NUREG/CP–0140
Vol. 2

Proceedings of the U.S. Nuclear Regulatory Commission

Twenty-Second Water Reactor Safety Information Meeting

Volume 2

– Severe Accident Research
– Thermal Hydraulic Research for Advanced Passive LWRs
– High–Burnup Fuel Behavior

Held at
Bethesda Marriott Hotel
Bethesda, Maryland
October 24–26, 1994

U.S. Nuclear Regulatory Commission

Office of Nuclear Regulatory Research

Proceedings prepared by
Brookhaven National Laboratory

AVAILABILITY NOTICE

Availability of Reference Materials Cited in NRC Publications

Most documents cited in NRC publications will be available from one of the following sources:

1. The NRC Public Document Room, 2120 L Street, NW., Lower Level, Washington, DC 20555-0001

2. The Superintendent of Documents, U.S. Government Printing Office, P. O. Box 37082, Washington, DC 20402-9328

3. The National Technical Information Service, Springfield, VA 22161-0002

Although the listing that follows represents the majority of documents cited in NRC publications, it is not intended to be exhaustive.

Referenced documents available for inspection and copying for a fee from the NRC Public Document Room include NRC correspondence and internal NRC memoranda; NRC bulletins, circulars, information notices, inspection and investigation notices; licensee event reports; vendor reports and correspondence; Commission papers; and applicant and licensee documents and correspondence.

The following documents in the NUREG series are available for purchase from the Government Printing Office: formal NRC staff and contractor reports, NRC-sponsored conference proceedings, international agreement reports, grantee reports, and NRC booklets and brochures. Also available are regulatory guides, NRC regulations in the *Code of Federal Regulations*, and *Nuclear Regulatory Commission Issuances*.

Documents available from the National Technical Information Service include NUREG-series reports and technical reports prepared by other Federal agencies and reports prepared by the Atomic Energy Commission, forerunner agency to the Nuclear Regulatory Commission.

Documents available from public and special technical libraries include all open literature items, such as books, journal articles, and transactions. *Federal Register* notices, Federal and State legislation, and congressional reports can usually be obtained from these libraries.

Documents such as theses, dissertations, foreign reports and translations, and non-NRC conference proceedings are available for purchase from the organization sponsoring the publication cited.

Single copies of NRC draft reports are available free, to the extent of supply, upon written request to the Office of Administration, Distribution and Mail Services Section, U.S. Nuclear Regulatory Commission, Washington, DC 20555-0001.

Copies of industry codes and standards used in a substantive manner in the NRC regulatory process are maintained at the NRC Library, Two White Flint North, 11545 Rockville Pike, Rockville, MD 20852-2738, for use by the public. Codes and standards are usually copyrighted and may be purchased from the originating organization or, if they are American National Standards, from the American National Standards Institute, 1430 Broadway, New York, NY 10018-3308.

DISCLAIMER NOTICE

NUREG/CP-0140
Vol. 2

Proceedings of the U.S. Nuclear Regulatory Commission

Twenty-Second Water Reactor Safety Information Meeting

Volume 2

- Severe Accident Research
- Thermal Hydraulic Research for Advanced Passive LWRs
- High–Burnup Fuel Behavior

Held at
Bethesda Marriott Hotel
Bethesda, Maryland
October 24–26, 1994

Manuscript Completed: March 1995
Date Published: April 1995

Compiled by: Susan Monteleone

Office of Nuclear Regulatory Research
U.S. Nuclear Regulatory Commission
Washington, DC 20555–0001

Proceedings prepared by
Brookhaven National Laboratory

ABSTRACT

This three-volume report contains papers presented at the Twenty-Second Water Reactor Safety Information Meeting held at the Bethesda Marriott Hotel, Bethesda, Maryland, during the week of October 24-26, 1994. The papers are printed in the order of their presentation in each session and describe progress and results of programs in nuclear safety research conducted in this country and abroad. Foreign participation in the meeting included papers presented by researchers from Finland, France, Italy, Japan, Russia, and United Kingdom. The titles of the papers and the names of the authors have been updated and may differ from those that appeared in the final program of the meeting.

PROCEEDINGS OF THE
22nd WATER REACTOR SAFETY INFORMATION MEETING

October 24-26, 1994

Published in Three Volumes

GENERAL INDEX

REGISTERED ATTENDEES (NON-NRC)
22ND WATER REACTOR SAFETY INFORMATION MEETING

H. ABE
NUCLEAR POWER ENGINEERING CORP.
3-13 4-CHOME TORANOMON
MINATO-KU TOKYO, 105 JAPAN

S. AHN
KOREA INSTITUTE OF NUCLEAR SAFETY
PO BOX 114
YUSUNG, TAEJON, 305-600 KOREA

R. ALLEN
BATTELLE PACIFIC NORTHWEST LABS
PO BOX 999, MS P8-10
RICHLAND, WA 99352 USA

R. AMADOR
COMISION NACIONAL DE SEGURIDAD NUC. Y SALVAGUARDIA
DR BARRAGAN NO 779, COL NARVARTE
MEXICO D.F., 03020 MEXICO

J. ANDREWS
B&W FUEL COMPANY
PO BOX 10935
LYNCHBURG, VA 24506-0935 USA

V. ASMOLOV
RUSSIAN RESEARCH CENTER KURCHATOV INST.
KURCHATOV SQUARE
MOSCOW, 123182 RUSSIA

T. BAKER
SHIFTWORK SYSTEMS, INC.
ONE KENDALL SQUARE, BLDG. 200, 4TH FLOOR
CAMBRIDGE, MA 02139 USA

A. BARATTA
PENN STATE UNIV., NUCLEAR ENGINEERING DEPT.
231 SACKETT BLDG.
UNIVERSITY PARK, PA 16802 USA

P. BAYLESS
IDAHO NATIONAL ENGINEERING LABORATORY
PO BOX 1625
IDAHO FALLS, ID 83415-3840 USA

S. BEUS
WESTINGHOUSE BETTIS
P.O. BOX 79
WEST MIFFLIN, PA 15122 USA

D. BHATTACHARYA
NUCLEAR POWER CORP. OF INDIA
BOMBAY, INDIA

S. ADDITON
TENERA (ARSAP)
1901 RESEARCH BLVD., SUITE 100
ROCKVILLE, MD 20850-3184 USA

M. ALAMMAR
GPU NUCLEAR CORP.
ONE UPPER POND RD.
PARSIPPANY, NJ 07054 USA

K. ALMENAS
UNIVERSITY OF MARYLAND
MAT. & NUC. ENERGY DEPT.
COLLEGE PARK, MD USA

L. ANDERMO
SWEDISH NUCLEAR POWER INSPECTORATE
BOX 27106
STOCKHOLM, S-102 52 SWEDEN

W. ANDREWS
SOUTHERN NUCLEAR OPERATING COMPANY
PO BOX 1295
BIRMINGHAM, AL 35201 USA

A. ASRANI
ATOMIC ENERGY REGULATORY BOARD
VIKRAM SARASHAI BHAVAN, ANUSHAKTI NAGAR
BOMBAY, 400 094 INDIA

M. BALE
B&W FUEL COMPANY
3315 OLD FOREST RD., PO BOX 10935
LYNCHBURG, VA 24506 USA

R. BARI
BROOKHAVEN NATIONAL LABORATORY
BLDG. 130, PO BOX 5000
UPTON, NY 11973 USA

L. BELBLIDIA
SCANDPOWER, INC.
101 LAKE FOREST BLVD., STE. 340
GAITHERSBURG, MD 20877 USA

C. BEYER
PACIFIC NORTHWEST LABORATORY
BATTELLE BLVD.
RICHLAND, WA 99352 USA

D. BLEY
BUTTONWOOD CONSULTING INC.
17291 BUTTONWOOD STREET
FOUNTAIN VALLEY, CA 92708 USA

A. AFZALI
NUS
910 CLOPPER ROAD
GAITHERSBURG, MD 20879 USA

A. ALEMBERTI
ANSALDO
C. 30 PERRONE 25
GENOVA, 16161 ITALY

A. ALONSO
POLYTECHNIC UNIVERSITY OF MADRID
JOSE GUTIERREZ ABASCAL, 2
MADRID, 28006 SPAIN

M. ANDOU
HITACHI WORKS, HITACHI LTD.
1-1, SAIWAI-CHO 3-CHOME
HITACHI-SHI, IBARAKI-KEN 317 JAPAN

S. ASAI
MINISTRY OF INT'L TRADE AND INDUSTRY
1-3-1, KASUMIGASAKI
CHIYODA-KU, TOKYO 100 JAPAN

M. AZARM
BROOKHAVEN NATIONAL LABORATORY
PO BOX 5000, BLDG. 130
UPTON, NY 11973-5000 USA

Y. BANG
KOREA INSTITUTE OF NUCLEAR SAFETY
PO BOX 114
YUSUNG, TAEJON, 305-600 KOREA

M. BARRIERE
BROOKHAVEN NATIONAL LABORATORY
PO BOX 5000, BLDG. 130
UPTON, NY 11973-5000 USA

K. BERGERON
SANDIA NATIONAL LABORATORIES
P.O. BOX 5800, MS 0743
ALBUQUERQUE, NM 87185-0743 USA

B. BHASIN
NUCLEAR POWER CORPORATION OF INDIA
TARAPUR ATOMIC POWER STATION
TARAPUR, MAHARASHTRA, INDIA

L. BOLSHOV
RUSSIAN ACADEMY OF SCIENCES/NUC. SAFETY INST.
B. TULSKAYA, 52
MOSCOW, 113191 RUSSIA

M. BONNER
BROOKHAVEN NATIONAL LABORATORY
BLDG. 197C, PO BOX 5000
UPTON, NY 11973-5000 USA

B. BOYACK
LOS ALAMOS NATIONAL LABORATORY
P.O. BOX 1663, MS K551
LOS ALAMOS, NM 87545 USA

R. BOYER
DUKE POWER CO.
8725 HORNWOOD CT.
CHARLOTTE, NC 28215 USA

G. BROWN
AEA TECHNOLOGY
THOMSON HOUSE, RISLEY
WARRINGTON, CHESHIRE WA36AT UK

W. BRUNSON
B&W FUEL COMPANY
PO BOX 10935
LYNCHBURG, VA 24506-0935 USA

R. BUDNITZ
FUTURE RESOURCES ASSOCIATES, INC.
2039 SHATTUCK AVE., SUITE 402
BERKELEY, CA 94704 USA

J. BUTLER
WESTINGHOUSE
P.O. BOX 355
PITTSBURGH, PA 15230 USA

C. CALLAWAY
NUCLEAR ENERGY INSTITUTE - NEI
1776 I ST., N.W., SUITE 400
WASHINGTON, DC 20006-3708 USA

A. CAMP
SANDIA NATIONAL LABORATORIES
PO BOX 5800
ALBUQUERQUE, NM 87185-0747 USA

G. CANAVAN
NEW YORK POWER AUTHORITY
123 MAIN ST.
WHITE PLAINS, NY 10601 USA

F. CARLIN
CIS BIO INTERNATIONAL
BP NO. 32
GIF-SUR-YVETTE CEDEX, F91192 FRANCE

D. CASADA
OAK RIDGE NATIONAL LABORATORY
PO BOX 2009, BLDG. 9102-1
OAK RIDGE, TN 37831-8038 USA

N. CAVLINA
UNIVERSITY OF ZAGREB
FACULTY OF ELEC. ENGINEERING, UNSKA 3
ZAGREB, CRO 41000 CROATIA

D. CHAPIN
MPR ASSOCIATES, INC.
320 KING ST.
ALEXANDRIA, VA 22314-3238 USA

F-B. CHEUNG
PENNSYLVANIA STATE UNIVERSITY
304 REBER BLDG., PENN STATE U.
UNIVERSITY PARK, PA 16802 USA

B. CHO
ILLINOIS DEPARTMENT OF NUCLEAR SAFETY
1035 OUTER PARK DRIVE
SPRINGFIELD, IL 62704 USA

D. CHO
ARGONNE NATIONAL LABORATORY
BLDG. 208, 9700 S. CASS AVE.
ARGONNE, IL 60439 USA

J. CHOI
KOREA INSTITUTE OF NUCLEAR SAFETY
151 DUKJIN-DONG YUSEONG-GU
TAEJON, KOREA, KOREA

S. CHOI
KOREA INSTITUTE OF NUCLEAR SAFETY
PO BOX 114
YUSUNG, TAEJON, 305-600 KOREA

A. CHRISTOU
MATERIALS & NUCLEAR ENG'G., U. OF MARYLAND
2135 BLDG. 090
COLLEGE PARK, MD 20742-2115 USA

T-L. CHU
BROOKHAVEN NATIONAL LABORATORY
BLDG. 130, P.O. BOX 5000
UPTON, NY 11973-5000 USA

T. CHU
SANDIA NATIONAL LABORATORIES
MS 1137, DEPT. 6422
ALBUQUERQUE, NM 87185 USA

N. CHUGO
TOSHIBA CORP.
8, SHINSUGITA-CHO, ISOGO-KU
YOKOHAMA, 235 JAPAN

A. COMBESCURE
CENTRE D'ETUDES DE SACLAY - DRN/DMT/SEMT
CENTRE D'ETUDES DE SACLAY
GIF SUR YVETTE CEDEX, 91191 FRANCE

L. COMES
SCIENCE & ENGINEERING ASSOCIATES, INC.
7918 JONES BRANCH DR., SUITE 500
MC LEAN, VA 22102 USA

L. CONNOR
SOUTHERN TECHNICAL SERVICES, INC.
3 METRO CENTER, SUITE 610
BETHESDA, MD 20814 USA

S. COOPER
SCIENCE APPLICATIONS INT'L. CORP.
11251 ROGER BACON DR., PO BOX 4875
RESTON, VA 22090 USA

R. COPELAND
SIEMENS POWER CORP.
2101 HORN RAPIDS RD.
RICHLAND, WA 99352 USA

B. CORWIN
OAK RIDGE NATIONAL LABORATORY
P.O. BOX 2008
OAK RIDGE, TN 37831-6151 USA

M. COURTAUD
COMMISSARIAT A L'ENERGIE ATOMIQUE
CENTRE D'ETUDES DE GRENOBLE 17, RUE DES MARTYRS
GRENOBLE, 38054 FRANCE

K. COZENS
NUCLEAR ENERGY INSTITUTE - NEI
1776 I ST., N.W., SUITE 400
WASHINGTON, DC 20006-3708 USA

M. CUNNINGHAM
PACIFIC NORTHWEST LABORATORY
PO BOX 999 K8-43
RICHLAND, WA 99352 USA

R. CURTIS
AECL RESEARCH
WHITESHELL LABORATORIES
PINAWA, MB ROE 1LO CANADA

V. DAJI
DUKE POWER COMPANY
9515 PONDSIDE LANE
CHARLOTTE, NC 28213 USA

R. DALLMAN
SCIENTECH, INC.
1700 LOUISIANA BLVD., NE STE. 230
ALBUQUERQUE, NM 87110 USA

J. DANKO
CONSULTANT - UNIVERSITY OF TENNESSEE
15818 SE 35TH ST
VANCOUVER, WA 98684 USA

J. DAVIS
NUCLEAR ENERGY INSTITUTE - NEI
1776 I ST., N.W., SUITE 400
WASHINGTON, DC 20006-3708 USA

B. DE BOECK
AIB-VINCOTTE NUCLEAIR
AVENUE DU ROI, 157
BRUSSELS, B-1060 BELGIUM

J. DE BOR
SCIENCE & ENGINEERING ASSOCIATES, INC.
7918 JONES BRANCH DR., SUITE 500
MC LEAN, VA 22102 USA

L. DEITRICH
ARGONNE NATIONAL LABORATORY
9700 SO. CASS AVE., BLDG. 208
ARGONNE, IL 60439 USA

D. DIAMOND
BROOKHAVEN NATIONAL LABORATORY
BLDG. 130, PO BOX 5000
UPTON, NY 11973-5000 USA

H. DIAMOND
PELCO ENERGY
965 CHESTERBROOK BLVD.
WAYNE, PA 19087 USA

H. DIETERSHAGEN
KNOLLS ATOMIC POWER LAB., INC. - MARTIN MARIETTA
RIVER ROAD - PO BOX 1072
SCHENECTADY, NY 12301-1072 USA

S. DOROFEEV
KURCHATOV INSTITUTE
KURCHATOV SQUARE 1
MOSCOW, RUSSIA, 123182 RUSSIA

R. DUBOURG
CEA-IPSN DES/SEPRI
BP 6
FONTENAY AUX ROSES, 92265 FRANCE

J. DUCO
INSTITUT DE PROTECTION ET DE SURETE NUCLEAIR
CEA, CEN/FAR 60-68 AVE. DU GENERAL LECLERC
FONTENAY AUX ROSES, 92265 FRANCE

R. DUFFEY
BROOKHAVEN NATIONAL LABORATORY
PO BOX 5000, BLDG. 197C
UPTON, NY 11973-5000 USA

J. EATON
NUCLEAR ENERGY INSTITUTE - NEI
1776 I ST., N.W., SUITE 400
WASHINGTON, DC 20006-3708 USA

R. EBERLE
SIEMENS-KWU
HAMMERBACHERSTRASSE 12+14
ERLANGEN, D-8520 GERMANY

M. ELI
LAWRENCE LIVERMORE NATIONAL LAB.
PO BOX 808, L-126
LIVERMORE, CA 94550 USA

F. ELIA
STONE AND WEBSTER ENG. CORP.
PO BOX 2325
BOSTON, MA 02107 USA

T. ENDO
NUCLEAR POWER ENGINEERING CORP.
FUJITA KANKO TORANOMON BLDG. 5F 17-1, 3-CHOME, TORA
MINATO-KU, TOKYO 105 JAPAN

R. ENNIS
TENERA
1901 RESEARCH BLVD., SUITE 100
ROCKVILLE, MD 20850 USA

T. EURASTO
FINNISH CENTRE FOR RADIATION & NUCLEAR SAFETY
PO BOX 14, FIN-00881
HELSINKI, FINLAND

M. FAKORY
S3 TECHNOLOGIES
8930 STAMFORD BLVD.
COLUMBIA, MD 21045 USA

D. FERETIC
UNIVERSITY OF ZAGREB
FACULTY OF ELEC. ENGINEERING, UNSKA 3
ZAGREB, CRO 41000 CROATIA

F. FERON
DIRECTION DE LA SURETE DES INSTALLATIONS NUCLEAIRES
20 AVENUE DE SEGUR
PARIS CEDEX 07 SP, 75353 FRANCE

A. FERRELI
DIR. FOR NUCLEAR SAFETY & HEALTH PROTECTION
VIA VITALIANO BRANCATI 48
ROME, 00186 ITALY

L. FIERO
ABB COMBUSTION ENGINEERING NUCLEAR FUEL
1000 PROSPECT HILL RD.
WINDSOR, CT 06095-0500 USA

M. FIRNHABER
GRS
SCHWERTNERGASSE 1
COLOGNE, 50667 GERMANY

J. FISHER
UTILITY RESOURCE ASSOCIATES, INC.
51 MONROE ST., SUITE 12000
ROCKVILLE, MD 20850 USA

M. FLETCHER
AECL TECHNOLOGIES INC.
9210 CORPORATE BLVD., SUITE 410
ROCKVILLE, MD 20850 USA

J. FOLSOM
GPU NUCLEAR CORP.
ONE UPPER POND RD.
PARSIPPANY, NJ 07054 USA

J. FORESTER
SANDIA NATIONAL LABORATORIES
DEPT. 6412
ALBUQUERQUE, NM 87185 USA

T. FUJISHIRO
JAPAN ATOMIC ENERGY RESEARCH INSTITUTE
TOKAI-MURA, NAKA-GUN
IBARAKI-KEN 319-11, JAPAN

A. FUKUDA
TOSHIBA CORP., ISOGO NUCLEAR ENGINEERING
8 SHINSUGITA-CHO, ISOGO-KU
YOKOHAMA, KANAGAWA 235 JAPAN

R. GAMBLE
GE NUCLEAR ENERGY
175 CURTNER AVE, M.C. 781
SAN JOSE, CA 95125 USA

R. GAUNTT
SANDIA NATIONAL LABORATORIES
PO BOX 5800, M.S. 1139
ALBUQUERQUE, NM 87185-1139 USA

J. GAUTHIER
COMMISSARIAT A L'ENERGIE ATOMIQUE
CE/FAR BP 6
FONTENAY AUX ROSES, 92265 FRANCE

S. GIBELLI
BROOKHAVEN NATIONAL LABORATORY
PO BOX 5000, BLDG. 130
UPTON, NY 11973-5000 USA

C. GIGGER
BETTIS
P.O. BOX 79
WEST MIFFLIN, PA 15122 USA

R. GILLILAND
OAK RIDGE NATIONAL LABORATORY
P.O. BOX 2009, MS 8051
OAK RIDGE, TN 37831-8051 USA

T. GINSBERG
BROOKHAVEN NATIONAL LABORATORY
PO BOX 5000, BLDG. 197D
UPTON, NY 11973-5000 USA

L. GOLDSTEIN
S.M. STOLLER CORP.
485 WASHINGTON AVE.
PLEASANTVILLE, NY 10570 USA

M. GOMOLINSKI
IPSN
321 RUE DE CHARENTON
PARIS, F 75012 FRANCE

A. GOPALAKRISHNAN
ATOMIC ENERGY REGULATORY BOARD
VIKRAM SARASHAI BHAVAN, ANUSHAKTI NAGAR
BOMBAY, 400 094 INDIA

M. GOTO
TOSHIBA CORP., ISOGO NUCLEAR ENGINEERING
8 SHINSUGITA-CHO, ISOGO-KU
YOKOHAMA, KANAGAWA 235 JAPAN

N. GOULDING
B&W NUCLEAR TECHNOLOGIES
PO BOX 10935
LYNCHBURG, VA 24506-0935 USA

M. GRANDAME
ATOMIC ENERGY CONTROL BOARD CANADA
C/O ONTARIO HYDRO, P.O. BOX 160
PICKERING, ONTARIO L1V2r5 CANADA

J. GREEN
UNIVERSITY OF MARYLAND
NUCLEAR ENG'G, 2135 BLDG. 080
COLLEGE PARK, MD 20742 USA

L. GROSSMAN
ABB COMBUSTION ENGINEERING
ADDISON ROAD
WINDSOR, CT 06095 USA

M. GROUNES
STUDSVIK NUCLEAR
S-61182 NYKOPING
NYKOPING, S-61182 SWEDEN

S. HABER
BROOKHAVEN NATIONAL LABORATORY
BLDG. 130, PO BOX 5000
UPTON, NY 11973-5000 USA

G. HACHE
INSTITUT DE PROTECTION ET DE SURETE NUCLEAIRE
CE CADARACHE BAT. 702
ST. PAUL LEZ DURANCE, 13108 FRANCE

R. HALL
BROOKHAVEN NATIONAL LABORATORY
BLDG. 130, PO BOX 5000
UPTON, NY 11973-5000 USA

L. HARROP
NUCLEAR INSTALLATIONS INSPECTORATE
ST. PETER'S HOUSE, BALLIOL RD
BOOTLE, MERSEYSIDE, L20 3LZ UK

E. HARVEGO
IDAHO NATIONAL ENGINEERING LABORATORY
PO BOX 1625
IDAHO FALLS, ID 83415 USA

C. HARWOOD
ATOMIC ENERGY CONTROL BOARD, CANADA
PO BOX 1046 STATION B, 280 SLATER ST.
OTTAWA, ONTARIO K1P 5S9 CANADA

H. HASHEMIAN
ANALYSIS & MEASUREMENT SERVICES CORP.
9111 CROSS PARK DR., NW
KNOXVILLE, TN 37923-4599 USA

M. HASSAN
BROOKHAVEN NATIONAL LABORATORY
PO BOX 5000, BLDG. 130
UPTON, NY 11973-5000 USA

H. HAYDEN
OAK RIDGE NATIONAL LABORATORY
P.O. BOX 2008, BLDG. 4500S
OAK RIDGE, TN 37831-8152 USA

J. HENRY
INSTITUT DE PROTECTION ET DE SURETE NUCLEAIRE
BP6
FONTENAY AUX ROSES, 92265 FRANCE

A. HEYMER
NUCLEAR ENERGY INSTITUTE - NEI
1776 I ST., N.W., SUITE 400
WASHINGTON, DC 20006-3708 USA

D. HIDINGER
MARTIN MARIETTA CORP. (KAPL, INC.)
PO BOX 1072
SCHENECTADY, NY 12302 USA

J. HIGGINS
BROOKHAVEN NATIONAL LABORATORY
BLDG. 130, PO BOX 5000
UPTON, NY 11973-5000 USA

A. HO
SIEMENS POWER CORP., NUCLEAR DIV.
PO BOX 130
RICHLAND, WA 99352 USA

R. HOBBINS
RRH CONSULTING
PO BOX 971
WILSON, WY 83014 USA

L. HOCHREITER
WESTINGHOUSE ELECTRIC COMPANY
P.O. BOX 355
PITTSBURGH, PA 15230 USA

S. HODGE
OAK RIDGE NATIONAL LABORATORY
PO BOX 2009 9104-1, MS 8057
OAK RIDGE, TN 37831-8057 USA

P. HOFMANN
NUCLEAR RESEARCH CENTER KARLSRUHE
PO BOX 3640
KARLSRUHE, D-76021 GERMANY

J. HOHORST
IDAHO NATIONAL ENGINEERING LABORATORY
PO BOX 1625
IDAHO FALLS, ID 83415 USA

H. HOLMSTROM
VTT ENERGY, NUCLEAR ENERGY
PO BOX 1604
ESPOO, 02044 VTT FINLAND

R. HOUSER
BETTIS ATOMIC POWER LABORATORY
173 MONTICELLO DR.
MONROEVILLE, PA 15146 USA

A. HOWARD
TOKYO ELECTRIC POWER CO
1901 L ST., NW
WASHINGTON, DC 20036 USA

T. HSU
VIRGINIA POWER
5000 DOMINION BLVD.
GLEN ALLEN, VA 23060 USA

H-Y HUANG
ATOMIC ENERGY COUNCIL, REP. OF CHINA
67 LANE 144, KEELUNG RD., SEC. 4
TAIPEI, TAIWAN ROC

S. HYTEN
WYLE LABORATORIES
PO BOX 077777
HUNTSVILLE, AL 35807-7777 USA

Y. IBE
NUCLEAR POWER ENGINEERING CORP.
3-13 4-CHOME TORANOMON
MINATO-KU TOKYO, 105 JAPAN

R. IRWIN
UNION ELECTRIC CO.
PO BOX 149, MC 470
ST. LOUIS, MO 63166 USA

H. ISBIN
NSRRC
2815 MONTEREY PKWY
MINNEAPOLIS, MN 55416-3959 USA

M. ISHII
PURDUE UNIVERSITY
SCHOOL OF NUCLEAR ENGINEERING
WEST LAFAYETTE, IN 47907 USA

J. JANSKY
BTB JANSKY GMBH
GERLINGER STR. 151
LEONBERG, 71229 GERMANY

T. JAYAKUMAR
INDIRA GANDHI CENTRE FOR ATOMIC RESEARCH
KALPAKKAM, INDIA

M. JIMINEZ
FLORIDA POWER & LIGHT
700 UNIVERSITY BLVD.
JUNO BEACH, FL 33407 USA

Y. JIN
KOREA ATOMIC ENERGY RESEARCH INST.
PO BOX 105, YUSEONG
TAEJON, 305-353 KOREA

J. JO
BROOKHAVEN NATIONAL LABORATORY
BLDG. 130, P.O. BOX 5000
UPTON, NY 11973-5000 USA

G. JOHNSEN
IDAHO NATIONAL ENGINEERING LAB
PO BOX 1625
IDAHO FALLS, ID 83415-3880 USA

R. JOHNSON
PACIFIC GAS & ELECTRIC CO.
333 MARKET ST., RM. 1061
SAN FRANCISCO, CA 94177 USA

A. KAKODKAR
BHABHA ATOMIC RESEARCH CENTRE
REACTOR DESIGN & DEV. GROUP
TROMBAY, INDIA

F. KAM
OAK RIDGE NATIONAL LABORATORY
PO BOX 2009
OAK RIDGE, TN 37831-8250 USA

S-P KAO
SIMULATION EXPERT SYSTEMS
23 HARBOR CLOSE
NEW HAVEN, CT 06519 USA

Y. KARINO
TOSHIBA CORP. (GE NUCLEAR ENERGY)
970 ST. ANDREWS DR., APT. 102
WILMINGTON, NC 28412 USA

H. KARWAT
TECHNISCHE UNIVERSITAT MUNCHEN
FORSCHUNGSGELANDE, D-85748 GARCHING
GARCHING, GARCHING D-85748 GERMANY

H. KASHIMA
MITSUBISHI HEAVY INDUSTRIES, LTD.
3-1, MINATOMIRAI 3CHOME, NISHI-KU
YOKOHAMA, 220 JAPAN

T. KATSUSHIGE
JAPAN POWER ENG'G & INSPECTION CORP.
SHIN-URAYASU BLDG., 9-2, MIHAMA 1 CHOME
URAYASU-SHI, CHIBA-KEN, 279 JAPAN

J. KAVANAGH
ATOMIC ENERGY CONTROL BOARD
280 SLATER ST
OTTAWA, ONTARIO K1P 5S9 CANADA

J. KELLY
SANDIA NATIONAL LABORATORIES
PO BOX 5800, MS 0742
ALBUQUERQUE, NM 87185-0742 USA

S. KERCEL
OAK RIDGE NATIONAL LABORATORY
PO BOX 2008, BLDG. 3508/MS 6318
OAK RIDGE, TN 37831-6318 USA

R. KERN
NETCORP
9 BANNISTER CT.
GAITHERSBURG, MD 20879 USA

B. KIM
KOREA INSTITUTE OF NUCLEAR SAFETY
PO BOX 114
YUSUNG, TAEJON, 305-600 KOREA

H. KIM
KOREA INSTITUTE OF NUCLEAR SAFETY
PO BOX 114
YUSUNG, TAEJON, 305-600 KOREA

I. KIM
BROOKHAVEN NATIONAL LABORATORY
BLDG. 130, PO BOX 5000
UPTON, NY 11973-5000 USA

I. KIM
KOREA ATOMIC ENERGY RESEARCH INSTITUTE
PO BOX 105, YUSEONG
TAEJON, 305-600 KOREA

K. KIM
KOREA INSTITUTE OF NUCLEAR SAFETY
151 DUKJIN-DONG YUSEONG-GU
TAEJON, KOREA, KOREA

S. KIM
KOREA INSTITUTE OF NUCLEAR SAFETY
PO BOX 114
YUSUNG, TAEJON, 305-600 KOREA

W. KIM
KOREA INSTITUTE OF NUCLEAR SAFETY
PO BOX 114
YUSUNG, TAEJON, 305-600 KOREA

S. KINNERSLY
AEA TECHNOLOGY
WINFRITH TECHNOLOGY CENTRE
DORCHESTER, DORSET DT2 8DH UK

J. KLAPPROTH
GE NUCLEAR
PO BOX 780, MC J26
WILMINGTON, NC 28402 USA

P. KLOEG
KEMA
UTRECHTSEWEG 310
ARNHEM, 6812 AR NETHERLANDS

Y. KOBAYASHI
NUCLEAR POWER ENGINEERING CORP.
FUJITA KANKO TORANOMON BLDG. 5F 17-1, 3-CHOME, TORA
MINATO-KU, TOKYO 105 JAPAN

K. KORSAH
OAK RIDGE NATIONAL LABORATORY
PO BOX 2008, BLDG. 3500, MS 6010
OAK RIDGE, TN 37831 USA

M. KOYAMA
JAPAN POWER ENG'G & INSPECTION CORP.
SHIN-URAYASU BLDG., 9-2, MINAMA 1 CHOME
URAYASU-SHI, CHIBA-KEN, 279 JAPAN

P. KRISHNASWAMY
BATTELLE PACIFIC NORTHWEST LABORATORY
505 KING AVE.
COLUMBUS, OH 43201 USA

B. KUCZERA
KERNFORSCHUNGSZENTRUM NUC. RESEARCH CENTER
PO BOX 3640
KARLSRUHE, D76021 GERMANY

Y. KUKITA
JAPAN ATOMIC ENERGY RESEARCH INSTITUTE
TOKAI, IBARAKI, IBARAKI 319-11 JAPAN

K. KUSSMAUL
MPA STUTTGART
PFAFFENWALDRING 32
STUTTGART, 70569 GERMANY

P. LACY
URA
51 MONROE STREET, SUITE 1600
ROCKVILLE, MD 20850 USA

J. LAKE
IDAHO NATIONAL ENGINEERING LABORATORY
PO BOX 1625
IDAHO FALLS, ID 83415-3895 USA

D. LAMPE
UTILITY RESOURCE ASSOCIATES, INC.
51 MONROE ST., SUITE 1600
ROCKVILLE, MD 20814 USA

P. LANG
U.S. DEPT. OF ENERGY
NE-451
WASHINGTON, DC 20585 USA

S. LANGENBUCH
GESELLSCHAFT FUR ANLAGEN U. REAKTORSICHERHEIT
FORSCHUNGSGELANDE
GARCHING, 85748 GERMANY

V. LANGMAN
ONTARIO HYDRO
700 UNIVERSITY AVE.
TORONTO, ONT M5G1X6 CANADA

D. LANNING
BATTELLE PACIFIC NORTHWEST LAB.
809 W. 22ND AVE.
KENNEWISK, WA 99337 USA

E. LANNING
NEBRASKA PUBLIC POWER DISTRICT
PO BOX 499
COLUMBUS, NE 68602-0499 USA

E. LANNING
NEBRASKA PUBLIC POWER DISTRICT
P.O. BOX 499
COLUMBUS, NE 68602-0499 USA

C. LECOMTE
INSTITUT DE PROTECTION ET DE SURETE NUCLEAIR
CEA, CEN/FAR 60-68 AVE. DU GENERAL LECLERC
FONTENAY AUX ROSES, 92265 FRANCE

C. LEE
KOREA ATOMIC ENERGY RESEARCH INSTITUTE
PO BOX 105, YUSONG
TAEJON, 305-606 KOREA

D. LEE
KOREA ELECTRIC POWER CORPORATION
103-16 MUNJI-DONG, YUSEONG-KU
TAEJEON, KOREA

J. LEE
KOREA INSTITUTE OF NUCLEAR SAFETY
P.O. BOX 114, YUSONG
TAEJON, KOREA, 305-600 KOREA

S. LEE
KOREA ATOMIC ENERGY RESEARCH INST.
PO BOX 105, YUSONG
TAEJON, 305-353 KOREA

J. LEHNER
BROOKHAVEN NATIONAL LABORATORY
PO BOX 5000, BLDG. 130
UPTON, NY 11973-5000 USA

M. LIVOLANT
INSTITUT DE PROTECTION ET DE SURETE NUCLEAIRE
CE/FAR BP M 6
FONTENAY-AUX-ROSES CEDEX, 92265 FRANCE

R. LOFARO
BROOKHAVEN NATIONAL LABORATORY
BLDG. 130, PO BOX 5000
UPTON, NY 11973-5000 USA

F. LOSS
MEA
9700-B M.L. KING JR. HWY.
LANHAM, MD 20706 USA

S. LU
LAWRENCE LIVERMORE NATIONAL LAB.
7000 EAST AVE.
LIVERMORE, CA 94550 USA

W. LUCKAS
BROOKHAVEN NATIONAL LABORATORY
PO BOX 5000, BLDG. 130
UPTON, NY 11973-5000 USA

L. MADNI
BROOKHAVEN NATIONAL LABORATORY
PO BOX 5000, BLDG. 130
UPTON, NY 11973-5000 USA

D. MAGALLON
CED-JRD ISPRA
JRC-EURATOM
ISPRA, VARESE 21020 ITALY

C. MANUEL
CEA-IPSN DES/SEPRI
BP 6
FONTENAY AUX ROSES, 92265 FRANCE

J. MARCON
FRAMATOME NUCLEAR FUEL
10, RUE JULIETTE RECAMIER
LYON, 69456 FRANCE

Y. MARUYAMA
JAPAN ATOMIC ENERGY RESEARCH INSTITUTE
2-4 SHIRANE, SHIRAKATA
NAKA-GUN, IBARAKI-KEN, 319-11 JAPAN

S. MASAMORI
MITSUBISHI HEAVY INDUSTRIES, LTD.
1-1-1 WADASAKI-CHO, HYOGO-KU
KOBE, 654 JAPAN

M. MASSOUD
BALTIMORE GAS & ELECTRIC
CALVERT CLIFFS NUCLEAR PLANT
LUSBY, MD 20657 USA

B. MAYKO
J. STEFAN INSTITUTE
JAMOVA 39
LJUBLJANA, SLOV. 61111 SLOVENIA

R. McCARDELL
EG&G IDAHO, INC.
167 NORTH 4200 EAST
RIGBY, ID 83442 USA

D. McCULLOUGH
KAPL, INC., MARTIN MARIETTA
RIVER ROAD
SCHENECTADY, NY 12301 USA

K. McDONOUGH
KNOLLS ATOMIC POWER LAB., INC. - MARTIN MARIETTA
RIVER ROAD - PO BOX 1072
SCHENECTADY, NY USA

T. McINTYRE
GE NUCLEAR ENERGY
175 CURTNER AVE, M.C. 781
SAN JOSE, CA 95125 USA

R. McMILLAN
AEA TECHNOLOGY
THOMSON HOUSE, RISLEY
WARRINGTON, CHESHIRE WA36AT UK

K. McMINN
AEA TECNOLOGY
WINFRITH TECHNOLOGY CENTER, DORCHESTER
DORSET, DT28DH UK

C. MEDICH
SOCIETA INFORMAZIONI EXPERIENZE TERMOIDRAULICHE
VIA N. BIXIO 27
PIACENZA, 29100 ITALY

N. MESHKATI
UNIVERSITY OF SOUTHERN CALIFORNIA
INST. OF SAFETY & SYSTEMS MGT, USC
LOS ANGELES, CA 90089-0021 USA

G. MEYER
B&W FUEL COMPANY
PO BOX 10935
LYNCHBURG, VA 24506-0935 USA

A. MEYER-HEINE
INSTITUT DE PROTECTION ET DE SURETE NUCLEAIRE
CE CADARACHE BAT. 702
ST. PAUL LEZ DURANCE, 13108 FRANCE

A. MIAO
CHARLES RIVER ANALYTICS, INC.
55 WHEELER ST.
CAMBRIDGE, MA 02138 USA

M. MILLER
DUKE POWER COMPANY
PO BOX 1439, MS ON01ES
SENECA, SC 29679 USA

R. MILLER
WESTINGHOUSE ELECTRIC CORP.
4350 NORTHERN PIKE WEC W 316
MONROEVILLE, PA 15146-2886 USA

S. MIRSKY
SCIENCE APPLICATIONS INT'L. CORP.
20201 CENTURY BLVD.
GERMANTOWN, MD 20874 USA

D. MITCHELL
B&W FUEL COMPANY
PO BOX 10935
LYNCHBURG, VA 24506-0935 USA

D. MODEEN
NUCLEAR ENERGY INSTITUTE - NEI
1776 I ST., N.W., SUITE 400
WASHINGTON, DC 20006-3708 USA

S. MODRO
INEL LOCKHEED IDAHO TECHNOLOGIES CO.
PO BOX 1625, MS 3890
IDAHO FALLS, ID 83415-3890 USA

D. MONHARDT
FRAMATOME
1 PLACE DE LA COUPOLE
COURBEVOIE, 92400 FRANCE

S. MONTELEONE
BROOKHAVEN NATIONAL LABORATORY
BLDG. 130, PO BOX 5000
UPTON, NY 11973-5000 USA

F. MOODY
GE NUCLEAR ENERGY
175 CURTNER AVE, M.C. 781
SAN JOSE, CA 95125 USA

D. MORRISON
THE MITRE CORPORATION
7525 COLSHIRE DR., MS W788
MCLEAN, VA 22102 USA

A. MOTTA
PENN STATE UNIV., NUCLEAR ENGINEERING DEPT.
231 SACKETT BLDG.
UNIVERSITY PARK, PA 16802 USA

K. MURAYAMA
HITACHI LTD.
1-1, SAIWAI-CHO 3-CHOME, HITACHI-SHI, IBARAKI-KEN
HITACHI-SHI, JAPAN

T. NAGAO
NUCLEAR POWER ENGINEERING CORP.
17-1, 3-CHOME TORANOMON
TOKYO, 105 JAPAN

D. NAUS
OAK RIDGE NATIONAL LABORATORY
PO BOX 2009, BLDG. 9204-1
OAK RIDGW, TN 37831-8058 USA

R. NG
NUCLEAR ENERGY INSTITUTE - NEI
1776 I ST., N.W., SUITE 400
WASHINGTON, DC 20006-3708 USA

M-S NI
ATOMIC ENERGY COUNCIL, REP. OF CHINA
67 LANE 144, KEELUNG RD., SEC. 4
TAIPEI, TAIWAN ROC

G. NIEDERAUER
LOS ALAMOS NATIONAL LABORATORY
M.S. K575
LOS ALAMOS, NM 87545 USA

L. NILSSON
STUDSVIK ECO & SAFETY AB
S-61182 NYKOPING
NYKOPING, S-61182 SWEDEN

S. NOWLEN
SANDIA NATIONAL LABORATORIES
MS0737, PO BOX 5800
ALBUQUERQUE, NM 87185 USA

A. NUNEZ
COMISION NACIONAL DE SEGURIDAD NUC. Y SALVAGUARDIA
DR BARRAGAN NO 779, COL NARVARTE
MEXICO D.F., 03020 MEXICO

N. ORTIZ
SANDIA NATIONAL LABORATORIES
PO BOX 5800, MS 0736
ALBUQUERQUE, NM 87185-0738 USA

D. OSETEK
LOS ALAMOS TECHNICAL ASSOCIATES
BLDG. 1, SUITE 400, 2400 LOUISIANA BLVD. NE
ALBUQUERQUE, NM 87110 USA

L. OSTROM
IDAHO NATIONAL ENGINEERING LABORATORY
P.O. BOX 1625
IDAHO FALLS, ID 83415-3855 USA

O. OZER
ELECTRIC POWER RESEARCH INSTITUTE
3412 HILLVIEW AVE.
PALO ALTO, CA 94304-1395 USA

B. PALAGI
COM ED COMPANY
P.O. BOX 767
CHICAGO, IL 60601 USA

J. PAPIN
INSTITUT DE PROTECTION ET DE SURETE NUCLEAIRE
CE CADARACHE BAT. 702
ST. PAUL LEZ DURANCE, 13108 FRANCE

B. PARK
KOREA NUCLEAR FUEL COMPANY
DAEJEON, 300 KOREA

Y. PARK
BROOKHAVEN NATIONAL LABORATORY
PO BOX 5000, BLDG. 475C
UPTON, NY 11973-5000 USA

M. PARKER
ILLINOIS DEPARTMENT OF NUCLEAR SAFETY
1035 OUTER PARK DRIVE
SPRINGFIELD, IL 62704 USA

J. PATE
OAK RIDGE NATIONAL LABORATORY
PO BOX 2008
OAK RIDGE, TN 37831-6158 USA

J. PELTIER
COMMISSARIAT A L'ENERGIE ATOMIQUE
BP 6
FONTENAY-AUX-ROSES-CEDEX, 92265 FRANCE

W. PENNELL
AMERICAN SOCIETY OF MECHANICAL ENGINEERS
PO BOX 2009, BLDG. 9204-1, MS-8058
OAK RIDGE, TN 37831-8058 USA

P. PERMEZEL
ELECT. DE FRANCE, SER. ETUDES ET PROJETS THERMIQUES
12-14 AV. DUTRIEVOZ
VILLEURBANNE, LYON 69628 FRANCE

M. PETRASKE
ABB COMBUSTION ENGINEERING
1000 PROSPECT HILL RD.
WINDSOR, CT 06095 USA

M. PEZZILLI
VIA ANGUILLARESE 301
S. MARIA DI GALERIA
ROMA, 00 ITALY

H. PFEFFERLEN
GENERAL ELECTRIC
175 CURTNER AVE, M.C. 781
SAN JOSE, CA 95125 USA

T. PIETRANGELO
NUCLEAR ENERGY INSTITUTE - NEI
1776 I ST., N.W., SUITE 400
WASHINGTON, DC 20006-3708 USA

B. PIKUL
THE MITRE CORPORATION
7525 COLSHIRE DR.
MC LEAN, VA 22102 USA

E. PILAT
YANKEE ATOMIC
580 MAIN ST.
BOLTON, MA 01740 USA

M. PILCH
SANDIA NATIONAL LABORATORIES
PO BOX 5800
ALBUQUERQUE, NM 87185-1137 USA

E. PIPLICA
WESTINGHOUSE
P.O. BOX 355
PITTSBURGH, PA 15230 USA

M. PODOWSKI
RPI
DEPT. OF NUCL. ENG. & ENG. PHYSICS
TROY, NY 12180 USA

S. POPE
SCIENTECH, INC.
11140 ROCKVILLE PIKE
ROCKVILLE, MD 20852 USA

G. POTTS
GE NUCLEAR
PO BOX 780, MC K05
WILMINGTON, NC 28402 USA

R. PRAKASH
EMBASSY OF INDIA
WASHINGTON, DC USA

W. PRATT
BROOKHAVEN NATIONAL LABORATORY
BUILDING 130
UPTON, NY 11973 USA

R. PROEBSTLE
GE NUCLEAR
PO BOX 780, MC A01
WILMINGTON, NC 28402 USA

V. PROKLOV
RRC KURCHATOV INSTITUTE
KURCHATOV SQUARE 1
MOSCOW, RUSSIA, 123182 RUSSIA

J. PUGA
UNESA
FRANCISCO GERVAS 3
MADRID, 28020 SPAIN

C. PUGH
OAK RIDGE NATIONAL LABORATORY
P.O. BOX 2009, MS 8063
OAK RIDGE, TN 37831 USA

T. RAJALA
ABB ATOM
FINNSLATTEN
VASTERAS, SWEDEN

D. RAPP
WESTINGHOUSE BETTIS LAB
P.O. BOX 79
WEST MIFFLIN, PA 15102 USA

J. RASHID
ANATECH RESEARCH CORP.
5435 OBERLIN DR.
SAN DIEGO, CA 92037 USA

S. RAY
WESTINGHOUSE ELECTRIC CORP.
PO BOX 355
PITTSBURGH, PA 15230 USA

K. REIL
SANDIA NATIONAL LABORATORIES
PO BOX 5800, M.S. 1139
ALBUQUERQUE, NM 87185-1139 USA

W. RETTIG
U.S. DOE, IDAHO OFFICE
850 ENERGY DRIVE
IDAHO FALLS, ID 83402 USA

J. RHODE
HEAD, SEVERE ACCIDENTS DEPT., GRS
SCHWERTNERGASSE 1
COLOGNE, 50667 GERMANY

L. RIB
AECL TECHNOLOGIES INC.
9210 CORPORATE BLVD., SUITE 410
ROCKVILLE, MD 20850 USA

A. RODRIGUEZ
COMISION NACIONAL DE SEGURIDAD NUC.Y SALVAGUARDIA
DR BARRAGAN NO 779, COL NARVARTE
MEXICO D.F., 03020 MEXICO

U. ROHATGI
BROOKHAVEN NATIONAL LABORATORY
BLDG. 475B, PO BOX 5000
UPTON, NY 11973-5000 USA

A. ROSCIOLI
PENNSYLVANIA POWER & LIGHT CO.
2 NORTH 9TH ST.
ALLENTOWN, PA 18101 USA

T. ROSS
PSE&G
PO BOX 236, MC a20
HANCOCKS BRIDGE, NJ 08038 USA

P. ROTHWELL
NUCLEAR INSTALLATIONS INSPECTORATE
ROOM 908 ST. PETER'S HOUSE, BALLIOL RD.
BOOTLE, MERSEYSIDE, L20 3LZ UK

T. ROWELL
WESTINGHOUSE ELECTRIC CORP.
PO BOX 353
PITTSBURGH, PA 15230 USA

J. ROYEN
OECD NUCLEAR ENERGY AGENCY
12 BLVD. DES ILES
ISSY-LES-MOULINEAUX, F92130 FRANCE

H. RYU
NUCLEAR POWER ENGINEERING CORP.
8F FUJITAKANKO TORANOMON BLDG. 17-1, 3-CHOME
MINATO-KU, TOKYO, 105 JAPAN

K. SAITO
NUCLEAR POWER ENGINEERING CORP.
17-1, 3-CHOME TORANOMON
TOKYO, 105 JAPAN

O. SANDERVAG
SWEDISH NUCLEAR POWER INSPECTORATE
SEHLSTEDT GT 11
STOCKHOLM, SWEDEN

M. SARRAM
NUCLEAR ENERGY INSTITUTE - NEI
1776 I ST., N.W., SUITE 400
WASHINGTON, DC 20006-3708 USA

K. SATO
HITACHI, LTD
3-1-1 SAIWAI-CHO
HITACHI-SHI, IBARAKI 317 JAPAN

K. SATO
MITSUBISHI ATOMIC POWER INDUSTRIES, INC.
3-3-1, MINATO MIRAI, NISHI-KU
YOKOHAMA-SHI, 220 JAPAN

M. SATO
TOSHIBA NUCLEAR MARKETING DEPT.
1-1-8, UCHISAIWAI-CHO
CHIYODA-KU, TOKYO 100 JAPAN

S. SAVOLAINEN
IMATRAN VOIMA OY/LOVIISA POWER PLANT
PO BOX 23
LOVIISA, FIN-07901 FINLAND

C. SAYLES
SOUTHERN CALIFORNIA EDISON
PO BOX 128
SAN CLEMENTE, CA 92672 USA

P. SCHEMERT
BETTIS ATOMIC POWER LABORATORY
PO BOX 79
WEST MIFFLIN, PA 15122 USA

F. SCHMITZ
CEA/IPSN
F-13108 ST. PAUL LEZ DURANCE CEDEX
, FRANCE

R. SCHULTZ
IDAHO NATIONAL ENGINEERING LABORATORY
P.O. BOX 1625
IDAHO FALLS, ID 83415 USA

A. SEKRI
ELECT. DE FRANCE, SER. ETUDES ET PROJETS THERMIQUES
12-14 AV. DUTRIEVOZ
VILLEURBANNE, LYON 69628 FRANCE

C. SEOK
300, CHUN-CHUN-DONG
SUWON, KOREA, 440-748 KOREA

S. SETH
THE MITRE CORPORATION
7525 COLSHIRE DR.
MC LEAN, VA 22102 USA

W. SHA
ARGONNE NATIONAL LABORATORY
9700 SOUTH CASS AVENUE
ARGONNE, IL 60439 USA

V. SHAH
IDAHO NATIONAL ENGINEERING LAB.
PO BOX 1625
IDAHO FALLS, ID 83415-3870 USA

J. SHIN
RAYTHEON E&C
2 WORLD TRADE CENTER, 87 FL.
NEW YORK, NY 10048 USA

D. SHURBERG
BROOKHAVEN NATIONAL LABORATORY
BLDG. 130, PO BOX 5000
UPTON, NY 11973-5000 USA

E. SILVER
OAK RIDGE NATIONAL LAB
BLDG. 9201-3, MS 8065, PO BOX 2009
OAK RIDGE, TN 37831-8065 USA

B. SINGH
JUPITER CORP.
2730 UNIVERSITY BLVD. W, STE. 900
WHEATON, MD 20902 USA

S. SNIDER
TU ELECTRIC COMPANY
400 NORTH OLIVE, L.B. 81/24SLIC
DALLAS, TX 75201 USA

M. SONG
KOREA INSTITUTE OF NUCLEAR SAFETY
PO BOX 114
YUSUNG, TAEJON, 305-600 KOREA

B. SOUBIES
INSTITUT DE PROTECTION ET DE SURETE NUCLEAIRE
B.P. 6
FONTENAY AUX ROSES, 92265 FRANCE

G. SRINIVASAN
NUCLEAR POWER CORPORATION OF INDIA
TARAPUR ATOMIC POWER STATION
TARAPUR, MAHARASHTRA, INDIA

K. ST. JOHN
YANKEE ATOMIC ELECTRIC CO.
580 MAIN ST
BOLTON, MA 01740 USA

W. STADTMULLER
MPA STUTTGART
PFAFFENWALDRING 32
STUTTGART, D-70569 GERMANY

D. STARCK
MPR ASSOCIATES, INC.
320 KING ST.
ALEXANDRIA, VA 22314-3238 USA

R. STEELE JR.
IDAHO NATIONAL ENGINEERING LABORATORY
P.O. BOX 1625
IDAHO FALLS, ID 83415 USA

R. STIRN
GE NUCLEAR
PO BOX 780, MC F24
WILMINGTON, NC 28402 USA

J. STONE
MPR ASSOCIATES, INC.
320 KING ST.
ALEXANDRIA, VA 22314-3238 USA

P. STOREY
HSE/NSD
BROADLANE
SHEFFIELD, S37HQ UK

V. STRIZHOU
NSI RHS
B. TULSKAYA, 52
MOSCOW, RUSSIA, 113191 RUSSIA

E. STUBBE
TRACTEBEL INGENIERIE
AVE. ARIANE 7, BTE 1
BRUSSELS, 1200 BELGIUM

R. SUMMERS
SANDIA NATIONAL LABORATORIES
P.O. BOX 5800, MS 0745
ALBUQUERQUE, NM 87185-0745 USA

B. SUN
SUNUTECH, INC.
PO BOX 978
LOS ALTOS, CA 94023 USA

J. SUN
ARGONNE NATIONAL LABORATORY
9700 SOUTH CASS AVENUE
ARGONNE, IL 60439 USA

A. SUSLOV
RRC KURCHATOV INSTITUTE
KURCHATOV SQUARE 1
MOSCOW, RUSSIA, 123182 RUSSIA

E. SWANSON
B&W NUCLEAR TECHNOLOGIES
PO BOX 10935
LYNCHBURG, VA 24506-0935 USA

L. SZABO
COMMISSARIAT L'ENERGIE ATOMIQUE
C.E. CADARACHE
ST. PAUL LES DURANCE, 13108 FRANCE

K. TAKIGUCHI
2-12-1 OH-OKAYAMA, MEGURO-KU
TOKYO, TOKYO 152 JAPAN

P. TALARICO
GILBERT/COMMONWEALTH, INC.
PO BOX 1498
READING, PA 19603 USA

T. TANAKA
SANDIA NATIONAL LABORATORIES
MS/0737, PO BOX 5800
ALBUQUERQUE, NM 87185 USA

P. TANGUY
ELECTRICITE DE FRANCE
32 RUE DE MONCEAU
PARIS, 75008 FRANCE

Z. TECHY
YEIKI
ZRINYI U. 1.
BUDAPEST, 1051 HUNGARY

C. THIBAULT
WYLE LABORATORIES
PO BOX 077777
HUNTSVILLE, AL USA

H. THORNBURG
ABB ATOM
901 S. WARFIELD DR.
MT. AIRY, MD 21771 USA

J. TOLY
CEA-IPSN DES/SEPRI
BP 6
FONTENAY AUX ROSES, 92265 FRANCE

M. TORCIVIA
KNOLLS ATOMIC POWER LAB.
PO BOX 1072
SCHENECTADY, NY 12301-1072 USA

N. TRIKOUROS
GPU NUCLEAR CORP.
ONE UPPER POND RD.
PARSIPPANY, NJ 07054 USA

A. TURRIAN
HSK SWISS FEDERAL NUC.SAFETY INSPECTORATE
WURENLINGEN
VILLIGEN-HSK, CH 5232 SWITZERLAND

W. URKO
ABB/COMBUSTION ENGINEERING
1000 PROSPECT HILL RD., DEPT. 9341-0421
WINDSOR, CT 06095 USA

K. VALTONEN
FINNISH CENTRE FOR RADIATION & NUCLEAR SAFETY
P.O. BOX 14
FIN-00881-HELSINKI, FINLAND

R. VAN HOUTEN
JUPITER CORP.
2730 UNIVERSITY BLVD., STE 900
WHEATON, MD 20902 USA

L. VANDEN HEUVEL
OAK RIDGE NATIONAL LABORATORY
PO BOX 2009, BLDG. 9201-3
OAK RIDGE, TN 37831-8065 USA

O. VESCOVI
SOCIETA INFORMAZIONI EXPERIENZE TERMOIDRAULICHE
VIA N. BIXIO 27
PIACENZA, 29100 ITALY

W. VESELY
SCIENCE APPLICATIONS INT'L CORP.
655 METRO PLACE SOUTH
DUBLIN, OH 43017 USA

J. WADE
ARIZONA PUBLIC SERVICE
P.O. BOX 52034
PHOENIX, AZ 85072-2034 USA

J. WALKER
AECL RESEARCH
CHALK RIVER LAB
CHALK RIVER, ONTARIO K0J1J0 CANADA

D. WALTERS
NUCLEAR ENERGY INSTITUTE - NEI
1776 I ST., N.W., SUITE 400
WASHINGTON, DC 20006-3708 USA

S-F WANG
INSTITUTE OF NUCLEAR ENERGY RESEARCH
1000 WENHUA RD., CHIAAN VILLAGE
LUNG-TAN, TAIWAN 325 ROC

W. WANG
STONE & WEBSTER ENG. CO.
P.O. BOX 5200
CHERRY HILL, NJ 08034 USA

A. WARE
IDAHO NATIONAL ENGINEERING LABORATORY
PO BOX 1625
IDAHO FALLS, ID 83415-3750 USA

P. WEBSTER
ATOMIC ENERGYCONTROL BOARD, CANADA
280 SLATER ST.
OTTAWA, ONTARIO K1P 5S9 CANADA

J. WHITCRAFT
BECHTEL POWER CORP.
9801 WASHINGTONIAN BLVD.
GAITHERSBURG, MD 20878 USA

D. WHITEHEAD
SANDIA NATIONAL LABORATORIES
PO BOX 5800, MS 0747
ALBUQUERQUE, NM 87185-0747 USA

K. WHITT
SOUTHERN NUCLEAR
40 INVERNESS CENTER PARKWAY
BIRMINGHAM, AL 35201 USA

G. WILKOWSKI
BATTELLE PACIFIC NORTHWEST LABORATORY
505 KING AVE.
COLUMBUS, OH 43201 USA

V. WILLEMS
GILBERT/COMMONWEALTH, INC.
P.O. BOX 1498
READING, PA 19603 USA

M. WILLIS
WESTINGHOUSE ELECTRIC CORP.
PO BOX 353
PITTSBURGH, PA 15230 USA

L. WOLF
UNIV. OF MARYLAND, DEPT. MATERIALS & NUCLEAR ENG'G
2135 BLDG. 090
COLLEGE PARK, MD 20742-2115 USA

K. WOLFERT
GESELLSCHAFT FUR ANLAGEN & REAKTORSICHERHEIT MBH
FORSCHUNGSGELANDE, D-85748 GARCHING
DEUTSCHLAND, GARCHING D-85748 GERMANY

J. WREATHALL
JOHN WREATHALL & CO.
4157 MACDUFF WAY
DUBLIN, OH 43017 USA

S. WRIGHT
SANDIA NATIONAL LABORATORIES
PO BOX 5800, MS 1145
ALBUQUERQUE, NM 87185-1145 USA

G. WROBEL
ROCHESTER GAS & ELECTRIC CORP.
49 EAST AVE.
ROCHESTER, NY 14649 USA

G. WU
NUCLEAR ENERGY INSTITUTE - NEI
1776 I ST., N.W., SUITE 400
WASHINGTON, DC 20006-3708 USA

M. YAMAGISHI
MITSUBISHI ATOMIC POWER INDUSTRIES, INC.
3-1, MINATOMIRAI 3-CHOME, NISHI-KU
YOKOHAMA, KANAGAWA 220 JAPAN

L. YEGOZOVA
RRC KURCHATOV INSTITUTE
ROGOV ST. 16, AP. 35
MOSCOW, RUSSIA

K. YOO
KOREA ATOMIC ENERGY RESEARCH INSTITUTE
PO BOX 105, YUSONG
TAEJON, 305-600 KOREA

Y. YOSHIZAWA
TOKYO INSTITUTE OF TECHNOLOGY
2-12-1 OH-OKAYAMA, MEGURO-KU
TOKYO, TOKYO 152 JAPAN

D. YU
KOREA ATOMIC ENERGY RESEARCH INST.
PO BOX 105, YUSONG
TAEJON, 305-353 KOREA

Y. YUNE
KOREA INSTITUTE OF NUCLEAR SAFETY
PO BOX 114
YUSUNG, TAEJON, 305-600 KOREA

G. ZACHARIAS
CHARLES RIVER ANALYTICS, INC.
55 WHEELER ST.
CAMBRIDGE, MA 02138 USA

D. ZANOBETTI
UNIVERSITY OF BOLOGNA
VIALE RISORGIMENTO 2
BOLOGNA, 40136 ITALY

P. ZMOLA
C&P ENGINEERING
5409 NEWINGTON RD.
BETHESDA, MD 20816 USA

PROCEEDINGS OF THE
TWENTY-SECOND WATER REACTOR SAFETY INFORMATION MEETING
October 24-26, 1994

CONTENTS - VOLUME 2

CONTENTS - VOLUME 2 (Cont'd)

CONTENTS - VOLUME 2 (Cont'd)

Closure of the Direct Containment Heating Issue for Zion

Martin M. Pilch, Michael D. Allen, Daryl L. Knudson[1],
Douglas W. Stamps, and Eden L. Tadios

Sandia National Laboratories
Albuquerque, NM

ABSTRACT

Supplement 1 of NUREG/CR-6075 brings to closure the DCH issue for the Zion plant. It includes the documentation of the peer review process for NUREG/CR-6075, the assessments of four new splinter scenarios defined in working group meetings, and modeling enhancements recommended by the working groups. In the four new scenarios, consistency of the initial conditions has been implemented by using insights from systems-level codes. SCDAP/RELAP5 was used to analyze three short-term station blackout cases with different leak rates. The SCDAP/RELAP5 output was used as input to CONTAIN to assess the containment conditions at vessel breach. The methodology originally developed in NUREG/CR-6075 was used to analyze the new splinter scenarios. Some enhancement of hydrogen combustion modeling was implemented for these analyses. A new computational tool--the two-cell equilibrium/Latin hypercube sampling (TCE/LHS) code--was developed for this effort to perform Monte Carlo sampling of the scenario distributions. The analyses of the new scenarios showed no intersection of the load distributions and the containment fragility curves, and thus the containment failure probability was zero for each scenario. These supplemental analyses complete closure of the DCH issue for Zion.

[1] Idaho National Engineering Laboratory, Idaho Falls, ID 83415

1.0 INTRODUCTION

In a light water reactor core melt accident, if the reactor pressure vessel (RPV) fails while the reactor coolant system (RCS) is at high pressure, the expulsion of molten core debris may pressurize the reactor containment building (RCB) beyond its failure pressure. A failure in the bottom head of the RPV, followed by melt expulsion and blowdown of the RCS, will entrain molten core debris in the high-velocity steam blowdown gas. This chain of events is called a high-pressure melt ejection (HPME). Four mechanisms may cause a rapid increase in pressure and temperature in the reactor containment: (1) blowdown of the RCS, (2) efficient debris-to-gas heat transfer, (3) exothermic metal/steam and metal/oxygen reactions, and (4) hydrogen combustion. These processes that lead to increased loads on the containment building are collectively referred to as direct containment heating (DCH). Understanding factors that enhance or mitigate DCH is necessary because the pressure load imposed on the RCB may lead to early failure of the containment.

Direct Containment Heating (DCH) is a prominent severe accident issue because of its potential for early containment failure. The Nuclear Regulatory Commission (NRC) has identified DCH as a major issue for resolution in the Revised Severe Accident Research Plan (NRC, 1992) and has sponsored a program at Sandia National Laboratories to resolve the DCH issue. The first step in this process was writing NUREG/CR-6075 (Pilch et al., 1994): "The Probability of Containment Failure by Direct Containment Heating in Zion." NUREG/CR-6075 assesses the probability of containment failure by DCH for the Zion Nuclear Power Plant (NPP). NUREG/CR-6075 was extensively reviewed by a panel of 15 experts representing national laboratories, universities, and industry. The review process included written comments by the peer reviewers, responses to the comments by the authors, and rebuttals by the reviewers (see Appendix A). Major issues that were identified as part of the peer review process, such as consistency of initial conditions and hydrogen combustion, are addressed in Supplement 1 of NUREG/CR-6075. Following the comment, response, and rebuttal process, two working group meetings of selected members of the original peer review group were held to resolve two residual concerns: initial conditions and model validity.

Supplement 1 to NUREG/CR-6075 focuses on closure of the DCH issue for the Zion plant. It contains the additional analyses that the working groups indicated were necessary to strengthen the original conclusions. The probabilistic framework for these analyses is described in Section 2 of this report. The working groups suggested four new possible scenarios for analyses using the methodology in NUREG/CR-6075. The scenarios are described and justified in Section 3. Quantification of the DCH phenomenon with the TCE model is discussed in Section 4, and quantification of the Zion fragility is described in Section 5. The probabilistic synthesis is carried out using a Monte Carlo sampling method in the TCE/LHS code, which is described in Appendix B. Section 6 contains the results of the calculations for the splinter scenarios. The conclusions and recommendations are summarized in Section 7.

The working group members stressed consistency of the DCH initial conditions. They recommended using insights from core melt progression analyses performed by the Idaho National Engineering Laboratory (INEL) with SCDAP/RELAP5 for the Zion plant. Consistent with that recommendation INEL analyzed three short-term station blackout cases for the Zion plant with different leak rates: (1) no leaks, (2) a leak rate of 250 gpm per pump, and (3) a leak rate of 480 gpm per pump. Failure of the hot leg or surge line resulting in depressurization of the primary system was observed well before core relocation and lower head failure in all three cases. However, the calculations were continued until the lower head failed in order to gain insights about conditions at lower head failure, such

as the melt mass and composition, reactor coolant system pressure, melting of upper plenum steel, and relocation of metallic core blockages into the lower plenum. These insights were applied in developing the distributions for the new scenarios defined in this supplement.

The NRC-sponsored experimental program has played a major role in developing an understanding of the key physical processes in DCH. The technical basis for these scaled experiments was developed by the Severe Accident Scaling Methodology Technical Program Group (SASM-TPG) (Zuber et al., 1992) and by Pilch et al. (1992). The extensive database from counterpart experiments by Sandia National Laboratories and Argonne National Laboratory has allowed the development and validation of simple analytical models for predicting the containment loads. In particular, the two-cell equilibrium (TCE) model is based on phenomenological insights from the experimental program and is used in the analyses presented here. The TCE model takes into account the coherence between the entrained debris and the RCS blowdown steam. Any noncoherence in the entrainment process limits the interactions that result in debris-to-gas heat transfer and in chemical reactions that produce hydrogen.

The methodology that has been developed in NUREG/CR-6075 and its supplement will be applied to the Surry plant in NUREG/CR-6109: "The Probability of Containment Failure by Direct Containment Heating in Surry." Extrapolation to other power plants is being addressed in another NUREG/CR report to be released soon.

1.1 References

NRC (December 1992). *Severe Accident Research Program Plan Update*, NUREG-1365, Rev. 1.

Pilch, M.M., M.D. Allen, and J.L. Binder (1992). "Counterpart and Replicate DCH Experiments Conducted at Two Different Physical Scales: The SNL/IET-1, 1R and the ANL/IET-1R, 1RR Experiments," Letter Report to the NRC.

Pilch, M.M., H. Yan, and T.G. Theofanous (1994). *"The Probability of Containment Failure by Direct Containment Heating in Zion,"* NUREG/CR-6075, SAND93-1535.

Zuber, N. et al. (1992). *An Integrated Structure and Scaling Methodology for Severe Accident Technical Issue Resolution*, Draft for Comment, NUREG/CR-5809, EGG-2659.

2.0 PROBABILISTIC FRAMEWORK

The basic understanding upon which this approach to resolving the DCH issue is based (and confirmed in repeated experiments) is that the intermediate (or steam generator) compartment traps most of the debris dispersed from the reactor cavity and that the thermal/chemical interactions during this dispersal process are limited by the incoherence in the steam blowdown and melt entrainment processes. To put it simply, for blowdowns that are sufficient to cause entrainment and significant thermal/chemical interactions, the entrainment time is short compared with the blowdown time so that the molten debris is exposed to only a small fraction of the steam from the primary system. Because this steam is the principal medium for carrying the melt energy and the hydrogen produced by steam/metal interactions to the main containment volume, this incoherence is a crucial mitigating factor. With this understanding, it is possible to reduce most of the complexity of the DCH phenomenon to a single parameter: the ratio of the melt entrainment time constant to the system blowdown time constant ($R_\tau = \tau_e/\tau_b$ in the TCE model). For simplicity, R_τ is referred to as a coherence ratio.

Besides these modeling factors, the DCH loads depend on parameters that characterize the system initial conditions; that is, primary system pressure, temperature and composition (i.e., hydrogen mole fraction), melt quantity and composition (zirconium and stainless steel mass fractions), initial containment pressure and composition (hydrogen mole fraction), and geometry (containment volume and the size of the breach). The key component of the framework, therefore, is the causal relation (CR1) between these parameters and the resulting containment pressure (and temperature) under the influence of the uncertainty in the coherence ratio, R_r. Of these parameters, some are fixed, some vary only over a narrow range, and some are so uncertain that they can be approached only in a very bounding sense. The following features were considered in coming up with the final choice of a framework:

1. *Geometry.* The specific geometry is fixed for a given plant; however, the basic features are that there is an intermediate compartment between the cavity and the main containment volume and that the lower head fails in a local (rather than global) manner. In addition, the geometry is characterized by the free volume of the containment and the primary system volume.

2. *Containment Conditions.* Typically, high-pressure scenarios evolve with significant primary system venting prior to vessel breach (see Section 3); this venting increases the containment pressure to ~0.25 MPa with temperatures near saturation. This pressure will be lower if any of the active containment heat removal systems are operational. The containment atmosphere will also contain hydrogen at a concentration of a few mole percent. Preexisting hydrogen is limited by the quantity of zirconium available to react in the core, and thus there is a constrained relationship between preexisting hydrogen in the containment and the hydrogen produced by steam/zirconium reactions in the DCH event.

3. *Primary System Conditions.* We emphasize here the reasonable consistency between reactor coolant system (RCS) pressure (and temperature) and melt mass and composition. Model predictions indicate that DCH loadings are insensitive to the temperature of the primary system (see Appendix D, NUREG/CR-6075), and accident analyses indicate that the primary system pressure can be enveloped rather than predicted (Section 3). This leaves only the expelled melt parameters in need of quantification: melt quantity, composition, and temperature. These are the variables that drive the DCH process; however, they are highly uncertain. They depend on the complex interactions and the many scenario bifurcations in the core meltdown, relocation, and lower head failure processes and are hence in need of very careful quantification. This is done in Section 3.

The probabilistic framework can be structured in the manner illustrated in Figure 2.1. As shown, the initial melt parameters are to be quantified as independent probability density functions, representing modeling uncertainty in the parameters (variations from stochastic processes are assessed as insignificant relative to modeling uncertainty). These functions are formed into a joint probability density function and then combined with CR1, under the parameter distribution function that represents model uncertainty for the DCH processes, R_r, to obtain a probability density function for the peak containment pressure. This distribution function is combined with the set of containment fragility curves (probabilistically distributed themselves) to obtain a probability distribution of the containment failure frequency.

The discrete probability distribution (DPD) method was used to propagate distributions through the probabilistic framework in NUREG/CR-6075. The ALPHA code, developed at the University of California at Santa Barbara (UCSB), was the software based on the DPD approach that was used in NUREG/CR-6075 to calculate containment failure probabilities. An alternative to using ALPHA was developed by Sandia for the present supplement document, with an eye towards continued use in future

extrapolation efforts. Sandia has developed software to perform either traditional Monte Carlo sampling or stratified Monte Carlo sampling (Latin Hypercube Sampling, LHS). The software, called LHS is user-friendly and has an established quality assurance pedigree, including code assessment and verification. Sandia chose to use a new numerical tool based on LHS to propagate distributions through the probabilistic framework. The resulting software is described more fully in Pilch et al. (1994) where LHS results are benchmarked against existing ALPHA predictions.

2.1 References

Pilch et al. (1994). *The Probability of Containment Failure by Direct Containment Heating in Zion*, NUREG/CR-6075, Supplement 1.

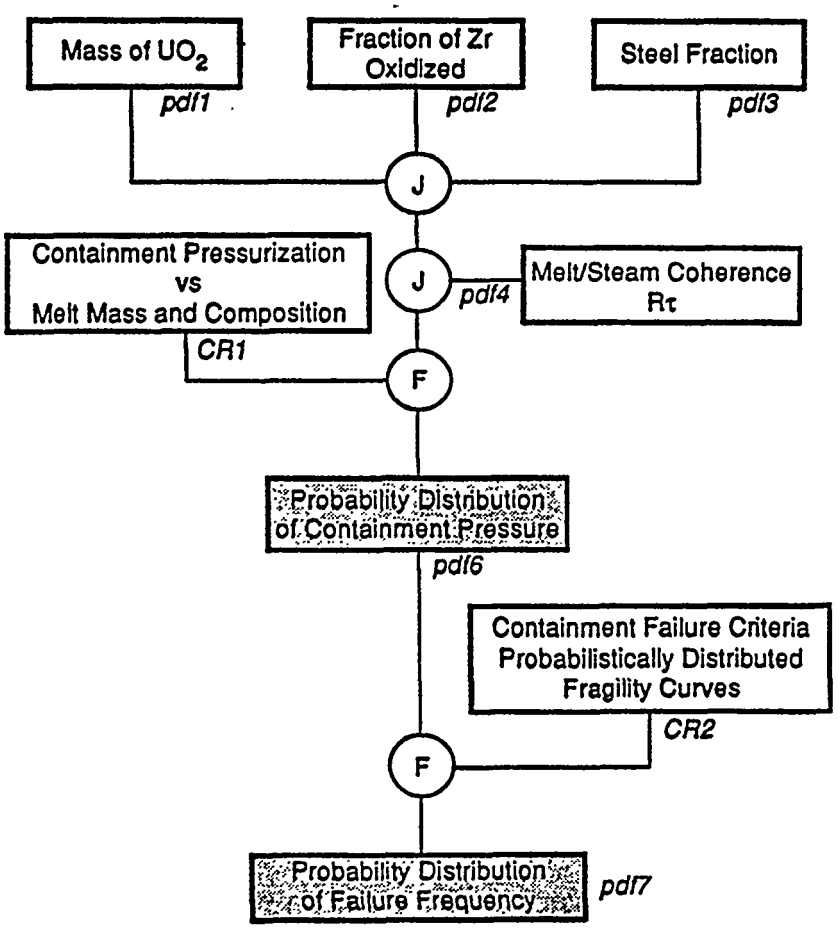

Figure 2.1. The probabilistic framework for containment failure under Direct Containment Heating scenarios. The (J) and (F) are the "joint" and "function" operations, respectively, as described in the text.

3.0 QUANTIFICATION OF INITIAL CONDITIONS

3.1 Introduction

DCH has traditionally been examined for a rather narrow range of hypothesized severe accident conditions: unmitigated station blackout at full system pressure, formation of a metallic blockage ceramic crust in the core that contains a large fraction of core in a molten state, sudden downward failure of this blockage and crust, resulting in a massive relocation of the melt into the lower plenum, failure of a penetration passing through the lower head of the reactor pressure vessel (RPV), rapid ablation of the resulting hole in the RPV from 5 to about 40 cm (Pilch and Tarbell, 1985), and high pressure melt ejection from the single hole followed by high-pressure steam blowdown. In attempts to address the DCH issue from either a systems point of view or an accident management point of view, intentional depressurization of the primary system has been examined (Hanson et al., 1990). Experiments have shown that the pressure must be very low (less than 1 MPa) to preclude the onset of dispersal from the cavity and to prevent the possibility of DCH (Tutu et al., 1988). Bounding calculations (Pilch and Tarbell, 1986) suggest that only 20 percent of the core (participating in DCH) could pose a threat for the containment. With this traditional understanding, containment- threatening loads from DCH can only be precluded if the RCS is almost fully depressurized. However, based on the understanding developed in NUREG/CR-6075 (Pilch et al. 1994a), a substantial reduction of DCH is achieved without having to invoke nearly complete depressurization of the RCS.

Quantification of melt release conditions was developed by attempting to envelope the physically possible behavior in a comprehensive and systematic manner. This means that we needed to examine all reasonably conceivable severe accident scenarios, identify key aspects of their phenomenology and respective ranges of behavior, and establish the few scenarios that envelope the DCH challenge to the containment.

Peer reviewers raised the following questions regarding the completeness of the splinter scenarios considered in NUREG/CR-6075:

1. Can full system pressure cases be ruled out?

2. Should operator intervention scenarios be analyzed?

3. Can dry core scenarios lead to melting and relocation of the metal (Zr) blockage from the core to the lower plenum?

Generally, the peer reviewers characterized initial condition quantifications in NUREG/CR-6075 as "optimistic." Specifically, they expressed concern that ~8 MPa RCS pressure might not be adequately bounding, that the melt mass distributions were too narrow, and that the melt composition did not contain sufficient metallics (Zr and steel). The reviewers also stressed that SCDAP/RELAP5 analyses be performed and used in a consistent manner in establishing initial conditions.

The NRC convened a working group to make recommendations on how to resolve these concerns. The group's minutes are included in Pilch et al. (1994b) and summarized in Section 3.2, where additional splinter scenarios are defined. SCDAP/RELAP5 calculations were performed to provide confirmatory insight into the working group recommendations. These calculations are discussed more fully in Pilch

et al. (1994b) and the relevant insights are summarized in Section 3.3. Quantifications for the new scenarios are presented in Sections 3.5 and 3.6.

3.2 Splinter Scenarios

Figure 3.1 depicts the four splinter scenarios analyzed in NUREG/CR-6075. The phenomenological complexity of severe accidents leads to the possibility of two major scenario bifurcations: one concerned with the quantity of melt that accumulates in the core region prior to its release and relocation into the lower plenum, and the other concerned with the mode and timing of lower head failure. The first bifurcation considers crucible formation/failure versus gradual relocation (no crucible) as the mechanism for melt relocation into the lower plenum. The second bifurcation considers a localized penetration failure of the lower head versus rupture.

Working group recommendations focused on four new splinter scenarios as shown in Figure 3.2. The intent was to place greater reliance on systems-level codes (SCDAP/RELAP5) in order to achieve better consistency between RCS pressure at vessel breach with melt mass and composition. Specifically, the working group emphasized that high RCS pressures are correlated with predominantly oxidic melts and that metallic melts are correlated with reduced RCS pressures. The rationale leading to these new splinter scenarios is discussed next.

The working group felt that there was no compelling need to further analyze scenarios with penetration failures. The INEL lower head failure analysis (Rempe et al., 1993) and the OECD-NEA-TMI-2 vessel investigation project (Stickler et al., 1993) both concluded that rupture was much more likely than a penetration-type failure. Marshall (1988) performed some scoping experiments on tube ejection. Specifically, he confirmed that binding caused by differential thermal expansion could prevent ejection of a penetration from the lower head (for the conditions and materials tested); however, ballooning of the lower head, which could induce ejection of a penetration as a precursor to rupture, was not modeled in these experiments. Fauske and Associates, Inc. (FAI) (Hammersley et al., 1993), under the sponsorship of the Electric Power Research Institute (EPRI), has examined melt penetration into in-core instrument guide tubes. Pressure-driven melt was observed to travel approximately 2 m, which is far enough to carry it well beyond the lower head. However, the melt mass is too small to threaten the integrity of the guide tube. These limited experiments confirm INEL and OECD conclusions that penetration-type failures are unlikely. NUREG/CR-6075 (Pilch et al., 1994a) showed that a penetration failure followed by ablation of the lower head would produce a hole about the same size as would be expected for a local rupture of the lower head. Finally, work reported in NUREG/CR-6075 showed that predicted loads for rupture scenarios bound predicted loads for penetration failure scenarios; consequently, penetration failures need not be considered further in the supplement assessments for Zion or in any extrapolation activities.

Scenario VI is very similar to Scenario II in NUREG/CR-6075. Here, the working group wanted to emphasize the presence of water in the lower head. They recommended the addition of a new TMI-like scenario (Scenario V) characterized by reflooding and repressurization ($\sim$16 MPa) of the RCS as a result of operator actions. Scenarios V and VI were envisioned as having water in the core (at least covering the bottom) during much of the core melt progression; consequently, slumping core material would form a crucible which could fail only locally. The melt composition would be largely oxidic, with most unoxidized Zr permanently retained as a metal blockage in the core.

The working group then recommended consideration of scenarios in which core melting would proceed without water in the core region and largely without water in the lower plenum. It was their expectation that these scenarios would evolve to much lower RCS pressures at vessel failure for typical small break loss-of-coolant accidents (SBLOCAs). At the lower pressures, the possibility of melting upper plenum steel without also failing the hot leg becomes possible; thus, both scenarios VII and VIII augment the oxidic melt with large quantities of upper plenum steel. Scenario VIII is distinguished from Scenario VII in that the metal blockage is also assumed to remelt, allowing large quantities of unoxidized Zr to relocate to the lower plenum.

NUREG/CR-6075 (Scenario IV) considered a gradual relocation scenario that progressed under high pressure (~8 MPa) with complete melting of upper plenum steel. Working group discussions pointed out that this scenario is overly conservative and that hot leg failure is strongly correlated with melting of upper plenum steel. In fact, a gradual relocation scenario has only been predicted in one MELPROG calculation for the Surry plant; and even here, hot leg failure was predicted before core relocation into the lower plenum. Should a gradual relocation scenario occur, working group members believed that it would look like Scenario VIII at the time of vessel failure.

SCDAP/RELAP5 calculations have been performed (based on working group recommendations) to confirm the basic features of Scenarios VII and VIII. Three cases were run with SCDAP/RELAP5 representing the full spectrum of expected SBLOCAs: no leaks, 250 gpm/pump, and 480 gpm/pump. The results are summarized in Section 3.3. The key conclusion, however, is that hot leg failure is predicted to occur before core relocation for all SBLOCAs leading to complete depressurization of the RCS before lower head failure. Consequently, Scenarios VII and VIII are not further analyzed.

3.3 Summary of SCDAP/RELAP5 and CONTAIN Insights

The initial and boundary conditions for the new scenarios analyzed in this supplement are based on insights from SCDAP/RELAP5 and CONTAIN calculations. These system code calculations are used to justify the initial and boundary conditions for the dry core splinter scenarios discussed in Section 3.2. In this report, "dry core" implies that the RPV water level is below the bottom of the core so that the potential exists for metallic blockages to relocate to the lower plenum. All of the cases analyzed produced "dry core" conditions.

Three dry core cases were run with SCDAP/RELAP5 at different leak rates: (1) no leaks, (2) 250 gpm per pump leaks, and (3) 480 gpm per pump leaks. The goal of these calculations was to develop a better understanding of the melt mass, melt composition, and RCS pressure at the time of lower head failure for dry scenarios. In each case, hot leg failure was allowed to occur, if predicted during the calculation. This failure would lead to depressurization and complete accumulator discharge. The output from SCDAP/RELAP5 for these cases was used in CONTAIN to determine the containment conditions at the time of lower head failure. The flow of steam, water, hydrogen, and nitrogen into the containment was provided to Sandia by INEL for use in CONTAIN. The hydrogen flow into the containment was assessed to determine if the hydrogen would burn as it entered the containment. A number of important insights were obtained from these calculations.

First, the SCDAP/RELAP5 calculations indicated that hot leg failure occurred prior to melt relocation into the lower plenum in all cases. The failure resulted in depressurization and accumulator discharge. In all cases, the RCS pressure was at containment pressure at the time of lower head failure. Owing to the significant amount of time between hot leg failure and lower head failure, we conclude that

the sequences, as calculated by SCDAP/RELAP5, will not result in a DCH threat. This supports the assessment in NUREG/CR-6075 that full system pressure scenarios can be excluded (except operator intervention accidents such as TMI-II). The SCDAP/RELAP5 calculations also confirm that the ~8 MPa bound in NUREG/CR-6075 is not only conservative, but perhaps excessively so unless the operator intervenes in the accident. This assumes, of course, that water injection does not arrest melt progression.

A second insight is related to the amount of metallic debris present in the melt in the lower plenum. We noted that the degree of upper plenum steel melting is limited in all cases and is strongly correlated with hot leg failure. The maximum amount of upper plenum steel that was predicted to melt was ~3 mt. We also noted that lower plenum steel was assumed to melt in all cases, representing an additional 5 mt of steel. Hence, the amount of steel in the melt is limited to ~8 mt. This ~8 mt of steel can be compared with the original 25 mt analyzed in Scenarios III and IV in NUREG/CR-6075. We conclude that the analyses confirm the conservatism in the original steel mass distributions.

With respect to zirconium in the melt, SCDAP/RELAP5 indicates that very little zirconium is predicted to relocate into the lower plenum. The maximum amount of zirconium in the lower plenum melt is ~0.5 mt. This result implies that melt-out of the metallic blockage in the core region is not predicted, even in dry core scenarios. Again, the SCDAP/RELAP5 predictions confirm NUREG/CR-6075 assessments.

The reason for this behavior can be seen by a careful review of the calculations. In all cases, the melt that relocated into the lower plenum is predicted to quench, but not all of the available water is vaporized. This is likely due to displacement of water from the lower plenum as the melt relocates. The water eventually settles back into the lower plenum, but a stratified condition exists, i.e., the water overlies the debris residing on the lower head. Owing to inefficient heat transfer between the debris and the water, the water is vaporized slowly and, in all cases, water remains in the lower plenum at the time of lower head failure. The presence of water and its slow vaporization appears to be sufficient to prevent melt-out of the in-core blockages. Hence, we conclude that the amount of zirconium in the melt in the lower plenum is expected to be very limited.

A third insight is related to the amount of hydrogen generated. We observed that the amount of hydrogen generated in Cases 2 and 3 corresponds to ~40 to 60 percent zirconium oxidation. Our expectation is that the 60 percent level is a likely upper bound since much of the remaining zirconium is contained in metallic blockages that are difficult to oxidize. The distributions for Zr oxidation in NUREG/CR-6075 envelope the SCDAP/RELAP5 predictions.

The fourth insight is related to the amount of molten material at the time of lower head failure. We noted that the amount of oxide material that relocated into the lower plenum varies from approximately 77 mt to 104 mt for the three cases, but the amount of *molten* oxide varies from 55 mt to 66 mt. Hence, while the amount of oxide material in the lower plenum shows some variation, the amount of *molten* oxide at vessel breach is limited to a rather narrow range. The SCDAP/RELAP5 predictions (~60 mt oxide) are about 10 mt higher than the assessments in NUREG/CR-6075, with most of the difference attributed to a NUREG/CR-6075 assessment that the crucible cannot fail at the bottom and drain completely, whereas SCDAP/RELAP5 analyses assume failure of the crucible results in complete drainage of the molten contents. However, sensitivity studies have shown that DCH loads are very insensitive to oxide mass.

The CONTAIN calculations were used to provide insights into the containment conditions at the time of lower head failure. The Zion containment was represented by four cells: one each for the cavity, steam generator compartments, annular region, and the dome. The SCDAP/RELAP5 predictions of the temperature and mass flow rates of water, steam, hydrogen, and nitrogen from the RCS were used as inputs to the CONTAIN calculations. Because of the complexity of the hydrogen combustion issues, CONTAIN was run with all burn models disabled. This allows the maximum accumulation of hydrogen at the time of RPV failure. Hydrogen combustion analyses were performed separately by examining sources from SCDAP/RELAP5 and CONTAIN predictions of the atmosphere composition in each cell to determine if hydrogen released prior to RPV failure would burn as it entered containment. Several insights were obtained from the CONTAIN calculations.

The CONTAIN calculations showed that the containment pressure at the time of lower head failure was in the range of 0.23 to 0.26 MPa for the three cases. These values are consistent with the ~0.25 MPa estimate used in NUREG/CR-6075. Condensation on internal structures and containment walls had a significant influence on the steam concentration in the containment atmosphere prior to vessel breach.

It was predicted that the gases would not accumulate in the steam generator compartments or in the containment annulus. This is consistent with gases released from relatively low release locations but the predictions were also influenced by the CONTAIN nodalization scheme and use of a lumped-parameter code.

During the time hydrogen was injected into the containment, the global mixtures were nonflammable for the three cases analyzed. In the dome, for example, the steam concentration varied between approximately 40 - 60 percent as the hydrogen was injected while the hydrogen concentration was typically below 5 percent.

Insights were obtained on non DCH-induced hydrogen combustion using both the SCDAP/RELAP5 and CONTAIN calculations. The SCDAP/RELAP5 predictions were analyzed to determine what fraction, if any, of the hydrogen injected into the containment would be consumed as an autoigniting jet. Furthermore, since the scenarios analyzed were station blackout scenarios, the autoigniting jets were considered to be the only possible ignition source for deflagrations in the containment. Therefore, CONTAIN predictions of the source compartments were analyzed to determine if mixtures were flammable at the time the jets autoignited.

It was determined that the only possibility of jet autoignition would occur at the hot leg break in Cases 1 and 3, and these cases would depressurize so quickly that they would not be a DCH threat. Otherwise, the temperatures of the gases (~600 K) released from the pilot-operated relief valves (PORVs) were too low for autoignition for all cases, and the hydrogen concentration in the jet never exceeded ~5 percent and usually was zero. Likewise, gases released from the RCPs likely would not autoignite in all of the cases analyzed because hydrogen concentrations in the jets were very low (~5 - 15 percent) during periods of high gas temperatures. Thus, the hydrogen concentration in the containment just prior to vessel failure can be simply determined by summing all hydrogen released from the RCS.

For Case 1, it was estimated that between 35 - 40 percent of the total hydrogen released into the containment could have burned as an autoigniting jet. Conditions for autoigniting jets were not satisfied for Case 2. For Case 3, it was estimated that approximately 1 - 2 percent of the total hydrogen released into the containment could have burned as an autoigniting jet. These results are for three cases that had

different leak rates for the reactor coolant pump seal but otherwise were the same. The large variation in the fraction of hydrogen that could have burned for the three cases illustrates that hydrogen is very scenario dependent.

Gases in the source compartments were not flammable during the time the jets were autoigniting for the three cases analyzed. The analyses accounted for the decrease in hydrogen that was consumed in the autoigniting jets. The containment pressure increase resulting from blowdown and autoignition of jets in Case 1 is ~0.03 MPa higher for a total pressure of ~0.30 MPa at the time (~2000 s) of jet combustion. This pressure is far from a containment- threatening load.

3.4 Characterization of the Zion Plant

Quantification of initial conditions for analyzing containment loads is based on the plant characteristics shown in Table 3.1. It is worth noting that approximately 30 percent of the core is within one fuel assembly distance to the edge of the core. This material, owing to its low decay power and high heat transfer to the core barrel, is difficult to melt, and it is an unlikely contributor to the core melt (in the lower plenum) at vessel breach. Although the core contains little steel, the upper and lower plenums contain large quantities of steel that might be added to the core melt, depending on the scenario. Here, we have restricted ourselves to relatively thin steel that has no substantial inertia to thermal loads that might be imposed on the structure. Based on a more careful examination of a TRAC deck for Zion, and in consultation with FAI (MAAP input deck), the quantity of meltable steel in the lower plenum has been revised from 15 mt (Pilch et al. 1994a) to 10 mt.

Figure 3.3 depicts the Zion NPP. Debris ejected from the reactor pressure vessel first enters the reactor cavity, where high-pressure blowdown gases can disperse the debris into the containment by one of two possible paths. The first is an annular gap around the RPV, which would allow debris to disperse directly to the upper dome. This annular gap is partially filled with reflective insulation and is blocked by neutron shielding and the eight nozzles near the top of the RPV. The SNL/IET-11 (Blanchat et al., 1994) experiment showed that if gas can carry debris into the gap, then the insulation will melt and be swept clear of the gap. Such a situation cannot be precluded at Zion; consequently, this potential flow path is explicitly bounded in the evaluation of containment loads evaluations.

As shown in Figure 3.3, the major dispersal path (by virtue of its large flow area) is through a tunnel leading from under the RPV, which exists so that in-core instrument guide tubes can have access to the lower head. Debris dispersed from the cavity through this path will enter the lower compartmentalized regions of the containment. In particular, a significant amount of debris will enter the containment basement, which comprises only ~6 percent of the containment volume. The TCE model treats this subcompartment room as part of its basic formulation, but it is found that DCH interactions are dominated by the interaction with the blowdown gas rather than any gas initially in the subcompartment. Consequently, this room plays no real role in DCH except to confine debris to an insignificant portion of the containment atmosphere. However, hydrogen produced in the cavity and basement during the DCH event will be pushed to the upper dome through vent paths by blowdown steam.

The seal table room sits over the cavity exit. Experiments have shown that some dispersed debris can reach the upper dome through the seal table room and through vents located above the reactor coolant pumps.

3.5 Scenario V - SBLOCA with Repressurization of the RCS by Operator Intervention

Scenario V represents a core melt accident that progresses with water still present in the lower portions of the core. Such conditions lead to formation of a crust within the core followed by a massive release of melt when the crust fails. Accumulation of core material on the lower head of the RPV causes the lower head to heat up, eventually to the point where its structural strength is so degraded it can longer withstand the stresses induced in the lower head by elevated RCS pressures. Thus, creep rupture of the lower head is the expected failure mechanism. The distinguishing feature of Scenario V is that operator actions are assumed to refill the RPV with water and to fully repressurize the RCS. Analysis of DCH for a repressurized RCS is deemed conservative because we expect operators to depressurize the RCS in a core damage accident.

Table 3.2 summarizes the initial conditions for this scenario. Operator actions are assumed to repressurize the RCS to 16 MPa. Operator intervention refills the RPV with water ($\sim$75 mt) to the hot leg nozzles and quenches any steam remaining in the RCS to near saturation ($\sim$700 K). Recall that a noncondensible gas bubble prevented operators from refilling the entire RCS at TMI-II. The RPV lower head must be heated by accumulated core material to the point that steel loses its strength ($\sim$1000 K), which leads to rupture of the lower head. The initial hole diameter is $\sim$0.40 m (Pilch et al., 1994) because of the likely presence of hot spots and because of stress concentrations associated with the existence and spacing of lower head penetrations. This rupture size is in accordance with working group recommendations (Pilch et al. 1994b). The final hole size ($\sim$0.46 m at the upper bound) is computed with the ablation model Eq. (4.2); however, ablation is not important for the large initial hole sizes associated with rupture of the lower head.

Oxidation of Zr occurs predominantly before significant core degradation, as demonstrated in various calculations. In earlier 2-D MELPROG calculations performed by Kelly et al. (1987), 80 percent of the Zr oxidation occurred prior to formation of a molten pool. SCDAP/RELAP5 calculations (Appendix C) performed specifically for this report confirm these early assessments and show that nearly 100 percent of the hydrogen is produced before core slump. Furthermore, most Zr will be permanently retained in core blockages, with any Zr remaining in the melt existing as a eutectic with the other (mainly oxidic) constituents. Little of this Zr is expected to oxidize during massive relocations. To first order then, Zr oxidation is independent of the core melt progression that follows the main oxidation event; and since oxidation occurs predominantly before molten pool formation, existing systems-level computer codes are technically adequate to assess the range of possible oxidation.

Referring then to SCDAP/RELAP5 calculations (Knudson and Dobbe, 1993; Knudson, 1993, Pilch et al. 1994b), MELPROG/PWR-MOD1 calculations (Kelly et al., 1987), and CORMLT calculations (Denny and Sehgal, 1983), we find that the fraction of Zr oxidized ranges from 20 to 60 percent with a mean around 40 percent. Consistent with NUREG-1150 expert elicitations, the extremes of the distributions are considered unlikely (P $\sim$0.01). The distribution is shown in Figure 3.4. The calculations cited were chosen because of their explicit treatment of recirculating flow patterns in the core.

Consistent with TMI-II, the potential release of molten material to the lower head is controlled by the formation of a hemispherical crucible that excludes only the outer assemblies of the core (Figure 3.5). The outer assemblies are generally not in a severely degraded state because the RPV is flooded. Asymmetries in crucible growth ensure that localized penetration of the outer assembly and the core barrel would most likely occur when the crucible has grown (on average) to the outer assembly.

The maximum volume of such a crucible is ~7 m^3 and it would be filled with a predominantly oxidic melt with a density of ~10,000 kg/m^3. This means that the crucible can hold a maximum of ~70 mt of molten material. The amount of melt released from the crucible is a function of where the crucible fails, with downward and sideward representing the two extremes. Recent studies by Schmidt and Humphries (1994), considering only conduction processes, suggest that bottom failure of a crucible is very unlikely. Natural convection patterns (which produce edge-peaked heat flux distributions) in the molten pool, should they develop, would only reinforce the prediction of side failure of the crucible. The MP-2 experiment (Gasser et al., 1994) tends to confirm that downward failure of an oxidic crust is unlikely, even in the absence of active cooling. To establish an upper bound (P ~0.01) on the UO_2 mass that relocates to the lower plenum, it was assumed that the crucible could fail at the bottom, releasing the entire ~70 mt of material to the lower plenum head.[2]

To fix the composition a little more closely, we note that ~80 - 90 percent of 70 mt (0.85 x 70 ~ 60 mt) is UO_2. As a best estimate, and consistent with TMI-II observations and working group recommendations, side failure of the crucible is expected to release about half of the material (~35 mt total) to the lower head. Likewise, the best estimate on the amount of relocated UO_2 is ~30 mt. On this basis, the distribution for the amount of UO_2 released from the crucible can be constructed as in Figure 3.6.

It should be noted that the amount of UO_2 released from the crucible exceeds the amount of *molten* material available to participate in DCH at the time of vessel failure. First, not all material released from the TMI-II crucible reached the lower head. Some froze between the core former plate and the core barrel and some additional material froze on other structures as it drained into the lower plenum. Second, some molten material will quench and freeze as it flows through the water in the lower plenum. Calculations using the THIRMAL code (Rempe et al., 1993) suggest that as much as ~50 percent might freeze during this process if the water is subcooled. Experiments (Spencer et al., 1994) tend to confirm this number if the water is subcooled, but suggest that only ~10 percent will quench if the water is saturated. Third, some of the molten material accumulated on the lower head will form an upper crust resulting from heat transfer to the overlying water. Finally, some of the molten material will freeze as it transfers heat to the lower head and drives it to failure.

The extent to which these solidified materials persist to vessel rupture is coupled to generation of decay heat within the debris and the time required to heat the vessel to rupture. SCDAP/RELAP5 calculations (Pilch et al. 1994b) indicate that ~20 - 25 mt of material are frozen on the lower head at the time of vessel breach. The SCDAP/RELAP5 calculations are themselves a lower bound since they do not account for water intrusion into the melt through cracks in the overlying crust or gaps along the vessel wall. These additional cooling mechanisms were identified as part of the TMI-II vessel investigation program (Stickler et al., 1993).

As a bound, we consider only melt freezing in the process of heating the lower head to rupture. Boucheron (referenced in Zuber et al., 1991) shows that ~10 - 15 mt of oxide will freeze (with decay heat coupling) in order to heat the lower head to a point where it loses its strength and ruptures. With this in mind, we shift the UO_2 distribution in Figure 3.6 an additional 10 mt to the left. The distribution of *molten* UO_2 at the time of vessel breach is then given by Figure 3.7. The best estimate is then

[2] As an upper bound, NUREG/CR-6075 assumed that 75 percent of the molten material bottled up in the crucible would relocate. The working group recommended that 100 percent relocation should be used as the upper bound.

centered at 20 mt, with an upper bound of 50 mt. We emphasize the conservative nature of this distribution given the additional quenching mechanisms that have been ignored.

The amount of molten ZrO_2 in the melt is controlled by the amount of oxidation that occurs prior to core melt. The amount of molten ZrO_2 can be estimated from

$$M_{ZrO2} = \frac{M_{UO2}(melt)}{M_{UO2}(core)} M^0_{Zr} f_{Zr} \frac{123}{91} \quad . \tag{3.1}$$

This expression assumes that ZrO_2 is contained in the melt in the same fraction to which the core is degraded M_{UO2}(degraded)/M_{UO2}(core) and that ZrO_2 relocates to the lower plenum in the same manner as the UO_2, that is, M_{UO2}(melt)/M_{UO2}(degraded).

The relocation of Zr metal within the core plays a key role in the ultimate formation of core blockages. Upon melting, most of the Zr metal and $(U,Zr)O_2$ relocates downward until it freezes in cooler portions of the core, forming partial or complete blockages, depending on the amount of relocating material. The subsequent melting of UO_2 and ZrO_2 allow molten oxides (at least initially) to settle and refreeze on top of the metallic blockages. In this way, the accumulating melt forms a crucible on top of the metallic blockage. This picture is consistent with SCDAP/RELAP5 calculations. This separation of molten oxides from the blockage, which consists of unoxidized clad and dissolution products, ensures that little metal enters the melt, except possibly through some additional formation of $(U,Zr)O_2$ eutectics, dripping of Zr from fuel stubs above the degraded region, or when the crust fails. However, SCDAP/RELAP5 predicts only negligible additional formation of eutectics and dripping is not predicted even in scenarios in which the core is completely dry. As observed in TMI-II, the crust is expected to fail locally (from inhomogeneities in the crust and asymmetries in crucible growth), carrying only small quantities of metal from the blockage into the lower plenum. The flooded core scenario precludes melting out of the blockage. Thus, little or no Zr is expected in the melt.

To account for uncertainties in eutectic formation and crucible failure (and consistent with the working group recommendations), we assume that the molten Zr mass is proportional to the mass of molten UO_2. Thus, the amount of molten Zr can be computed from

$$M_{Zr} = 0.029\ M_{UO2} \ . \tag{3.2}$$

Consistent with working group recommendations, we assume that ~2 mt of Zr is associated with the upper bound of the UO_2 distribution, which we take as ~70 mt. The ~70 mt of UO_2 is actually associated with Scenario VI; so that for Scenario V, the amount of Zr associated with the upper limit of the UO_2 distribution (~50 mt) is 1.45 mt. In this way, Scenarios V and VI are both treated consistently. This formulation is equivalent to a hypostoichiometry of urania, which can be expressed as UO_{2-x}, where $x \sim 0.17$.

In a wet core scenario such as this, the control rod material will be an initial contributor to the metal blockage in the core and the flooded core scenario precludes melting out of the blockage. Consequently, only trivial quantities (~0 mt) of control rod will be present in the melt at the time of vessel breach.

Melting of upper plenum steel is strongly correlated with failure of the surge line or hot leg nozzle at high system pressures (~8 MPa). Specifically, gas temperatures that are hot enough to melt upper plenum steel (~1700 K) are also hot enough to induce rupture (under pressure) of the hot leg or surge

line. Upper plenum steel is a potential contributor to melt mass and composition only in those scenarios (Scenarios VII and VIII) that proceed to relatively low pressures at the time of vessel breach; and even then, SCDAP/RELAP5 predicts failure of the hot leg. In any case, melting of upper plenum steel cannot be important when operators reflood the RPV as they did in TMI-II. The small amount of steel initially in the core, like cladding and control rod material, is largely retained in core blockages, which cannot melt out in a flooded core scenario.

The melting of lower plenum steel by relocated core material is the only source of molten steel of potential importance in a DCH event. Only thin lower plenum steel (e.g., nozzles) that is submerged in the accumulating core material is assumed to melt. The quantity of submerged steel depends on the volume of core material in the lower plenum and can be computed from

$$M_s = M_{s,LP}\,\frac{\dfrac{M_{UO2}}{\rho_{UO2}} + \dfrac{M_{ZrO2}}{\rho_{ZrO2}} + \dfrac{10x10^3}{\rho_{UO2/ZrO2}} + \dfrac{M_{Zr}}{\rho_{Zr}} + \dfrac{M_{CRM}}{\rho_{CRM}}}{V_{LP}} \qquad (3.3)$$

where the densities (kg/m^3) are $\rho_{UO2} = 10400$, $\rho_{ZrO2} = 5900$, $\rho_{UO2/ZrO2} = 9660$, $\rho_{Zr} = 6500$, and $\rho_{CRM} = 9250$. Note that the quenched 10 mt must be taken into account because it is part of the volume of core material. We note that submerged nozzles at TMI-II did not all melt; consequently, Eq. (3.3) gives a conservative result.

Consideration of natural convection in volumetrically heated pools (Theofanous, 1988; Epstein and Fauske, 1989) indicates that the melt superheat cannot exceed ~200 K under steady state conditions. These assessments are also consistent with SCDAP/RELAP5 analyses. The UO_2/ZrO_2 eutectic melts at about 2800 K, so the maximum temperature on relocation is about 3000 K (~2900 K has been estimated for TMI-II), but some cooling on relocation is expected. Thus, we believe that a conservative bounding value of ~2800 K is appropriate for Scenario V.

MAAP calculations (Henry, 1993) for the Zion plant indicate that the containment pressure at vessel breach is about ~0.25 MPa and the conditions are saturated (~380 K). CONTAIN calculations (Tutu et al., 1990) for the Zion plant produced 0.3 MPa at vessel breach. The most recent CONTAIN calculations (Appendix D), using sources from SCDAP/RELAP5 (Pilch et al. 1994b), show containment pressures in excess of ~0.25 MPa up to and through the period of accumulator discharge. As a result, ~0.25 MPa is chosen as representative for our purposes, which is consistent with NUREG/CR-6075 (Pilch et al., 1994a). Appendix D in NUREG/CR-6075 (Pilch et al., 1994a) concludes that DCH loads are insensitive to reasonable choices of initial containment pressure. The Zion containment is initially at atmospheric pressure, so approximately 0.1 MPa (400 K/314 K) ≈ 0.13 MPa of the pressure at vessel breach is air. Consequently, the initial steam concentration is ~48 percent.

The containment conditions discussed above assume that active containment cooling systems (i.e., fan coolers or sprays) are not operational. We note that fan coolers were operational at TMI-II and that containment conditions were P ~ 0.11 MPa, T ~ 326 K, X_{STM} ~0.035, and X_{H2} ~0.079. Thus, there was little steam in the containment. This situation will also be analyzed in Section 6.

The core-wide oxidation of Zr also controls the amount of preexisting hydrogen that can exist in the containment building at the time of vessel breach. The RCS retains very little of this hydrogen because it is produced early in the accident and most is vented to the containment. This is supported by earlier

SCDAP/RELAP5 calculations (Knudson, 1993) where more than 90 percent of the H_2 was released to the containment. The most recent SCDAP/RELAP5 calculations (Pilch et al. 1994b) indicate that essentially all the in-vesssel produced hydrogen will be released to the containment. Steam/H_2 sources from SCDAP/RELAP5 are sometimes very hot and there is a possibility that hydrogen will burn as it enters the containment. However, recent CONTAIN assessments using SCDAP/RELAP5 sources suggest that this effect is minimal except in the event of a hot leg failure, which precludes a DCH event. Consequently, we assume that all hydrogen produced in-vessel will be released to containment, where it will not burn prior to vessel breach. The moles of preexisting hydrogen in the containment are given by:

$$N_{H2}\ (g \cdot mole) = \frac{2}{0.091} f_Z M^0_{Zr}\ (core) \tag{3.4}$$

or alternatively, a concentration can be specified

$$X_{H2} = \frac{N_{H2}}{N^0_{ATM}} \ . \tag{3.5}$$

We note that at TMI-II there was ~7.9 percent H_2 in the atmosphere and essentially no steam. Since these conditions are in the flammable regime, we cannot guarantee that an ignition source (unless intentional) will burn off hydrogen prior to the DCH event if the flammability limits are exceeded.

3.6 Scenario VI - SBLOCA Under Wet Core Conditions

Table 3.2 also summarizes the initial conditions for Scenario VI. In the absence of any RCS leaks, SCDAP/RELAP5 (Pilch et al. 1994b) predicts surge line failure long before bottom head failure. These cases fully depressurize and are of no interest to DCH. We then seek SBLOCAs of just the right size to depressurize sufficiently that natural circulation degrades to the point that surge line or hot leg failure is not assured. Such an intermediate state was not found. In fact, SCDAP/RELAP5 predicts hot leg failure before core relocation for the full spectrum of SBLOCAs; consequently, Scenario VI can only exist as the consequence of partial operator intervention. For the expected SBLOCAs, SCDAP/RELAP5 predicts depressurization to the ~4 MPa range. However, repressurization spikes due to accumulator injection or melt relocation could sometimes repressurize the RCS to ~8 MPa, which is consistent with NUREG/CR-6075 (Pilch et al., 1994a) assessments. Thus, the ~8 MPa RCS pressure used in NUREG/CR-6075 is adequately bounding, particularly in light of SCDAP/RELAP5 predictions that the hot leg will fail before core relocation. Owing to the similarity in Scenarios V and VI, we emphasize only the differences in RCS temperature, melt mass, and composition, with all other parameters developed in a manner similar to Scenario V.

The RCS gas at the time of vessel breach clearly must be superheated. In conjunction with the pressure and volume, the moles of gas in the RCS can be computed with the RCS temperature. The gas temperatures in each region of the RCS are estimated from SCDAP/RELAP5 output (Pilch et al. 1994b). Given this assessment, a lower bound of ~1000 K is assigned to this scenario.

The potential release of molten material to the lower head is again controlled by the formation and failure of a crucible in the core region. Water occupies only the lowest regions of the core, so radial cooling of a growing crucible is reduced in this situation, and consistent with SCDAP/RELAP5

predictions, the crucible could take on the bounding shape of an upright cylinder as depicted in Figure 3.8. Again, the outer assemblies are largely excluded, although SCDAP/RELAP5 does predict some localized degradation of the outer assemblies.

In the extreme of this geometry, ~80 percent of the core can be contained in the crucible. The upper bound to the UO_2 distribution is then 0.8 x 100 mt ~ 80 mt if the crucible fails on the bottom. Again, the calculations of Schmidt and Humphries (1994) favor side failure before the crucible obtains these extreme proportions. As a best estimate we assume ~40 mt of UO_2 can be released. With this in mind, the distribution of UO_2 released from the crucible can be constructed as indicated in Figure 3.9. Again allowing (~10 mt) only for melt freezing in order to heat the lower head to rupture, the distribution of molten UO_2 at the time of vessel failure is given by Figure 3.10.

The fraction of Zr oxidized remains unchanged. This, in conjunction with the causal relations (Equations 3.1 - 3.4) developed in Section 3.5, defines the remaining melt constituents and atmosphere compositions.

CONTAIN calculations, using sources from SCDAP/RELAP5, show containment pressures in excess of ~0.25 MPa during the period of accumulator discharge. Consistent with the coupled SCDAP/RELAP5 and CONTAIN calculations, we take P^0_{RCS} ~0.25 MPa and T^0_{RCS} ~400 K. The steam concentration in the containment is ~50 percent.

3.7 References

Blanchat, T.K. et al. (April 1994). *Experiments to Investigate Direct Containment Heating Phenomena With Scaled Models of the Surry Nuclear Power Plant*, NUREG/CR-6152, SAND93-2519.

Denny, V.E. and B.R. Sehgal (1983). "Analytical Prediction of Core Heatup/Liquefaction/Slumping," *Proceedings International Meeting on Light Water Reactor Severe Accident Evaluation*, Aug. 28-Sept. 1, Cambridge, MA.

Epstein, M. and H.K. Fauske (1989). "The Three Mile Island Unit 2 Core Relocation -- Heat Transfer Mechanisms," *Nuclear Technology*, Vol. 87, 1021.

Gasser, R.D. et al. (1994 draft). *Late Phase Melt Progression Experiment--MP-2, Results and Analysis*, NUREG/CR-6167, SAND93-3931.

Hammersley, R.J., M. Merilo, and R.E. Henry (Jan. 26-29, 1993). "Experiments to Address Lower Plenum Response Under Severe Accident Conditions," Proceedings of the International Topical Meeting on Probabilistic Safety Assessment (PSA93), Clearwater Beach, FL.

Hanson, D.J. et al. (October 1990). *Depressurization as an Accident Management Strategy to Minimize the Consequence of DCH*, NUREG/CR-5447.

Henry, R.E. (1993). Personal Communications, Fauske & Associates, Inc., Burr Ridge, IL.

Kelly, J.E., R.J. Henninger, and J.F. Dearing (January 1987). *MELPROG-PWT/MODI Analysis of a TMLB' Accident Sequence*, NUREG/CR-4742, SAND86-2175.

Knudson, D.L. (April 1993). Transmittal of SCDAP/RELAP5/MOD3 Results for the Zion Power Station, Private Communication at NRC request.

Knudson, D.L. and C.A. Dobbe (November 1993). *Assessment of the Potential for High Pressure Melt Ejection Resulting from a Surry Station Blackout Transient*, NUREG/CR-5949, EGG-2689.

Marshall, B.W. (1988). *Reactor Safety Research Semi-annual Report July-December 1987*, NUREG/CR-5039, SAND87-2411, Vol. 2, pp. 244.

Pilch, M. and W.W. Tarbell (September 1985). *High Pressure Ejection of Melt from a Reactor Pressure Vessel: The Discharge Phase*, NUREG/CR-4383, SAND85-0012.

Pilch, M. and W.W. Tarbell (July 1986). *Preliminary Calculations on Direct Heating of a Containment Atmosphere by Airborne Core Debris*, NUREG/CR-4455, SAND85-2439.

Pilch, M.M., H. Yan, and T.G. Theofanous (1994a). *The Probability of Containment Failure by Direct Containment Heating in Zion*, NUREG/CR-6075, SAND93-1535.

Pilch, M.M. et al. (1994b). *The Probability of Containment Failure by Direct Containment Heating in Zion*, NUREG/CR-6075, Supplement 1.

Rempe, J.L. et al. (Oct. 1993). *Light Water Reactor Lower Head Failure Analysis*, NUREG/CR-5642, EGG-2618.

Schmidt, R.L. and L.L. Humphries (1994). *Late Phase Melt Progression Scoping and Sensitivity Studies*, Draft, SAND92-2831.

Spencer, B.W. et al. (Feb. 1994). *Fragmentation and Quench Behavior of Corium Melt Streams in Water*, NUREG/CR-6133, ANL-93/32.

Stickler, L.A. et al. (Oct. 1993). *Calculations to Estimate the Margin to Failure in the TMI-2 Vessel*, TMI V(93)EG01.

Theofanous, T.G. (1988). "Some Considerations of Severe Accidents at Loviisa," Report Prepared for Imatron Voima 04, Helsinki, Finland.

Tutu, N.K., T. Ginsberg, and L. Fintrok (1988). "Low Pressure Cutoff for Melt Dispersal from Reactor Cavities," *Fourth Proceedings of Nuclear Thermal Hydraulics*, 29-37.

Tutu, N.K. et al. (January 1990). *Estimation of Containment Pressure Loading Due to Direct Containment Heating for the Zion Plant*, NUREG/CR-5282, BNL-NUREG-52181.

Williams, D.C. (1990). Personal Communications, Sandia National Laboratories, Albuquerque, NM.

Zuber, N. et al. (1991). *An Integrated Structure and Scaling Methodology for Severe Accident Technical Issue Resolution*, NUREG/CR-5809, EFF-2659.

3.8 Nomenclature

f_{Zr} = fraction of Zr oxidized core-wide
M_{CRM} = mass of control rod material in melt
M^0_{Zr} = mass of Zr initially in core
M_s = mass of steel in melt
$M_{s,LP}$ = mass of steel in lower plenum
M_{UO2} = mass of UO_2 in melt
M_{Zr} = mass of Zr in melt
M_{ZrO2} = mass of ZrO_2 in melt
N^0_{ATM} = atmosphere moles
N_{H2} = mole of H_2 produced from Zr oxidation
P^0_{RCS} = initial RCS pressure
T^0_{RCS} = initial RCS temperature
V_{LP} = volume of lower plenum
X_{H2} = H_2 concentration

Greek

ρ_{CRM} = mass density of control rod material
ρ_{UO2} = mass density of UO_2
$\rho_{UO2/ZrO2}$ = mass density of UO_2/ZrO_2 eutectic
ρ_{Zr} = mass density of Zr
ρ_{ZrO2} = mass density of ZrO_2

Table 3.1 Characterization of the Zion plant

Parameter	Value
Thermal power (MW)	3238
Core height (m)	3.66
Core diameter (m)	3.39
Number of fuel assemblies	193
Number of fuel assemblies at edge of core	64
Fuel assembly dimensions (m)	0.214
Number of in-core instruments	58
RCS volume (m^3)	353
Lower head ID (m)	4.2
Lower head thickness (m)	0.14
Core inventory (mt) UO_2 Zr Steel CRM	 98.2 20.0 3.2 3.6
Thin upper plenum steel	20
Thin lower plenum steel	10
Lower plenum volume (m^3)	30
Containment volume (m^3)	76.9×10^3
Subcompartment volume (m^3)	4.83×10^3
Cavity volume (m^3)	190
Containment pressure (MPa)	0.1
Containment temperature (K)	316

Table 3.2 Summary of initial condition quantification

Parameter	SCENARIO	
	V	VI
RCS pressure (MPa)	16	8
RCS temperature (K)	700	1000
RPV water (mt)	75	10
RPV temperature (K)	1000	1000
Initial hole dia. (m)	0.4	0.4
Final hole dia. (m)	Eq. 4.3	Eq. 4.3
Fraction Zr oxidized	Fig. 3.4	Fig. 3.4
UO_2 mass (mt)	Fig. 3.7	Fig. 3.10
Zr mass (mt)	Eq. 3.2	Eq. 3.2
ZrO_2 mass (mt)	Eq. 3.1	Eq. 3.1
Steel mass (mt)	Eq. 3.3	Eq. 3.3
CRM mass (mt)	0.0	0.0
Melt temp. (K)	2800	2800
Fraction of Zr blockage relocated	0.0	0.0
Containment pressure (MPa)	0.25	0.25
Containment temperature (K)	400	400
Preexisting H_2	Eq. 3.4	Eq. 3.4
Autoignition temperature (K)	1100	1100
Melt fraction ejected into cavity	1.0	1.0
Ejected fraction dispersed from cavity	0.85	0.85
Fraction dispersed through gap	0.09	0.09
Fraction dispersed through seal table room and SG vents	0.05	0.05
Coherence ratio	Eq. 4.2	Eq. 4.2

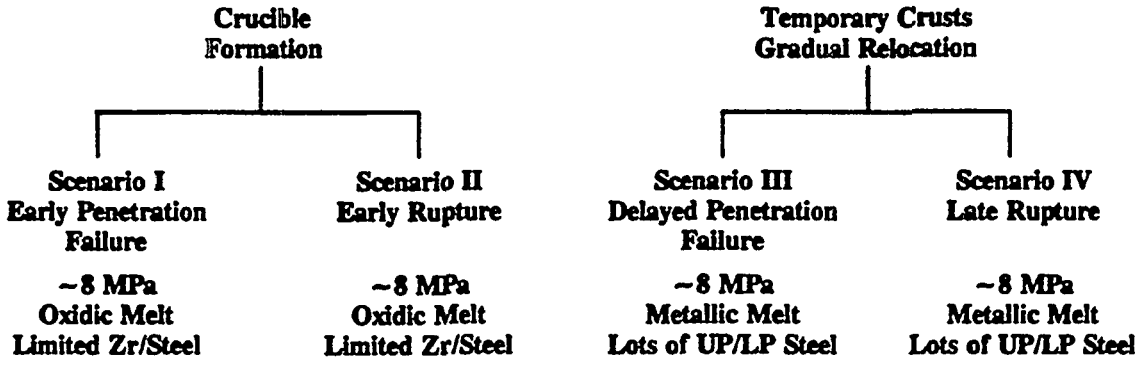

Figure 3.1. Splinter DCH scenarios used in NUREG/CR-6075.

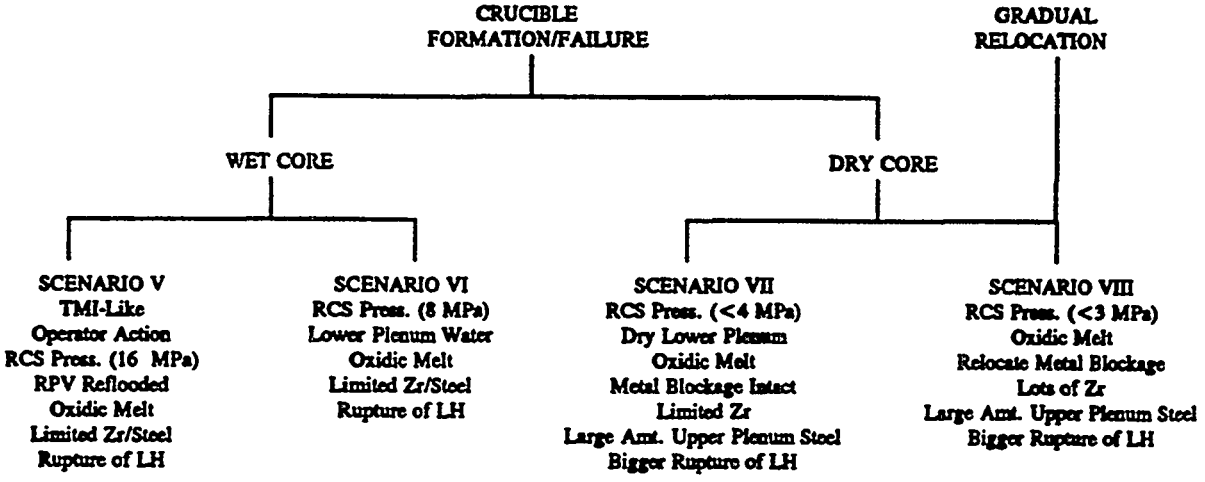

Figure 3.2. Splinter DCH scenarios reflecting working group recommendations.

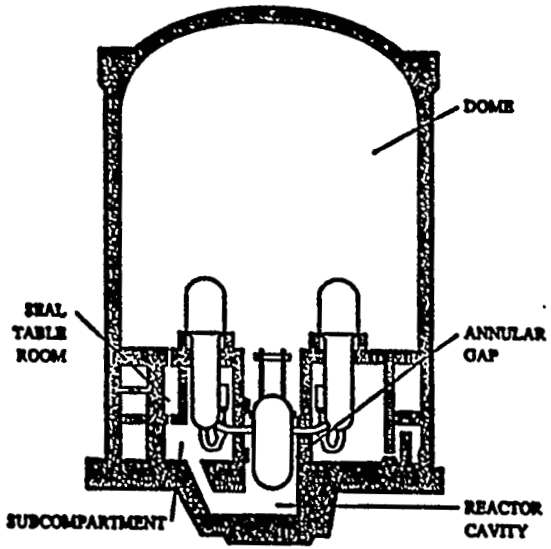

Figure 3.3. Zion nuclear power plant.

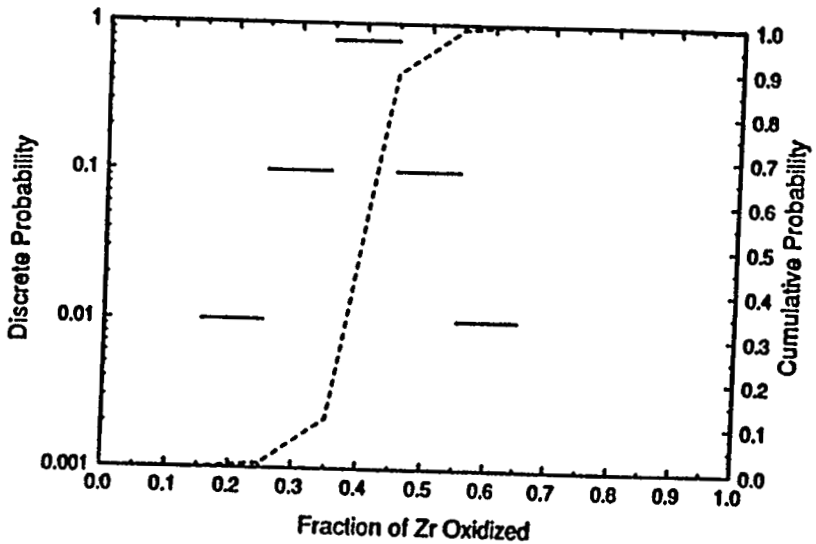

Figure 3.4. Distribution for fraction of Zr oxidized (core-wide) in Scenarios V and VI.

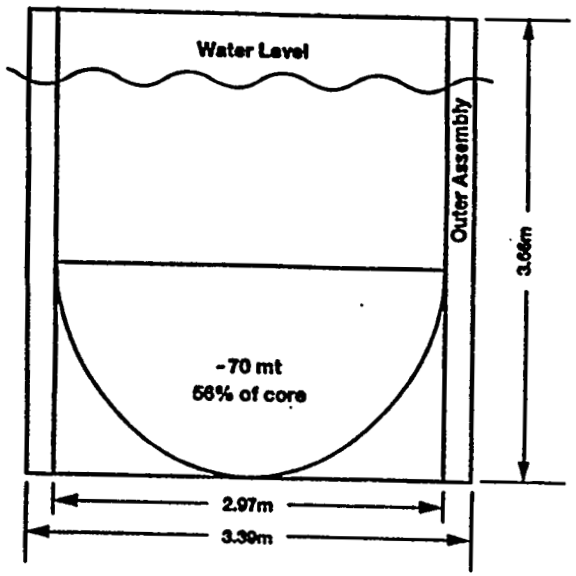

Figure 3.5. Crucible formation in a flooded RPV - Scenario V.

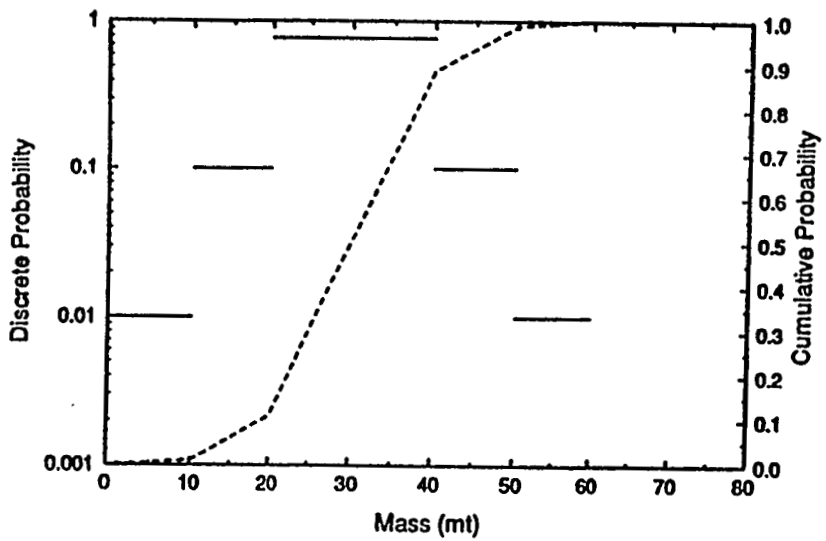

Figure 3.6. Distribution for UO_2 release from the crucible in Scenario V.

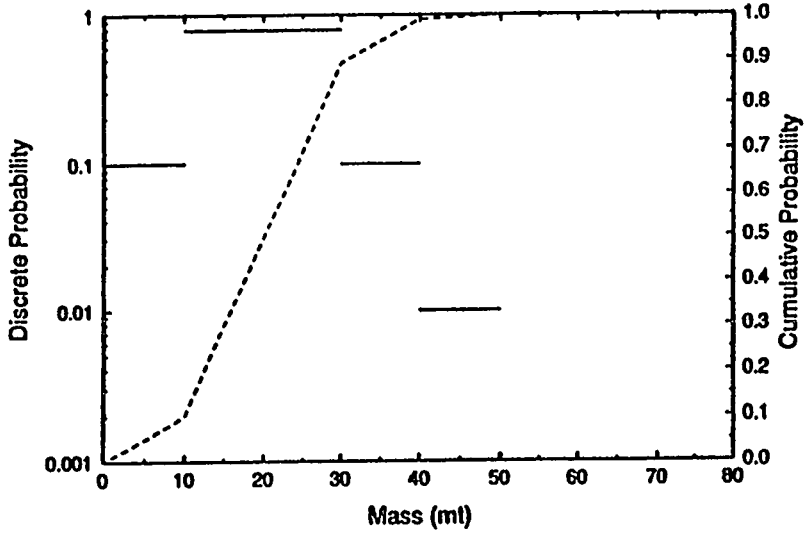

Figure 3.7. Distribution for molten UO_2 in the lower plenum at the time of vessel rupture for Scenario V.

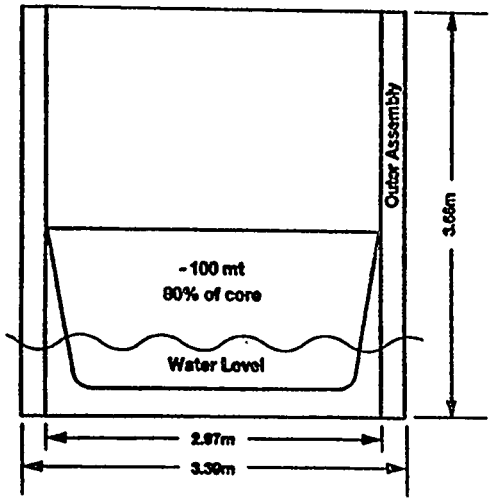

Figure 3.8. Crucible formation in wet core scenario with partial operator intervention - Scenario VI.

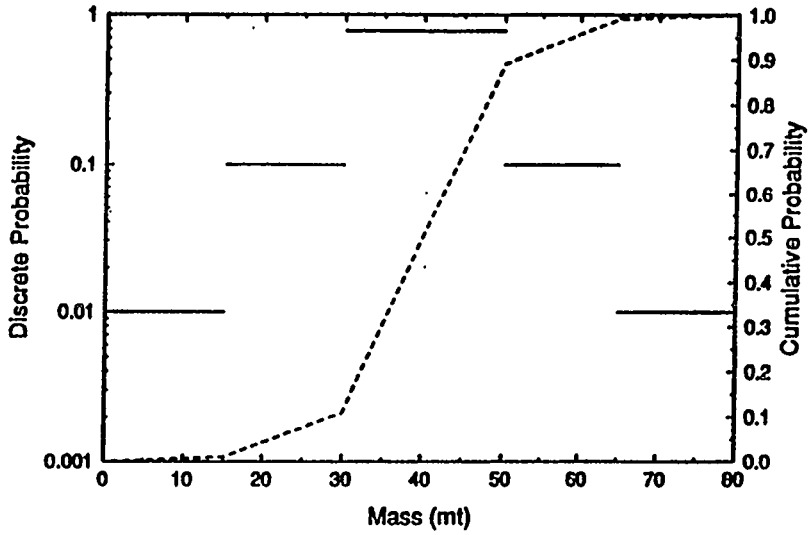

Figure 3.9. Distribution for UO_2 release from the crucible in Scenario VI.

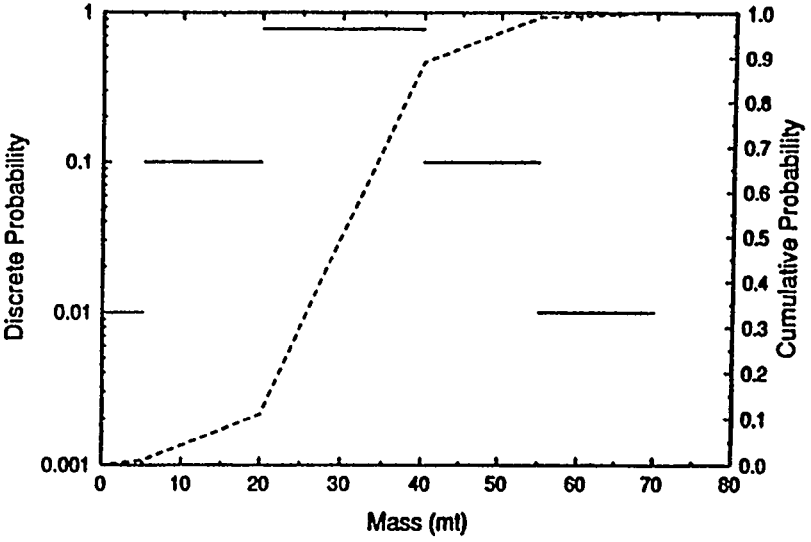

Figure 3.10. Distribution for molten UO_2 in the lower plenum at the time of vessel rupture for Scenario VI.

4.0 QUANTIFICATION OF THE DCH PHENOMENON

The quantification of the DCH phenomenon is carried out by means of a causal relation (CR1) for the containment load. CR1 is fulfilled here by the two-cell equilibrium model, which is developed in Appendix E of NUREG/CR-6075 (Pilch et al., 1994a). In the TCE model, the containment pressurization can be written in terms of the various energy sources (blowdown, latent and sensible heat of debris, oxidation of metallic debris constituents, and hydrogen combustion) that can contribute to DCH,

$$\frac{\Delta P}{P^0_{RCB}} = \eta \frac{\sum \Delta E_i}{U^0(1 + \psi)} , \tag{4.1}$$

where η is an efficiency that accounts for mitigation of DCH due to the compartmentalized geometry of the containment and accounts for mitigation due to the noncoherence of debris dispersal and blowdown processes. Figure 4.1 compares model predictions with the relevant database.

Working group discussions defined two new scenarios (V and VI) which involve significant quantities (~10 - 75 mt) of nearly saturated water that would be coejected with the melt into the reactor cavity. This is a situation that has not been addressed by the existing database; however, the working group expressed an opinion that water in the primary system at vessel breach is expected to mitigate the impact of DCH. We note that a related experiment involving large quantities of cavity water (IET-8B; Allen et al., 1994) suggest that DCH energies went entirely into vaporizing water, pressurizing the containment to levels comparable to containment pressures observed in (essentially) dry DCH tests. RPV water (unlike cavity water) will partially flash to steam during isentropic blowdown. The contribution to containment pressure from this mechanism is less than ~0.075 MPa. The calculations and results presented here are performed by ignoring any impact of coejected water. The margins to failure are high enough for Zion so that the impact of coejected water can be ignored in these analyses; however, it may become necessary to address this phenomenon explicitly in the extrapolation effort.

We note that the Zion reactor cavity will be deeply flooded in certain scenarios. A deeply flooded cavity would submerge the RPV, which may prevent its failure (although this is an area of ongoing research). The SNL/IET-8B experiment indicated that melt ejection into a half full cavity would fully quench the melt reducing the DCH event to a non-threatening steam spike. We expect that more deeply flooded situations would exhibit similar quenching behavior.

Most input parameters in the TCE model are related to initial conditions and material properties. The key modeling parameter in the TCE model is the melt-to-steam coherence ratio. Because the entrainment time is short compared with the blowdown time, molten debris is exposed to a small fraction of the primary system steam during the dispersal process. Since this steam is the medium for carrying the melt energy and the hydrogen produced by steam/metal interactions to the main containment volume, this incoherence is a crucial mitigating factor. With this understanding, it is possible to reduce most of the complexity of cavity phenomena to the coherence ratio ($R_\tau = \tau_e/\tau_b$ in the TCE model). We now focus on the coherence ratio and its quantitative representation in the calculations (i.e., *pdf4*, see Figure 2.1).

Appendix E in NUREG/CR-6075 (Pilch et al., 1994a) develops a correlation for the coherence ratio based on experiment values obtained by a procedure best suited to the TCE model. For this application, the Zion data are best correlated by

$$R_r = 9.661\, f_d \left[\frac{T^0_{RCS}}{T^0_d}\right]^{\frac{1}{4}} \left[C_d \frac{M^0_d}{M^0_g} \frac{A_h V^{\frac{1}{3}}_{cav}}{V_{RCS}}\right]^{\frac{1}{2}} . \tag{4.2}$$

It is assumed that R_r values are distributed normally about the mean given by Equation 4.2 with a relative standard deviation of 29 percent as indicated by the database. The database for the coherence ratio largely overlaps the range of individual parameters that are of interest to reactor applications. However, the database does not include all possible combinations of parameters for each of the potential applications; consequently, the correlation for the coherence ratio is required to fill gaps in the database. It is significant that this process is one of interpolation rather than extrapolation.

Rapid ejection of hot melt through a breach in the RPV leads to ablation, which increases the initial hole size. Appendix J in NUREG/CR-6075 (Pilch et al. 1994a) develops a model for hole ablation. The final hole size can be computed from

$$\frac{\Delta D_h}{D^0_h} = \frac{\frac{\tau_M}{\tau_D}}{1 + 0.6934 \left[\frac{\tau_M}{\tau_D}\right]^{2/3}} \tag{4.3}$$

where

$$\tau_M = \frac{M^0_d}{\dot{M}_d} = \frac{M^0_d}{\rho_d C_d \frac{\pi (D^0_h)^2}{4} \left[\frac{2}{\rho_d}(P^0_{RCS} - P^0_c)\right]^{1/2}} \tag{4.4}$$

is the characteristic time to eject all the melt from the RPV in the absence of ablation and where

$$\tau_D = \frac{D^0_h}{\dot{D}_h} = \frac{D^0_h}{\left[\frac{2\, h_{d,w}\,(T^0_d - T_{mp,w})}{\rho_w \left[C_{p,w}(T_{mp,w} - T_w) + h_{f,w}\right]}\right]} \tag{4.5}$$

is the characteristic time to double the initial hole size by ablation. Ablation does not significantly increase the hole size for rupture of the lower head.

A second phenomenological uncertainty concerns hydrogen combustion during DCH. The working group emphasized that hydrogen combustion should be treated in a manner consistent with the expected conditions in the containment. Pilch et al. (1994b) addresses the issue of jet combustion, entrainment into a jet, stratification, global mixing, and volumetric combustion phenomenology in more detail. Our conclusions regarding hydrogen combustion during DCH events can be summarized as follows:

1. DCH-produced hydrogen (plus some entrainment of H_2 from the preexisting atmosphere) can burn as a jet in the dome and contribute to peak containment pressures. This is consistent with NUREG/CR-6075.

2. Stratification of jet combustion products will occur in the dome, thus impeding the mixing of combustion products with the preexisting atmosphere.

3. Flame propagation is difficult to achieve in a stratified containment atmosphere and the burning process is too slow and inefficient to contribute to peak loads except possibly at the upper end of H_2 distribution. Explicit treatment of this process (not considered in NUREG/CR-6075) to better define and bound uncertainties in hydrogen combustion is included in the supplement analyses. The fraction of the preexisting hydrogen that can burn on DCH time scales and contribute to peak loads is given by

$$f_{pre} = \eta \left[1 - \frac{\dot{E}_{HT}}{\dot{E}_{H2}} \right] . \qquad (4.6)$$

   Even for finite combustion completeness (η), heat transfer to structures can exceed the energy release rate due to the deflagration so that the deflagration does not contribute to peak DCH loads. These enhancements had negligible impact on the predicted containment load distributions for scenarios with ~50 percent steam in the containment atmosphere. Deflagration enhanced DCH loads are predicted for a TMI-like scenario with essentially no steam in the atmosphere, but the increased pressure is offset by the lower initial pressure in the containment.

4. Slow volumetric combustion of preexisting hydrogen does not contribute to peak loads.

5. Sudden volumetric combustion (autoignition) of preexisting hydrogen is essentially impossible in a stratified atmosphere because heating of the containment atmosphere is mixing limited. However, to better bound uncertainties in hydrogen combustion phenomena, we have reduced the autoignition temperature from 1100 K (NUREG/CR-6075) to ~950 K.

6. Combustion initiated by mixing of hot gases with the preexisting atmosphere is too slow to contribute to peak pressure. This is because the mixing (and combustion) time scale is long compared to the heat transfer time scale.

These insights and recommendations are consistent with peer review comments concerning the autoignition temperature and the need to consider partial combustion of the preexisting hydrogen. These recommendations have been factored into the calculated results presented in Section 6.

The amount of material participating in DCH is typically less than the melt mass on the lower head at the time of bottom head failure. The SNL/ANL counterpart experiments exhibited melt retention in both the crucible (scaled to the bottom head of the RPV) and the reactor cavity below the RPV. On average, 93 ± 4.4 percent of the melt was ejected into the cavity in these experiments. A conservative upper bound of 100 percent is used for all the scenarios in the supplement. The SNL/ANL counterpart experiments have also shown that only 76 ± 7.2 percent of the melt in the cavity is dispersed into the containment. We assign a dispersal fraction of 85 percent to all scenarios in order to bound the experiment results. These assessments are fully consistent with NUREG/CR-6075.

The SNL/ANL counterpart experiments have shown that 8.5 percent of the debris dispersed from the cavity through the instrument tunnel (not the annular gap) will enter the upper dome, some through the seal table room (located directly over the cavity exit) and some through vents above the reactor coolant pumps (RCPs). Ishii et al. (1993) report 3 percent transport to the dome in experiments using water. Of this, 2 percent is carried to the dome through the vents above the RCPs surrounding the steam generators located on either side of the cavity exit. The remaining 1 percent, which is carried to the dome through the seal table room, is nonprototypic because of low film velocities at the cavity exit. Minimal transport to the dome is supported by additional scoping experiments using water (FAI, 1991; Ginsberg, 1988). This transport to the dome is accounted for in the TCE evaluations of containment loads. For the evaluations in this supplement to NUREG/CR-6075, we assume 5 percent transport through the seal table room and RCP vents to the upper dome. Such treatment, however, is deemed conservative because the experiments did not model the seal table that blocks access into the seal table room; because the experiments did not model the "penthouse" over the cavity exit (a steel enclosure with blowout panels intended to deny unauthorized personnel access into the cavity); and because the experiments did not model the vast array of in-core instrument guide tubes that may be dispersed from the cavity with the debris (Allen et al., 1990). These assessments are consistent with NUREG/CR-6075.

A second possible flow path to the upper dome is the annular gap around the RPV. The SNL/IET-11 experiment showed that the melt-laden gas will melt the insulation and sweep it from the gap. The SNL/HIPS-8C experiment also simulated the gap without insulation. Analysis of these two experiments indicates that the fraction of dispersed debris that goes through the gap is equivalent to the minimum flow area through the gap divided by the sum of the minimum gap and tunnel flow areas (see Appendix K in NUREG/CR-6075). For Zion, the minimum tunnel flow area is ~ 5.6 m^2 and the minimum gap flow area (at the level of the nozzles) is ~ 0.54 m^2. Consequently, ~ 9 percent of all dispersed debris will be transported through the gap to the dome. This can be added to the ~ 5 percent transport through the seal table room and RCP vents, so that 14 percent of all dispersed debris will enter the dome. These assessments are consistent with NUREG/CR-6075.

4.1 References

Allen, M.D., R.T. Nichols, M. Pilch (1990). *A Demonstration Experiment of Steam-Driven, High-Pressure Melt Ejection: The HIPS-10S Test*, NUREG/CR-5373, SAND89-1135.

Allen, M.D. et al. (May 1994). *Experiments to Investigate Direct Containment Heating Phenomena with Scaled Models of the Zion Nuclear Power Plant in the SURTSEY Test Facility*, NUREG/CR-6044, SAND93-1049.

FAI (1991). *Zion IPE Position Paper on Direct Containment Heating*, FAI/91-18, Submitted to Commonwealth Edison Co.

Ginsberg, T., and N.K. Tutu (1988). *Progress in Understanding Direct Containment Heating Phenomena in Pressurized Light Water Reactors*, BNL-NUREG-41751.

Ishii, M. et al. (March 1993). *Separate Effects Experiments on Phenomena of Direct Containment Heating - Air-Water Simulation Experiments in Zion Geometry*, PU NE-93/1.

Pilch, M.M. et al. (1994b). *The Probability of Containment Failure by Direct Containment Heating in Zion*, NUREG/CR-6075, Supplement 1.

4.2 Nomenclature

A_h	=	breach area in RPV
C_d	=	discharge coefficient (0.6)
$C_{p,w}$	=	heat capacity of RPV steel
D^0_h	=	initial hole diameter
f_d	=	fraction dispersed
$h_{d,w}$	=	ablation heat transfer coefficient
$h_{f,w}$	=	heat of fusion for RPV steel
M^0_d	=	initial melt mass
M^0_g	=	initial RCS gas mass
P^0_c	=	initial containment pressure
P^0_{RCS}	=	initial RCS pressure
R_γ	=	coherence ratio
T^0_d	=	debris temperature
T^0_{RCS}	=	RCS gas temperature
$T_{mp,w}$	=	melting temperature of RPV
T_w	=	temperature of RPV lower head
U^0	=	internal energy of cont. atmos.
V_{cav}	=	cavity volume
V_{RCS}	=	RCS volume

Greek

ΔD_h	=	change in hole diameter
ΔE_i	=	energy contribution of DCH process
ΔP	=	pressure increase due to DCH
ρ_d	=	mass density of debris
ρ_w	=	mass density of RPV steel
σ_{bias}	=	relative bias
σ_{rms}	=	relative (root mean squared) standard deviation
τ_D	=	doubling time for hole size
τ_M	=	melt ejection time
ψ	=	ratio of debris/atm total heat capacity

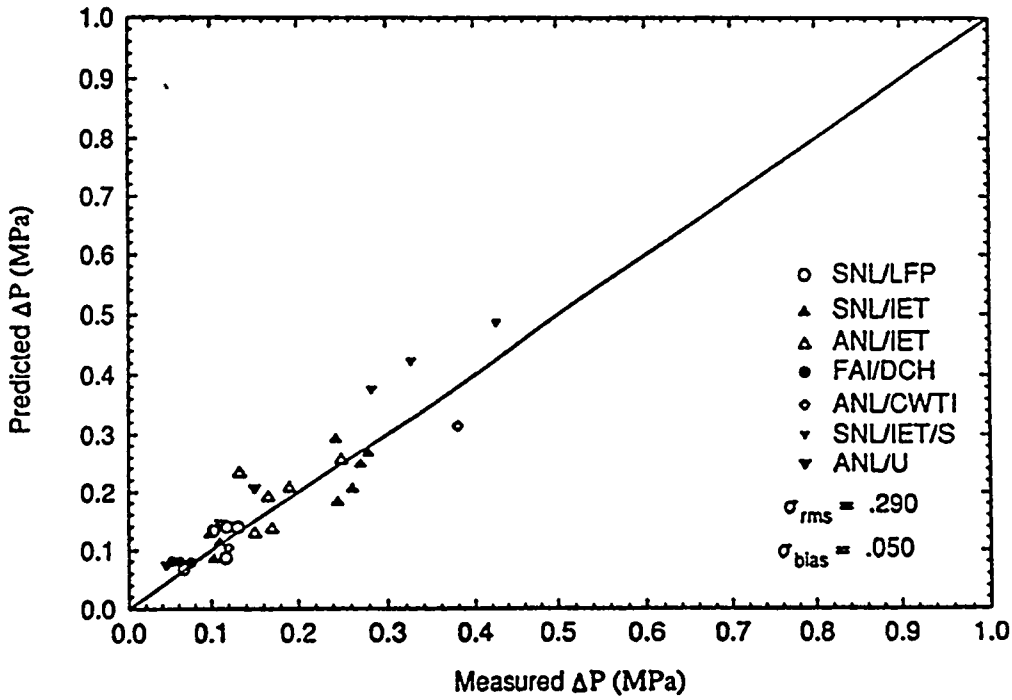

Figure 4.1. Validation of the two-cell equilibrium model against all experiments with compartmentalized geometry.

5.0 QUANTIFICATION OF CONTAINMENT FRAGILITY

This section characterizes the strength of the Zion containment in probabilistic terms. The pressure capacity of the Zion containment is treated as a random variable because of the variability in material properties, of unknown differences between the as-built and design conditions, and modeling uncertainties. The probability that the containment failure pressure is less than a specified pressure is known as the containment overpressure fragility curve.

Fragility curves represent a probabilistic estimate of the capacity of the containment, and as such are not directly derivable from existing data or full-scale experiments. In general, they are derived from a combination of material property data, tolerances in dimensions from drawings, and judgment of the analyst. Analyst judgment is used in determining what level of analysis is required and what failure mechanisms are considered to govern the containment capacity. In addition, analyst judgment is utilized in translating the results of material property tests into a probabilistic estimate of the variability of the various material properties involved. Finally, judgment is exercised in assigning "modeling" uncertainty to the models to characterize the analyst's confidence in the ability of the selected models to represent the actual failure mechanisms involved. Modeling uncertainty could, in principle, be reduced with further analysis or testing. Funding constraints, however, usually require the analyst to exercise his judgment to reflect the uncertainty involved.

In addition, it should be noted that a containment fragility curve is, in fact, a plant- specific entity. It is to be anticipated that the fragility curves derived for a specific containment are sensitive to local design details, tolerances, and the design philosophy used for that particular containment. While it is likely that various submodels representing different local containment failure modes may be applicable to a variety of containments of a given type, it is also true that the combination of failure mechanisms existing in a given containment is unique. Thus, the reader is cautioned against reading any generic applicability into the fragility curves developed for any specific containment.

The Zion containment is a prestressed, post-tensioned concrete cylinder with a shallow-domed roof. The foundation is a reinforced concrete slab. The containment is lined with welded 6.35-mm (0.25-inch) steel plate. The post-tensioning system is composed of 63 dome tendons, 216 vertical tendons, and 555 hoop tendons. The design pressure and temperature are 0.42 MPa-abs and 376 K (47 psig and 217°F). The free volume is about 76.9×10^3 m^3 (2.7 million cubic feet).

The containment fragility curve used for this study (Figure 5.1) is taken from the Zion IPE (1992). This curve reflects the most recent judgment of the licensee of the plant. The Zion IPE did not tabulate values nor did any of the supporting documentation; consequently, the authors of NUREG/CR-6075 digitized the numerical data required for the calculations from the available plot.

Working group members criticized this process as being potentially inaccurate and unphysical in the extreme of very low failure frequencies. Specifically, the digitizing process is subject to human error and is dependent on the quality of the curve that is digitized. In addition, low failure frequencies are obtained only as extrapolations of a theoretical curve which is fit to physically based analytical results defining the middle portions of the fragility curve. Although numerically feasible, excessive extrapolation to low failure frequencies could lose the physical basis on which most of the curve rests.

To address these issues, the NRC requested that Fauske and Associates Inc. (FAI, 1994) provide the actual pressure/frequency pairs making up the IPE fragility curve. Graphic presentation of this

information is shown in Figure 5.1 where it is compared with the fragility curve that was used in NUREG/CR-6075. The coefficient of variation (COV) for the FAI-supplied IPE curve is slightly smaller than the COV of the NUREG/CR-6075 curve. At low failure frequencies, the FAI-supplied curve produces (for a given pressure) lower failure frequencies than the NUREG/CR-6075 approximation. In addition, FAI recommended truncation of the curve at 0.791 MPa (failure frequency ~0.01) because, in their judgment, extrapolation to lower pressures would be unphysical. This can be compared with a threshold (failure frequency = 0.0) of 0.689 MPa used in the NUREG/CR-6075 approximation. The FAI-supplied fragility curve was used in the supplement analyses for Zion.

5.1 References

FAI (1994). Fauske and Associates, Inc., 16W070 West 83rd Street, Burr Ridge, IL, 60521.

Zion IPE (April 1992). *Commonwealth-Edison Zion Station: Individual Plant Evaluation*, NRC Doc. No 9204290315.

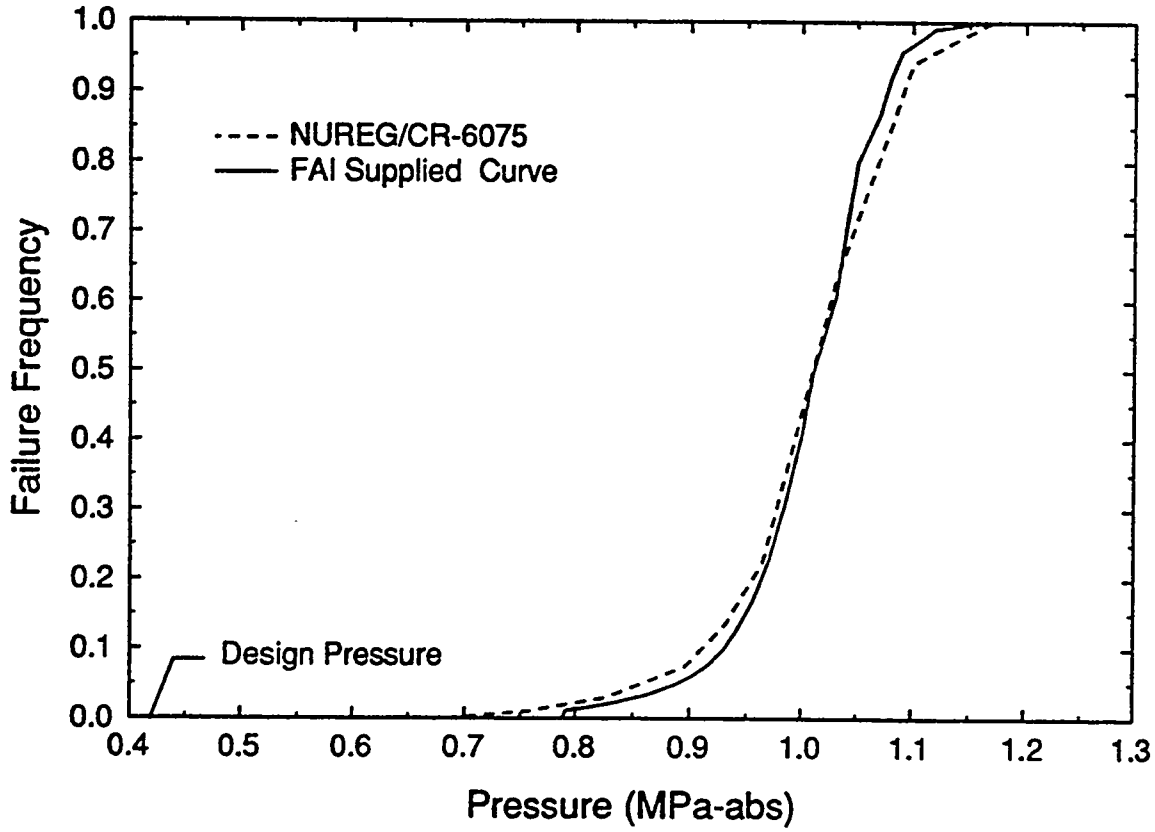

Figure 5.1. Comparison of the FAI-supplied Zion fragility curve with the approximation used in NUREG/CR-6075.

6.0 RESULTS

Each scenario identified in Section 3, supplemented by the respective coherence ratio distribution as discussed in Section 4 and the fragility curve of Section 5, was run through the arithmetic defined by the probabilistic framework of Section 2 to produce probability distributions for the final hole size, coherence ratio, containment temperature, and containment pressure. Finally, the containment failure probability was computed. The calculations were carried out using the computer code TCE/LHS.

Table 6.1 provides a concise summary of the range of the calculated parameter organized as lower bound (LB), best estimate (BE), and upper bound (UB). The distributions for containment pressure (Figure 6.1) are provided so the reader can see firsthand the range over which this key result varies. No intersection of the load distribution with containment fragility is predicted; therefore, we conclude that probability of containment failure by DCH in the Zion plant is negligible for the scenarios analyzed.

Scenario V is an operator intervention accident with features roughly similar to the TMI-II accident. The TMI-II accident differs from Scenario V in that fan coolers were operational so that there was essentially no steam in the reactor building (compared with ~48 percent steam in Scenario V). To examine this scenario, we ran a TMI-like case with containment pressure (0.11 MPa), temperature (326 K), and atmosphere composition (X_{STM} ~ 0.039) consistent with TMI. All other parameters were the same as in Scenario V.

A hydrogen burn occurred at TMI-II when the hydrogen concentration in the dome was ~7.9 percent, which was above the local flammability limit of ~4.0 percent. Consequently, we cannot guarantee an ignition source, which would burn off the hydrogen in the containment prior to the DCH event. Deflagrations, which contribute to peak containment pressure, are expected in this scenario because of the high hydrogen concentration and the low steam concentration in the atmosphere. The deflagration model adequately handles this situation.

Figure 6.1 shows the results of Scenario Va with TMI-like containment conditions. The upper bound pressure is 0.474 MPa, which is well below the threshold (~0.79 MPa) for Zion's containment fragility. The predicted pressure for TMI-like conditions is only slightly higher than for Scenario V, which had much more steam in the building. This is because the increased pressures resulting from the deflagration in the TMI-like case are offset by the lower initial containment pressure.

Table 6.1 Summary of results

Distribution/Result	Scenario V	Scenario VI
	Range *	Range *
Hole size (m)	0.403 LB 0.429 BE 0.459 UB	0.405 LB 0.444 BE 0.483 UB
Coherence ratio	0.021 LB 0.214 BE 0.544 UB	0.057 LB 0.479 BE 1.15 UB
Containment temperature (K)	424 LB 500 BE 572 UB	438 LB 574 BE 675 UB
Containment pressure (MPa)	0.324 LB 0.382 BE 0.437 UB	0.295 LB 0.387 BE 0.455 UB
Containment failure probability	0	0

* LB, lower bound; BE, best estimate; UB, upper bound.

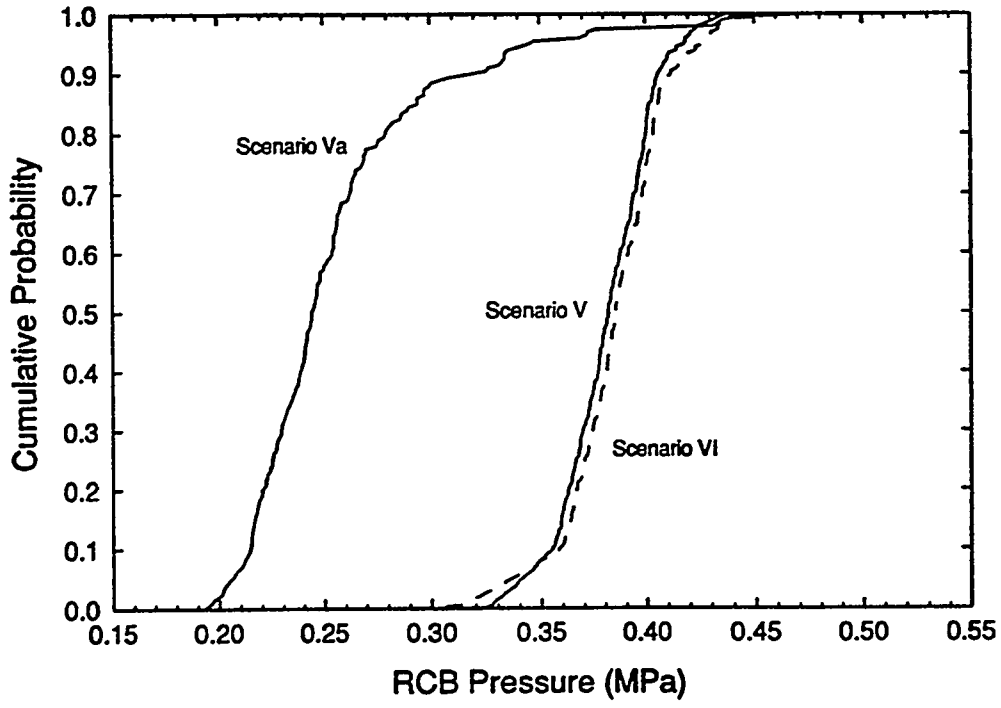

Figure 6.1. Calculated distribution for the containment pressure.

7.0 CONCLUSIONS AND RECOMMENDATIONS

The conclusions listed below are the result of insights from SCDAP/RELAP5 and CONTAIN analyses of three short-term station blackout cases with different leak rates and of analyses of new splinter scenarios defined in working group meetings using the methodology developed in NUREG/CR-6075.

1. SCDAP/RELAP5 was used to analyze a short-term station blackout scenario with three different leak rates: (1) no leaks, (2) 250 gpm per pump, and (3) 480 gpm per pump. In all cases analyzed, the RCS depressurized to roughly containment pressure well before lower head failure. Therefore, the RCS pressure selected in NUREG/CR-6075 (8 MPa) is conservative.

2. SCDAP/RELAP5 analyses indicate that only a very small amount of metallic debris relocates to the lower plenum. In-core metallic blockages tend to stay in place, i.e., they do not relocate to the lower plenum. The amount of metallics in the lower plenum at vessel breach predicted by SCDAP/RELAP5 were $\approx$0.5 mt Zr, $\approx$5 mt lower plenum steel, and no upper plenum steel. These amounts of metallics are less than the distributions initially considered in NUREG/CR-6075.

3. The SCDAP/RELAP5 analyses predict *molten* UO_2 masses at lower head failure that are similar to the original UO_2 melt mass distributions in NUREG/CR-6075.

4. CONTAIN calculations using input from the three cases run with SCDAP/RELAP5 resulted in containment conditions similar to those initially analyzed in NUREG/CR-6075.

5. The new splinter scenarios defined in the working group meetings were analyzed using the methodology developed in NUREG/CR-6075. There were no load-to-strength intersections and thus the containment failure probabilities were zero for the scenarios analyzed. Therefore, the primary conclusion of this supplement to NUREG/CR-6075 is that DCH is not a problem for Zion.

Deliberate Ignition of Hydrogen-Air-Steam Mixtures Under Conditions of Rapidly Condensing Steam*

Thomas K. Blanchat and Douglas W. Stamps
Sandia National Laboratories
Albuquerque, NM 87185

Abstract

A series of experiments was conducted to determine hydrogen combustion behavior under conditions of rapidly condensing steam caused by water sprays. Experiments were conducted in the Surtsey facility under conditions that were nearly prototypical of those that would be expected in a severe accident in the CE System 80+ containment. Mixtures were initially nonflammable owing to dilution by steam. The mixtures were ignited by thermal glow plugs when they became flammable after sufficient steam was removed by condensation caused by water sprays. No detonations or accelerated flame propagation was observed in the Surtsey facility. The combustion mode observed for prototypical mixtures was characterized by multiple deflagrations with relatively small pressure rises. The thermal glow plugs were effective in burning hydrogen safely by igniting the gases as the mixtures became marginally flammable.

Program Description

A hydrogen-air-steam mixture that is initially nonflammable because it is diluted by steam may be rendered flammable when water sprays cause rapid condensation of steam. If the condensation process is sufficiently rapid, then a question arises as to whether a detonation could occur in such mixtures if thermal glow plugs were active during the operation of the water sprays. Detonations may be possible if: (1) ignition by thermal glow plugs is delayed until enough steam has been removed to make the mixture intrinsically detonable or (2) ignition occurs early near the flammability limits but the time for the entire mixture to burn is so long that any unburned mixture can be made intrinsically detonable by the action of the water sprays before the burn is complete.

The effect of water sprays on the combustion of hydrogen-air-steam mixtures was investigated in a 2048-m^3 spherical vessel [1]. Unlike the scenario described earlier, however, the water sprays and the combustible gas mixture were at the same temperature so that there was no steam condensation. Since the steam concentration did not change, the chemical sensitivity of the flammable mixture was fixed prior to activation of the igniters. Similar experiments were also performed using water sprays with hydrogen-air mixtures [2-3]. In all of these experiments, the mixtures were flammable prior to the activation of the igniters. These experiments did not address the issue of mixtures becoming more reactive by the removal of steam during the same time the igniters were active. This issue was investigated for hydrogen-air-steam mixtures without water sprays in a 17-liter quasi-spherical vessel [4]. By using water-cooled coils around the outside of the vessel, the steam condensation time could be reduced to less than 10 minutes. However, the condensation

* A final report will be published under SAND94-1676

time can be significantly shorter when the steam is condensed by internal water sprays. Furthermore, the effect of the spray-generated turbulence on the combustion behavior was not investigated. The purpose of the current set of experiments was to investigate the combustion behavior of initially nonflammable mixtures that rapidly became flammable through the action of water sprays when the igniters were activated the entire time.

Depending on the location and the conditions under which hydrogen is released into the containment, the hydrogen may be either stratified or well mixed. Under stratified conditions, the hydrogen is concentrated in the upper part of the containment. If steam were absent, these mixtures would be more sensitive to detonation than if the same quantity of hydrogen was released at a low location and well mixed throughout the entire containment. For the CE System 80+ containment, the well-mixed concentration of hydrogen is approximately 13.6% on a dry basis assuming 100% metal-water reaction of the active cladding [5]. If all of this hydrogen accumulates above the operating deck, the average concentration in that region would be approximately 19.3%.The ability of water sprays to mix stratified mixtures is an important factor in determining the resulting combustion mode.

The combustion mode that results when initially nonflammable mixtures are rendered flammable by rapid condensation of steam caused by water sprays depends on the competition among three processes: (1) the removal of steam by water sprays, (2) the consumption of hydrogen by chemical reaction, and (3) for stratified mixtures, the mixing of hydrogen by water sprays. If the time required to remove steam is slow relative to the other time scales, then combustion can be initiated as the mixture first becomes flammable and a slowly propagating flame will result.

The objectives of this program were developed to cover the conditions of well-mixed or stratified hydrogen-air-steam mixtures prior to the operation of the water sprays. The program objectives were to determine: (1) if detonations or other forms of energetic combustion are possible when originally nonflammable mixtures are rendered flammable by water sprays, (2) the effectiveness of water sprays in mixing hydrogen-stratified mixtures, and (3) the effect of hydrogen stratification on the maximum combustion pressure.

Experiments were conducted in the modified Surtsey vessel shown in Figure 1. The vessel is a domed cylinder 3.6 m in diameter, 5.6 m high, and has a volume of 59.1 m^3. The vessel was instrumented with pressure transducers, gas grab sample bottles, and thermocouple rakes. A deliberate ignition system was installed which was composed of actual plant igniters (GM AC7G thermal glow plugs) at three locations. The effect of igniter location was tested using one or more igniters at these three locations. For most tests, the target water spray mass flux was scaled to one spray train at runout flow in the CE System 80+ standard design. Owing to the characteristics of the nozzle used in the tests, the spray mass flux was the same as for the CE System 80+ but the volumetric condensation rate for the tests was 1.63 times the CE System 80+ rate. For these tests, a full-cone spray nozzle (Lechler model 461.148 having a 120° nozzle spray angle) was installed at the top of the dome. When the water spray mass flux was scaled to the operation of both CE System 80+ independent spray trains, a high-capacity full-cone spray nozzle (Lechler model 461.206 having a 90°nozzle spray angle) was installed at the top of the dome.

The experiments were conducted under conditions scaled to be nearly prototypical of those expected in hypothetical severe accidents in the CE System 80+ containment. The quantities that were scaled included the spray mass flux and hydrogen mass flow rates for stratified tests.

Eleven combustion tests were conducted: 8 were well-mixed tests and 3 were stratified tests. The main parameters that were tested in these experiments were hydrogen concentration, steam condensation rate as determined by the water spray flow rate, and igniter location. Table 1 shows the initial conditions of the tests; Table 2 shows the conditions at the first burn; and Table 3 shows the conditions at the end of the tests after the water sprays were turned off. The first test, HIT-1, was performed to collect data and test gas grab sample techniques and igniter design. After test HIT-1, the time to purge gas sample lines was increased and gas sample data were considered more accurate. Results for HIT-7 were influenced by a small leak (~0.003 MPa/hr) in the facility since the test was conducted over a long (23-hour) period. This leak did not have any significant influence on the results of the other tests because the test times were short (~20 minutes). Results from HIT-7 were analyzed assuming the steam was saturated and that the remaining constituents leaked out in proportion to their composition in the facility. A steam condensation experiment was conducted before the combustion tests to determine the steam condensation rate owed to water sprays in a nonflammable helium-air-steam mixture. Three mixing tests were performed at ambient conditions to determine if stratified conditions could be created for the combustion tests and to measure the mixing time with the water sprays.

Results

In all of the combustion tests, one or more relatively slow deflagrations were recorded: no detonations were observed. The combustion behavior of the well-mixed tests can be loosely categorized into one of two types: (1) multiple deflagrations with relatively small pressure rises and (2) a single deflagration with a pressure rise greater than those observed in the multiple deflagrations but lower than the theoretical adiabatic constant volume value. The combustion behavior of the stratified tests was similar to that of the well-mixed tests. This is because the sprays were very effective in mixing the hydrogen before the mixture became flammable.

For mixture compositions that have directionally dependent flammability limits, multiple deflagrations with relatively small pressure rises were observed. Within the range of experimental uncertainty, these mixtures lie below the "nose" of the flammability limits curve. Combustion behavior was not dependent on igniter location. Since these mixtures have directionally dependent flammability limits (upward, horizontal, and downward propagation criteria), the upward propagation criterion was satisfied first and a marginal burn occurred. The combustion was incomplete and the pressure rise was small (1-10 kPa). The partial burn temporarily inerted the mixture, which did not become flammable again until additional steam was condensed by the water sprays. The partial burns were responsible for the multiple deflagrations. This behavior is illustrated in Figure 2, which shows the results of HIT-2, a well-mixed test with 13.5% hydrogen on a dry basis. The pressure rises were larger (up to 30 kPa) in the well-mixed tests with 13.5% hydrogen on a dry basis but having larger steam condensation rates. Multiple deflagrations, however, were again observed. This behavior is illustrated in Figure 3, which shows the results of

HIT-10, a well-mixed test with 13.5% hydrogen on a dry basis and a spray flow rate nominally twice that of test HIT-2.

For mixture compositions that do not have directionally dependent flammability limits, a single deflagration with a pressure rise greater than those observed in the multiple deflagrations but lower than the theoretical adiabatic constant volume value was observed. Once these mixtures were rendered flammable by the water sprays, the flame could propagate in all directions, which consumed nearly all of the hydrogen. This resulted in a single deflagration with a pressure rise closer to the adiabatic constant volume value. The increase in pressure did not achieve peak theoretical values because of heat losses from the relatively slow deflagration near the flammability limit. This behavior is illustrated in Figure 4, which shows the results of HIT-3, a well-mixed test with a stoichiometric mixture (29.5% hydrogen on a dry basis).

Three stratified tests were conducted with different spray flow rates but all having a near stoichiometric mixture in the upper part of the vessel. The target condition for each test was a stratified mixture with 29.5% hydrogen (dry basis) in the upper part of the vessel but having an equivalent well-mixed concentration of 13.5% hydrogen (dry basis). Different spray flow rates were used: 0.0 kg/second, 1.35 kg/second, and 3.17 kg/second. The behavior of these tests was similar to that of the comparable well-mixed tests with 13.5% hydrogen. This behavior is illustrated in Figure 5, which shows the results of HIT-6, a stratified test with approximately 24% hydrogen (dry basis) in the upper part of the vessel. The sprays rapidly mixed the hydrogen in the vessel prior to the mixture becoming flammable so that the hydrogen was essentially uniform at 13.5% (dry basis) before ignition.

The mixing time was determined using newly developed hydrogen microsensors which provided spatially resolved real-time continuous output of hydrogen concentrations. A stratified test was conducted at ambient conditions with approximately 19% hydrogen (dry basis) in the upper part of the vessel. The hydrogen was mixed by water sprays with a flow rate of 1.58 kg/second. As shown in Figure 6, the mixing time was approximately 20 seconds for most of the vessel and less than 1 minute even for the lowest levels.

Conclusions

Multiple deflagrations with relatively small pressure rises or single deflagrations with pressure rises greater than those observed in the multiple deflagrations but lower than the theoretical adiabatic constant volume values were observed when igniters were on during the entire experiment. This is because ignition occurred near the flammability limit and the combustion time was fast relative to the time to condense steam. Detonations or other forms of energetic combustion (flame acceleration or DDT) were not observed in hydrogen-air-steam mixtures which were initially nonflammable owing to steam dilution but were rendered flammable by steam condensation caused by water sprays. Mixtures with hydrogen concentrations above approximately 24% (dry basis) exhibited a single deflagration with a relatively large pressure rise. Such mixtures cannot exist under globally well-mixed conditions in the CE System 80+ or AP600 containments. These containments will have approximately 13.5% hydrogen (dry basis) on a well-mixed basis, assuming a 100% metal-water reaction of the active cladding. If the hydrogen accumulates above the operat-

ing deck level, the concentration could be as high as 19.3% (dry basis) on a well-mixed basis above the floor of the operating deck. Mixtures having 19.3% hydrogen or less exhibited multiple deflagrations with relatively small pressure rises.

Thermal glow plugs functioned as intended: ignition occurred near the flammability limits. The flammability limits for mixtures with water sprays were similar to previously obtained flammability limits for quiescent hydrogen-air-steam mixtures.

Stratified mixtures and well-mixed mixtures yielded similar combustion pressures owing to the effective mixing by water sprays. Stratified hydrogen in the Surtsey vessel was made essentially uniform by the water sprays in less than 1 minute.

Acknowledgments

The support and guidance of the NRC program managers A. Malliakos and C. Tinkler is gratefully acknowledged. The authors would like to thank M. Allen and M. Pilch for their useful discussions during the experimental program. The authors express their gratitude to R. Nichols, the lead mechanical engineer and site manager; to M. Oliver and T. Thornhill, who were the electronics and instrumentation engineers; to J. Ross and T. Covert, who were the mechanical technicians; and R. Hudgens and J. Andazola, who provided technical support during the experiments.

This work was supported by the U.S. Nuclear Regulatory Commission and performed at Sandia National Laboratories, which is operated for the U. S. Department of Energy under Contract No. DE-AC04-94AL85000.

References

1. Ratzel, A. C., "Data Analyses for Nevada Test Site (NTS) Premixed Combustion Tests," Sandia National Laboratories, SAND85-0135, NUREG/CR-4138, Albuquerque, NM, May 1985.
2. Nelson, L. S., "Behavior of Hydrogen Igniters During Operation of Water Sprays in Containment," presented at the Twelfth Water Reactor Safety Research Information Meeting, Gaithersburg, MD, October 22-26, 1983, published as an NRC report, NUREG/CP-0058, Vol. 3, pp. 371-387, Washington, DC, January 1985.
3. Shebeko, Yu. N., Tsarichenko, S. G., Eremenko, O. Ya., Keller, V. D., and Trunev, A. V., "Combustion of Lean Hydrogen-Air Mixtures in an Atomized Water Spray," *Fizika Goreniya i Vzryva*, Vol. 26, No. 4, pp. 58-61, July-August 1990.
4. Tamm, H., Ungurian, M., and Kumar, R. K., "Effectiveness of Thermal Ignition Devices in Rich Hydrogen-Air-Steam Mixtures," Electric Power Research Institute report, EPRI NP-5254, AECL-8363, Palo Alto, CA, July 1987.
5. CESSAR Design Certification, Appendix 19.11K, "Assessment of the System 80+ Hydrogen Mitigation System for Application in a Severe Accident Environment," ABB-Combustion, Combustion Engineering, Inc., Windsor Locks, CT, October 1993.

Table 1. Initial conditions in the HIT experiments

		HIT-1	HIT-2	HIT-3	HIT-4	HIT-5	HIT-6	HIT-7	HIT-8	HIT-9	HIT-10	HIT-11
Test Date		1-12-94	1-20-94	1-26-94	2-9-94	2-16-94	2-21-94	4-13-94	4-20-94	5-2-94	5-9-94	5-16-94
Hydrogen condition wm - well-mixed, strat - stratified		wm	wm	wm	wm	wm	strat	strat	wm	wm	wm	strat
Vessel pressure (MPa)		0.4642	0.4351	0.4686	0.4386	0.4142	0.4552	0.3279	0.4608	0.4040	0.3926	0.4427
Vessel gas temperature (K)		416	413	412	419	411	416	401	408	405	406	411
Vessel gas moles (g • moles)		7934	7491	8083	7443	7162	7771	5808	8030	7098	6882	7653
Gas composition *	Steam	69.3	67.6	63.1	67.5	63.7	68.9	58.0	65.4	62.9	64.5	67.5
(mole%)	Air	26.5	28.0	25.9	28.1	29.3	26.9	36.2	26.1	29.6	30.6	28.0
Wet basis-well mixed	H_2	4.2	4.4	11.0	4.4	7.0	4.2	5.8	8.5	7.5	4.9	4.5
Gas composition	Steam	00.0	00.0	00.0	00.0	00.0	00.0	00.0	00.0	00.0	00.0	00.0
(mole%)	Air	86.5	86.4	70.3	86.5	80.7	86.5	86.2	75.3	79.8	86.2	86.3
Dry basis-well mixed	H_2	13.5	13.6	29.7	13.5	19.3	13.5	13.8	24.7	20.2	13.8	13.7
Spray nozzle model #461		.148	.148	.148	.148	.148	.148	.148	.148	.206	.206	.206
Spray drop Sauter mean diameter (μm)		850	850	850	850	850	850	n/a	850	500	500	500
Spray flow rate (kg/s)		1.68	1.35	1.61	1.63	1.46	1.48	n/a	1.45	3.15	3.17	3.15
Spray temperature (K)		332	296	291	289	298	292	n/a	289	289	291	291
Igniter temperature (K)		1072	1307	1202	1204	1204	1224	1290	1235	1268	1251	1240
Igniter location (m) (from floor/from wall)		4.5/1.8 3.7/0.5 1.1/1.8	3.1/1.8 0.6/1.8	3.1/1.8 0.6/1.8	3.1/0.5	3.1/0.5	3.1/0.5	4.5/1.8	3.7/0.5	3.7/0.5	3.7/0.5	3.7/0.5
Surtsey vessel volume (m^3)		59.1										

* Gas concentrations at initial conditions are based on the calculated amounts of air and hydrogen gases that were added; steam concentrations are based on the ideal gas law.

Table 2. Conditions at the first burn in the HIT experiments.

		HIT-1	HIT-2	HIT-3	HIT-4	HIT-5	HIT-6	HIT-7	HIT-8	HIT-9	HIT-10	HIT-11
Elapsed time (min)		10.9	9.3	3.0	4.3	5.5	5.8	8.8 hr	4.0	0.8	1.3	1.7
Vessel pressure (MPa)		0.2321	0.2517	0.3382	0.2700	0.2436	0.2682	0.1886	0.3302	0.3093	0.2645	0.2697
Vessel gas temperature (K)		384	385	400	391	386	388	367	391	391	384	385
Vessel gas moles (g • moles)		4299	4650	6018	4904	4486	4909	3653	5997	5625	4899	4976
Gas composition • (mole%) Wet basis-well mixed	Steam	43.4	47.9	50.5	50.7	42.0	50.8	43.3	53.7	53.3	50.2	50.0
	N_2	38.3	35.2	27.2	33.3	36.5	33.2	38.2	27.2	29.1	33.5	33.7
	O_2	10.3	9.4	7.3	8.9	9.8	8.9	10.3	7.3	7.8	9.0	9.0
	H_2	7.7	7.1	14.7	6.7	11.2	6.7	7.8	11.4	9.4	6.9	6.8
Gas composition (mole%) Dry basis-well mixed	Steam	00.0	00.0	00.0	00.0	00.0	00.0	00.0	00.0	00.0	00.0	00.0
	N_2	67.5	67.5	54.9	67.5	63.0	67.5	67.3	58.8	62.3	67.3	67.4
	O_2	18.1	18.1	14.7	18.1	16.9	18.1	18.1	15.8	16.7	18.1	18.1
	H_2	13.5	13.6	29.7	13.5	19.3	13.5	13.8	24.7	20.2	13.8	13.7
Pressure increase at 1st burn (kPa)		1	3	604	10	11	13	7	515	164	29	29
Temperature increase at 1st burn (K)		1	1	447	5	7	4	3	457	122	15	10

• Gas concentrations at first burn conditions are based on the assumption that the noncondensible gas moles remain constant at their initial values and steam concentrations are based on the ideal gas law. Wet basis concentrations for HIT-7 were estimated assuming saturated steam conditions. For details on HIT-7, see text in Program Description section. Gas compositions do not include trace air constituents.

Table 3. Final conditions in the HIT experiments

		HIT-1	HIT-2	HIT-3	HIT-4	HIT-5	HIT-6	HIT-7	HIT-8	HIT-9	HIT-10	HIT-11
Elapsed time (min)		18.9	23.7	18.2	19.3	21.5	20.9	23 (hr)	21.7	9.8	9.8	9.9
Vessel pressure (MPa)		0.1697	0.1227	0.1270	0.1261	0.1080	0.1225	0.1083	0.1728	0.1150	0.1198	0.1212
Vessel gas temperature (K)		371	338	346	326	344	338	333	365	330	331	334
Vessel gas moles (g • moles)		3248	2583	2611	2750	2232	2580	2313	3366	2478	2575	2579
Gas composition * (mole%) Wet basis-well mixed	Steam	27.9	17.3	32.3	23.4	6.9	19.2	18.4	47.2	21.1	18.2	17.0
	N_2	50.6	63.3	62.7	59.4	73.4	63.2	57.8	48.5	66.1	63.8	65.0
	O_2	12.3	14.4	3.9	12.3	12.3	12.8	14.8	3.9	9.4	13.3	13.1
	H_2	6.8+	4.2	0.3	3.8	5.4	4.0	7.8+	0.2	3.5	3.9	3.9
Gas composition (mole%) Dry basis-well mixed	Steam	00.0	00.0	00.0	00.0	0.0	00.0	00.0	00.0	00.0	00.0	00.0
	N_2	70.2	76.5	92.5	77.6	78.8	78.2	70.8	91.8	83.8	77.9	78.3
	O_2	17.1	17.4	5.7	16.0	13.3	15.8	18.1	7.4	12.0	16.3	15.7
	H_2	9.4	5.1	0.5	5.0	5.9	5.0	9.5	0.3	4.4	4.7	4.7
Oxygen burned (g • moles)		41	67	338	102	163	107	21	306	205	97	112
Hydrogen burned (g • moles)		109	220	876	223	381	223	117	680	446	236	239
2 x O_2 burned / H_2 burned		0.75	0.61	0.77	0.91	0.86	0.96	0.37	0.90	0.92	0.82	0.94

* Gas concentrations at final conditions are based on the gas grab sample results; steam concentrations are based on the ideal gas law. Gas compositions in HIT-1 were influenced by the gas sample procedure (see text in Program Description section for more details). Wet basis concentrations for HIT-7 were estimated assuming saturated steam conditions. Gas compositions do not include trace air constituents.

\+ Burns were still occurring at the end of the test. They were confined to a region near the igniter and, for HIT-7 in particular, there was no mixing caused by water sprays.

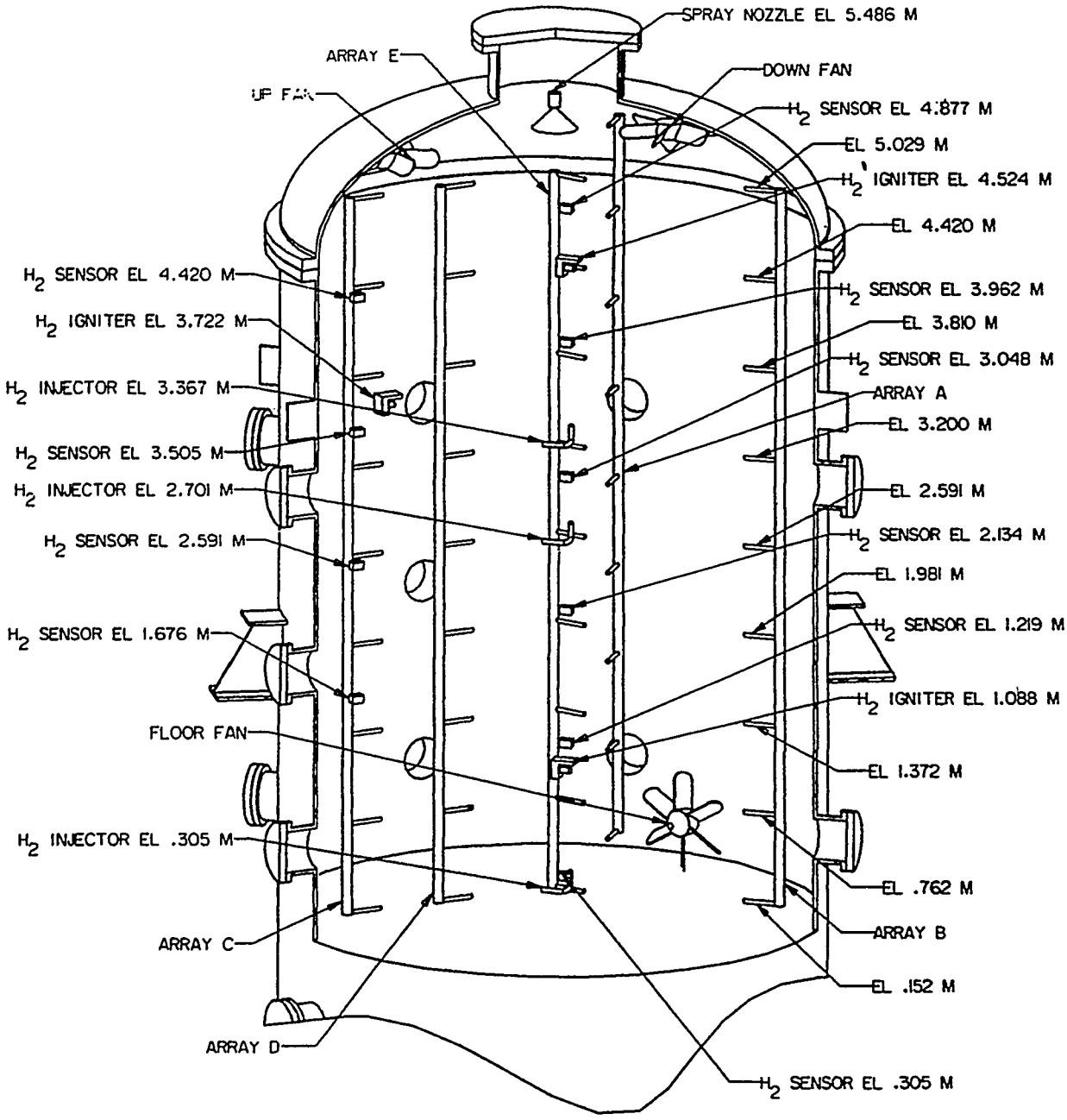

Figure 1. Schematic of the Surtsey facility.

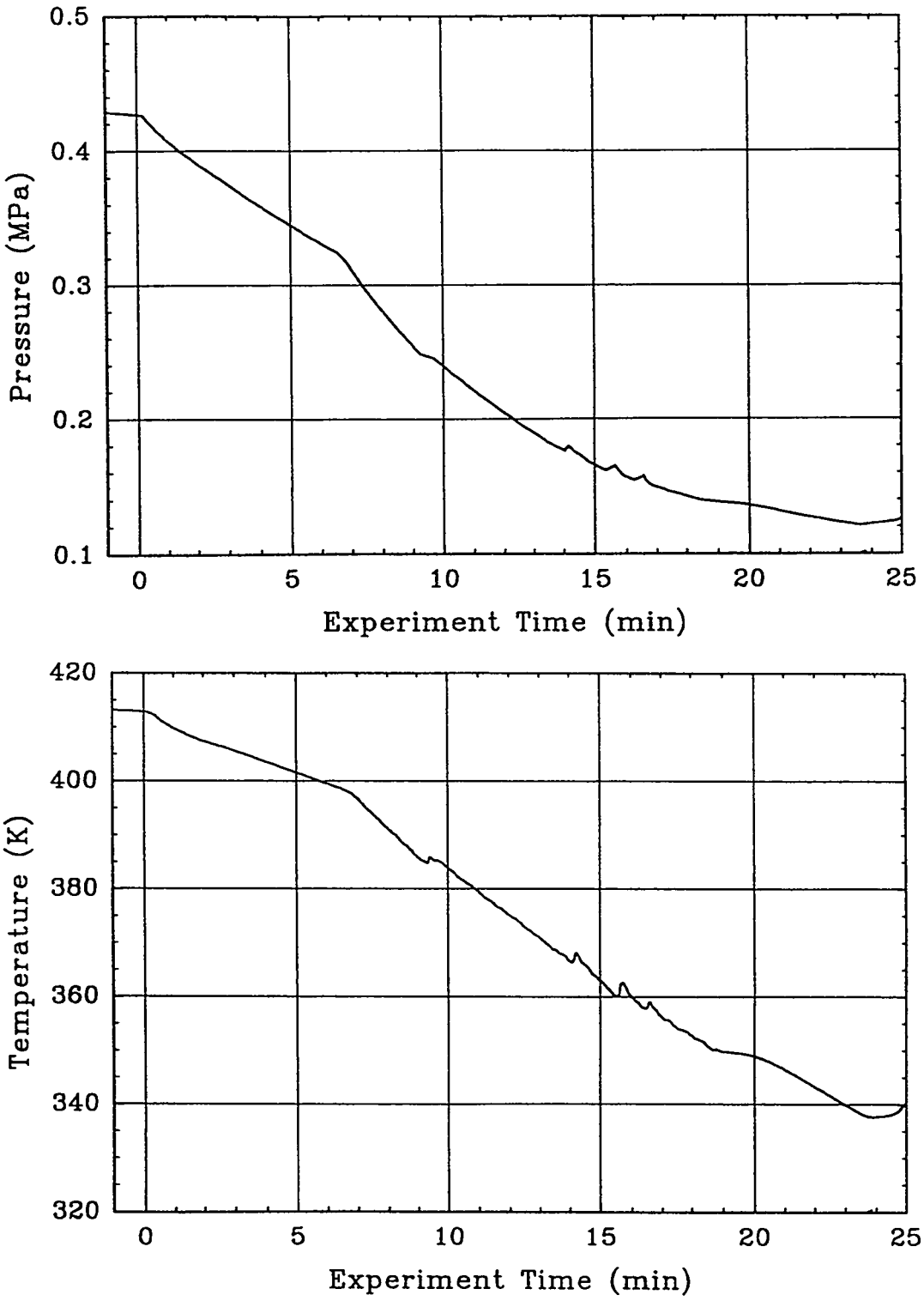

Figure 2. Pressure and temperature from experiment HIT-2.

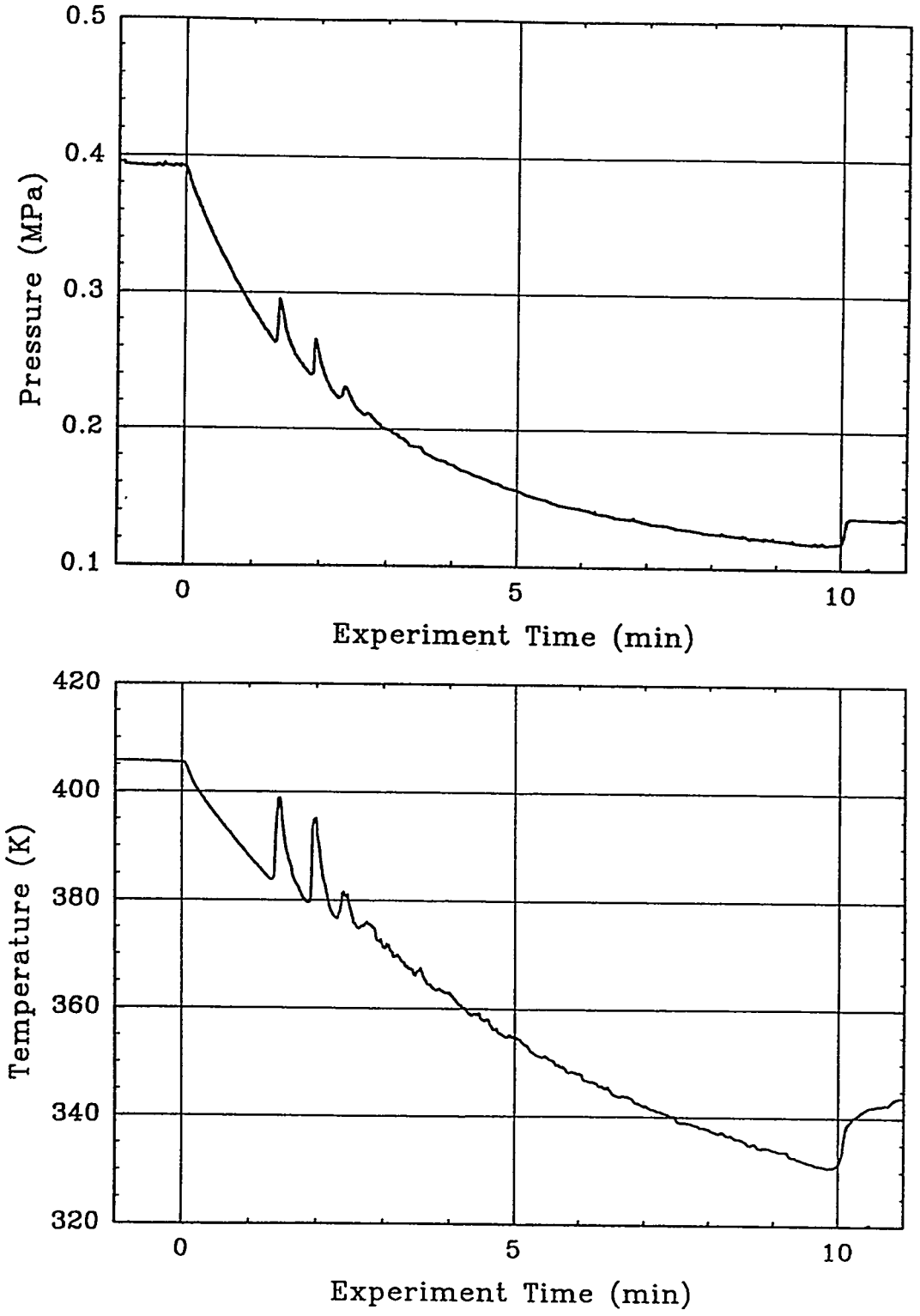

Figure 3. Pressure and temperature from experiment HIT-10.

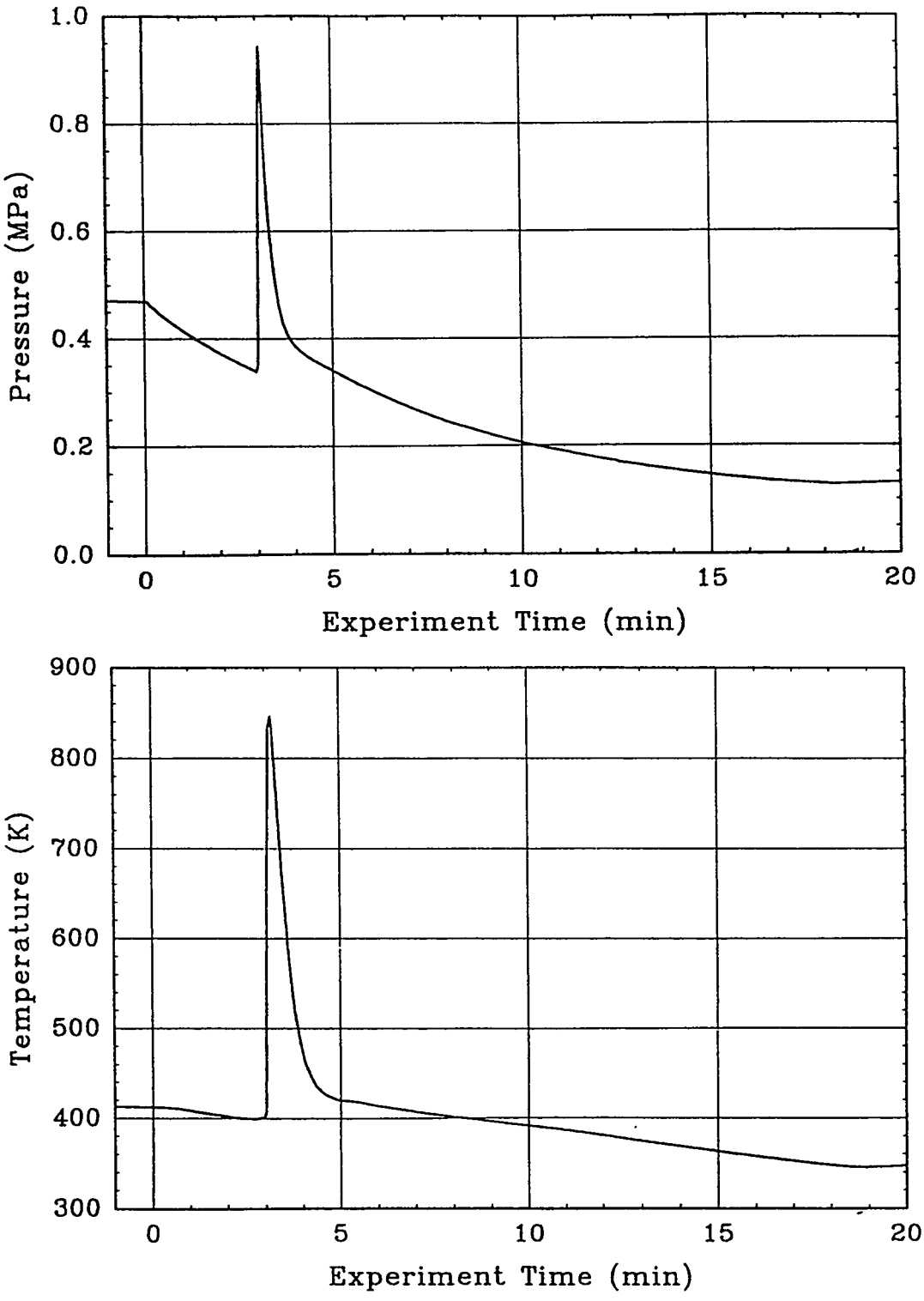

Figure 4. Pressure and temperature from experiment HIT-3.

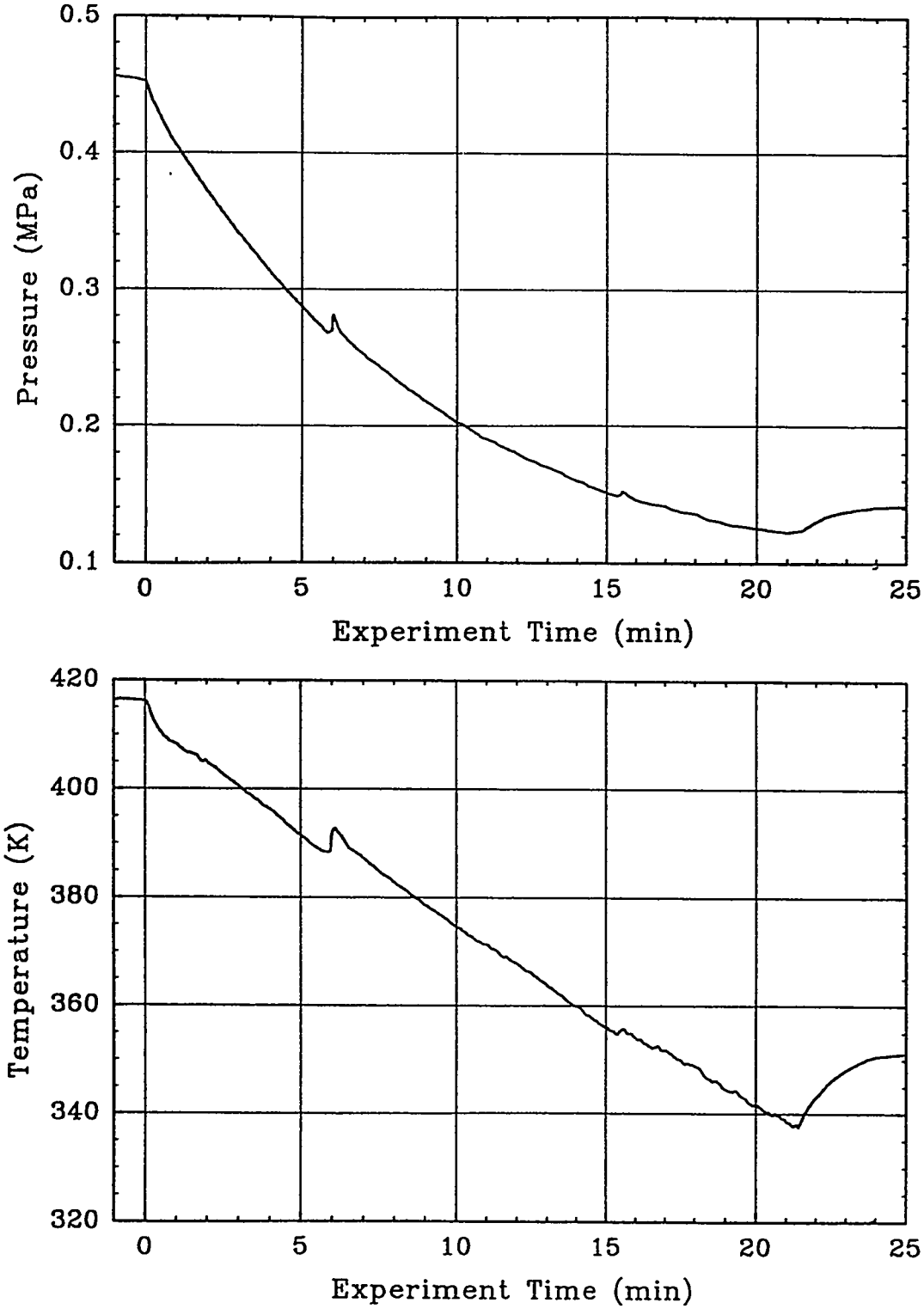

Figure 5. Pressure and temperature from experiment HIT-6.

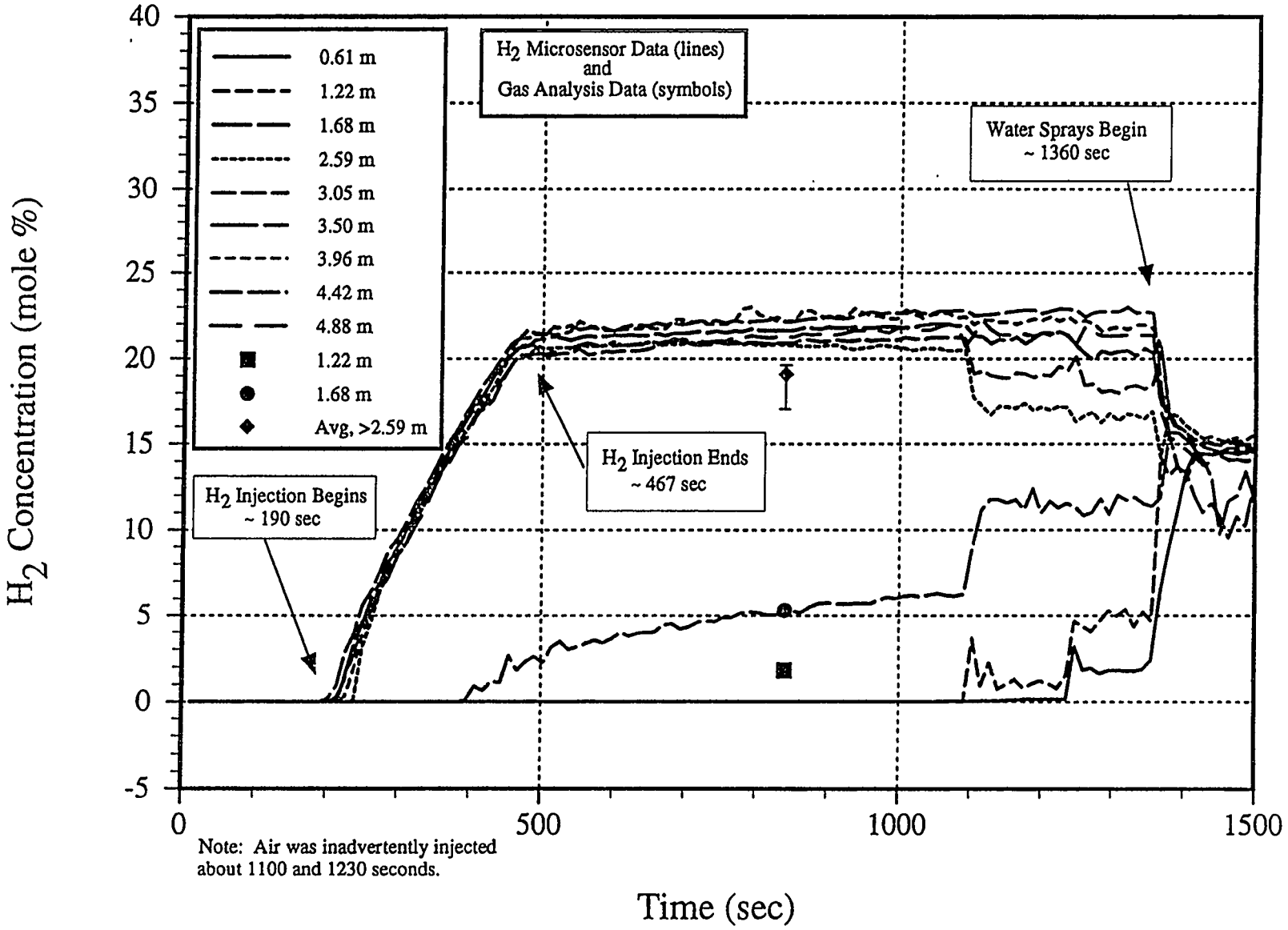

Figure 6. Hydrogen concentration measurements by microsensors and gas grab samples in a stratification test.

Recent Developments in the CONTAIN Project

R. O. Griffith, K. K. Murata, D. C. Williams,
J. Tills, and E. L. Tadios

Sandia National Laboratories
Albuquerque, NM

CONTAIN is a detailed computer code developed by Sandia National Laboratories under USNRC sponsorship to provide integrated analysis of containment phenomena. Several targeted applications have been identified for CONTAIN, including LWR plant analysis, experimental analysis, and detailed analysis for specific technical issues. New LWR modeling capabilities have been added to CONTAIN, including models for direct containment heating (DCH) and core-concrete interactions (CORCON-Mod3). Models for advanced light water reactor (ALWR) applications have also been added, including an independent mass and energy accounting/tracking system, a duct channel quasi-steady flow model, a water film tracking model, improved heat transfer modeling, improved modeling of water pools, and a new hybrid flow solver. Several assessment and validation studies have been performed using SNL DCH experiments, NUPEC hydrogen mixing and distribution experiments, GE sponsored separate effects tests, and the Westinghouse Large Scale Tests (LST). CONTAIN also recently completed the peer review process, in which the review committee found that in general CONTAIN fulfills its design objectives and target applications. CONTAIN 1.2 was recently released as a beta test version.

CONTAIN is a detailed computer code developed by Sandia National Laboratories under USNRC sponsorship to provide integrated analysis of containment phenomena [MUR89]. CONTAIN provides the knowledgeable analyst with the capability to predict nuclear reactor containment loads, radiological source terms, and associated physical phenomena under accident conditions. The purpose of CONTAIN is to provide the USNRC with predictive containment analysis capabilities, and to serve as a tool which can be used to provide technical information in support of

regulatory decisions. CONTAIN represents a balance between the current state of the art in containment phenomenological understanding, simpler parametric models, insight from experimental data, and capabilities to explore phenomenological uncertainties.

Several targeted applications have been identified for CONTAIN. These include LWR plant analysis to predict the physical, chemical, and radiological conditions inside containment, and fission product releases as a result of containment failure; experimental analysis and support for containment related severe accident experimental programs such as HDR, LACE, NTS, and Surtsey, and analysis of relevant ALWR test programs such as the Westinghouse large scale tests (LSTs); selected detailed analysis for specific technical issues such as hydrogen combustion and transport, build-up of non-condensible gases, DCH, and accident management evaluations; MELCOR benchmarking, assessment, and model test bed; and ALWR design basis and severe accident evaluation.

A number of new LWR modeling capabilities have been added to CONTAIN over the last year. Models for direct containment heating (DCH) have been extended to include reactor pressure vessel (RPV) and cavity phenomena. Models for RPV phenomena describe the vessel blowdown, gas blowthrough, exit quality, and hole ablation. Models for cavity and containment phenomena describe the entrainment rate, entrained fraction, debris transport with gas slip, multifield debris particle size, forced convection heat transfer, gas side and drop side mass transfer, multiple species chemical reactions, Kutateladze Criterion debris trapping, and interaction of gases with non-airborne debris (NAD). The DCH models in CONTAIN have been assessed against a large experimental data base [WIL94]. Improved models for core-concrete interactions were incorporated as part of CORCON-Mod3, and include improved models for axial/radial heat transfer to concrete, the addition of a model for condensed phase chemical reactions between the metallic and oxidic phases, the addition of models for interlayer mixing due to entrainment and stratification due to settling of entrained droplets, the inclusion of the VANESA model as a subroutine of CORCON, and improved coolant heat transfer models. The CORCON-Mod3 models have been validated through comparison to experimental results [BRO93].

Several models for advanced light water reactor (ALWR) applications have also been added to the code. An independent mass and energy accounting/tracking system has been implemented to ensure that mass and energy are conserved during calculations. A duct channel quasi-steady flow model has also been implemented to speed up long-term code calculations for plant designs such as the AP600, which includes a passive containment cooling system

(PCCS). If conditions in the channel are approaching steady-state, the quasi-steady flow model overcomes Courant limitations on the flow timestep by replacing channel cells with fixed flow boundary conditions for most of the system timestep if the replaced cell meets user specified tolerances for the rate of change on quantities such as the gas volume, temperature, and mass. The quasi-steady model also uses the mass and energy accounting system to ensure that conservation errors remain at acceptable levels.

A film tracking model has also been incorporated to aid in representing important features of passive containment designs. Although the model was motivated by the AP600 PCCS, it can also be used to represent dynamic laminar and turbulent water films on inner containment structures, and allows an arbitrary network of structures to represent striping, dry patches, and runoff diversion. However, the resolution of dryout or striping is limited to the size of the specified structures. The fall of droplets through the containment atmosphere is not explicitly represented, but dripping to the sump is captured.

A number of improvements have been made to the heat transfer models, including the incorporation of generalized heat transfer correlations with user-specifiable constants. Heat transfer models now incorporate improved Grashoff number and boundary layer properties which include composition effects more consistently. Previously, the gas temperature and composition effects were not handled consistently. In the improved models, the gas temperature is now consistently evaluated as the average of the wall and bulk gas temperatures, and evaporation and condensation effects are consistently incorporated when evaluating the gas composition. Enhanced output is now provided for describing heat transfer, including Nu and Sh numbers and a complete reporting of the amounts of energy transferred by various heat transfer mechanisms.

A series of major architectural changes were made to the code to improve the modeling of liquid water in cells, particularly the modeling of deep water pools. Water pools of arbitrary height are now modeled, including water-solid cells, along with gas and liquid flow in flowpaths and multiple vents. A new hybrid flow solver has also been developed to permit improved modeling of gas stratification and mixing. Control volume codes tend to overpredict mixing, and the hybrid flow solver is intended to improve CONTAIN's ability to capture these effects.

A number of assessment and validation studies and plant calculations have also been performed. A large assessment effort for the new DCH models in the code has been completed, with comparisons against a large experimental database consisting of

the Limited Flight Path (LFP), Wet Cavity (WC), and Integral Effects Tests (IET) experiments conducted at SNL [WIL94]. In addition, the ISP-29 and ISP-35 standard problems as well as the NUPEC M-7-1, M-4-3, M-5-5, M-8-1, and M-8-2 tests were modeled with CONTAIN. The comparisons against the NUPEC hydrogen mixing and distribution experiments used different nodalization schemes, analysis methods, and flow solvers. The study also assessed the treatment of sprays, and a general procedure was recommended for lumped parameter code analysis of problems dominated by sprays [STA94].

In support of ALWR applications, an assessment of the SBWR PCCS was performed. Heat transfer correlations were assessed for the GE sponsored separate effects tests, and the film flow model was used to mechanistically capture PCCS effects. The CONTAIN PCCS model was compared to experiments for single tube condensers. Additional assessment and verification of the film model will be provided by the assessment of the GE scaled experiments GIRAFFE, PUMA, PANDA, and PANTHERS. The GIRAFFE assessment is nearly complete, with the other facilities to be modeled in 1995. In addition, four of the Westinghouse Large Scale Tests (LST) for the AP600 were modeled with CONTAIN, and additional analyses are planned to be completed in early 1995. A number of DCH plant calculations have been performed in support of DCH issue resolution, along with preliminary scoping analyses for the SBWR and AP600 plants. The hybrid flow solver will also be assessed against various experimental programs.

Perhaps the most important recent activity in the CONTAIN project has been the peer review, which was a necessary and critical step in the evolution of the code. The CONTAIN Peer Review had several major objectives. First, the committee determined whether CONTAIN met its design objectives and target applications. Next, given the code's design objectives and targeted applications, the committee assessed individual CONTAIN models for adequacy, assessed the integrated CONTAIN code for adequacy, and assessed documented code applications. The assessment of individual CONTAIN models and the integrated CONTAIN code corresponded to a "bottom-up" and "top-down" type review methodology. Finally, the committee made recommendations for changes and improvements to CONTAIN and its documentation.

A number of specific observations were made by the committee. In general, CONTAIN fulfills its design objectives and target applications. CONTAIN demonstrated the capability to cross the boundary between severe accident and DBA space. In addition, the code demonstrated good transportability and was numerically robust. Models of key physical processes are present and functioning as a whole. Finally, CONTAIN was found potentially adequate for ALWR applications, although the committee noted that development and assessment activities for

ALWR applications are still in progress.

The committee also noted several specific areas where improvements could be made. The first area for improvement is in the treatment of momentum driven flows and buoyancy driven flows at the extremes of each type of flow. The second is in melt water interactions, including fuel-coolant interactions (FCI), DCH with water, and debris coolability. Currently, CONTAIN has no models for either FCI or debris coolability. CONTAIN does have the ability to treat water in DCH scenarios, but the models are partially parametric and have not been fully validated. The final area for improvement noted by the committee is that the aerosol physics models no longer reflect the state of the art. The final peer review report has been completed, and is awaiting publication.

CONTAIN 1.2 was recently released as a beta test version for general LWR applications, and in support of the RELAP/CONTAIN link project for ALWR applications. This version of the code includes all of the recent modeling improvements described above, including the DCH models, CORCON-Mod3, mass and energy accounting, water film tracking, quasi-steady duct flow, heat transfer improvements, and water pool modeling improvements. In addition, the CONTAIN 1.2 code manual is under final preparation and review, and will be released in 1995. CONTAIN 1.2 represents a mature, assessed, peer-reviewed LWR containment analysis tool ready for application to problems and issues identified by the NRC. One envisioned application of this code will be to audit vendor severe accident and DBA calculations. Ongoing model development to allow the code to capture other unique aspects of the ALWR designs and assessments against ALWR experiments will be discussed with the NRC, and CONTAIN 1.2 will be used to support the ALWR certification process.

REFERENCES

BRO93 Brockmann, J. E., and Griffith, R. O., "CORCON-Mod3 Validation Study", SAND93-0295, Sandia National Laboratories, Albuquerque, NM, 1995.

MUR89 Murata, K. K., et. al, "User's Manual for CONTAIN 1.1: A Computer Code for Severe Nuclear Reactor Accident Containment Analysis", NUREG/CR-5026, SAND87-2309, Sandia National Laboratories, Albuquerque, NM, 1989.

STA94 Stamps, D. W., "CONTAIN Assessment of the NUPEC Mixing Experiments", SAND94-2880, Sandia National Laboratories, Albuquerque, NM, 1994.

WIL94 Williams, D. C., Griffith, R. O., Tadios, E., and Washington, K. E., "Assessment of the CONTAIN Direct Containment Heating (DCH) Model", SAND94-1174, Sandia National Laboratories, Albuquerque, NM, to be published.

INITIAL HYDROGEN DETONATION DATA FROM THE HIGH-TEMPERATURE COMBUSTION FACILITY*

T. Ginsberg, G. Ciccarelli, J. Boccio, J. Curtiss, C. Economos,
C. Finfrock, L. Gerlach, J. Jahelka, M. Kinoshita[1], K. Sato[1], and H. Tagawa[1]

Brookhaven National Laboratory
Department of Advanced Technology
Upton, NY 11973

ABSTRACT

The Brookhaven National Laboratory High-Temperature Combustion Facility (HTCF) is described and data from initial hydrogen detonation experiments are presented. The HTCF was designed to provide a capability to investigate detonation phenomena characteristics of hydrogen-air-steam mixtures at initial temperature up to 700K and initial pressures up to 3 atmospheres. The Large Detonation Vessel used in the experiments is a 27-cm diameter, 21.3-m long, stainless steel detonation tube, constructed in modular 3.05-m long sections. The vessel can be heated to 700K in five hours to a uniformity of $\pm$14K.

The initial phase of the inherent detonability experimental program is described. Detonations are initiated in hydrogen-air test mixtures using an oxyacetylene gas driver system, together with a high-voltage capacitor discharge system. Test gases thus far tested are hydrogen-air mixtures at one atmosphere initial pressure and temperatures in the range 300K-650K. Measurements of detonation pressure, wave speed, and detonation cell size have been made.

The data from these experiments are consistent with the earlier SSDA test results. The HTCF results confirm the conclusion from the SSDA program that the effect of gas temperature is to decrease the cell size and, therefore, to increase the sensitivity of mixtures to undergo detonation. The data from the larger HTCF test vessel, however, also demonstrates that the effect of increased scale is to extend the range of detonable mixtures to lower concentration.

Additional data will be obtained at several temperatures for leaner mixtures of hydrogen and air, and the detonability limits will be obtained. Experiments with steam will be conducted at 400K-650K, with steam content up to about 50 percent steam. Cell size data will be obtained for high-temperature mixtures in order to provide an extensive database for assessment of the Zel'dovich-von Neumann-Doring (ZND) model for detonation cell size.

---

*This work was performed under the auspices of the U.S. Nuclear Regulatory Commission. This program is a joint research project involving the U.S. Nuclear Regulatory Commission and the Nuclear Power Engineering Corporation (NUPEC) of Japan.

[1]Visiting Research Engineer, Nuclear Power Engineering Corporation, Tokyo, Japan.

1. INTRODUCTION

The Brookhaven National Laboratory (BNL) High-Temperature Combustion Facility (HTCF) has been constructed as an experimental research tool for the purpose of characterizing the influence of elevated gas mixture temperature on:

- the inherent sensitivity of hydrogen-air-steam mixtures to undergo detonation,
- the potential for deflagration-to-detonation transition (DDT),
- the phenomena of hot jet initiation of detonation, and
- detonation transmission.

Previously, high-temperature gaseous detonability data, and their interpretation, have been presented from experiments conducted in the BNL Small-Scale Development Apparatus (SSDA) [1]. The HTCF was designed to study a broader range of test conditions, which required a larger-scale test apparatus than the SSDA. Table 1 shows the range of conditions which are the focus of the experimental program in the HTCF.

This paper presents a description of the facility, describes the initial inherent detonability test program, and presents results of experiments performed as part of the initial phase of the planned testing program.

2. DESCRIPTION OF THE HTCF

The HTCF consists of the Large Detonation Vessel (LDV) and the support facilities which are required in order to perform high-temperature detonations within the test vessel. Figure 1 is a schematic of the HTCF site, and Figure 2 is a photographic view of the site. Table 2 summarizes the essential systems of the facility and the work that was performed in order to support the experimental effort. The schematic diagram shows the LDV located within a 10-ft diameter underground tunnel and shows the various support systems which are located at the site, including the gas storage pad, electrical distribution house, and vacuum house. Figure 2 shows these structures along with the ventilation and gas purging equipment located over the tunnel.

The central feature of the facility is the Large Detonation Vessel (LDV), a 27-cm diameter, 21.3-m long, stainless steel detonation tube, constructed in modular, flanged, 3.05-m long sections. Figure 3 is a photographic view of the vessel within the tunnel. The Maximum Allowable Working Pressure of the LDV, fabricated to ASME Boiler Code requirements, is 100 atm. The vessel is electrically heated using heating blankets which surround the tube and the flanges and was designed to operate at a maximum temperature of 700K and with a temperature uniformity of $\pm$ 14K. The HTCF is capable of serving as a test vehicle for detonation experiments using gaseous mixtures of hydrogen, air, and steam at initial pressures up to 3 atm and initial temperatures up to 700K. Additional gases, such as nitrogen, carbon monoxide, carbon dioxide, and oxygen, can also be introduced as components of the test mixtures.

Figure 4 is a schematic of the instrumentation configuration of the LDV. Instrumentation includes distributed thermocouples (TC), ion probes (IP) to measure flame front position vs. time, pressure transducers (PT) to measure detonation pressure, pressure transducers (PS) to measure initial vessel pressure, and sampling ports to permit measurement of initial composition. Detonation cell width is

measured using smoked foils, which are carbon soot coated foils of aluminum inserted into the test vessel prior to an experiment. When a detonation wave passes over the foil, it leaves a pattern of cells imprinted on the foil, from which a measure of cell size can be obtained. The available instrumentation provides measurements of detonation wave speed, detonation pressure, and detonation cell width.

The inherent detonability test program requires initiation of a detonation in a gaseous test mixture of hydrogen, air, and steam. Measurement of the detonation characteristics as the detonation propagates along the test vessel is also required. In the BNL program, detonations are initiated using a "gaseous driver system," described below in more detail. Figure 4 shows a schematic representation of the driver gas system. Oxygen and acetylene are mixed, and the mixture is used as the driver gas. A pair of electrodes penetrate the vessel into the driver gas mixture. A high-voltage discharge circuit (not shown) is used to discharge a capacitor across the electrodes, thereby initiating a detonation in the oxyacetylene mixture.

Figure 5 is a schematic of the gas delivery system, which shows the method of introduction of combustible test mixture in the test vessel. Sources of hydrogen, air, steam (and nitrogen for purging purposes) are available. The gases are supplied, controlled, and metered using choked venturis and flow through the mixing chamber, where they form a homogenous mixture. The gases are preheated to the desired temperature prior to entering the test vessel through the end flange. The gas concentrations are determined by ratio of the volumetric flowrates and are checked by sampling and gas chromatography.

3. INHERENT DETONABILITY EXPERIMENT DESCRIPTION

The initial phase of the HTCF test program addresses the effect of temperature on the sensitivity of gaseous mixtures to undergo detonations and on the limits of detonability of the HTCF test vessel. An experimental run begins with drawing a vacuum on the test vessel and preheating the vessel to the desired temperature. Upon reaching the desired temperature, the gas delivery system, shown schematically in Figure 5, is activated remotely at a computer-control console. Gases are metered and heated and delivered at the desired temperature and composition into the test vessel, and the gases fill the vessel to the desired initial pressure. A small volume of driver gas is then delivered to the initiation end of the LDV, and the detonation firing circuit initiates a detonation in the oxyacetylene mixture. The detonation propagates in the driver gas which is about 2-3 meters long and transmits the detonation to the test mixture of hydrogen, air, and steam. The detonation in the test gas then propagates down the remaining 15 meters of the vessel.

Measurements are made of the detonation cell width and detonation wave speed, which provide the necessary data for assessment of mixture sensitivity and (lean) detonability limits. The cell size data are compared with predictions based upon the ZND detonation model [2], and the wave speed data are compared with Chapman-Jouget (C-J) [3] calculations.

4. INHERENT DETONABILITY EXPERIMENTAL RESULTS

As indicated in Table 1, experiments are conducted in the HTCF using hydrogen-air-steam mixtures with compositions up to 50 percent hydrogen (all compositions are by volume), steam fractions greater than 30 percent, initial pressure in the range 1 to 3 atm, and initial temperature between 300K-650K. (Temperatures greater than 650K could not be tested because of observed preignition chemical reactions.)

Initial Cold Detonation Experiments

The HTCF test program was initiated with experiments using mixtures of hydrogen and air at one atmosphere and at 300K. Hydrogen composition varied between 14 percent and 50 percent. The objective of these early "cold" experiments was to establish that the data are consistent with results obtained from experiments reported previously in the literature and to determine the limits of detonability of the HTCF vessel at 300K. The speed of the detonation wave was constant along the vessel and also was in agreement within 2 - 3 percent of the detonation speed predicted by the C-J theory, as shown in Figure 6. Figure 7 shows that the detonation cell width data are in good agreement with previous data, both from the BNL Small-Scale Development Apparatus experiments and from experiments performed at other laboratories. These results indicate that the detonations are stable and fully developed and, therefore, that the method of initiation of the detonation is successful at cold temperatures. Additional data demonstrates that the lean limit for detonation of hydrogen-air mixtures at 300K in the Large Detonation Vessel (270-mm diameter) is 14 percent hydrogen, compared with 16 percent hydrogen in the SSDA vessel (100-mm diameter).

Thermal Calibration Experiments

Thermal calibration experiments were performed to measure and document the temperature uniformity of the LDV. A total of 55 thermocouples were used to measure the temperature distribution along the entire length of the vessel. The thermocouples were placed on the inside and outside surfaces of the vessel, at locations representative of all major structural elements of the vessel. The vessel was heated to 500K and to 650K in approximately 5 hours, at which time the final temperatures were recorded. The experimental data demonstrates that the temperatures reached steady-state conditions and that the uniformity specification of $\pm$ 14K was satisfied.

Additional Operational Testing

Extensive testing was performed to measure and document the gaseous mixture composition along the axis of the LDV. These experiments have led to the conclusion that the uniformity of hydrogen concentration along the vessel axis is acceptable. Additionally, extensive gas driver detonation initiation system testing was performed to demonstrate that the minimum quantity of driver gas was being used.

Initial Heated Detonation Experiments

Initial heated detonation experiments were carried out with hydrogen-air mixtures at 500K and at 650K. The preliminary results for detonation velocity and cell size are shown in Figures 8 and 9. The results

indicate that the detonation velocities agree with the C-J calculations and that the detonation wave speed agrees with data from the SSDA experiments.

5. SUMMARY AND FUTURE PLANS

The HTCF has been completed, operational testing has been completed, and the inherent detonability experimental program has been initiated.

Detonation experiments at 300K have been performed. Within the applicable range of hydrogen concentrations, detonation wave speed and detonation cell size data from the LDV are consistent with the SSDA test vessel. Preliminary high-temperature detonation experiments have been performed at 500K and at 650K, with mixtures of hydrogen and air. The data from these experiments are also consistent with the earlier SSDA test results. The HTCF results confirm the conclusion from the SSDA program that the effect of gas temperature is to decrease the cell size and, therefore, to increase the sensitivity of mixtures to undergo detonation. The data from the larger HTCF test vessel, however, also demonstrates that the effect of increased scale is to extend the range of detonable mixtures to lower concentration.

Much additional data will be obtained in the inherent detonability test program. Additional data will be obtained at all temperatures for leaner mixtures of hydrogen and air, and the detonability limits at all temperatures tested will be obtained. Experiments with steam will be conducted at 400K-650K, with steam content up to about 50 percent steam. For each hydrogen-air ratio tested, the steam detonability limit will be determined. Cell size data will be obtained over a broad range of conditions in order to provide an extensive database for assessment of the ZND model for detonation cell size.

6. ACKNOWLEDGEMENTS

The authors acknowledge the advice and encouragement of Dr. Asimios Malliakos, Program Manager, U. S. Nuclear Regulatory Commission, Office of Nuclear Regulatory Research, Division of Systems Technology, Accident Evaluation Branch, during the course of this work.

The help of Ms. Jean Frejka in preparation of this manuscript for publication is appreciated.

7. REFERENCES

1. Ciccarelli, G., et al., "High-Temperature Hydrogen-Air-Steam Detonation Experiments in the BNL Small-Scale Development Apparatus," Brookhaven National Laboratory, NUREG/CR-6213, BNL-NUREG-52414, August 1994.

2. Zel'dovich, Y. B., "The Theory of Propagation of Detonation in Gaseous Systems," Expt. Theor. Phys. S. S. S. R., Vol. 10, p. 542, 1940; Translation, NACA TM 1261, 1950.

3. Chapman, D. L., Phil. Mag., Vol. 47:Series 5, No. 284, pp. 90-104, 1899.

Table 1 - Experimental Conditions for HTCF Large Detonation Vessel

PARAMETER	RANGE
Temperature	300 K - 650 K
Scale	27-cm diameter (10 cm - SSDA)
Pressure	1 - 3 atm
Mixtures*	< 15% hydrogen at 300K < 11% hydrogen at 500K < 10% hydrogen at 650K
Steam Dilution	> 30% steam, off-stoichiometric mixtures

*Mixtures with greater hydrogen content were the focus of the SSDA experiments.

Table 2 - Major Systems of the High-Temperature Combustion Facility

FACILITY SYSTEM	WORK PERFORMED
Large Detonation Vessel	Vessel fabricated to BNL specs to satisfy research objectives; installed, integrated with other systems and tested
Electrical Power Supply System and Vessel Heating System	Connection to preexisting high-voltage power transformer; switchgear, distribution hardware and enclosure designed and built; vessel heating system designed, tested, installed with vessel
Gas Storage and Handling System	Gas storage pad, gas pipe distribution and gas handling and metering equipment designed, installed, tested
Vacuum System	Existed previously; connections made to vessel
Ventilation and Purge System	Tunnel ventilation system, vessel purge, elevated release, and cooling air system installed; connect to interlock system
Safety and Interlock Systems	Design and reviewed for safety. Preexisting interlock system interfaced with present apparatus; gas detection and alarms system added
Control and Data Acquisition System	Adapted and expanded system used for SSDA
Detonation Instrumentation	Adapted from techniques used in SSDA

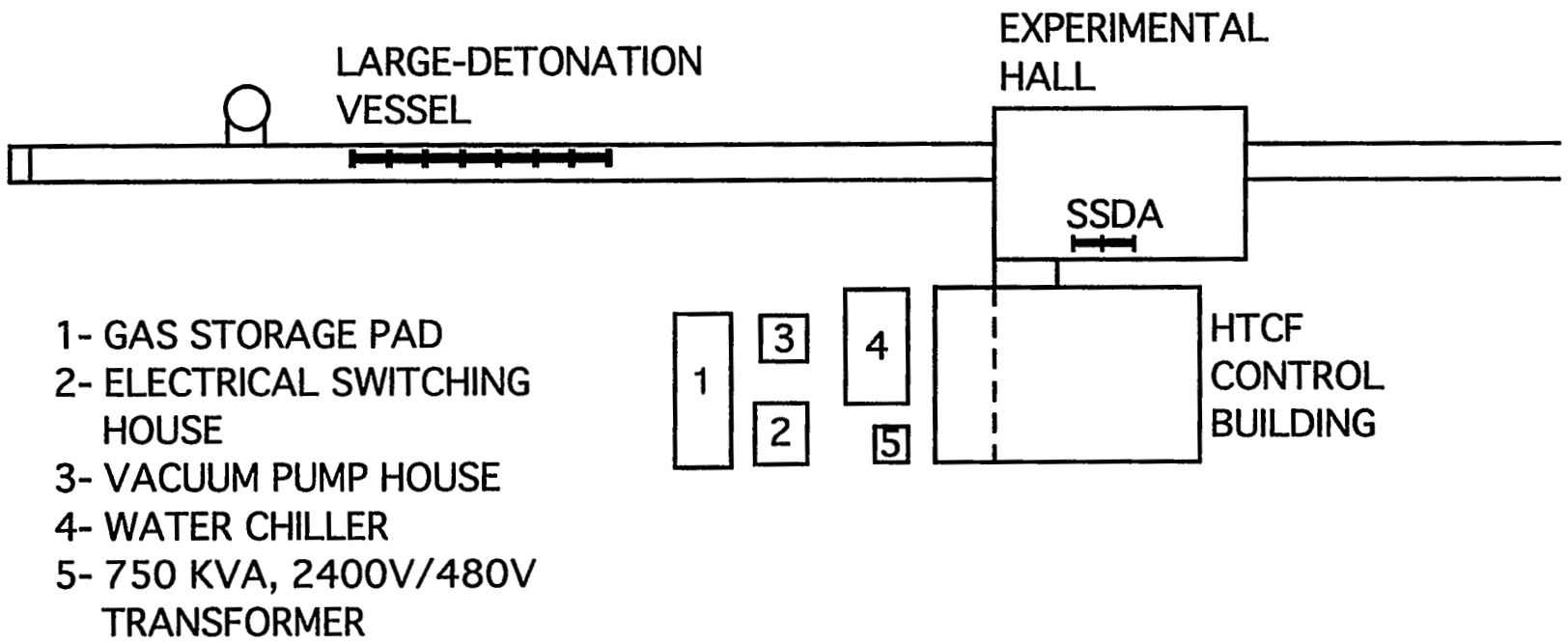

Figure 1: High-temperature combustion facility site layout

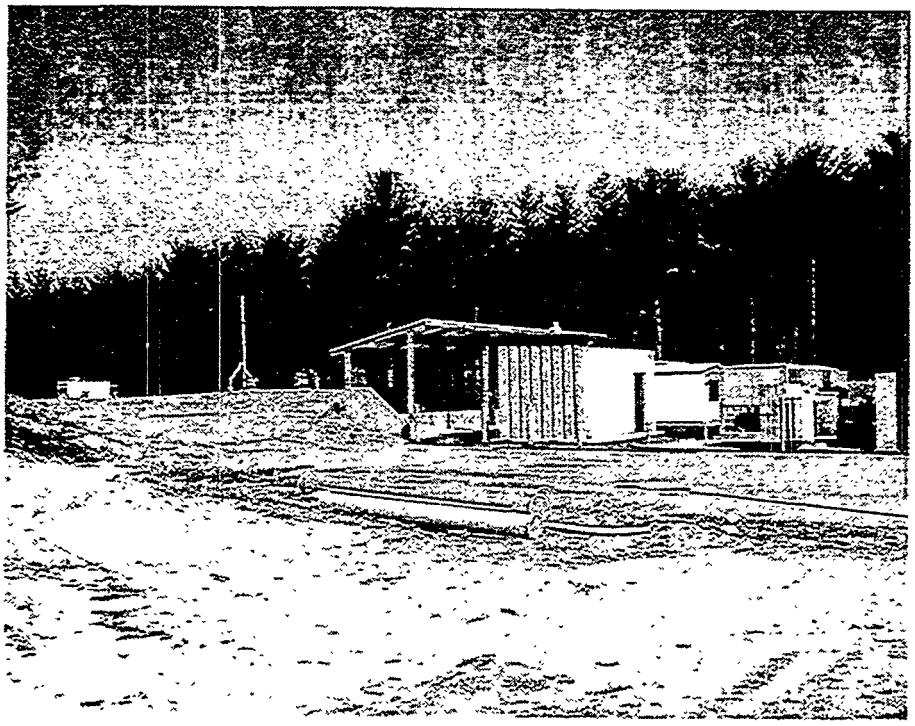

Figure 2 - Major Features of High-Temperature Combustion Facility Site

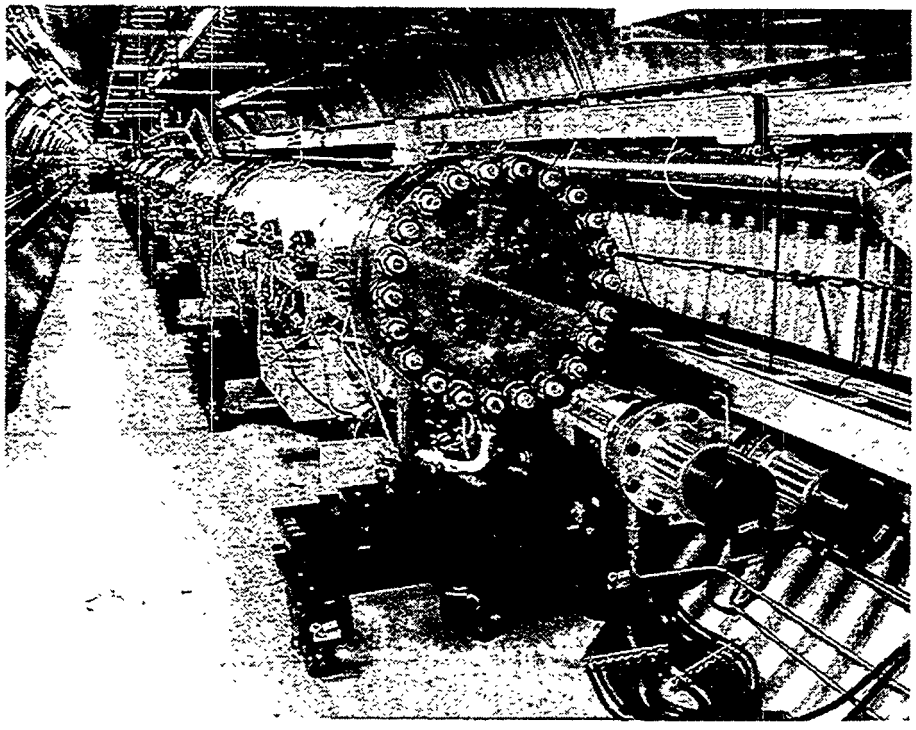

Figure 3 - High-Temperature Combustion Facility Large Detonation Vessel

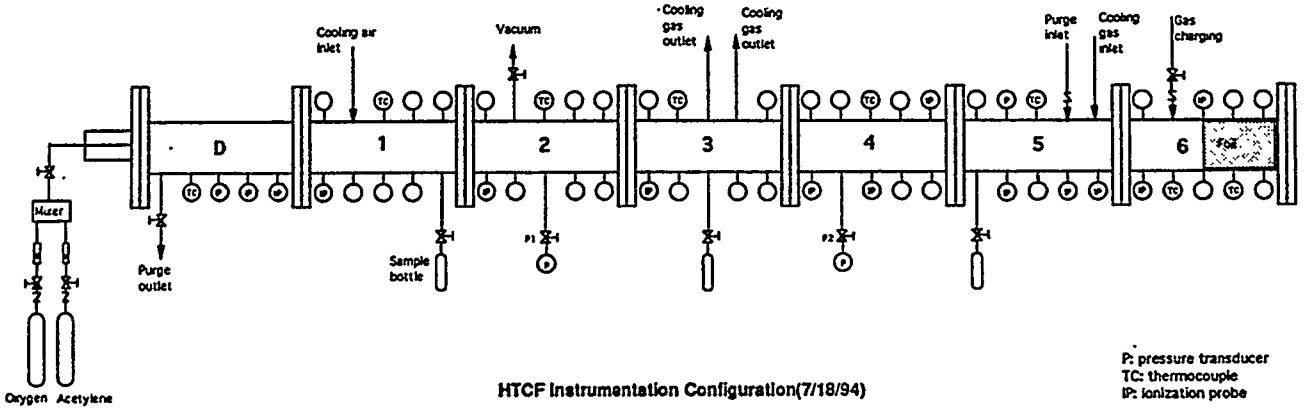

Figure 4 - Schematic of Instrumentation Configuration on the Large Detonation Vessel

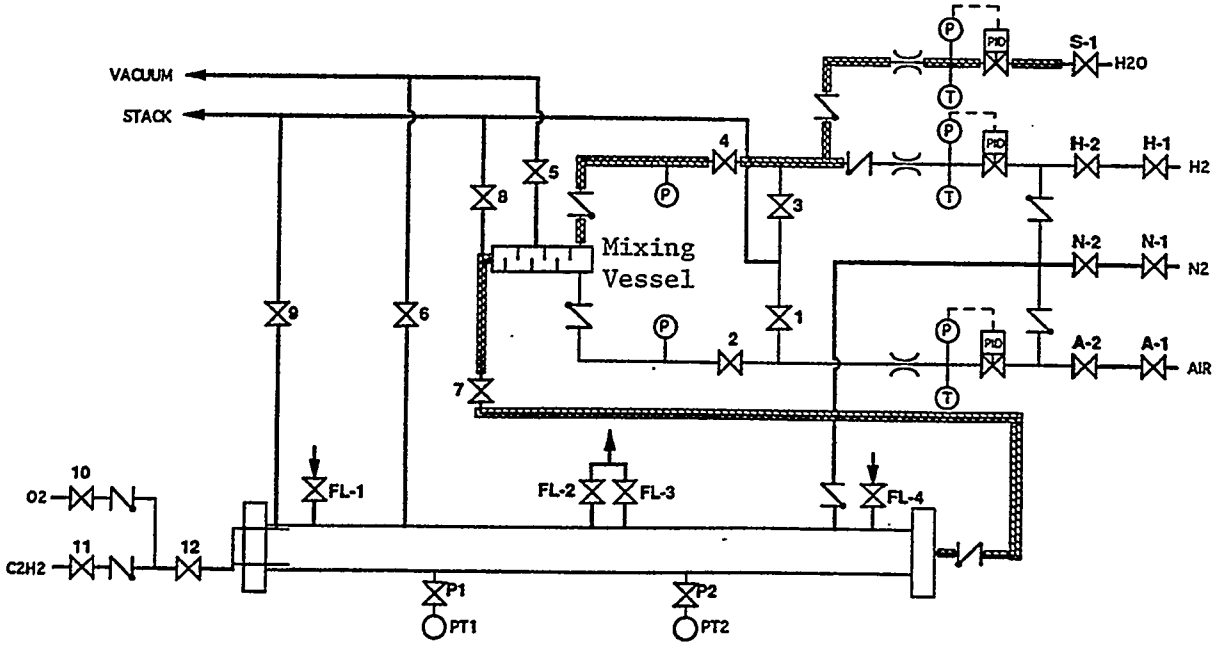

Figure 5 - HTCF Gas Delivery System With Axial Mixture Injection

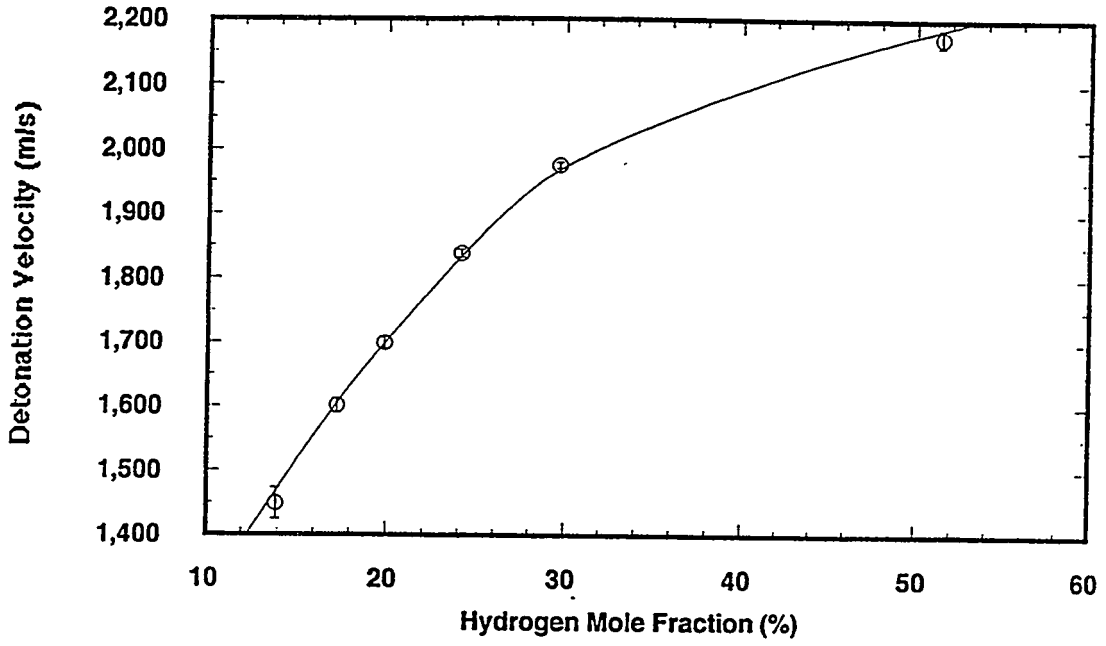

Figure 6 - Detonation Velocity for Hydrogen-Air Mixtures at 300K and 1 atm

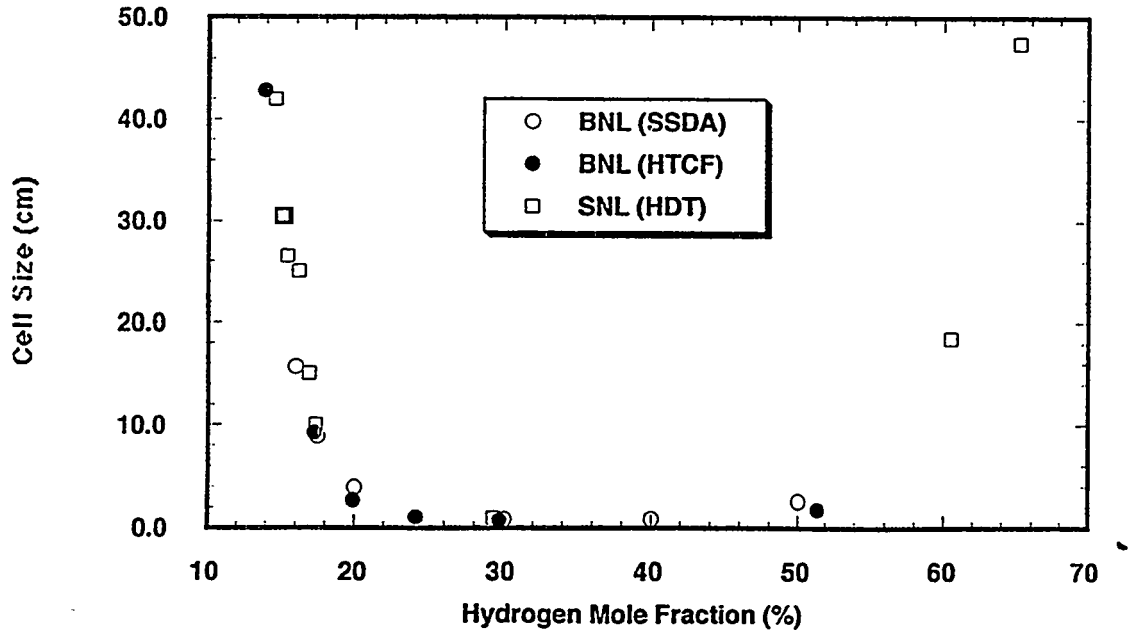

Figure 7 - Cell Size for Hydrogen-Air Mixtures at 300K and 1 atm

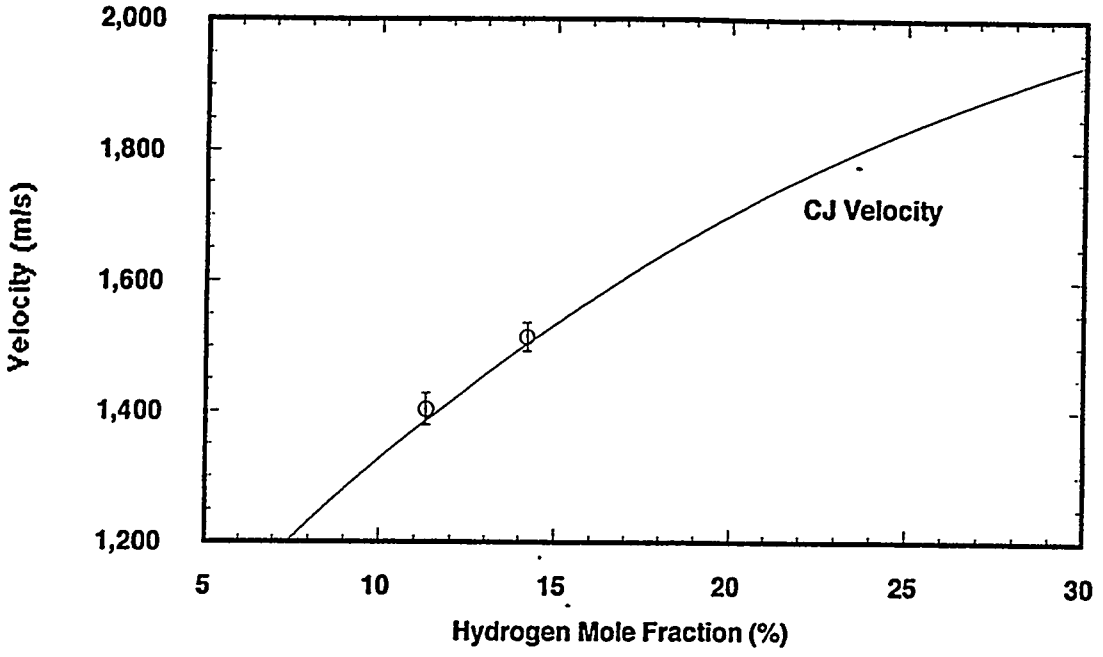

Figure 8 - Detonation Velocity for Hydrogen-Air Mixtures at 650K and 1 atm

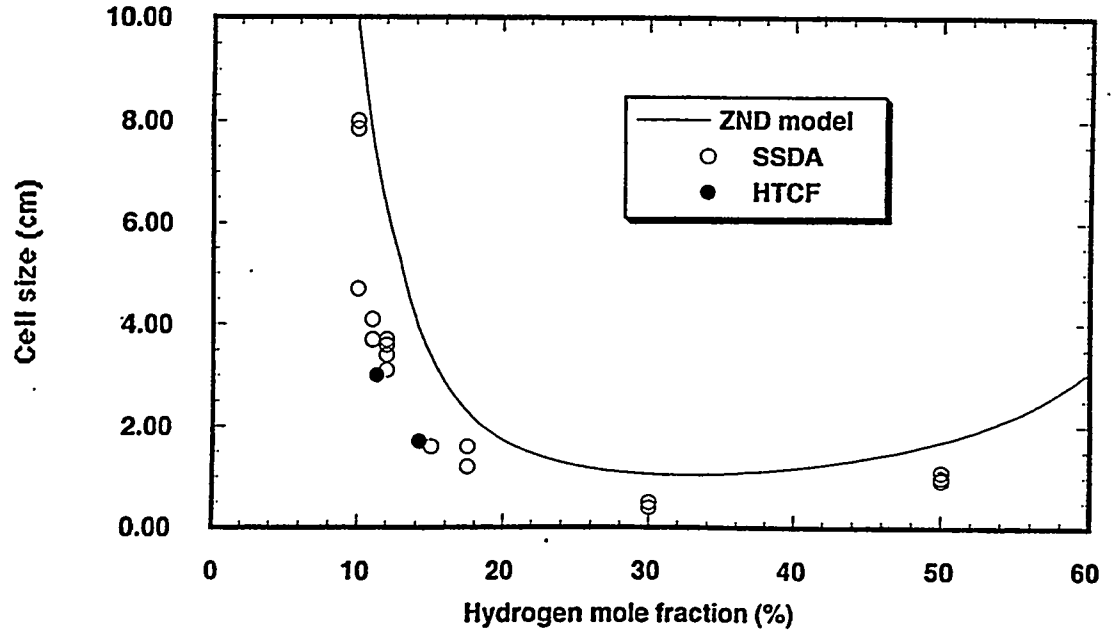

Figure 9 - Detonation Cell Size for Hydrogen-Air Mixtures at 650K

Progress in MELCOR Development and Assessment *

Randall M. Summers
Randall K. Cole, Jr.
Arnold E. Elsbernd
Lubomyra N. Kmetyk
Russell C. Smith
David S. Stuart
Samuel L. Thompson
Modeling and Analysis Department
Sandia National Laboratories
Albuquerque, NM 87185-0739

Recent efforts in MELCOR development to incorporate CORCON- Mod3 models for core-concrete interactions, new models for advanced reactors, and improvements to several other existing models have resulted in release of MELCOR 1.8.3. In addition, continuing efforts to expand the code assessment database have filled in many of the gaps in phenomenological coverage. Efforts are now under way to develop models for chemical interactions of fission products with structural surfaces and for reactions of iodine in the presence of water, and work is also in progress to improve models for the scrubbing of fission products by water pools, the chemical reactions of boron carbide with steam, and the coupling of flow blockages with the hydrodynamics. Several code assessment analyses are in progress, and more are planned.

1. INTRODUCTION

Recent activities in the MELCOR development project have led to the release of MELCOR 1.8.3,[1] a much-improved version of the code. Several important modeling improvements and other new features have been incorporated into the code and are described in Section 2. Concurrent with code development efforts, continuing assessment of the code has resulted in a significantly expanded database of calculations and sensitivity studies. These efforts have demonstrated the ability of the code to successfully calculate a variety of phenomena important to severe accident analyses, and they have also identified many problems with the code and phenomenological models that have subsequently been corrected. These analyses and modeling improvements have resulted in substantially increased credibility of the code. Three assessment studies[2,3,4] completed in the last year are described in Section 3.

Work was completed shortly after the MELCOR 1.8.3 release on two additional models[5] related to reactor vessel failure. Work is now in progress in a number of additional areas related to fission product transport and chemistry, and efforts are continuing to couple the effects of flow blockages during late-phase melt progression to the hydrodynamic models. Furthermore, new models[6,7] are being developed at Oak Ridge National Laboratory (ORNL) for phenomena important in boiling water reactors (BWRs) during early core heatup and degradation. These efforts are all described in Section 4.

---

*This work was supported by the U.S. Nuclear Regulatory Commission and was performed at Sandia National Laboratories, which is operated for the U.S. Department of Energy under Contract Number DE-AC04-94AL85000.

2. MELCOR 1.8.3 IMPROVEMENTS

MELCOR 1.8.3 was released to the international reactor safety community in August 1994 following substantial testing on a suite of plant calculations to demonstrate its robustness and reliability for many different accident scenarios on a variety of computer systems. This version of the code incorporates a number of new features, corrections, and other changes that have been made since the release of MELCOR 1.8.2.

Perhaps the most significant modification has been the incorporation of CORCON-Mod3[8] into MELCOR. This implementation was part of a joint effort to simultaneously implement CORCON-Mod3 into CONTAIN,[9] and it included significant restructuring of CORCON to minimize future duplication of effort. No changes were made to the basic phenomenological models, but now the central phenomenological routines are identical in the stand-alone, MELCOR, and CONTAIN versions, and additional modeling improvements to CORCON can now be made in all versions with a minimum amount of effort. During the course of implementation, previous modifications made to MELCOR and CONTAIN to address difficulties with CORCON in a systems code environment were retrofitted to the new version. Several other numerical deficiencies with CORCON-Mod3 have also been addressed, including instabilities in the interlayer mixing model and a general lack of robustness. The numerical implementation of the interlayer mixing model was completely redone, and the oscillations that have been observed in calculations that utilized this model have been eliminated.

A few CORCON modeling issues that have previously been identified are still unresolved. Releases of fission products calculated by the VANESA model as a metal phase vanishes are still incorrect, but a possible modification to the model developed by the Nuclear Safety Institute (NSI) in Russia may be incorporated that will remedy this problem. The adjustment made to the oxygen potential in VANESA to account for unequal metal and oxide temperatures is inadequate; a patch has been made to prevent code aborts, but a more permanent modeling fix is still needed. Finally, the non-ideal oxide chemistry model is not functional in CORCON-Mod3, but investigations by others (e.g., NSI) have questioned the need for and practicality of this model.

Another major improvement to MELCOR has been the upgrade of the hydrodynamics solution algorithm to include the mass and energy transfer terms associated with bubble separation from a two-phase pool in the implicit numerical solution scheme. This was needed to stabilize computed void fractions and pool surface elevations, which had exhibited severe oscillations in many calculations that had a strong negative impact on the functioning of several other models. As a part of this effort, many of the low-level hydrodynamic modeling algorithms were completely recoded to enhance their future maintainability. Other hydrodynamic improvements include adding the capability for the user to define momentum flux terms for a two-dimensional network of control volumes for use in fine-scale natural circulation calculations in the core region. A new input format for mass and energy sources has been added to allow direct reference to external data files and to allow scaling. Also, the option to write various flow variables to external data files has been added.

A number of improved modeling capabilities and new input options have been added to the heat structure models. The model for film condensation and evaporation on heat structure surfaces has been substantially enhanced by modeling the water film surface as an additional temperature node and explicitly accounting for the thermal resistance across the film. The mass transfer expressions were generalized to remove inappropriate limitations so that they would be applicable to both pure steam and noncondensible gas mixture environments. A new film tracking model was also added to allow condensate to drain from one structure to another, thus allowing modeling of passive containment cooling systems proposed for certain advanced light water reactors (ALWRs). New optional input to allow scaling of heat and mass transfer coefficients for specified surfaces has been added, and an option to allow the use of the maximum heat transfer coefficient given by the correlations for forced and natural convection and for laminar and turbulent flows has been added as an alternative to the existing interpolation scheme for transitions between those flow regimes. (Late in MELCOR 1.8.3 testing, we discovered situations where the default scheme can significantly under-predict the true heat transfer coefficient.)

Several new modeling features have been added to other packages as well. The capability to initialize the core in a degraded state with debris materials and oxidized cladding and canister materials has been added to the Core package, and the high-pressure melt ejection model in the Fuel Dispersal Interactions (FDI) package has been extended to treat oxidation and heat transfer for debris that is deposited on heat structures. Automatic mass conservation accounting for fission products has been implemented in the RadioNuclide (RN) package. New input has been added to the Containment Sprays (SPR) package to allow spray sources to be associated with control volume pools, thus permitting a recirculation mode of operation.

Many additional changes have been made to correct errors of varying degrees of severity. These include fixes to errors that caused the code to abort in one or more calculations, such as floating point numbers divided by zero or array subscripts out of range. They also include logic errors that led to code shutdown, poor execution performance, numerical sensitivity, or incorrect phenomenological behavior. Additional improvements to the user interface and code input/output capabilities have been made. User input has been provided for additional control and flexibility in some models, and input checking in a number of areas has been strengthened to ensure consistency and prevent later problems from arising due to bad input. Several control function arguments and plot variables have been added, and output for some packages has been improved. Several more enhancements to warning and error message processing have been made.

New modeling capabilities specific to BWRs have been added as well to the BWR Lower Plenum Debris Bed (BH) package by ORNL MELCOR development staff. Treatment of radiation heat transfer among the lower plenum debris, the core plate, the core shroud, and the vessel wall has been added, and a model to simulate the melting of heat structures used to treat the core shroud has been added (but is currently only available in conjunction with the BH package models. A model to calculate the effects of water interacting with the debris bed has been added, and fission product release from the debris using either the CORSOR or

CORSOR-M models has been added. Mass and energy conservation accounting is now calculated within the BH package, though it has not yet been fully integrated with the global MELCOR accounting scheme. New models have been added to the BH package to simulate operation of the PCCS and ICS in ALWRs.

In preparation for distribution to external MELCOR users, MELCOR was subjected to a number of tests as required by our Software Quality Assurance Plan (SQAP). This testing was done primarily to ensure robustness of the code; however, calculations were also quickly reviewed for physical reasonableness and plausibility. The following full-plant calculations were selected for this testing:

1. Grand Gulf large break loss-of-coolant accident (LOCA) during shutdown (POS 5) with 40-day decay heat levels.

2. Grand Gulf low pressure boiloff during shutdown (POS 5) with open containment, closed upper head vent, 2 safety relief valves open, and 24-hr decay heat levels.

3. Surry S2D sequence (hot leg small break LOCA).

4. Surry AG sequence (hot leg large break LOCA).

5. LaSalle high-pressure short-term station blackout with failed emergency core cooling and automatic depressurization systems.

6. Advanced boiling water reactor (ABWR) loss of all core cooling with failure to depressurize.

7. DEMO calculation distributed with the software (simplified coarse nodalization for idealized plant).

MELCOR 1.8.3 was required to run each of these calculations to completion without aborting, terminating prematurely (necessitating restart with a different time step), or using an excessive amount of computational time because of numerical difficulties. These calculations collectively were run on various machines (IBM, HP, and SUN workstations, and IBM PC), although any individual calculation was run on only one or two machines.

3. MELCOR ASSESSMENT

Significant progress continues to be made in MELCOR assessment, and most phenomenological areas within the code have been or are being assessed against at least one experiment. Recently completed assessments include the MP-1 and MP-2 late-phase melt progression experiments conducted at the Annular Core Research Reactor at Sandia,[10] the General Electric large vessel level swell tests,[2] which measured void fraction distributions and bubble rise velocities, and the containment spray experiments conducted in Pacific Northwest Laboratory's Containment Systems Experiment vessel.[3] The SURC-2 core-concrete interactions test conducted at Sandia was used to verify the correct implementation of

CORCON-Mod3 in MELCOR;[4] a more complete assessment against this test was conducted for stand-alone CORCON-Mod3.[11] All assessments conducted at Sandia include a systematic search for and identification of numeric effects from time step and machine dependencies, in addition to the identification of other code problems and limitations requiring developer attention. Extensive sensitivity studies also provide the basis for development of user guidelines.

The GE large vessel blowdown and level swell experiments are a set of primary system thermal/hydraulic separate effects tests studying the level swell phenomenon for BWR transients and LOCAs. This experiment series includes both top blowdown tests with vapor blowdown, characteristic of accidents such as steam line breaks, and bottom blowdown tests with liquid and two-phase blowdown, more characteristic of recirculation line breaks. The test facility includes a 4.5-m^3 steel-shell vessel containing saturated steam/water at 7 MPa and a 10-inch diameter blowdown line with a dip tube extension. Assessment against this data allowed an evaluation of the ability of MELCOR to predict the inventory loss, and hence time to core uncovery and heatup, in the early stages of transients and accidents in BWRs. Also, an implicit bubble separation algorithm has been implemented recently in the MELCOR hydrodynamics models, and analysis of the GE tests was intended to validate this algorithm for general use.

MELCOR was able to calculate reasonable agreement with the depressurization and break flow data for all tests. Although the code predictions for the liquid level showed good agreement with experimental data for the bottom blowdown tests, MELCOR underpredicted the level swell for the top blowdown tests with the base case nodalization and model parameters, generally reaching a maximum value that is significantly below the maximum two-phase levels in the test data and then beginning to decline earlier in the calculations than in the tests. Sensitivity studies showed that the break flow and depressurization rate were sensitive to the time step during the two-phase portion of the calculated blowdown and that the calculated level swell is very sensitive to nodalization and bubble rise model parameters.

Eight experiments have been performed in the CSE containment vessel to evaluate the performance of aqueous sprays as a means of decontaminating containment atmospheres. The 595-m^3 steel-shell vessel is subdivided into a dome, lower drywell, middle and lower rooms, and wetwell. Uranium aerosols were generated to represent core materials that have very low vapor pressures and low solubilities in water, and cesium aerosols were generated to represent volatile solids highly soluble in water. Iodine was injected as both elemental iodine and methyl iodide. Six intermittent, multiple spray experiments conducted after the aerosols and iodine had been injected involved either STP air or steam/air at 3 atm and 400 K, different spray rates and timing, both fresh and recirculating sprays, different spray solutions, and different nozzle types and distributions. Two continuous spray tests were conducted with concurrent aerosol/vapor injection.

Results of MELCOR assessment analyses demonstrated that MELCOR correctly reproduces the qualitative thermal/hydraulic, aerosol washout, and vapor decontamination response to containment spray injection. In particular, MELCOR reproduced the relative responses observed when the spray flow rate and droplet size distribution were varied. Also, the accuracy and reasonableness of the predicted results generally improved as more MAEROS

components and sections were used to model the aerosol size distributions. Quantitatively, MELCOR predicts more efficient steam condensation and equilibration of drops with the atmosphere than shown by experimental data. Removal of aerosols and vapors by sprays is generally underpredicted by the code, which also shows the same proportional effects for each spray period, while the data shows the first spray period being much more effective in removing contaminants than later spray periods. Major sensitivities include the fraction of the spray assumed to interact with the atmosphere, the spray droplet size and distribution, and the fog water droplet evaporation and condensation.

The major purpose of our calculational efforts for SURC-2 were to verify the correct implementation of CORCON-Mod3 in MELCOR by comparing MELCOR results for the same analysis with those of stand-alone CORCON-Mod3. This verification effort showed no significant differences; most results showed no distinguishable differences at all in the plots, and the few minor observable differences were readily traced to unavoidable coding differences associated with the interface to MELCOR. One sensitivity study was performed to examine the effects of the input options for multiple debris layers vs. a single homogeneous layer (now the default in MELCOR). Results with multiple layers and using the interlayer mixing model were different only at very early times when the debris was stratified. Results with the old CORCON-Mod2 layer configuration agreed with those using the interlayer mixing model.

Work is currently in progress to assess code thermal/hydraulic behavior for Surry plant calculations with pressurizer surge line failure. Assessment calculations of aerosol scrubbing by water pools are to be conducted for two sets of Electric Power Research Institute experiments one set involving superheated steam and the other involving noncondensible gases.

4. POST-1.8.3 MODEL DEVELOPMENT ACTIVITIES

Work was completed shortly after MELCOR 1.8.3 release on two additional models related to reactor vessel failure.[5] The capability to treat heat transfer from the exterior surface of the lower head to a liquid pool surrounding the lower vessel has been added, using boiling heat transfer correlations specifically applicable to downward-facing surfaces. This model is needed for simulation of flooded reactor cavities for accident scenarios involving advanced reactor designs. Experimental correlations relating the critical heat flux and the film boiling heat flux to the surface orientation are used to determine the heat transfer coefficient from the external surface of the vessel, and several user control options were added to provide additional flexibility, as this is an ongoing area of research still with large uncertainties.

Also, models for creep rupture failure of the lower head were implemented in the code after 1.8.3 release. These models are based on Larson-Miller time-to-rupture correlations and application of a life fraction rule to calculate the cumulative damage fraction for transient conditions. Options in the model include the ability to treat the lower head stress as a zero-dimensional membrane stress or to calculate the one-dimensional stress distribution through the thickness of the head.

Fission product chemistry models are being developed to treat the chemical deposition of cesium and tellurium compounds on structural surfaces. Preliminary design of the model calls for the modeling of chemisorption as an addition to the current mass transfer processes. Experimentally based mass transfer coefficients for CsOH and CsI chemisorption on stainless steel and Inconel surfaces would be factored into the TRAP-MELT equations used in MELCOR for normal condensation and evaporation. The chemisorbed mass would not be considered for release from the structure unless very high temperatures were reached, in which case a general refractory vapor pressure curve could be utilized to return vapor to the atmosphere. We do not propose applying the model for tellurium, hydrogen iodide, or iodine by default, as the mass transfer coefficient values are not based upon sufficient data, but we plan to incorporate the capability to perform these calculations at the user's option.

Models are also being developed to capture the important chemical reactions of iodine in the presence of water. Preliminary design of the model includes submodels to calculate release of I_2 from a water pool to the atmosphere in the presence of steam condensation or evaporation, which will either inhibit or enhance iodine diffusion through the boundary layer, and to calculate the pH of the water pool based on the concentrations of boric acid and alkali metal hydroxides. Radiolysis and pyrolysis processes may also be considered in the pH model, and the formation, release, and destruction of methyl iodide will be modeled.

Fission product vapor scrubbing is being implemented by incorporating updated models from SPARC-90.[12] The enhanced modeling capabilities will be demonstrated through testing, which will verify that the new models are giving reasonable results. Implementation of these models should also lay to rest questions about the decontamination factors predicted by the aerosol scrubbing models.

Coupling of flow blockages to the hydrodynamic models by automatically reducing flow areas and increasing loss coefficients is being developed to enhance natural circulation capabilities during late-phase melt progression. We have proposed a limited model for the increased flow resistance associated with formation of core debris ("core blockage") based on correlations developed for flow in porous media. Consistency of representation between core models and hydrodynamic models will require that much of the geometry now defined by flow path input will have to be derived internally from core input.

Finally, new equilibrium chemistry models for the reactions of boron carbide with steam and the partitioning of those reactions with competing eutectic reactions of the boron carbide with steel are being implemented. The advanced chemistry models are based on minimization of the Gibbs free energy and have been taken from models developed by Oak Ridge National Laboratory. The methane produced by these models will be provided to the fission product iodine chemistry models for determining the formation of methyl iodide in water suppression pools and its release to the containment atmosphere.

Oak Ridge National Laboratory is also working on models for the allocation of steam among core components during oxidation and for gamma heating of other core components, particularly those in the interstitial region in boiling water reactors. These model upgrades should give a more accurate simulation of the internal heating rates and oxidation of BWR canister walls and control blades.

Longer term development plans include the examination of models developed by the Nuclear Safety Institute under a cooperative agreement with the Russian Research Center for in-vessel fuel-coolant interactions, ex-vessel debris coolability, melt spreading, and reflood hydrodynamics, followed by the development of simplified models for implementation in MELCOR. Additional improvements in a few areas are also needed to address some residual concerns identified during the MELCOR peer review.

5. REFERENCES

1. R. M. Summers et al., MELCOR Computer Code Manuals, Version 1.8.3, September 1994, NUREG/CR-6119, SAND93-2185, Sandia National Laboratories, Albuquerque, NM (being printed).

2. L. N. Kmetyk, MELCOR 1.8.3 Assessment: GE Large Vessel Blowdown and Level Swell Experiments, SAND94-0361, Sandia National Laboratories, Albuquerque, NM July 1994).

3. L. N. Kmetyk, MELCOR 1.8.3 Assessment: CSE Containment Spray Experiments, SAND94-2316, Sandia National Laboratories, Albuquerque, NM (December 1994).

4. R. K. Cole, Jr., "Verification of CORCON-Mod3 Implementation into MELCOR using the SURC-2 Experiment," Sandia National Laboratories letter report from R.M. Summers to S. Basu, USNRC, Albuquerque, NM (July 21, 1994).

5. R. C. Smith and R. M. Summers, "Lower Vessel External Heat Transfer and Larson-Miller Failure Criterion for Lower Head Failure," Sandia National Laboratories letter report from R. M. Summers to S. Basu, USNRC, Albuquerque, NM (June 14, 1994).

6. C. R. Hyman, "COR Package Steam Allocation Model Preliminary Design Report," Oak Ridge National Laboratory letter report from C. R. Hyman to S. Basu, USNRC, Oak Ridge, TN (July 13, 1994).

7. R. L. Sanders, "Fission Product Gamma Heating of Non-Fuel Core Structures for MELCOR," Oak Ridge National Laboratory letter report from R. L. Sanders to S. Basu, USNRC, Oak Ridge, TN (August 15, 1994).

8. D. R. Bradley et al., CORCON-Mod3: An Integrated Computer Model for Analysis of Molten Core-Concrete Interactions User's Manual, NUREG/CR-5843, SAND92-0167, Sandia National Laboratories, Albuquerque, NM (October 1993).

9. K. K. Murata et al., User's Manual for CONTAIN 1.1: A Computer Code for Severe Nuclear Reactor Accident Containment Analysis, NUREG/CR-5026, SAND87-2309, Sandia National Laboratories, Albuquerque, NM (November 1989).

10. T. J. Tautges, MELCOR 1.8.2 Assessment: The MP-1 and MP-2 Late Phase Melt Progression Experiments, SAND94-0133, Sandia National Laboratories, Albuquerque, NM (May 1994).

11. J. E. Brockmann, R. O. Griffith, and D. R. Bradley, CORCON-Mod3 Validation Study, SAND93-0295, Sandia National Laboratories, Albuquerque, NM (1993).

12. P. C. Owczarski and K. W. Burk, SPARC-90: A Code for Calculating Fission Product Capture in Suppression Pools, NUREG/CR-5765, PNL-7723, Pacific Northwest Laboratory, Richland, WA (October 1991).

METALLIC CORE- MELT BEHAVIOR IN DRY-CORE BWR ACCIDENTS: THE EX-REACTOR EXPERIMENTS

Randall 0. Gauntt, Paul H. Helmick, Rodney C. Schmidt
Sandia National Laboratories, Albuquerque, NM
Larry Humphries
SAIC, Albuquerque, NM

ABSTRACT

The XRl-l and XRl-2 (Ex-Reactor) experiments, investigating metallic core-melt relocation in boiling water reactor (BWR) geometry, were performed in August and November of 1993. The XRl tests represented the BWR control blade and channel box structures in the lower part of the BWR core as metallic core materials are beginning to melt and drain downwards. The purpose of this experiment program is to examine the behavior of downward-draining molten metallic core materials in a severe reactor accident in a dry BWR core, and to determine conditions under which the molten materials drain out of the core region, or freeze to form blockages in the lower portion of the core. In the event that the draining metallic materials do not form stable blockages in the lower core region, and instead, erode the lower core structures such as the lower core plate, then the subsequent core melt progression processes may proceed quite differently than was observed in the TMI-2 accident with correspondingly different impact on vessel loading and vessel release behavior.

The results of the XR1 simple channel experiments show some variations in blockage formation behavior associated with the melting and draining of the control blades in the BWR core, that are attributed principally to the axial thermal gradient. A greater degree of downward melt penetration was observed in the high gradient XR1-2 test than in the low gradient XR1-1 test. The XR1-2 test indicated that a significant degree of control blade melt drainage can be expected when the thermal gradient in the lower core is on the order of 2000K/m. Both tests showed a significant degree of channel box destruction, which alters the melt flow pathways available to the control blade melt as well as the later melting zircaloy materials.

A follow-on set of experiments, designated as the XR2 tests, are described which include fuel rods in the test bundles, along with more detailed representations of the lower core plate, fuel support pieces, and control blade velocity limiter structures. Prototypic materials are to be used in these tests. Furthermore, the XR2 tests will include a second Zr-melt pour following the control blade melt pour. These additions are included in the XR2 experiments to fully represent the melt relocation events considered typical for the BWR dry-core accident scenario, and will provide information needed to determine BWR core blockage or drainage behavior.

1. Introduction and Background

The XR experiments are being conducted at Sandia National Laboratories to aid in the resolution of a major uncertainty in the core melt progression process associated with a severe accident in a boiling water reactor (BWR) where loss of reactor core coolant inventory has occurred. Specifically, the class of accidents of concern are those that involve core melting under dry core conditions, such as an unrecovered Station Blackout accident with manual vessel depressurization.[1] In

these accidents, a manual vessel depressurization is to be carried out by the plant operators when the core water level drops to ~35% below the top of the core. This procedure is intended to cool down the reactor core before the onset of severe fuel damage from oxidation and over-temperature conditions by the steam blowdown and cooling effect, and to permit the activation of any potentially available low pressure coolant injection systems. After vessel depressurization, the water level in the vessel would be below the lower core plate, but above the jet pump intake nozzles. The procedure also delays severe damage to the core by about a half an hour, assuming that reintroduction of water into the core does not subsequently occur. In the event that core cooling is not regained, the severe core damage processes resulting from the continued core heatup takes place under comparatively "dry core" conditions because of the low water level in the reactor vessel, with very low steam flow through the core.

Without vessel depressurization, "wet core" conditions would exist, with the lower core generating comparatively large amounts of steam from the boiling coolant present there. Wet core conditions were present in the TMI-2 accident, which, as a result of subsequent core melt progression processes, are believed, in general, to lead to a blocked core configuration with the formation of a growing molten ceramic fuel pool. The water in the lower core causes relocating molten core materials to freeze, forming a dense crust. Subsequent melt collects upon the crust blockage until a molten pool forms. Later, as the pool growth reaches a boundary of the core, the contents of the molten pool (principally molten ceramic fuel) will be released and relocation to the lower vessel head follows, as occurred in the TMI-2 accident. The blocked core "TMI-like" melt progression scenario is illustrated in Figure 1.

In the case of the BWR "dry core" melt progression scenario, it is not clear that the blocked core, molten pool configuration, discussed in the previous paragraph will result since the heat sink associated with water in the lower core is not present. An alternative "continuous drainage" melt progression pathway has been proposed for these dry-core conditions, which does not lead to the formation of a large in-core molten ceramic pool, but instead, follows a continuous drainage behavior, where molten material drains from the core region without the formation of any stable crusts or blockages. This alternative melt progression pathway is also illustrated in Figure 1, and can be seen to lead to very different melt relocation behavior and different vessel head loading conditions. The TMI-like blocked core pathway results in a sudden relocation of ~3000K molten ceramic fuel material, which subsequently comes into contact with the lower vessel head. The alternative continuous drainage pathway results in the gradual and continuous drainage of materials from the core region, first the lower melting point metallic core materials (control blades and zircaloy materials), and later solid or molten ceramic fuel materials. In this case, the metallic materials will collect on the lower head, followed later by overlying ceramic fuel materials. Because these two melt progression pathways lead to important differences in the timing and mode of vessel failure, in addition to differences in the rate, temperature and composition of those materials that are ultimately released into the containment environment, it is important to understand under what conditions which melt progression scenario will result, so that the consequences of these two different pathways can be assessed. Complicating the analytical assessment of these pathways is the complexity of the BWR lower core geometry, which is comprised of fuel

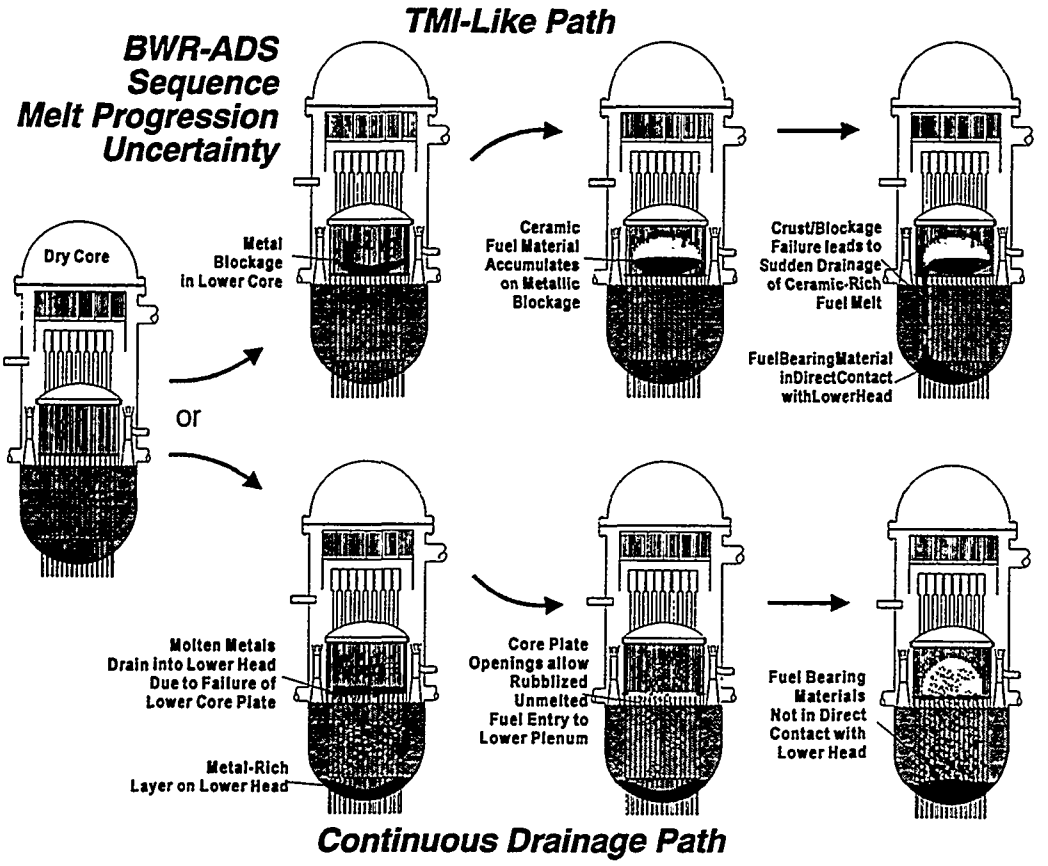

Figure 1: Illustration of the melt progression branchpoint uncertainty for "dry core" and "wet core" scenarios.

canisters with rods, control blades, and inter-canister gaps, as well as lower canister nosepieces, control rod drive tubes, the lower core plate structure, and numerous flow pathways. These geometrical complexities are illustrated in Figure 2. These complexities, together with uncertainties concerning material eutectic interactions (Zr-Fe for example), stability of core structures during melt relocation, and the freezing and blockage behavior of relocating metallic melts has prompted an experimental, and companion analytical, program to address this melt progression issue. The Ex-reactor experiments are intended to provide the experimental evidence necessary to develop and assess predictive models of this phase of the melt progression process, which are required to resolve the uncertainty in this crucial melt progression pathway branchpoint.

2. Experimental Program

In order to determine the conditions under which BWR dry core melt progression will follow either the "blocked core, TMI-like" path, or alternatively, the continuous drainage pathway, a series of experiments is currently underway to characterize the behavior of the draining metallic core materials in the geometry of the BWR lower core region. If the molten metallic core materials form stable blockage

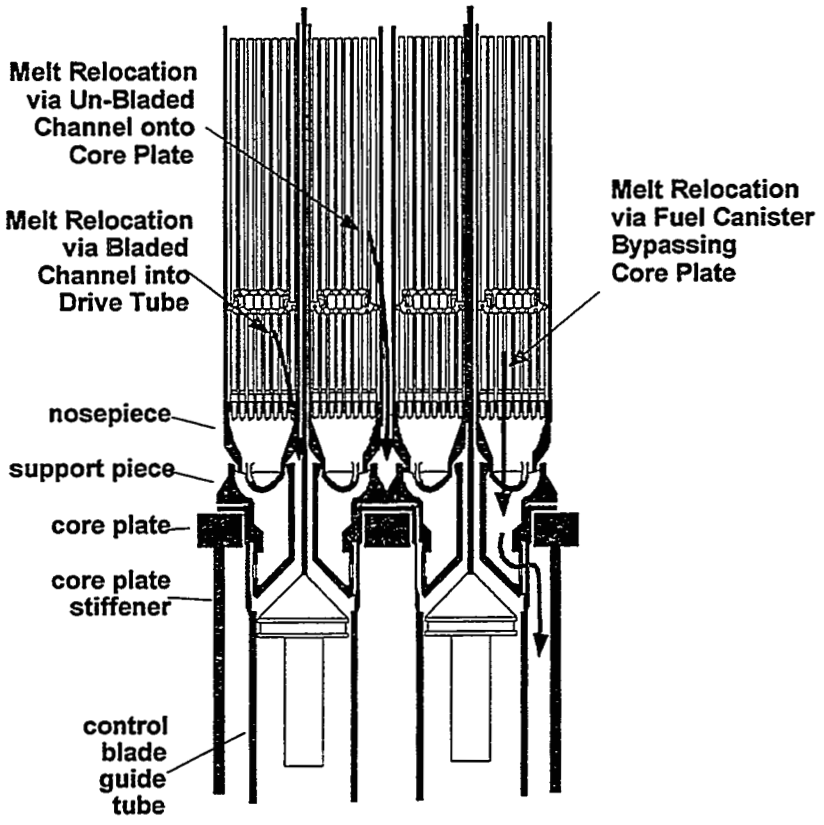

Figure 2: Diagram of the complex lower core structure in the BWR.

configurations in the lower BWR core region under dry core conditions, then it is considered likely that the TMI-like melt progression pathway, involving the formation of a ceramic fuel melt pool, will also apply to BWRs. It should be kept in mind, however, that under typical dry-core conditions, there is only marginally sufficient thermal heat sink available to freeze the relocating stainless steel control blade melt and the subsequently relocating zircaloy channel box and cladding materials. This together with the complex BWR lower core geometry, with many possible melt drainage pathways (Figure 2) and many potential material interaction effects, would suggest that stable blockages might not form, and that the continuous drainage melt progression pathway might be favored.

The general approach taken in the Ex-Reactor experiments is to simulate the lower 1/2 to 1 meter of the BWR core geometry in full scale at the time that the molten metallic core materials are beginning to drain from the upper regions of the core into the lowermost regions. A test section is constructed, including important geometrical features such as zircaloy fuel canister walls, B_4C-filled stainless steel control blade structure, fuel canister nosepieces, lower core plate, bladed and unbladed inter-canister gaps, and so on. Prototypic materials are used in the conduct of these experiments. Figure 3 shows a cross sectional view of two test section designs used in these experiments. In the upper view, a simple channel design used in the XR1 tests is shown where only the fuel canister walls (channel box) and the control blade features are included. The lower view shows the cross section for the

Lateral Geometry Considered in XR Series 1 and Series 2 Tests

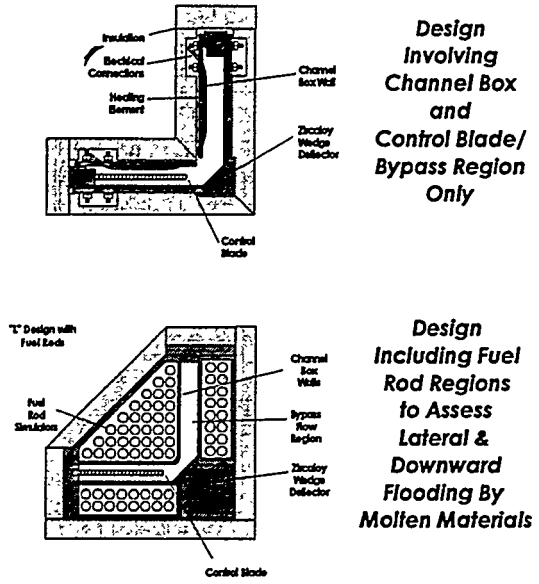

Figure 3: Cross sectional views of test bundles for the XR1 (top view) and XR2 (bottom view) tests.

Experimental Approach Used in the Ex-Reactor Metallic Melt Relocation Experiments

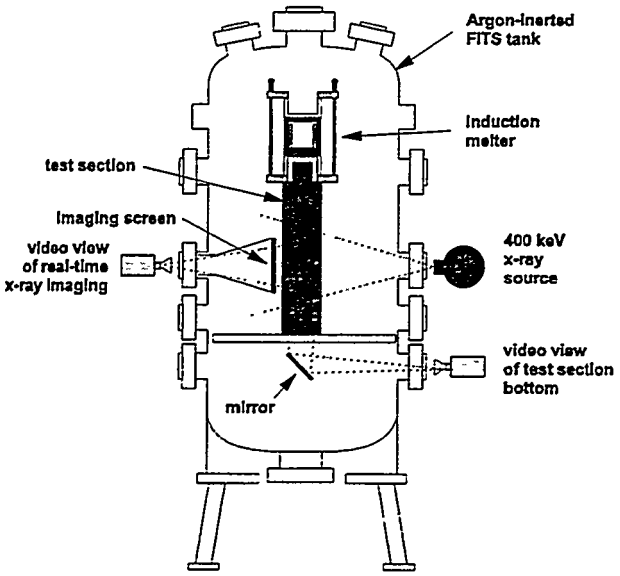

Figure 4: Facility for conducting the Ex-Reactor experiments.

more prototypic geometry XR2 tests which include arrays of zircaloy clad fuel rods in addition to the channel box and control blade structures. The lateral scale of the XR2 test section is designed to represent all of the lateral degrees of freedom with respect to the draining of molten materials, and was selected based on symmetry principles (the XR2 test section is approximately a 1/8 symmetric section extracted from the 4-canister repeating array of the BWR core).

The tests are conducted by pouring molten metallic materials (molten control blade steel and molten zircaloy components - fuel rod cladding and channel boxes) into the upper, open end of the heated test section, thereby simulating the melting and draining of the upper core metallic materials in the overheating reactor. The test sections are heated using electrical heating on the periphery so that a prototypic axial thermal gradient is imposed over the length of the test section. The object is to characterize the nature of any blockages that are formed as the melt enters the test geometry, and to provide information on melt drainage pathways through the lower core region.

Figure 4 shows the test facility used to conduct the XR experiments. The test section is placed within the argon-inerted test chamber to prevent air oxidation of the test section components and the draining metallic melts (control blade and zircaloy). The test section is instrumented with thermocouples to measure the thermal gradient prior to introducing the molten metals, and to characterize the melt flow and blockage behavior of the melt flowing into the test section. In addition to thermocouples, a real-time x-ray imaging system provides a video image

of the melt flow as it enters the test section, showing flow behavior and blockage formation.

The melt flow in the package is provided by an inductively powered melter system, situated above the test section (Figure 4). The total amount of metallic melt delivered to the test section is representative of that available from the entire axial extent of the core above the lower 1/2 to 1 meter region, and so, the tests include the full amount of incoming melt mass and enthalpy that would be typical of actual accident conditions.

Figure 5 and Figure 6 show the melting rates and thermal conditions expected for the conditions of interest. The axial gradient in the lower part of the BWR core at the time of initial control blade melting and draining is between 1000 and 2000 K/m. The melting of the control blades, as estimated by MELCOR, takes place over approximately a 10 minute duration. After the control blades have melted and relocated, the temperatures in the upper core reach zircaloy melting temperatures and the draining of the melting fuel rod cladding and channel boxes takes place, as predicted from the MELCOR calculations for short term station blackout (Figure 5).

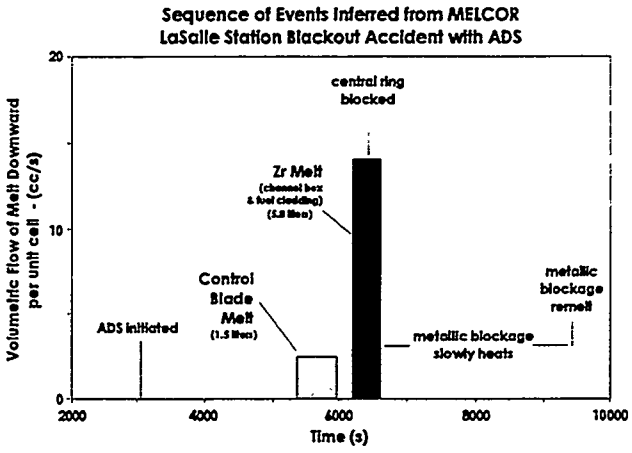

Figure 5: Flow rate of molten metallic materials from upper core into lower core.

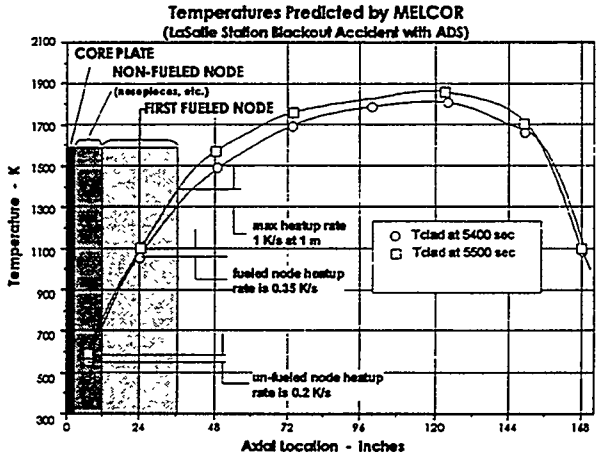

Figure 6: Axial thermal gradient in the lower BWR core for Dry-Core (Station Blackout with depressurization).

3. Results of XR1 Simple Channel Tests

The XR1 "Simple Channel" tests (XR1-1 and XR1-2) were performed to develop the techniques necessary to perform the more conclusive XR2 "Prototypic Geometry" experiments, and to gain insight into the effects of the major experiment parameters to be explored by these tests. A description of these initial two experiments and their results follows.

Table 1 Conditions Used in the XR1 Experiments

Test Condition	XR1-1	XR1-2
Channel Length	1 m	.5 m
Thermal Gradient	1000 K/m	2000 K/m
Channel Surface Oxide Layer	2 μm	2 μm
Melt Mass	12 kg	12 kg
Melt % B_4C	4.4w%	4.4w%
Melt Pour Duration	10 min	15 min

3.1 Test Conditions

As described in Section 2, the geometry of the XR1 experiments was simplified to include only the zircaloy channel box and control blade structures, as illustrated in Figure 3. Consistent with this simplification, the melt which was introduced into the XR1-1 and XR1-2 test channels consisted only of control blade melt (stainless steel and boron carbide) and was introduced to the "bladed" wing of the L-shaped channel, thereby simulating the melting and draining of the upper core blade structure into the lower core region. A simplified core plate structure was included in the XR1 test section design, as were some approximate details of the BWR fuel canister nosepieces. The principal test parameter varied between the two XR1 tests (Table 1) was the axial thermal gradient, with the XR1-1 test having a nominal 1000 K/meter axial gradient, and the XR1-2 test having a 2000 K/meter gradient. It is important to point out that the gradient was attained in both tests by holding the lower core plate region of the test at ~500 K, and heating the upper part of the test channel essentially to the melting point of the control blade structure (~1500 K). This simulates the conditions when molten blade material begins to drain into the lower part of the core. This also implies that the XR1-1 test channel was nominally 1 meter in length and that the XR1-2 test channel was nominally 0.5 meter in length. Test XR1-2, therefore, presented less thermal heat sink for the formation of blockages from the draining melt than did test XR1-1.

3.2 Melt Flow and Blockage Behavior

Both tests XR1-1 and XR1-2 showed some similar behavior in response to the control blade melt. In both tests the upper control blade was eroded away, partly in response to the radiant heat load from the upper inductively heated melter (~1700 K), and partly due to the added enthalpy carried with the molten control blade melt draining from the melter. In both tests, temporary blockages tended to form in the bladed and unbladed channels, where initial channel temperatures were between ~900 to 1100 K. These blockages led to the pooling of subsequently draining control blade melt within the zircaloy walls of the test section. The formation of these blockages and the pool accumulation were clearly observed in the real time video x-ray images of the test section. After a time (~2 minutes), the molten pool of control blade melt was observed to suddenly drain into the lower regions of the test section. In both XR1-1 and XR1-2, the drainage path was in the large channel gap region near the tip of the control blade where the bladed and unbladed channel gaps meet. Figure

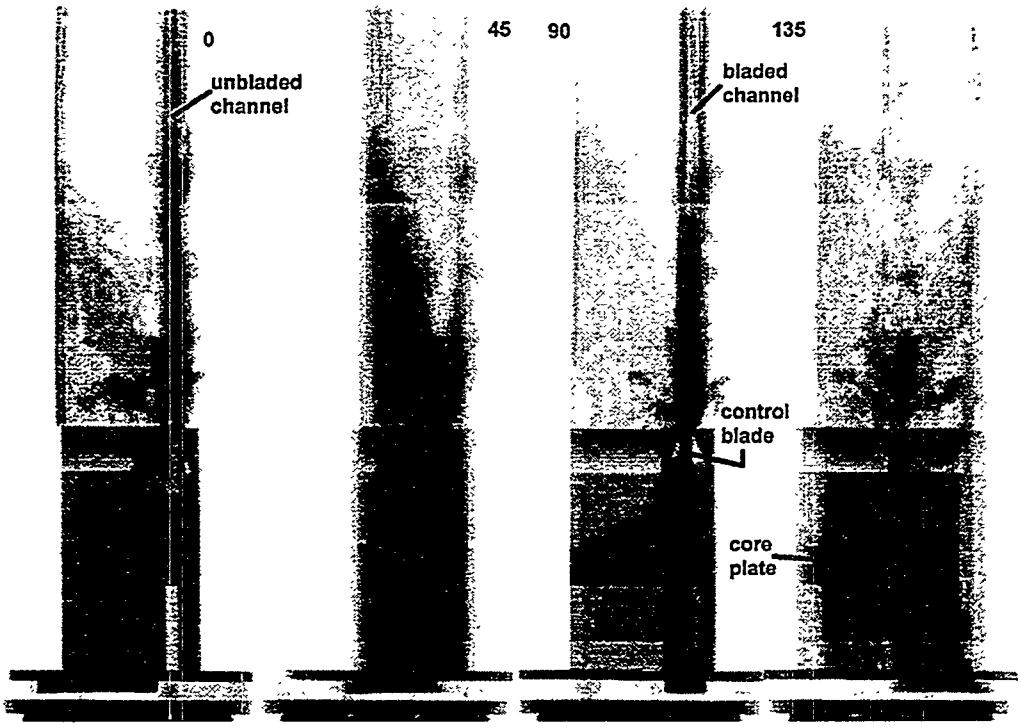

Figure 7: X-ray projection images of the XR1-2 test (.5m test section) seen from four directions (0, 45, 90 and 135 degrees).

7 shows x-ray projection images of the XR1-2 test section blockages after termination of the test. Four views of the test section are shown. The view indicated as 90 degrees shows a view normal to the unbladed channel, where the core plate is clearly visible. The 0 degree view is normal to the bladed channel, and the view indicated as 135 degrees shows an oblique view of both the bladed and unbladed channels. The oblique view of both channels best shows the remnants of the metallic melt pool, where the funnel-shaped voided region in the center mid-section of the channel is clearly seen. This voided region shows the drainage path taken when the melt relocated to the bottom regions of the channel. Part of the melt drained onto the core plate, as seen in the radiograph, and part drained into the bladed region below the core plate.

In comparing the results of the XR1-1 and XR1-2 tests, some differences in behavior were also seen. The downward penetration of molten material in the XR1-1 (1-meter channel with 1000 K/m thermal gradient) was not as great as was observed in the XR1-2 test (.5 meter channel with 2000 K/m gradient). In both tests, melt reached the lower core plate and accumulated there, however, very little material relocated below the core plate in XR1-1, whereas, much more material relocated below the core plate in test XR1-2. This trend is consistent with the higher thermal gradient in the shorter bundle (lower heat sink available for freezing), but also probably reflects the random nature of the melt draining process with respect to the

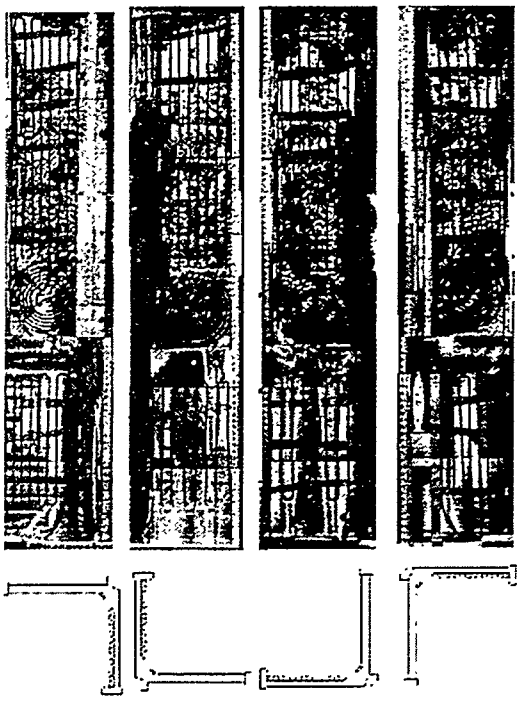

Figure 8: External views of the XR1-2 test section showing severe zircaloy wall attack from molten control blade melt.

precise path taken by the melt. Both tests also exhibited considerable interaction between the molten draining control blade melt and the zircaloy channel walls. The molten blade material dissolved the zircaloy walls locally and penetrated partially into the insulating material behind the channel walls. These effects were especially pronounced where the molten control blade material pooled over underlying blockages. The evidence suggests that the wall destruction was not instantaneous, and that some time is required to breach the surface oxide layer on the channel walls before penetration results.

The insulated region in the XR1 tests corresponds to the region in the BWR core that would normally be occupied by fuel rods, as seen in the XR2 series test section (Figure 3). In that the insulation behind the zircaloy walls prevented the intrusion of the control blade melt into the region normally occupied by fuel rods, the melt relocation observed in the XR1 tests was confined to the inter-canister gaps to a greater degree than would be expected had fuel rods been in the place of the insulation board. The zircaloy wall attack and penetration by the control blade melt can be seen in the external views of the XR1-2 test section shown in Figure 8.

4. Approach to XR2 Prototypic Geometry Tests

The XR2 experiments, currently under preparation, will include a much greater degree of prototypicality with respect to the geometrical details and test conditions which govern the behaviors under investigation. This includes a high degree of realism in the geometrical details by including fuel rods, and by using actual BWR core structural components. Additionally, the second melt pour of molten zircaloy into the lower core region (see Figure 5) will also be included and will be distributed across the entire cross section of the XR2 test channel (see Figure 3).

4.1 Detailed Prototypic Geometry

The XR2 test bundle is shown in cross section in Figure 3. In addition to including the fuel rod regions, considerable realism is also included in the lower

geometrical details of the test package. Actual BWR structural components, such as those shown in Figure 9, will be used in the fabrication of the test section, including the fuel canister nose piece, fuel rod tie plate, and fuel canister support piece. Realistic representation of the control rod guide tube, core plate, and control blade velocity limiter will also be included.

4.2 Melt Delivery System

One of the major technical challenges in the conduct of the XR2 experiments is the preparation and introduction of the appropriate molten materials into the correct regions of the test section. Molten control blade material must be delivered to the bladed section of the test bundle, whereas molten zircaloy must be directed over both the fuel rods and the channel box walls in order to simulate the melt relocation processes. The timing and rate of melt flow into the test section must also be controlled to correctly represent the accident conditions. In the XR1 tests, involving only control blade melt (stainless steel and boron carbide), a pot of molten metal was prepared by inductive heating techniques, and the molten charge was drained over the control blade region. Because of the extreme difficulties associated with containing molten zircaloy, a different approach is being taken in preparing the melts to be used in the XR2 experiments. The melter being developed for the XR2 tests is shown schematically in Figure 10. In this concept, wire is fed into an inductively heated graphite susceptor which is held at near 3000 K. The wire is melted within the melter by radiative heating from the graphite and the melt is directed over the desired locations at the entrance to the test section. The melting rate is determined by the rate at which the wire is fed into the melter. A wire feed system controls the velocity of the wire entering the melter. The regions requiring a zircaloy melt are fed with 1/16th inch diameter zirconium wire, and the regions requiring control blade

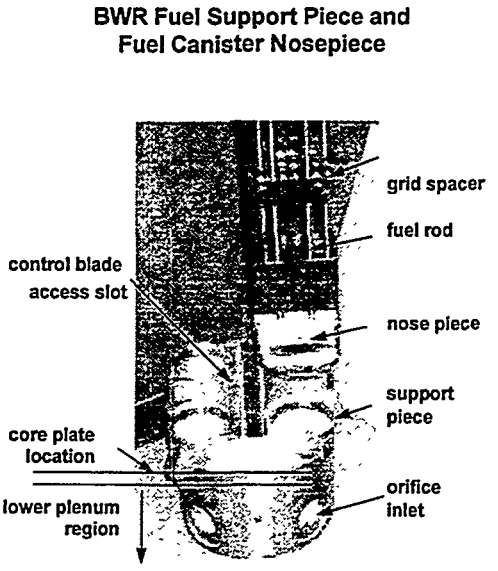

Figure 9: Photograph of BWR structural components that will be used in the fabrication of the XR2 test sections.

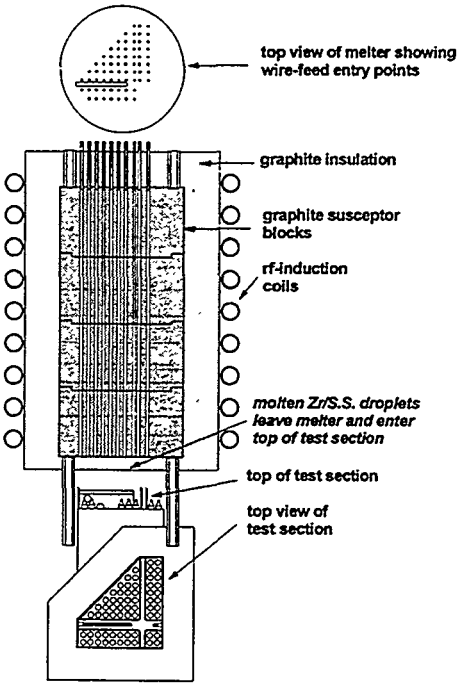

Figure 10: Wire fed melt delivery system developed for the XR2 experiments.

melt are fed with a drawn B_4C-loaded stainless steel wire composite (also 1/16th inch). The melter also provides a downward radiant heat flow of ~10 kW to the top of the test section which is situated below the melter, as shown in Figure 4.

5. Conclusions

The XR1 "simple channel" tests, XR1-1 and XR1-2, investigating the behavior of draining control blade melt in the lower BWR core under severe accident "dry core" conditions have been completed. These tests were primarily developmental in emphasis, but have provided useful insight into the operative phenomena in the reactor core during this phase of the accident. These tests showed that temporary blockages can form in the gaps between the channel box walls in the lower core due to the freezing of the initially relocating molten control blade materials. Due to material interactions between the molten blade material and the zircaloy channel walls and due to the continued enthalpy addition of subsequently relocating blade material, these blockages are breached, allowing the continued downward drainage of molten metal. During these processes, the zircaloy channel boxes become heavily attacked, allowing intrusion of control blade materials into the fuel rod regions of the core. Some blade material accumulates on the lower core plate, but some material can relocate to regions below the core plate by flowing into the fuel canister nosepieces. The initial melting and draining of the control blades causes significant degradation of the lower channel boxes, thus influencing the relocation pathways available to the subsequently melting zircaloy materials, which contain significantly more melt enthalpy in comparison to the molten control blade materials. The XR2 tests, currently under preparation, will include greater geometrical detail in the test section design and will include a zircaloy melt phase in addition to the initial control blade melt phase. The initial control blade melt phase will condition the test bundle by causing the initial damage and blockage effects observed in the XR1 tests, so that the subsequently introduced zircaloy melt will encounter prototypic conditions, structures, and melt drainage pathways. The XR2 tests either will show that the draining metallic zircaloy melt is so aggressive in eroding the lower core structures that melt drainage into the lower plenum is anticipated (continuous drainage pathway in Figure 1), or will reveal the configuration of in-core blockages that instead result. In the event that blockage, and not melt drainage, is observed (the TMI-like path in Figure 1), the configuration revealed by the experiments can be further analyzed by other analytical means to evaluate the timing of any subsequent metallic blockage meltout or ceramic melt release.

REFERENCES

1 F.P. Griffin and L.J. Ott, "Development of the BWR Dry Core Initial and Boundary Conditions for the SNL XR2 experiments," ORNL/NRC/LTR-94/38, 1994.

OBSERVATION OF THE DYNAMIC BEHAVIOR OF THE TWO-PHASE BOUNDARY LAYERS IN THE SBLB EXPERIMENTS

F.B. Cheung and K.H. Haddad
Department of Mechanical Engineering
The Pennsylvania State University, University Park, PA 16802

ABSTRACT

Subscale boundary layer boiling (SBLB) experiments were performed under controlled laboratory conditions to simulate the process of downward facing boiling on the external bottom surface of a reactor vessel. The objectives were to observe the dynamic behavior of the two-phase boundary layer and to determine the local variation of the critical heat flux. Transient quenching and steady-state boiling experiments were conducted under both saturated and subcooled conditions. For all cases explored in the experiments, strong subcooling effects were observed on the size and dynamics of the vapor bubbles. The local boiling curves deduced from the quenching data showed significant variations along the vessel wall. In particular, the CHF value increased significantly from the bottom center to the upper edge of the vessel. As the degree of subcooling was increased, considerably higher values of CHF were obtained throughout the entire heating surface. Results of the present study indicated that with subcooling of the water in a flooded cavity, much higher heat fluxes from the core melt resulting from a severe accident could be accommodated by nucleate boiling on the external surface of the reactor lower head.

INTRODUCTION

The concept of external cooling of core melt by cavity flooding has been considered a desirable means of decay heat removal during a severe core-meltdown accident in an advanced light water reactor. In this concept, the decay heat generated in the melt is removed from the external bottom surface of the reactor vessel by downward facing boiling of water in the flooded cavity. The feasibility of this concept depends largely on the critical heat flux on the external bottom surface of the reactor vessel. For the case in which the critical heat flux is higher than the local heat flux from the core melt, nucleate boiling will be the prevailing mode of heat transfer. The wall temperatures can be maintained well below the failure temperature of the steel structure. However, if the downward facing boiling situation and the thermal loading conditions are such that the local heat flux from the core melt exceeds the critical heat flux, then transition to film boiling will occur on the external bottom surface. Under such circumstances, the wall temperatures could rise rapidly toward the failure temperature of the steel structure, and the integrity of the reactor lower head could be severely jeopardized.

In spite of its practical importance, very little is known about the boiling phenomena and the critical heat flux on a downward facing curved surface. Most studies of nucleate boiling have been focused on the effects of liquid properties and surface conditions, with the effects of shape

and size of the surface being treated to be of secondary importance (Nishikawa and Fujita 1990). The reported results on the influence of surface orientation are limited to those for boiling on inclined flat plates or disks of relatively small dimensions with no curvature on the surface.

For inclined flat surfaces, it has been found that the rate of nucleate boiling can be significantly affected by the orientation of the heating surface. An upward shift of the boiling curve as the surface changes from a horizontally upward facing to a vertical position was observed by Class et al. (1959) for liquid hydrogen, Githinji and Sabersky (1963) for isopropyl alcohol, and Marcus and Dropkin (1963) for water. Upward shifts in the boiling curve with an increase of inclination angle were also observed by and Littles and Wallis (1970) for Freon 113, Vishnev et al. (1976) for liquid helium, and Chen (1978) for Freon 11. Recently, Nishikawa et al. (1984), Jung et al. (1987), and Beduz et al. (1988) used water, R-11, and liquid nitrogen, respectively, as the working fluid to study nucleate boiling on inclined flat surfaces and reported that at low heat fluxes the boiling curves shifted considerably upward with an increase of inclination angle from the upward facing to downward facing direction. However, at high heat fluxes, the boiling curves for various inclination angles appeared to merge together into a single curve, implying that the surface orientation had very little effect on nucleate boiling in the high-heat-flux regime.

The effects of surface orientation on the critical heat flux have been reported by Ishigai et al. (1961), Costello and Adams (1963), Lyon (1965), Anderson and Bova (1971), Styrikovich and Polyakov (1973), Bewilogua et al. (1975), Vishnev et al. (1976), Beduz et al. (1988), and Guo and El-Genk (1991, 1992). Bewilogua et al. (1975) measured the critical heat flux for liquid helium on a disk heater inclined with an angle ϕ against a horizontal plane. At a given pressure, the critical heat flux, q_{CHF}, was related to the referenced value, q_{CHF} (0), for a horizontally upward facing disk heater (i.e., $\phi = 0$) by

$$q_{CHF}/q_{CHF}(0) = [1 - \phi/190°]^{1/2} \qquad (1)$$

The same relationship was obtained by Vishnev et al. (1976) for liquid helium on an inclined flat plate. The data of Beduz et al. (1988) obtained with liquid nitrogen generally supported the trend predicted by equation (1), although their results lie just under the low end of the data scatter. While equation (1) works quite well for cryogenic fluids, it does not appear to be valid for water (Ishigai et al. 1961, Guo and El-Genk 1991, 1992).

Ishigai et al. (1961) and Anderson and Bova (1971) observed that the critical heat flux was related to the time duration for a vapor mass to remain on the heating surface. The longer a vapor mass stayed on the heating surface, the lower the CHF value would be. For a downward facing surface, vapor bubbles tend to stay on the surface longer and coalesce underneath the surface due to buoyancy, leading to a smaller value of CHF. Costello and Adams (1963) reported a reduction of 25% in the CHF value from upward facing to downward facing boiling, Lyon (1965) reported a reduction of a factor of four, and Styrikovich and Polyakov (1973) reported a reduction of 40%. Recently, Guo and El-Genk (1991) performed quenching experiments using

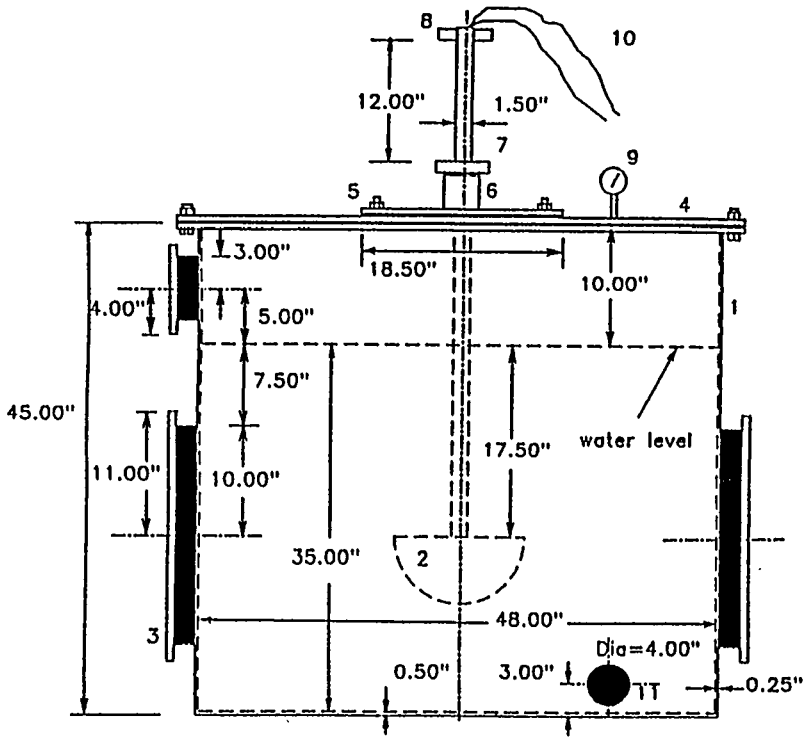

1 Cylindrical Tank
2 Hemispherical Vessel
3 Viewing Window
4 Tank Cover
5 Tank Acess Hole Cover
6 Vertical Guidance Mechanism
7 Stopping Mechanism
8 Handle
9 Pressure Gage
10 Thermocouples and Power Supply Lines
11 Immersion Heater

Figure 2. Front View of the SBLB Pressurized Water Tank with the Hemispherical Test Vessel.

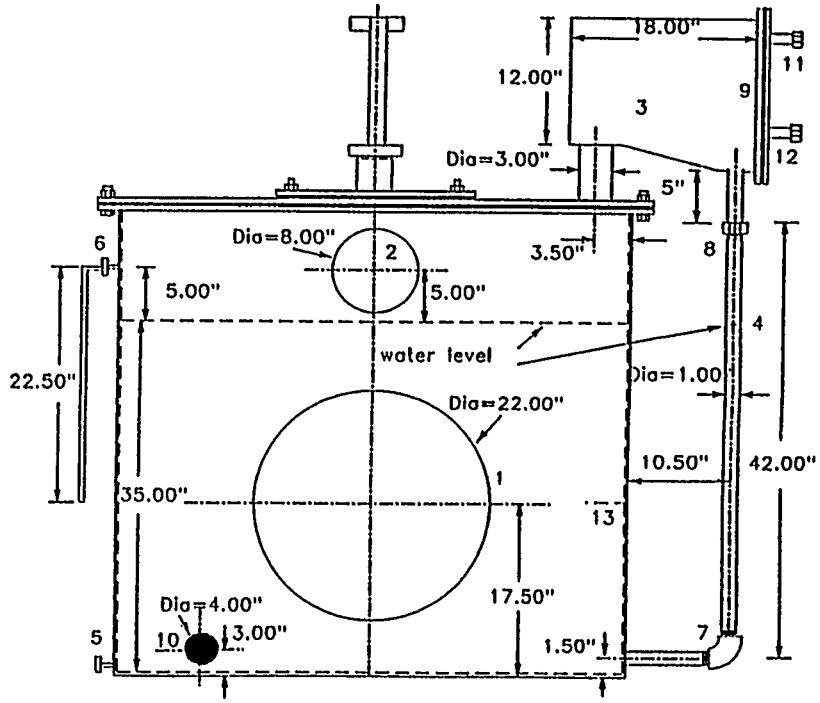

1 Large Viewing Window
2 Small Viewing Window
3 Condenser
4 Condensate Return
5 Drain
6 Water Inlet and Pressure Relief Valve
7 Elbow
8 Pipe Connection
9 Condenser Access Door
10 Immersion Heater
11 Cold Water Inlet
12 Hot Water Outlet
13 Thermocouple Access Hole

Figure 3. Side View of the SBLB Pressurized Water Tank with the Condenser Unit.

vessels of varying sizes made of different wall materials could be easily installed and tested under identical conditions one at a time.

To minimize heat loss from the water tank, thermal insulation material was applied to cover all the exterior surfaces of the tank and the condenser unit, leaving only the viewing windows exposed to the room air. With the insulation material in place, the bulk water temperature dropped less than 0.7°C per hour with the water being saturated and the immersion heaters in the off position. This small amount of heat loss could easily be compensated by turning on the immersion heaters for a couple of minutes every hour. Thus the same experimental setup was suitable for both steady-state boiling and transient quenching experiments.

Two Strawberry Tree ACPC-16 data acquisition boards were installed inside a 386 IBM personal computer. Each board could monitor up to 16 thermocouples with a resolution that could be selected in the range between 12 to 16 Bits. The connections between the boards inside the PC and the thermocouples were accomplished through the use of Strawberry Tree T21 terminal panels. These panels had a large isothermal plate with screw terminals for analog inputs and digital I/O. The isothermal plate attenuated temperature differences at the cold junction connector. Each of these panels was precalibrated at the factory with the ACPC board with which it was intended to be used. These factory calibrations were found to be satisfactory when the thermocouple readings were checked against thermometer readings at the freezing and the boiling points of water. A total of 24 thermocouples were connected to the data acquisition system. The first 16 of these sensors were placed at the locations corresponding to the nodes in the finite difference analysis used to deduce the boiling heat flux. The rest were placed at various locations inside the vessel wall to assess the uniformity of the heating of the test vessel before each run.

Based on estimates of the time constant of the vessel at the critical heat flux state, it was decided to use a sampling rate of 0.1 s which also allowed the resolution to be set to 16 Bits for maximum accuracy. For higher sampling rates, the resolution might have to be decreased since readings at a higher frequency take longer to achieve than those at a lower frequency. A computer program was developed to read the temperatures from the thermocouples. After the thermocouples were scanned once, the readings were stored in memory before the sensors were scanned again after 0.1 s. It was only at the end of the process that all the thermocouple readings were transferred into a file for later analysis.

EXPERIMENTAL PROCEDURE

Two types of experiments were conducted in this study. These were transient quenching experiments and steady-state boiling experiments. The transient quenching experiments were used to simulate the transient decay heat removal process in a delayed cavity flooding situation whereas the steady-state boiling experiments were employed to simulate the situation of long-term external cooling of a reactor lower head in a flooded cavity. To prepare for either type of experiments, the tank was filled with water to a desired level, leaving a 0.25m air gap on the top

downward facing inclined flat plates. They found that the CHF value decreased from about 0.8 MW/m^2 in the vertical position to nearly 0.21 MW/m^2 in the horizontally downward facing position, a reduction of almost a factor of four. Although a similar trend was observed by various investigators for the effect of the inclination angle, there were significant quantitative differences in the measured values of CHF. Note that in all of the above studies, the size of the heating surface was relatively small (on the order of 10 to 50 mm), and no spatial variation of the CHF value was observed along the downward facing, inclined surface.

Despite the quantitative differences in the measured values of CHF and the lack of spatial variation of the critical heat flux along the heating surface, the above results cannot be applied to the case of downward facing boiling on the external bottom surface of a reactor vessel. This is because the reactor configuration is not only downward facing but also curved. Moreover, the area of the heating surface is not a constant but increases from the bottom center to the upper portion of the vessel. Thus the external bottom surface of a reactor vessel cannot be approximated by downward facing flat plates with varying inclination angles. To realistically simulate the reactor situation, a subscale boundary layer boiling (SBLB) test facility was developed by Cheung et al. (1994 a,b) to study the phenomena of downward facing boiling on the external surface of a heated hemispherical vessel. A two-phase liquid-vapor boundary layer was clearly observed on the external surface of the vessel under both steady-state and transient quenching conditions. Local boiling curves were deduced from the quenching data for the case of saturated boiling and were found to vary significantly along the curved heating surface. In particular, the local CHF value increased by almost 100% from the bottom center to the upper edge of the vessel.

In this study, the SBLB test facility was employed to investigate the phenomena of downward facing boiling on the external surface of a heated hemispherical vessel under both saturated and subcooled boiling conditions. The objectives were: (i) to quantify the local variation of the critical heat flux, (ii) to determine the effects of subcooling, and (iii) to seek a clear physical insight of the dynamic behavior of the two-phase boundary layers.

DESCRIPTION OF THE SBLB TEST FACILITY

The subscale boundary layer boiling (SBLB) test facility was developed specifically for simulating the phenomena of downward facing boiling on the external bottom surface of a reactor vessel. As shown schematically in Figure 1, the facility consisted of three major components, i.e., a pressurized water tank with a condenser unit, a heated hemispherical/toroidal vessel, and a data acquisition/photographic system. The water tank with a condenser unit at the top for mass flux measurement, was completely sealed and designed to sustain a pressure up to 20 psig (~2.4 bars). It was 1.22m in diameter and 1.14m in height, and had two large and one small viewing windows (see Figure 2 for detailed dimensions). The small window was located above the water level and was used to determine the initial position of the test vessel before submergence in water. On the other hand, the large windows were located below the water level and were used to observe the dynamic behavior of the two-phase boundary layer during downward facing boiling of water on

the external surface of the vessel. Three immersion heaters were installed near the bottom of the tank for preheating water to a prescribed temperature before a run. The condenser unit was connected to the cover of the tank assembly through a 76mm steel pipe, as shown in Figure 3. The condensate return, on the other hand, was connected to the bottom of the tank assembly through a 25.4mm steel pipe. With this arrangement, the water level in the tank could be maintained constant. Pressurization of the tank could be accomplished in two different ways. One was to boil the water in the tank for a prolonged period of time by turning on all three immersion heaters without operating the condenser unit. The other was to inject high-pressure air into the tank through the pressure relief valve.

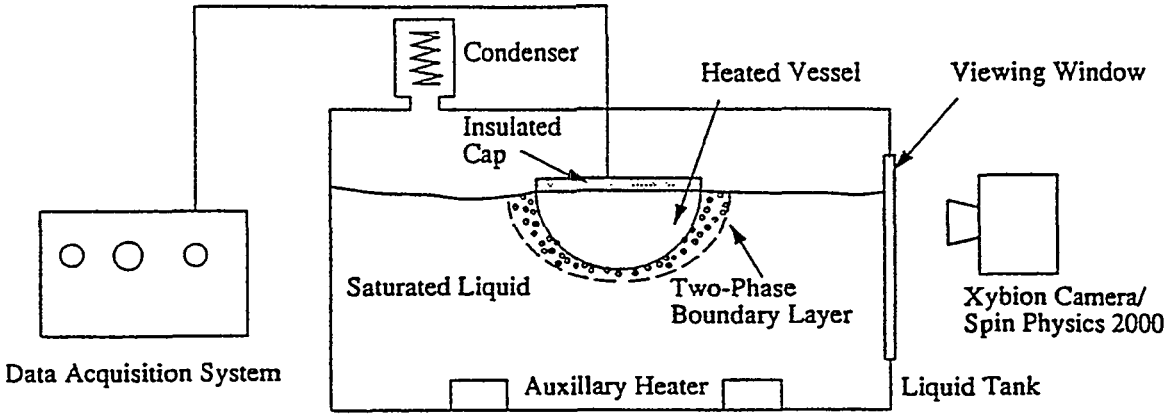

Figure 1. Schematic of the Subscale Boundary Layer Boiling (SBLB) Test Facility.

Three different types of test vessels were prepared for use as the heating surface in the SBLB experiments. These were continuous hemispherical vessels, segmented hemispherical vessels, and continuous toroidal vessels. This paper reports only the results obtained using the continuous hemispherical vessels. This type of test vessels was fabricated by connecting a stainless steel or aluminum hemisphere to a top cover made of the same metal, with a high-temperature rubber gasket placed in-between for thermal insulation and leak tightness. The top cover was welded at its center to a pipe coupling that could screw tightly onto a vertical guidance mechanism (see Figure 2). The vessel as a whole was suspended in the center of the water tank by the vertical guidance mechanism that allowed the vessel to travel freely in the vertical direction while keeping the tank leak tight. Pre-shaped nichrome coils with a prescribed power density were applied uniformly on the interior surface of the hemisphere for heating the vessel to desired temperatures. The electric power supply lines were connected to the nichrome coils through the hollow space in the vertical guidance mechanism. Also connected through the hollow space were 30 gage chromel-alumel thermocouples that were embedded in the vessel wall at various locations for temperature measurement. The thermocouple and power supply lines were securely fixed inside the vertical guidance mechanism so that no tension would be applied on them when changing the position of the heated vessel. Cleaning/polishing and replacement of the vessel was made by opening the tank access hole cover located in the middle of the tank cover. In this way,

(see Figure 2). The water was then purified and upgraded using a filter system consisting of a Porta pump (1/2 HP) and a high-grade replaceable filter. This was done by circulating the water through the filter system at least twice to remove all particles in the water. The water was then boiled for a long period of time to degas, and was allowed to cool down to room temperature. It was then circulated through the filter system again to remove whatever particles precipitated from the water during boiling. After the water in the tank had been conditioned, the external surface of the hemispherical vessel was polished with fine emery paper (#220) and cleansed with acetone. The vessel was then suspended in the air gap near the top of the water tank by using the vertical guidance mechanism. The heating elements (i.e., the nichrome coils) and the thermocouples inside the vessel were connected to the power supply and the data acquisition system, respectively, through the hollow space in the guidance mechanism. The immersion heaters were then turned on to bring the water in the tank to a prescribed temperature. This completed the procedure to prepare for a run.

Both stainless steel and aluminum vessels having diameters of 8" (~0.2m) and 12" (~0.3m) were tested in this study under saturated and subcooled boiling conditions. In the former case, the water temperature was maintained at 100°C whereas in the latter case, the water temperature was kept either at 90°C, 93°C, or 97°C. To conduct a transient quenching experiment, the immersion heaters were turned off once the water in the tank was raised to the prescribed temperature. A sufficiently long waiting period was given to allow the water to become completely quiescent. During the waiting period, power was supplied to the nichrome coils in the vessel to gradually heat the vessel wall to a uniform temperature in the range of 300°C to 350°C. Once the vessel reached the prescribed temperature, the power supply was turned off, and the data acquisition system was activated. The vessel was quenched into the water by suddenly lowering the vertical guidance mechanism to a prescribed position. Usually, it took less than two seconds to submerge the vessel in a relatively smooth manner. By the time the vessel assumed its final position, the external surface of the vessel was still in the film boiling regime. As long as the initial temperature of the vessel was above 300°C, the measured CHF values and the corresponding wall superheats were found to be virtually independent of the initial vessel temperature.

Transient responses of the local wall temperatures during the quenching process were recorded by scanning the embedded thermocouples (a total of 24) once every 0.1 second. However, a higher sampling rate was found to be needed for the case with the water temperature at 90°C, as the quenching time was relatively short. In that case, the thermocouples were scanned once every 0.05 seconds. Throughout the quenching event, the data acquisition system controlled with a 386 IBM personal computer was used for temperature recording. In the meantime, the downward facing boiling process and the dynamic behavior of the two-phase boundary layer on the vessel outer surface were video taped through the large viewing windows in the water tank using a high-resolution CCD video camera by Sony. An in-house inverse heat conduction code was employed to deduce the local boiling curves from the transient temperature data. The data reduction analysis is presented in the next section.

Steady-state boiling experiments were also performed in this study under both saturated and subcooled conditions. However, no quantitative heat transfer data were taken in this series of experiments. Only visual observation of the dynamic behavior of the two-phase boundary layer in the nucleate boiling regime was made. The primary objective was to seek a better physical insight of the effect of subcooling on the local behavior of the two-phase boundary layer. To conduct a steady-state boiling experiment, the test vessel was submerged in the middle of the water tank once the water temperature reached 90°C. The immersion heaters were then turned off, and the power control unit was turned on and set at a prescribed level to supply power at a given rate to the nichrome coils in the vessel. The power input was maintained constant and a sufficiently long waiting period was given to allow the boiling process to reach a steady state. The attainment of a steady-state boiling situation was assumed when there were no further changes in the temperature readings of the embedded thermocouples. The steady-state boiling process and the behavior of the two-phase boundary layer on the vessel outer surface were video taped. When the recording was done, the immersion heaters were turned on to raise the water temperature in the tank. As the water temperature reached the next level, i.e., 93°C, the immersion heaters were turned off. Video taping of the boiling event was made as a new steady state was attained. The above procedure was repeated until the saturated boiling case was done.

DATA REDUCTION

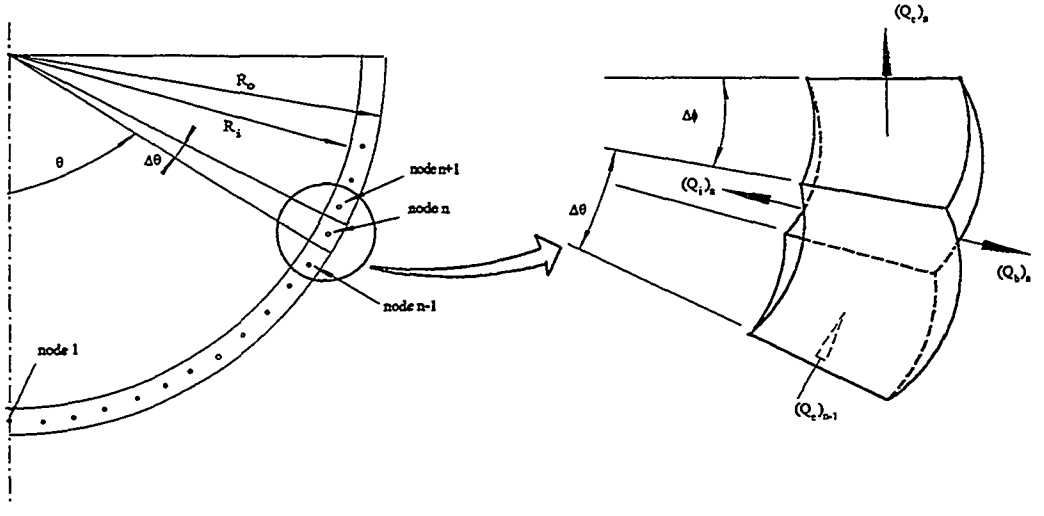

Figure 4. Configuration of the Control Volume and the Node Distribution in the Data Reduction Analysis.

An inverse heat conduction code was developed for deducing the local boiling curves from the transient temperature data recorded in the quenching experiments. The code was based on the finite difference method using the control volume approach. Figure 4 shows the configuration of the control volume and the node distribution. The wall thickness was not drawn to scale in the

figure. For all test vessels used in the transient experiments, the wall thickness was two orders of magnitude smaller than the vessel diameter. In view of this, the control volume for node n was chosen to be

$$V_n = \frac{1}{3}(R_o^3 - R_i^3)[\cos\theta - \cos(\theta + \Delta\theta)] \tag{2}$$

where R_o is the outside radius of the vessel, R_i the inside radius, and θ the local angle of inclination, and Δθ the node size in the θ-direction. A total of 16 nodes were used along the curved heating surface with the temperature at each node given by the corresponding thermocouple reading. An energy balance on the control volume represented by node n gives

$$\rho\, C_p V_n\, (T_n^k - T_n^{k-1}) = [(Q_c)_{n-1} - (Q_c)_n - (Q_b)_n - (Q_i)_n]\,\Delta t \tag{3}$$

where T_n^{k-1} and T_n^k represent the local temperatures at the time steps $k-1$ and k, respectively, Δt the time step, ρ the density of the wall material, C_p the specific heat, $(Q_c)_{n-1}$ the heat conducted into the control volume in the θ-direction, $(Q_c)_n$ the heat conducted out of the control volume in the θ-direction, $(Q_b)_n$ the local heat removal from the outer surface by boiling, and $(Q_i)_n$ the heat loss to the interior of the vessel. Since all the test vessels were tightly sealed, the quantity $(Q_i)_n$ was found to be almost two orders of magnitude smaller than the others. Hence, it was neglected in the calculations. The other three quantities are given by

$$(Q_c)_{n-1} = \frac{1}{2\Delta s}\sin\theta\,(R_o^2 - R_i^2)\,\lambda\,(T_{n-1}^k - T_n^k) \tag{4}$$

$$(Q_c)_n = \frac{1}{2\Delta s}\sin(\theta + \Delta\theta)\,(R_o^2 - R_i^2)\,\lambda\,(T_n^k - T_{n+1}^k) \tag{5}$$

$$(Q_b)_n = R_o^2[\cos\theta - \cos(\theta + \Delta\theta)]\,(q_b'')_n \tag{6}$$

where $(q_b'')_n$ is the local boiling heat flux for node n, λ the thermal conductivity of the wall, and Δs the distance between nodes given by

$$\Delta s = \frac{1}{2}(R_i + R_o)\,\Delta\theta \tag{7}$$

For the node at the bottom center of the vessel, the same approach was used except that the quantity $(Q_c)_{n-1}$ was set equal to zero due to symmetry.

From the transient temperature data, equations (2) to (7) were used to solve for the values of $(q_b'')_n$. The time step Δt was chosen to be the same as the sampling time of the data acquisition system employed in the experiments. Note that a total of 24 thermocouples were embedded in the wall. The first 16 of them were placed at the locations corresponding to the nodes shown in Figure 4. Each of these sensors were embedded half way through the wall. The remaining eight thermocouples were placed at other selected locations and were embedded at various depths in the wall. From the readings of these eight thermocouples, it was found that the thermocouple

located at the center of each node represented closely the instantaneous average temperature of the node during transient quenching.

RESULTS AND DISCUSSION

Dynamic Behavior of the Two-Phase Boundary Layer During Transient Quenching

The transient quenching events were examined in detail by playing the video tapes in slow motions. The rate of quenching was found to increase substantially with increasing subcooling. As the water temperature was decreased from 100°C to 90°C, the time required to quench the vessel from the same initial temperature reduced by almost an order of magnitude. However, the time evolution of the boiling process on the vessel outer surface was essentially the same for both saturated and subcooled boiling. A typical sequence of events is reproduced in Figures 5 and 6.

In the initial stage of quenching, the entire external surface of the vessel was covered by a continuous vapor film, as shown in Figures 5(a) and 5(b). The picture shown in Figure 5(a) was taken immediately after the vessel was submerged in water. At that moment, the wall temperature was well above the minimum film boiling temperature. The vapor film was quite wavy, especially in the upper portion of the vessel. Evidently, the two-phase boundary layer was in the turbulent film boiling flow regime. As the wall temperature dropped toward the minimum film boiling temperature, the vapor film became very smooth. This situation corresponded to the moment when the picture shown in Figure 5(b) was taken. At that time, the two-phase boundary layer was in the laminar film boiling flow regime.

Once the local wall temperature dropped below the minimum film boiling temperature, transition boiling began to take place, eventually leading to the occurrence of CHF on the vessel outer surface. This intermediate stage of quenching was represented by the sequential pictures shown in Figures 5(c), 5(d), 6(a) and 6(b). It was in this stage that significant local variations of the two-phase boundary layer configuration were observed. Changes in the boiling regime did not occur uniformly over the entire surface. Rather, transition boiling first took place near the upper edge of the vessel, as shown in Figure 5(c). It then propagated downward along the curved surface, and eventually reached the bottom center of the vessel. By the time transition boiling took place at the bottom center, the upper portion of the vessel was already in the state of CHF, as shown in Figure 5(d). Immediately after the CHF state, the local wall temperatures dropped very quickly toward the saturation temperature. This situation was shown in Figure 6(a). No vapor bubbles were generated near the upper edge of the vessel, and the local surface was non-boiling. The state of CHF continued to spread downward along the curved surface until it reached the bottom center (see Figure 6b), marking the end of the intermediate stage.

Beyond the CHF state, nucleate boiling became the only mechanism of vapor production on the vessel outer surface. The quenching process thus entered into its final stage. In this stage, vapor bubbles were generated mainly in the bottom center region. Elsewhere on the vessel outer surface, it was non-boiling, as shown in Figure 6(c). The presence of vapor bubbles in the upper

5(a)

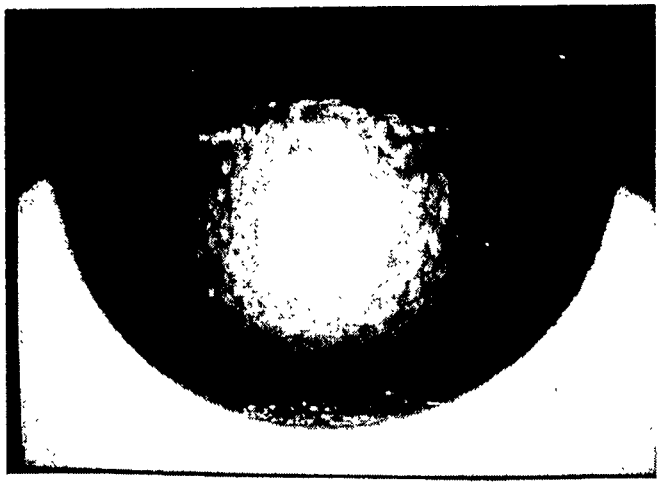

5(c)

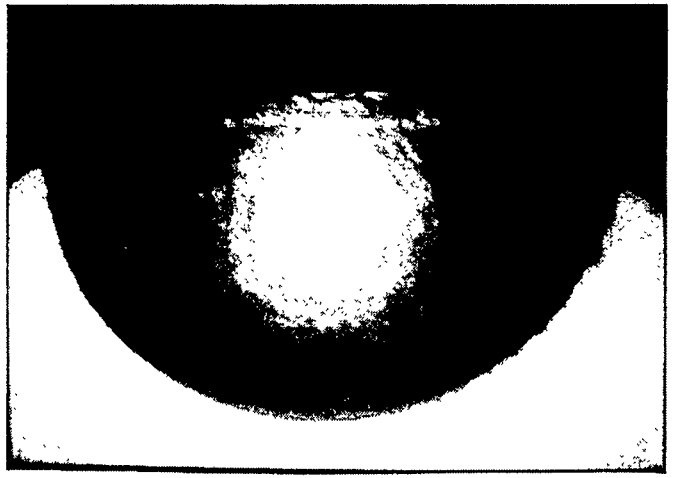

5(b)

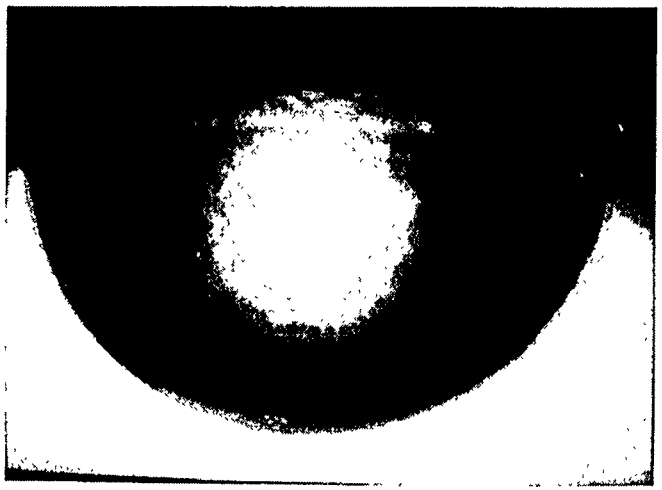

5(d)

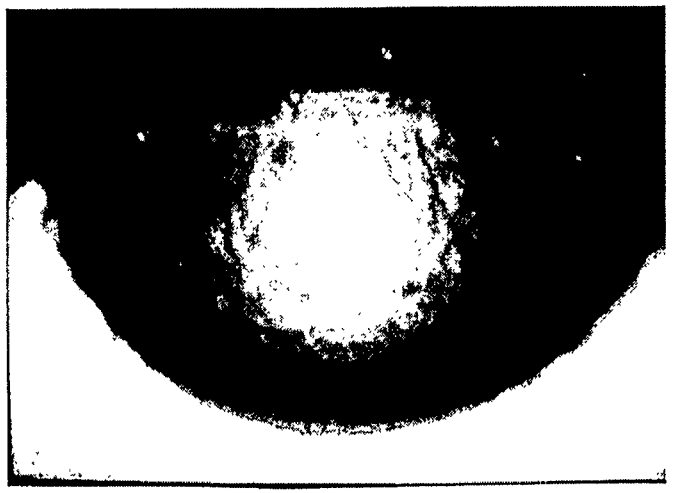

Figure 5. Sequence of Events Observed in the Initial and Intermediate Stages of Quenching.

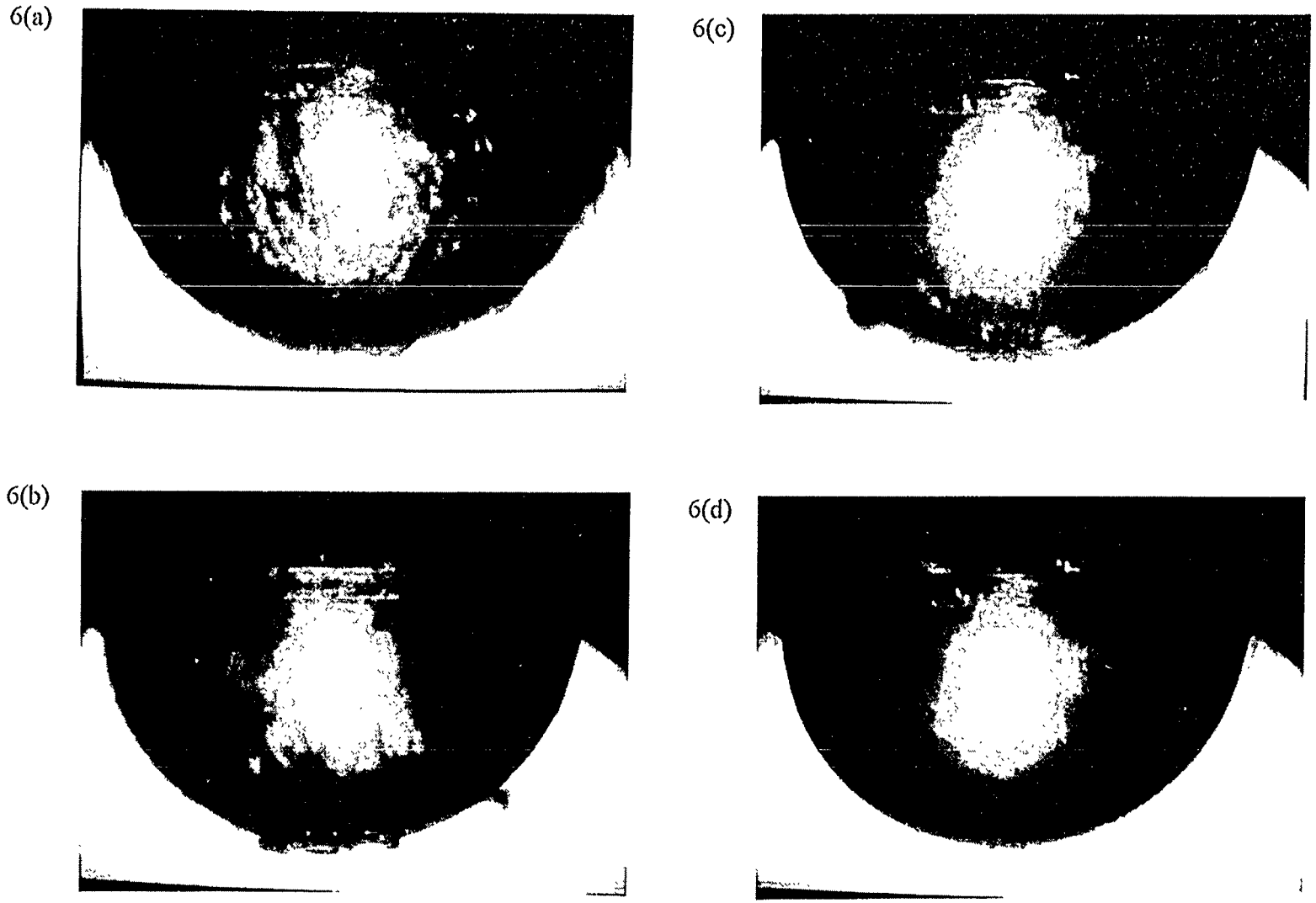

Figure 6. Sequence of Events Observed in the Intermediate and Final Stages of Quenching.

portion of the vessel was due entirely to the upstream effect of the two-phase boundary layer flow along the curved surface. Eventually, the bottom center was cooled down toward the saturation temperature, and no further vapor bubbles were generated beyond this point, marking the end of the quenching process (see Figure 6d).

When the water was subcooled, the time duration occupied by each of the above three stages of quenching was found to decrease substantially. In general, the larger the subcooling, the shorter was the time duration. For the cases with water temperatures at 90°C and 93°C, the intermediate stage was so short that the state of CHF was attained almost immediately after the onset of transition boiling. Also, the turbulent film boiling flow regime was not observed in the initial stage of quenching. This was probably due to the fact that the minimum film boiling temperature might have increased with subcooling. It should be noted that with subcooling, there was natural convection cooling of the vessel at the end of the quenching process. Although the entire vessel outer surface was non-boiling, the wall temperature continued to drop until it reached the subcooled water temperature.

From the above observation, it is obvious that the dynamic behavior of the two-phase boundary layer depended strongly upon the water subcooling as well as the local position along the curved heating surface. For all cases explored in the experiments, the local rate of quenching was highly non-uniform. Although the bottom center of the vessel was submerged in the water before the other parts of the vessel, it took a longer time to quench than the rest of the vessel. Conceivably, the local boiling curve and thus the local critical heat flux could vary significantly from the bottom center to the upper edge of the vessel. In addition to the spatial variation, subcooling also had significant influence on the local boiling curve and the local CHF value. A detailed discussion of the spatial variation and subcooling effects will be presented in the following sections.

Dynamic Behavior of the Two-Phase Boundary Layer During Steady-State Boiling

To seek a better physical understanding of the dynamic behavior of the two-phase boundary layer, steady-state boiling experiments were conducted under both saturated and subcooled conditions. In all cases, a buoyancy-driven two-phase boundary layer flow was clearly observed on the external surface of the heated hemispherical vessel, as shown in Figure 7. The shape and size of the vapor bubbles as well as their growth and departure behavior were found to vary significantly along the curved heating surface. For saturated boiling, the vapor bubbles in the bottom center region of the vessel were an order of magnitude larger than those observed in the upper portion of the vessel. The vapor bubbles at the bottom center were elongated and had a shape resembling a pancake whereas those in the upper portion were almost spherical. Upon departure, the vapor bubbles from the bottom center gradually transformed into the shape of a spherical cap while washing away the growing bubbles in the downstream locations. Evidently, the nucleate boiling process taking place in the downstream locations depended strongly on the upstream conditions (i.e., the vapor bubble activities in the bottom center region), and thus it could not be treated as a localized event.

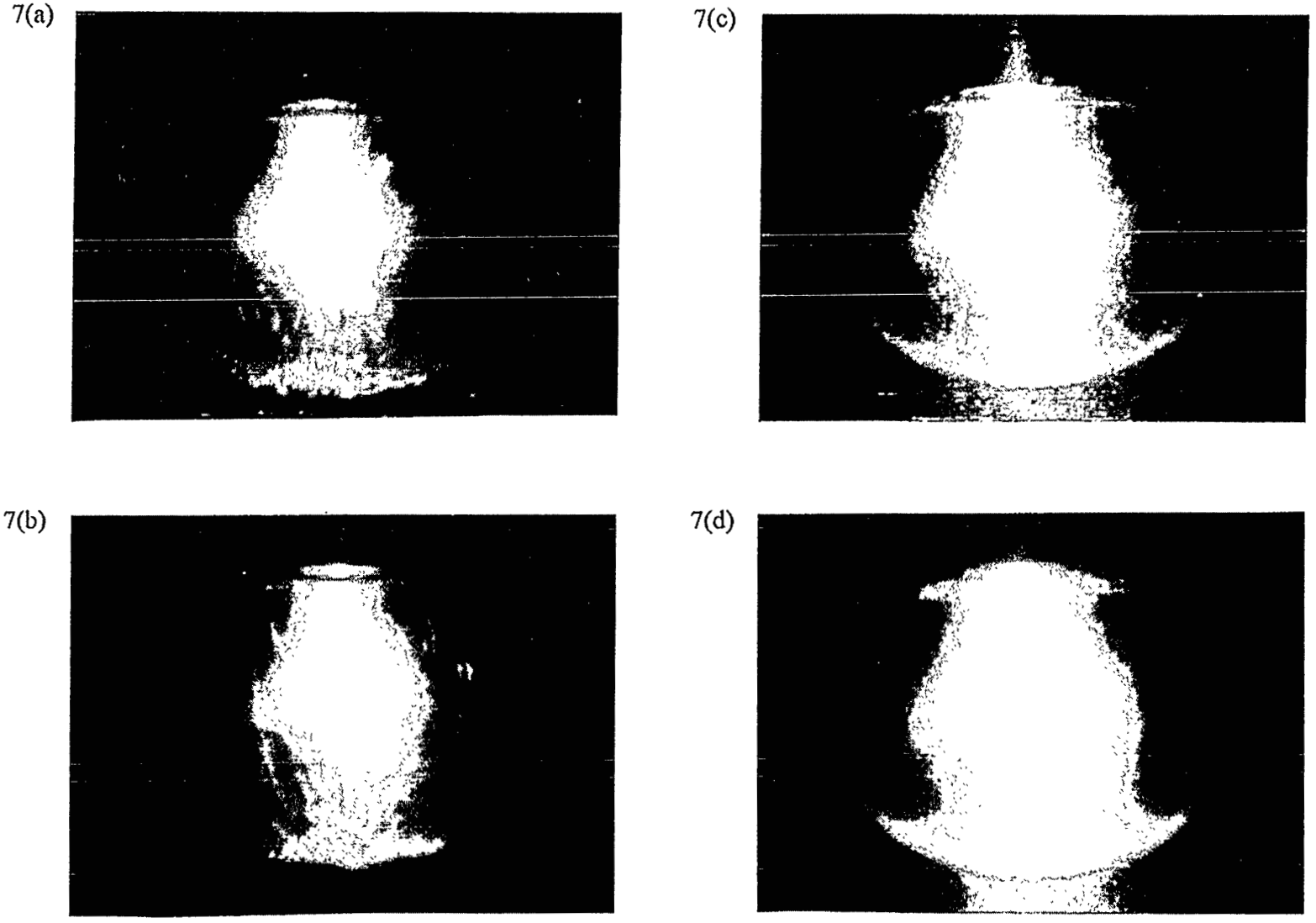

Figure 7. Configurations of the Two-Phase Boundary Layer During Steady-State Boiling.

For subcooled boiling, higher bubble growth and departure frequencies were observed. However, the bubble sizes were found to decrease considerably. The vapor bubbles, particularly those from the bottom center, shrank quickly after departing from the heating surface, apparently due to condensation. With large subcooling, the vapor bubbles in the bottom center region were almost an order of magnitude smaller than those observed in the saturated boiling case. This situation can be seen by comparing the pictures shown in Figures 7(c) and 7(d) for subcooled boiling with those shown in Figures 7(a) and 7(b) for saturated boiling. Large variations of the vapor bubble sizes are shown in Figures 7(a) and 7(c) where the pictures were taken by freezing the two-phase motions. On the other hand, significant differences in the vapor flow configuration are shown in Figures 7(b) and 7(d) where the pictures were taken using multiple exposure.

It should be stressed that for both saturated and subcooled boiling, the two-phase boundary layer flow was three-dimensional although it was axisymmetrical. The downward facing boiling process on the curved heating surface depended strongly upon the upstream flow conditions, particularly the activities of those large elongated bubbles in the bottom center region. Conceivably, it is not possible to simulate the boiling phenomena by performing two-dimensional experiments.

Local Boiling Curves for Saturated Boiling

The transient quenching data obtained in this study included results from quenching 8" (~0.2 m) and 12" (~0.3 m) stainless steel and aluminum hemispherical vessels in water. Local boiling curves were deduced using the data reduction method described in the previous section. When compared at the same dimensionless wall location, l/D, having a value of zero at the bottom center and unity at the upper edge of the vessel, the local boiling curves for the two vessel sizes and two wall materials were found to be essentially the same. The differences were well within the uncertainties of the experiments. Since the boiling data for the 12" (~0.3 m) aluminum vessel were most complete, they were chosen to be presented in this paper.

Typical temperature-time histories recorded at various wall locations during a transient quenching experiment are shown in Figure 8. Initially, the vessel was cooled by natural convection in air. The rate of cooling was very small. Upon submergence in water, the rate of cooling increased substantially as a result of boiling of water on the vessel outer surface. Thus there was a sharp change in the slope of the temperature curve at the point of submergence. The local wall temperature decreased continuously in time as boiling proceeded. When the local CHF state was reached, there was a large drop in the wall temperature over a very short period of time, as indicated in the figure. The quenching event was practically over beyond this point.

Figure 9 shows the local boiling curves deduced from the quenching data for the case of saturated boiling. Consistent with the observed behavior of the two-phase boundary layer, the local boiling curves showed significant variations along the vessel wall. In general, the local boiling curve shifted upward as the local wall position was raised, i.e., as l/D was increased. The local critical heat flux, having the lowest value at the bottom center of the vessel (i.e., at $l/D = 0$),

increased monotonically with increasing value of *l*/D. On the other hand, the local wall superheat corresponding to the CHF state varied only slightly from the bottom center to the upper position of the vessel.

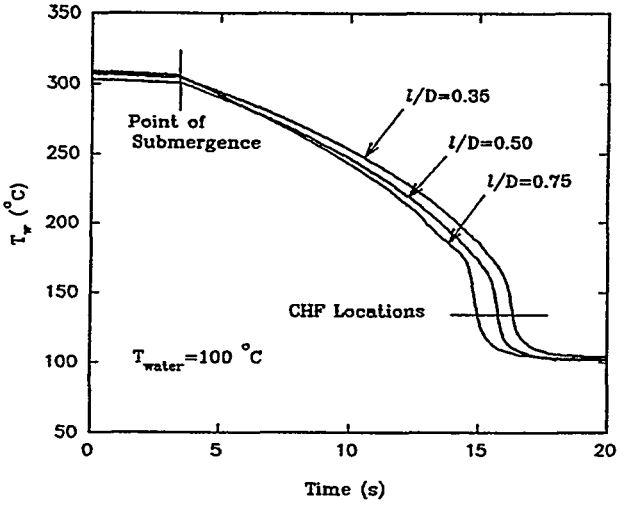

Figure 8. Typical Temperature-Time Histories Recorded at Various Wall Locations During Quenching.

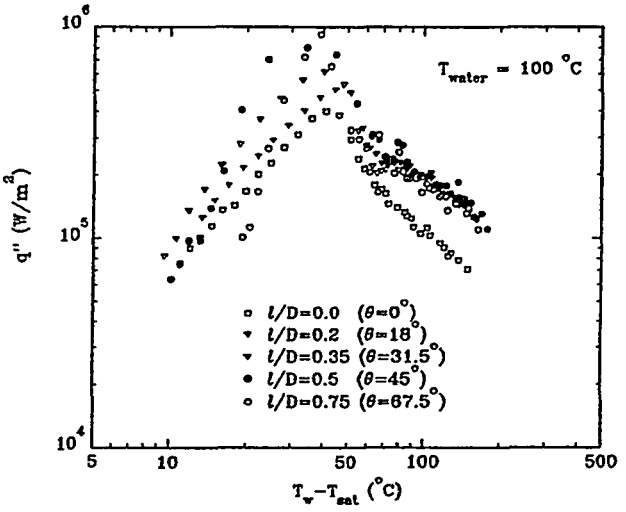

Figure 9. Local Boiling Curves for Saturated Boiling on theVessel Outer Surface (Water Temperature at 100°C).

Note that the present results were substantially different than those for an inclined flat plate (Guo and El-Genk 1991, 1992). In the latter case, the local wall superheat corresponding to the CHF state was a strong function of the angle of inclination. Specifically, the local wall superheat increased by almost a factor of three (i.e., from 12°C to 35°C) as the heating surface was changed from a horizontally downward facing position to a vertical position. In addition, significant changes in the CHF value (from 0.21 MW/m^2 to 0.34 MW/m^2) and corresponding wall superheat (from 12°C to 23°C) were observed as the angle of inclination was increased from zero to 5°. These abrupt changes over such a narrow range of inclination angles were not observed in this study. As shown in Figure 9, the CHF value increased only moderately and the corresponding wall superheat remained almost unchanged as the local inclination angle was increased from zero (i.e., *l*/D = 0) to 18° (i.e., *l*/D = 0.2).

From the above discussion, it is evident that the process of downward facing boiling on the external bottom surface of a hemispherical vessel is quite different than the process of downward facing boiling on an inclined flat plate. While the former case involves a 3-D two-phase boundary layer flow along a curved heating surface, the latter case involves a 2-D flow along a flat surface. Both the divergent effect of the flow and the buoyancy-driven two-phase boundary layer along the curved heating surface in the former case cannot be simulated in the latter case.

Local Boiling Curves for Subcooled Boiling

The local boiling curves deduced from the transient quenching data under subcooled boiling conditions are shown in Figures 10 to 12 for water temperatures of 90°C, 93°C, and 97°C, respectively. In all three subcooling cases, the local boiling curves showed significant variations along the external surface of the heated vessel. Similar to the behavior observed in saturated boiling, the local critical heat flux assumed the lowest value at the bottom center, and had considerably higher values in the upper positions of the heating surface. On the other hand, the corresponding local wall superheat exhibited a substantially different behavior than the one observed for saturated boiling. With subcooling, much larger values of the local wall superheat corresponding to the CHF state were found in the bottom center region of the vessel. This result is consistent with the behavior of the two-phase boundary layer observed in the steady-state boiling experiments, where strong subcooling effects were observed mainly in the bottom center region. Elsewhere on the vessel outer surface, subcooling effects were not as important. With large subcooling (i.e., the cases of 90°C and 93°C), the large elongated vapor bubbles that were observed at the bottom center of the vessel under saturated boiling conditions disappeared altogether. The size of the vapor bubbles at the bottom center was an order of magnitude smaller than those for saturated boiling. Conceivably, much higher local wall superheats were required for the occurrence of CHF at the bottom center under subcooled boiling conditions.

To further explore the effect of subcooling, the boiling curves obtained at a given wall location for different water temperatures were plotted in the same graph for comparison, as presented in Figures 13 to 17. As can be seen from these figures, subcooling had important effects on the boiling curves at all wall locations. However, the strongest effects were found at the bottom center of the vessel (i.e., $l/D = 0$). At this horizontally downward facing position, both the local critical heat flux and the corresponding wall superheat increased significantly as the degree of subcooling was increased. Moreover, the boiling curve in the nucleate boiling regime depended strongly on the degree of subcooling. This strong dependence of the nucleate boiling heat flux on subcooling was not observed in conventional pool boiling studies (Carey 1992). Note that the effects of subcooling became much smaller in the region away from the bottom center (i.e., for $l/D = 0.2$, 0.35, 0.5 and 0.75). In these downstream locations, only the local CHF value was found to increase with subcooling. The corresponding wall superheat as well as the nucleate boiling heat fluxes were weakly dependent upon the water temperature.

Variations of the Local Critical Heat Flux

Figure 18 shows the variations of the local CHF values with the degree of subcooling at five dimensionless wall locations. For a given value of l/D, a higher local critical heat flux was always obtained as the degree of subcooling was increased. To the first approximation, the local CHF values for all five locations were found to vary almost linearly with subcooling. This behavior is qualitatively similar to those reported in the conventional pool boiling studies (Carey 1992). The major difference is the magnitudes of the local critical heat fluxes. For the case of saturated boiling, the CHF value at the bottom center of the vessel was found to be 0.40 MW/m^2,

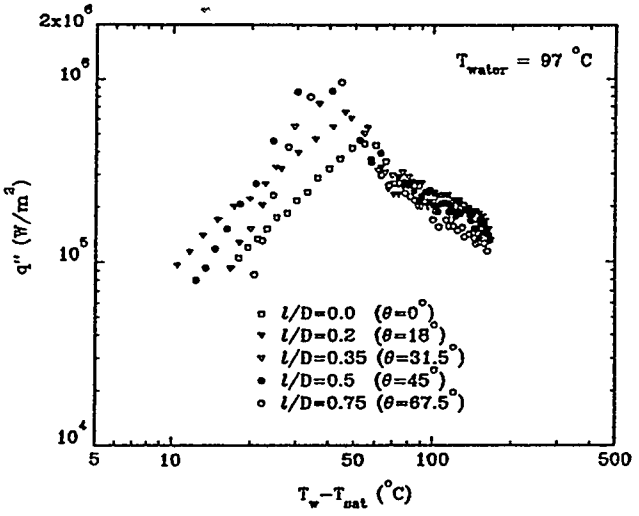

Figure 10. Local Boiling Curves for Subcooled Boiling on the Vessel Outer Surface (Water Temperature at 97°C).

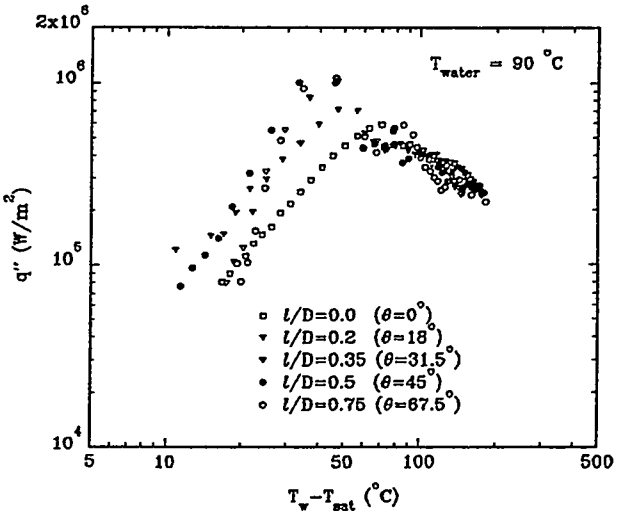

Figure 12. Local Boiling Curves for Subcooled Boiling on the Vessel Outer Surface (Water Temperature at 90°C).

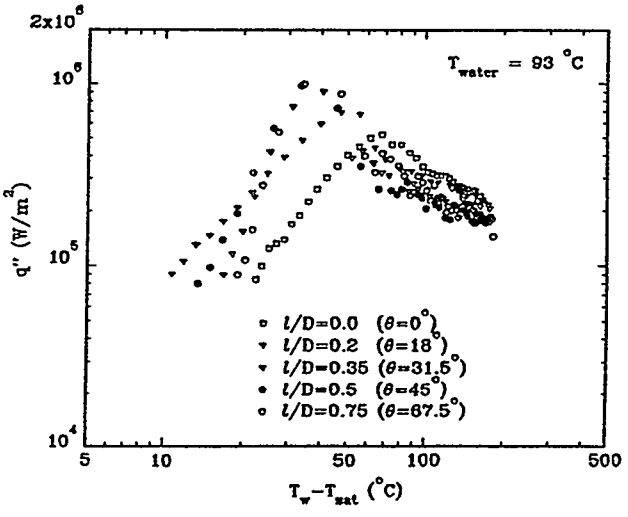

Figure 11. Local Boiling Curves for Subcooled Boiling on the Vessel Outer Surface (Water Temperature at 93°C).

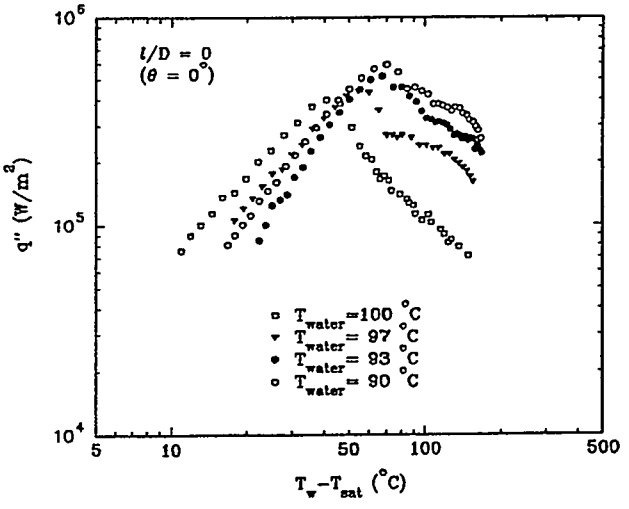

Figure 13. Effect of Subcooling on the Local Boiling Curve (l/D = 0).

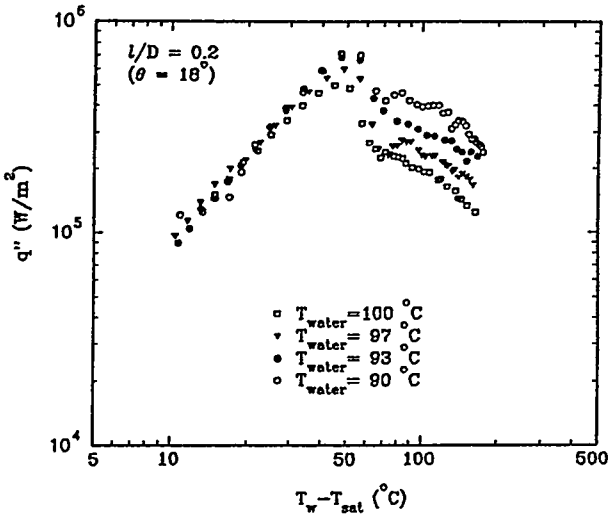

Figure 14. Effect of Subcooling on the Local Boiling Curve (l/D = 0.2).

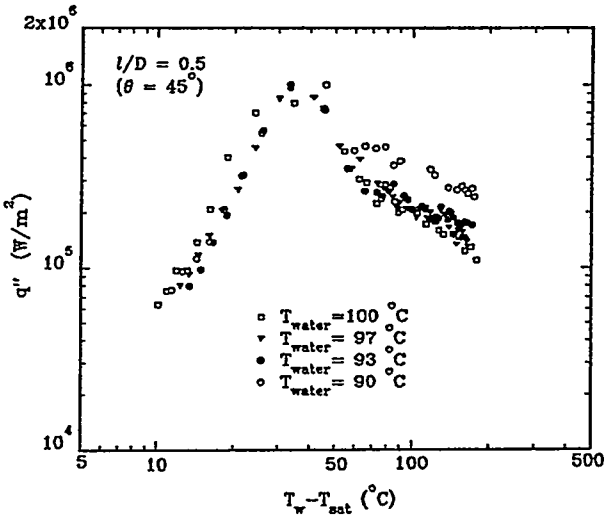

Figure 16. Effect of Subcooling on the Local Boiling Curve (l/D = 0.5).

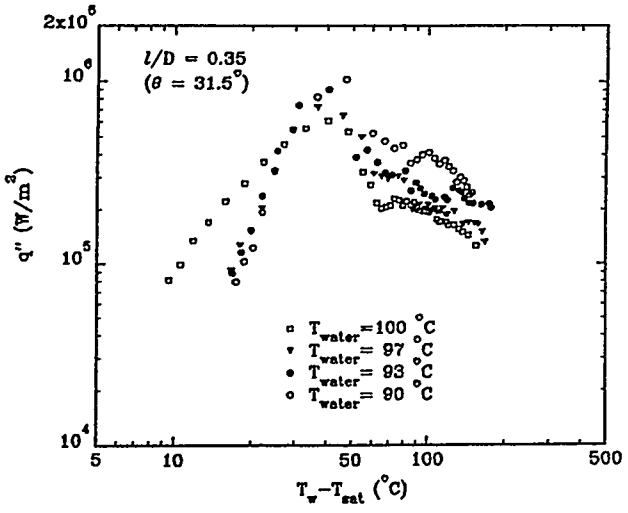

Figure 15. Effect of Subcooling on the Local Boiling Curve (l/D = 0.35).

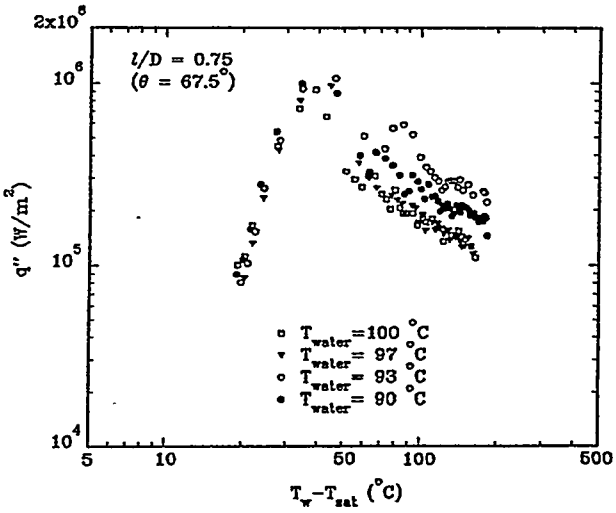

Figure 17. Effect of Subcooling on the Local Boiling Curve (l/D = 0.75).

which was only one third of the value for an upward facing flat surface. With a subcooling of, say, 10°C, the CHF value at the bottom center increased to 0.59 MW/m^2, which was about one half of the value for an upward facing flat surface. It should be reiterated that there was a significant spatial variation of the critical heat flux along the vessel outer surface. In the upper positions of the vessel, the local CHF values were only slightly below the conventional pool boiling value. Evidently, with subcooling, a local CHF value above 1.0 MW/m^2 can be expected in the upper portion of the vessel.

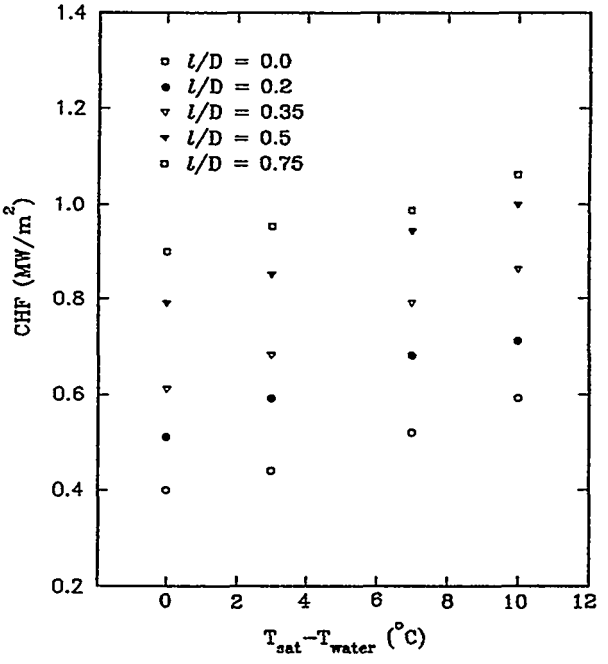

Figure 18. Variation of the Local Critical Heat Flux with Subcooling.

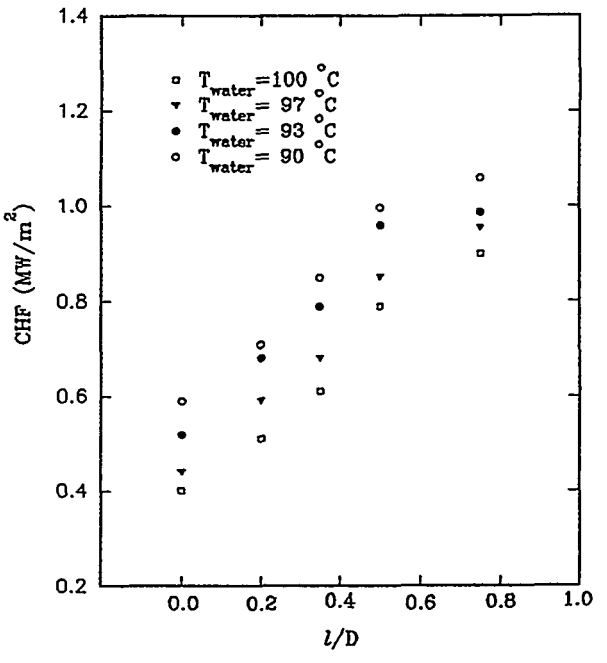

Figure 19. Variation of the Local Critical Heat Flux on the Vessel Outer Surface.

The spatial variations of the critical heat flux along the curved heating surface under both saturated and subcooled boiling conditions are shown in Figure 19. For all water temperatures, significant variations of the local critical heat flux were observed on the vessel outer surface. Over the range of subcooling (0°C to 10°C) explored in the experiments, a nearly 100% increase in the local critical heat flux from the bottom center to the upper position of the vessel was observed. Note that the spatial variation was not linear. A relatively large change in the local CHF value was found in the middle (i.e., at *l*/D = 0.5) of the vessel outer surface. On the other hand, there was no sharp change in the local CHF value in the region adjacent to the bottom center. This behavior is quite different than that for an inclined flat plate. In the latter case, an abrupt change in the CHF value was found as the inclination angle was increased from zero to 5° (Guo and El-Genk 1991, 1992). Evidently, the results for inclined flat plates cannot be used to predict the local variation of the critical heat flux on the external surface of a hemispherical vessel.

PHYSICAL SIGNIFICANCE OF THE RESULTS

The present work represents the first attempt to observe the phenomena of downward facing boiling and the critical heat flux on the external surface of a heated hemispherical vessel. Many new results have been obtained. Substantial differences in the behavior of the two-phase boundary layer and the local boiling curves have been found between the present results and those for downward facing inclined flat plates. The dependence of the local critical heat flux on the dimensionless wall location and the degree of subcooling obtained in this study should provide a useful database for model development and validation. They should also be useful in establishing a proper scaling law.

The findings of this study are very encouraging. First, it is widely recognized that the local heat flux from a melt pool increases from the bottom center to the upper edge of the pool. The local variation of the critical heat flux on the external bottom surface of the vessel observed in this study is similar to the heat flux distribution of the melt pool. With both the local heat flux from the core melt and the CHF for downward facing boiling varying in the same manner, the likelihood for a local hot spot to develop on the vessel wall would be substantially reduced. Second, the fact that the critical heat flux increases appreciably with subcooling throughout the external surface of the vessel is highly favorable from a safety standpoint. With subcooling, considerably higher heat fluxes from the core melt can be accommodated. It should be noted that subcooling is an important factor as the water level in the flooded cavity is likely to be well above the location of the reactor lower head.

To further illustrate the above points, the present results are applied to the AP600 specific geometry. Based on the assumption that 100% of the core fuel would relocate to the reactor lower head (with an inside diameter of 3.99 m), the size of the resulting melt pool would be approximately 13.9 m^3 in volume and 1.8 m in height. At a typical decay power level of 16 MW, the volumetric heat generation rate of the melt pool would be 1.15 MW/m^3. Using the heat transfer correlations for internally heated melt pools bounded from below by circular segments (Mayinger et al. 1976, Gabor et al. 1980), the average downward heat flux to the hemispherical lower head can be estimated to be 0.25 MW/m^2. Assuming the minimum local heat flux at the bottom center to be approximately one-half the average reactor heat flux and the maximum local heat flux at the upper edge of the melt pool to be approximately twice the average value, the local reactor heat flux from the melt pool to the vessel outer surface can be determined. The result is shown graphically in Figure 20. Also shown in the figure is the anticipated variation of the local critical heat flux (upper dashed curve). Because of gravity head, the water near the bottom center of the vessel is likely to be subcooled. Assuming the degree of subcooling to be between 7°C to 10°C at the bottom center and 0°C to 3°C at the upper edge, the upper dashed curve was constructed as shown. The difference in the heat flux level between the upper dashed curve (i.e., the local critical heat flux for downward facing boiling) and the lower dashed curve (i.e., the local reactor heat flux from the melt pool) represents the available thermal margin. Evidently, a nearly constant thermal margin is available throughout the entire vessel outer surface in this sample case. A local hot spot is not likely to develop under such circumstances.

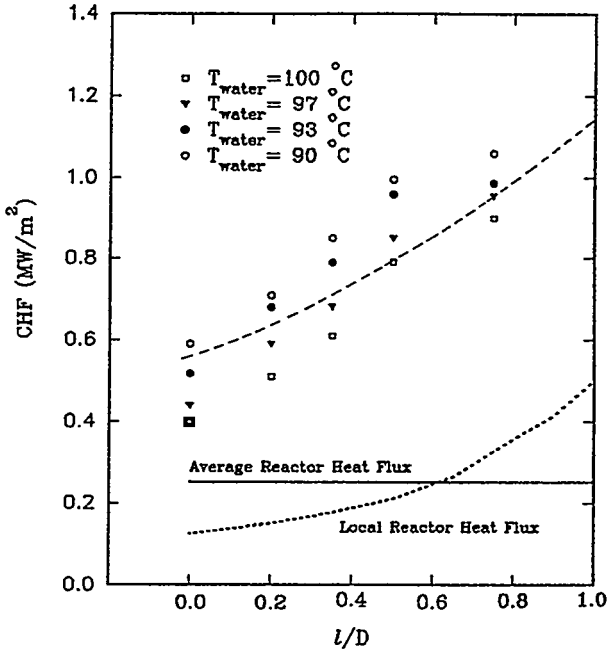

Figure 20. Thermal Margin between the Local Critical Heat Flux on the Vessel Outer Surface and the Local Heat Flux from the Core Melt.

CONCLUSIONS

Based upon the flow observations and the heat transfer results obtained in this study, the following conclusions can be made:

1. The two-phase boundary layer configuration exhibits significant spatial variations during quenching. The rate of heat removal is highly non-uniform on the vessel outer surface and depends strongly on subcooling.

2. For steady-state boiling, large elongated vapor bubbles tend to form at the bottom center whereas those in the upper positions of the vessel are usually an order of magnitude smaller. Subcooling tends to increase the bubble frequency while decreasing the bubble size.

3. For both saturated and subcooled boiling, the two-phase boundary layer flow is three-dimensional although it is axisymmetrical. Strong upstream influences are observed as a result of the activities of large elongated bubbles in the bottom center region of the vessel. These 3-D flow configurations as well as the divergent effect of the flow cannot be simulated by two-dimensional experiments or by downward facing inclined flat plates (Guo and El-Genk 1991, 1992).

4. The local boiling curves and the critical heat flux vary significantly along the vessel outer surface. In particular, the local critical heat flux increases by almost 100% from the bottom center to the upper edge of the vessel under both saturated and subcooled boiling conditions.

5. Considerably higher CHF values are obtained with subcooling. Also, much larger values of the local wall superheat corresponding to the CHF state can be expected in the bottom center region of the vessel when the water is subcooled.

6. Significant quantitative as well as qualitative differences in the boiling curves, the CHF values, and the corresponding wall superheats exist between the present results and those for downward facing inclined flat plates (Guo and El-Genk 1991, 1992).

7. The critical heat flux has the lowest value of 0.4 MW/m^2 at the bottom center of the vessel under saturated boiling conditions. The local CHF value is highest near the top of the vessel, and is approximately 1.06 MW/m^2 with subcooling of 10°C.

8. The present results are very encouraging. When applied to AP600 specific geometry, a nearly constant thermal margin is found between the local critical heat flux on the vessel outer surface and the anticipated local heat flux from the core melt. Under such circumstances, a local hot spot is not likely to develop.

ACKNOWLEDGMENT

This work was sponsored by the U.S. Nuclear Regulatory Commission under Contract No. NRC-04-93-061.

REFERENCES

Anderson, R.P. and Bova, L., 1971, "The Role of Downfacing Burnout in Post-Accident Heat Removal," *Trans. Am. Nucl. Soc.*, Vol. 14, pp. 294.

Beduz, C., Scurlock, R.G., and Sousa, A.J., 1987, "Angular Dependence of Boiling Heat Transfer," *Advances in Cryogenic Engineering*, Vol. 33, pp. 363-370.

Bewilogua, L., Knoner, R. and Vinzellerg, H., 1975, "Heat Transfer in Cryogenic Liquids under Pressure," *Cryogenics*, Vol. 15, pp. 121-127.

Carey, V.P., 1992, Liquid-Vapor Phase-Change Phenomena, Chapter 7, p. 252, Hemisphere Publishing Corp.

Chen, L.T., 1978, "Heat Transfer to Pool-Boiling Freon from Inclined Heating Plate," *Letters in Heat and Mass Transfer*, Vol. 5, pp. 104-108.

Cheung, F.B., and K.H. Haddad, 1994a, "Determination of Boiling Curves on a Downward Facing Hemispherical Surface," Presented at *CSARP Meeting,* Bethesda, MD, May 2-6.

Cheung, F.B., K.H. Haddad, L.M. Charma, F. Otero, and A.L. Brundage, 1994b, "Boundary Layer Boiling on the External Bottom Surface of a Hemispherical Vessel," Accepted for presentation at the *ANS Winter Meeting,* Washington, D.C., November 13-17.

Class, C.R., Dehaan, J.R., Piccone, M. and Cost, R.B., 1959, "Boiling Heat Transfer to Liquid Hydrogen from Flat Surfaces," *Adv. Cryog. Eng.*, Vol. 5, pp. 254-260.

Costello, C.P. and Adams, J.M., 1963, "The Interrelation of Geometry, Orientation, and Acceleration in the Peak Heat Flux Problem," *AIChE J.*, Vol. 9, No. 5, pp. 663-670.

Gabor, J.D., Baker, L. Cassulo, J.C., Erskline, D.J., Warner, J.G., 1980, "Heat Transfer to Curved Surfaces from Heat Generating Pools," *J. Heat Transfer,* Vol. 102, pp. 519-524.

Githinji, P.M. and Sabersky, R.H., 1963, "Some Effect of the Orientation of the Heating Surface on Nucleate Boiling," *Trans. ASME J. Heat Transfer,* Vol. 85, pp. 379.

Guo, Z. and El-Genk, M., 1991 "An Experimental Study of the Effect of Surface Orientation on Boiling Heat Transfer During Quenching," Paper No. 91-WA-HT-1, *ASME Winter Annual Meeting,* Atlanta, GA, Dec.

Guo, Z. And El-Genk, M.S., 1992, "An Experimental Study of Saturated Pool Boiling from Downward Facing and Inclined Surfaces," *Int. J. Heat Mass Transfer,* Vol. 35, pp. 2109-2117.

Ishigai, S., Inoue, K., Kiwaki, Z., and Inai, T., 1961, "Boiling Heat Transfer from a Flat Surface Facing Downward," *Intl. Developments in Heat Transfer,* Part II, No. 26, pp. 224-229.

Jung, D.S., Venart, J.E.S., and Sousa, A.C.M., 1987, "Effects of Enhanced Surfaces and Surface Orientation on Nucleate and Film Boiling Heat Transfer in R-11," *Int. J. Heat Mass Transfer,* Vol. 30, pp. 2627-2639.

Littles, J.W. and Wallis, H.A., 1970, "Nucleate Pool Boiling of Freon 113 at Reduced Gravity Levels," ASME Paper No. 70-HT-17.

Lyon, D.N., 1965, "Boiling Heat Transfer and Peak Nucleate Boiling Fluxes in Saturated Liquid Helium between the λ and Critical Temperatures," *Intl. Advances in Cryogenic Engineering,* Vol. 10, pp. 371-379.

Marcus, B.D. and Dropkin, D., 1963, "The Effect of Surface Configuration on Nucleate Boiling Heat Transfer," *Int. J. Heat Mass Transfer,* Vol. 6, pp. 863-869.

Mayinger, F., Jahn, M., Reineke, H.H., and Steinbrenner, U., 1976, "Examination of Thermohydraulic Processes and Heat Transfer in a Core Melt," BMRT R8 48/1, Institute fur Verfahrenstechnik der T.U., Hannover.

Nishikawa, K. and Fujita, Y., 1990, "Nucleate Boiling Heat Transfer and Its Augmentation," *Advances in Heat Transfer,* Vol. 20, pp. 1-82.

Nishikawa, K., Fujita, Y., Uchida, S., and Hota, H., 1984, "Effect of Surface Configuration on Nucleate Boiling Heat Transfer," *Int. J. Heat Mass Transfer,* Vol. 27, pp. 1559-1571.

Styrikovich, M.A. and Polyakov, G.M., 1973, Cited from Vishnef, I.P., "Effect of Orienting the Hot surface with Respect to the Gravitational Field on the Critical Nucleate Boiling of a Liquid," *J. Engng. Phys.,* Vol. 24, No. 1, pp. 43-48.

Vishnev, I.P., Filator, I.A., Vinokur, Y. G., Gorokhov, V.V. and Svalov, G.G., 1976, "Study of Heat Transfer in Boiling of Helium in Surfaces with Various Oreintations," *Heat Transfer Sov. Res.,* Vol. 8, pp. 104-108.

ADVANCE IN THE FARO/KROTOS MELT QUENCHING TEST SERIES[a]

H. Hohmann, D. Magallon, I. Huhtiniemi, A. Annunziato, A. Yerkess
Commission of the European Union
Joint Research Centre
Safety Technology Institute
I - 21020 Ispra (Va)

ABSTRACT

The FARO programme of JRC-Ispra includes three main activities centred on the FARO facility: large scale melt quenching experiments, small scale KROTOS FCI tests, code development and test analysis. Four FARO tests involving up to 151 kg of $76.7^{W}/_{O}$ UO_2 + $19.2^{W}/_{O}$ ZrO_2 + $4.1^{W}/_{O}$ Zr melt at 2800 K quenched in 608-kg, 2-m-depth saturated water at pressure 5.0 MPa have been performed. In KROTOS the melt is poured into a water column height 1.10 m, and diameter either 95 mm or 200 mm. An explosion can be artificially triggered. Five tests performed recently involved 3 kg of prototypical core materials ($80^{W}/_{O}$ UO_2 + $20^{W}/_{O}$ ZrO_2) and one test involved 1.5 kg of simulant (Al_2O_3). Modelling and test analysis are focused on the development and validation of the JRC-Ispra COMETA computer code and the University of Wisconsin TEXAS-III code, and analysis of the FARO and KROTOS tests by these codes. The paper presents the recent results and progress in each activity.

INTRODUCTION

The FARO tests have been designed to provide the experimental data base on melt jet/water quenching and mixing with information from tests performed with 150-kg-scale of real corium in prototypical conditions. Basically, the penetration of the molten corium into the water of the lower plenum and its subsequent settling on the bottom head of the RPV are simulated. The melt quantity is of about one order of magnitude higher than what has been performed so far in this field. Thus, the data represent a major contribution in evaluating the potential of water to quench the core material before it reaches the bottom of the reactor pressure vessel and the subsequent early thermal load on the bottom structure, and further help in validating the computer models for melt/water mixing. So far high pressure (5.0 MPa) core melt down scenarios have been simulated.

Two preliminary tests known as L-06 and L-08 were performed with 18 and 44 kg of pure oxide melts ($80^{W}/_{O}$ UO_2 + $20^{W}/_{O}$ ZrO_2)[1], respectively, poured into

[a]The present FARO-LWR Test Programme is performed in collaboration with USNRC in the frame of Technical Exchange Agreement n° 4086-90-09 TG ISP USA.

1-m-depth water at saturation at 5.0 MPa (537 K) from a nozzle of diameter 100 mm. They have shown that, although significant breakup and thus quenching of the melt occurred, part of the corium (~1/3) reached the bottom plate still molten. Nevertheless, the thermal load on the bottom plate remained rather mild with a temperature increase of the plate contact face around 275 K and a maximum downward heat flux of 0.8 MW/m^2. More recently two larger size tests known as L-11 (or Base Case Test: BCT) and L-14 have been performed. They involved up to 151 kg of melt quenched in 2-m-depth water at saturation at 5.0 MPa. The melt composition was varied from 76.7 $^{w}/_{o}$ UO_2 + 19.2 $^{w}/_{o}$ ZrO_2 + 4.1 $^{w}/_{o}$ Zr to 80 $^{w}/_{o}$ UO_2 + 20 $^{w}/_{o}$ ZrO_2 for L-11 and L-14, respectively. These tests, together with the two preliminary tests, allow quantifying the effect of melt mass, H_2 generation and water depth on the quenching process. In the first part of the paper the results of the large melt mass tests are reported and compared with those of the two lower size tests L-06 and L-08.

The KROTOS FCI tests aim at providing benchmark data to examine the effect of fuel/coolant initial conditions and mixing on explosion energetics. Experiments, fundamental in nature, are performed in well-controlled geometries and are complementary to the FARO large scale tests. An explosion can be triggered from the base of the water column using a gas trigger device. In the past, fuel simulants, e.g. Sn (7.5 kg at 1370 K)[2] or Al_2O_3 (1.5 kg at 2650 K)[3] were poured into a water column of ≤1.20 m in height, 95 mm in diameter.

Recently, a new test series was started using prototypical core materials (80 $^{w}/_{o}$ UO_2, 20 $^{w}/_{o}$ ZrO_2). Four tests have been performed in the test tube of diameter 95 mm with different subcooling levels (10-80K) and with and without an external trigger. No spontaneous energetic FCI has been observed in these corium tests. This is in contrast with the energetic FCI's observed in the previously reported aluminium oxide tests which had the same initial conditions (pressure and subcooling)[3]. However, the analysis of the corium experiments indicated that strong vaporisation at the melt/water contact led to a partial expulsion of the melt from the test section into the expansion vessel. Thus, a precise comparison with aluminium oxide tests could not be made at this point. In order to obtain a good penetration and premixing of the corium melt, further tests have been performed with a test tube of inner diameter 200 mm instead of 95 mm, thus increasing the quantity of water from 7.5 kg to 35 kg. A test with aluminium oxide in the same condition has also been performed for comparison. In the second part of the paper, a synthesis of the test results is presented.

Modelling and test analysis activities are focused on development of the JRC-Ispra COMETA computer code, and analyses of the FARO and KROTOS tests by COMETA and TEXAS-III codes. So far, COMETA was used only for the

interpretation of the FARO tests. A brief description of COMETA and comparisons with the FARO experimental data are presented and discussed in the third part of the paper. Results obtained by TEXAS-III in analysing the FARO data are also reported.

FARO FULL-SIZE EXPERIMENTS

Objectives of the FARO Tests

The main objectives of the tests were:

1. determine the melt quenching rate prior to debris settling on the bottom plate;
2. evaluate the global rate of zirconium oxidation and subsequent hydrogen production;
3. assess the influence of zirconium oxidation process on melt quenching;
4. determine the early thermal load on the bottom structure;
5. characterise the debris structure.

FARO Test Apparatus

The experimental arrangement for performing the FARO large size tests is shown in Figure 1. The interaction vessel TERMOS (designed for 10 MPa, 573K) is connected to the UO_2-ZrO_2 melting furnace via the release channel and isolated from it during interaction by the valve S02. After melting in the FARO furnace, the melt is first delivered to the release vessel, and then released into the water. The release vessel, located in the upper head (so-called dome) of the test vessel, can contain about 1000 m of 1.2 mm diameter Zr wire (7 kg) uniformly distributed in the whole volume. In that case (L-11 test) the superheated oxide melt coming from the furnace induced the melting of the zirconium and the formation of a homogenous mixture UO_2-ZrO_2-Zr.

The test vessel TERMOS is connected downstream to a condenser via a steam/water separator and exhaust valves (Figure 2). The purpose of this unit is to vent and condense part of the steam produced during the melt quenching should the pressure in the interaction vessel TERMOS exceed a pre-established value (9.3 MPa for the tests reported here). The high pressure steam/water separator is connected to TERMOS by a pipe with an internal diameter of 146 mm. From the separator the steam is distributed to four circuits, each including an exhaust valve (full lift safety valve) with a discharge diameter of 32 mm. Downstream to the valves the steam is vented to a low pressure condenser (design pressure 0.8 MPa). The unit was conservatively designed on the basis of predictions from several computer models. Non-condensable gases (such as the hydrogen

produced by zirconium oxidation or the argon possibly initially present in TERMOS) can be stored in the 2.5 m^3 free-board volume of the condenser.

FARO Test Procedure

Initially, the release vessel is at the same low pressure as the furnace (0.2 MPa). After transfer of the UO_2-ZrO_2 mixture to the release vessel, the intersection valve SO1 and the isolation valve SO2 are closed, and the release vessel is pressurised to the TERMOS pressure (i.e. 5.0 MPa) by using an argon supply. Upon pressure equalisation, the two melt catcher flaps automatically open. The lower flap allows the melt to be released to the water by gravity . The side flap, of the same diameter as the melt release flap, prevents against pressure differences between the release vessel and TERMOS during the melt release. After mixing with the water, the corium is collected in the debris catcher. If the pressure in the TERMOS vessel reaches the threshold pressure of the exhaust valves, steam/gas venting to the condenser occurs.

FARO Instrumentation

The principal quantities measured in the test vessel during the corium quenching are pressures and temperatures both in the freeboard volume and in the water, and temperatures in the debris catcher bottom plate. Tungsten ultrasonic temperature sensors are mounted in the release vessel for measuring the temperature of the melt. A total of about 250 signals are loaded to 6 different recorders of the data acquisition system. KELLER pressure transducers (piezoresistive, 5-kHz frequency response) measure the vessel pressurisation. VIBRO-METER pressure transducers (piezoelectric, 15-kHz frequency response) are located in the water for rapid transient records in case of an energetic FCI. They are protected by stainless steel grids. The gas-phase K-thermocouples are protected from direct radiation of the melt jet by large shells. The water K-thermocouples are essentially sacrificial thermocouples used to determine the downward progression and radial expansion of the melt jet. Those not destroyed during melt penetration record the long time water temperature histories. The centreline thermocouples in the water are sustained by thin (0.2 mm) stainless steel wires crossing the test section. The opening of the melt catcher flaps is indicated by the rupture of two 0.5 mm K-thermocouples (OD1, OD3). Another 0.5 mm K-thermocouple (OD2) is placed on the centreline of the vessel, 250 mm below the lower face of the release flap, for detecting the passage of the melt. The level swell is measured by means of four resistance probes installed every 0.25 m for a distance of 1.00 m above the initial water level, and a continuous level-meter based on the time domain reflectrometry method. Experimental probes for testing the capability to quantify the hydrogen produced by the oxidation of the zirconium are mounted.

These probes are ultrasonic sensors based on the absorption of hydrogen by palladium.

The instrumentation includes also absolute pressure transducers and thermocouples in the separator, on the downstream side of each valve and in the condenser. Water level measurements are made by differential pressure probes mounted both in the separator and in the condenser. Magnetic indicators show the ON/OFF positions of the exhaust valves.

FARO Experimental Conditions

Table 1 summarises the experimental conditions of large size tests L-11 (BCT) and L-14, together with those of tests L-06 and L-08 made with reduced quantities of melt and water[1]. The melt delivery conditions have been deduced mainly from the thermocouple signals and are, therefore, subject to some uncertainties. The main difference between L-11 and L-14 is the quality of the melt. The Base Case Test L-11 was specially designed to meet objectives 2 and 3. It has to be noted that the measured melt temperature in L-14 is 250 K higher than the estimate value for L-11. However, due to the difference of the melting point of the two mixture (2860 K for L-14 mixture and 2723 K for L-11 mixture), the difference in superheating is only around 100 K.

The pressure equalisation procedure used for the two start-up tests L-06 and L-08 did not allow for a pure gravity delivery to the water. In fact, the pressure in the release vessel oscillated but was damped during melt delivery. The maximum amplitudes of the oscillations were +0.26/-0.15 MPa for L-08 at the beginning of the delivery. For L-06 however, a crust 10 mm thick formed above the melt in the release vessel, thus explaining the long delivery time with respect to the quantity of melt.

FARO Results and Discussion

Table 2 summarises the main experimental data of the four tests. For all the tests, time zero corresponds to the start of melt delivery to the water from the release vessel, at the end of the pressure equilibration between TERMOS and the release vessel.

Pressure histories during quenching are reported in Figure 3 (-2.5<time <25s) and Figure 4 (-1<time<6s) for all the tests. The curves present two main maxima, roughly corresponding to the end of melt fall and to the debris cooling (Figure 3). Even though the melt mass in L-14 was 17% lower that in L-11, the influence of the zirconium oxidation during the melt quenching is evidenced by the significant difference of the rate of pressure increases and of the maximum values of the pressure reached at the end of the melt fall

Table 1. Summary of experimental conditions

			Scoping Test (L-06)	Quenching Test-2 (L-08)	L-14	Base Case Test (L-11)
Melt	composition UO_2	w/o	80	80	80	76.7
	ZrO_2	w/o	20	20	20	19.2
	Zr	w/o	0	0	0	4.1
	temperature	K	2923[a]	3023[a]	3073±50[b]	2823[a]
	discharged mass	kg	18	44	125	151
	delivery time	s	0.28	0.37	~ 1	~ 1
	mean mass flow rate	kg/s	64	119	125	151
	hydrostatic head in release vessel	m	0.34	0.47	0.57	0.59
	Δp delivery		~gravity	~gravity	gravity	gravity
	initial discharge diameter	m	0.1	0.1	0.1	0.1
	final discharge diameter	m	0.084	0.095	0.092	0.095
	free fall in gas	m	1.66	1.53	1.04	1.09
Water	mass	kg	120	255	623	608
	height	m	0.87	1.00	2.05	2.00
	diameter water container	m	0.470	0.710[c]	0.710[c]	0.710[c]
	inital mean temperature	K	539	536	537	535
	fuel/coolant mass ratio		0.15	0.17	0.21	0.25
Free-board	gas composition steam	w/o	83	70	77	77
	argon	w/o	17	30	23	23
	volume	m^3	0.464	0.875	1.260[d]	1.280[d]
	initial mean temperature	K	543	536	536	536
Exhaust valves	start opening pressure P_s	MPa	-	-	9.3 ± 0.15	
	full opening pressure[e]		-	-	1.05 P_s	
	full opening time[e]	s	-	-	< 0.1 from 1.05 P_s	
	flow area at full opening[e]	m^2	-	-	8.04×10^{-4}	
	sensitivity to back pressure[e]		-	-	no if < 0.5 P_s	
Condenser	overall volume	m^3	-	-	4.0	
	water mass	kg	-	-	1440	
	initial water temp.	K	-	-	290	

[a]inferred from measurements in previous test; [b]measured in the test; [c]test vessel itself; [d]includes separator and piping up to exhaust valves; [e]valve manufacturer data - proportional opening up to 1.05 P_s corresponding to 20% of full discharge capacity, then full opening.

phase for each test (Figure 4). A maximum pressure of 10 MPa is obtained for L-11 despite 48 kg of steam were discharged to the condenser starting at 9.3 MPa, while the maximum pressure is only 7.8 MPa in L-14. As melt quenching was more efficient during the melt fall for L-11 than for L-14, the debris cooling maximum is higher for L-14 than for L-11 (8.3 MPa for L-14 against 7.7 MPa for L-11, see Figure 3).

Table 2. Summary of experimental data

			Scoping Test (L-06)	Quenching Test-2 (L-08)	L- 14	Base Case Test (L-11)
Melt	mean velocity in gas phase	m/s	4	5	2.9	2.9
	mean velocity in water	m/s	2.3	3.7	4.8	2.4 /1.17[a]
	broken up	kg	12	30	105	151
	conglomerated on bottom plate	kg	6	14	20	0
	mean size of fragments	mm	4.5	3.8	4.8	3.5
	melt/debris rejection		no	no	no	no[b]
Bottom Plate	maximum temperature increase[c]	K	n.a.	275	330	20
	maximum downward heat flux	MW/m^2	n.a.	0.8	0.5	negligible
	state		intact	intact	intact	intact
Pressure Increase	melt fall stage maximum	MPa	1.1	1.8	2.8	5.1
	long term maximum	MPa	1.6	1.8	3.4	2.8
	maximum rate	MPa/s	1.6	3.3	2.4	4.8
	steam explosion		no	no	no	no
Temp. Increase	gas phase	K	43	40	38	44
	water	K	15	23	28	27
Level swell	Maximum measured	m	0.130	0.410	0.600	0.800
Venting Phase	duration	s	-	-	-	3.8
	debris in separator	kg	-	-	no	5(< 1mm)
	water added to condenser	kg	-	-	venting	48
	pressure increase in condenser	MPa	-	-	in this	0.17
	mean water temperature increase in condenser	K	-	-	test	20

[a]2.4 m/s: from level 2.00 m down to 0.6 m, 1.17 m/s=constant: from 0.6 m down to bottom plate; [b]about 5 kg of debris <1 mm entrained by the steam/gas flow into the separator; [c]contact face.

In Figure 5 the pressure histories in TERMOS and at the outlet of the separator are compared. It is seen that the TERMOS and separator traces are identical up to the time at which the gas started discharging to the condenser (time 1.44s). Later on, the pressure difference between TERMOS and separator indicates the gas flow through the connecting pipe. The gas venting started at 9.3 MPa, as expected, but the pressure continued to increase in TERMOS up to about 10.0 MPa. This pressure-overshoot in the test vessel was due to the fact that the venting system never reached its full discharging capabilities. The exhaust valves are sensitive to the pressure at the outlet of the separator. This pressure never increased beyond 9.7 MPa which was the lower limit for a full opening of the valves. Because of the ±0.15 MPa uncertainty on the set pressure, some valves opened completely, but some only partially. The valve behaviour has been identified and characterised on the basis of experimental results[4]. This point is further analysed by COMETA in the last section of the paper. Although a pressure difference between TERMOS and the separator is clearly observed only up to time 3.15 s in Figure 5, a residual gas discharge through the valves continued up to time 5.0 s, i.e. when the pressure reached 7.3 MPa (evidenced in Figure 3). Then, the pressure in TERMOS increased again up to reaching the debris cooling maximum at time 22.2s. From Tables 1 and 2, it is deduced that the 48 kg of water added to the condenser during the venting phase contained 130 MJ, which corresponds to about 50% of the total heat content of the melt (including the heat of the Zr/H_2O reaction, i.e., ~40 MJ).

So far, it has not been possible to determine the hydrogen production rate from the H_2 probes for L-11. However, X-ray diffraction analysis of the debris indicated that Zr was no longer present as a metallic phase. Furthermore, all the melt experienced breakup during L-11. Analysis of the water thermocouple signals indicated that complete breakup of the melt was achieved from 0.8 to 0.6 m height above the bottom plate (breakup length between 1.2 and 1.4 m). This leads one to believe that the zirconium oxidation was nearly completed at the end of the melt fall phase. Therefore, most of the heat from the chemical reaction and, consequently, of the hydrogen (partial pressure of 0.5 MPa for 0.272 kg in the test conditions) were released during that period. This contributed to enhance the pressurisation of the test vessel.

The fact that in L-11 all the melt experienced breakup well before reaching the bottom plate is in contrast with all the FARO tests performed so far and, particularly, with L-14. One can easily conclude that the Zr/H_2O chemical reaction also enhanced breakup of the melt jet. This further contributed to the overpressurisation noted in L-11 with respect to L-14.

It is remarkable that for the UO_2-ZrO_2 melt tests, the proportion of melt which did not experience breakup apparently did not depend on the melt mass

and varied linearly with the water depth. It is also remarkable that the temperature increases in both the water and the gas phase were of the same order for all the tests (see Table 2), except for L-06 (18 kg of melt).

Level swell measurements give an indication of the global void fractions reached during the tests. Using the values of Table 2 and assuming a uniform distribution of the two-phase steam/water mixture, one finds values of the void fraction equal to 0.13, 0.29, 0.29 and 0.23 for L-06, L-08, L-11 and L-14, respectively.

The particle size distribution of the debris of all tests is reported in Figure 6. In this test, a few kilograms of particles (size of the order of 1 mm) were entrained into the separator during the gas discharge. The mean particle in test L-14 is sensibly higher than for L-11 (4.8 mm against 3.5 mm). This could explain the relatively high settling velocity (5 m/s) observed in L-14 (Table 2). As could be expected from the extensive melt breakup observed in L-11, the thermal load on the bottom plate was negligible. The collection of molten material on the bottom plate in L-14 (20 kg) gave rise to a maximum heat flux of 0.5 MW/m^2. As for the previous tests with a conglomerate found on the bottom, the plate was not damaged by the melt. Only a brown coloured spot evidenced the position of the conglomerate melt on the plate in L-14.

Calculation of the Quenching Rate

From the pressure and temperature data it is possible to calculate the quenching rate and the energy released to the steam-water system as a function of time. The following formula are used:

$$E = m_{liq} h_{liq} + m_{vap} h_{vap}$$

$$P = \frac{dE}{dt} = (m_{liq} + m_{vap}) \frac{dh_{liq}}{dt} + V \frac{d}{dt} \left[\frac{h_{vap} - h_{liq}}{\sigma_{vap}} \right]$$

where:

E	energy of the system;
P	quenching rate;
m_{liq}	mass of liquid water;
m_{vap}	mass of steam;
h_{liq}	enthalpy of liquid;
h_{vap}	enthalpy of steam;
σ_{vap}	specific volume of steam;
V	freeboard volume.

The results of the calculations are presented in Figures 7, 8a and 8b, and in Table 3. In the data presented, the superheating of the steam has been neglected and the enthalpies of steam and water at the total pressure of the system have been used.

Table 3. Energy release and quenching rates

		Scoping Test (L-06)	Quenching Test-2 (L-08)	L- 14	Base Case Test (L-11)
energy of the melt: E_{melt}	MJ	27	66	190	265[a]
energy released at first pressure maximum (~ melt fall): E_{fall}	MJ	6	24	83	170
ratio E_{fall} / E_{melt}		0.22	0.36	0.44	0.64
energy released (calculated max.)	MJ	13	43	136	181
maximum quenching rate	MW	7	22	57	157
maximum quenching rate per kg of broken up melt	MW/kg	0.58	0.73	0.54	0.89[b]
maximum quenching rate per kg of melt	MW/kg	0.39	0.50	0.46	0.89[b]

[a] includes the energy of the Zr/H_2O chemical reaction, i.e.~40 MJ; [b] related to the equivalent melt mass corresponding to the total energy content, i.e. 177 kg.

In particular, it is seen from Table 3 that the proportion of energy released during the melt fall phase with respect to the energy content of the melt increases with increasing melt and water masses (or water depth) from 0.22 for L-06 to 0.64 for L-11 (for which, however, the Zr oxidation has to be accounted for). The maximum quenching rate also increases from 7 MW for L-06 to 157 MW for L-11 (Figure 8a). However, related to the melt mass, the differences are smoothed and the range reduces to 0.39 - 0.89 MW per kilogram of available melt and to 0.58 - 0.89 MW per kilogram of broken up melt (Figure 8b).

KROTOS Tests

In support of the large-scale FARO tests the KROTOS facility was used for FCI studies in the molten UO_2-ZrO_2/water system. The objectives of these tests were to investigate in 1-D and 2-D geometries the premixing of molten fuel jets with nearly saturated and subcooled water.

KROTOS Facility

A detailed description of the KROTOS facility and the results of aluminium oxide-water experiments have already been given in a previous publication[3]. Therefore, only the general features and important changes from the previous configuration are given here.

Figure 9a illustrates the main components of the facility: the radiation furnace, release tube and test section. Figure 9a also indicates the locations of pressure and temperature sensors (temperature sensors in the test section are at the same elevations as pressure sensors). Two different test section designs were used in this test series: a narrow test section with an internal diameter of 95 mm, as depicted in Figure 9a, and a wide test section with an internal diameter of 200 mm, illustrated in Figure 10. The sensors were placed at the same elevations in both the test section designs.

A pre-test series with UO_2-ZrO_2 melts showed that some modifications of the facility were required with respect to the previous test series with molten tin and aluminium oxide. At high temperatures (up to 3273 K) involved in the UO_2 melting, the use of graphite heaters caused material problems due to unexpected chemical reactions. For these reasons the graphite heater elements were replaced by tungsten heaters. The pre-tests also demonstrated that helium was better suited as furnace cover gas than argon. Furthermore, due to the high temperatures in these tests only tungsten could be used as the material for the melt crucible and the puncher (the device for perforating the crucible bottom), see Figure 9b. Extensive work had to be done to refine the sophisticated fabrication techniques to machine the bottom membrane of the tungsten crucibles according to the required dimensions (0.2-0.3 mm thickness).

In the tests, KROTOS 32-37, about 3 kg of melt composed of 80 $^{w}/_{o}$ UO_2 and 20 $^{w}/_{o}$ ZrO_2 (density 7960 m^3/kg) at temperatures ranging from 3018 to 3063 K was used. The melt was contained in the W-crucible of 3 mm wall thickness and dropped from the furnace onto the W-puncher where the bottom membrane was ruptured (Figure 9b) allowing the melt to exit into the funnel and through the nozzle. The pure tin brake disk used in the previous test series with aluminium oxide was not used because the pre-test showed that the UO_2-ZrO_2 melt would develop a crust upon touching it. This crust was observed to block the melt injection into the test tube (KROTOS 31). Instead, the KROTOS 35 test was performed with a Woods metal-tin alloy disk with a melting point of about 140 °C. The nozzle exit (30 mm diameter) was positioned 0.45 m above the water free surface in the test tube. At the upper part of the narrow test tube, a steel vessel of 205 mm inner diameter was mounted and filled up with water to the test tube water level. In this vessel (Figure 9c), two level-meters were

placed to measure the water level swell during melt/coolant mixing. One float-type and one Time Domain Reflectometry (TDR) level-meter were used. However, with the wide test section, the level-meter vessel was not needed and two level-meters of TDR-type were mounted along the inside wall of the test section. The data from these sensors allow to estimate the integral vapour void fraction in the test section. A strong gas trigger device, shown in Figure 9d, was mounted to the bottom of the test section in selected tests to provide an external pressure pulse to trigger an explosion. It consists of a gas chamber (volume 15 cm^3) pressurised to about 12.5 MPa and closed by a 0.2 mm thick steel membrane. Either a thermocouple signal or a predetermined time delay can be used to activate the destruction of the membrane to generate a pressure pulse that propagates vertically upwards through the melt/water mixture.

The zero-time signal for the data acquisition was generated by the falling crucible fracturing a copper wire in the release tube. This signal is the time reference for all measurements.

KROTOS Experimental Results

Up to now five experiments with UO_2-ZrO_2 have been performed. The objective of this test series was to study premixing of UO_2-ZrO_2 melts with water at both low and high subcoolings and to determine if an energetic FCI could take place under such conditions. The main test parameters and some results are summarised in Table 4. The KROTOS test programme has been evolutionary in nature, the outcome of previous results contributing significantly to the planning of the future experiments. To reduce the number of test variables, the following parameters have been fixed in these tests: the initial system pressure (0.1 MPa), release nozzle diameter (30 mm), fall height (0.45 m) and the water depth (approximately 1.1 m).

In the next sections a brief description of the tests and results is given. The discussion is subdivided into two classes as "saturated water conditions" and "subcooled water conditions" following the same convention as before when the results of the aluminium oxide/water system were reported[3].

KROTOS Experiments in "Saturated Water Conditions"

In the KROTOS 32 test, approximately 3 kg of UO_2-ZrO_2 was heated up to 3063 K in a tungsten crucible. After the test sequence initiation, the crucible was released and fell down onto the puncher. Since the test was performed without a brake disk, the melt was free to stream out through the punctured crucible bottom and funnel into the water without any time delay. A Plexiglas liner

(2 mm thick) was used in the test section to reduce the risk of a spontaneous steam explosion upon the melt contacting the walls of the test section.

The thermocouple data gives an estimate of 4.2 m/s for the leading edge velocity using the thermocouples TC6 and TC7 as melt arrival indicators. This value is significantly lower than the value considering a gravity release of the melt from the furnace. Evidently, the puncher and funnel assembly slowed down the release rate. Thermocouples in the water allowed for the estimation of the melt velocity after penetration into the water. The estimated velocity of the melt jet between TC5 and TC6 was approximately 1.5 m/s. The thermocouple data demonstrates that the coherent jet penetrated at least down to TC5.

Table 4. KROTOS Experimental Conditions and Results

	KROTOS Test n°		32	33	35	36	37
Melt	composition UO_2	w/o	80.8	81.2	79	79	79
	ZrO_2	w/o	19.2	18.8	21	21	21
	discharged mass	g	3030	3170	3102	3027	3222
	temperature	K	3063	3063	3023	3025	3018
	brake disk		no	no	yes[a]	no	no
	initial jet diameter	mm	30	30	30	30	30
	free fall in gas	m	0.46	0.46	0.46	0.46	0.46
Water	mass	kg	7.1	7.7	7.7	7.7	34.5
	height	m	1.08	1.08	1.08	1.08	1.105
	inital temperature	K	351	298	363	294	294
	subcooling	K	22	75	10	79	79
Test	initial pressure (He)	MPa	0.1	0.1	0.1	0.1	0.1
Section	internal diameter	mm	95	95	95	95	200
	Plexiglas liner		yes	no	no	no	no
	gas trigger		no	no	yes	yes	yes
Results	confirmed penetration depth of the melt jet		TC5	TC4	n.a.[b]	TC5	TC4
	maximum pressurisation	MPa	0.23	0.14	0.17	0.13	0.07
	steam explosion		no	no	no	no	no
	total debris[c]	g	2608	2802	1424	2801	2925
	debris in test section	g	1402	1705	331	1142	2925

[a]Tin/Woods metal alloy ($T_m \approx 140°C$). [b]Thermocouple wires destroyed by melt ejection from the test section. [c]Found in test section, level-meter vessel and pressure vessel.

No energetic interactions occurred, and the pressurisation of the expansion volume was only due to the steam generation of the quenching melt (see Figure 11). The initial pressure increase reached approximately 0.23 MPa and then the pressurisation fell quickly to the quasi steady-state value of about 0.05 MPa due to condensation heat-transfer onto the cooler test section walls.

The KROTOS 35 test was essentially a repeat of the KROTOS 32 experiment except that the test section did not have a Plexiglas liner and a Woods metal-tin brake disk was installed to reduce the melt release rate. Additionally, a gas trigger device (Figure 9d) was mounted. The gas trigger was configured to trigger when TC3 sensed the melt arrival. Furthermore, if the melt jet could not reach TC3 or by-passed it, a backup operation of the trigger was ensured by activating it after a predetermined time delay.

After the initial melt injection, a rapid pressurisation of the expansion vessel was observed. This initial rapid pressurisation lasted longer than in KROTOS 32. This difference was likely caused by the lower subcooling of the water (10 K as opposed to 22 K in KROTOS 32). The observed peak pressurisation of 0.17 MPa is lower than in KROTOS 32, because the vigorous steaming lead to an early expulsion of significant fraction of unquenched melt (77%). Unfortunately, some of melt swept out from the test section damaged the thermocouple and level-meter cables on the outside of the test section. Thus the trigger device activated only after the set time delay (2.6 s), but no steam explosion took place. However, the time delay might have been too long for an appropriate triggering, i.e. it is believed that significant fraction of the melt was already quenched.

Experiments in Subcooled Conditions

The KROTOS 33 test was essentially a repeat of the KROTOS 32 test except that the water subcooling was higher (75 K) and that the Plexiglas liner was removed from the test section. A similar estimate to KROTOS 32 for the leading edge velocity was obtained. The TC6 and TC7 data indicated a somewhat higher velocity of 8 m/s prior to melt penetration into the water. Once in the water, the jet decelerated rapidly from the average velocity of 4.4 m/s between TC6 and TC5 to 0.9 m/s between TC5 and TC4. Due to the higher subcooling, the pressurisation of the expansion volume is less than in KROTOS 32 with a maximum of about 0.14 MPa and a quasisteady-state level of about 0.025 MPa, see Figure 11.

The KROTOS 36 test was performed with the same conditions as KROTOS 33 except that a trigger device was mounted. The trigger device was set to activate with the TC3 signal as in the KROTOS 35 test. Moreover, the results from the KROTOS 35 test allowed for a better estimate of the appropriate back-

up time delay for triggering. Melt injection was successful but again vigorous steaming at the melt-water contact lead to a partial expulsion of the melt from the test section. The gas trigger device was activated by the TC3 signal at 1.6 s. However, no energetic propagating explosion was observed. Immediate rapid pressurisation and melt sweep-out lead to the conclusion that the melt mass participating in the premixing process was limited due to the flow constraint imposed by the narrow test tube.

The KROTOS 37 test was a repeat of the KROTOS 36 test with a new, larger diameter test section (20 cm vs. 9.5 cm). The larger test section was utilised to reduce the superficial steam velocity above the water thus reducing early (fall stage) jet breakup, levitation and sweep-out of the melt as observed in previous tests. In KROTOS 37, the melt jet was successfully injected into the test section with an insignificant amount of sweep-out. The coherent melt jet penetrated at least down to the TC4 level. The trigger activated with the TC3 signal at 1s, but no interaction was observed. However, due to the larger test section, the magnitude of the propagating trigger pulse was reduced from the previous tests because the trigger energy (200 J) was kept constant. The pressurisation of the expansion vessel, shown in Figure 12, was lower than the previous one (KROTOS 33) because of the greater mass of subcooled water (34 kg).

It is interesting to contrast the UO_2-ZrO_2 results with the previous ones from the aluminium oxide test series where supercritical explosions were observed[3]. However, to make consistent comparisons, it was imperative to repeat an aluminium oxide test with the larger diameter test section to see if lessening the constraint of the narrow test tube would indeed affect the outcome (normally an energetic interaction). Such a test (KROTOS 38) was performed recently with 1.5 kg of aluminium oxide (at 2670 K). A spontaneous energetic explosion took place before the trigger system was activated. Peak dynamic pressures up to 67 MPa were observed in the test section. The expansion vessel pressurisation for this test is shown with the KROTOS 37 result in Figure 12. A different type of premixing behaviour with UO_2-ZrO_2 and aluminium oxide is evident by comparing the initial pressurisation rates of the expansion vessel. Significantly greater steam generation with the UO_2-ZrO_2 melt is further illustrated by the level swell data, shown in Figure 13. This preliminary data would therefore suggest that less breakup of the melt occurred and that the void fraction in the mixing region was smaller prior to triggering in the case of aluminium oxide. These observations have important implications concerning tests with simulants. The differences between UO_2-ZrO_2 and aluminium oxide melts, in this respect, should be well understood. Currently, experimental investigations are pursued to study the differences between the prototypic UO_2-ZrO_2 melts and aluminium oxide simulant melts within the frame of general objectives of the KROTOS programme.

MODELLING AND ANALYSIS OF THE FARO EXPERIMENTS

Description of the COMETA code

COMETA (Core Melt Thermal-hydraulic Analysis) is a two field code: the water/steam/non-condensable gases field and the corium field[5].

The water/steam/non-condensable gases field is described by an Eulerian 6-equation model including mass, momentum and energy conservation equations for water and steam, and mass conservation equations for each non-condensable gas. The interface relations are represented by momentum and energy exchanges depending on the flow pattern. Thermal and mechanical equilibrium are assumed for the non-condensable gases. A network of fluid volumes connected at their top, bottom, or one of their two sides (external or internal) is constructed. Specific macro-volumes and macro-junction structures are present in the code, thus allowing 2-D nodal schemes.

The corium field is represented by three sub-components: the jet, the droplets and the fused debris bed. They are described in Lagrangian coordinates. The jet is released with the appropriate velocity from a tank and is fragmented during its fall according to jet breakup length correlations available in the literature.

The heat exchange between jet, droplets, fused debris bed and the steam-water mixture is controlled by heat transfer coefficients which are dependent on the local thermal hydraulic conditions. Heat slabs can be specified to represent the vessel walls or possible heaters.

A simple correlation for hydrogen production from the water/zirconium reaction has been implemented. This correlation determines the hydrogen production as a function of the fragmentation rate. The gas produced represents a non-condensable mass source for the actual volume, a mass sink and an energy source for the water which reacts with the zirconium.

The code has been written to run both on a PC or on a UNIX workstation and it produces on-line plots and automatic nodalisation drawing schemes showing volume void fractions. It is currently applied to the prediction of the FARO facility behaviour and test interpretation.

Calculation of the Base Case Test by COMETA

A 1-D pre-test calculation of the L-11 test has been made. The corresponding pressure history is presented in Figure 14, and compared to the experimental data. The prediction is in reasonable agreement with the data, considering the fact the real conditions understandably differed from that assumed in the calculation. In particular, in the simulation the valves were supposed to open completely and to operate around the set point (9.3 MPa), which was actually not the case (see description of the test in the first chapter).

A post-test calculation using initial and boundary conditions closer to that observed in the test was made. The corresponding pressure history is also reported in Figure 14. The pressure increase was still over-predicted but the behaviour of the valves was significantly improved. In particular, almost the same magnitude of the pressure peak was calculated. However, the pressure fluctuation at the beginning of the venting phase was not caught. It was suggested that the second pressure increase after the fluctuation had been induced by an enhancement of the steam production because part of the water had already reached saturation when the valves opened. In the 1-D simulation the saturation conditions were reached later on.

A 2-D calculation was then performed to account for possible non-uniform radial heating of the water. The result is presented in Figure 15. The pressure increase is still slightly overpredicted but the pressure trend at valves opening is significantly improved with respect to the 1-D simulation. Also the time dependent temperature distribution in the vessel is correctly predicted (Figure 16). Internal temperatures initially increased faster than the external ones and, later on, became lower than the external ones. This behaviour was already shown and predicted for the L-08 Test (Quenching Test-2).

The hydrogen distribution at valves opening is presented in Figure 17. It is possible to see that before the valves opening most of this gas is concentrated in the vessel area while after the valves opening a redistribution tends to make the gas fraction more uniform.

Calculation of the Base Case Test by TEXAS-III

In collaboration with the University of Wisconsin (USA), modifications have been added to the 1-D computer code TEXAS-III in order to improve its simulation capabilities for the FARO and KROTOS experiments. A simple diffusion based hydrogen generation model, developed by Corradini and Murphy[6] is now included. This model assumes that if a fuel droplet contains a metallic

component then it is always available at the droplet surface and that the hydrogen gas production matches the removal of water vapour surrounding the melt in a 1:1 molar ratio. It is also assumed that all the energy liberated from this metal/water exothermic reaction is deposited into the melt particles and that the thermodynamic properties of the water vapour are compensated by using the partial pressure of the water vapour, not the total system pressure. The simplistic addition of the diffusion based oxidation equation will only provide meaningful results when the mole fraction of hydrogen gas produced is small compared to the existing water vapour.

TEXAS-III has now been modified to allow the input of a non-uniform jet, according to a recommendation made recently[7]. Modelling more correctly the non-uniform jet flow experienced in the first two FARO quenching tests, L-06 and L-08, it is now possible to have consistent agreement with experiment for both particle settling times (including melt cake production) and pressure profiles. Assuming a uniform jet is far too restrictive to account for all the physical phenomena that occur during the melt fall and quenching.

A simple valve-opening simulation has been incorporated into TEXAS-III to account for the relief of the system pressure in the TERMOS vessel. The top boundary condition is switched from a "closed boundary" to an "open boundary condition" at a particular gas pressure, and vice versa. The cross-sectional area of the top boundary cell is equivalent to the total area of the valves.

All the above modifications have been used to model the FARO Base Case test, L-11. Figure 18 shows the discretisation of the TERMOS vessel, condenser and exhaust valves. The melt jet is modelled as a coherent jet, diameter 10 cm, with a few discrete particles at the leading edge to account for some dispersion which probably occurs during the opening phase of the release vessel. The jet exit velocity profile from the release vessel was calculated by an independent program. The condenser is not modelled, thus when the valves open it is assumed that the gas flows out of the system into the atmosphere rather than build up a pressure in a condenser. Figure 19 compares a TEXAS pressure prediction with the experimental pressure where it is assumed that the valve flow area remains constant until the pressure falls to 7.3 MPa.

CONCLUSIONS

The main objectives of the two large melt mass tests in FARO have been achieved. The melt quenching rate and the importance of the zirconium oxidation have been determined. In particular, it has been found that:

- The zirconium oxidation was completed during the melt fall phase;
- The Zr/H_2O chemical reaction induced an increase of the early quenching of the melt with respect to a pure oxide melt, and, consequently, led to a significant increase of the steam production and vessel pressurisation, and a decrease of the thermal load on the bottom plate.

From the FARO tests performed so far, including those with reduced quantities of melt and water, it does not seem that a "limit to quenching" during the melt fall have been reached in the test conditions. This point will be investigated further by using a large mass of oxide melt (150 kg) in a reduced depth of water (1 m). The water depletion phenomena in case of multiple jets has still to be investigated as well. These will be the objectives of the next FARO tests. To draw more general conclusions applicable to the reactor case still require a sound analysis of the tests with the help of analytical tools.

Concerning KROTOS tests, it is important to note that the following conclusions are based on preliminary trends observed so far with only a few tests and need to be confirmed with further tests. The experimental results from the KROTOS UO_2-ZrO_2 programme so far indicate:

- Significant breakup of the melt into relatively fine debris;
- No energetic interaction within the range of the following investigated parameters: low subcooling (10-20 K), high subcooling (80 K) and external trigger (energy of 200 J);
- Due to lack of energetic interactions so far with UO_2-ZrO_2 melts, the data on effects of geometric constraints on explosions and the far field effects are limited to results from aluminium oxide tests;
- Significant differences between the behaviour of prototypic UO_2-ZrO_2 and simulant aluminium oxide melts have been observed and more data is needed to understand them.

Further development of COMETA will consist of introducing additional models for fuel fragmentation (Corradini-Tang and Bürger models) and specific models for low pressure cases, and modelling the 2-D behaviour of the fuel drops. Further improvements to TEXAS are required to model more correctly the valve opening sequence, the system of piping and the separator.

ACKNOWLEDGEMENTS

The authors greatly acknowledge the work and efforts of the whole FARO team.

REFERENCES

1. D. Magallon and H. Hohmann, High Pressure Corium Melt Quenching Tests in FARO, CSNI Specialist Meeting on Fuel Coolant Interaction, Santa Barbara (CA), 5-8 Jan. 1993.

2. M. Bürger, K. Müller, M. Buck, S. H. Cho, A. Schatz, H. Schins, R. Zeyen and H. Hohmann, Examination of Thermal Detonation Codes and Induced Fragmentation Models by Means of Triggered Propagation Experiments in a Tin/Water Mixture, Nucl. Engrg. Des. 131 (1991).

3. H. Hohmann, D. Magallon, H. Schins and A. Yerkess, FCI Experiments in the Aluminiumoxide/Water System, CSNI Specialist Meeting on Fuel Coolant Interaction, Santa Barbara (CA), 5-8 Jan. 1993.

4. A. Annunziato, Evaluation of FARO L-11 Test Parameters Relevant to the Optimisation of the COMETA Post-Test Analysis, Technical Note I.94.100, JRC-Ispra, June 1994.

5. A. Annunziato and C. Addabbo, COMETA (Core Melt Thermalhydraulic Analysis): a Computer Code for Melt Quenching Analysis, Int Conf on "New Trends in Nuclear System Thermohydraulics", May30th-June 2nd, 1994, Pisa, Italy.

6. M. Corradini and J. Murphy, private communication, 1993.

7. A. Yerkess and M. Corradini ,"Analysis of FARO Tests with the TEXAS Code", Int Conf on "New Trends in Nuclear System Thermohydraulics", May 30th-June 2nd, 1994, Pisa, Italy.

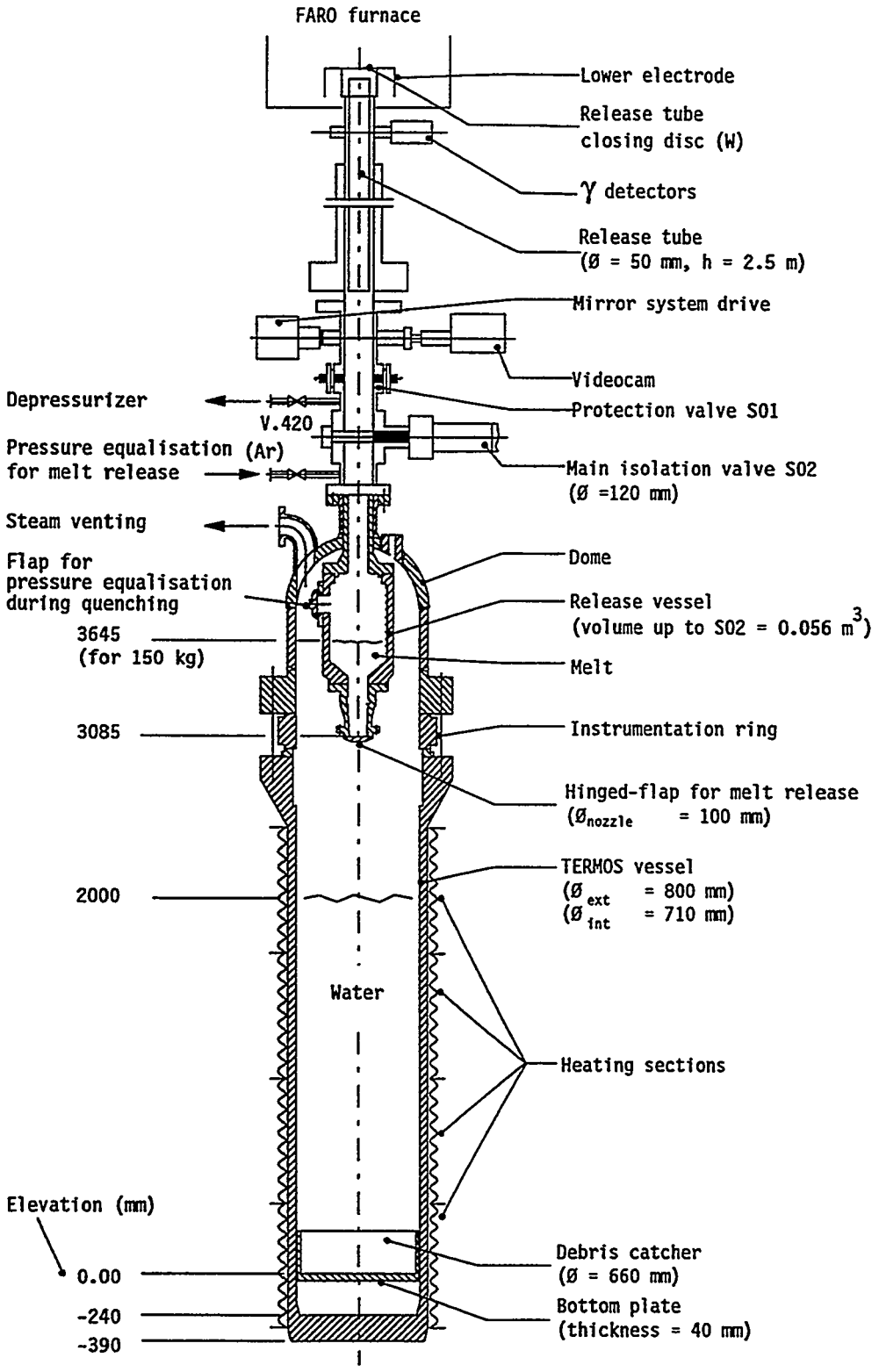

Figure 1. FARO Test Arrangement

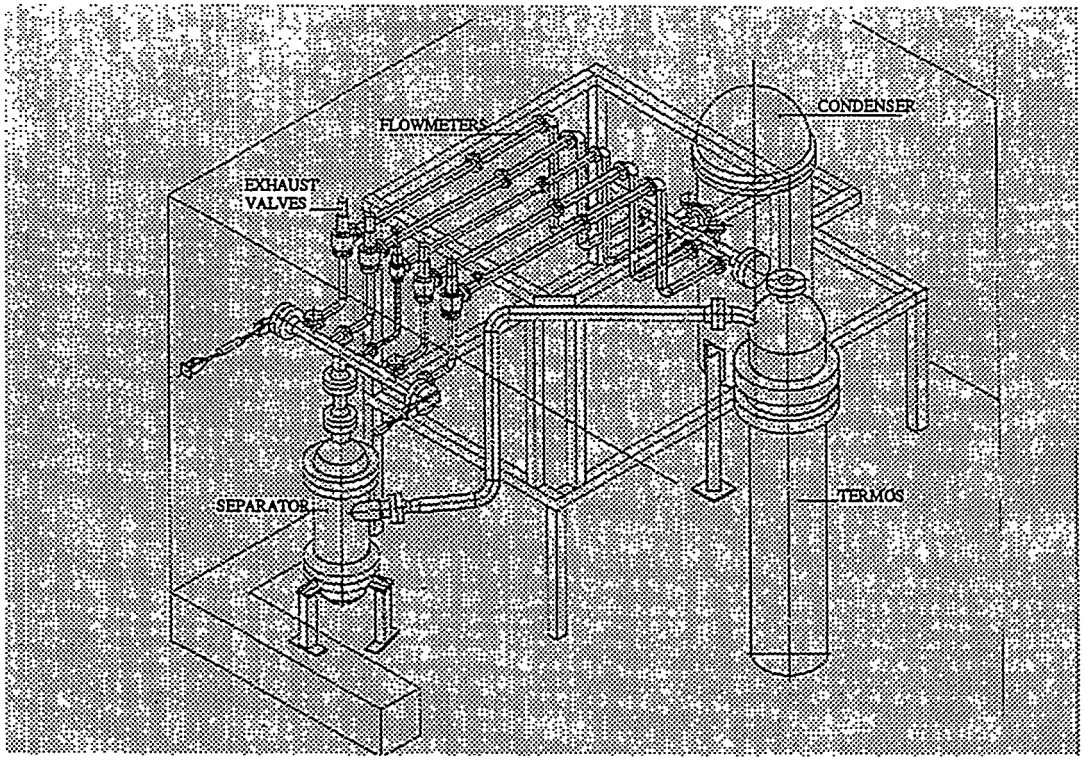

Figure 2. FARO Venting System

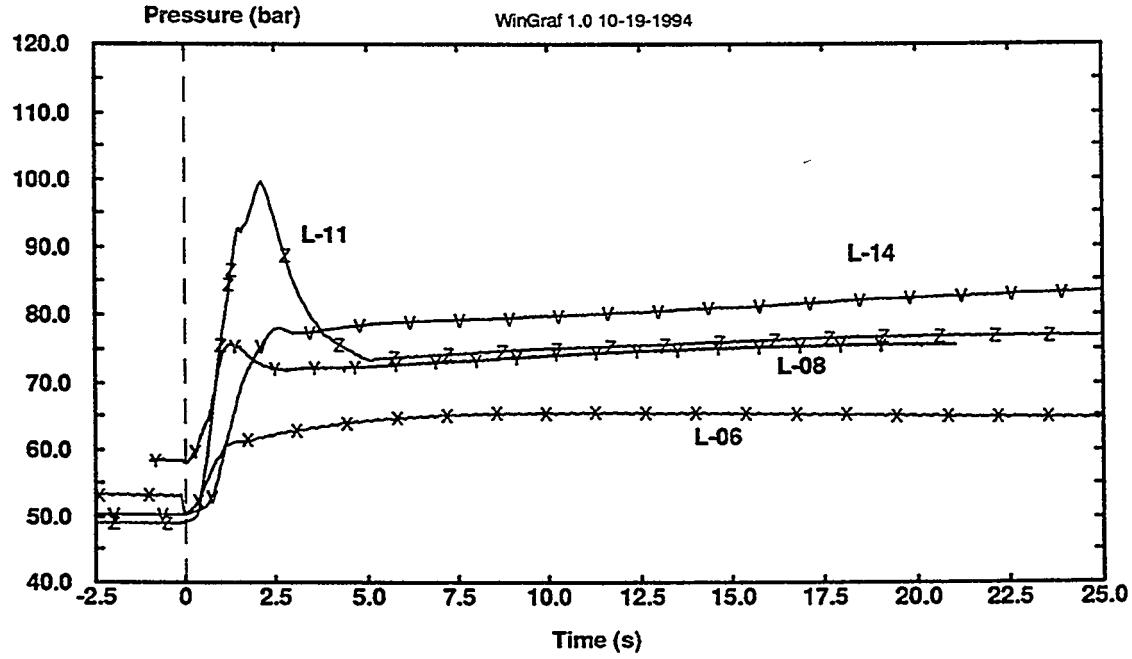

Figure 3. Test Vessel Pressure (-2.5s<t<25s)

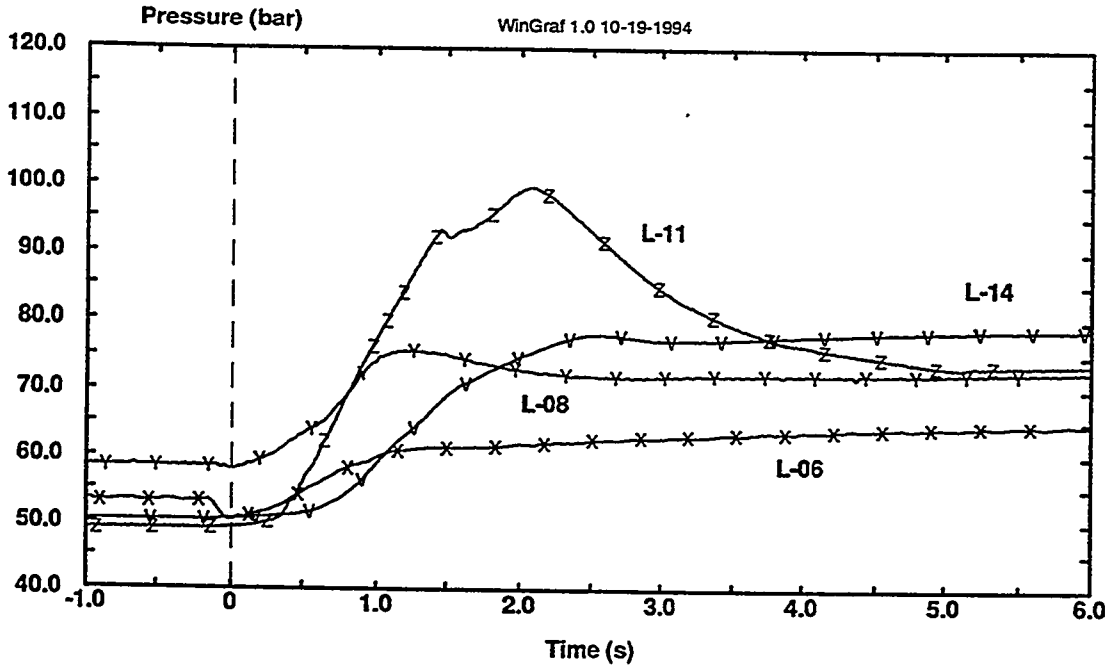

Figure 4. Test Vessel Pressure (-1s<t<6s)

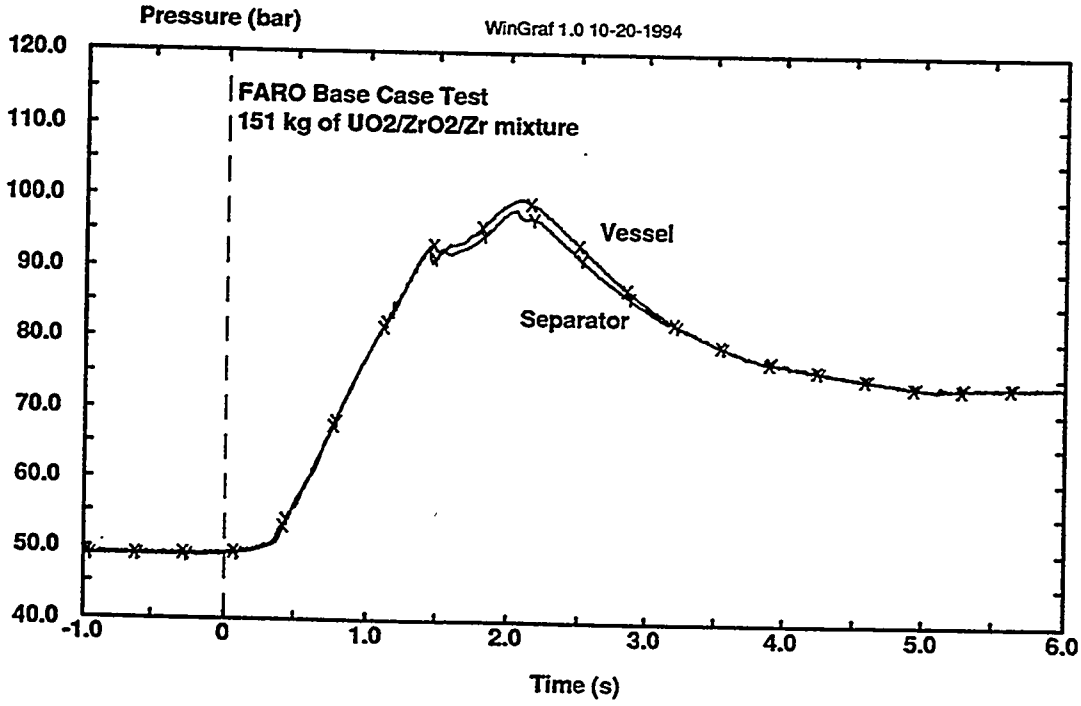

Figure 5. Vessel and Seperator Pressures in L-11 (-1s<t<6s)

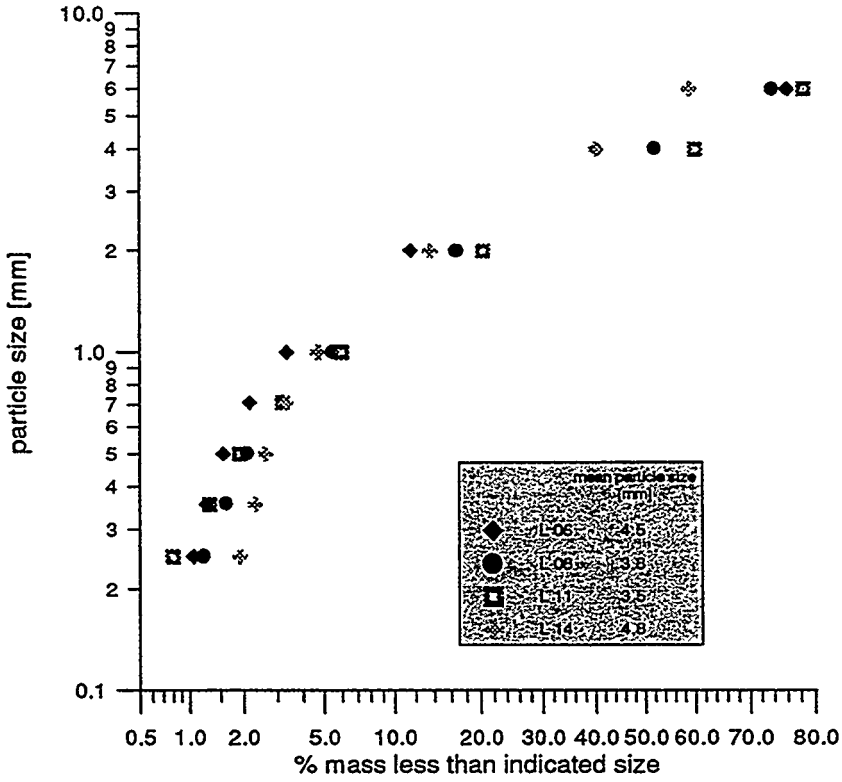

Figure 6. Particle Size Distribution

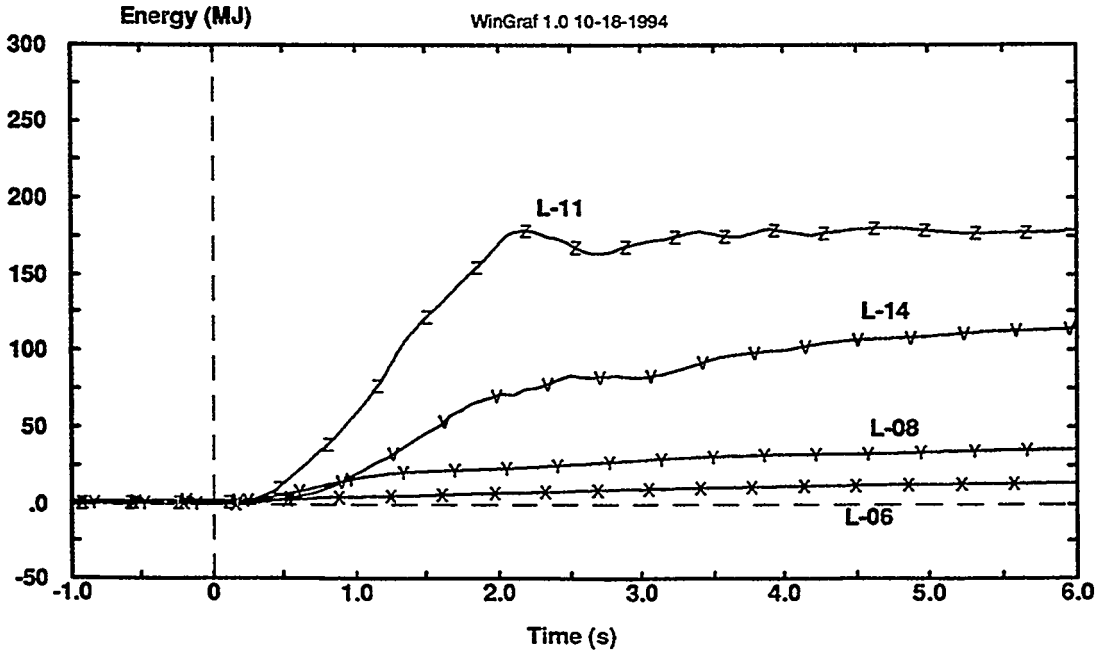

Figure 7. Energy Released to the Water

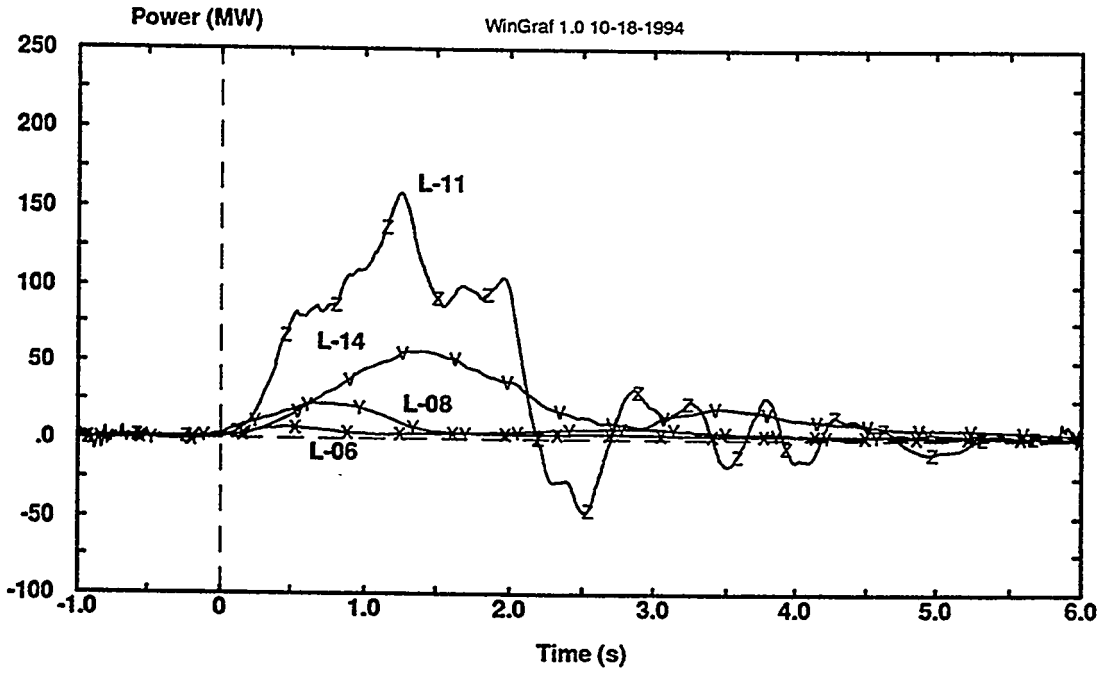

Figure 8a. Quenching Rate

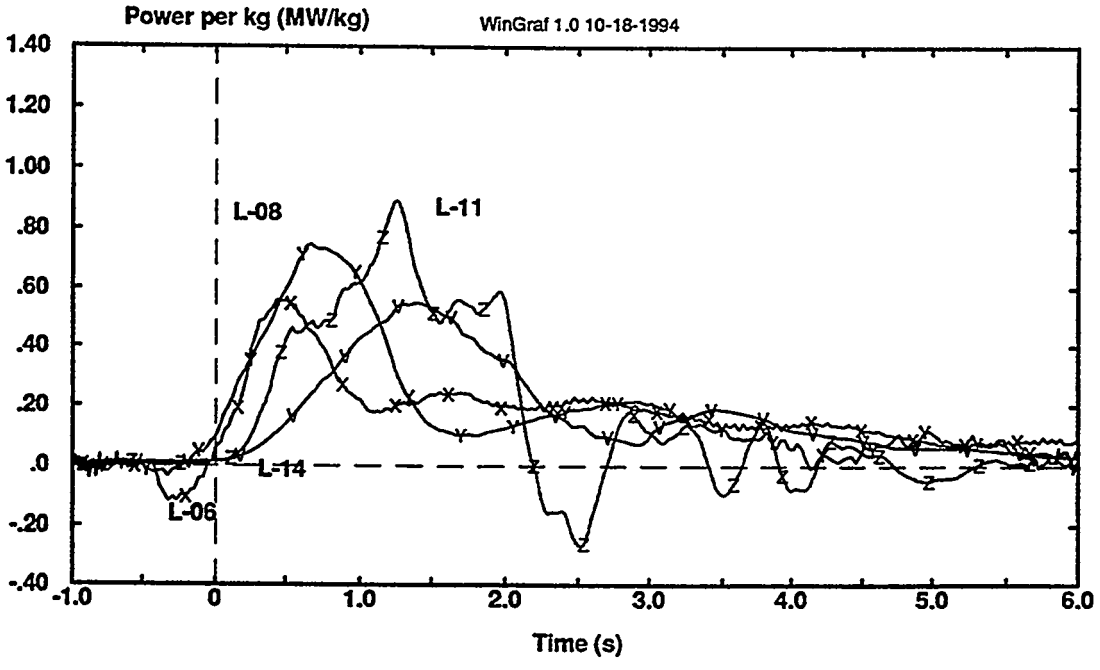

Figure 8b. Quenching Rate per Kilogram of Broken up Melt

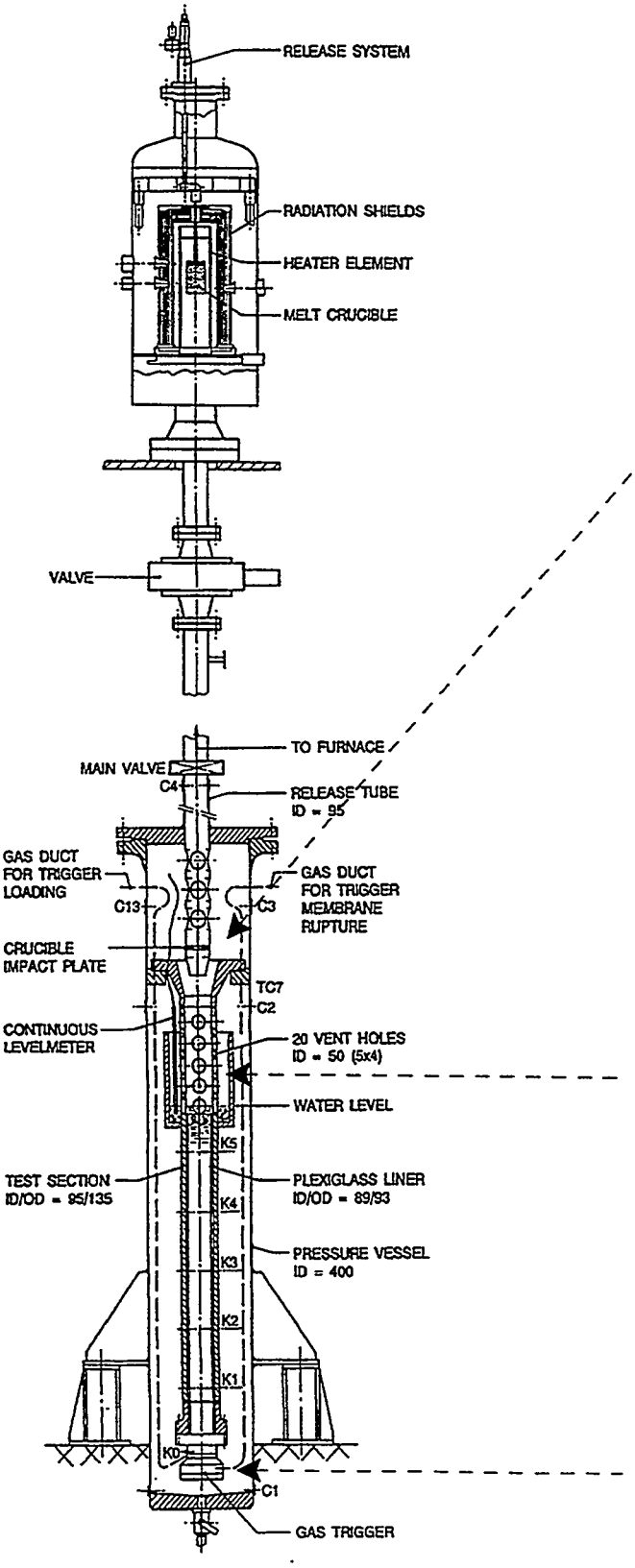

Figure 9a. Krotos Test Facility

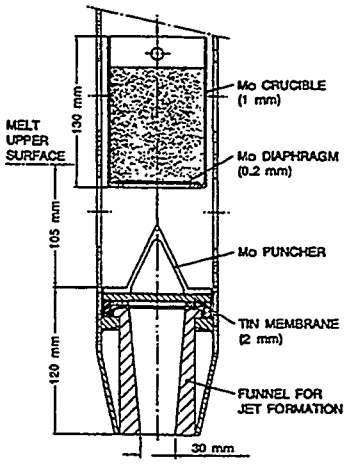

Figure 9b. Crucible and Puncher

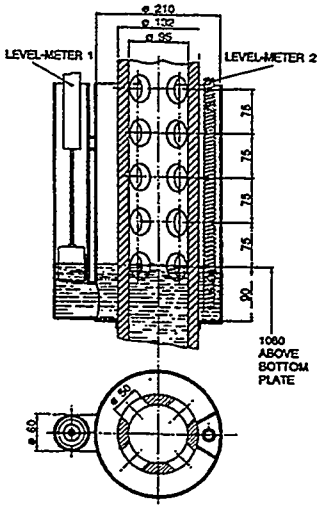

Figure 9c. Level-meter Vessel

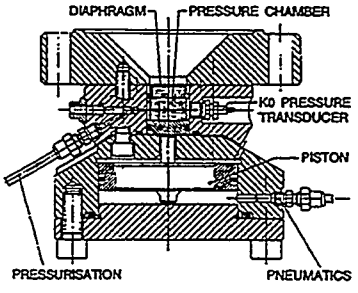

Figure 9d. Gas Trigger Device

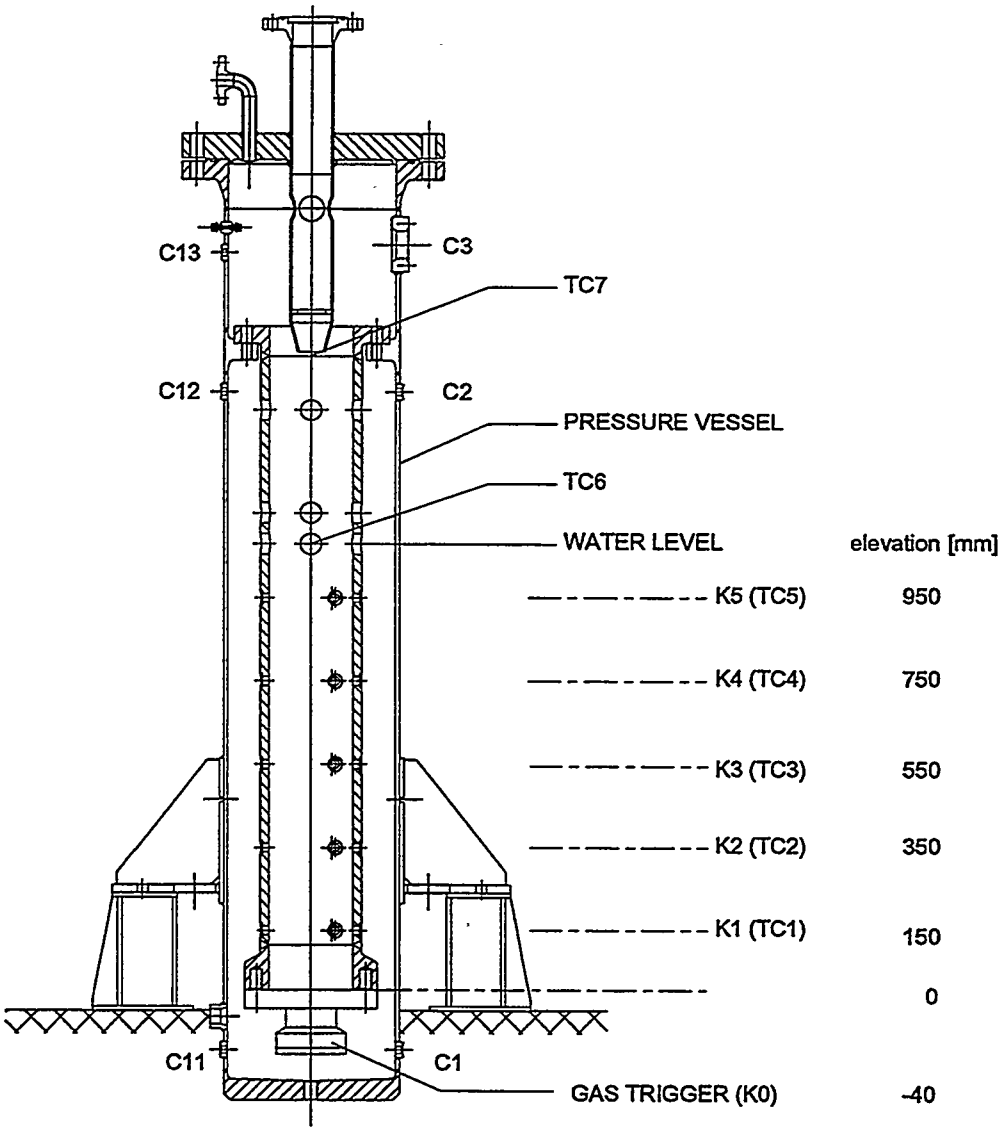

Figure 10. Wide Test Section and Instrumentation in KROTOS Tests

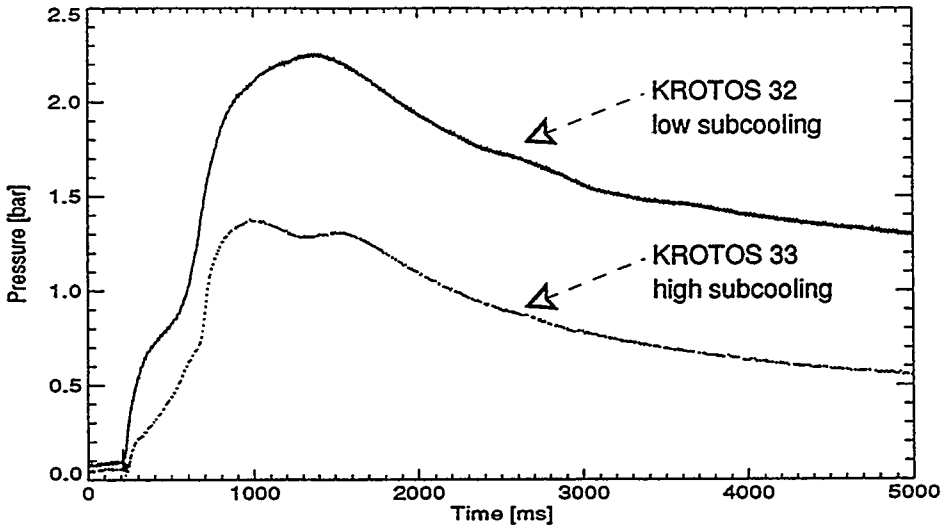

Figure 11. Expansion Vessel Pressurisation

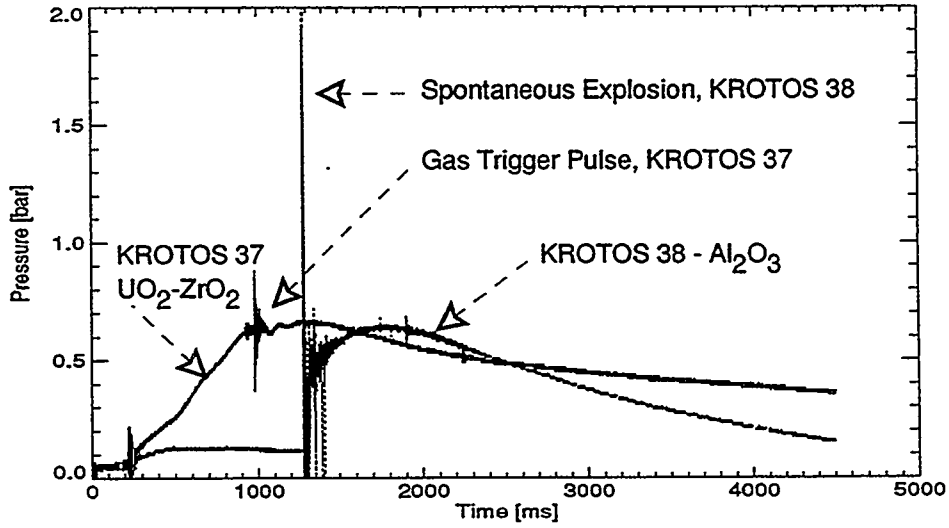

Figure 12. Expansion Vessel Pressurisation (Wide Test Section)

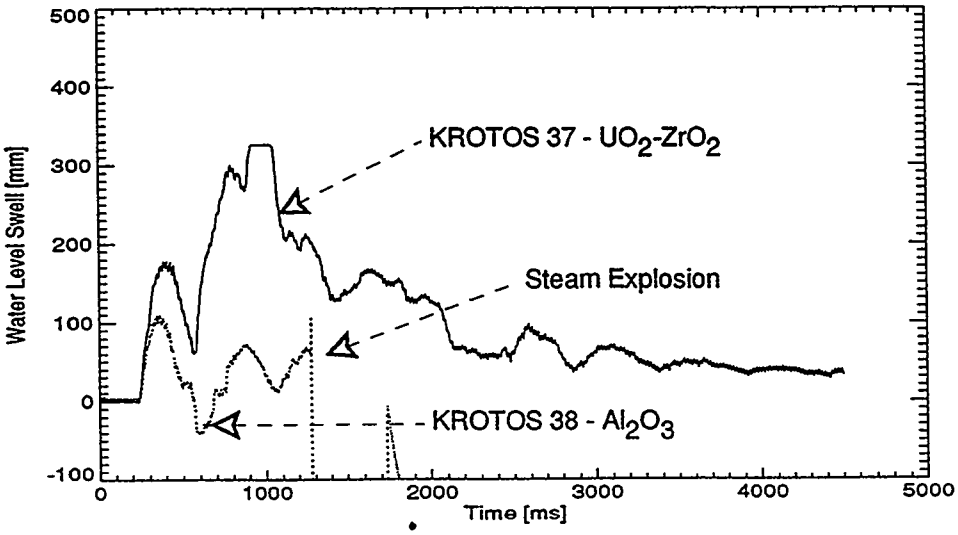

Figure13. Water Level Swell

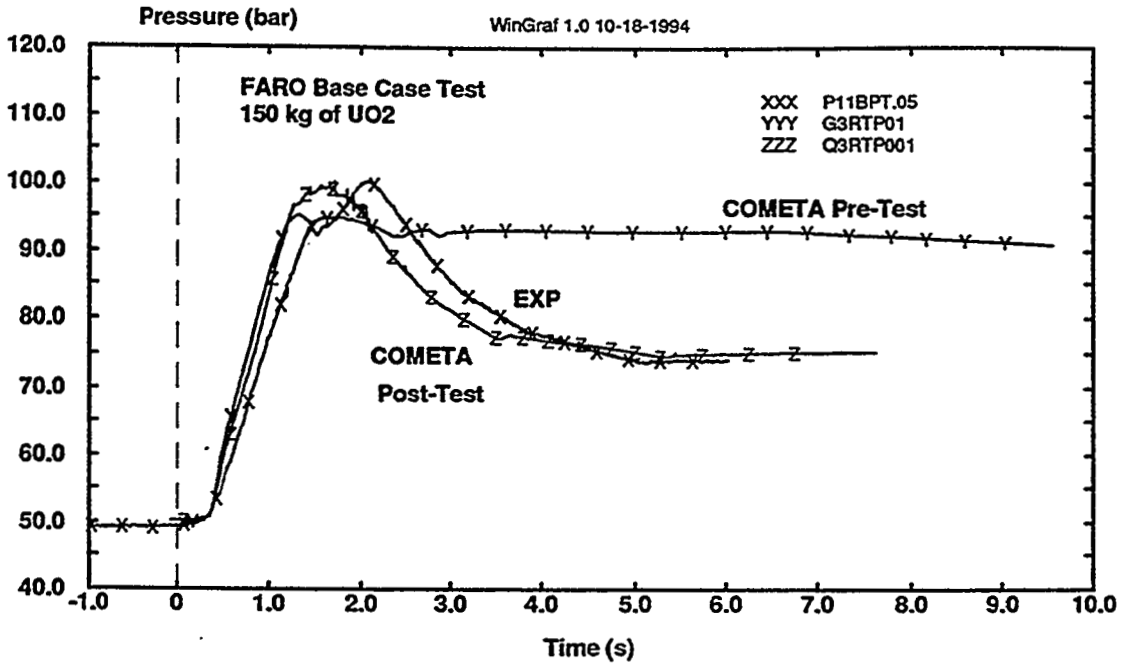

Figure 14. COMETA 1-D Pre-Test and Post-Test Calculations of the FARO L-11: Test Vessel Pressure

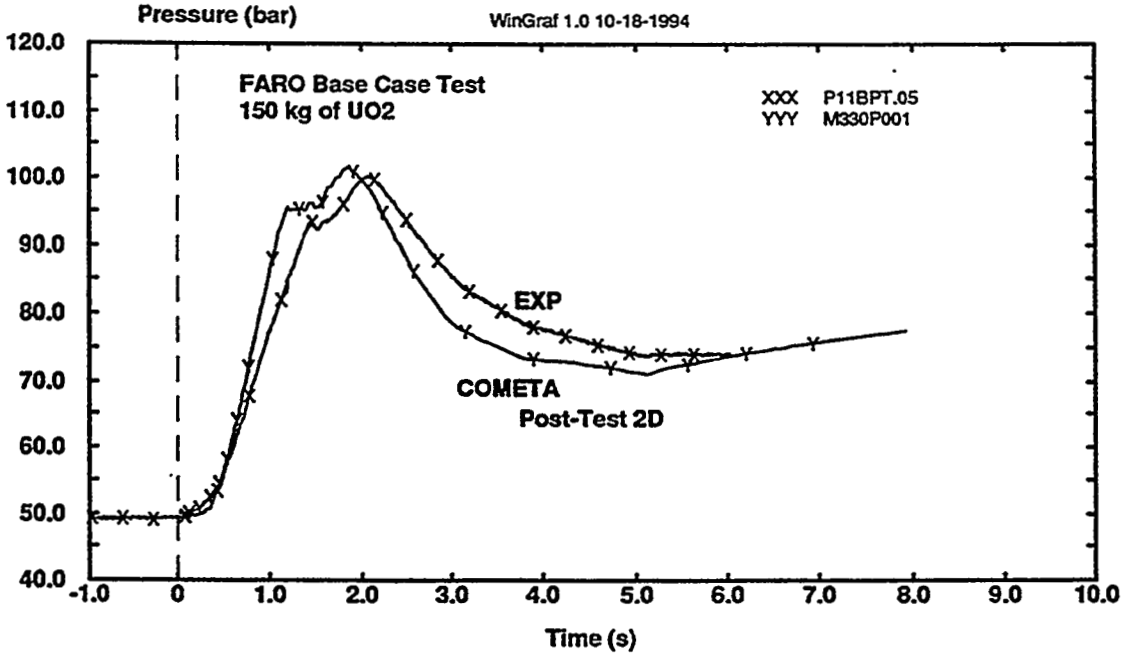

Figure 15. COMETA 2-D Post-Test Calculation of FARO Test L-11: Test Vessel Pressure

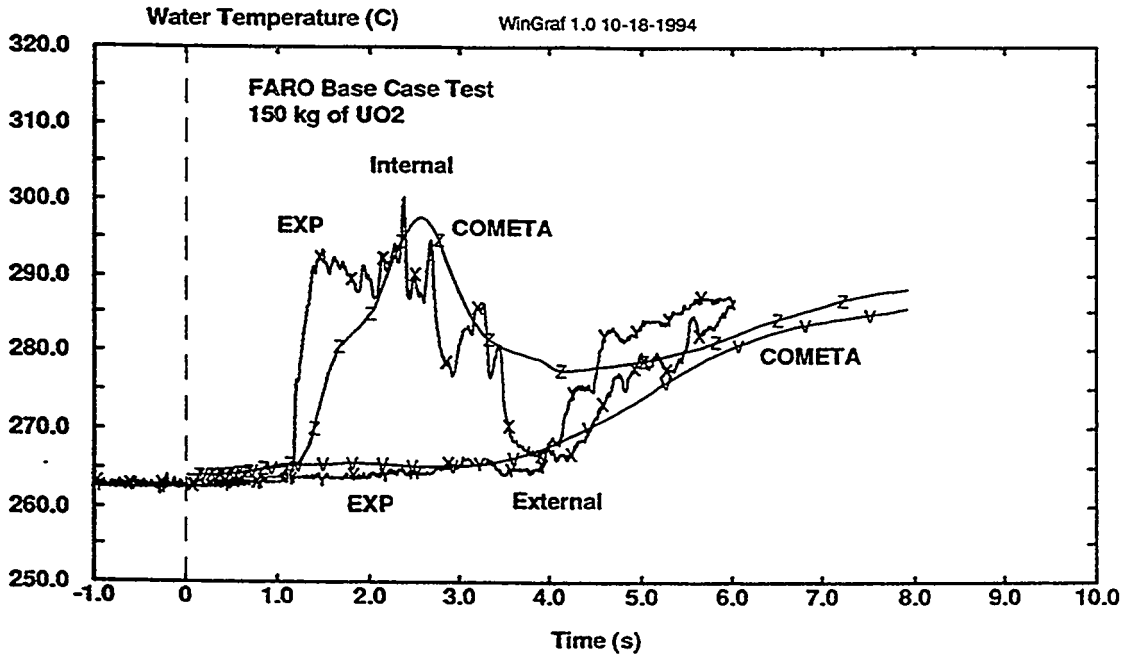

Figure 16. COMETA 2-D Post-Test Calculation of FARO Test L-11: Test Vessel Temperature

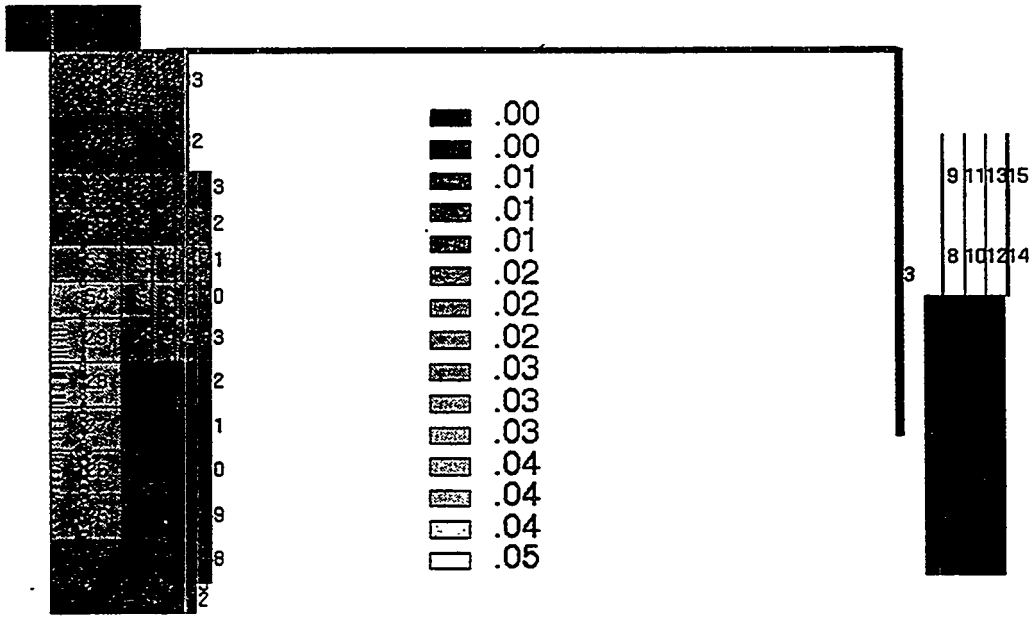

Figure 17. COMETA 2-D Post-Test Calculation of FARO Test L-11: Hydrogen Distribution (volumetric fraction)

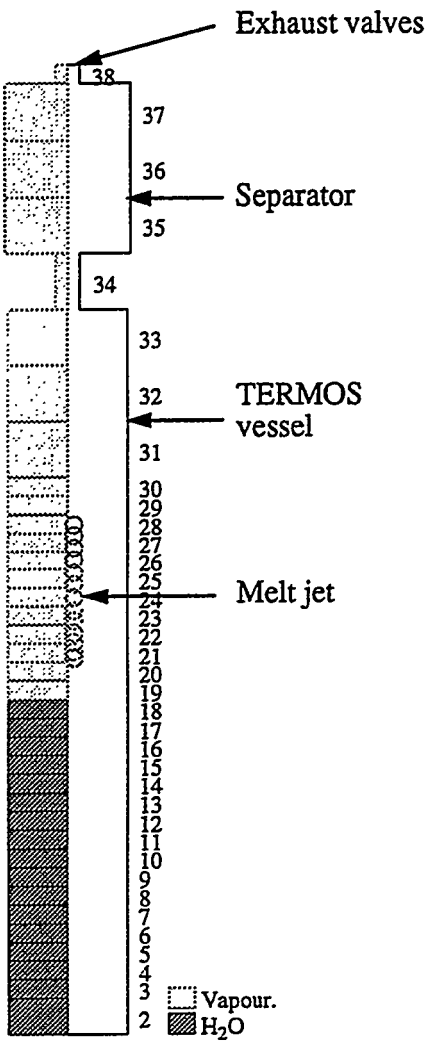

Figure 18. TEXAS Discretisation of the FARO Test Region

In TEXAS the exhaust valves are fully opened from 9.3 to 7.3 MPa

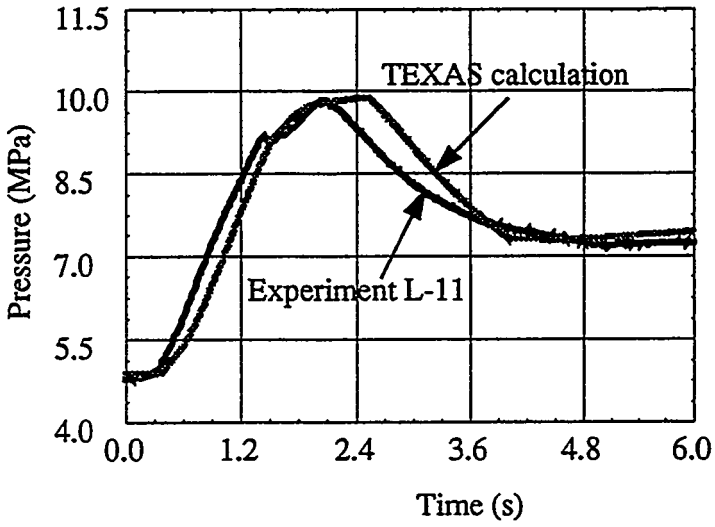

Figure 19. TEXAS Calculation of FARO Test L-11: Test Vessel Pressure

IFCI Validation Using Small Scale Coarse Mixing Experiments

Freddie Joe Davis, Jr.

Sandia National Laboratories
Albuquerque, New Mexico

Abstract

The Integrated Fuel-Coolant Interaction Code (IFCI 6.0) [Dav94] is a tool for the numerical investigation of Fuel-Coolant Interaction (FCI) phenomenology. FCIs are possible in a variety of severe accidents. FCIs may involve a variety of fuel-coolant contact modes as well as a variety of energy releases up to and including steam explosion events. One of the most crucial considerations in FCI is the mixing of the fuel and coolant, and the effects of steam production.

IFCI is operable and able to produce plausible results. [Dav93] As part of a complete code validation effort, and in preparation for a peer review of the code, IFCI 6.0 calculations are being compared with a matrix of experimental results. The matrix covers a spectrum of FCI contact modes and range of energetics. The list of experiments in the validation includes, but is not limited to the following experiments : 1) single drop experiments; 2) stratified layer experiments; 3) FARO; 4) KROTOS; 5) NPR/FCI EXO-FITS; 6) ALPHA; 7) MAGICO; 8) MIXA. Due to the critical nature of fuel-coolant mixing on the possibility and severity of a steam explosion, the first assessments performed are against mixing experiments.

This paper describes the validation of IFCI 6.0 against the MIXA-06 experiment. The MIXA experimental series provides data for steam generation rates, and time dependent results for melt distribution and vapor pressure [Den92]. MIXA provides data for small scale (3kg) prototypic melts.

The simulation effort revealed two shortcomings of IFCI that have been corrected. IFCI calculations for pressure rise and melt front progression are presented in this paper. This paper also describes animation sequences of the melt and water volume fractions. The steam generation rate, not normally an IFCI output variable, is also discussed in the context of a corrected finding.

The IFCI simulations demonstrate that the local distributions of material during the mixing phase are reasonable. However, there is some room for improvement. The simulations further show that IFCI captures parameters for system analysis, such as pressure history, to within a few percent.

Introduction

The Integrated Fuel-Coolant Interaction Code (IFCI 6.0) [Dav94] is a tool for the investigation of Fuel-Coolant Interaction (FCI) phenomenology. FCIs are possible in a variety of severe accidents. FCIs may involve a variety of fuel-coolant contact modes as well as a variety of energy releases up to and including steam explosion events. One of the most crucial considerations in FCI is the mixing of the fuel and coolant. Mixing includes the separation of the two liquids by steam production.

The operability of IFCI and its ability to produce plausible results have been demonstrated. [Dav93] As part of a complete code validation effort, and in preparation for a peer review of the code, IFCI 6.0 calculations are being compared to a matrix of experimental results. The list of experiments in the validation includes, but is not limited to the following experiments : 1) single drop experiments; 2) stratified layer experiments; 3) FARO; 4) KROTOS; 5) NPR/FCI EXO-FITS; 6) ALPHA; 7) MAGICO; 8) MIXA. FCI probability and consequences are tightly coupled to the degree of mixing of the melt, water, and vapor. Fuel-coolant mixing is critical to the possibility and severity of a steam explosion. Therefore, the first assessments performed are against mixing experiments. As part of the IFCI validation effort, IFCI has been used to simulate the MIXA-06 experiment. The MIXA experimental series provides data for the mixing and steam generation from a pour of prototypic hot melt droplets into a quenching medium.[Den92]

Experimental Description

The MIXA experimental series investigates the quenching of kilogram quantities of molten core simulant (in the form of 6 mm diameter droplets of 81% uranium dioxide and 19% molybdenum metal) at prototypic temperature (3600 K) into a saturated coolant pool near atmospheric pressure[Den94]. The pool was 0.6 m in depth and contained in a square vessel, 0.37 m on a side. The vessel was open to the atmosphere via a vent line. The vent line contained a flow meter to measure the steam production.

The following results from MIXA-06 affect the validation of IFCI. First, no steam explosion was observed. This validates only latent energy effects. Second, steam generation and level swell obscured the inflow region for a large portion of the inflow period. Local void fraction calculations cannot be validated. Third, melt holdup near the surface and extensive steam void in the mixing region was observed. This provides a qualitative basis for validation. Fourth, the melt initially reached the water surface with a velocity of ~5 m/s, slightly larger (~10%) than that from a gravity pour. The melt pour lasted approximately 1.5 s. The delivery of the melt into the system and particularly into the coolant pool is not precisely known. Finally, the peak pressure rise of 0.031 MPa, occurs approximately 1 second after the melt arrives at the water surface. This provides a basis for validation of the energy transfer models, and to a lesser degree the transport calculations.

IFCI Modeling Description

The following values were used in modeling of the MIXA-06 experiment. All of the following values are common to the entire suite of MIXA-06 simulations. The Fletcher and Denham paper I.7 from CSNI Specialist meeting in Santa Barbara, CA is the primary reference. [Fle93]

Vessel Radius	=	0.21	m
Vessel Height	=	1.5	m
Water Level	=	0.6	m
Droplet size	=	0.006	m
Jet Radius(60mm)	=	0.06	m
Melt Mass In	=	3	kg
Melt Density	=	8400	kg/m3
Jet Col. Ht.	=	0.48	m

Table 1. Parameters Used in the IFCI MIXA-06 Model.

The vessel radius is based on an area equivalent to that of the 0.37 m x 0.37 m vessel. Water depth is 0.6 m, as specified in section III of the reference document. The vessel height, droplet size, jet diameter, melt mass, melt density and jet column height are all provided in section IV of the reference document.

IFCI simulations were performed using a 7 x 24 and a 11 x 36 mesh that bound, by number of cells, the calculation results presented from the CHYMES validation. [Fle93]

Validation Findings and Corrections

Simulations of the MIXA-06 experiment produced two primary findings. The first finding was a considerable variation in results with nodalization. Figure 1 illustrates the large variation in pressure calculated using different nodalizations. Due to the highly dynamic and rapidly evolving nature of FCI, bifurcations may exist for even subtle differences in values. Therefore, slight variations with nodalization are unavoidable. However, it was clear that different nodalizations tracked the melt jet much differently. After considerable investigation, it was determined that the initialization of matrices was being performed incorrectly for the melt field equations. The error caused melt tracking to be dependent on the nodalization and solutions were highly divergent as a result. The source code was corrected and the results shown in the Final Results section are calculations from the corrected source code.

The second finding was an underprediction of the pressure rise in the upper plenum vapor region. Unfortunately, having corrected the melt tracking problem previously identified, no combination of user parameters enabled IFCI to reproduce the pressure values reported from the experiment. Figure 2 is a representative IFCI pressure calculation.

A brief description of the modeling of the coolant pool is in order, as it was critical in the discovery process. The coolant pool was modeled as uniformly at saturation at a pressure of 0.1 MPa. These conditions are not equilibrium throughout the coolant pool due to the small but not negligible static head of the liquid. The reason the static head is not negligible is that it causes regions below the surface to activate the subcooled boiling mode. This tests the adequacy and robustness of the subcooled boiling and condensation models. Since the melt energy is insufficient to place the coolant pool into a dominantly bulk boiling regime, the subcooled boiling and condensation models were investigated.

The inability of IFCI to match the experimental pressure rise results indicate some error in the heat transfer models, equations of state, or application thereof. Steam generation and the pressure rise are coupled results. The error was not in the generation of steam, but an excessive condensation of steam, while submerged in the slightly subcooled pool. The rapid condensation in the pool prevented the steam from being released to the atmosphere and elevating system pressure.

The source code was modified to inhibit, by a factor of 1000, the steam condensation rate. This effectively precluded the rapid condensation of vapor produced by subcooled boiling. The subsequent calculations for steam generation and pressure, with condensation suppressed, compare to within 10-25 percent of the reported experimental values. Suppression of essentially all of the condensation allows the pressure and steam generation to be bounded on the high side. This indicates that IFCI can reproduce the experimental values. However, it is not clear that the suppression of the condensation applied to this case is applicable to all simulations. It does indicate the need for further study and model improvement for subcooled effects.

Final Results

After addressing the deficiencies described previously a suite of final calculations was performed. This suite of calculations investigates two issues. First, how sensitive are the results to variations in delivering the melt to the coolant? This addresses the issue of how well melt delivery must be characterized in order to provide useful information to numerical models and simulations, and hopefully how sensitive FCI are to melt delivery. Second, what are the effects of nodalization on the overall solution? This is investigated using the pressure in the vapor plenum region.

The initial configuration of melt, coolant, and vessel geometry for each nodalization is shown in Figure 3. It is assumed for the first calculation that the melt falls unaffected through the vapor space and that the melt can accurately be represented as in tact, just above the water surface, with an initial downward velocity of 5 m/s, as reported from the experimental observations. The initial velocity is applied uniformly to the melt region above the water. This may produce some error as the melt in cells at higher locations will have the additional gravitational potential associated with elevation. This error is believed to be minimal as melt holdup will dominate the melt motion within milliseconds of water contact and vapor generation. Figure 4, a-d, shows the average vapor pressure calculated by IFCI, for several different cases. Error bars indicate the maximum and minimum

calculated pressure within the solution domain. The thinner line, w/o error bars, represents the experimental pressure. The maximum calculated pressure exceeds the experimental value. If the calculated pressure response is smoothed for comparison to the pressure traces, which may or may not be justifiable based on the pressure transducer response characteristics, then the pressure agrees to about 10%. The timing of the peak pressure lags the experimental result slightly. There is some concern about the experimental zero time. The zero time is reported as, "melt water contact and steam generation." The detection of steam generation may not correspond exactly to melt water contact, so some temporal shift may be present.

The second simulation (Figure 4b) shows the calculation for releasing the melt from above the pool surface with zero initial velocity. The calculated values compare reasonably well with the experimental results. The maximum pressure rise is again overpredicted. This could be a result of more efficient fuel coolant mixing, or an indication that the adjustment to mitigate condensation effects is excessive. However, this simulation closely matches the timing of the maximum pressure, and the slopes of pressure increase and decrease are very similar.

Two different nodalizations were selected for study of variations with nodalization. The 7 x 24 and 11 x 36 meshes, shown in Figure 3, are roughly to scale. Fluid transport codes are generally sensitive to extreme cell aspect ratios. The nodalization schemes employed here maintain a suitable aspect ratio (on the order of 2). These nodalizations intentionally are not one double the other. It is hoped that the variations which result from meshing will be highlighted by these two meshes.

Figures 4c and 4d show the IFCI simulations performed for a 7 x 24 grid. Those results show some differences from the 11 x 36 calculations. This is expected and will be discussed in the following paragraph. The overall characteristics of the upper plenum vapor pressure are the same for all four calculations shown.

As mentioned previously, some variations with nodalizations are expected. This is for the following reasons. First, IFCI uses a lower volume fraction threshold to decrease computational time and avoid singular matrices. In a given cell, if the volume fraction of a field, melt, water, or vapor, is below that threshold, the equations for that field will not be incorporated into the solution. Thus, for cells of different volumes, if the same amount of a field is transported into those cells, the resulting volume fractions of the material in question will differ between the small and large cell. Consequently, at a particular time, the field may be solved for one nodalization and not for the other, and results will be slightly different. Second, IFCI calculates the timestep used. The timestep is based on limits of transport across cell interfaces and on relative phase change within a cell. Both depend on the nodalization scheme employed. Thus, nodalization will effect the results to a small degree. It is hoped that no severe bifurcations exist in the phenomenology, such that any slight changes in local characteristics will have a dramatic effect on global results.

The advance of the leading edge of the melt through the coolant pool was also reported from the experiment. This information can also provide insight into the quality of the IFCI calculations for this experiment. Figure 5 shows three values; the 5 m/s line corresponding to the reported velocity of the melt incident on the coolant surface, the

progression of the melt front calculated by IFCI, and, the data points reported from the experiment. The penetration of the melt front compares well for the initial phases of fuel coolant mixing (a little more than one-tenth of a second). After that time, the experimental measurement shows some hold-up of the melt progression that IFCI does not predict. The discrepancy may be a result of modeling the melt as intact at the surface of the pool at time zero. Modeling the melt as a pour from an elevated location may produce different melt progression results. This is currently being pursued. Unfortunately, the disparity between calculated melt tracking and that reported from the experiment may also indicate an error in the multi-field drag correlation.

Animation Observations

In addition to the history plots shown in this paper, an animation sequence was generated for the melt and water volume fractions calculated on the 11 by 36 grid. This section briefly describes the observations from those animations. Further details can be obtained by direct inquiry to the author.

The first animation is for the cell wise melt volume fractions. Initially the 'stack' of melt begins to sink into the coolant pool region. Some lateral spreading along the top of the coolant pool occurs. Then, at about 0.3 seconds, the top level of the melt begins to rise. This corresponds to level swell. Significant vapor formation occurs at about 0.6 seconds that accelerates some fraction of the melt upward. Radial spreading of the melt, beneath the surface of the coolant pool possesses a characteristic fireball shaped spreading below the coolant surface.

As melt falls from the top of the vessel, the continued vapor generation accelerates the melt back upward once again. This continues in a quasi-cyclic fashion, until the rate of vapor formation significantly decreases. Melt eventually accumulates at the vessel bottom.

The animation of the water volume fraction supports some of the occurrences described in the previous paragraph. In the animation the minimum water volume fraction utilized is 0.25. This corresponds to the lower end of a continuous liquid phase. As melt displaces and boils water, the water level rises on the outer half of the region. At about 0.6 seconds, some water is accelerated upward as with the melt in the previous animation. Water strikes the vessel top and spreads radially outward returning down the outer side walls in somewhat of a convection loop. Steam/water slug flow is established upward in the center regions of the vessel. Counter-current flow is observed on the periphery. There is generally less and less water in the system as boiling continues and escapes the outlet.

Whereas the pressure history for the upper plenum space provides a basis for the evaluation of the global parameters calculated by IFCI, the animation sequence provides some confidence that the underlying processes of fuel-coolant mixing are being readily calculated. These animations provide confidence in the IFCI simulations of MIXA-06.

Conclusions

The results of the MIXA-06 simulation revealed two shortcomings in the IFCI code. One of these, melt field initialization and tracking, has been corrected by source code modification. The other, excessively rapid condensation, has been addressed through a model correction factor. The net effect and overall applicability of the latter correction still require validation. The simulations also show that IFCI captures the MIXA-06 pressure well subject to a calibration of the condensation model. IFCI tracks melt front progression well in the early stage of mixing. Further investigation is required for later stages. Animations show that IFCI captures the qualitative characteristics of FCI mixing. IFCI is poised to continue with further validation.

References

F. J. Davis, and M. F. Young, "Integrated Fuel-Coolant Interaction (IFCI 6.0) Code : User's Manual," Sandia National Laboratories, SAND94-0406, NUREG/CR-6211, Albuquerque, NM, April 1994.

F. J. Davis, "Integrated Fuel-Coolant Interaction Code : Assessment of Stand-Alone Version 6.0," Twenty-first Water Reactor Safety Meeting, NUREG/CP-0132, Bethesda, MD, October, 1993.

M. K. Denham, A. P. Tyler, and D. F. Fletcher, "Experiments on the Mixing of Molten Uranium Dioxide With Water and Initial Comparisons With Chymes Code Calculations," Fifth International Meeting on Reactor Thermal Hydraulics, NURETH-5, Salt Lake City, UT, September, 1994.

D. F. Fletcher and M. K. Denham, "Validation of the Chymes Mixing Model," presented at the CSNI Specialists Meeting, Santa Barbara, CA, January, 1993.

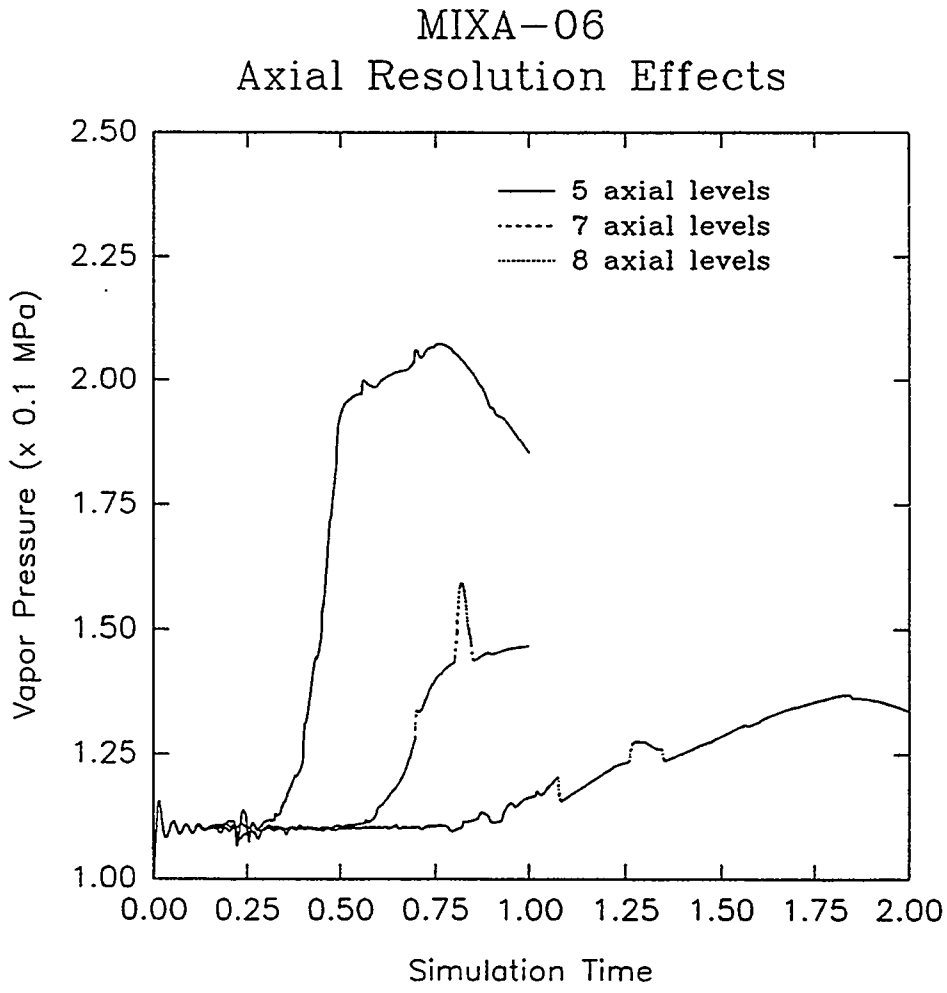

Figure 1. Nodalization Effects on Pressure Response.

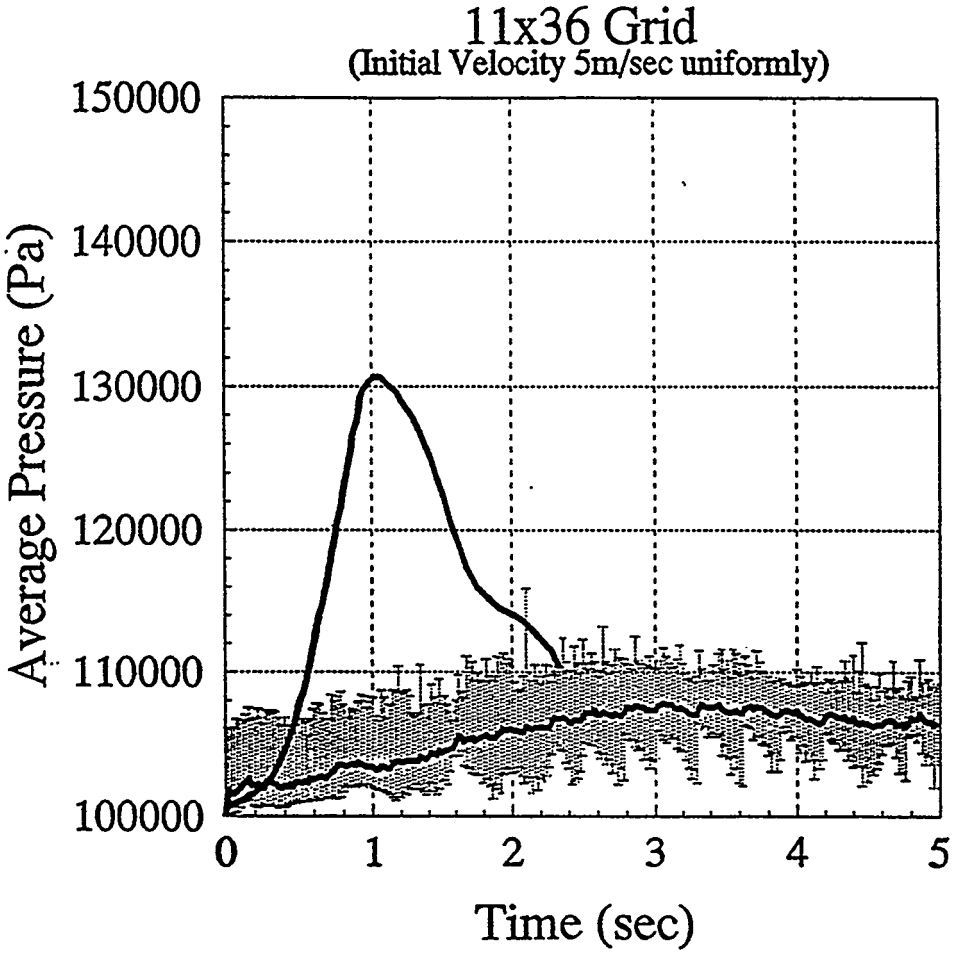

Figure 2. Example of the Underpredicted Pressure.

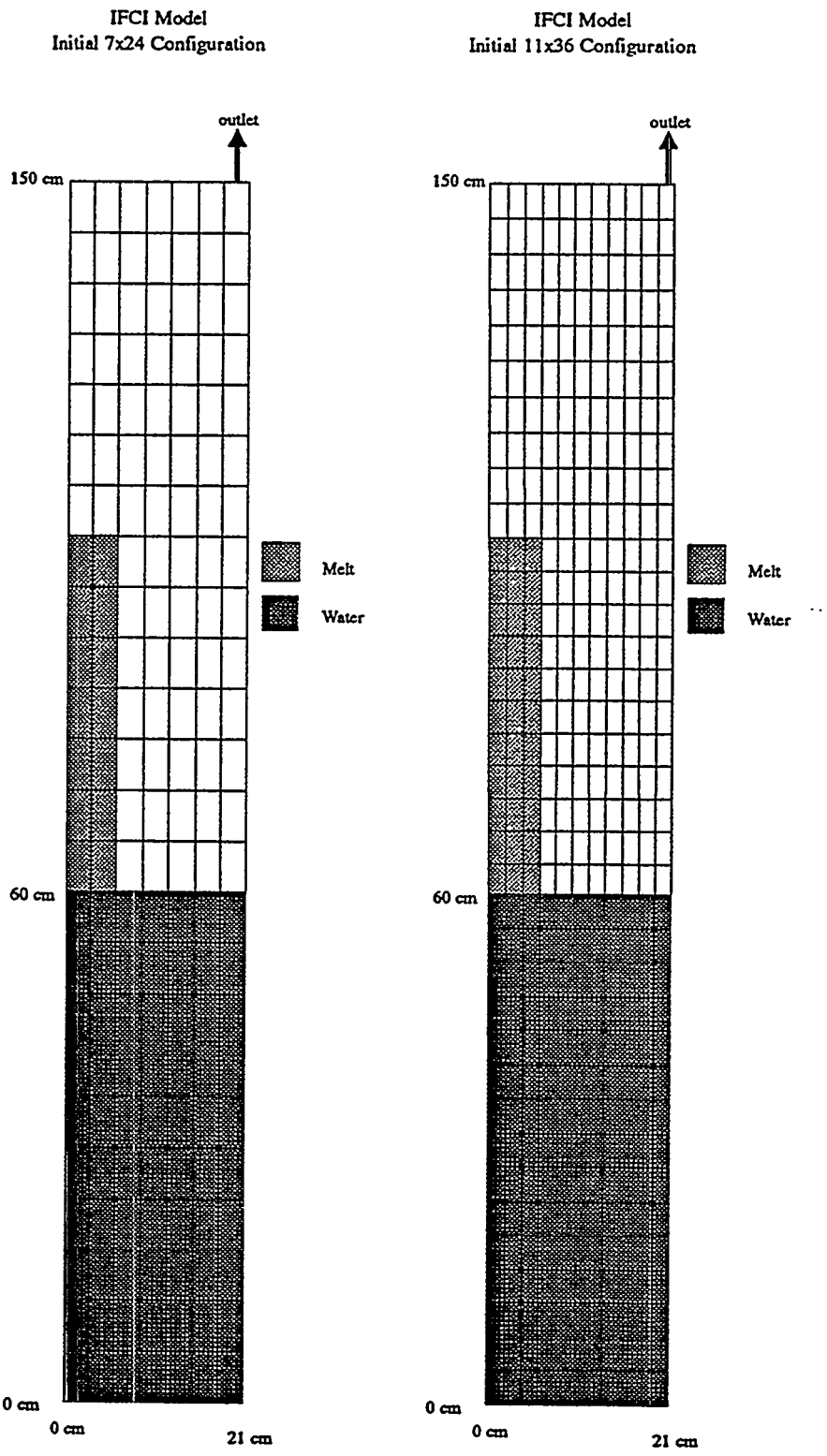

Figure 3. Nodalizations used in IFCI Simulations of MIXA-06.

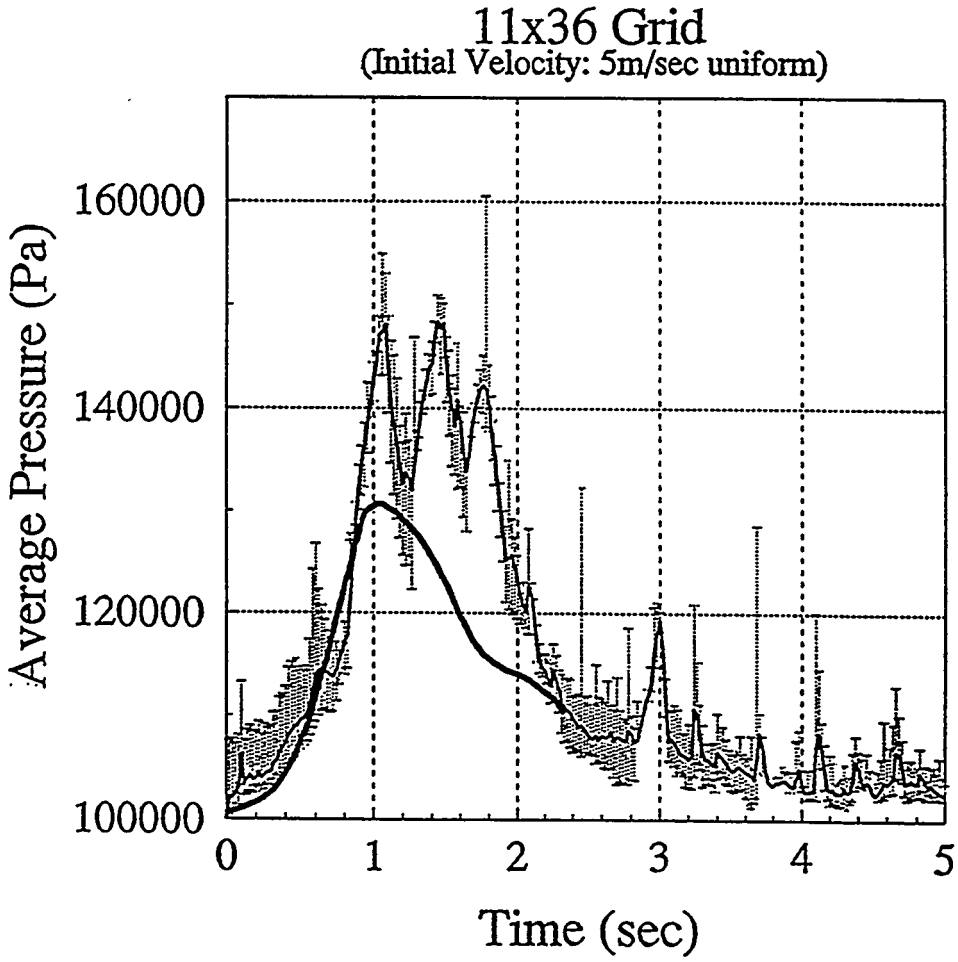

Figure 4a. IFCI Simulations of MIXA-06, 11 x 36 Grid, 5 m/s.

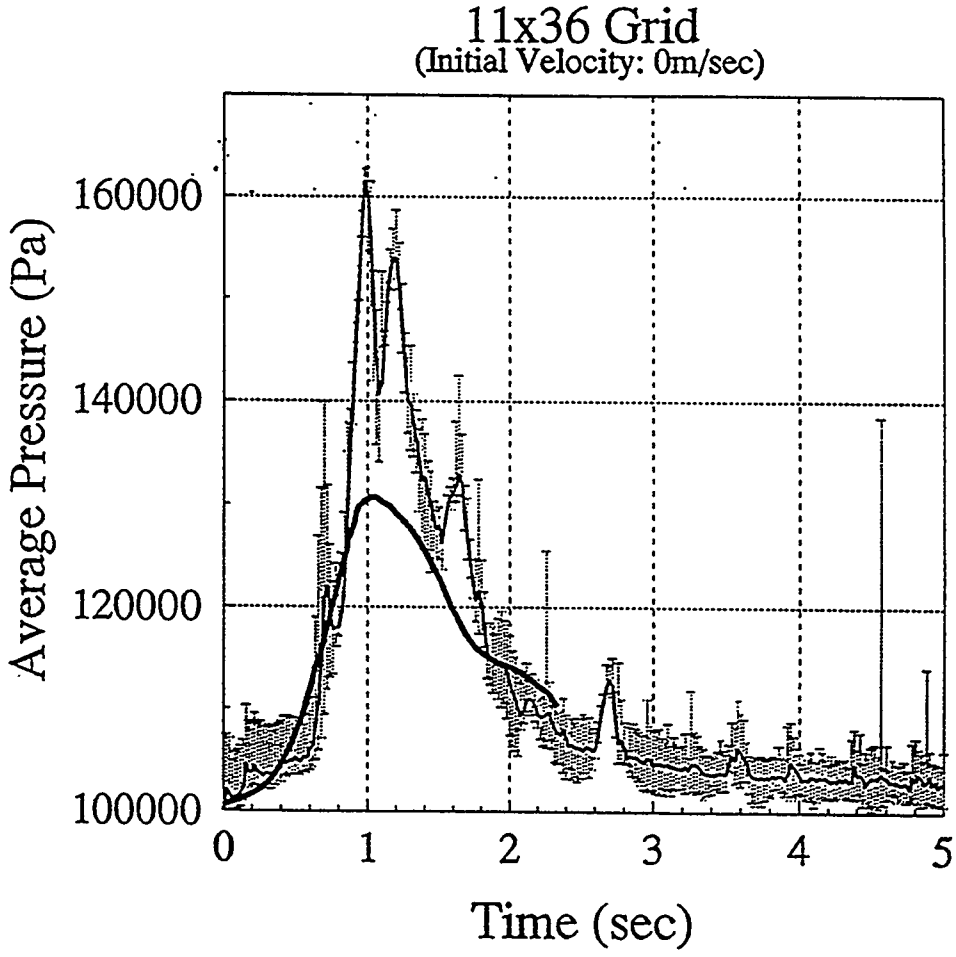

Figure 4b. IFCI Simulations of MIXA-06, 11 x 36 Grid, 0 m/s.

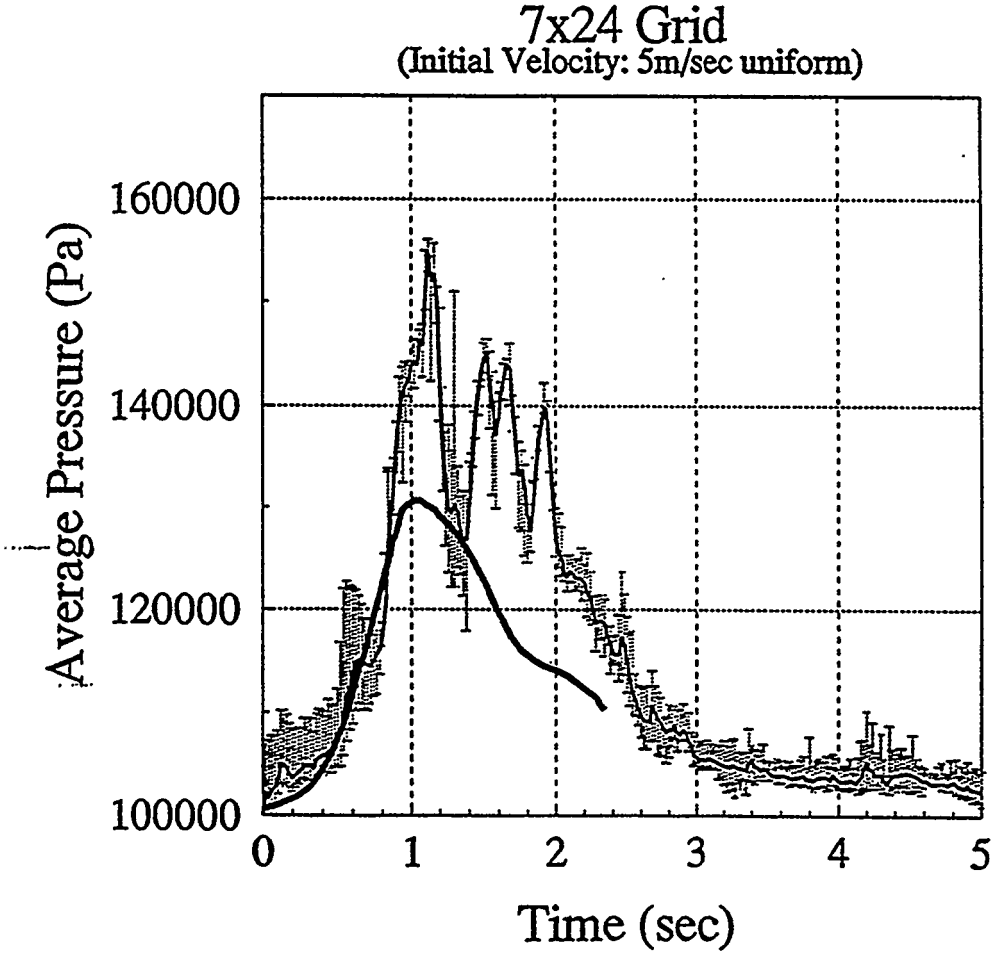

Figure 4c. IFCI Simulations of MIXA-06, 7 x 24 Grid, 5 m/s.

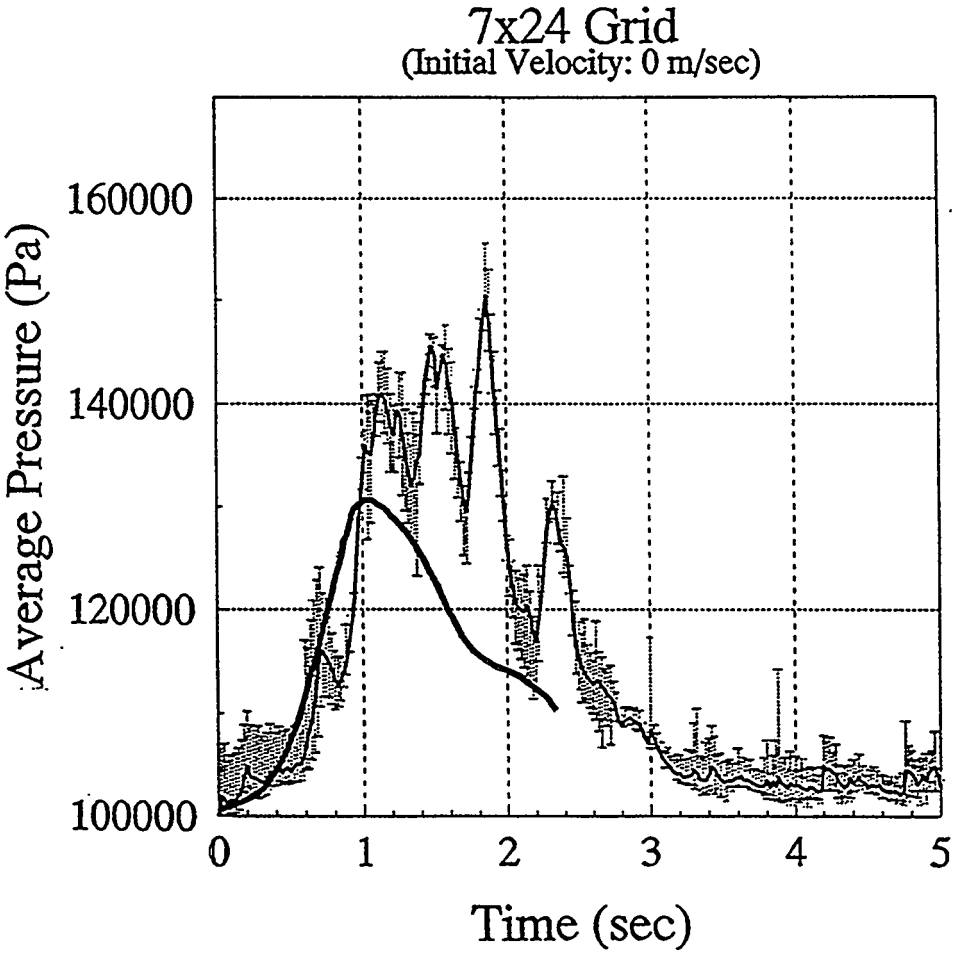

Figure 4d. IFCI Simulations of MIXA-06, 7 x 24 Grid, 0 m/s.

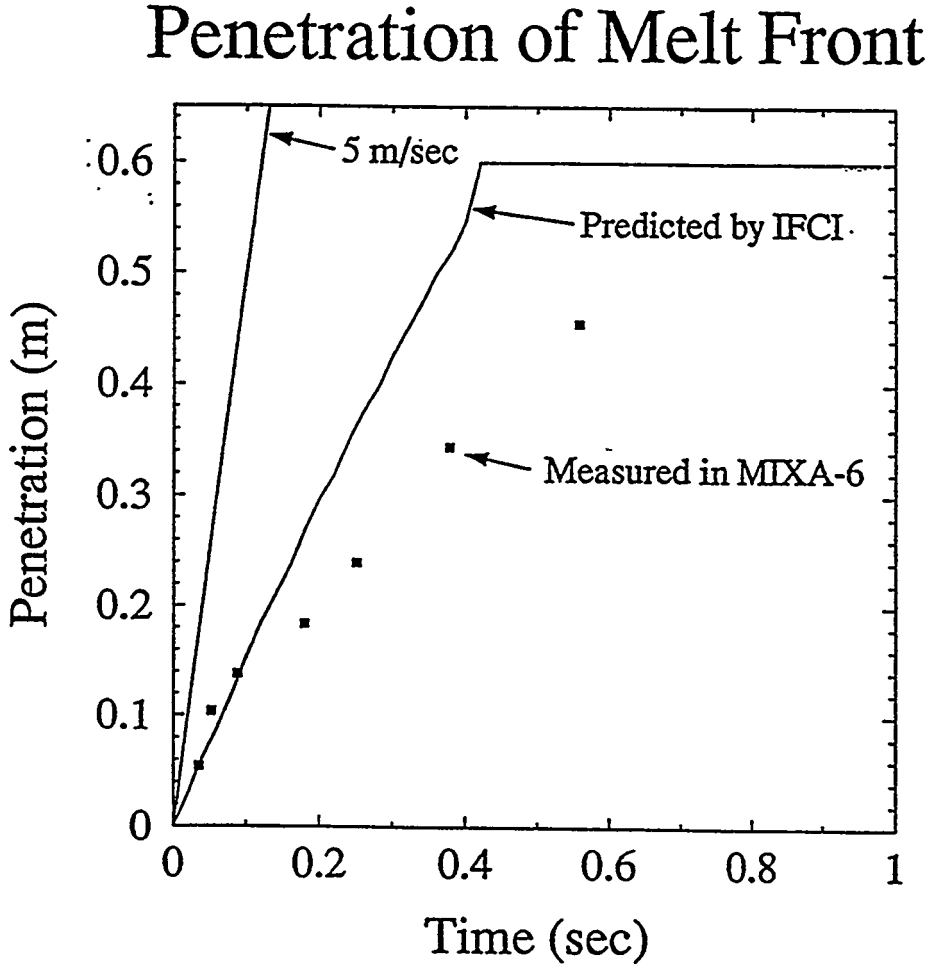

Figure 5. Penetration of the Melt Leading Edge.

TMI-2 ANALYSIS USING SCDAP/RELAP5/MOD3.1

J. K. Hohorst
S. T. Polkinghorne
L. J. Siefken
C. M. Allison
C. A. Dobbe

Idaho National Engineering Laboratory
P. O. Box 1625
Idaho Falls, Idaho 83415

Work supported by the U.S. Nuclear Regulatory Commission, Accident Evaluation Branch, under DOE Contract No. DE-AC07-94ID13223

ABSTRACT

SCDAP/RELAP5/MOD3.1 an integrated thermal hydraulic analysis code developed primarily to simulate severe accidents in nuclear power plants, was used to predict the progression of core damage during the TMI-2 accident. The version of the code used for the TMI-2 analysis described in this paper includes models to predict core heatup, core geometry changes, and the relocation of molten core debris to the lower plenum of the reactor vessel. This paper describes the TMI-2 input model, initial conditions, boundary conditions, and the results from the best-estimate simulation the TMI-2 accident as well as the results from several sensitivity calculations.

1.0 INTRODUCTION

The SCDAP/RELAP5/MOD3.1 computer code[1,2,3] was used to predict the progression of core damage during the TMI-2 accident. SCDAP/RELAP5/MOD3.1 is an integrated thermal-hydraulic analysis code developed primarily to simulate severe accidents in nuclear power plants. It includes models to predict core heatup, core geometry changes, and the relocation of molten core debris to the lower plenum of the reactor vessel. This paper briefly describes the TMI-2 input model, including the initial and boundary conditions used for the analysis, and discusses results from the best-estimate simulation of the TMI-2 accident as well as the results from several sensitivity calculations. The primary objectives of this analysis were to (a) calculate all of the relevant phenomena believed to have occurred during the TMI-2 accident, (b) exercise and assess various core damage models and options, and (c) determine if the most recent version of SCDAP/RELAP5 is better able to predict the progression of core damage during the TMI-2 accident than previous code versions.

All major components of the TMI-2 primary system were modeled using the SCDAP/RELAP5/MOD3.1 code package. The RELAP5 module was used to simulate the thermal-hydraulics of the reactor vessel, primary coolant loops, steam generators, and pressurizer. Steam generator secondary side coolant levels, pressures, and feedwater temperatures, and primary side makeup and letdown flow rates were supplied as boundary conditions. The SCDAP module was used to simulate the reactor core, which was divided into five radial regions by grouping similarly powered fuel assemblies together.

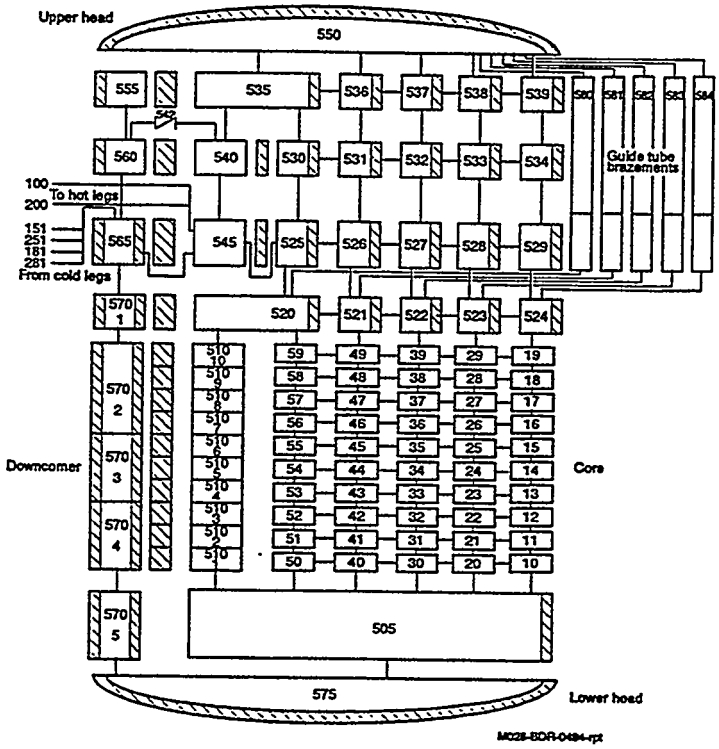

Figure 1: RELAP5 nodalization of the reactor vessel and core.

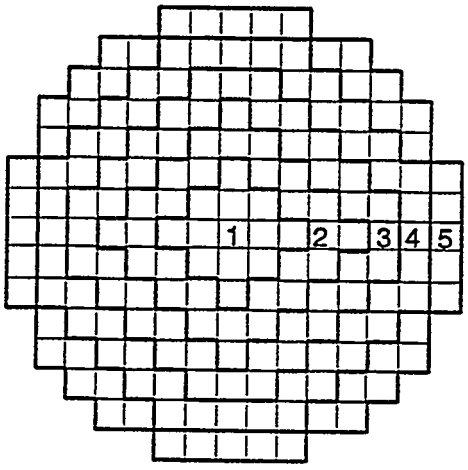

Region	Radial Peaking Factor
1	1.245
2	1.136
3	1.074
4	1.061
5	0.733

M028-BDR-0494-001

Figure 2. Cross-section of core showing fuel assembly grouping and radial peaking factors.

Table 1. TMI-2 axial power peaking factors.

Distance From Bottom of Fuel (m)	Power Factor				
	Region 1	Region 2	Region 3	Region 4	Region 5
0.183	0.665	0.674	0.729	0.690	0.670
0.549	0.933	0.919	0.962	0.951	0.944
0.914	1.134	1.099	1.112	1.132	1.145
1.280	1.216	1.164	1.112	1.168	1.213
1.646	1.248	1.202	1.138	1.192	1.238
2.012	1.262	1.221	1.153	1.206	1.248
2.377	1.225	1.232	1.251	1.241	1.222
2.743	1.078	1.124	1.174	1.131	1.083
3.109	0.792	0.853	0.880	0.834	0.794
3.475	0.448	0.512	0.488	0.455	0.442

One SCDAP fuel rod component is used to represent all the fuel rods in each core region. One SCDAP control rod component is used to represent all the full- and part-length control rods, all the guide tubes (including those containing burnable poison rods), and all the instrument tubes in each core region (except region five which contains no control rods).[a] The control rod radii in regions one through four have been adjusted so that the total mass of Zircaloy, Ag-In-Cd absorber, and stainless steel is conserved (the burnable poison mass is neglected). In core region five, a dummy fuel rod component is used to represent all the guide and instrument tubes. By specifying a small fuel diameter and zero power, this component essentially behaves as a hollow Zircaloy tube. The SCDAP grid spacer model is used to represent the eight Inconel spacer grids that are uniformly distributed along the length of each fuel assembly.

Much of the SCDAP input data was obtained from Reference 9 and is summarized in Table 2. Table 3 lists the total number of fuel assemblies, fuel rods, control rods, burnable poison rods, and orifice rods in each core region.

2.4. Initial Conditions

Table 4 compares the initial conditions in the SCDAP/RELAP5 model to those recommended in the TMI-2 data base.[b] With the exception of steam generator pressures and temperatures, the calculated (or specified) initial conditions are in good agreement with the data base. For steady-state calculations, a control system is used in the SCDAP/RELAP5 model to automatically adjust steam generator pressures (by varying the flow areas of the main steam valves) until user-specified cold leg temperatures are obtained. For simplicity, the target coolant temperature for all four

a. Component models specifically for burnable poison rods and instrument tubes have not been developed for SCDAP/RELAP5.

b. All initial conditions correspond to the time of turbine trip: 04:00:37 hours on March 28, 1979.

Table 2. Total fuel assemblies, fuel rods, and control rods in each core region.

Core Regions	Fuel Assemblies	Fuel Rods	Full-Length Control Rods	Part-Length Control Rods	Burnable Poison Rods	Instrument Tubes	Orifice Rods
1	13	2704	144	0	64	13	0
2	28	5824	256	0	192	28	0
3	40	8320	192	128	320	40	0
4	48	9984	384	0	384	48	0
5	48	9984	0		128	48	640
Total	177	36816	976	128	1088	177	640

Table 3. SCDAP input parameters.

Parameter	Value
Fuel Rods	
Active height (m)	3.568
Rod Pitch (m)	1.443×10^{-2}
Cladding inner radius (m)	4.788×10^{-3}
Cladding outer radius (m)	5.461×10^{-3}
Fuel pellet radius (m)	4.699×10^{-3}
Fuel density (% T.D.)	92.5
Mass of He fill gas (kg) (estimated)	1.265×10^{-4}
Upper and lower plenum void volume (m^3)	1.490×10^{-5}
Control Rods	
Guide tube inner radius (m)	6.325×10^{-3}
Guide tube outer radius (m)	6.731×10^{-3}
Cladding inner radius (m)	5.055×10^{-3}
Cladding outer radius (m)	5.588×10^{-3}
Absorber radius (m)	5.004×10^{-3}
Instrument Tubes	
Tube inner radius (m)	5.601×10^{-3}
Tube outer radius (m)	6.261×10^{-3}
Grid Spacers	
Grid spacer mass (kg)	0.86
Grid spacer height (m)	3.30×10^{-2}
Grid spacer thickness (m)	5.08×10^{-4}

Table 4. TMI-2 initial conditions at turbine trip.

Parameter	ICBC Data Base	SCDAP/RELAP5
Reactor power (MW)	2700	
Primary system pressure (Mpa)	15.2	15.2
Pressurizer level (m)	5.77	5.76
Pressurizer heater power (MW)	1.39	1.39
Loop A coolant flow (kg/s)	8280	
Loop B coolant flow (kg/s)	8560	
Cold leg temperature 1A (K)	561	565
Cold leg temperature 1B (K)	565	
Cold leg temperature 2A (K)	548	565
Cold leg temperature 2B (K)	565	
Hot leg temperature loop A (K)	592	593
Hot leg temperature loop B (K)	592	593
Makeup flow (kg/s)	5.44	0.0
Letdown flow (kg/s)	4.18	0.0
PORV flow (kg/s)	2.59	0.0
Steam generator A feedwater flow (kg/s)	723	
Steam generator B feedwater flow (kg/s)	717	
Feedwater temperature (K)	513	
Steam generator A pressure (Mpa)	7.31	6.34
Steam generator B pressure (Mpa)	7.24	6.28
Steam generator A steam temperature (K)	586	576
Steam generator B steam temperature (K)	585	582

Table 5. Steam generator initial conditions.

Parameter	Reference 12	SCDAP/RELAP5
Main feedwater temperature (K)	513	
Steam generator A feedwater flow (kg/s)	722	723
Steam generator B feedwater flow (kg/s)	718	717
Steam generator A pressure (Mpa)[a]	6.38	6.34
Steam generator B pressure (Mpa)[a]	6.24	6.28
Steam generator A steam temperature (K)	586	576
Steam generator B steam temperature (K)	586	582
Steam generator A riser level (cm)	526	197
Steam generator B riser level (cm)	538	183
Steam generator A downcomer level (cm)	660	559
Steam generator B downcomer level (cm)	669	543
Steam generator A power (MW)	1346	1332
Steam generator B power (MW)	1339	1378

a. The pressures reported in Reference 12 are average steam line pressures measured 10 to 0.1 min before turbine trip.

cold legs was specified to be 565 K. Table 5 compares the calculated initial conditions on the secondary side of each steam generator to the initial conditions recommended in Reference 10. It is seen that the calculated steam generator pressures are in much better agreement with the Reference 10 than with those presented in Reference 8.[a]

2.5. Boundary Conditions

All boundary conditions, except HPI/makeup flow rates, were obtained from Reference 8. The HPI/makeup flow rate history reported in Reference 11 was adjusted until the time of core uncovery (as inferred from hot leg temperature measurements), the time of initial fuel rod cladding failure (as inferred from containment radiation measurements), and the primary system pressure history were predicted reasonably well.[b]

Calculated steam generator coolant levels, steam generator pressures, and letdown flow rates were compared to Reference 8 data and found to be in good agreement. For transient calculations, a control system is used in the SCDAP/RELAP5 model to automatically add auxiliary feedwater to the steam generators whenever calculated boiler levels are less than levels given in the TMI-2 data base. Core power as a function of time for the first 400 s following reactor scram was estimated using the reactor (point) kinetics and decay heat models in the RELAP5 code. The decay power from 400 s onward was obtained from Reference 12. Figure 3 shows the reactor power versus time curve used in the SCDAP/RELAP5 model.

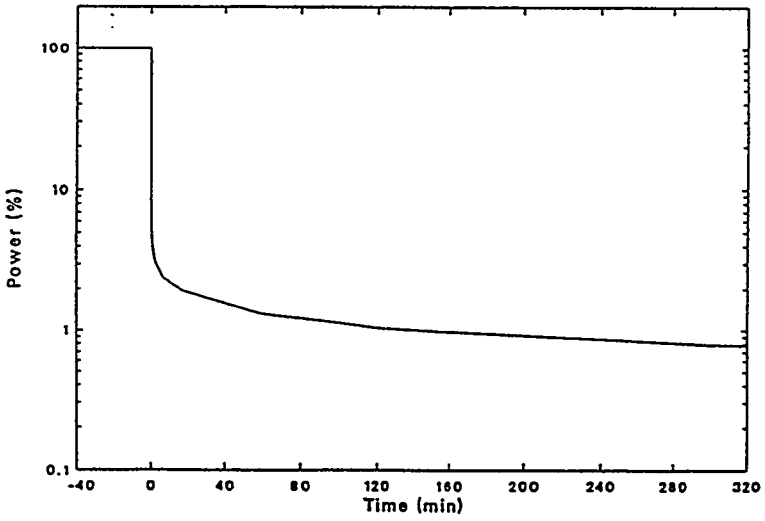

Figure 3. Reactor power versus time curve used for TMI-2 calculation.

---

a. The pressures reported in Reference 13 are average steam line pressures measured 10 to 0.1 min before turbine trip.

b. The HPI/makeup flows were not measured resulting in large uncertainties.[11,13]

3. RESULTS

3.1 Base case best-estimate calculation

This section describes the results of the base case best-estimate analysis.[a] Best-estimate conditions were based on the results of sensitivity studies, discussed in Section 3.2, performed with variations in the makeup flow rates. The best-estimate conditions were selected by comparing predicted system pressure, vessel liquid level, and initial clad failure time with those in the TMI-2 data base and the hypothesized core damage prior to the 2B-pump transient. The makeup flow rates used for the best-estimate calculation are shown in Figure 4. For comparison purposes, the nominal letdown flow, used as the other input flow boundary condition, makeup flow, and calculated flow through the PORV are shown in Figure 5. As shown in this figure, letdown flows were approximately 9 kg/s and the calculated flows through the PORV varied between 10 and 55 kg/s, considerably greater than the makeup flow rates. Calculated flows through the PORV show large spikes associated with system pressure fluctuations prior to the closure of the block valve at 139 minutes.

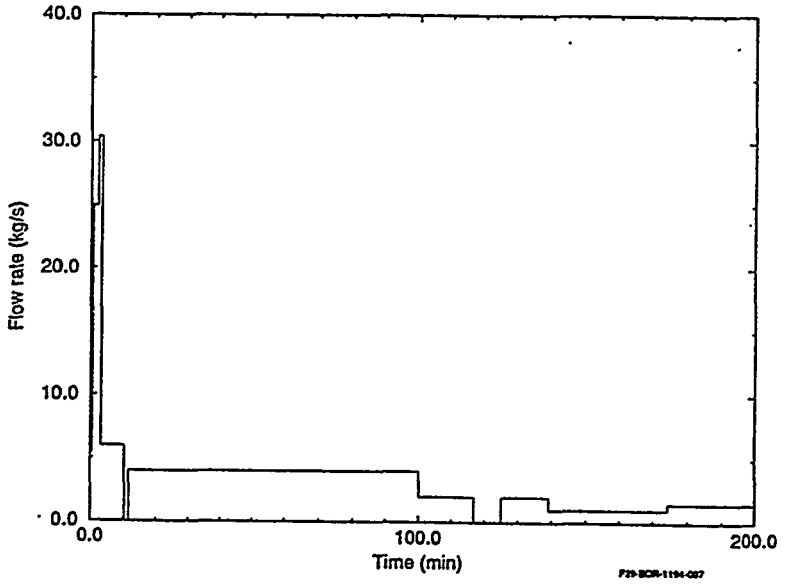

Figure 4. Makeup flow rate used for the best-estimate calculation.

---

a. These results include the correction of an error in the oxidation model identified during the analysis of the results from the sensitivity studies on core liquid level. The error resulted in the suppression of the oxidation in a region that contained relocated material due to the interaction of Inconel spacer grids with fuel rod cladding.

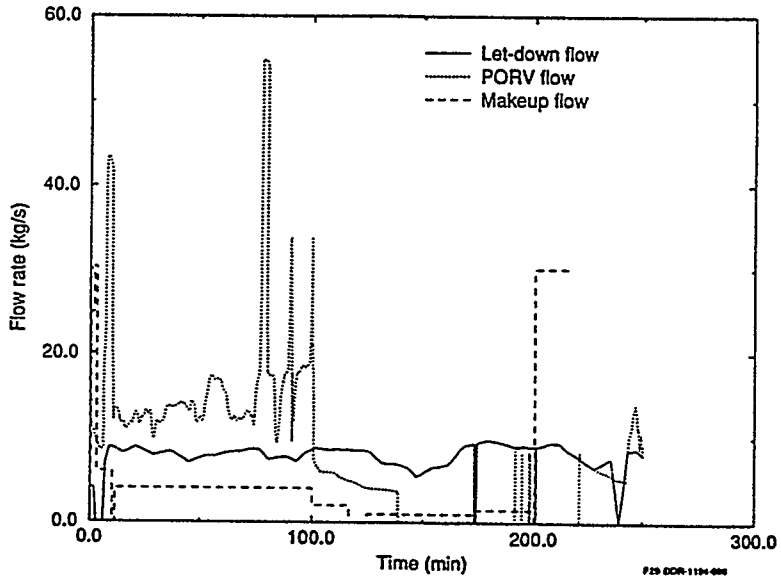

Figure 5. Makeup, letdown, and calculated PORV flows from the best-estimate case.

As shown in Figure 6, the predicted pressure during the core heating and melting prior to the 2B pump transient was significantly less than that measured. As discussed later, this is attributed to the underprediction of oxidation and hydrogen production during this phase of the accident. Figures 7 and 8 show the predicted best-estimate collapsed liquid level, and integral hydrogen production. As shown in Figure 8, hydrogen production is predicted to begin 135 min into the accident with a significant rise in production prior to the 2B pump transient. However, the total amount of hydrogen predicted during the accident is still significantly less than that estimated during the accident. The code predicted 430 kg hydrogen to be produced during the accident. Henrie and Postma estimated the total hydrogen produced during the accident to be 460 kg[14]. This underprediction is consistent with other code-to-data hydrogen production comparisons of bundle reflood tests as noted in References 2 and 3.

It was estimated from containment radiation measurements that the fuel rod cladding began rupturing about 139 minutes into the accident. The best-estimate calculation predicted fuel rod clad ballooning and rupture to occur at 138.7 minutes. A comparison of the best-estimate and hypothesized core damage state at 173 minutes shows that the code predicted the formation of a molten pool and associated flow blockages in relatively good agreement with the hypothesized core damage state. The code also predicted partially oxidized and embrittled fuel rods in the upper core which is consistent with the formation of a loose debris bed late in the accident. Figure 9 shows the hypothesized TMI core damage state prior to the 2B pump transient. The predicted core damage state is shown in Figure 10.

The 2B pump was throttled to inject 30 m^3 of water. Once water started entering the core additional damage was predicted to occur. The molten pool continued heating as did some regions immediately above the pool. As material continued heating it moved downward into the pool, creating voided regions. Rubble beds continued to form above and below the molten pool as cold water contacted embrittled cladding. Small quantities of cohesive debris formed in the outer channels. Although rubble beds were predicted above and below the molten pool and in core region four, the pool was not calculated to slump into the lower plenum since the molten pool did not extend to the outer periphery

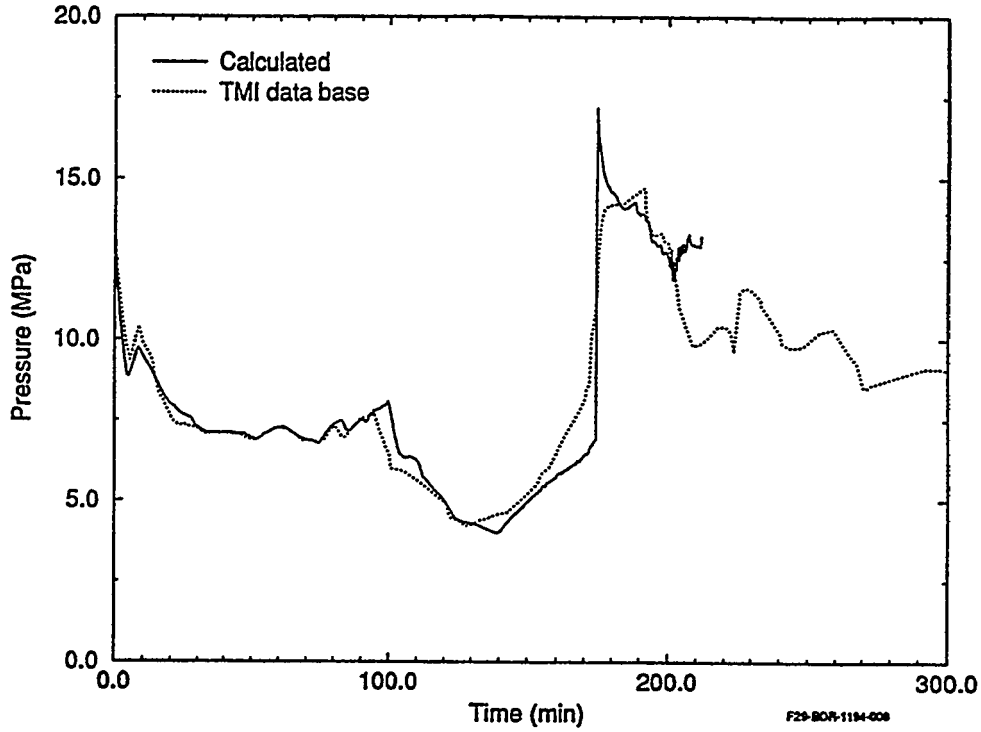

Figure 6. Calculated best-estimate and measured pressures.

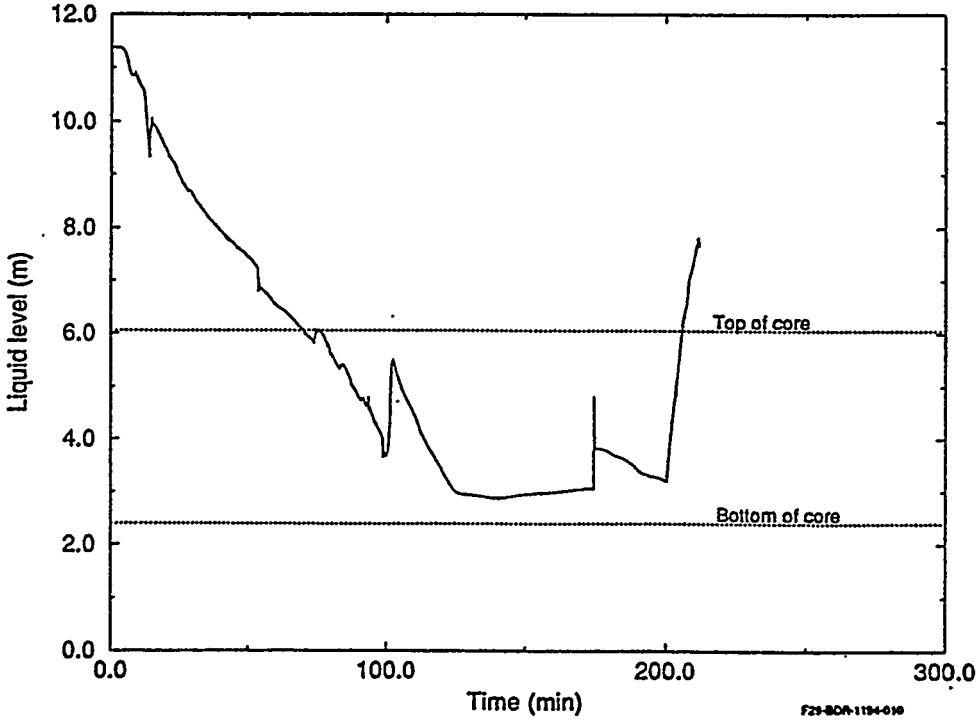

Figure 7. Predicted best-estimate collapsed liquid level.

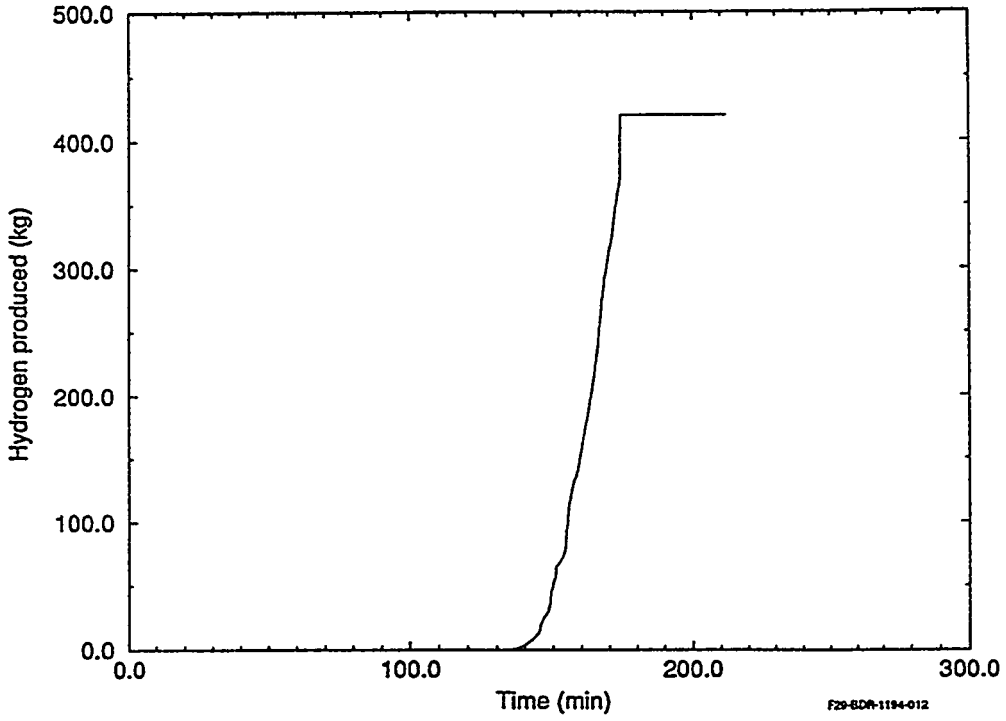

Figure 8. Predicted best-estimate integral hydrogen production.

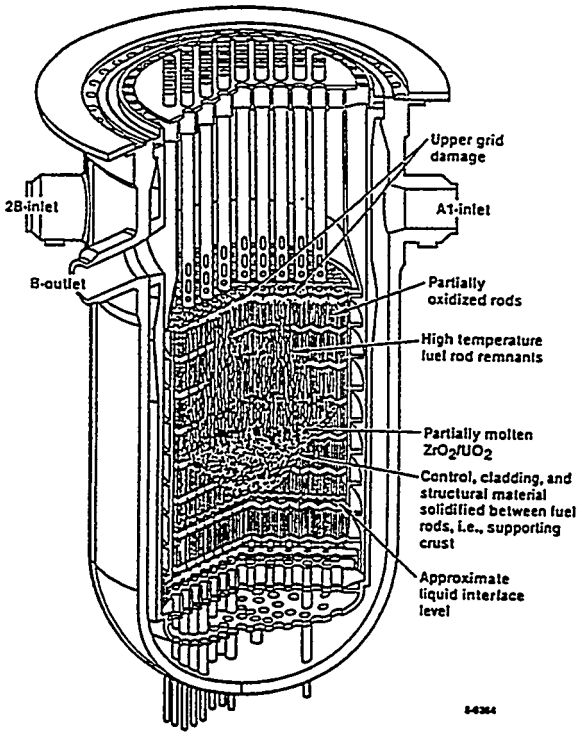

Figure 9. Hypothesized TMI-2 core damage state prior to the 2B pump transient.

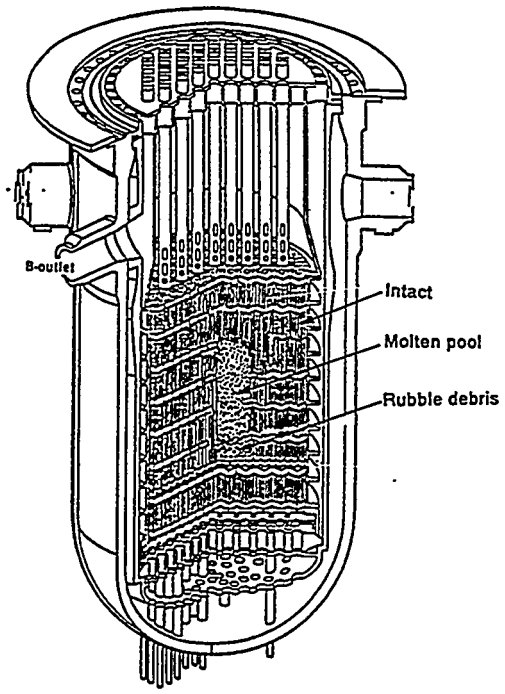

Figure 10. Predicted TMI-2 core damage state prior to the 2B pump transient.

of the core. The calculation was stopped at 226 minutes as the core appeared to have cooled considerably and the formation of additional rubble or relocation of the molten pool to the lower head did not appear imminent. The predicted end state of the reactor core had a smaller void region, and a slightly smaller molten pool. Figure 11 shows the hypothesized end-state of the core after HPI injection. The predicted end-state of the core is shown in Figure 12.

Figures 13 and 14 show the predicted radial temperature profiles of cladding temperatures at two elevations in the core region, 2.19 and 2.56 m. Each elevation was predicted to contain molten material during the TMI-2 accident prior to the 2B pump transient. As shown in the figures a molten pool was predicted to form in the centermost channel prior to the core reflood associated with the restart of the 2B pump when the predicted temperatures reached 2873 K. Also, the figures show channels 2 and 3 reaching temperatures in excess of the eutectic melting point for UO_2 and ZrO_2, 2600 K, and the two peripheral channels reaching temperatures near 2800 K with the production of superheated steam in conjunction with the core reflood during the 2B pump transient.

The predicted peak temperatures in the outer channels are important since complete blockage of the channels and the formation of a molten pool is not predicted to occur until a temperature of 2870 K is reached.[a] As described in Reference 2, the maintenance of coolable geometries in a reactor core to temperatures in excess of 2870 K has been observed in a number of severe accident experiments. Consequently even though extensive melting and loss of geometry in the outer channels was predicted to occur, the assemblies in these channels were predicted to remain coolable. As shown in Figures 13 and 14 the temperatures drop sharply to near 1200 K in channels 2 through 5 immediately after the restart of the 2B pump. However temperatures in the

---

a. As described in Reference 2, the maintenance of coolable geometries to temperatures in excess of 2870 K has been observed in a number of experiments. This temperature is the lowest melting point of a mixture of UO_2 and ZrO_2.

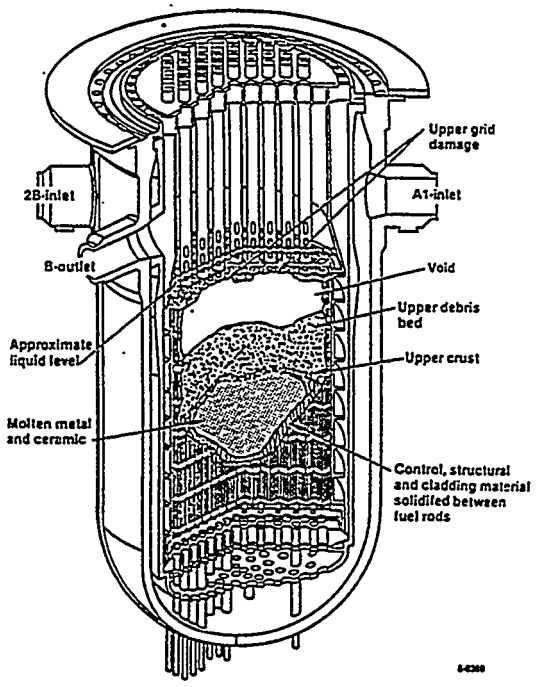

Figure 11. Hypothesized end-state of the TMI-2 core.

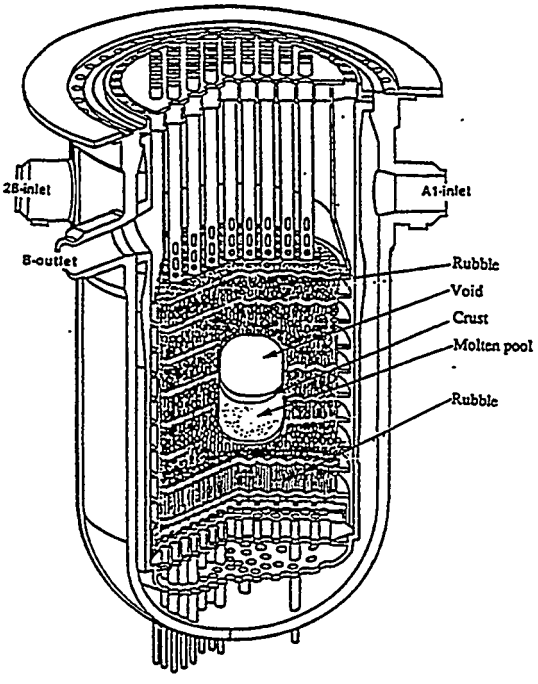

Figure 12. Predicted end-state of the TMI-2 core.

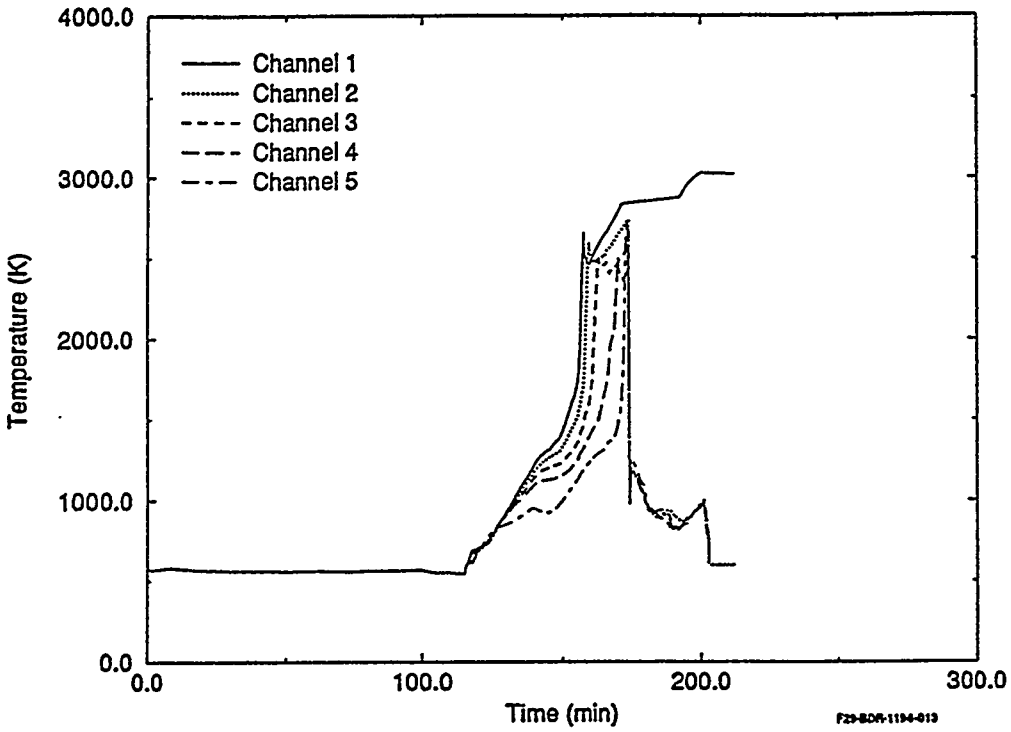

Figure 13. Predicted radial temperature profile at the 2.19 m elevation.

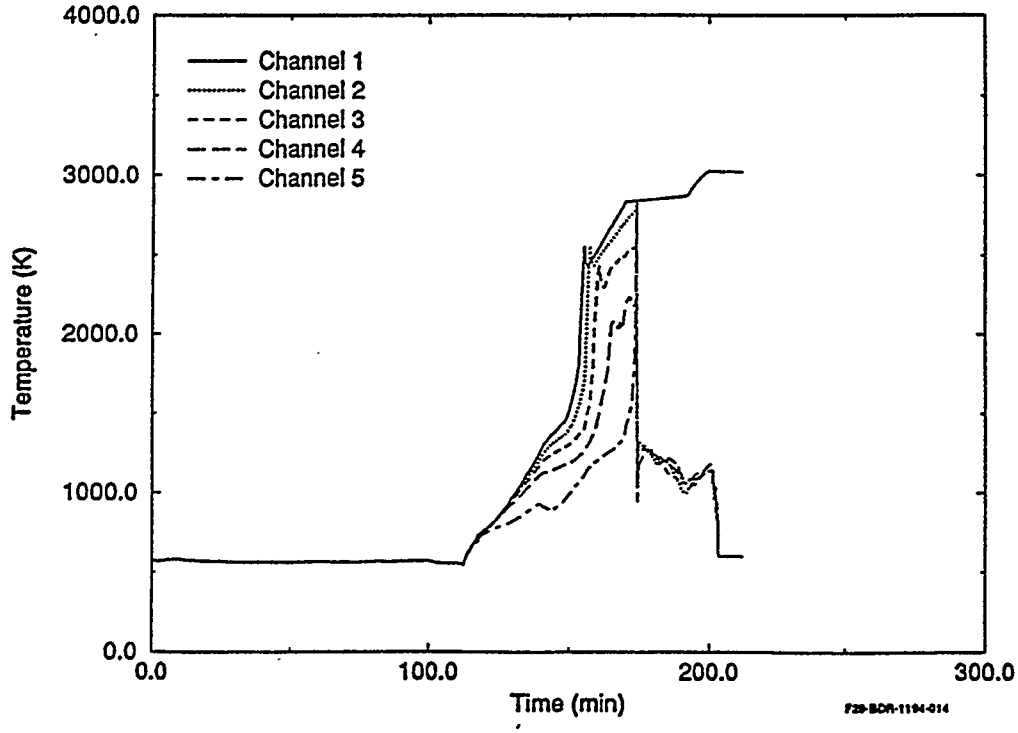

Figure 14. Predicted radial temperature profile at the 2.56 m elevation.

central core regions containing molten ceramic material remained high since these regions were not immediately coolable. The code predicted the formation of metallic melts in all core channels along with the melting and relocation of grid spacer and control material between 1250 and 1500 K, as indicated by the change in heating rate in this temperature range. Molten control and grid spacer materials are predicted to relocate to the bottom of the reactor vessel and solidify in the water at the bottom of the vessel.

3.2 Influence of Makeup Flow

Table 6 summarizes the different makeup flow rates used for this sensitivity study. Tables 7 through 9 summarize the damage progression at three different stages of the TMI-2 accident, namely at a time prior to the 2B pump transient, after the 2B pump transient, and after sustained HPI injection began. As shown in these tables, a small change in makeup flow can influence core damage dramatically. Case 1, where 4 kg/s makeup was allowed to flow into the core from 139 to 200.2 minutes, showed the least core damage. A small fraction, 5%, of the core was predicted to be in a damaged state prior to the 2B pump transient. After the 2B pump was restarted, some additional fragmentation of embrittled cladding occurred increasing the total core damage to nearly 12 percent and total hydrogen production by approximately 50 kg to 142 kg. The other 5 cases showed initial core damage prior to the 2B pump transient ranging from 9 to 14 percent of the core, with a molten pool size varying from 2 percent of the core, for case 2, to 14 percent for case 5. Cases 2 and 6 showed no predicted increase in the size of the molten pool during the 2B pump transient and sustained HPI injection, whereas cases 4 and 5 showed pool growth during the 2B pump transient. The size of the molten pool increased slightly during the 2B pump transient for case 4 and from 13 to 16 percent of the core for case 5. All cases, except case 5, showed increased hydrogen production during the 2B pump transient and no increase during sustained HPI injection. Case 5 showed increase hydrogen production during both the 2B pump transient and HPI injection. During sustained HPI injection,

Table 6 Summary of variation in makeup flow

Case No.	Time(min)	Flow rates(kg/s)
1	100-139	3.0
	139-200.2	4.0
2	100-139	3.0
	139-200.2	2.0
3	100-139	3.0
	139-200.2	0.0
4	100-122.3	3.0
	122.3-200.2	0.0
5	100-116.7	2.0
	116.7-125	0.0
	125-174	1.0
	174-200.2	1.5
6	100-116.7	2.0
	116.7-125	0.0
	125-200.2	2.0

Table 7. Core damage prior to the 2B pump transient

Case Number	Extent of Core Damaged (%)	Extent of Core Molten (%)	Hydrogen Produced (Kg)
1	5	0	93
2	13	2	227
3	12	7	321
4	10	8	353
5	14	9	300
6	9	6	297

Table 8. Core damage after the 2B pump transient

Case Number	Extent of Core Damaged (%)	Extent of Core Molten (%)	Hydrogen Produced (Kg)
1	12	0	142
2	21	2	240
3	12	7	365
4	11	8	395
5	17	9	362
6	12	6	348

Table 9. Core damage after sustained HPI injection

Case Number	Extent of Core Damaged (%)	Extent of Core Molten (%)	Hydrogen Produced* (Kg)
1	15	0	142
2	26	2	240
3	17	7	365
4	32	8	395
5	30	9	375
6	52	6	348

*Total estimated hydrogen production was 460 kg.

additional fragmentation of embrittled cladding occurred. Cases 2 through 5 showed considerable differences in core damage during the sustained HPI injection phase of the accident.

Figure 15 compares the calculated system pressure for all cases with the measured system pressure, while Figures 16 through 18 show the calculated collapsed liquid level, maximum core temperature, and total hydrogen produced for each case. As shown in Figure 15, the predicted system pressure is consistently less than measured during core heatup and melting. Figure 16 shows the predicted collapsed liquid level for each sensitivity case. Predicted liquid level reflects the quantity water entering the core as makeup prior to the 2B pump transient. For each case, except case 1, less than 1 m of water was predicted to be in the core prior to the restart of the 2B pump and water level was predicted to increase to slightly more than 2 m prior to sustained HPI injection. For all cases, water filled the core to the bottom of the hot legs after sustained HPI injection. The maximum core temperature for all cases, Figure 17, shows clearly the effect of variation in makeup flow on the formation of a molten pool. The formation of a molten pool, shown by the leveling of temperature near 2850 K, occurs at different times during the accident for each case. Case 1 shows temperature spikes but gives no indication of a molten pool forming in the core region. As shown in Figure 18, cases 5 and 6 show similar hydrogen production behavior up to and through the 2B pump transient, with case 6 predicting the production of approximately 18 kg more during the 2B pump transient. The code predicted an additional 45 kg hydrogen to be produced during sustained HPI injection for case 5 and no additional hydrogen production for case 6. As shown in the tables, a small change in the quantity of water entering the core during the accident causes large differences in core damage, pressure response, and predicted collapsed liquid level in the reactor vessel.

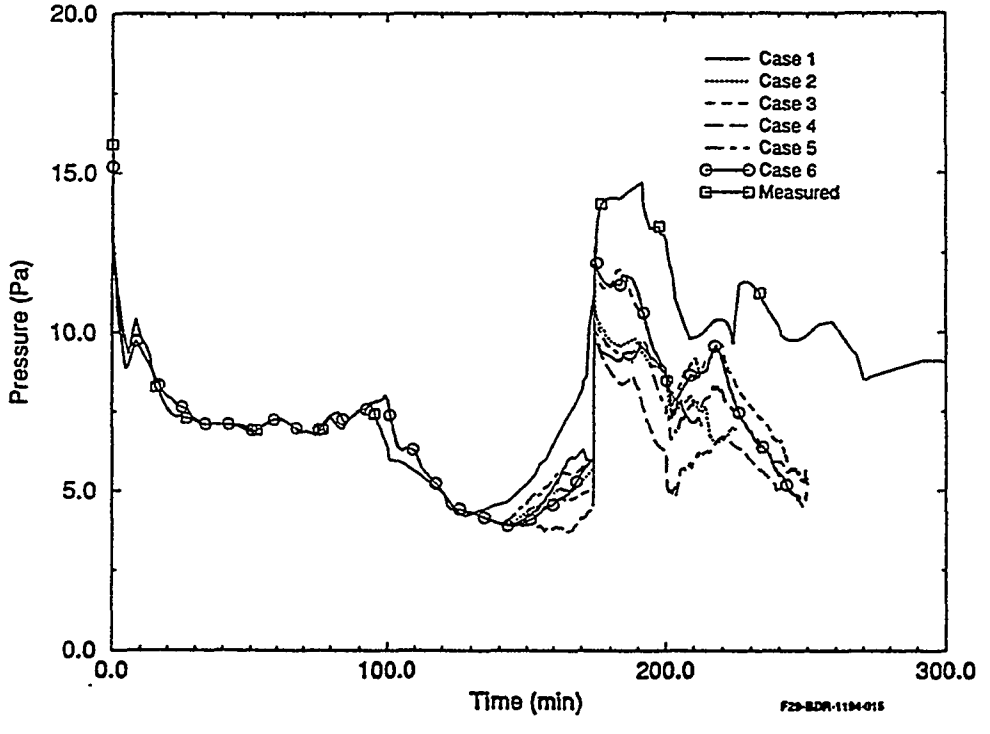

Figure 15. Calculated system pressure from sensitivity study.

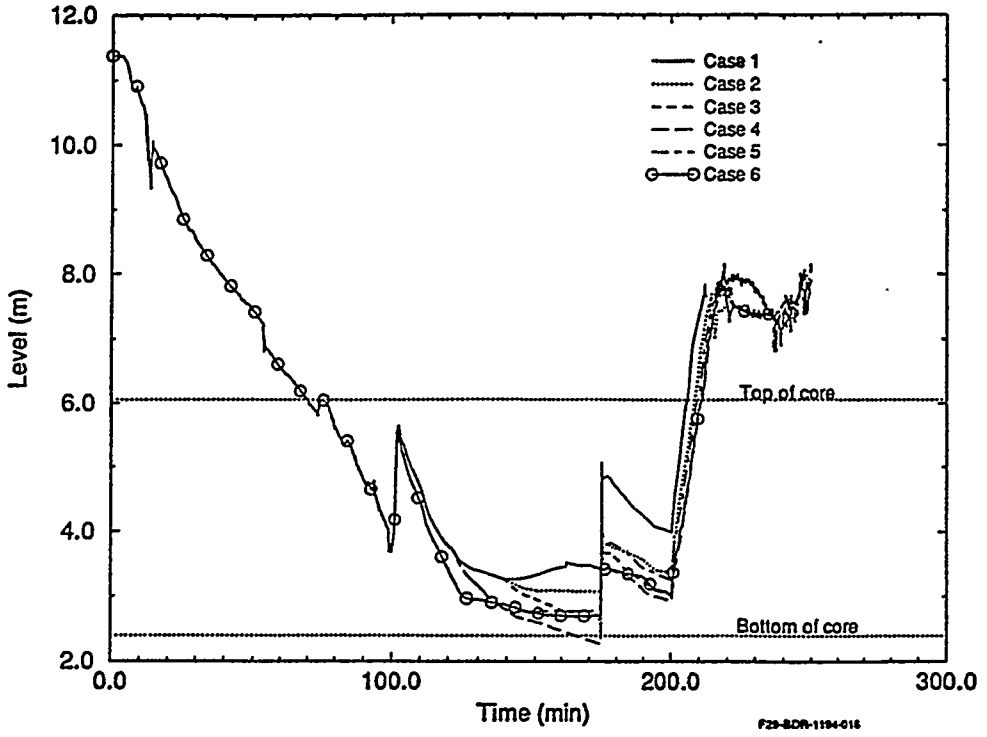

Figure 16. Calculated collapsed liquid level from sensitivity study.

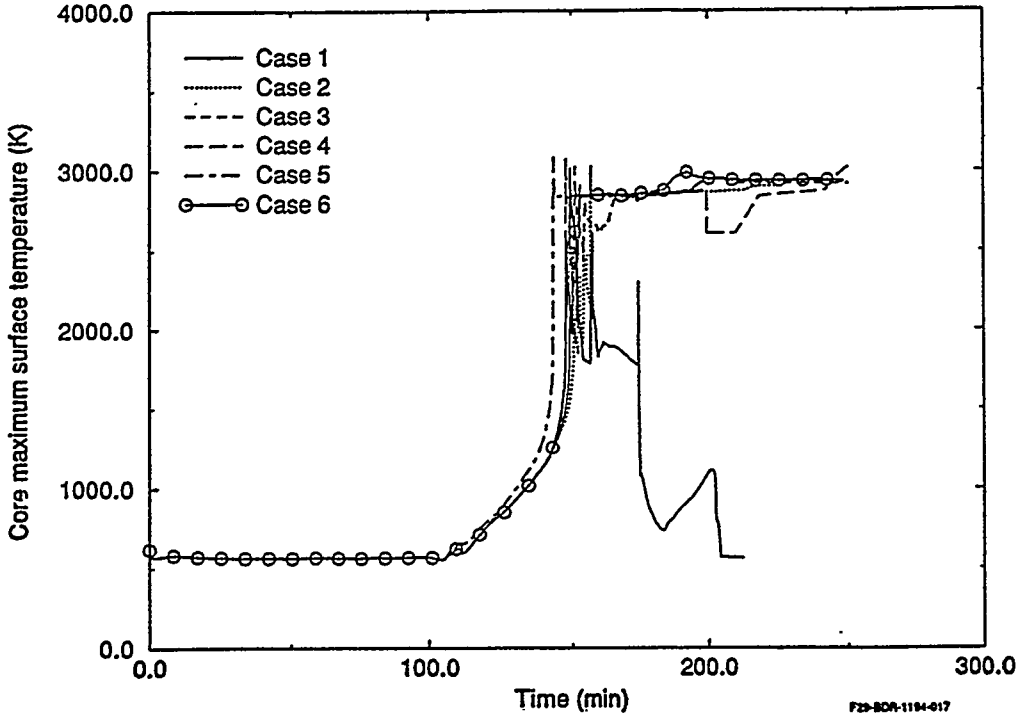

Figure 17. Calculated maximum core temperatures from sensitivity study.

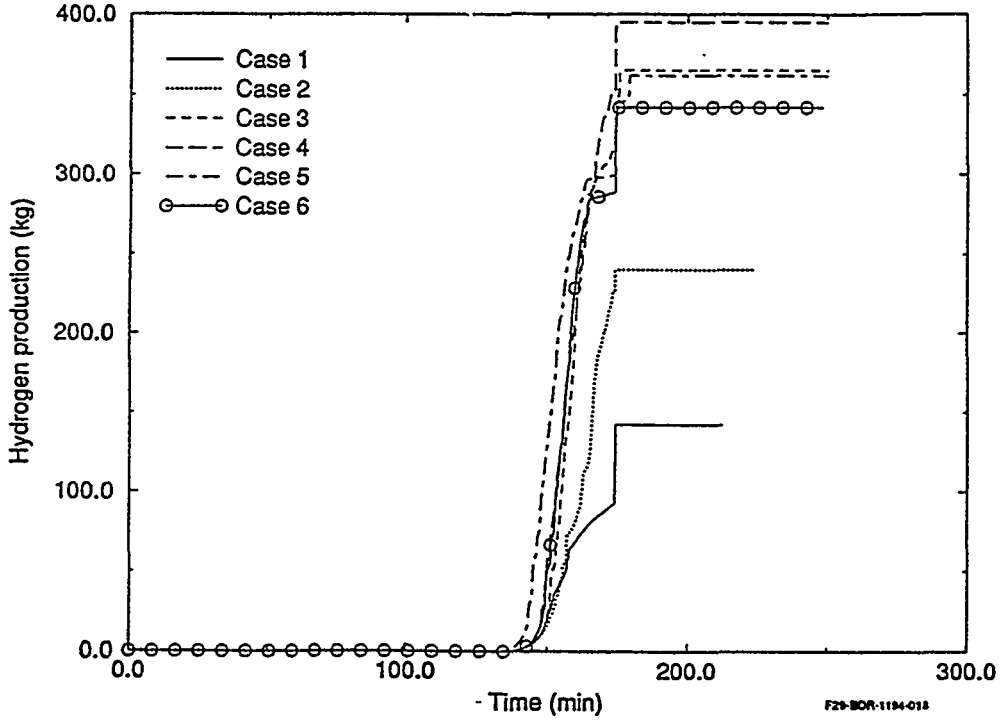

Figure 18. Integral hydrogen production from sensitivity study.

4. CONCLUSIONS

SCDAP/RELAP5/MOD3.1 clearly cannot predict the major events occurring in the TMI-2 accident following the 2B-pump transient. Even though the uncertainties in the system thermal hydraulics boundary conditions are very large, these uncertainties do not appear to be a significant factor in the later stages of the accident. The most obvious deficiency in the predictions following the 2B pump transient is that the radial extent of the blockage and resulting molten pool is significantly underpredicted. As a consequence, the molten pool and core remains in a coolable geometry. When the core is reflooded, the molten ceramic remains within the core and eventually cools.

Although all of the factors leading to the underprediction of the radial spreading of the molten pool are not yet known, two main factors seem to be the dominant contributors;

1. The systematic underprediction of the oxidation, and resulting heat generation, during the initial melting and relocation of core material prior to and during the 2B-pump transient. - There are two direct indications of the underprediction of the oxidation heat generation. First the total predicted hydrogen production is 90% or less than that estimated for the accident; Second, the system pressure response during this period is systematically underpredicted. Although system pressure is a function of the heat removed from the system, it is also directly related to the hydrogen generation rate. The underprediction of oxidation and hydrogen production for this period is also consistent with the results from the MOD3.1 developmental assessment using data from reflood experiments such as CORA-13 and PBF SFD-ST.

2. The enhanced cooling of the outer assemblies during the initial heating and melting phase of the central portion of the core - Even though the outer assemblies reached temperatures near the ceramic melting point,

their heating rates were slowed because of the diversion of steam from the center assemblies to the outer assemblies as damage in the centermost portions of the core grew more severe. The possible overprediction of the flow diversion associated with the initial stages of damage, such as fuel rod ballooning and the metallic melt relocation, is also consistent with the results of the MOD3.1 assessment where the flow diversion in the LOFT LP-FP-2 experiment was overpredicted. This enhanced cooling, in conjunction with the assumption that complete blockage of the outer assemblies will not occur until the ceramic melting point is reached, means that the outer assemblies did not become blocked during this period of the accident. As a result, these assemblies were relatively quickly cooled when the core was reflooded. Therefore, it was not possible for the molten pool to continue to grow out to the outer periphery of the core.

Even though MOD3.1 did not predict the relocation of melt into the lower plenum while earlier version of the code did, MOD3.1 did not predict slumping of the molten pool for the right reasons, while earlier versions predicted slumping for the wrong reasons. In earlier versions of the code, the core was predicted to block off as the result of metallic melt relocation and then the molten pool slumped because the metallic layer under the molten pool started to thin. Both of these earlier assumptions are clearly at odds with the experimental evidence that we now have.

5. REFERENCES

1. C. M. Allison et al., SCDAP/RELAP5/MOD3.1 Code Manual, Volumes I-III, NUREG/CR-6150, EGG-2720, October 1993.

2. SCDAP/RELAP5/MOD3.1 Code Manual Volume V: Developmental Assessment, NUREG/CR-6150, EGG-2720, December, 1993.

3. C. M. Allison et al., "SCDAP/RELAP5/MOD3.1 Code Development and Assessment," Proceedings of the 21st Water Reactor Safety Meeting, NUREG/CP-0133, Vol. 2, April 1994.

4. D. F. Guessing, "The Three Mile Island Analysis Exercise," Nuclear Technology, 87, August 1989, pp. 298-301.

5. J. M. Broughton, P. Kuan, D. A. Petti, and E. L. Tolman, "A Scenario of the Three Mile Island Unit 2 Accident," Nuclear Technology, 87, August 1989, pp. 34-53.

6. J. R. Wolf et al., TMI-2 Vessel Investigation Project Integration Report, NUREG/CR-6197, TMI V(93)EG10, EGG-2734, March 1994.

7. D. A. Brownson, L. N. Haney, and N. D. Chien, Intentional Depressurization Accident Management Strategy for Pressurized Water Reactors, NUREG/CR-5837, EGG-2688, April 1993.

8. R. W. Brower, L. J. Fackrell, D. W. Golden, M. L. Harris, and C. L. Olaveson, ICBC Version 3.1, TMI-2 Initial and Boundary Conditions Data Base, GEND-INF-078, January 1988.

9. D. Coleman, "As-Built Design and Material Characteristics of the TMI-2 Core," Part III in TMI-2 Accident Core Heat-Up Analysis, A Supplement, NSAC-25, June 1981.

10. J. L. Anderson, TMI-2 Once Through Steam Generator Secondary Level Analysis, EGG-TMI-7359, January 1987.

11. J. L. Anderson, Recommended HPI Rates for the TMI-2 Analysis Exercise (0-300 Minutes), EGG-TMI-7833, September 1987.

12. T. R. England and W. B. Wilson, TMI-2 Decay Power: LASL Fission-Product and Actinide Decay Power Calculations for the President's Commission on the Accident at Three Mile Island, LA-8041-MS, Revised, March 1980.

13. D.W.Golden and N. Ohnishi, SCDAP/RELAP5 Demonstration Calculation of the TMI-2 Accident, EGG-TMI-8473, March 1989.

14. J. O. Henrie and A. K. Postma, Lessons Learned from Hydrogen Generation and Burning During the TMI-2 Event, GEND-061, May 1987.

Simulation of BWR Core Meltdown Accidents using the APRIL and MAAP Computer Codes

M.Z. Podowski and W. Luo
Department of Nuclear Engineering
and Engineering Physics
Rensselaer Polytechnic Institute
Troy, NY 12180-3590

R. F. Kirchner
Niagara Mohawk Power Co.
301 Plainfield Road
Syracuse, NY 13212

ABSTRACT

The objective of the present work was to analyze the progression and consequences of hypothetical severe accidents in a reference BWR power plant using the APRIL and MAAP severe accident computer codes. The APRIL-based numerical simulations of various accident scenarios were conducted at RPI and their results were compared against similar calculations performed at Niagara Mohawk Power Company (NMPC) using MAAP. The observed differences in the predictions by these two codes, as well as the results of parametric studies using APRIL, have been analyzed and used to assess the uncertainties in BWR severe accident predictions. The comparison between the APRIL and MAAP codes has revealed that whereas these two codes produce similar long-term results in most cases analyzed, several significant differences have also been observed in the predicted timing of specific events and the values of selected parameters governing accident progression.

I. INTRODUCTION

In recent years, both experimental and theoretical studies have contributed to the development of severe accident computer codes. However, the complexity of the phenomena being modeled and the random character of events such as the reactor core meltdown and melt relocation, do not allow for eliminating various uncertainties in the results of calculations and tracking the melting progression in a precise manner using deterministic models. One way to improve the understanding of the reasons behind those uncertainties, to identify, and possibly develop methods of reducing, their major sources, is to perform comparative studies using different computer codes for the same accident scenarios in a given nuclear power plant. Although limited studies of this kind were undertaken in the past, the existing results [1, 2] clearly indicate the potential benefits for future individual plant examinations.

The objective of the present work was to analyze the progression and consequences of hypothetical severe accidents in a reference BWR power plant using the APRIL and MAAP severe accident computer codes. This objective has been accomplished by conducting at RPI the APRIL-based numerical simulations of various accident scenarios and comparing the results against similar calculations performed at Niagara Mohawk Power Company (NMPC) using MAAP.

II. OVERVIEW OF THE APRIL AND MAAP CODES

APRIL (Accident Progression and Radioactive Isotope Location) is a computer code [3-7] developed at Rensselaer Polytechnic Institute under the sponsorship of Oak Ridge National Laboratory and Empire State Electric Energy Research Corporation (ESEERCO). Some of the features of the APRIL code which make this code a useful tool for the present analysis are:

- APRIL has been developed especially for BWRs. It contains mechanistic models of several severe accident phenomena, such as: gradual relocation of molten materials and their refreezing in contact with cold structures, channel blockage and crust remelting, heatup and possible failure of the lower core plate, steam separator/dryer, and reactor pressure vessel.
- Several models in the APRIL code have been validated against detailed experimental data [8-11], including those taken at Rensselaer and elsewhere. In particular, the comparisons against the SANDIA DF-4 and CORA BWR-series experiments have shown good agreement between the APRIL predictions and the experimental results.
- Extensive testing of APRIL on various computers have been performed, including: VAX 750, 386/486-PC, RS/6000, IBM-3090, and CRAY.
- APRIL is a fast running code. For example, on a RS/6000 (model 320) computer the CPU time is comparable to, or faster than, the real time (a similar estimate applies to 486-PC). This feature is very useful when a parametric analysis is to be performed for various user-specified parameters and different accident conditions.

The MAAP code has been developed by the Industry Degraded Core Rulemaking Program for simulating core and containment conditions during a severe accident. MAPP models core heatup and degradation, reactor pressure vessel (RPV) failure, containment response and fission product behavior. Details concerning the MAAP modeling and code structure can be found in this code's user's manual [12].

Several differences can be noticed in the modeling concepts used in the APRIL and MAAP codes. Examples include: the evaluation of the fuel melting temperature, and the model of melt relocation. It is assumed in MAAP that the core materials (including fuel pellets) melt at a fixed temperature (4040F in the present study). This temperature is between the melting temperature of Zircaloy (3365F) and UO2 (4960F in the APRIL calculations), and reflects in a simplified form the effect of Zircaloy-UO2 eutectics formation. On the other hand, APRIL models separately the melting of individual core materials, such as stainless steel (control rods), Zircaloy (cladding and canister walls) and UO2. The eutectic reaction between Zircaloy and UO2 is accounted for using a quasi-binary phase diagram. Concerning the melt relocation phenomena, MAAP assumes that in order for the core materials to relocate and move into the lower plenum, one of the lowest code nodes must be completely molten. APRIL uses mechanistic models to evaluate the gradual melting, melt relocation, and refreezing of the various core materials, both inside the core and on the lower core plate. Melt release to the lower plenum occurs in APRIL as a result of (local) failure of the lower core plate. The molten debris includes both the core materials and, possibly, the molten steel from the upper vessel structures. The melting and heatup of these structures, i.e. the upper shroud, stand pipes and the steam separator/dryer complex are explicitly modeled in the APRIL code.

III. SITUATIONS ANALYZED

The purpose of the present work was two-fold. First, the effects of uncertainties in selected physical parameters and modeling assumptions have been studied with the APRIL code. This study has been performed using a short-term station blackout as a reference accident scenario. Next, a comparative analysis has been performed between the APRIL and MAAP predictions for four different accident scenarios. A detailed discussion of all the cases studied is given below, including a description of the individual scenarios, the results of simulations and their analysis.

III.1. The APRIL-based Analysis of Short-Term Station Blackout

The station blackout accident analyzed here includes both loss of offsite power as an initiating event and the loss of emergency AC power. In the analysis, it is assumed that the station blackout is due to equipment failures at the emergency buses or 115 KV supplies, and the situation is not recoverable. Similarly, the emergency diesels are not recoverable. Thus, all coolant injection systems fail to supply emergency cooling to the reactor. The operators will attempt to establish effective reactor vessel injection; nevertheless, by the definition of this accident sequence, these efforts will fail. Without reactor vessel injection, the vessel water level cannot be maintained above the top of the core. With the core partially uncovered and the vessel water level decreased to the top of active fuel (TAF), the operator is supposed to manually open the ADS (Automatic Depressurization System) valves to depressurize the reactor pressure vessel. This action provides flashing of water in the core region and in the lower plenum, and also provides desired temporary cooling for the uncovered region of the core.

The emergency depressurization causes all the water in the core region and, partially, the water in the lower plenum, to be flashed. At the end of the depressurization, the vessel water level falls below the lower core plate, and into the lower plenum. Thereafter, the remaining water inventory will be confined to the lower plenum, the core will be completely uncovered and start heating up. If the operator fails to open the ADS valves to depressurize the reactor pressure vessel, the vessel water level will continue to decrease to very low levels until the core is completely uncovered. Thereafter, the accident sequence proceeds into a severe core damage phase during which the molten materials released from the core are discharged into the lower plenum. This leads to steam evaporation in the lower plenum and failure of the reactor pressure vessel.

The main purpose of this series of tests was to demonstrate the consistency of APRIL calculations by parametrically varying selected parameters and/or modeling assumptions in the numerical simulations of a hypothetical station blackout accident. The reference accident scenario (denoted as Case-1) is described in Table 1. In addition, parametric calculations were performed, in which the effects of selected input parameters on the accident progression were quantified. Specifically, Cases-2 and 3 address the fact (observed, among others, in the CORA-series experiments) that the UO2-Zr eutectic reaction decreases the melting temperatures of both UO2 and Zircaloy during the fuel damage phase.

Accident Progression for the Reference Case (Case-1)

The sequence of the main events as calculated by APRIL is shown in Table 2. The station blackout accident causes loss of feedwater to the reactor vessel, and the reactor system pressure to rise rapidly to SRV setpoint. The SRVs open in response to a higher reactor vessel pressure.

Since feedwater flow has stopped, the reduction in water inventory thereafter causes the RPV

Table 1: Descriptions of Input Conditions for Station Blackout Accident Analysis (Case-1)

No.	Input Description
1	Loss of all ECCS injection
2	No ADS valve opening
3	No CRD flow
4	Reactor core power is only due to decay heat
5	Nuclear fuel (UO2) melting temperature is 4960 F
6	The Zircaloy melting temperature is 3365 F
7	Time step for the reactor core thermal-hydraulic calculation is 1 second
8	The reactor core is divided into 5 radial zones with equal volume in each zone, and 10 axial nodes of equal length in each zone
9	Local failure of the vessel lower head is due to the drain plug meltdown

water level to drop. The downcomer water level shortly reaches the HPCS and RCIC setpoints as a result of steam evaporation in the core due to the decay power generation. However, because of the loss of station power, no ECCS water is injected into the reactor vessel. Thus, the water level in the core/riser region begins to decrease. Eventually, the downcomer water level drops to the ADS setpoint. However, due to the nature of this accident and the assumption of no manual actuation of ADS by the operator, the ADS cannot be opened to depressurize the reactor system.

The reactor heat-up starts immediately after the core water level drops below the top of active fuel (TAF). The Zircaloy oxidation, together with increasing cladding temperature, rapidly weaken the mechanical properties of the cladding tubes. When the calculated stress reaches the allowable stress limit, cladding rupture is assumed to occur. Cladding failure results in the release of gaseous fission products, and makes the internal gap between the fuel pellets and the cladding accessible for steam. After Zircaloy melting the molten cladding, exposed to steam, will undergo a rapid oxidation and produce additional heat. A part of the molten Zircaloy may form Zr-UO2 eutectic mixture. When a substantial amount of Zircaloy is oxidized or melted in any node, the nodal section of cladding may not be able to support the weight of the materials in all nodes located above. As a result, the node may collapse, forming a localized rubble bed. Thereafter, the node height diminishes and causes a relocation of all the nodes above. Eventually, the molten material may release to the lower core plate, or may cool down and freeze, forming a partial channel blockage.

As a result of heating by the combined decay power and the exothermal reaction of Zircaloy oxidation, the APRIL code predicts the hottest fuel element to reach the UO2 melting temperature at approximately 84 min. from the beginning of core uncovering. As core melting is in progress, the molten materials released from the degraded core will eventually reach the lower core plate.

The predicted time of molten materials being dropped into the lower core plate is about 116 min. In APRIL, the lower core plate is treated as a combination of the fuel support unit and the plate unit, and the code calculates the gradual delivery of molten materials from the core onto the lower core plate complex. The molten materials may lose most of their heat in contact with the highly subcooled plate. The failure of the plate is assumed to be due to the total tensile stress exceeding the temperature-dependent ultimate tensile strength of the plate; this local plate failure mechanism may occur prior to plate melt-through. The predicted time of lower core plate failure is about 164 min.

Following the failure of the lower core plate, the molten materials are released into the lower plenum which contains water. The accumulated mass released from the core to the lower plenum is illustrated in Fig.1. The molten corium first comes in contact with the upper parts of the CRD tubes and the instrument guide tubes. Subsequently, it may collect on the lower head of the reactor pressure vessel. There, the corium may interact with the lower head itself.

The molten corium in the lower plenum may partially solidify and, at the same time, heat up the solid steel structures. Excessive heating and melting of these structures may lead to a loss of vessel integrity and discharge of water and melt from the lower plenum to the drywell of the reactor containment. The actual sequence of events depends on the history of core meltdown, the melt release to the lower plenum, and the progression of solid structure melting in the lower plenum.

The molten corium released from the core transfers some of its heat to the remaining water in the lower plenum. Consequently, any water in the lower plenum serves as a heat sink for the molten debris, preventing, or delaying, the process of lower head melting and failure. At the same time, a substantial amount of steam can be produced to reduce the inventory of water in the lower plenum, and cause rapid oxidation of the remaining metallic Zircaloy in the core. Fig. 2 shows that the mass of water in the lower plenum begins to decrease immediately after the molten corium is delivered from the core.

It is assumed in the APRIL model that early failure of the lower plenum is due to either the failure of the drain plug or of the CRD tubes. The drain plug is a thin tube, about 0.25 inch thick, located at the center of the lower head. It can easily heat up and melt in contact with the hot molten corium. It is also assumed that the CRD tube failure occurs if the tube wall outside the vessel completely melts. The following three criteria are used for the drain plug failure:

(1) the total stress exceeds the ultimate tensile strength of the tube prior to complete debris solidification in the drain plug, or
(2) all debris is solidified and the drain plug wall is melted-through, or
(3) the total stress imposed on the crust-filled drain plug exceeds the ultimate tensile stress of the crust.

In the present case, the APRIL code predicts the reactor pressure vessel failure at about 168 min. into the transient, due to the drain plug failure. Following the vessel failure, the system pressure drops immediately and the remaining water in the lower plenum is discharged to the drywell of the reactor containment. The history of fuel mass left in the reactor core is illustrated in Fig. 3.

Effect of Melting Temperature of Fuel (Case-2)

UO2 and Zircaloy are chemically active with each other. At high temperatures, chemical interactions are therefore expected to form eutectics which can influence the integrity of the fuel rods and the fission product release. For example, the CORA experiments, performed in Germany,

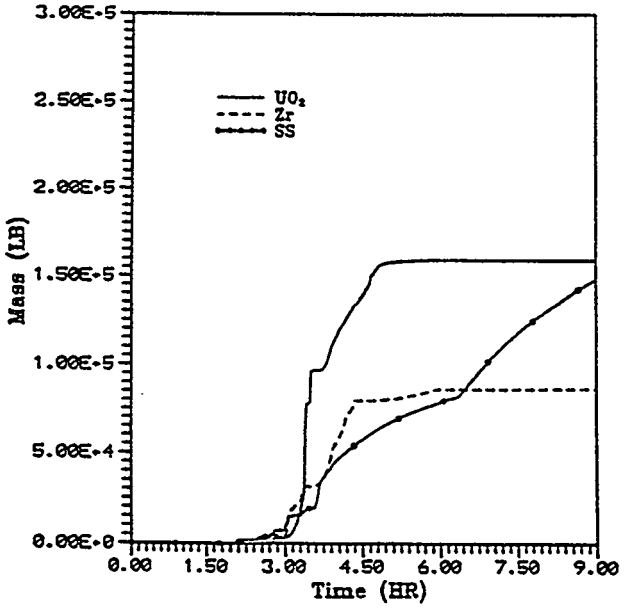

Figure 1. Accumulated mass released from the core to the lower plenum; station blackout, Case-1

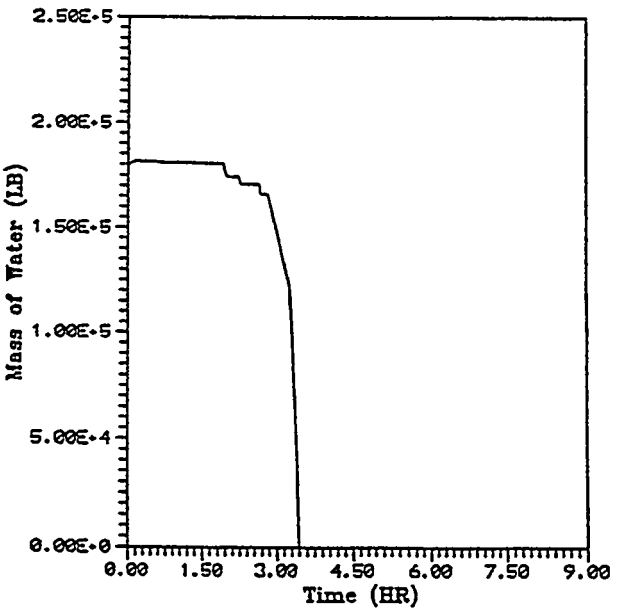

Figure 2. Mass of water in the lower plenum; station blackout, Case-1

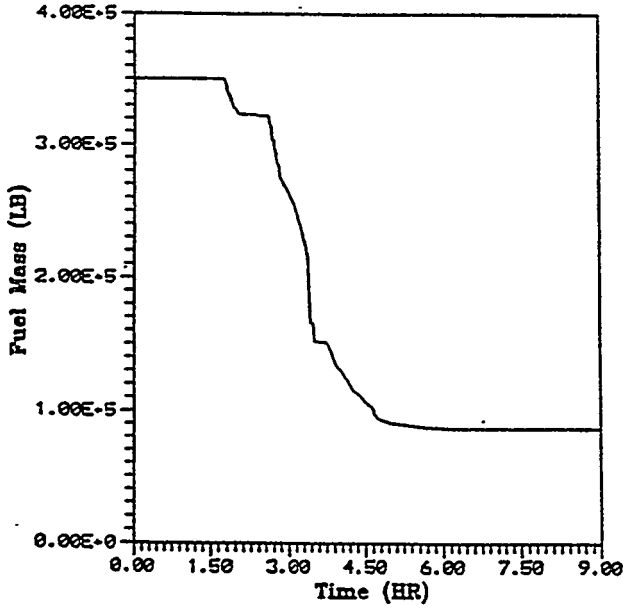

Figure 3. Mass of UO2 in the core; station blackout, Case-1

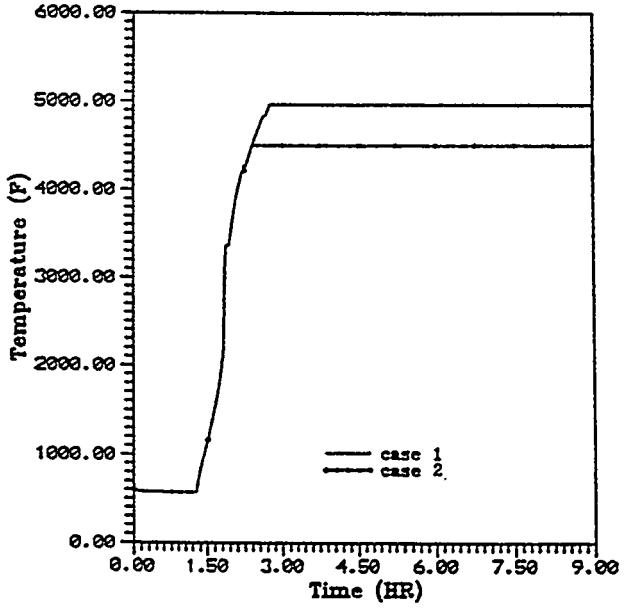

Figure 4. Maximum temperature in the core; station blackout, Cases 1&2

Table 2: APRIL Calculated Main Events in a Station Blackout Accident (Case-1)

Events	Time into transient (min.)
Reactor scram after loss of offsite power	1.0
Beginning of core uncovering (swollen water level falls below TAF)	57.3
Oxidation of Zircaloy begins	93.9
Melting of fuel begins	105.3
Reactor core completely uncovered	116.3
Beginning of Zircaloy relocation onto lower core plate	118.0
Lower core plate fails	164.2
Molten debris starts collecting on the lower head of the vessel	165.7
Reactor vessel fails	168.4
Loss of all water in the lower plenum	206.5

indicated that during the fuel damage phase the UO2 - Zr eutectic reaction may decrease below the melting temperature of both UO2 and Zircaloy.

In order to parametrically test the effect of decreased melting temperature on the core damage and other related results, calculations were performed using a lower melting temperature of fuel, i.e., 4500 F, compared to 4960 F in Case-1.

The interaction between fuel and cladding can take the form of one of two basic phenomena, depending on the cladding temperature. First, below the melting point of Zircaloy, the extent of reaction depends on the fuel/cladding contact conditions. If a solid contact occurs due to external overpressure or different thermal expansions of the fuel and cladding at high temperature, Zircaloy-UO2 reaction occurs to form several layers. For a temperature at, or above, the melting point of Zircaloy, the solid fuel can be partially dissolved by the molten Zircaloy, and structural changes may occur in the fuel pellets.

Although several experiments have been reported, and analytical models have been developed, to evaluate the extent of the interaction, substantial uncertainties still exist. Especially, when the core temperatures are higher than the melting point of Zircaloy.

In the APRIL code, the interaction between molten Zircaloy and UO2 is evaluated based on a conservative assumption that UO2 is instantly dissolved in molten Zircaloy to reach an equilibrium state. This process continues until the molten Zircaloy flows out through a cladding breach. The mole fraction of fuel in the Zircaloy melt is a function of the fuel temperature, and this parameter is calculated in the APRIL code. The dissolved fuel is released through the cladding breach in the form of mixture with molten Zircaloy.

In the present case (Case-2) both the input data, except for the fuel melting temperature, and all the modeling assumptions are the same as in Case-1. Hence, these two cases yield identical results until the fuel temperature reaches the Case-2 melting temperature of 4500 F, including the initial phase of UO2 liquefaction due to the eutectic reaction after the fuel element temperature reaches the Zircaloy melting point of 3365 F (see Figs. 4 and 5). The accelerated melting phase that follows is delayed in Case-1 by about 25 min., which is the time needed to increase the UO2 temperature to 4960F. With an earlier (and faster) faster fuel melting in the core in Case-2, a larger amount of molten fuel material is released onto the lower core plate and, thereafter, to the lower plenum. Therefore, the failure of the vessel lower head in Case-2 occurs about 50 min. earlier than in Case-1, as indicated by the vessel depressurization time in Fig. 6.

Effect of Melting Temperature of Zircaloy (Case-3)

As mentioned before, the UO2 - Zr eutectic reaction decreases the melting temperature of both UO2 and Zircaloy during the fuel damage phase. In order to parametrically test the effect of decreased Zircaloy melting temperature on core damage progression, calculations were performed by reducing the melting temperature of Zr from 3365 F to 3327 F.

In the APRIL code the mole fraction of fuel in the Zircaloy melt is calculated based on the oxygen-stabilized zirconium-uranium dioxide quasi-binary phase diagram [5, 13]. It is known from this diagram that when the fuel temperature is below 2103 K (3326 F), there is no fuel dissolved in the Zircaloy melt. Therefore, in this calculation, the melting temperature of Zircaloy has been decreased to 3327 F. Other parameters are the same as Case-1.

Fig. 7 compares the fuel mass left in the core for Cases-1 and 3. It can be seen that initially the mass of fuel in the core in Case-3 decreases faster than in Case-1. Interestingly, this trend reverses after about 3.5 hours into the transient. This result can be explained by the accelerated core heatup and melting driven by the Zircaloy oxidation reaction during the depressurization after the reactor vessel failure. With more molten materials released onto the lower core plate and into the lower plenum, both the core plate failure and the lower head failure occur earlier in Case-3 than in Case-1 (see Fig. 8). On the other hand, the delay results in higher core temperatures at the time of vessel failure in Case-1 and, thus, has a stronger effect on the exothermal chemical reaction during depressurization, and on the resultant core melting. After the vessel failure, the molten materials are released into the containment.

Based on the results provided by the APRIL code, it can be concluded that the eutectic-reaction-induced reduction in the melting temperature of Zircaloy may significantly affect the timing and consequences of an accident. Specifically, a decrease in the Zr melting temperature by only 38 F (21 K) may accelerate the reactor vessel failure by about 40 min. On the other hand, such a change may also slow down the long-term core melting, reducing the amount of molten UO2 by as much as 10% or more.

III.2. Comparative Analyses of Core Meltdown Accidents Predicted by the APRIL and MAAP Codes

A comparative analysis of the hypothetical core meltdown accidents predicted by the APRIL and MAAP codes has been performed for four basic cases. The MAAP calculations were performed at NMPC, whereas the APRIL code was run at RPI. The results obtained for each case are discussed below, including the effects of the differences in the modeling concepts between the MAAP and APRIL codes on the predictions of accident progression by these codes, and an

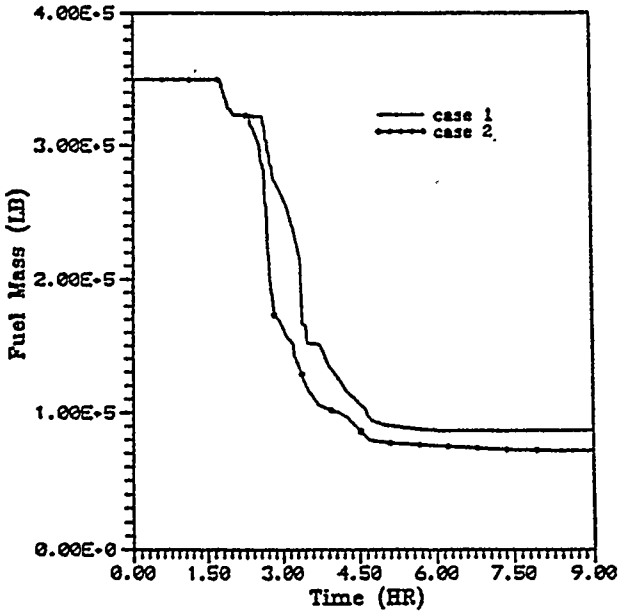

Figure 5. Mass of UO2 in the core; station blackout, Cases-1&2 .

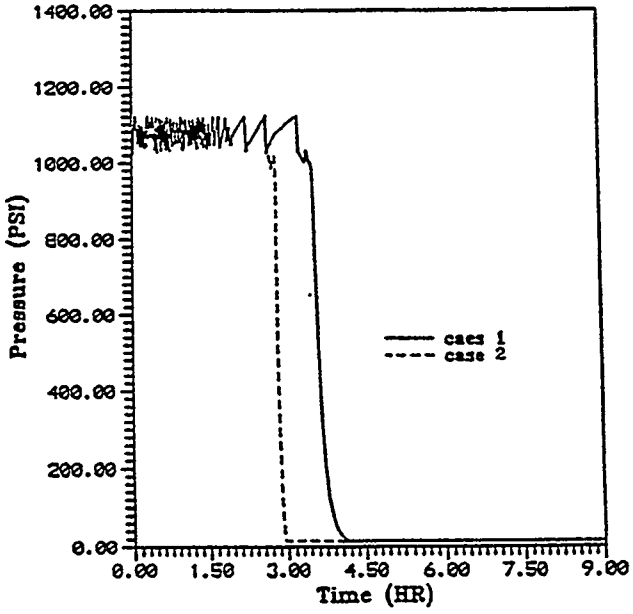

Figure 6. Pressure in the primary system; station blackout, Cases-1&2

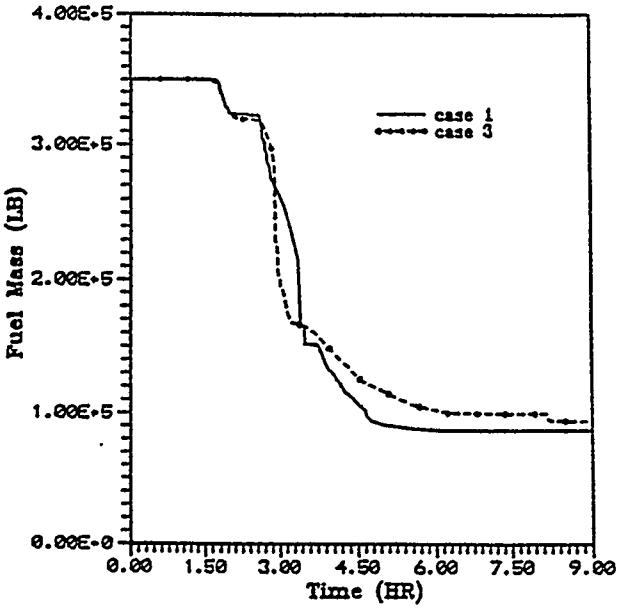

Figure 7. Mass of UO2 in the core; station blackout, Cases-1&3

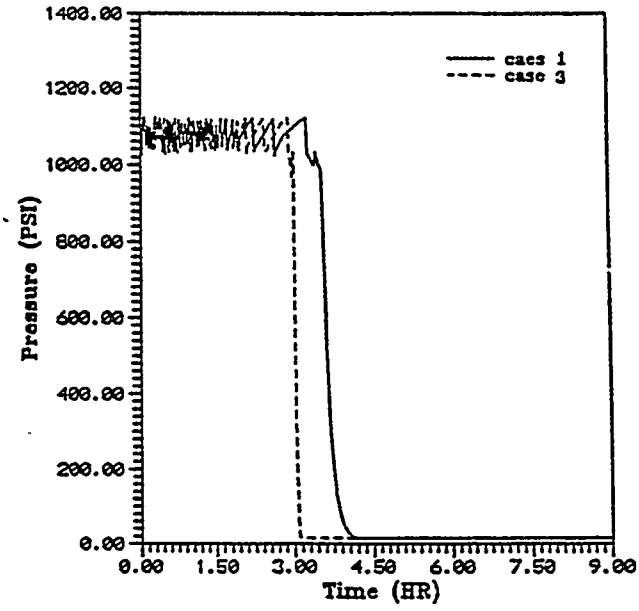

Figure 8. Pressure in the primary system; station blackout, Cases 1&3

assessment of some of the major modeling uncertainties.

Sequence-1: Loss of All Injection and No ADS Actuation

In this core meltdown accident, it is assumed that all of the ECCS injections and the ADS system are unavailable. Most assumptions used in this case, and thus the basic accident progression and core melting /relocation phenomena, are similar to those used in the analysis of the station blackout accident described in Section III.1.

The APRIL and MAAP-calculated heights of the collapsed water level in the downcomer and lower plenum are shown in Fig. 9. It can be noted that the MAAP-calculation shows only the downcomer level and is not applicable after the water level falls below the bottom of the jet pump diffusers. The MAAP code predicts early core uncovering, which results in early core heatup and temperature increase, as illustrated in Fig. 10. It can be seen from these results that although the fuel melting temperatures used in APRIL (4,960 F) and MAAP (4,040 F) are significantly different, similar long-term core average temperatures are predicted by both codes. The reason for using a lower fuel melting temperature in the MAAP code can be attributed to the effect of Zircaloy-UO2 eutectic reaction in the core. In the APRIL code, the effect of this reaction is modeled based on the oxygen-stabilized zirconium-uranium dioxide quasi-binary phase diagram, as described in Section II.

Although there are clear differences in the time of core heatup and fuel melting, both MAAP and APRIL predict approximately the same time of lower core plate failure and pressure vessel failure. Therefore, the APRIL computations agree well with the MAAP code predictions of the time of primary system depressurization and water mass change in the lower plenum, as shown in Table 3.

A comparison of the fuel mass left in the reactor core is shown in Fig. 11. The APRIL code predicts gradual core melting and molten material relocation throughout the transient, whereas the MAAP results indicate that large portions of the fuel melt and relocate in a very short time. This is due to the different modeling concepts used in these codes. At the same time, however, there are several similarities in the long-term accident consequences predicted by these two independently developed computer codes, using entirely different numerical methodologies and employing different modeling concepts.

Sequence-2: ATWS

ATWS (Anticipated Transient Without Scram) is an event sequence in which a reactor transient event is coupled with a failure to insert control rods into the core. Thus, in this event, there is insufficient negative reactivity available to scram the reactor. The postulated failure of the reactor scram system may be attributed to mechanical or electrical failures. ATWS sequences typically involve early and large containment failures, potentially leading to larger radionuclide releases than in other accidents.

In the present hypothetical ATWS scenario, the accident is initiated by MSIV closure, followed by failure to scram and a successful trip of the recirculation and feedwater pumps. In particular, the following assumptions have been made in the present APRIL simulations:

(a) ADS valves are actuated at a time of 4,060 s into the transient to depressurize the reactor primary system; this action is triggered at containment failure in the MAAP calculations,

(b) HPCS system is assumed to start automatically when water level in the downcomer falls

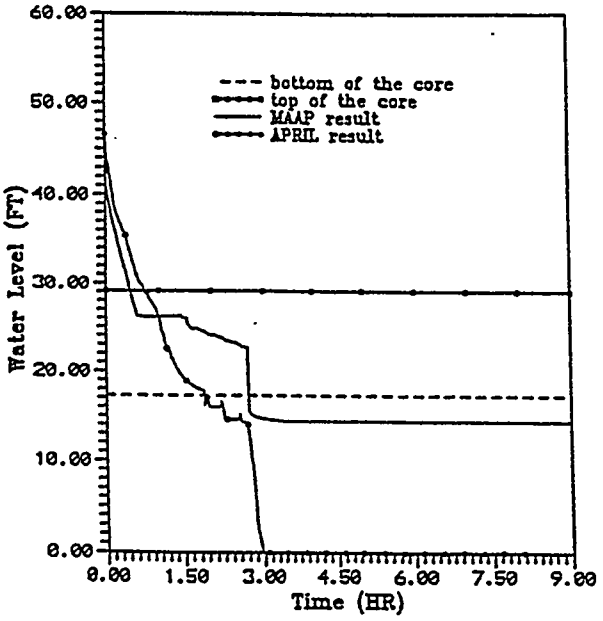

Figure 9. Water level in the downcomer and lower plenum; Sequence-1

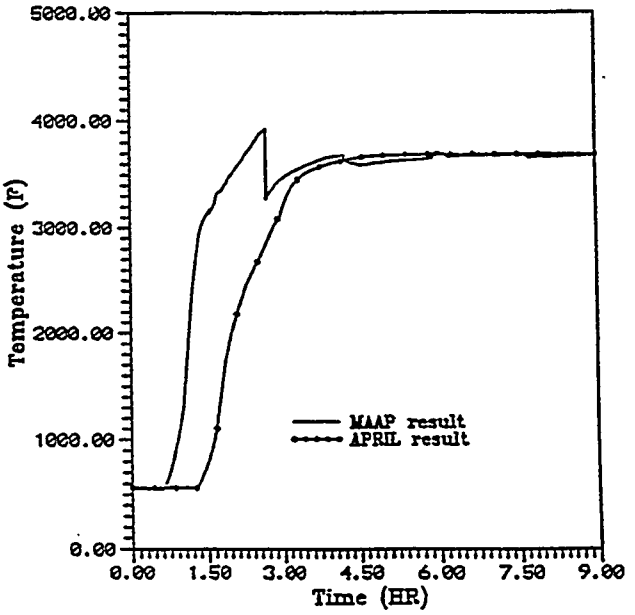

Figure 10. Average core temperature; Sequence-1

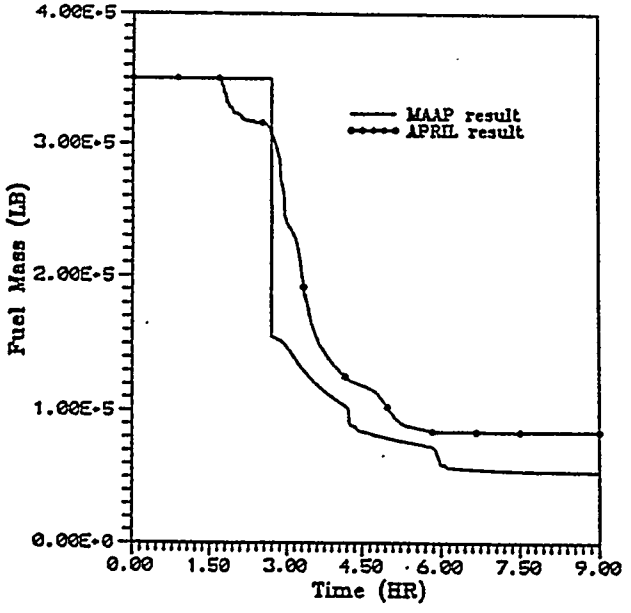

Figure 11. Mass of UO_2 in the core; Sequence-1

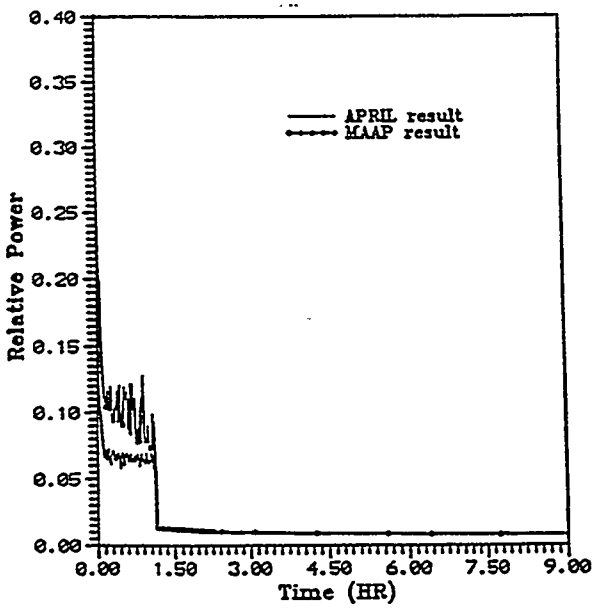

Figure 12. Reactor core relative power; Sequence-2

Table 3: APRIL and MAAP predicted main events for loss of all injections at high RPV pressure

Main Events (Sequence-1)	MAAP	APRIL	Explanation Of APRIL Results
MSIV closure and loss of feedwater	0.0 min	0.0 min	From MAAP
Water level in the downcomer region drops to TAF	31.0 min	46.8 min	Calculated
Two-phase water level in the core region drops to TAF	36.0 min	57.0 min	Calculated
Beginning of fuel heat-up	40.2 min	64.0 min	Calculated
Beginning of Zr melting	60.9 min	103.0 min	Calculated
Beginning of Zr-UO_2 eutectic reaction and the resultant fuel melting	N/A	104.0 min	Calculated
Fuel temperature reached melting temperature (MAAP: 4040F, APRIL: 4960F)	65.1 min	147.0 min	Calculated
Reactor core becomes totally uncovered	158.3 min	135.0 min	Calculated
Lower core plate failure	161.4 min	155.4 min	Calculated
Pressure vessel failure	161.5 min	160.4 min	Calculated
Molten materials release to the pedestal room	161.6 min	162.3 min	Calculated
Loss all of water in the lower plenum	162.1 min	176.5 min	Calculated
Mass of molten fuel in the core after 9 hours into the transient	296,000 lb	266,000 lb	Calculated
Reactor core average fuel temperature after 9 hours into the transient	3669 F	3685 F	Calculated

below 40 ft (ref. to the bottom of the vessel), with a time delay of 27 s after vessel depressurization; the HPCS flow rate is 936,000 lb/hr,

(c) CRD pumps deliver a constant flow of water (31,800 lb/hr) until pressure vessel depressurization, after which there is no CRD flow.

Fig. 12 compares the calculated reactor core relative power, which is a sum of the decay power and ATWS power. It can be seen that the MAAP-calculated ATWS power is higher than that of APRIL. This is probably due to the different water levels in the downcomer, calculated by each code, as shown in Fig. 13. Again, the constant MAAP-calculated level below the bottom of the core corresponds to the bottom of the jet pumps. Since these two codes have different thermal-hydraulic models, and the calculated ATWS powers are different from each other, the computed water level behavior and the onset of core uncovery are also different. Before the ADS actuation, the APRIL and MAAP-calculated heights of the collapsed water level in the vessel shroud remain

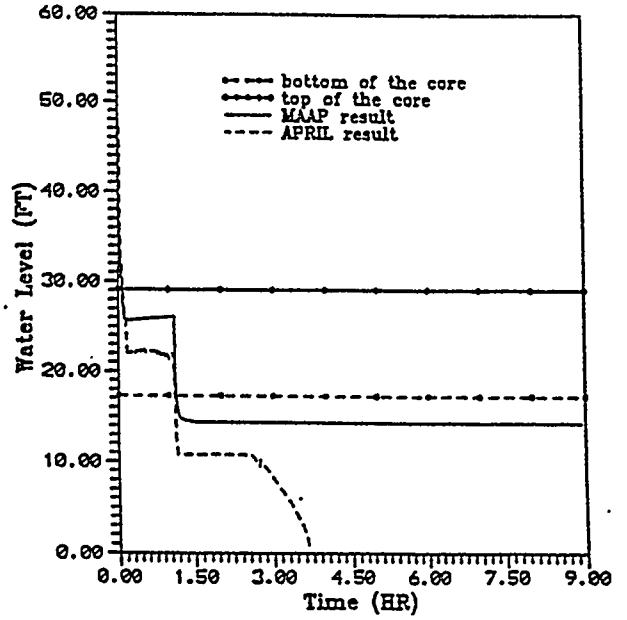

Figure 13. Water level in the downcomer and lower plenum; Sequence-2

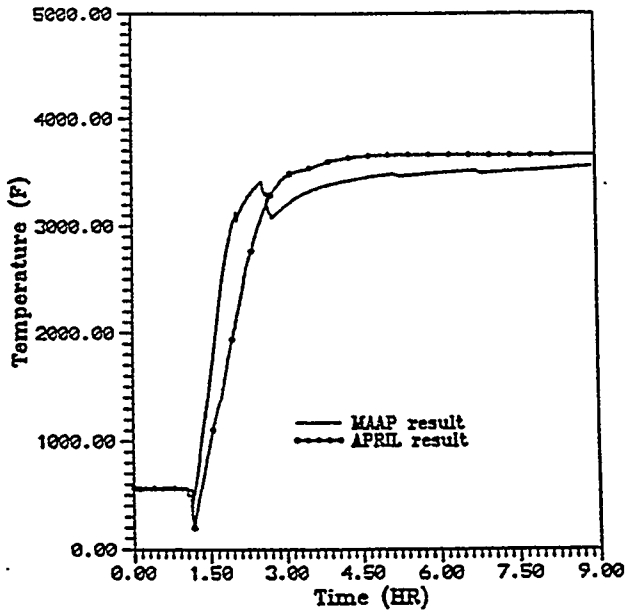

Figure 14. Average core temperature; Sequence-2

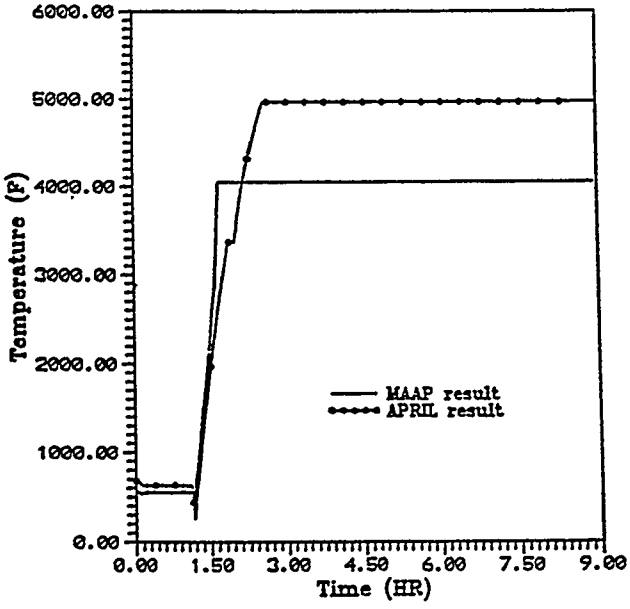

Figure 15. Maximum temperature in the core Sequence-2.

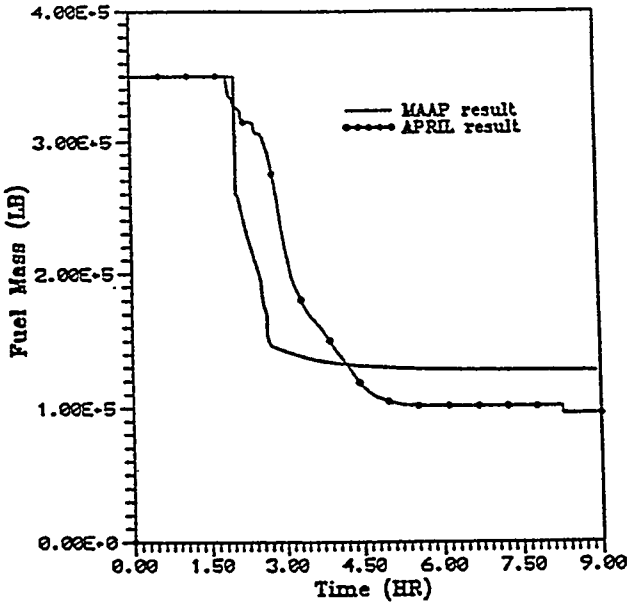

Figure 16. Mass of UO_2 in the core; Sequence-2

approximately steady.

Both the MAAP and APRIL codes predict very similar histories of core heatup and temperature increase, as illustrated in Fig. 14. However, the fuel melting temperatures used in APRIL and MAAP are different again (see Fig. 15). A comparison of the fuel mass left in the reactor core is shown in Fig. 16. APRIL computes a gradual core melting and molten material relocation throughout the transient, whereas the MAAP result indicates a large amount of fuel melting and relocation in a very short time. As illustrated in Fig. 17, the MAAP code predicts almost immediately loss of all water in the lower plenum after pressure vessel failure. On the other hand, the APRIL code results show a gradual loss of water in the lower plenum due to the discharge through the break and because of steam evaporation in the lower plenum (including the effect of mass reduction due to flashing and partial refill due to the inflow from the core and downcomer after the end of sudden depressurization). The former effect is mainly due to the mode of RPV failure predicted by APRIL. Specifically, the drain plug failure opens a small flow area, which, even with the effect of ablation by molten corium discharged from the vessel, only allows for a relatively low flow rate of water through the break. The main events calculated by both codes are listed in Table 4.

Sequence-3: Large LOCA

This LOCA accident is initiated with a 18 inch pipe break inside the RHR room. The assumptions used in the analysis include: successful reactor scram, loss of feedwater and all ECCS injections, and no ADS actuation. Because this accident is a large LOCA, the time of events and the operator actions are limited, and no operator action and equipment are needed to depressurize the RPV. The ECCS injection failure, combined with a large loss of coolant from the vessel, result in significant core damage.

The discharge from RPV occurs in the downcomer region via the pipe break. Due to a large two-phase discharge flow and immediate system depressurization, the water level in the vessel drops quickly below the lower core plate. Thereafter, the reactor is totally uncovered, and the core begins to heat up and melt.

Both the MAAP and APRIL codes predict the core heat-up and temperature increase at almost the same time, as illustrated in Fig. 18. It can also be seen from these results that due to the differences in the modeling assumptions, the fuel heatup rate predicted by MAAP is much faster than that in APRIL. The higher heatup rate and lower fuel melting temperature in the MAAP calculations result in early fuel melting predicted by this code.

A comparison of the fuel mass left in the reactor core is shown in Fig. 19. The APRIL code predicts less fuel left in the core than MAAP. The predictions of all major events are summarized in Table 5.

Sequence-4: Loss of RPV Makeup at Low Pressure

In this core meltdown accident, it is assumed that all of the ECCS injections are unavailable, the ADS system is initiated when the water level decreases to the top of active fuel (TAF), and the LPCS injection is put into operation just before the vessel failure. The ADS valves are opened when the downcomer water level drops below TAF. Then, a fast system depressurization results in the swollen water levels to increase quickly. The heights of the collapsed water levels in the downcomer/lower plenum regions, as calculated by both MAAP and APRIL, are shown in Fig.

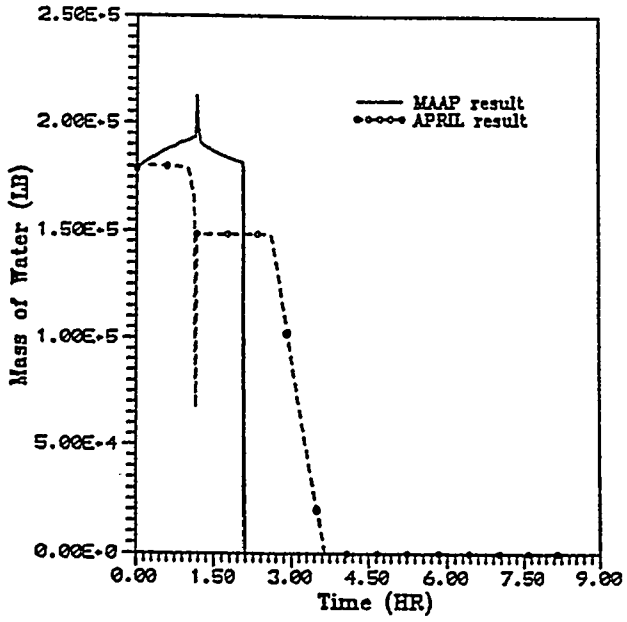

Figure 17. Mass of water in the lower plenum; Sequence-2

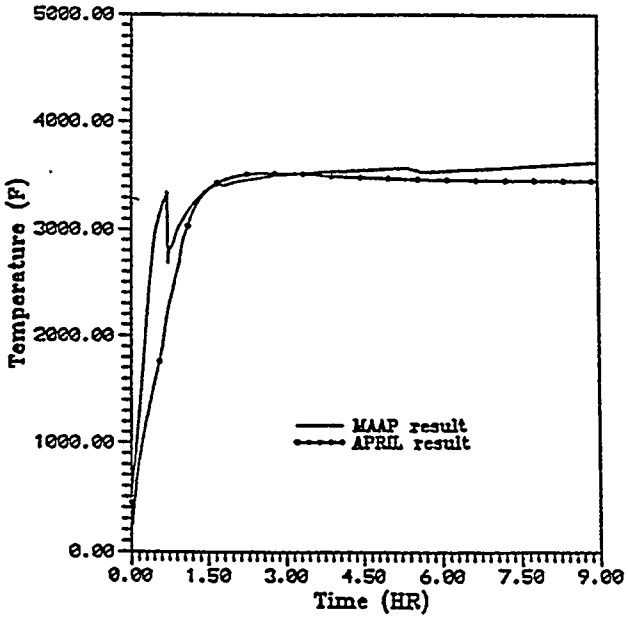

Figure 18. Average core temperature; Sequence-3

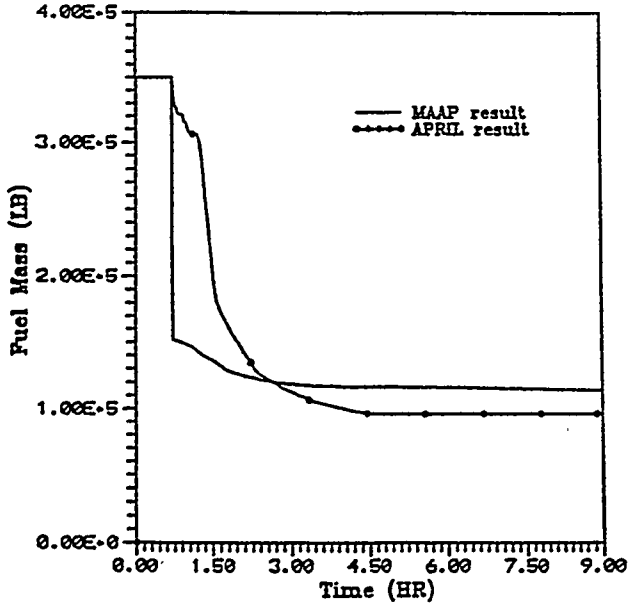

Figure 19. Mass of UO_2 in the core; Sequence-3

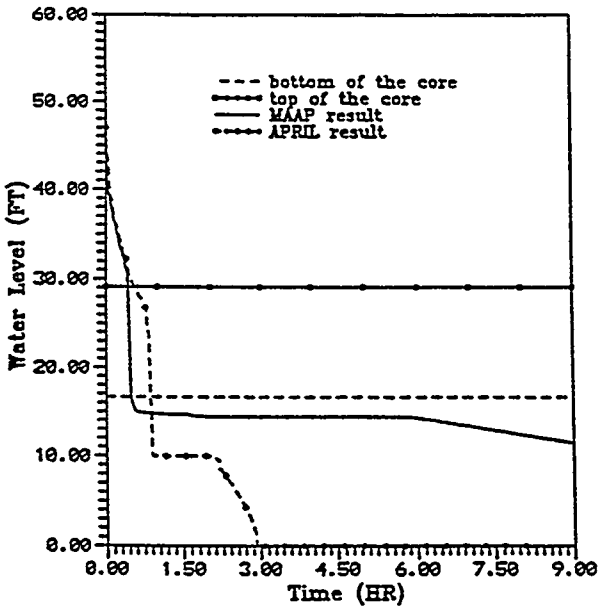

Figure 20. Water in the downcomer; Sequence-4

Table 4: APRIL and MAAP predicted main events for ATWS accident

Main Events (Sequence-2)	MAAP	APRIL	Explanation Of APRIL Results
MSIV closure and loss of feedwater	0.0 min	0.0 min	From MAAP
HPCS initiation	0.8 min	0.8 min	From MAAP
Onset of core uncovering	4.4 min	6.1 min	Calculated
ADS valves opened	67.5 min	67.5 min	From MAAP
HPCS & CRD flow trip off	67.5 min	67.5 min	From MAAP
Reactor core becomes totally uncovered	69.7 min	68.9 min	Calculated
Beginning of fuel heat-up	69.4 min	71.8 min	Calculated
Beginning of Zr melting	98.3 min	112.0 min	Calculated
Beginning of Zr-UO_2 eutectic reaction and the resultant fuel melting	N/A	112.6 min	Calculated
Fuel temperature reaches UO_2 melting temperature	101.6 min	150.0 min	Calculated
Lower core plate failure	122.8 min	151.4 min	Calculated
Pressure vessel failure	122.9 min	155.4 min	Calculated
Loss of all water in the lower plenum	126.0 min	219.1 min	Calculated
Mass of molten fuel in the core after 9 hours into the transient	127,000 lb	96,030 lb	Calculated
Reactor core average fuel temperature after 9 hours into the transient	3548 F	3653 F	Calculated

20. Due to the early ADS actuation, the MAAP code predicts early total core uncovering, which results in an early core heatup and temperature increase, as illustrated in Fig. 21. It can be seen from the MAAP results that the fuel temperature reaches the melting point (4040 F) very quickly after system depressurization.

The MAAP code predicts the lower core plate failure at 91.7 min into the transient. After the failure of the lower core plate, the LPCS system is initiated, with a flow rate of 1,028 lb/sec. The spray of a large amount of subcooled water into the core causes core temperature to decrease immediately.

Three cases have been analyzed using the APRIL code. In Case-1, the timing of LPCS actuation in APRIL was assumed the same as in the MAAP calculations. The resultant fuel temperatures are shown in Fig. 22. In the Case-2 calculations, the LPCS was actuated after the APRIL-calculated failure of the lower core plate at 127.4 min. The calculated fuel temperatures are

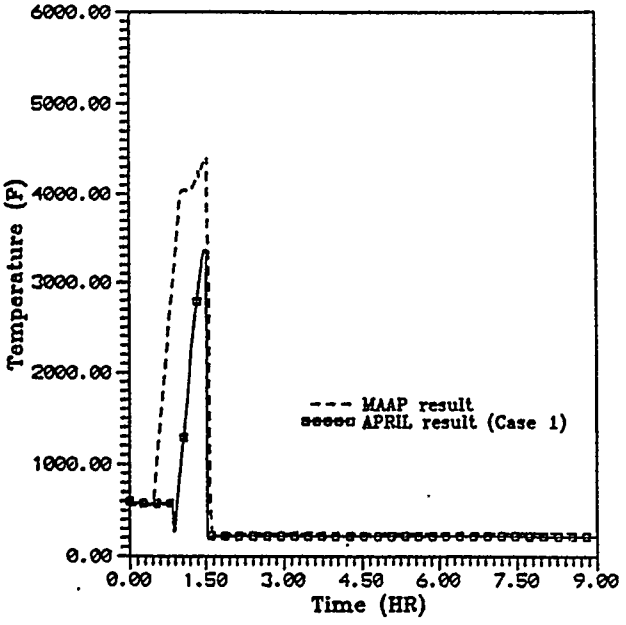

Figure 21. Maximum core temperature; LPCS initiated at 91.7 min. for APRIL; Sequence-4

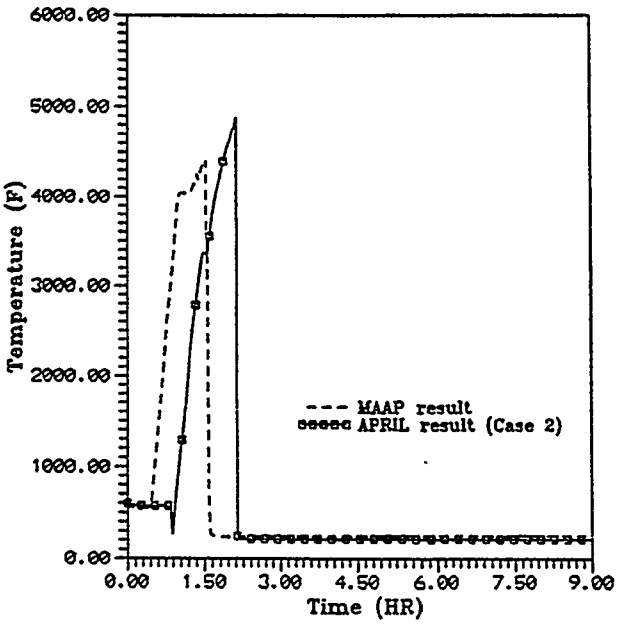

Figure 22. Maximum core temperature; LPCS initiated at 127.4 min. for APRIL; Sequence-4

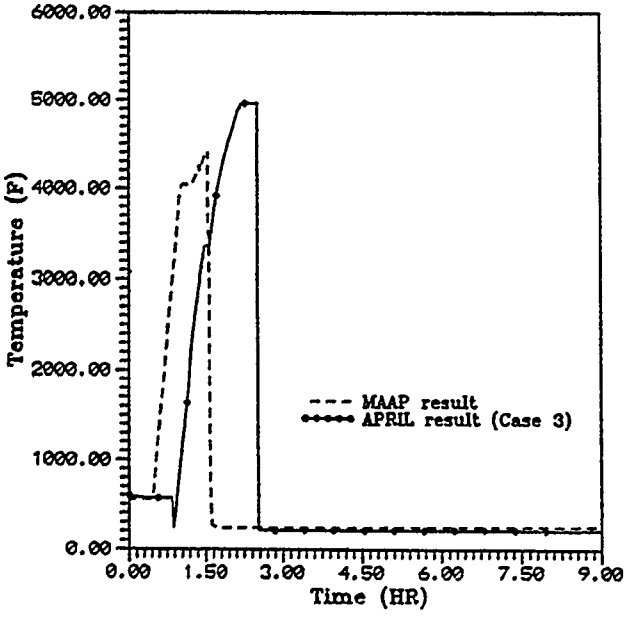

Figure 23. Maximum core temperature; LPCS initiated at 150 min. for APRIL; Sequence-4

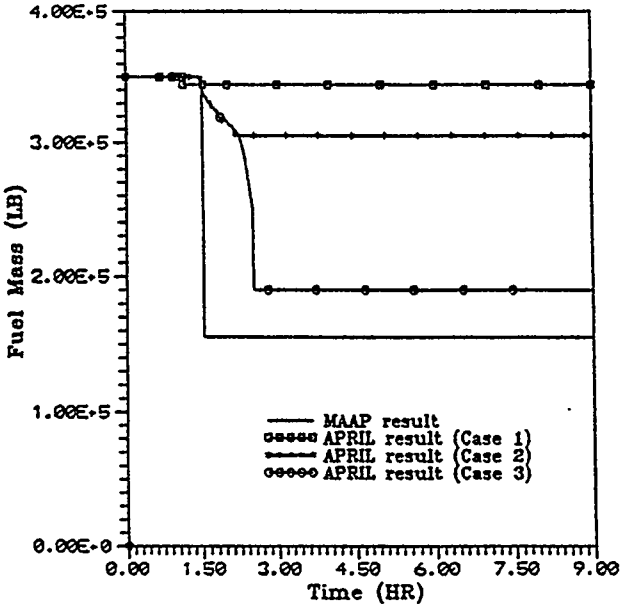

Figure 24. Mass of UO_2 in the core, calculated by MAAP nad APRIL; Sequence-4

Table 5: APRIL and MAAP predicted main events for large LOCA

Main Events (Sequence-3)	MAAP	APRIL	Explanation Of APRIL Results
Onset of large LOCA	0.0 min	0.0 min	From MAAP
Onset of core uncovering	1.3 min	0.9 min	Calculated
Reactor core becomes totally uncovered	2.0 min	1.7 min	Calculated
Beginning of fuel heat-up	2.1 min	2.6 min	Calculated
Beginning of Zr melting	18.8 min	43.0 min	Calculated
Beginning of Zr-UO_2 eutectic reaction and the resultant fuel melting	N/A	43.9 min	Calculated
Fuel temperature reaches UO_2 melting temperature	22.9 min	70.3 min	Calculated
Lower core plate failure	42.9 min	72.3 min	Calculated
Pressure vessel failure	43.0 min	76.5 min	Calculated
Loss of all water in the lower plenum	56.7 min	174.5 min	Calculated
Mass of molten fuel in the core after 9 hours into the transient	113,800 lb	96,000 lb	Calculated
Reactor core average fuel temperature after 9 hours into the transient	3629 °F	3450 °F	Calculated

shown in Fig. 22. In Case-3, in order to simulate more fuel melting in the core, the LPCS system was initiated 22 min. after the lower core plate failure. The effect of this delay on the APRIL-calculated fuel temperature are shown in Fig. 23. As can be seen, the heatup rate slowed down after the temperatures reached the melting point of Zircaloy.

A comparison of the fuel mass left in the reactor core is shown in Fig. 24. Furthermore, a comparison between the APRIL and MAAP calculated hydrogen productions are shown in Fig. 25. The main events according to APRIL and MAAP predictions are listed in Table 6.

IV. CONCLUSIONS

The APRIL computer code has been used to simulate the progression of severe accidents at a reference BWR. The input data for the APRIL calculations were prepared based on the MAAP code parameter file obtained from NMPC. In addition to the reference accident scenario, several runs were performed in order to test the sensitivity of results to various input parameters and modeling assumptions, and to quantify some of the major uncertainties in the modeling of severe accident phenomena.

An extensive comparison (for four different accident scenarios) was performed between the

Table 6: APRIL and MAAP predicted main events for loss of RPV makeup at low pressure

Main Events (Sequence-4)	MAAP	APRIL			Explain. Of APRIL Results
		Case 1	Case 2	Case 3	
MSIV closure and loss of feed-water	0.0 min	0.0 min	0.0 min	0.0 min	From MAAP
Water level in the core region at TAF	25.3 min	49.3 min	49.3 min	49.3 min	Calc.
ADS valves opened	25.3 min	49.3 min	49.3 min	49.3 min	Calc.
Onset of core uncovering	26.6 min	45.2 min	45.2 min	45.2 min	Calc.
Beginning of fuel heat-up	27.2 min	52.9 min	52.9 min	52.9 min	Calc.
Beginning of Zr melting	55.5 min	86.8 min	86.8 min	86.8 min	Calc.
Beginning of Zr-UO2 eutectic reaction and the resultant fuel melting	N/A	87.1 min	87.1 min	87.1 min	Calc.
Fuel melting reached (MAAP: 4040F, APRIL: 4960F)	61.1 min	N/A	125.9 min	125.9 min	Calc.
Lower core plate failure	91.7 min	No failure	127.4 min	127.4 min	Calc.
LPCS initiated	91.7 min	91.7 min	127.4 min	150.0 min	Input
Pressure vessel failure	91.8 min	No failure	No failure	131.1 min	Calc.
Mass of molten fuel in the core after 9 hours into the transient	155,700 lb	345,100 lb	305,000 lb	190,100 lb	Calc.

APRIL and MAAP codes, and the observed differences in the obtained results have been analyzed and used to assess the uncertainties in BWR severe accident predictions.

The obtained results can be summarized as follows:

1. The depressurization of the reactor vessel by opening the ADS valves when the downcomer level is already below TAF (but at least 60-70% of the active fuel height) may provide, due to the combined effects of level swelling and steam flow, a desired temporary cooling of the uncovered region of the core. Therefore, this action will delay core heat-up and melting.
2. It is known that the UO2-Zr eutectic reaction decreases the melting temperature of both fuel and Zircaloy during the core damage phase. With a lower assumed fuel melting temperature, more molten materials are released to the core plate/lower plenum and the failure of the vessel lower head occurs earlier. The simulations are even more sensitive to the assumed melting temperature of Zircaloy/UO2 eutectic. A small decrease in this temperature may accelerate the predicted vessel failure by several minutes, and its impact on long-term core melting is even more complex.

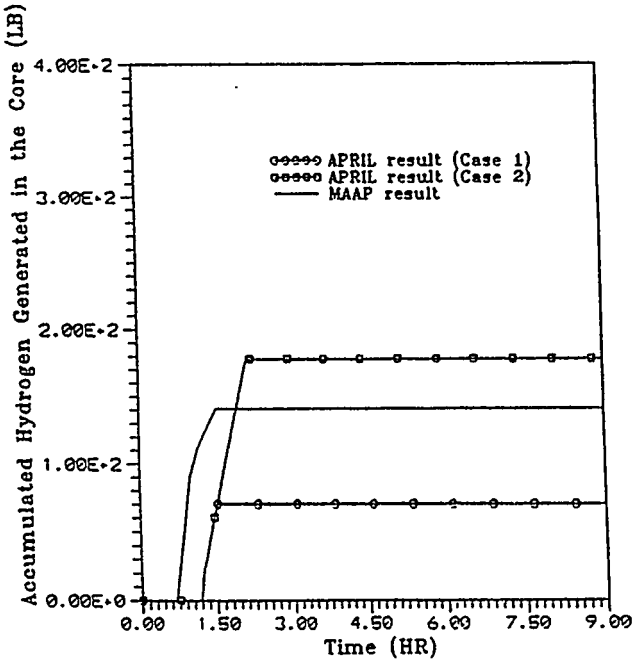

Figure 25. Comparison between the MAAP and APRIL-calculated mass of H_2; Sequence-4

3. The consequences of hypothetical core meltdown accidents predicted by the APRIL and MAAP codes have been compared against each other. The major observations are as follows:
   - These two independently developed computer codes, using entirely different numerical methodologies and different modeling concepts, produce similar long-term results in most cases analyzed. Both MAAP and APRIL predict approximately the same time of lower core plate failure, pressure vessel failure, and primary system depressurization.
   - At the same time, however, several significant differences has been observed in the predicted timing of specific events and the values of selected parameters, such as: core heatup, fuel melting, and ATWS power. The APRIL code predicts gradual core melting and molten material relocation throughout the transient, whereas the MAAP code results indicate that a large amount of core fuel melting and relocation occurs in very short time.
   - The fuel melting temperatures used in the APRIL (4,960 F) and MAAP (4,040 F) are significantly different. The use of an assumed lower fuel melting temperature in the MAAP code can be attributed to the effect of Zircaloy-UO2 eutectic formation. In the APRIL code, the effects of eutectic reaction are modeled based on the zirconium-uranium dioxide quasi-binary phase diagram, whereas the melting of the remaining fuel pellets is modeled using the actual melting temperature of UO2.
   - The MAAP code predicts a loss of all water in the lower plenum almost immediately after the pressure vessel failure; the APRIL code results show a gradual loss of water in the lower plenum due to the combined effects of: (a) discharge through the break caused by drain plug failure, and (b) of water evaporation on the lower plenum.

REFERENCES

1. Abramson, P. and Komoriya, H., "BWR Source Term Codes Comparison", ESEERCO Report EP86-19, 1988.
2. Podowski, M. Z., Lahey, R.T., Jr. and Burger, J. M., "The Analysis of Core Meltdown Progression in BWRs", Proceedings of the Fourth International Topical Meeting on Nuclear Reactor Thermal-Hydraulics, Karlsruhe, FRG, 1989.
3. Koh, B. R., Kim, S. H., Taleyankhan, R. P., Podowski, M. Z. and Lahey, R. T., Jr., "The Modeling of BWR Core Meltdown Accident for Application in the MELRPI-MOD2 Computer Code", NUREG/CR-3889, 1985.
4. Kim, S. H., Kim, D. H., Koh, B. R., Pessanha, J., SiAhmed, El-K., Podowski, M. Z. and Lahey, R. T., Jr., "The Development of APRIL.MOD2 - A Computer Code for Core Meltdown Accident Analysis of Boiling Water Nuclear Reactors", NUREG/CR-5157, 1988.
5. Lahey, R.T., Jr. and Podowski, M.Z., "Degraded BWR Core Modeling; APRIL.MOD3 Severe Accident Code", ESEERCO Report, EP84-4, 1990.
6. Podowski, M.Z., Lahey, R.T. Jr., Kim, S.W., Kurul, N., Luo, W. and Moraga, F., "The Upgrading and Validation of APRIL.MOD3X as an Interactive Computer Code for BWR Severe Accident Analysis", Research Report EP84-4, ESEERCO, July 1994.
7 Podowski, M.Z. Lahey, R.T. Jr., Cho, C.S., Jia, H., Kim. D.H., Kim, S.H., Kim, S.W., Kurul, N. and Luo, W., "APRIL.MOD3X User's Manual", with, N. Kurul, C. Cho, H. Jia, D.H. Kim, S.H. Kim, S.W. Kim, W. Luo, M.Z. Podowski, R.T. Lahey, Jr., RPI Report, June 1994.
8. Pessanha, J., SiAhmed, El.-K. and Podowski, M.Z., "Theoretical and Experimental Analysis of Liquefied Material Relocation During Severe Reactor Accidents", ANS Proceedings, 1988 National Heat Transfer Conference, Houston, Texas, HTC-Vol. 3, 1988.
9. SiAhmed, El-K., Podowski, M.Z. and Lahey, R.T. Jr., "An Experimental and Theoretical Investigation of Melt Propagation in a Rubble Bed, with Application in Severe Accident", Fourth ANS Proceedings on Nuclear Thermal-Hydraulics, Washington, DC, 1988.
10. Cho, C.S., Lahey, R.T. Jr. and Podowski, M.Z., "Multidimensional Analysis of Natural Convection in MARK-I Containments during BWR Core Meltdown Accidents", ANS Proc, Vol. 6, 1992.
11. Kim, S.W., Podowski, M.Z. and Lahey, R.T. Jr., ""Numerical Simulation of DF-4 and CORA-16/17 Severe Fuel Damage Experiments using APRIL.MOD3", Proc. of the Fifth International Tropical Meeting on Nuclear Reactor Thermal-Hydraulics (NURETH-5), 1992.
12. FAI, "MAAP User's Manual", 1986.
13. "MATPRO - A Handbook of Materials Properties for Use in the Analysis of Light Water Reactor Fuel Rod Behavior", NUREG/CR-0497, 198).

ROSA/AP600 TESTING: FACILITY MODIFICATIONS AND INITIAL TEST RESULTS

Y. Kukita, T. Yonomoto, H. Asaka, H. Nakamura, H. Kumamaru and Y. Anoda
Japan Atomic Energy Research Institute
Tokai, Ibaraki, Japan

T.J. Boucher, M.G. Ortiz, R.A Shaw and R.R. Schultz
Idaho National Engineering Laboratory
Idaho Falls, Idaho

ABSTRACT

The Japan Atomic Energy Research Institute (JAERI) and the United States Nuclear Regulatory Commission (USNRC) are jointly conducting high-pressure, confirmatory, integral testing on the Westinghouse AP600 rector transient responses by using the ROSA-V Large Scale Test Facility of JAERI. This facility, built originally for the simulation of conventional 4-loop pressurized water reactors (PWRs), has been modified by adding components specific to the AP600 design. The modified LSTF provides a full-pressure, full-height, 1/30.5 volumetrically-scaled simulation of AP600. Seven loss-of-coolant experiments have been performed for the break locations of cold leg, Pressure Balance Line (PBL) and Direct Vessel Injection (DVI) line. The experimental results generally indicate satisfactory core cooling and decay heat removal performances of the AP600 passive safety components.

I. INTRODUCTION

The Japan Atomic Energy Research Institute (JAERI) and the United States Nuclear Regulatory Commission (USNRC) entered a cooperative research agreement in 1992 to perform a series of high-pressure integral tests on the safety response of the Westinghouse AP600 design using the Large Scale Test Facility (LSTF) of JAERI. The primary objective of this test series is to provide thermal/hydraulic data of phenomena that would be expected during an AP600 transient; those data will then be used for assessment of safety analysis codes.

Under this agreement, the USNRC funded the modifications of LSTF to perform simulations of AP600 transient responses. The major modifications included the addition of two Core Makeup Tanks (CMTs), a Passive Residual Heat Removal System (PRHR), an In-Containment Refueling Water Storage Tank (IRWST), CMT Pressure Balance Lines (PBLs) and an Automatic Depressurization System (ADS). Also, a new, full-height pressurizer was installed, and the two existing accumulator tanks were modified to allow nitrogen discharge to follow the discharge of the scaled water inventory. The design specifications for these changes were developed by the Idaho National Engineering Laboratory (INEL) based on RELAP5/MOD2.5 comparative analyses

of the AP600 and modified-LSTF responses to selected accident scenarios. The modified LSTF now provides a 1/30.5 volumetrically-scaled full-height model of AP600.

After the completion of above modifications in February 1994, a facility "shakedown" experiment[1] and seven matrix experiments were conducted by the end of October 1994. This paper summarizes the facility modifications and findings from the first five experiments.

II. FACILITY MODIFICATIONS

The ROSA-V LSTF[2] was built in 1985 as a 1/48 volumetrically scaled, full-height, full-pressure model of a conventional Westinghouse-type 4 loop (3423 MWt) PWR. The LSTF has two primary loops each including one cold leg, one hot leg, an active inverted-U tube steam generator (SG), and an active reactor coolant pump. Each SG contains 141 full-height U-tubes. The LSTF pressure vessel includes an annular downcomer and contains 1008 electrically heated rods capable of operating at 10 MW, or 14% of the scaled full power for the reference PWR. The heater rod dimensions and pitch are the same as those for the 17x17 fuel assembly used in the reference PWR core. The existing components are approximately full-height and ~1/30 volumetrically scaled as compared to those in AP600.

INEL conducted a series of RELAP5/MOD2.5 calculations[3] to explore different levels of LSTF modifications for the simulation of AP600 transients. The scenarios chosen for these calculations were: 3- and 1-inch cold leg breaks, 3-inch PBL break, one and three SG U-tube ruptures (SGTRs), and a main steam line break. The modifications were evaluated in terms of their capability in reproducing the AP600 response, predicted by using the same code and the same modeling approach, in such parameters as the depressurization rate, mass inventory, and energy distribution.

Based on considerations of these analysis results, cost estimates, past testing experience with LSTF[4-6], and impacts on the LSTF capability on performing tests on conventional PWR design, the USNRC and JAERI agreed to implement the following modifications to LSTF:

- Add two CMTs.
- Add one PRHR and one IRWST.
- Add 4-stage ADS, with catch tanks for the stage-4 valves.
- Add connecting lines for the above components [including pressurizer surge line, CMT PBLs, CMT and IRWST discharge lines and Direct Vessel Injection (DVI) lines].
- Replace the existing pressurizer with a full-height one.
- Add a stand pipe to the two accumulator tanks to allow nitrogen discharge to follow the discharge of the scaled water inventory.
- Reduce the depth of cold leg loop seals.
- Increase the flow paths between the upper plenum and the upper head, and between the upper head and the downcomer.

The modified LSTF provides a 1/30.5 volumetrically-scaled full-height model of AP600. The AP600 design changes which were announced by Westinghouse in February 1994 were implemented before the first matrix experiment was conducted in April 1994.

A schematic of the modified LSTF is given in **Fig. 1**. The loop on the left hand side in this figure (A-loop) represents the P-loop in AP600 to which PRHR and the pressurizer are connected. The other loop (B-loop) represent the AP600 C-loop to which CMTs are connected. Since LSTF has only one cold leg per loop, the two CMTs are connected to the same cold leg in the standard experiment geometry; however, for the PBL break and DVI line break experiments, the unaffected CMT is connected to the P-loop cold leg, while the affected CMT is still connected to the C-loop, to avoid atypical influence of the break on the behavior of the unaffected CMT.

The break is always located in the simulated C-loop and represented by using a quick opening valve and a limiting nozzle. The break flow is routed to a catch tank (not shown in **Fig. 1**), where the steam component is condensed, to estimate the time-integrated break mass flowrate on the basis of the level increase in the catch tank.

Measurement of transient parameters are made for approximately 2300 channels including about 300 channels for the newly-added AP600 components. The final data reduction is made off-line, but real-time displays are available in the control room not only for directly-measured quantities but also for derived quantities including the spatial distributions of coolant inventory and subcooling which are calculated from measured differential pressures, densities, temperatures and pressures.

III. EXPERIMENTAL RESULTS

III.1 INITIAL AND BOUNDARY CONDITIONS

The seven experiments conducted to date simulated loss-of-coolant scenarios with different break sizes and break locations as follows:

Exp. ID.	Date*	Scenario
AP-CL-03[8]	April 14	1-in. cold leg break
AP-AD-01[9]	May 17	Inadvertently open ADS
AP-CL-04[10]	June 7	0.5-in. cold leg break
AP-PB-01[11]	June 28	2-in. PBL break
AP-CL-05	August 2	1-in. cold leg break with failure of ADS 1-3
AP-PB-02	September 20	1-in. PBL break, with failure of unaffected CMT
AP-DV-01	October 12	Double-ended break of DVI line

(*: All Conducted in 1994.)

The experiments were initiated from initial pressures and temperatures typical of AP600 rector rated operating conditions. Since the LSTF maximum core power was limited to 10 MW, or 16% of the scaled AP600 rated core power, the initial core flow rate was set to 16% of the scaled

rated flow to obtain cold leg-to-hot leg temperature difference typical of AP600 rated operating conditions. INEL developed a core decay power curve which takes into account the small-than scaled initial core power. With this power curve, the time-integrated core power was scaled starting from 21.3 s after reactor trip. Other test boundary conditions including the ADS flow areas, the pump coastdown curve, and the component trip logics were also developed by INEL and implemented by JAERI for testing.

The experiments conducted to date generally indicated that the passive safety components had sufficient capabilities to maintain the core cooling and decay heat removal in simulated LOCA situations. Major findings from these experiments are briefly described below.

III.2 GENERAL SYSTEM RESPONSES

Figure 2 depicts the reactor coolant system (RCS) and SG secondary-side pressures during Experiment AP-CL-03 (1-inch cold leg break) with timings of major events indicated. Post-test analysis for this experiment has been done by INEL using the RELAP5/MOD3 code[12].

The initial events in this experiment (reactor trip, SG isolation) were similar to those in a SBLOCA in a conventional PWR, except that both CMTs and PRHR were tripped on by a low pressurizer liquid level signal.

Despite the small break size, the RCS pressure became lower than the SG secondary-side pressures early in the transient as shown in **Fig. 2**. This occurred because most of the RCS liquid inventory was kept subcooled by the PRHR and CMT flows, even after the SGs no longer extracted heat from the RCS. The core temperature distribution is shown in **Fig. 3**. The core was entirely subcooled until ADS came on at 3533 s. (Also, the cold leg break flow was subcooled until that time.) The RCS was thermally decoupled from the SGs after the U-tubes voided completely at ~800 s for SG-A and ~2000 s for SG-B. The asymmetric response of the two SGs resulted from the pressurizer outsurge which flowed into the SG-A primary side and thus fed the SG-A primary side with hotter fluid than SG-B.

The collapsed liquid level distribution in the facility at 3005 s, before ADS actuation, is shown in **Fig. 4**. The steam which filled the upper portions of RCS resulted from flashing; there was no steam production in the core.

The response of the AP600 components in the initial five experiments (from Experiment AP-CL-03 to AP-PB-01) are summarized in the following subsections.

III.3 PRHR RESPONSE

The LSTF represents the two banks of PRHR heat exchanger (HX) tubes in AP600. The tubes are full-size but the number of tubes (45) is scaled. The PRHR energy removal rate, calculated from the flow rate and temperature drop, is compared to the core decay power in **Fig. 5** for Experiment AP-CL-03. The energy removal amounted to 4% core decay power for an inlet

temperature of 550 K; so it exceeded the core decay power soon after scram occurred in the experiment[13]. With other energy sinks (CMTs and break flow) available, the RCS inventory cooled down and depressurized continuously.

After the primary loop natural circulation through the SGs had stopped, the cold PRHR return flow entered the pressure vessel without being mixed with the hot loop flow. This resulted in an accumulation of highly subcooled water in the lower parts of the vessel; the core inlet flow was kept subcooled throughout all the experiments conducted so far, except the double-ended DVI line break experiment (AP-DV-01) in which the core was saturated entirely. Since the core flow was nearly stagnant after the cessation of the loop natural circulation, a strong thermal stratification formed in the core as shown in **Fig. 3** for Experiment AP-CL-03.

After the PRHR inlet flow became two-phase flow, the steam component condensed in the upper horizontal leg of the C-shaped HX tubes. For the 2-inch PBL break case (Experiment AP-PB-01) the PRHR return flow indicated notable fluctuations synchronized with temperature fluctuations in the upper part of HX tubes. The temperature fluctuations were significant for those tubes which opened above the water level in the PRHR inlet plenum. The axial and temporal changes of fluid temperatures inside these tubes suggested that steam condensed not only on the HX tube walls but also on the surface of subcooled water which existed in these tubes as shown in **Fig. 6.**

The HX tubes were filled and inactivated by the nitrogen gas which discharged from the accumulator gas phase, soon after the accumulators became empty of liquid. Significant gas discharge occurred only after the ADS actuation which lowered the system pressure to nearly atmospheric pressures. The HX tube water level dropped to the bottom, as illustrated in **Fig. 7,** as the gas accumulated in the tubes. Since PRHR did not play any important role after ADS actuation, the above nitrogen effect did not affect much the system overall responses.

III.4 CMT RESPONSE

Opening the CMT discharge valve initiated a liquid-phase natural circulation flow in the loop formed by each CMT, PBL, cold leg and downcomer. Hot water from the PBLs replaced the initial cold water inventory of the CMT. This replacement occurred first at the top of each CMT and progressed downward. The axial temperature profiles of the CMT inventory are shown in **Fig. 8** for Experiment AP-CL-03.

The CMT started draining down when saturation was reached at the top of the CMT. The axial temperature profile in the CMT at this time depended on the length of the natural circulation period and the time history of cold leg temperature during the natural circulation. For the simulated 1- and 0.5-inch breaks, the duration of natural circulation was long enough to allow hot water to accumulate above the cold water inventory before the CMT started draining. This hot water inventory continually flashed as the RCS depressurized. The boundaries between the cold, hot and saturated water zones are shown in **Fig. 9** together with the water level. As shown in this figure, one-dimensional calculation based on the measured CMT discharge flow rate was

able to predict the bottom-edge height of the hot zone. This indicate that axial diffusion in the liquid phase was small.
For the larger breaks (2-inch break and inadvertently-open ADS scenarios), the natural circulation was interrupted early in the transient because of the quick depressurization. In these cases, the CMT water surface became subcooled during the late drain-down phase because of heat transfer to the CMT wall which was initially cold. Because the accumulators were discharging nitrogen by this time, this nitrogen accumulated above the water surface in CMTs, preventing the direct-contact condensation of steam on the subcooled water surface from occurring. The axial temperature profile for the inadvertently open ADS scenario (Experiment AP-AD-01[10]), **Fig. 10**, indicates gas phase temperatures significantly lower than the saturation temperature because of high concentration of nitrogen.

III.5 ADS AND IRWST RESPONSE

The ADS stages 1, 2, and 3 valves, all connected to the top of the pressurizer, were opened by the CMT level signal after specified delay times. The discharge through these valves resulted in a quick system depressurization, as shown in **Fig. 2** for Experiment AP-CL-03, and a liquid holdup in the pressurizer, as shown in **Fig. 7**. The increase in the accumulator flow during the depressurization interrupted the CMT discharge flow, since these two flows entered the same line (DVI line) connected to the vessel downcomer.

The opening of ADS moved the hot water inventory in the upper plenum into the pressurizer surge line. The cold leg inventory flashed as shown in the coolant inventory distribution, **Fig. 7**, and forced the cold water in the vessel lower portions into the core as can be seen in the core temperature profile, **Fig. 3**. Since this cold water was brought into contact with steam in the upper portions of the RCS, causing direct-contact condensation of steam, oscillatory changes in core differential pressure were recorded in Experiments AP-CL-03 and AP-CL-04; however, the core inventory was entirely subcooled during such oscillations, and thus there was no problem in the core cooling capability.

The injection from the IRWST initiated only after the ADS stage-4 valves, connected to the hot legs, had opened. The injection flow was initially oscillatory. The flow oscillations were coupled with changes in the pressurizer and hot leg water levels, the ADS stage-4 flows, the vessel pressure and the core steaming rate. The pressurizer level and IRWST flow rate are plotted in **Fig .11** for Experiment AP-CL-03[8]. The flow became steady after the pressurizer had emptied.

IV. CONCLUDING REMARKS

The ROSA/AP600 testing program have conducted seven high-pressure integral experiments on AP600 reactor response to postulated LOCA scenarios. In all these experiments, adequate core cooling was maintained and the RCS depressurized automatically to such a level as allowing continuous injection from IRWST driven by gravity alone.

The PRHR indicated a high cooling capability and created significant subcoolings in the RCS

liquid phase. The subcooling in the cold leg affected the CMT drain-down behavior. Also, the significant subcooling in the vessel lower portions caused a potential for direct-contact condensation when the hotter water beneath the steam-water interface was taken away by ADS.

The nitrogen discharged from the accumulator gas phase blocked the PRHR HX tubes, but only after ADS was actuated. The gas also limited the condensation in CMTs which occurred for relatively-large breaks, and thereby stabilized the CMT drain-down behavior.

Future experiments in the ROSA/AP600 testing program will include simulations of station blackout, multiple SGTR and main steam line break scenarios. Currently, it is planned to conduct a total of 14 experiments by June 1995.

V. REFERENCES

[1] Shaw, R.A., et al., "Quick Look Report for ROSA/AP600 Experiment AP-CL-02," JAERI unpublished report (Aug. 1994).

[2] ROSA-IV Group, "ROSA-IV Large Scale Test Facility (LSTF) System Description for the Second Simulated Fuel Assembly," JAERI-M 90-176 (Oct. 1990).

[3] Ortiz, M.G., et al., "Investigation of the Applicability and Limitations of the ROSA Large Scale Test Facility for AP600 Safety Assessment," NUREG/CR-5853, EGG-2670 (1992).

[4] Kukita, Y., Yonomoto, T. and Anoda, Y, "ROSA-AP600 Program; Confirmatory Testing of AP600 Design at the ROSA-V Large Scale Test Facility," Proc. 20th Water Reactor Safety Information Meeting, Bethesda, MD, Oct. 21-23, 1992.

[5] Yonomoto, T., Kukita, Y. and Anoda, Y., "Passive Safety Injection Experiment at the ROSA-V Large Scale Test Facility," Proc. 1993 National Heat Transfer Conf., Atlanta, Aug. 8-11, 1993.

[6] Yonomoto, T. et al., "Passive Safety Injection Experiments with a Large-Scale PWR Simulator," Proc. Int. Topical Mtg. Advanced Reactor Safety (ARS'94), Pittsburgh, Apr. 17-21, 1994.

[7] Rhee, G.S., Bessette, D.E. and Shotkin, L.M., "NRC Confirmatory Safety System Testing in Support of AP600 Design Review," Proc. Int. Topical Mtg. Advanced Reactor Safety (ARS'94), Pittsburgh, Apr. 17-21, 1994.

[8] Shaw, R.A., Yonomoto, T. and Kukita, Y., "Quick Look Report for ROSA/AP600 Experiment AP-CL-03," JAERI unpublished report (Oct.. 1994).

[9] Nakamura, H., Shaw, R.A. and Kukita, Y., "Quick Look Report for ROSA/AP600 Experiment AP-AD-01 (Draft)" (Aug. 1994).

[10] Kumamaru, H., Kukita, Y. and Shaw, R.A., "Quick Look Report for ROSA/AP600 Experiment AP-CL-04 (Draft)" (Oct. 1994)

[11] Anoda, Y., et al., "Quick Look Report for ROSA/AP600 Experiment AP-PB-01 (Draft)" (Oct. 1994).

[12] Schultz, R.R. et al., "ROSA-AP600 Characterization Tests and Analysis of 1-Inch Cold Leg Break Test," to be presented at the 22nd Water Reactor Safety Inf. Mtg., Bethesda, MD., Oct. 24-26, 1994.

[13] Yonomoto, T., Shaw, R.A., and Kukita, Y., "Cold Leg 1-Inch Break LOCA Experiment for the ROSA-AP600 Project," submitted for presentation at the 3rd JSME-ASME Int. Conf. on Nuclear Engineering (ICONE-3), Kyoto, Apr. 23-27, 1995.

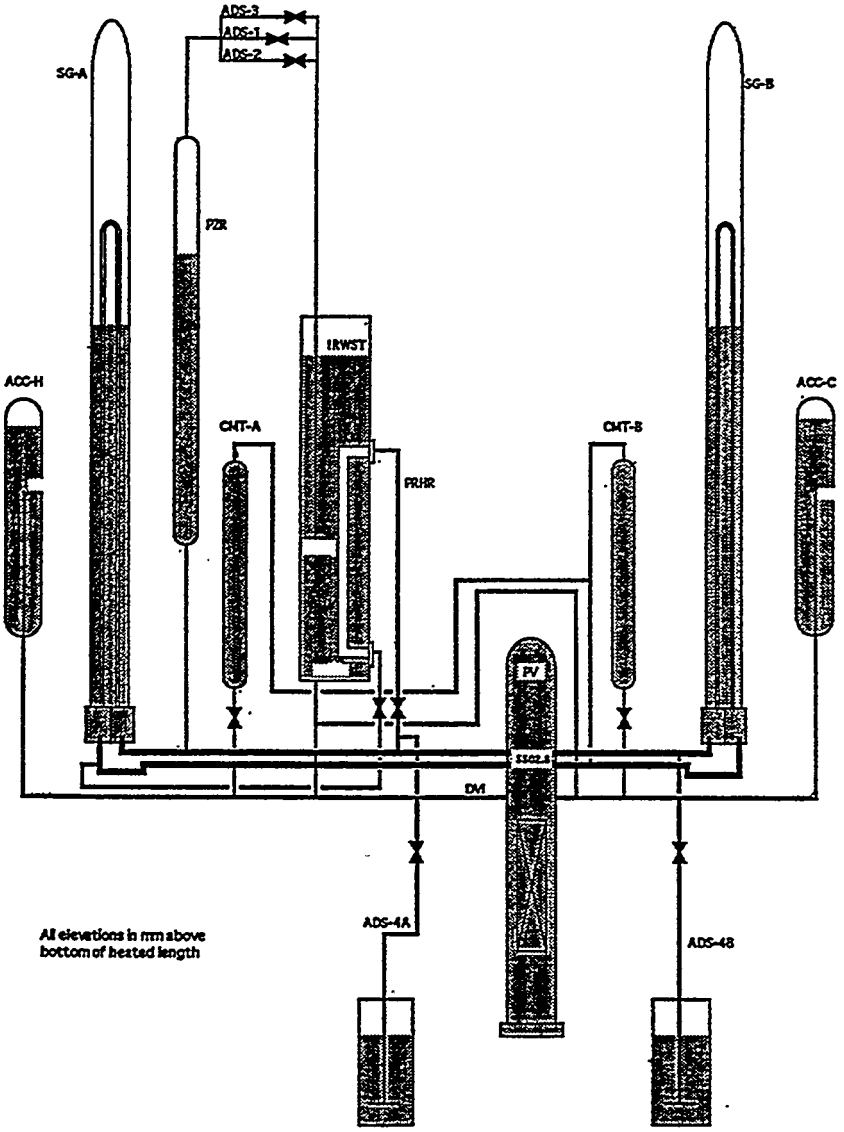

Fig. 1 Schematic of LSTF in ROSA/AP600 Configuration

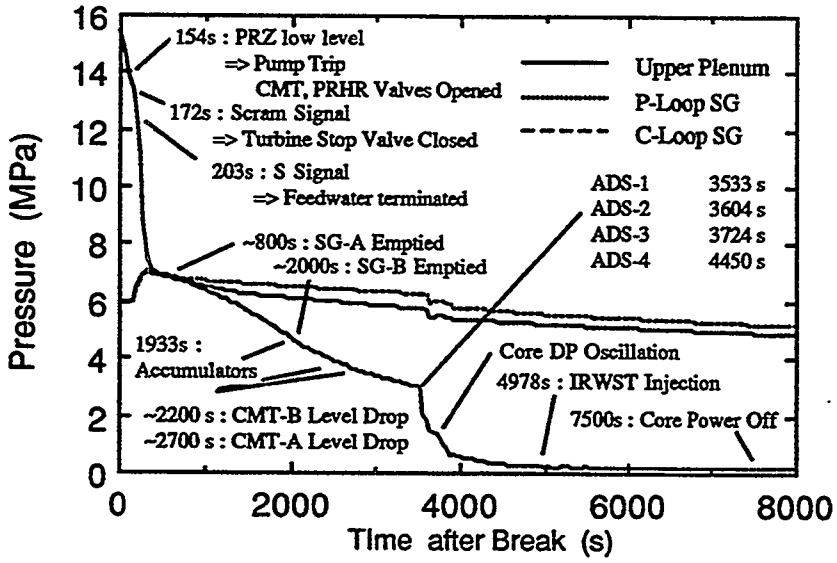

Fig. 2 RCS and SG Secondary Side Pressures during Experiment AP-CL-03 with Timings of Major Events.

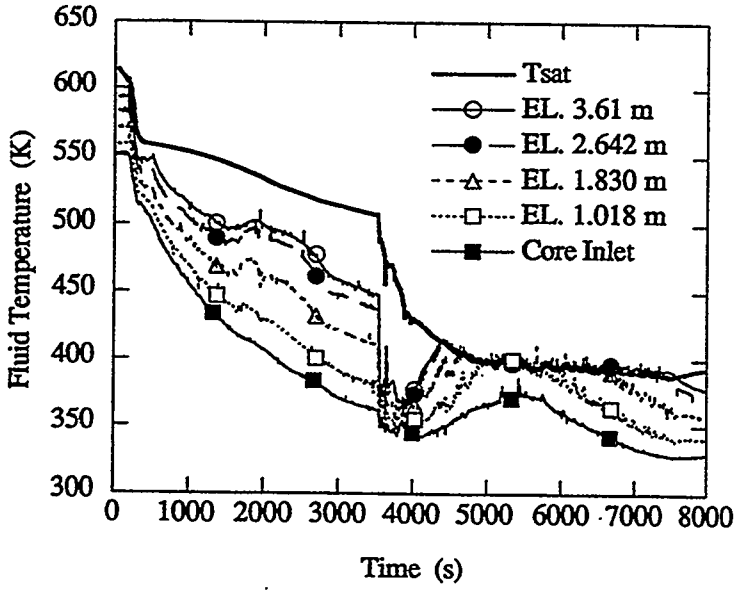

Fig. 3 Core Fluid Temperature Distribution during Experiment AP-CL-03 (EL = Height above the Bottom of Core Heated Length in m)

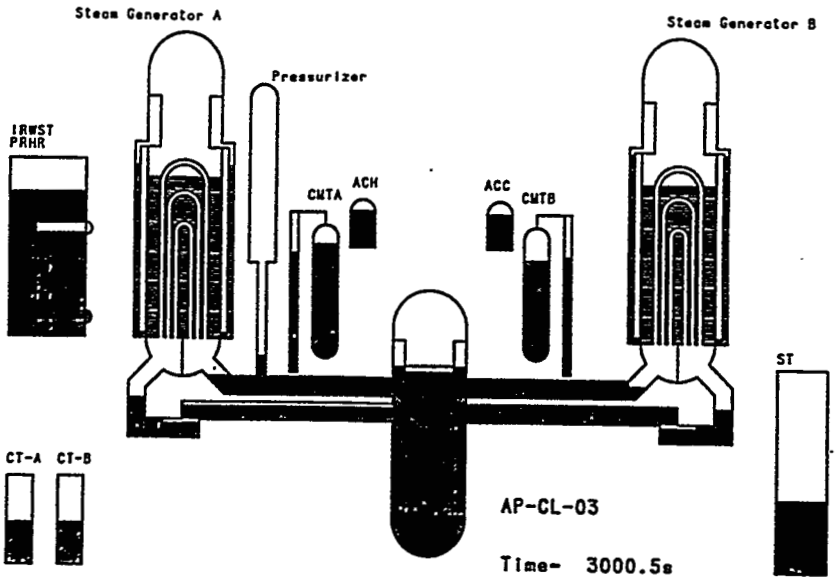

Fig. 4 Collapsed Liquid Level Distribution at 3005 s after Break (before ADS Actuation) in Experiment AP-CL-03

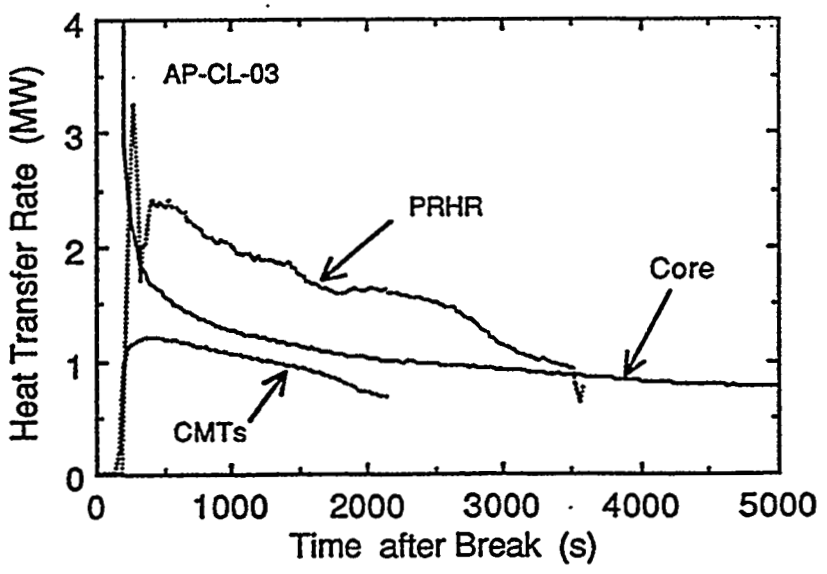

Fig. 5 Energy Removal Rates of PRHR and CMTs Compared to the Core Decay Power during Experiment AP-CL-03[13].

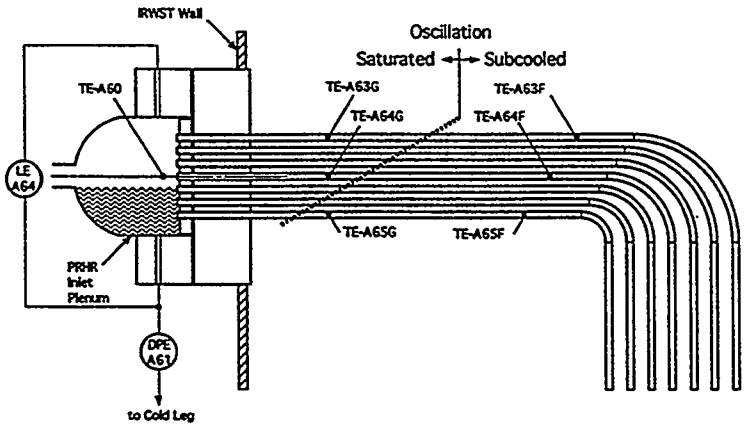

Fig. 6 PRHR Two-Phase Flow Oscillations Observed in Experiment AP-PB-01[11].

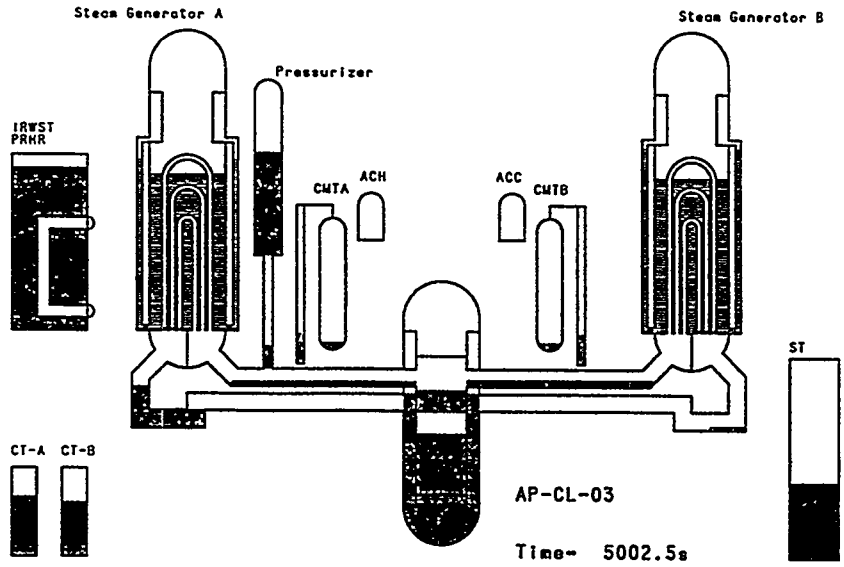

Fig. 7 Collapsed Liquid Level Distribution at 5000 s after break (after ADS Actuation) in Experiment AP-CL-03.

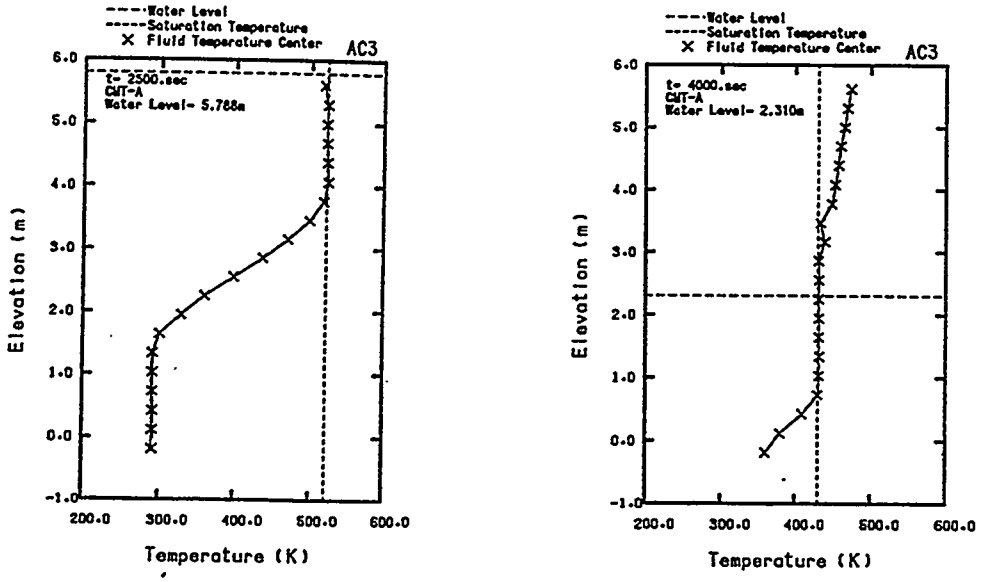

Fig. 8 Axial Distribution of CMT Fluid Temperature in Experiment AP-CL-03.

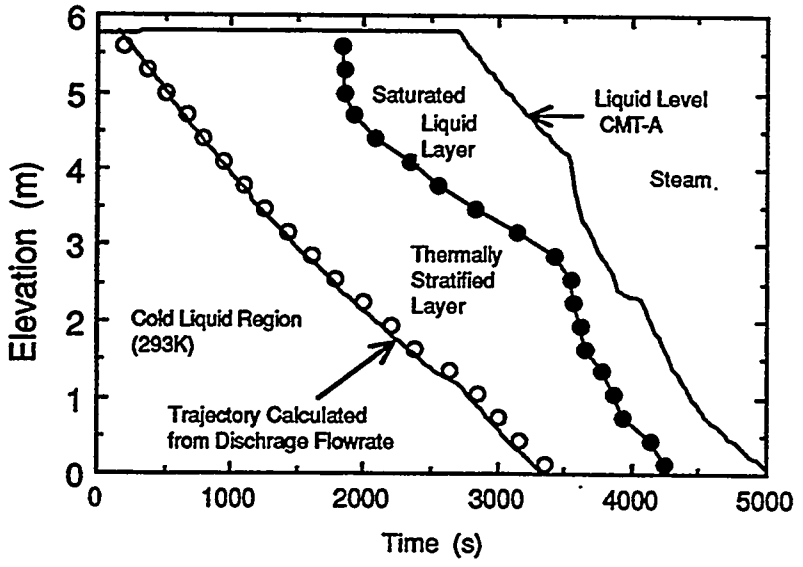

Fig. 9 Elevations of Boundaries between Steam, Saturated, Hot and Cold Water in CMT during Experiment AP-CL-03[13].

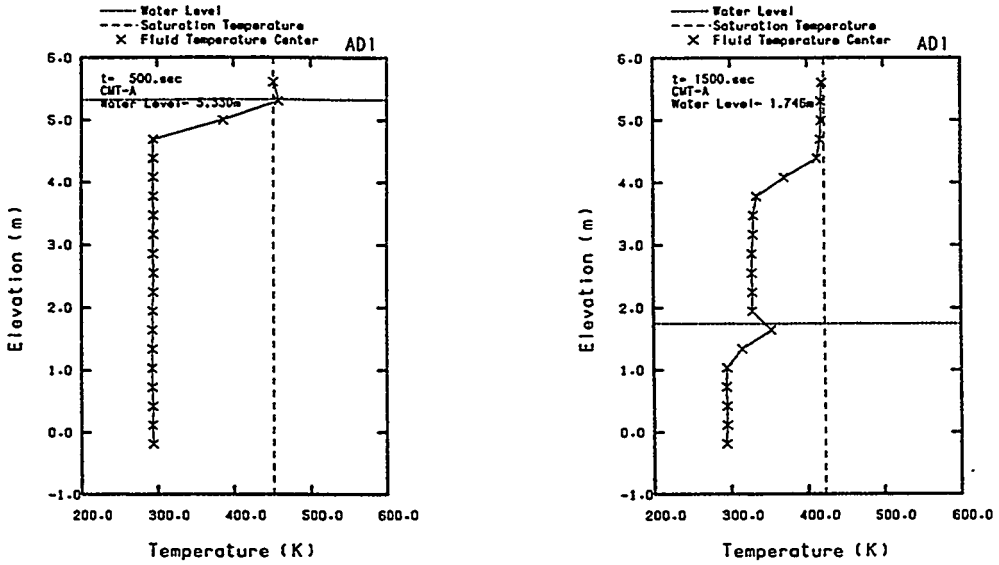

Fig. 10 Axial Distribution of CMT Fluid Temperature in Experiment AP-AD-01.

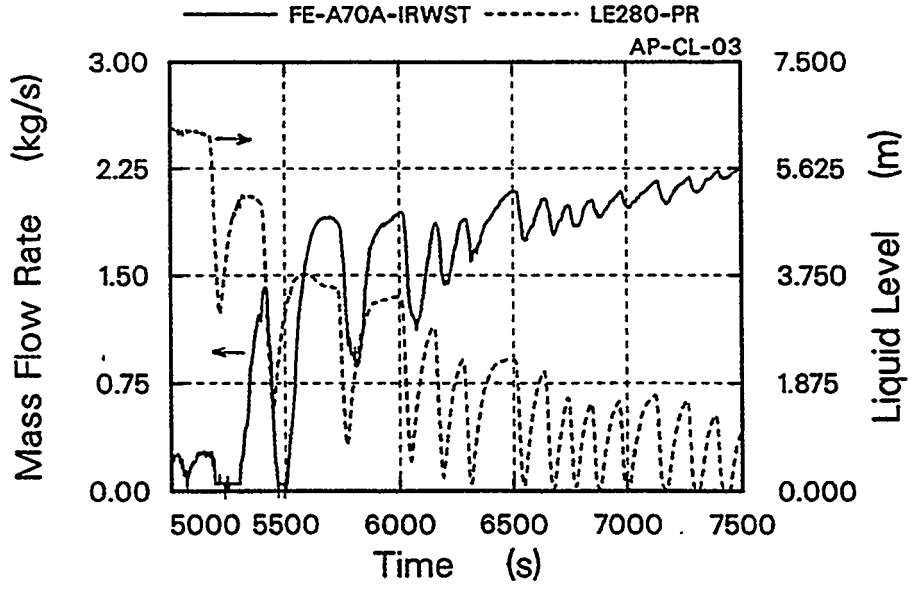

Fig. 11 Coupled Fluctuations of IRWST Flow (Solid Line) and Pressurizer Collapsed Liquid (Dotted Line) in Experiment AP-CL-03[8].

ROSA/AP600 Characterization Tests and Analysis of 1-Inch Cold Leg Break Test

R.R. Schultz, J.M. Cozzuol, R.A. Shaw
Idaho National Engineering Laboratory

T. Yonomoto, Y. Kukita
Japan Atomic Energy Research Institute

ABSTRACT

The United States Nuclear Regulatory Commission (USNRC) and the Japan Atomic Energy Research Institute (JAERI) are jointly performing tests at the ROSA-AP600 facility located in Tokai, Japan. The first test, a simulation of a 1-inch break, oriented downward and located in one of the cold legs, was performed in April, 1994. The paper discusses and summarizes the important results of the test and shows a comparison between a calculation performed using the RELAP5/MOD3 code and the data. The calculational results show reasonable agreement with the data.

INTRODUCTION

In response to a request for certification of Westinghouse Electric Co's new advanced passive 600 MWe nuclear plant design (AP600), the U.S. Nuclear Regulatory Commission (USNRC) recently initiated testing at the 1/30.5-volume scaled ROSA-AP600 Facility in Tokai, Japan. The cooperative test effort is being conducted using the help and expertise of the Japan Atomic Energy Research Institute (JAERI). The facility, located on the JAERI campus in Tokai, Japan, has all the passive-safety system components inherent to the AP600-system and was designed to study all phases of the AP600 transients of interest.

The first test, performed in April, 1994, was a simulation of a 1-inch downward-oriented break in one of the cold legs of the AP600 system. This test was performed to: (i) generate code assessment data and (ii) study the behavior of the ROSA-AP600 system during a small break loss-of-coolant accident (SBLOCA) scenario. Even though the test was performed only a few days after Westinghouse announced major changes to the AP600 design (for example, elimination of the pressurizer pressure balance lines and various important modifications to the passive safety system initiation logic) all the announced changes were included in the ROSA-AP600 facility. In fact, the test (labeled AP-CL-03) generated the first data from an integral-effects system subsequent to the Westinghouse hardware/system logic modifications.

The test was a success and has formed the basis for performing subsequent tests with other size breaks placed in other locations. The following paragraphs describe: (i) the facility and test procedures, (ii) the thermal-hydraulic behavior occurring in the test together with a comparison to the RELAP5/MOD3 calculation, and (iii) conclusions.

ROSA-AP600 FACILITY & TEST PROCEDURES

The ROSA-AP600 Program tests are being performed in a full-height 1/30.5-volume scaled facility (see Fig. 1). All the passive-safety systems and other AP600-specific systems included in the AP600 plant are contained in the ROSA-AP600 facility, viz.: the automatic depressurization system (ADS), the core makeup tanks (CMTs), the passive residual heat removal system (PRHR), the in-containment refueling water storage tank (IRWST), and the accumulators.

One of the first activities undertaken by the ROSA-AP600 experimentalists was designed to measure the loss coefficients and friction factors of the facility hardware. Since the flow rates and flow distribution in the AP600 system are governed by fluid density gradients in large measure, the facility was designed to have resistances equivalent to those in the AP600 plant. The systems characterization tests provided data for direct comparison with the design specifications. Comparisons between the design specifications and the measured data from the systems characterization tests showed the facility to have acceptable flow resistance characteristics.

The 1-inch cold leg break test was performed by first achieving a steady-state at ROSA-AP600 rated conditions. The transient was begun at time zero by opening the break valve.

THE 1-INCH COLD LEG BREAK TRANSIENT

The 1-inch cold leg break transient was begun at time zero by opening the break in the cold leg. The break nozzle had a throat diameter of 4.6 mm and was oriented downward.

Three distinct phases were noted during the transient (see Fig. 2): the high pressure phase, the ADS phase, and the long-term cooling phase. The time of transition from one phase to the next is given in Table 1.

Table 1: Time of Transition From One Phase to Next

Phase=¢ Test or Calculation	High Pressure to ADS Blowdown	ADS Blowdown to Long Term Cooling
Test	3425.	4375.
Calculation	4100.	5050.

High Pressure Phase

The high pressure phase began at time zero and ended when the ADS opened. The phase was characterized by the following behavior and phenomena:

i. A rapid depressurization over the first 380 s (475 s for calculation) from 15.5 MPa to the secondary pressure level, followed by a moderate depressurization lasting until ADS actuation;

ii. Formation of large regions of subcooling in the primary caused by the action of the PRHR and CMT recirculation. In particular, the core remained subcooled throughout its length for the high pressure phase;

iii. Formation of fluid zones with large thermal gradients (in excess of 170 K in the cold leg fed by the PRHR and in excess of 90 K across the core);

iv. A net decrease in primary energy as the PRHR energy removal and CMT energy removal exceeded the core power input;

v. Subcooled break flow;

vi. Accumulator discharge began (the primary pressure was less than 4.9 MPa).

The behavior and the effect of the phenomena summarized in items i through vi are shown in Figs. 2 through 8 for the test data and the RELAP5/MOD3 calculation.

The depressurization phase between time zero and about 230 s, observed in the test, occurred as the pressurizer drained (see Fig. 2) and energy was transferred from the primary to the secondary. Shortly thereafter the primary briefly equilibrated with the secondary system and secondary to primary energy transfer began. Even so the continuous draining stemming from the break and the heat removal to (a) the IRWST from the PRHR and (b) the CMTs (both beginning at about 165 s) resulted in a continuation of the primary depressurization until ADS was initiated, but at a reduced rate. Similar behavior was shown in the calculation but with events occurring at slightly different times due to different (with respect to the data), but reasonably close, recirculation flow rates and break flows.

The PRHR, using the IRWST as its heat sink, proved to be a remarkably effective means of removing energy from the primary system. Comparisons between the calculated and measured PRHR inlet and outlet temperatures are shown in Fig. 3. Initially the PRHR cooled the incoming fluid in excess of 235 K (the initial

calculated cooling was approximately 15 K less than measured). As the transient proceeded the PRHR inlet fluid temperature decreased together with the primary pressure. However the PRHR outlet temperature remained at a relatively constant value just slightly above the IRWST secondary fluid temperature at the lower elevation of the PRHR heat exchanger tubes.

The effectiveness of the PRHR (and the CMTs) can be seen by comparing the total integrated energy removed by the PRHR compared to the integrated core power. The integrated energy removal by the PRHR and the CMTs versus the integrated energy addition from the core beginning at the initiation time for the PRHR and CMT systems are shown in Fig. 4. Shortly after 1000 s the PRHR system began to remove more energy than was added to the primary from the core. Thus considering the CMTs together with the PRHR it is evident the PRHR and CMT systems were important contributors in the primary system depressurization prior to actuation of the ADS.

As the PRHR effluent moved into the ROSA-AP600 crossover leg (A-Loop) it mixed with the A-Loop loop flow moving through the crossover leg enroute to the A-Loop cold leg and thence into the vessel (see Fig. 1). The resulting mixture entered the pressure vessel downcomer 5.5 m above the core inlet elevation. The PRHR effluent combined with the CMT discharge, entering the downcomer from the direct vessel injection (DVI) lines, moved to the vessel lower plenum and from thence to the core inlet. The action of the combined CMT and PRHR effluent can be easily seen by viewing the temperature decrease measured and calculated at the core inlet and shown in Fig. 5. As the transient proceeded the core inlet subcooling increased.

Although natural circulation-driven loop flow was present in both loops at the start of the transient, the measured loop flows were not sustained beyond 400 s and 1750 s in the A-Loop and B-Loop piping respectively (500 s and 1700 s respectively in the calculation). Termination of A-Loop loop natural circulation is apparent by studying the measured and calculated core inlet temperature (see Fig. 5) and occurred as a significant portion of the A-Loop loop flow began to circulate through the PRHR instead of the U-tubes. Termination of A-Loop natural circulation-driven loop flow resulted in a more rapidly decreasing core inlet temperature (at 410 s for data and 600 s for calculation). Termination of B-Loop loop natural circulation is apparent by the indicated increase in the core exit temperature shown in Fig. 5 (1720 s for data and 1770 s for calculation) and the sudden downturn of the fluid temperature at the pressure balance line (PBL) inlet (see Fig. 6--1700 s for data and 1720 s for calculation).

The increase in core exit temperature and corresponding decrease in PBL inlet temperature were caused by a shift in the pressure vessel downcomer flow distribution triggered by termination of the B-Loop natural circulation. Once

flow from the B-Loop cold leg to the downcomer decreased sufficiently, the very subcooled fluid present in the downcomer (from the PRHR and CMT systems) began to move into the B-Loop cold leg toward both the break plane and the PBL inlet. Concurrently the core flow decreased, the core fluid residence time increased, and the core exit temperature increased.

Of particular significance is the termination of natural circulation-driven loop flow in the B-Loop. Prior to termination the flow moving into the PBL and thus transported to the CMTs was fluid circulated through the steam generator U-tubes. The PBL fluid was near saturation prior to termination of loop flow natural circulation. However, after natural circulation-driven loop flow ceased, the PBL fluid became increasingly subcooled (see Fig. 6). By 2800 s the measured PBL flow subcooling was 38 K (83 K subcooling in calculation).

Following termination of B-Loop natural circulation-driven loop flow but before reaching maximum subcooling of the PBL inlet flow, the primary pressure was decreased sufficiently by energy removal through the break, the PRHR system, and the CMT systems that the accumulator injection pressure was achieved. Accumulator injection began at 1934 s in the test and at 2050 s in the calculation.

Throughout the high pressure phase, following opening of the CMT isolation valve, the CMT fluid temperatures (from top to bottom of the tank) showed the history of the fluid fed to the CMTs through the PBLs (see Fig. 7). Recirculation through the CMTs began immediately after the isolation valve opened. The temperature at the 5.3 m (above the bottom of the CMT) rapidly increased indicating the arrival of cold leg fluid. Similar behavior is shown in the calculation. The arrival of warm fluid at each elevation is indicated by a rapid increase in the temperature by the resident thermocouples. The calculation indicates a more gentle increase in temperature at each elevation and by an earlier indication of a temperature increase at lower elevations due to numerical diffusion. Physical fluid thermal stratification cannot be properly modelled by the code without a special model designed specifically to simulate such behavior (currently being developed).

Termination of CMT recirculation and the beginning of draining in both CMTs occurred due to flashing in the fluid near the top of the CMTs. Draining began in the test at 2200 s in the B-Loop CMT (see Fig. 8) followed by the A-Loop CMT at ~2700 s (the CMTs were calculated to begin draining shortly thereafter: ~2900 s). The automatic depressurization system (ADS) Stage 1 signal was generated when the 67.5% volumetric level was reached (3425 s and 4100 s in the test and calculation respectively). Thus ended the high pressure phase.

ADS Phase

The ADS phase began when the Stage 1 valve opened and ended when the ADS Stage 4 valves opened. The phase was characterized by the following behavior and phenomena:

vii. A rapid depressurization of the primary system occurred as each successive ADS stage opened;

viii. The pressurizer filled and became liquid solid;

ix. Fluid discharge from the accumulators and the CMTs rapidly increased;

x. The fluid in the upper reaches of the core became saturated.

xi. The break flow became saturated;

xii. Flashing occurred in various regions in the primary;

xiii. Condensation occurred in various regions of the primary (even while other local regions flashed as noted in item xii) as steam (in some cases superheated) came in contact with subcooled liquid;

xiv. The accumulators were fully discharged and nitrogen from the accumulator gas volumes entered the primary system;

xv. The PRHR became ineffective.

The rapid primary system depressurization during the ADS phase is shown in Fig. 9. Over a 500 s time interval the measured primary pressure decreased 2.7 MPa (calculated primary pressure decreased ~1.7 MPa in 300 s). The measured and calculated primary depressurization rates were similar (see Fig. 9--following opening of the ADS).

The pressurizer filled by 3825 s (4650 s in calculation) (see Fig. 10). Thus the ADS discharge varied from being single-phase steam (when ADS Stage 1 opened) to single-phase liquid (when the pressurizer became liquid solid).

As the ADS blowdown continued and the CMTs drained sufficient volume was lost from the CMTs to trigger ADS Stage 4 (see Fig. 8: at 4375 s for test and 5050 s for calculation).

Long-Term Cooling

Initial behavior of the system during the long-term cooling phase transient phase is shown in Figs. 11 through 14. The long-term cooling phase began when the Stage 4 valves opened and continued to the end of the transient. The phase was characterized by the following behavior and phenomena:

xvi. The CMTs emptied;

xvii. A slow primary depressurization continued;

xviii. The primary pressure decreased to less than hydrostatic driving head of IRWST. Gravity-driven IRWST flow commenced;

xix. A slow primary system oscillation developed with slow decreases in pressurizer level balanced with rises in the downcomer liquid level, rises in core inventory average temperature level, rises in the primary pressure level, and corresponding decreases in IRWST flow rate;

xx. As flow from the IRWST increased the degree of core subcooling and the subcooled fraction of the core increased.

The criteria for terminating the test was continuous flow from the IRWST. The test was terminated at 7527 s after it was confirmed continuous IRWST injection was achieved.

The character of the long-term cooling phase for the test (see Figs. 11 and 13) and the calculation (see Figs. 12 and 14) can be seen by studying the behavior of the pressurizer level, the downcomer liquid level, the mid-core fluid temperature, the upper plenum pressure, and the IRWST mass flow rate.

After the ADS Stage 4 valves opened, the primary system fluid level began to decrease as ADS Stage 4 effluent was discharged from the hot legs. By 4975 s (5910 s in the calculation) IRWST injection began. As the pressurizer level decreased corresponding increases in the downcomer liquid level and the upper plenum pressure can be observed. Coupled with the downcomer liquid level increase was a calculated flow reversal in the core region--resulting in a net average core inventory temperature increase, an increased core steaming rate and a corresponding increase in primary system pressure. The IRWST mass flow rate increased with an increase in primary pressure.

CONCLUSIONS AND OBSERVATIONS

The test data, discussed in the paragraphs above, give some insights into the expected behavior and effects of the passive safety systems inherent to the ROSA-AP600 facility:

1. *The core remained covered throughout the 1-inch cold leg break simulation and remained subcooled for most of the transient.*

2. *The PRHR system played a key role in the transient progression.* From the time of the S-signal (when the PRHR isolation valve was opened) until the ADS was initiated, the core was very subcooled.

3. *Once IRWST flow was initiated the degree of core subcooling and the subcooled fraction of the core increased.* Even though the test was terminated before equilibrium was reached it is expected the core would ultimately be fully subcooled.

Throughout the transient the code did a good job of calculating the event chronology and phenomena.

Figure 1. ROSA AP600 Facility

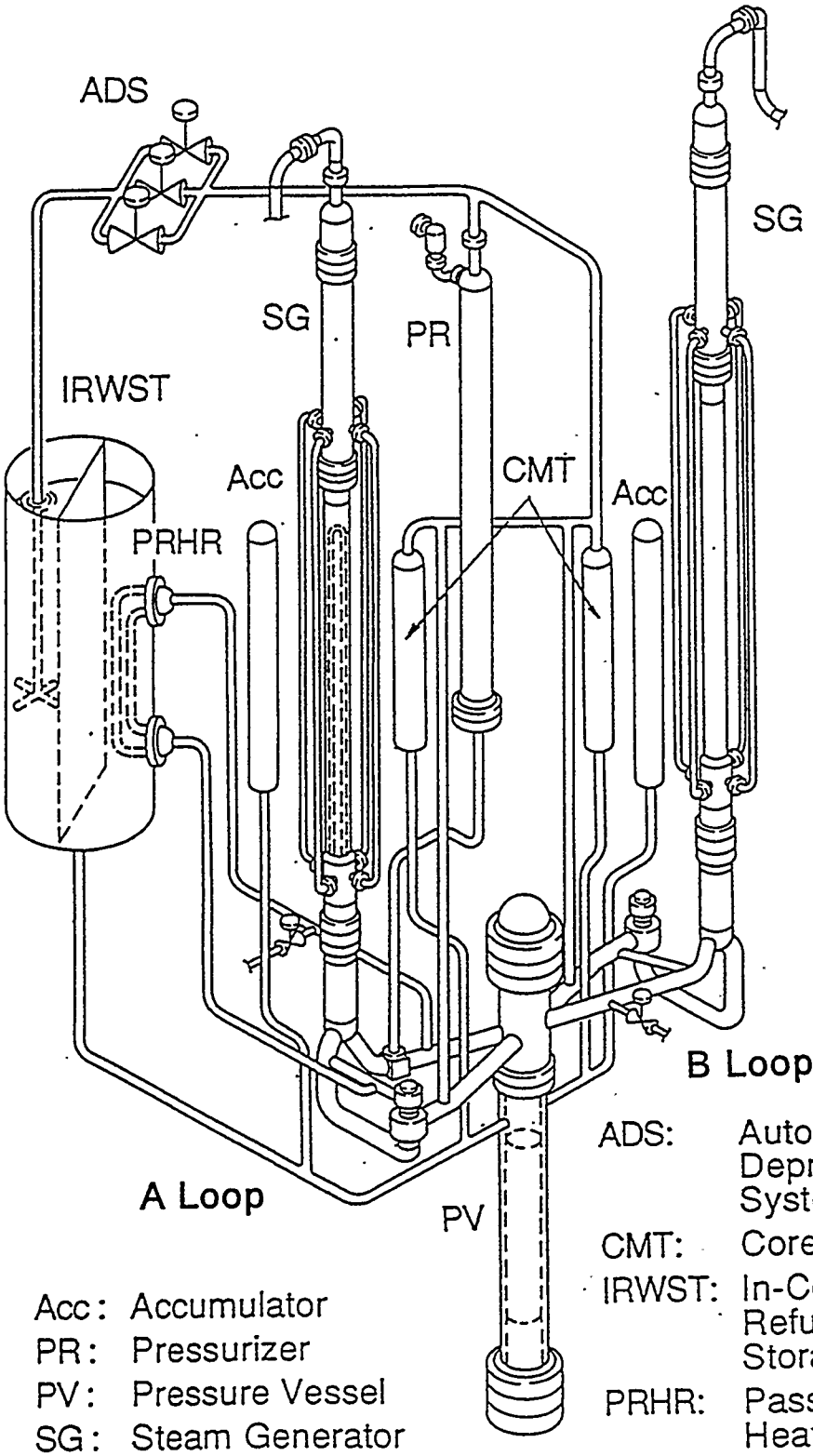

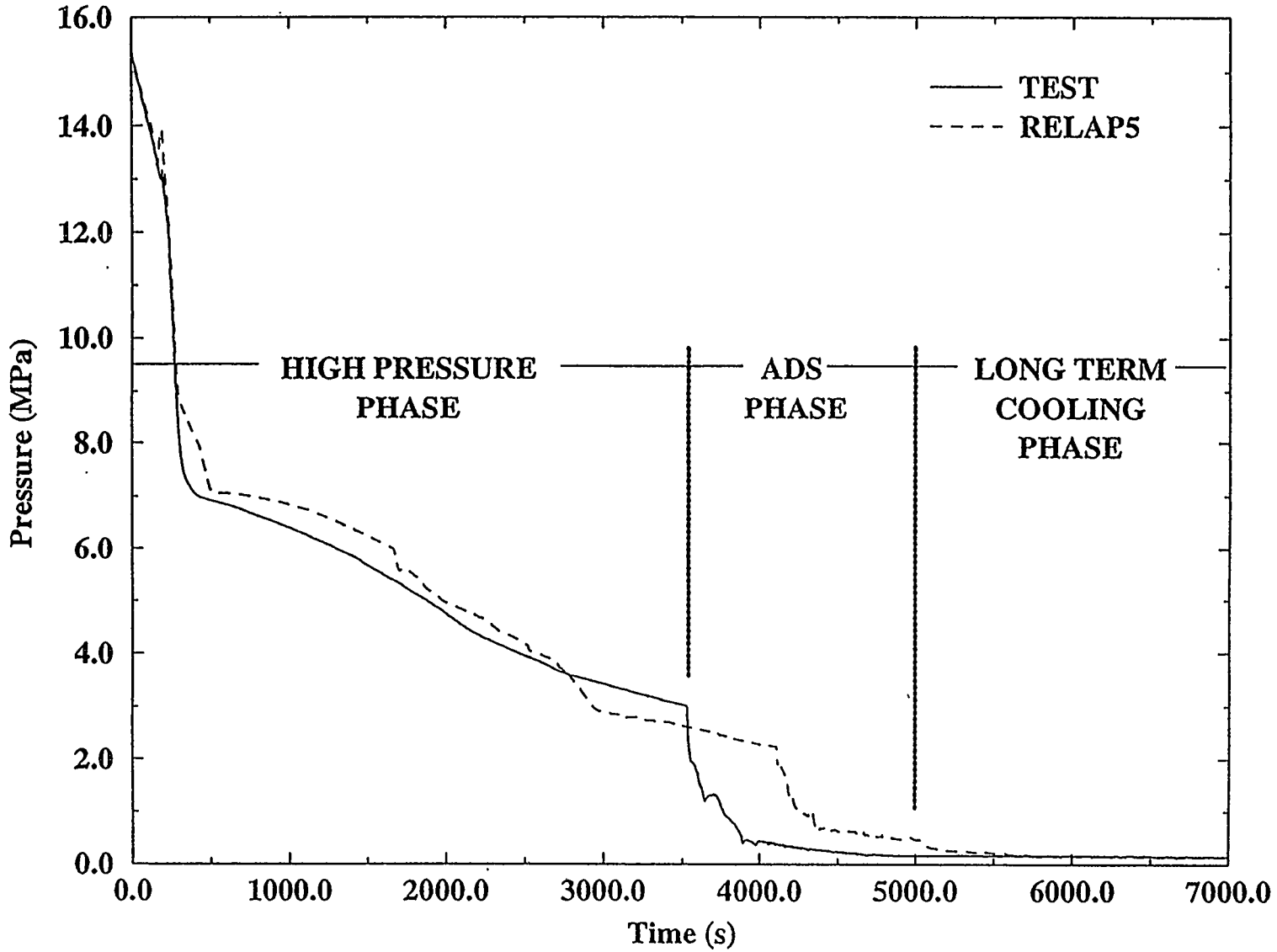

Figure 2. Comparison of calculated and measured primary pressure

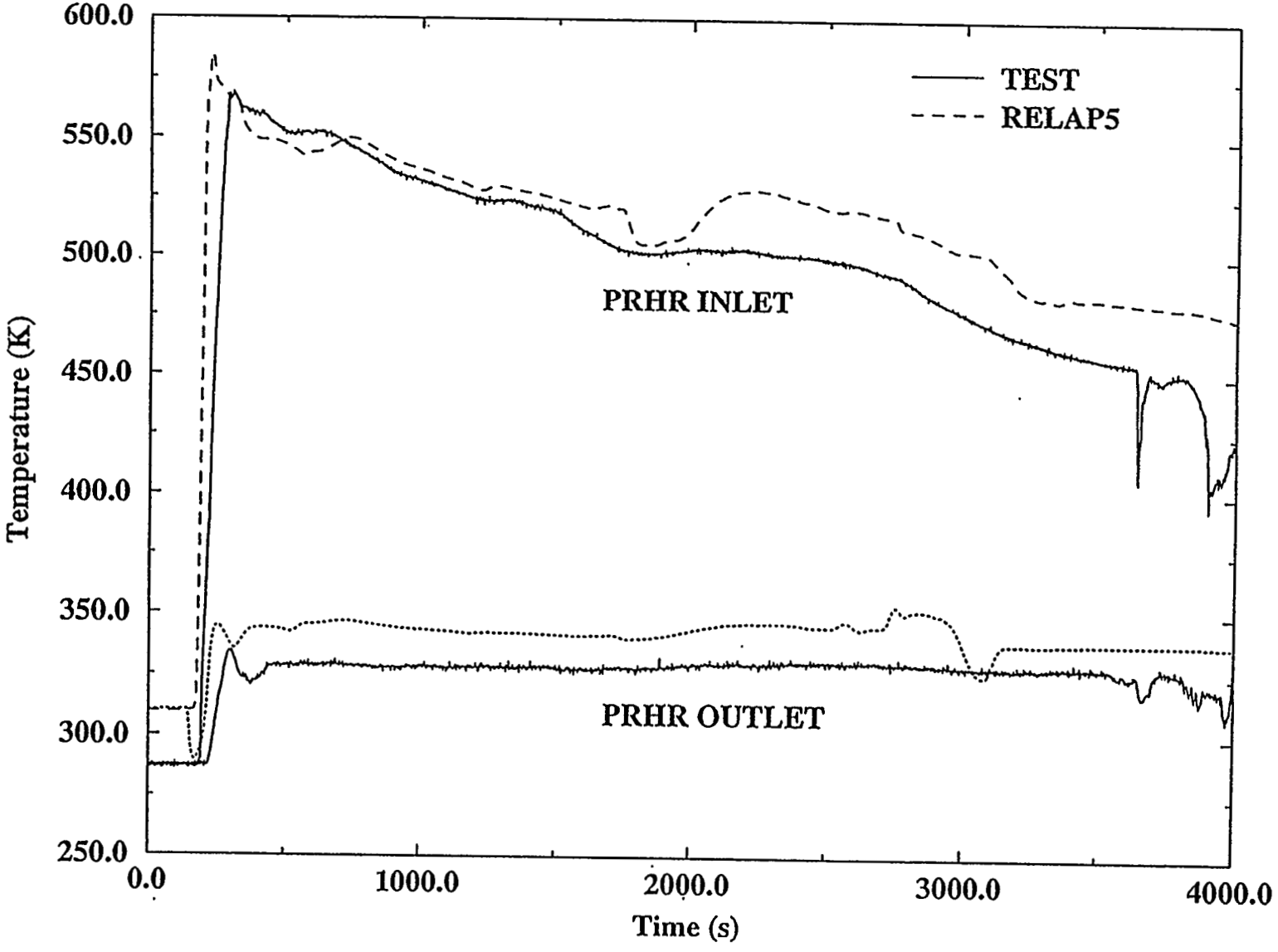

Figure 3. Comparison of calculated and measured PRHR inlet and outlet temperatures

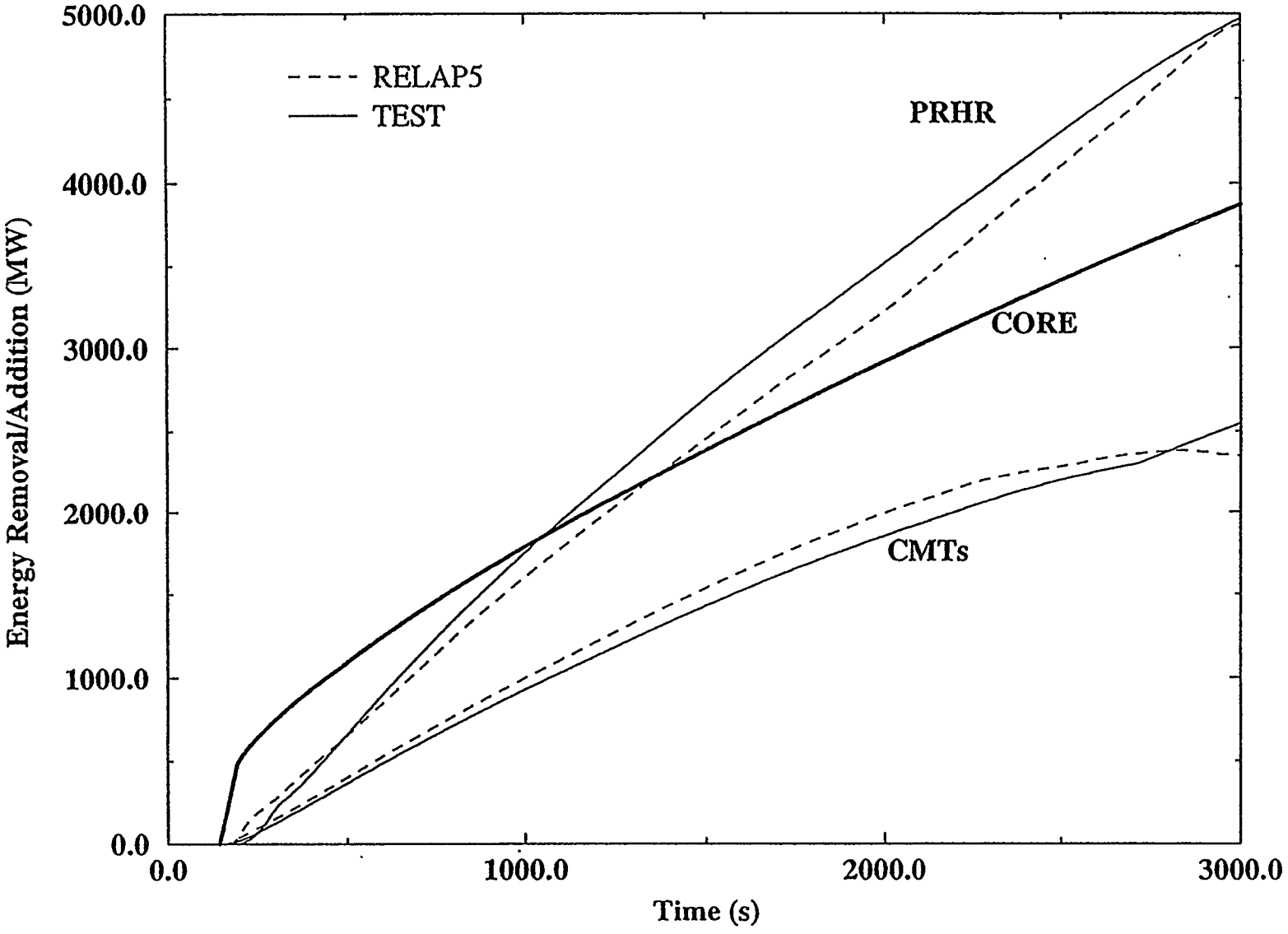

Figure 4. Comparison of calculated and measured integrated energy removed by PRHR and CMTs to core energy addition

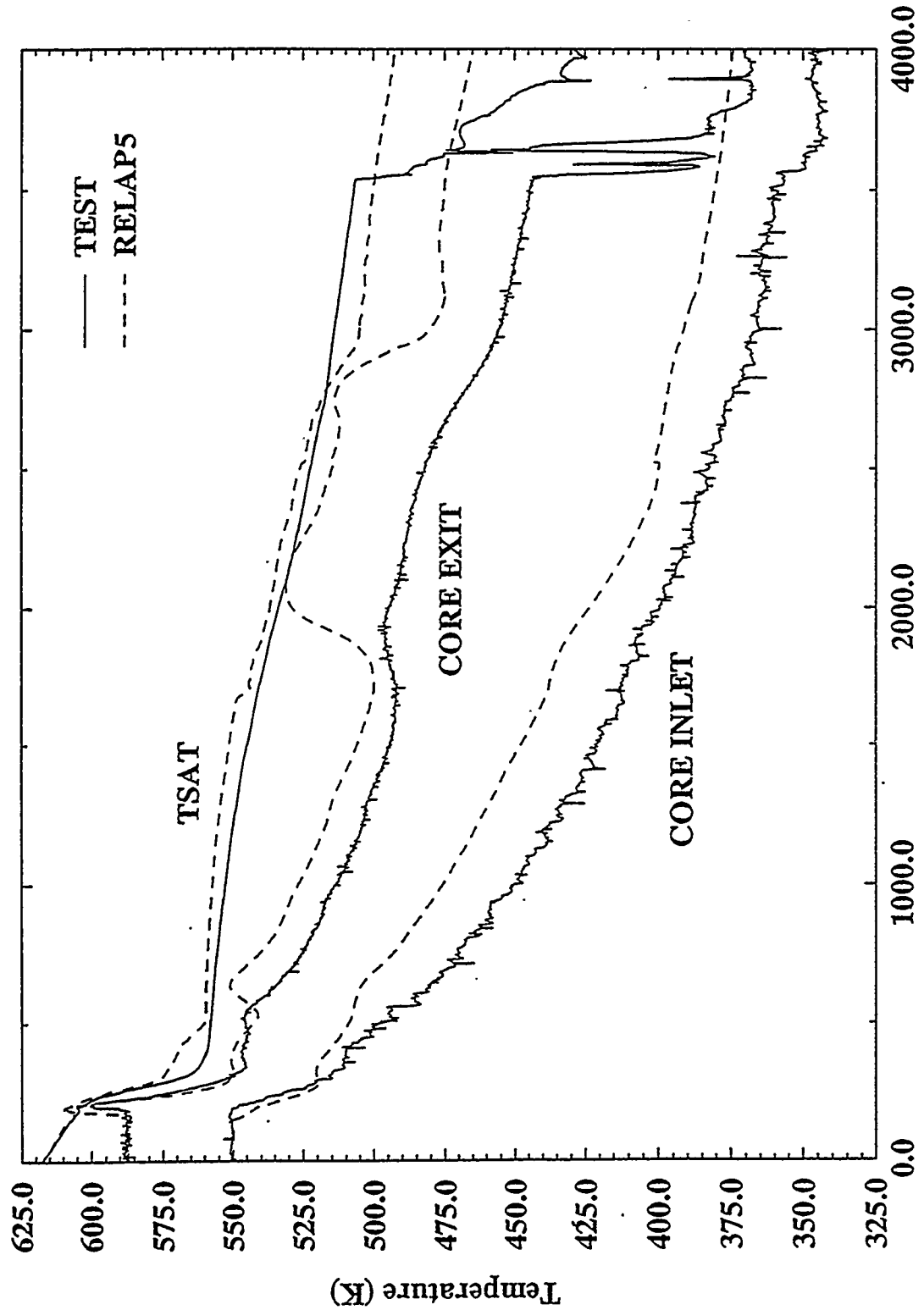

Figure 5. Comparison of calculated and measured core inlet and exit temperatures to saturation temperature

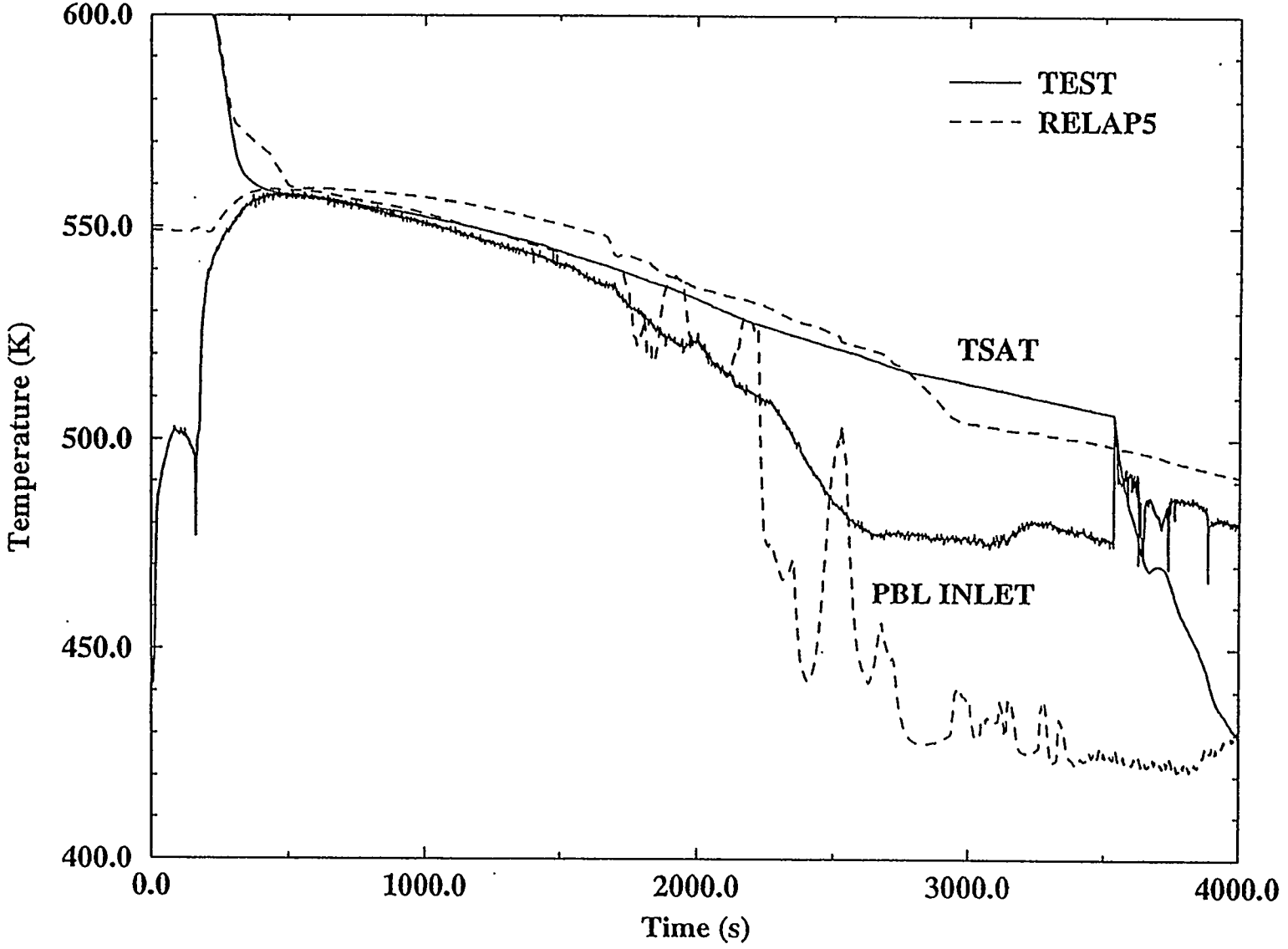

Figure 6. Comparison of calculated and measured fluid temperatures at PBL inlet to saturation temperature

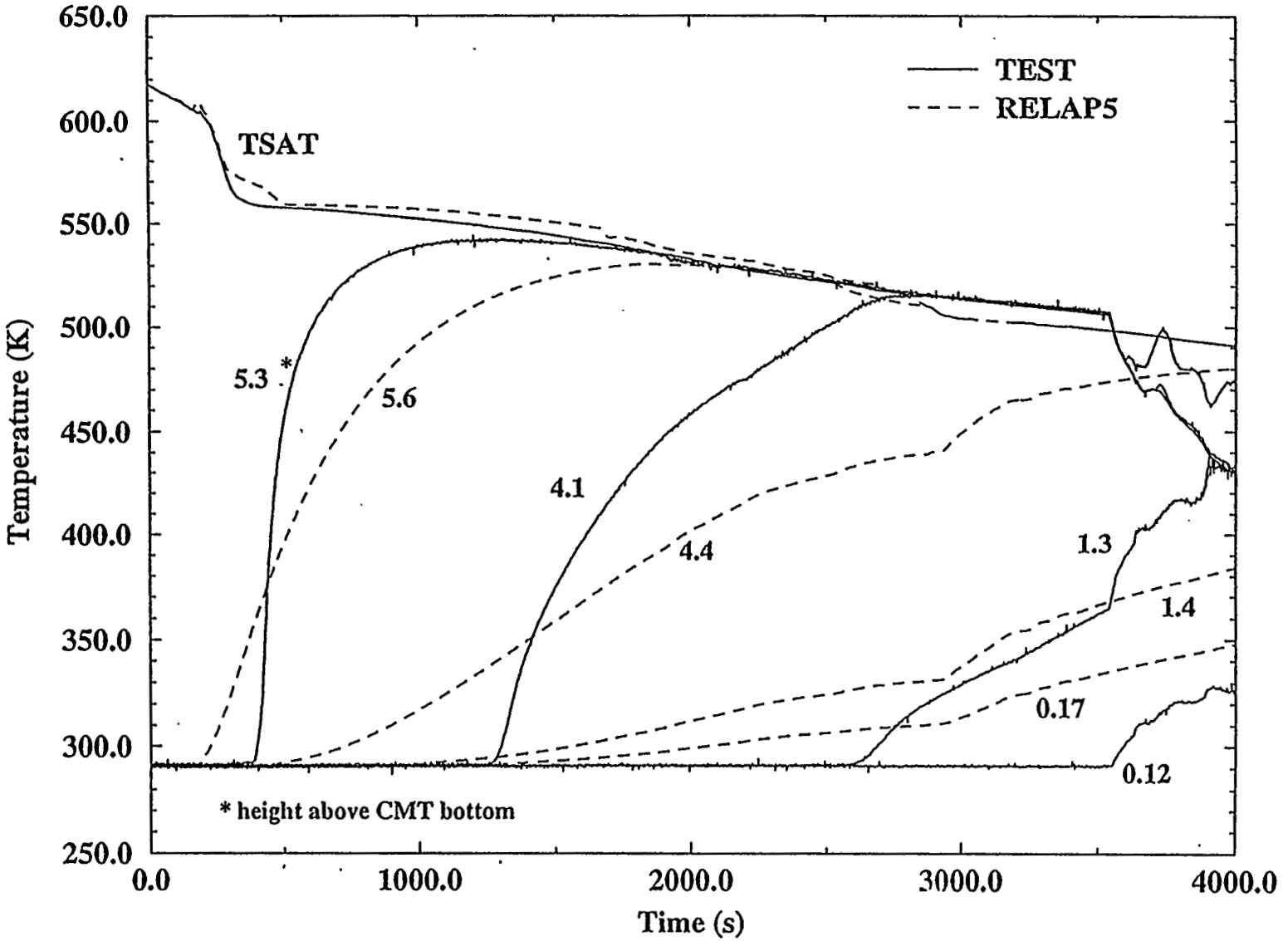

Figure 7 Comparison of calculated and measured fluid temperatures at various elevations in the CMT to saturation temperature

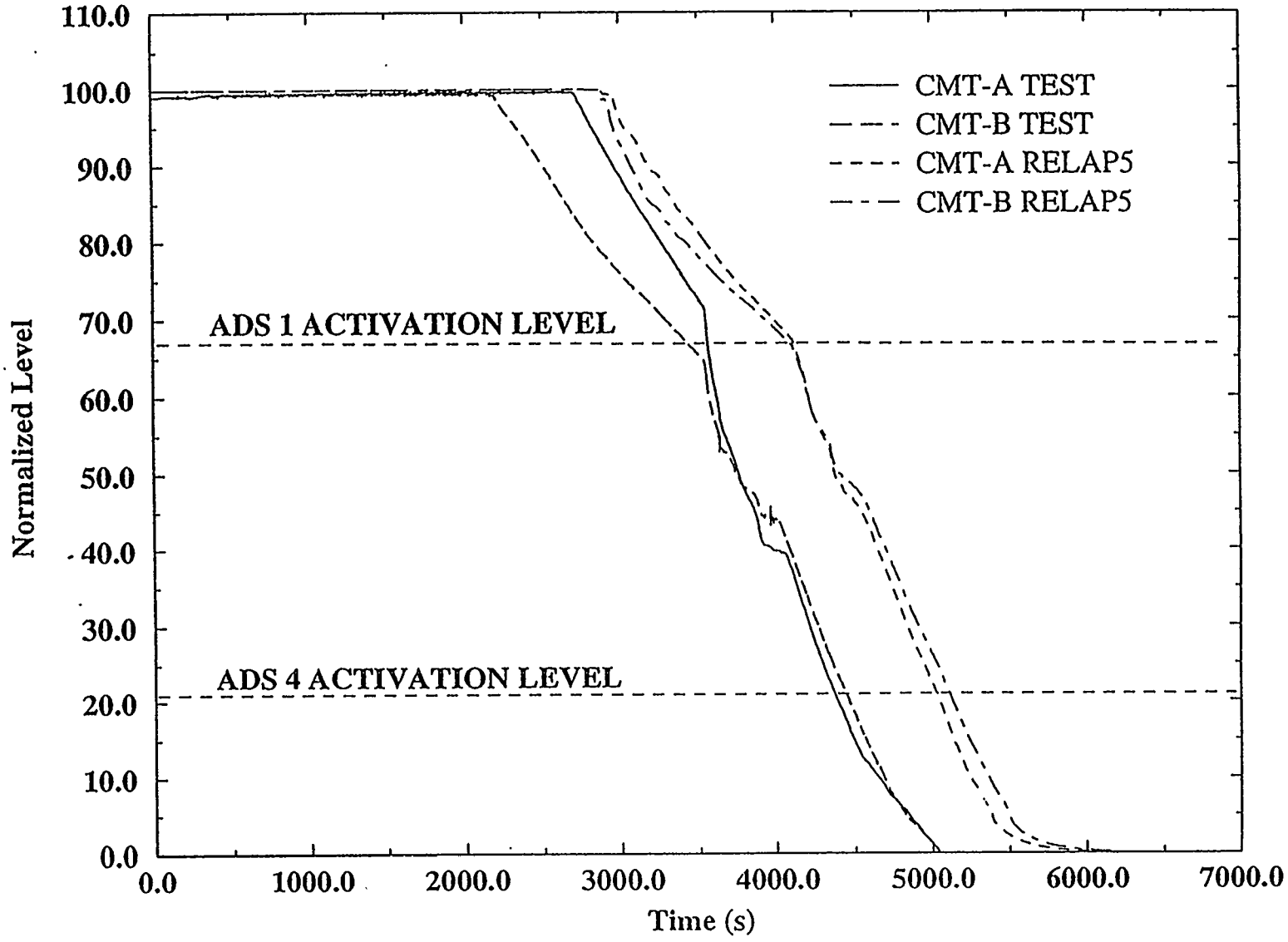

Figure 8. Comparison of calculated and measured CMT normalized levels

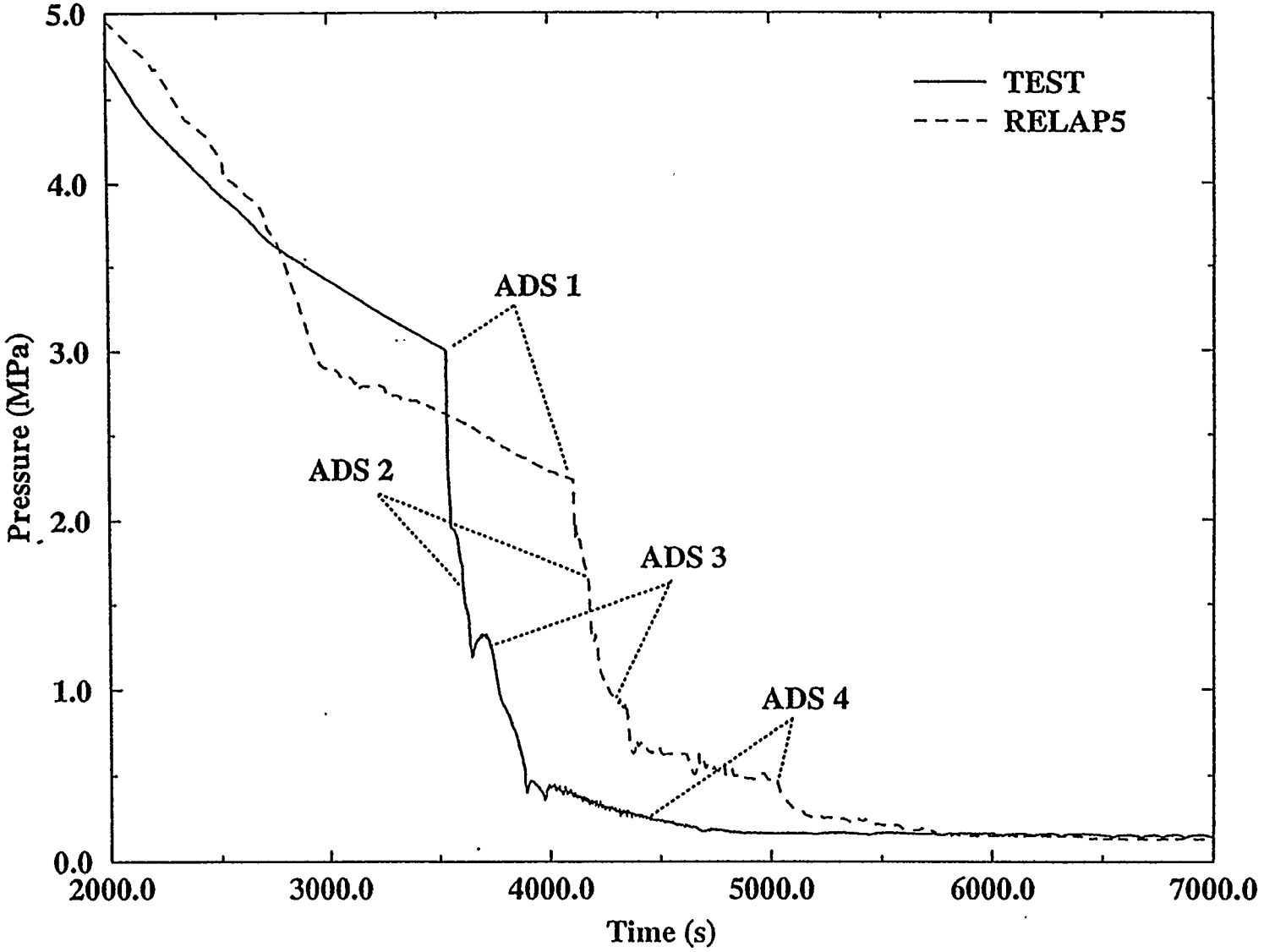

Figure 9. Comparison of calculated and measured primary pressure during ADS actuation

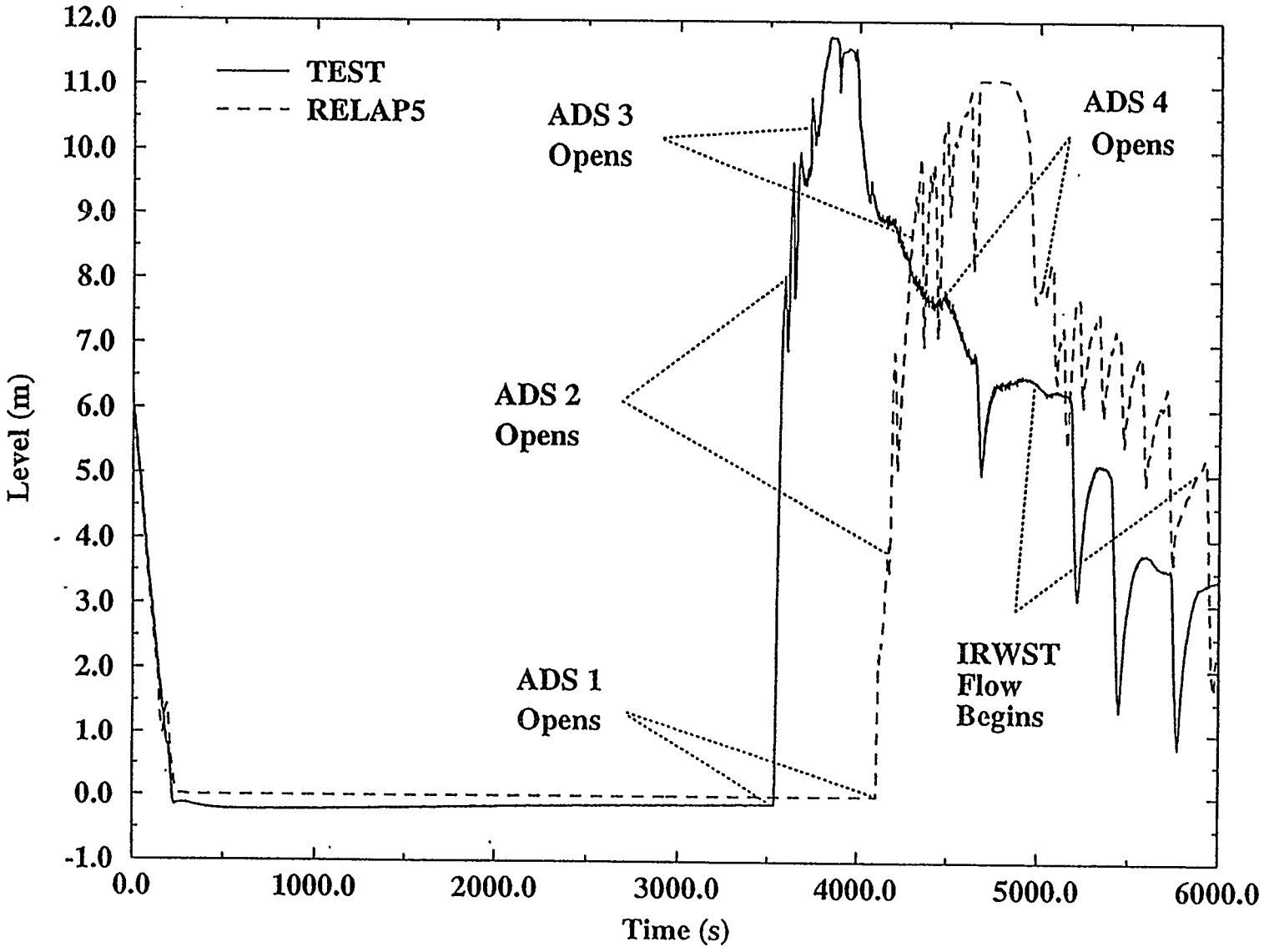

Figure 10. Comparison of calculated and measured pressurizer level

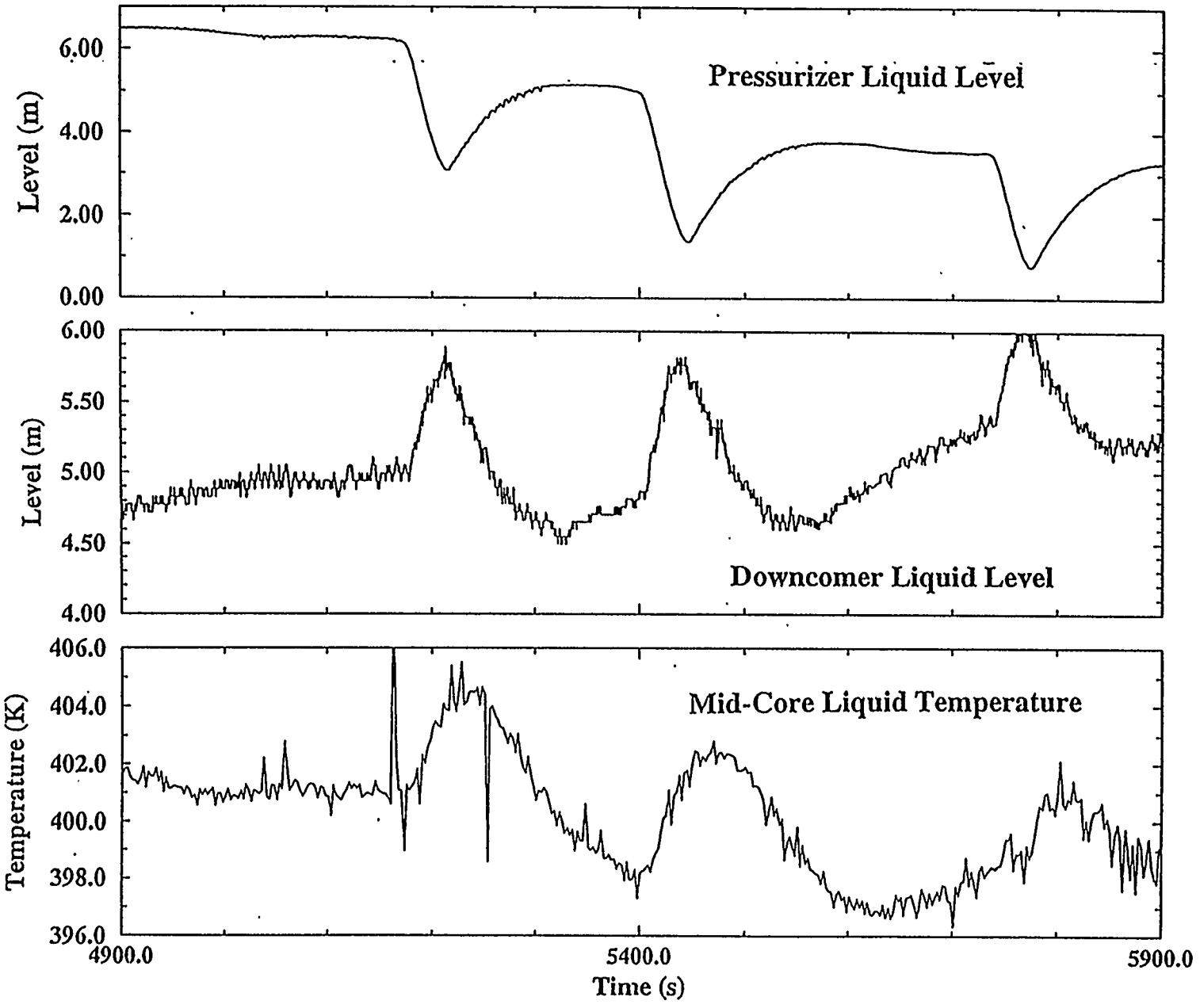

Figure 11. Comparison of measured liquid levels in the pressurizer and downcomer and measured mid-core liquid temperature

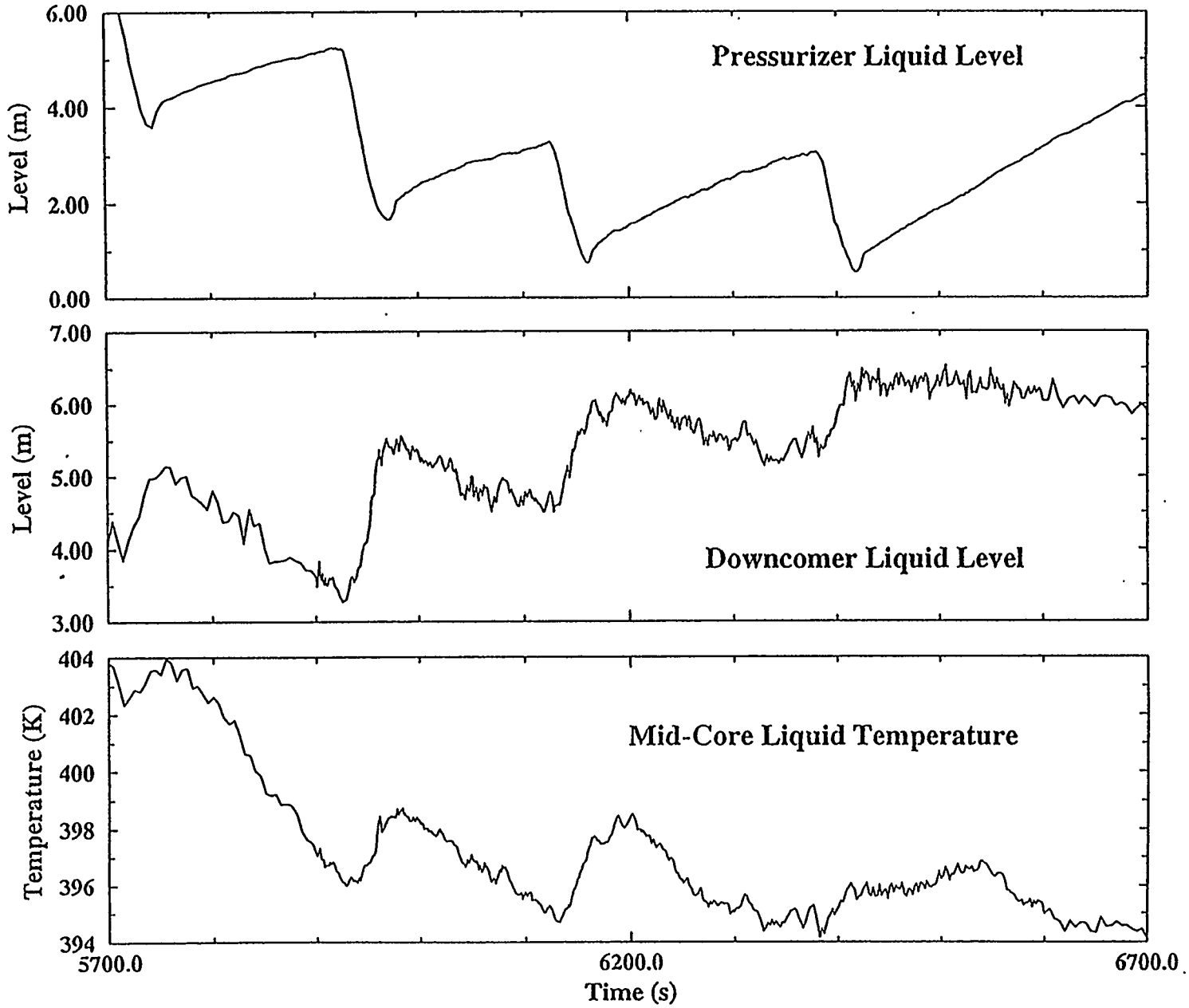

Figure 12. Comparison of calculated liquid levels in the pressurizer and downcomer and measured mid-core liquid temperature

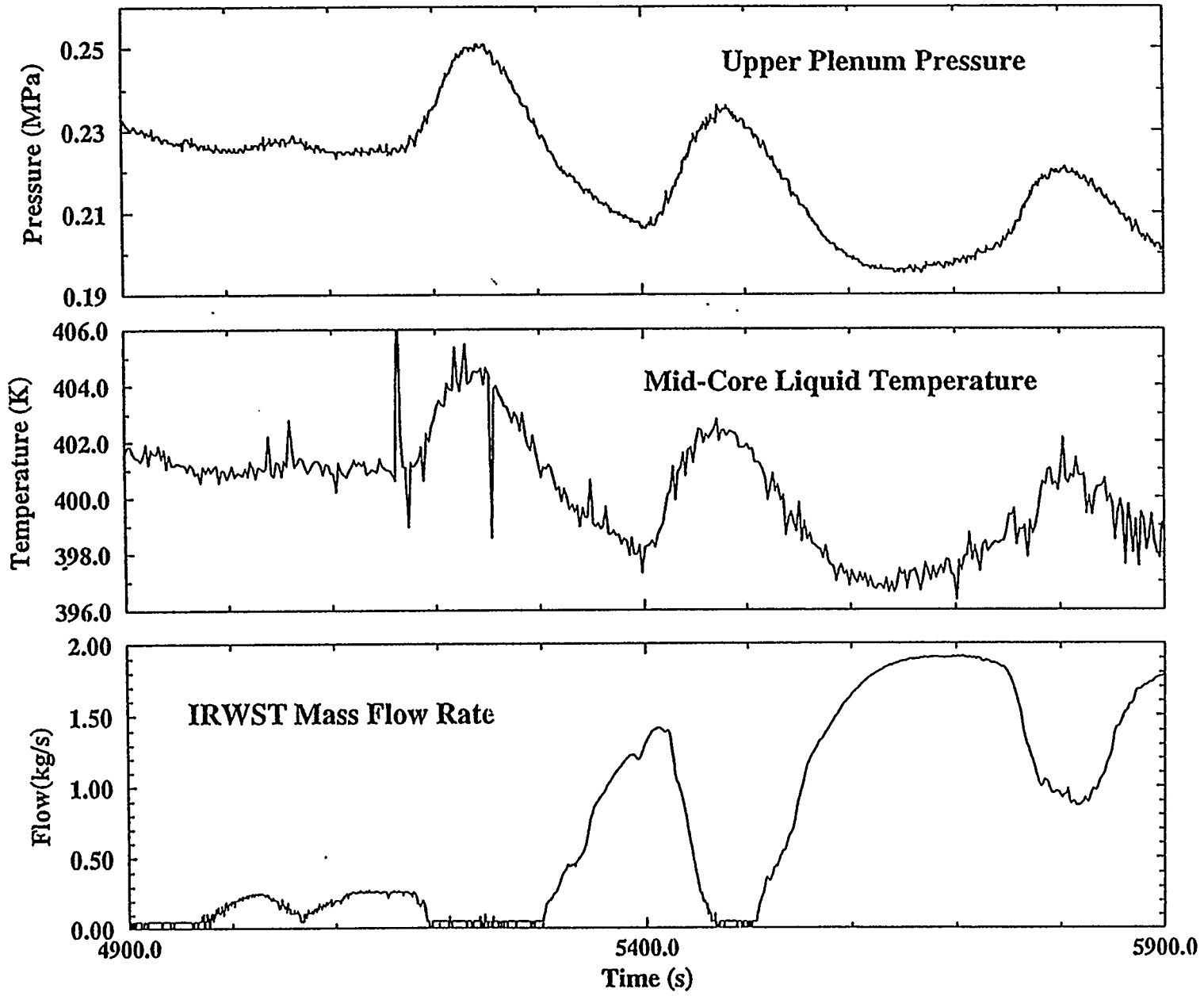

Figure 13. Comparison of measured upper plenum pressure, mid-core liquid temperature and IRWST mass flow rate

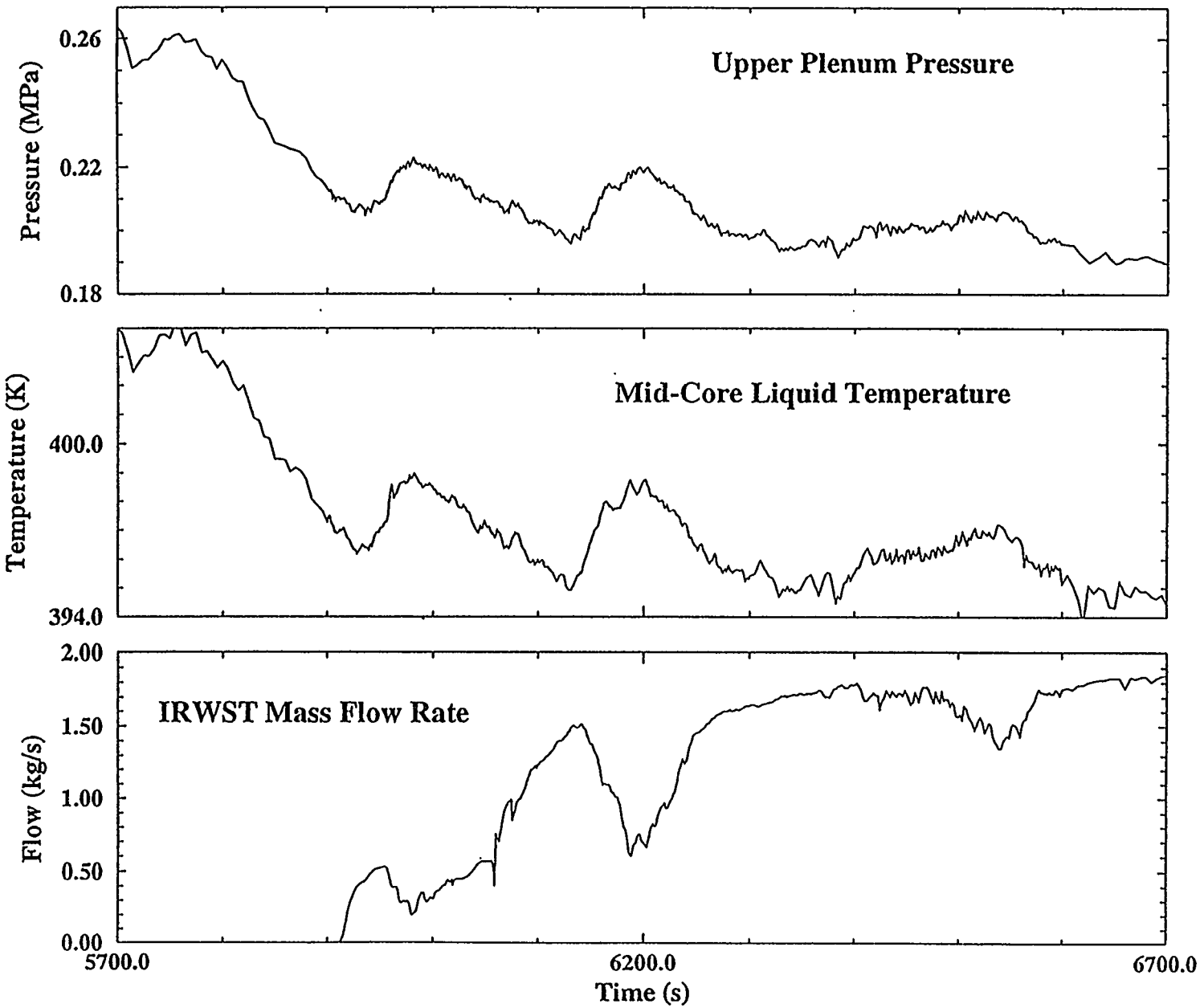

Figure 14. Comparison of calculated upper plenum pressure, mid-core liquid temperature and IRWST mass flow rate

AP600 Analyses and Sensitivity Studies

Paul D. Bayless
Idaho National Engineering Laboratory

Abstract

Analyses of the transient response of the AP600 design are being performed to support the U.S. Nuclear Regulatory Commission's evaluation of the plant safety. Transient calculations with the RELAP5/MOD3 computer code are being performed to characterize the plant response. Sensitivity studies are being performed to investigate the behavior of specific plant systems or components. Transients investigated to date have included small break loss of coolant accidents in both the hot and cold legs, and main steam line breaks. None of the transients investigated thus far are predicted to result in core heatup or damage.

Introduction

Plant transient calculations are being performed with the RELAP5/MOD3 computer code to investigate the behavior of the AP600 reactor system design. The analyses of the transient behavior support the U.S. Nuclear Regulatory Commission's evaluation of AP600 safety. Sensitivity studies are also being performed to investigate the influence or significance of specific system or component behavior on the plant transient response. The range of calculations being performed also provides a general characterization of the plant behavior. These studies complement earlier scoping analyses performed for a previous version of the AP600 design. The results of the analyses also feed back to the phenomena identification and ranking table (PIRT) that has been, and is being, developed for the AP600.

The primary safety concern for the AP600 design relates to the behavior of the passive safety systems. Are there periods of time during which there is no emergency core coolant (ECC) injection to the reactor coolant system? How do the passive systems interact with each other? How well do the passive systems perform? Do the interactions detract from the expected individual system performances?

Of particular interest is the automatic depressurization system (ADS) performance, since most transients rely on the ADS to depressurize the reactor coolant system to allow injection from passive low pressure safety systems. The ADS controls the mass and energy loss from the system. If the flow through the ADS valves is mostly steam, both the depressurization rate and the liquid inventory in the system are maximized; if the flow is of lower quality,

both the depressurization rate and the liquid inventory decrease. The former scenario tends to decrease the likelihood of core heatup, while the latter tends to increase it.

In the AP600 design, as the pressure decreases, the driving head for flow from the passive safety features also decreases. This holds indirectly for the core makeup tanks as well, which will drain as the reactor coolant system pressure decreases, thereby reducing the injection flow from the tanks. This behavior is different from plants with active, pumped ECC injection, in which the decreasing system pressure allows more coolant to be injected. With low driving forces for ECC injection, the plant may be very sensitive to small changes in conditions. Intermittent flow from the in-containment refueling water storage tank (IRWST) to the reactor coolant system has been predicted in several calculations. If the vessel liquid inventory falls low enough during the periods of no injection, a core heatup might occur.

The way the plant is designed, the potential for large asymmetries between the two coolant loops exists. The passive residual heat removal system is connected to only one of the loops. In a transient, the preferential cooling of that loop may influence the transient progression. While the one loop cools down and stays liquid solid, the other loop may stay stagnant and relatively warm, resulting in liquid flashing as the plant depressurizes.

A detailed RELAP5/MOD3[1] input model has been developed for the AP600 design. This model represents best available design information. Detailed input for the reactor coolant system and passive safety features are provided. The secondary system in the containment is modeled. The complete model contains 724 control volumes, 927 junctions, and 638 heat structures

Mass Inventory Required to Keep the Core Cooled

An inadvertent ADS opening transient was used to determine the minimum inventory required to cool the core. This information is needed to help define the safety margin in other plant analyses. The minimum reactor vessel inventory in a given calculation can be compared to the amount required to keep the core cooled, thereby giving an indication of the margin to core uncovering for that transient.

The transient is initiated by opening the first stage ADS valves. This action alone is not sufficient to scram the reactor; that occurs on low pressurizer pressure. Opening of the other three stages of ADS valves occurs normally, based on decreasing core makeup tank (CMT) level. In order to allow a core heatup to occur, injection of coolant from the IRWST was prevented. Normally, injection from the IRWST would occur long before core heatup could. The liquid in the reactor vessel was allowed to boil off, until core heatup began. In the base transient calculation, fuel heatup began with a core collapsed liquid of about 45%.

In addition to the base calculation, sensitivity calculations were run to determine the influence of containment back pressure and interphase drag in

the core on the inventory required to keep the core cooled. These are two areas of uncertainty in the calculations. Changing the interphase drag in the core had a minor effect on the minimum inventory required to keep the core cooled. Increasing the average drag by about 20% allowed the core to remain cool with a lower inventory (about 4%), because liquid from the lower part of the core was entrained further up the length of the fuel rods. Conversely, reducing the drag by about 10% reduced the entrainment, allowing the core heatup to begin with more liquid in the reactor vessel (about 2%).

A much greater impact on the core heatup was effected by the containment back pressure. In the sensitivity calculation, the containment was held constant at atmospheric pressure, compared to a pressure of about 30 psia in the base calculation. With the lower pressure, about 14% less mass was required to keep the core cooled, as a higher froth level was maintained in the core. In this case, the collapsed liquid level in the core was near 30% when the heatup began.

Containment Back Pressure Effect

Containment back pressure was the subject of a sensitivity study for a 0.05-m (2-in.) cold leg break. Containment pressure in the two calculations was held at 14.7 and 45 psia, respectively. These pressures are expected to bound the actual containment pressure during a transient. While the core remained cooled in both calculations, the injection flow from the IRWST was different. With the higher containment pressure, the flow from the IRWST to the reactor vessel was continuous. With the atmospheric containment pressure, the IRWST injection flow was intermittent, although no core heatup was predicted to occur.

Phase Separation Effects on ADS Performance

Phase separation effects on ADS performance have been investigated in two locations, the upper plenum and the surge line connection to the hot leg. For the upper plenum investigation, the base transient was a 0.05-m (2-in.) cold leg break; for the surge line investigation, an inadvertent ADS opening transient was used. Both analyses used calculations with nominal, maximum, and minimum entrainment of liquid. Maximum entrainment was achieved by specifying no slip between the liquid and vapor phases. Minimum entrainment was achieved by updating the RELAP5 code so that no liquid was allowed to pass through the subject location until the upstream void fraction was less than 15%.

The intent of these analyses was to determine how much difference in mass and energy flow through the ADS would be effected by altering the phase separation in the upper plenum or the surge line inlet. Neither set of calculations was significantly affected by the difference in liquid entrainment. Slight differences in the transient timing were observed. In neither case was core cooling in question, as the reactor vessel inventory remained well above the minimum required to keep the fuel cooled.

Asymmetric Loop Effects

A main steam line break transient has been used to investigate asymmetric loop effects. The steam line break causes the blowdown of one steam generator. The resultant cooling of the reactor coolant system leads to temperature differences between the cold legs, with the temperature of the liquid returning from the affected steam generator being much lower than that flowing to the reactor vessel from the intact generator. The objective of the analysis was to determine how much of the cold leg temperature difference is attenuated in the reactor vessel, to help guide the modeling detail needed for similar calculations.

This analysis used both RELAP5 and COMMIX[2] code calculations. A RELAP5 transient calculation was performed first to determine the cold leg mass flow rates and temperatures entering the reactor vessel. This information was then used in a three-dimensional COMMIX calculation of the fluid behavior in the reactor vessel. The COMMIX calculations showed that with cold leg temperature differences of 70 K, the temperature of the liquid entering the core is nearly uniform across the reactor vessel; nearly complete mixing occurred in the downcomer and lower plenum.

Main Steam Line Break with Maximum Cooldown

A main steam line break with maximum cooldown has also been investigated. The purpose of this analysis was to determine whether ADS might be actuated during a main steam line break. This was a question raised during the development of the PIRT. This analysis differed from the other plant analyses in that bounding modeling assumptions and boundary conditions were used, rather than best-estimate conditions. If ADS actuation did not occur with bounding assumptions designed to encourage it, ADS would not be expected to be actuated with best-estimate conditions.

To provide maximum cooling of the primary coolant system, liquid entrainment in the break flow was minimized. A range of break sizes was modeled, and the break was placed on either loop to account for differences between the coolant loops. In all of the calculations, the CMTs remained subcooled and liquid full. ADS actuation during a main steam line break is therefore unlikely.

Conclusions and Future Work

The results of the analyses performed thus far have provided insight into the expected transient response of the AP600 design. Less inventory is required to keep the core cooled at lower system pressures than at higher pressures. Phase separation in the reactor vessel upper plenum and at the surge line connection to the hot leg did not have a significant impact on the ADS performance, or the transient progression, for the transients investigated. Based on the results of a main steam line break calculation, there is sufficient mixing in the downcomer and lower plenum that thermal asymmetries between the cold legs have essentially disappeared by the time the flow reaches the core inlet. ADS actuation during a main steam line break is

not likely to occur, even if bounding boundary conditions are assumed. Finally, core heatups have only been observed in transients in which the injection from the IRWST was prohibited.

Analysis of postulated transients in the AP600 design is continuing. Further sensitivity calculations related to ADS performance will be performed. Of particular interest are plant calculations that can be compared to data obtained from the various scaled experimental facilities, as well as the associated code calculations of those experiments. These comparisons, and the assessment of the RELAP5/MOD3 code against the experiment data, will provide information on scaling distortions in the facilities and on the ability of the RELAP5 code to predict the important phenomena and transient behavior of the AP600 design.

References

1. Carlson, K. E., et al., *RELAP5/MOD3 Code Manual*, NUREG/CR-5535, EGG-2596, June 1990 (Draft).

2. Domanus, H. M., et al., *COMMIX-1C: A Three-Dimensional Transient Single-Phase Computer Program for Thermal-Hydraulic Analysis of Single-Component and Multicomponent Engineering Systems*, NUREG/CR-5649, ANL-90/33, Vol. 1 and 2, November 1990.

SCALING OF THE PURDUE UNIVERSITY MULTI-DIMENSIONAL INTEGRAL TEST ASSEMBLY (PUMA) DESIGN FOR SBWR

by

M. Ishii, S. T. Revankar, R Dowlati, M. L. Bertodano, I. Babelli,
W. Wang, H. Pokharna, V. H. Ransom and R. Viskanta
School of Nuclear Engineering
Purdue University
West Lafayette, IN 47907

The scaling study of the Purdue University Multi-dimensional Integral Test Assembly (PUMA) design has been carried out. The PUMA facility is to be built at Purdue under the "Confirmatory Integral System Testing for the GE SBWR Design" contract sponsored by the U.S. Nuclear Regulatory Commission. The scaling is based on a three-level scaling method developed for this task. The first level of scaling, the integral scaling, is based on a well-established approach obtained from the application of integral response function to the thermal-hydraulic system. This level ensures that the steady-state as well as dynamic characteristics of the thermal-hydraulic loops will be similar between SBWR and PUMA. The second scaling level addresses the boundary flow of mass and energy between components, insuring flow and inventory similarity. The third scaling level focuses on the similarity of key local phenomena governed by constitutive relations. The PUMA facility has 1/4 height and 1/100 area ratio scaling. This corresponds to the volume scale of 1/400. The PUMA power scaling based on the integral scaling is 1/200. The present scaling method predicts that PUMA time scale will be one-half that of SBWR. The system pressure for PUMA is full scale, therefore, a prototypic pressure is maintained. PUMA is designed to operate at and below 1.03 MPa (150 psi), which allows it to simulate the prototypic SBWR accident conditions below 1.03 MPa (150 psi). The facility includes models for all the major components of SBWR safety and non-safety systems that are important to the transient response to postulated LOCA and other transients.

1. Introduction

The General Electric Nuclear Energy (GE) has developed a new boiling water reactor called the Simplified Boiling Water Reactor (SBWR) [1]. Major differences between the current Boiling Water Reactors (BWRs) and the SBWR are in the simplification of the coolant circulation system and the implementation of passive emergency cooling systems. There are no recirculation pumps to drive the coolant in the vessel of the SBWR. The engineered safety

systems and safety-grade systems in the SBWR are: (1) the Automatic Depressurization System (ADS), (2) the Gravity-Driven Cooling System (GDCS), (3) the Passive Containment Cooling System (PCCS), (4) the Isolation Condenser Systems (ICS), and (5) the Pressure Suppression Pool (SP). The GDCS and PCCS are new designs unique to the SBWR and do not exist in operating BWR's. The ICS is similar to those in some operating BWRs. Both the GDCS and PCCS are designed for low-pressure operation (less than 1.03 MPa or 150 psia), but the ICS is capable of high pressure operation as well (up to 7.58 MPa or 1100 psia). It is necessary to study the performance of the new safety system and interaction between the safety systems to assess the response of the SBWR under postulated accident conditions. Since it is not feasible to build and test a full power prototypical system, a scaled integral facility is the best alternative. This paper addresses the scaling method used in the design of a model facility called PUMA

The integral test facility scaling method should provide a rational basis by which to scale- up the integral model test results to the prototype conditions. Therefore, it is necessary to have rational scaling method that establishes the interrelationship between the important physical variables associated with mass, force and energy of the prototypical system and the model. In view of this a well balanced and justifiable scaling approach has been developed for the design of the SBWR integral test facility. For this task a three level scaling approach is used. This three level scaling approach consists of; (1) integral scaling, (2) boundary flow scaling, and (3) local phenomena scaling. The integral scaling is derived from the integral response functions for major variables in single and two-phase flow. This scaling insures that both the steady state and dynamic conditions are simulated. It also determines the geometrical requirements and time scale. The integral scaling results in the simulation of all the major thermalhydraulic parameters. The boundary flow scaling simulates the mass and energy inventory of each component and flow among these components.

The third level scaling is used to insure that key local phenomena can be reasonably well scaled. Even under the global simulation of flow, mass and energy, various local phenomena which affect the constitutive relations should be addressed through this third level of scaling. Local phenomena scaling scaling have been carried out in detail.

2. General Scaling Consideartions

The scaling criteria for a natural circulation loop under single-phase and two-phase flow conditions were developed by Ishii, et al. [2-4]. The criteria include the effects of fluid properties, so one can also use them for reduced-pressure system scaling. For a single-phase flow, continuity, integral momentum and the energy equations in one-dimensional area averaged forms are used. First, relevant scales for the basic parameters are determined, then the similarity groups are obtained from the conservation equations and boundary conditions. The heat transfer between the fluid and structure can be included in the analysis by using the energy equation for the structure. From these considerations, the geometrical similarity groups, friction number, Richardson number, characteristic time constant ratio, Biot number and heat source number are obtained. It should be noted that the simulation of a long, large pipe section by a small scale

model may encounter some difficulties if the prototype system does not have a reasonably large loss coefficient in addition to the wall frictional loss.

For a two-phase natural circulation system, similarity groups have been developed from a perturbation analysis based on the one-dimensional drift flux model. The set of mass, momentum and energy equations are integrated along the loop, and the transfer functions between the inlet perturbation and various variables are obtained. The scaling parameters are developed from the integral transfer functions, represent the whole-system similarity conditions, and are applicable to transient thermal-hydraulic phenomena.

The scaling approach that has been used for the design of many existing NRC thermal-hydraulic research facilities is summarized in an NRC NUREG Report prepared by Condie, et al. [5]. The so-called "full pressure full-height method" was used for most of these facilities. The scaling approach recommended by the NRC, based on the experience accumulated from extensive LOCA studies in scaled integral test facilities, is summarized in a comprehensive paper by Boucher, et al. [6].

3. Global Scaling

3.1 Integral System Scaling (1st Level)

It is imperative to have the single-phase flow similarity requirements as a ready reference, as they are needed to simulate the single-phase to two-phase flow transition. The system consists of a thermal energy source, energy sink and connecting piping system between components. For a natural circulation loop under single-phase flow condition the similarity parameters are obtained from the integral effects of the local balance equations (continuity momentum and energy) along the entire loop.

The fluid continuity, integral momentum, and energy equations in one-dimensional, area-averaged forms are used along with the appropriate boundary conditions and the solid energy equation. From the non-dimensional form s of these equations, important dimensionless groups characterizing geometric, kinematic, dynamic and energetic similarity parameters are derived.

If similarity is to be achieved between processes observed in the prototype and in a model, it is necessary to satisfy the following requirements:

$$A_{iR} = (a_i/a_o)_R = 1 \qquad (1)$$

$$L_{iR} = (l_i/l_o)_R = 1 \qquad (2)$$

$$\left[\sum_i F_i/A_i^2\right]_R = \left[\sum_i \left[f_i \frac{l_i}{d_i} + K_i\right] / (a_i/a_o)^2\right]_R = 1 \tag{3}$$

$$R_R = (\beta \Delta T_o l_o / u_o^2)_R = 1 \tag{4}$$

$$St_{iR} = (h l_o / \rho_f c_{pf} u_o d_i)_R = 1 \tag{5}$$

$$T^*_{iR} = [(l_o/u_o)/(\delta^2/\alpha_s)_i]_R = 1 \tag{6}$$

$$B_{iR} = (h\delta/k_s)_{iR} = 1 \tag{7}$$

$$Q_{siR} = (q'''_s l_o / \rho_s c_{ps} u_o \Delta T_o)_{iR} \tag{8}$$

where subscript i designates a particular component and R denotes the ratio of the value of a model to that of the prototype, i.e.,

$$\psi_R \equiv \frac{\psi_m}{\psi_p} = \frac{\psi \text{ for model}}{\psi \text{ for prototype}} \tag{9}$$

The reference velocity, u_o, and temperature difference, ΔT_o are obtained from the steady-state solution. If the heated section is taken as the representative section, these characteristic parameters are expressed as follows:

$$u_o = \left[\frac{4\beta g \left[\frac{q'''_o l_o}{\rho_f c_{pf}}\right]\left[\frac{a_{so}}{a_o}\right] l_h}{\sum_i \left[F_i/A_i^2\right]}\right]^{1/3} \tag{10}$$

and

$$\Delta T_o = \left[\frac{q'''_o l_o}{\rho_f c_{pf} u_o}\right]\left[\frac{a_{so}}{a_o}\right] \tag{11}$$

where the subscript o here denotes the heated section.

The frictional similarity requirement, Eq. (3), can be satisfied independently of the remaining scaling requirements [2-4]. Hence, from the remaining scaling requirements, it can be shown that the following conditions should be satisfied for a complete simulation:

$$(u_o)_R = \left[\frac{\beta q_o''' l_o^2}{\rho_s c_{ps}} \right]_R^{1/3} \tag{12}$$

$$(\Delta T_o)_R = \left[\frac{q_o''' l_o}{\rho_s c_{ps} u_o} \right]_R \tag{13}$$

$$(\delta_i)_R = (\delta)_R = \left[\frac{\alpha_s l_o}{u_o} \right]_R^{1/2} \tag{14}$$

$$(d_i)_R = (d)_R = \left[\frac{\rho_s c_{ps}}{\rho_f c_{pf}} \right]_R \left[\frac{\alpha_s l_o}{u_o} \right]_R^{1/2} \tag{15}$$

$$(h_i)_R = (h)_R = (k_s)_R \left[\frac{u_o}{l_o \alpha_s} \right]_R^{1/2} \tag{16}$$

where the parameters without the component subscript, i, denote universal values that must be satisfied in all components. In addition to the above, the geometric similarity requirements dictate that

$$\left[\frac{l_i}{l_o} \right]_R = 1 \quad \text{and} \quad \left[\frac{a_i}{a_o} \right]_R = 1 \tag{17}$$

must also be met.

With these conditions, Eqs. (12-17) and Eq. (3), the effects of each term in the conservation equations are preserved in the model and prototype without any distortions. If some of these requirements are not satisfied, then the effects of some of the processes observed in the model and prototype will be distorted.

It is important to note that the above set of requirements does not put constraints on the power density ratio, $\dot{q}_{oR}$. However, they do put a restriction on the time scale as follows:

$$\tau_R \equiv \left[\frac{l_o}{u_o}\right]_R = \frac{l_{oR}}{[(\beta q_o''' l_o^2)_R/(\rho_s c_{ps})_R]^{1/3}} \tag{18}$$

The small perturbation technique and integral response function have been used by Ishii and Kataoka [2] to develop similarity criteria for two-phase flow systems. The important dimensionless groups that characterize the kinematic, dynamic and energetic fields are given as follows:

$$\text{Phase Change No.} \quad N_{pch} \equiv \left[\frac{4q_o''' \delta l_o}{du_o \rho_f \Delta h_{fg})}\right] \left[\frac{\Delta\rho}{\rho_g}\right] = N_{Zu} \tag{19}$$

This phase change number has been renamed as the Zuber number, N_{Zu} recently in recognition of Zuber's significant contribution to the field.

$$\text{Subcooling No.} \quad N_{sub} \equiv \left[\frac{\Delta h_{sub}}{\Delta h_{fg}}\right] \left[\frac{\Delta\rho}{\rho_g}\right] \tag{20}$$

$$\text{Froude No.} \quad N_{Fr} \equiv \left[\frac{u_o^2}{g l_o \alpha_o}\right] \left[\frac{\rho_f}{\Delta\rho}\right] \tag{21}$$

$$\text{Drift–Flux No.} \quad N_{di} \equiv \left[\frac{V_{gj}}{u_o}\right]_i \text{ (or Void–Quality Relation)} \tag{22}$$

$$\text{Time Ratio No.} \quad T_i^* \equiv \left[\frac{l_o/u_o}{\delta^2/\alpha_s}\right]_i \tag{23}$$

$$\text{Thermal Inertia Ratio } N_{thi} \equiv \left[\frac{\rho_s c_{ps} \delta}{\rho_f c_{pf} d}\right]_i \tag{24}$$

$$\text{Friction No.} \qquad N_{fi} \equiv \left[\frac{fl}{d}\right]_i \left[\frac{1+x(\Delta\rho/\rho_g)}{(1+x\Delta\mu/\mu_g)^{0.25}}\right] \left[\frac{a_o}{a_i}\right]^2 \tag{25}$$

$$\text{Orifice No.} \qquad N_{oi} \equiv K_i\,[1+x^{3/2}\,(\Delta\rho/\rho_g)] \left[\frac{a_o}{a_i}\right]^2 \tag{26}$$

where V_{gj}, Δh_{fg}, Δh_{sub}, and x are the drift velocity of the vapor phase, heat of evaporation, subcooling and quality, respectively In addition to the above-defined physical similarity groups, several geometric similarity groups such as (l_i/l_o) and (a_i/a_o) are obtained.

The Froude, friction and orifice numbers, together with the time ratio and thermal inertia groups, have their standard significance. Subcooling, Zuber and drift-flux numbers are associated with the two-phase flow systems. Their physical significance is discussed in detail elsewhere [2-4].

Eqs. (19) through (26) represent relationships between the dimensionless groups and the generalized variables of a two-phase flow system. The dimensionless groups must be equal in the prototype and model if the similarity requirements are to be satisfied. Hence, the following conditions result:

$$(N_{Zu})_R = 1\,,\ (N_{sub})_R = 1\,,\ (N_{Fr})_R = 1\,,\ (N_{di})_R = 1$$

$$(T_i^*)_R = 1\,,\ (N_{thi})_R = 1 (N_{fi})_R = 1\,,\ \text{and}\ (N_o)_R = 1\ . \tag{27}$$

It can be shown from the steady-state energy balance over the heated section that N_{Zu} and N_{sub} are related by

$$N_{Zu} - N_{sub} = x_e \left[\frac{\Delta\rho}{\rho_g}\right] \tag{28}$$

where x_e is the quality at the exit of the heated section. Therefore, the similarity of the Zuber and subcooling numbers yields

$$(x_e)_R \left[\frac{\Delta\rho}{\rho_g}\right]_R = 1 \tag{29}$$

This indicates that the vapor quality should be scaled by the density ratio. When combined with Eqs. (25) and (26), Eq. (29) shows that the friction similarity in terms of N_{fi} and N_{oi} can be approximated by droping the terms related to the two-phase friction multiplier. Furthermore, by definition it can be shown that $N_d = (\Delta\rho/\rho_g\, x)\,[\rho_g/\Delta\rho\alpha - 1] - 1$. Therefore, similarity of the drift-flux number requires void fraction similarity

$$(\alpha_e)_R \left[\frac{\Delta\rho}{\rho_f}\right]_R = 1 \qquad \text{or } (\alpha_e)_R \simeq 1 \tag{30}$$

Excluding the friction, orifice and drift-flux number similarities from the set of similarity requirements, Eq. (27), and solving the remaining equations, one obtains the following similarity requirements:

$$(u_o)_R = (l_o)_R^{1/2} \tag{31}$$

$$(\Delta h_{sub})_R = \left[\frac{\Delta h_{fg}\rho_g}{\Delta\rho}\right]_R \tag{32}$$

$$(q_o''')_R = \left[\frac{\rho_f\rho_g\Delta h_{fg}}{\Delta\rho}\right]_R (\frac{d}{\delta})_R\, (l_o)_R^{-1/2} \tag{33}$$

$$\delta_R = (l_o)_R^{1/4}\, (\alpha_s)_R^{1/2} \tag{34}$$

$$d_R = \left[\frac{\rho_s c_{ps}}{\rho_f c_{pf}}\right]_R (l_o)_R^{1/4}\, (\alpha_s)_R^{1/2} \tag{35}$$

The velocity scale shows that, in contrast to the case of single-phase flow scaling, the time scale for a two-phase flow is not an independent parameter. From Eq. (31), the time scale in two-phase flow is uniquely established. Thus,

$$\tau_R = \left[\frac{l_o}{u_o}\right]_R = (l_o)_R^{1/2} \tag{36}$$

This implies that if the axial length is reduced in the model, then the time scale is shifted in the two-phase flow natural circulation loops. In such a case, the time events are accelerated (or shortened) in the scaled-down model by a factor of $(l_{oR})^{1/2}$ over the prototype.

3.2 Mass and Energy Inventory and Boundary Flow Scaling (2nd Level)

The scaled mass and energy inventory histories must be preserved for integral similarity to be achieved. The integral system response scaling methods assure this similarity when friction-dominated loop flow is considered. However, when vessel or system discharges occur that are dominated by non-frictional momentum effects, such as at a point of choked flow or any nozzle flow in which the pressure drop-flow relation is dominated by kinetic loss or by cavitation effects, then additional constraints apply. At such discharge points the fluid velocity depends upon the local pressure ratio across the device, which is preserved in a full-pressure scaled system such as the PUMA facility. In nonfrictional momentum-dominated flows, the fluid velocity is the same in the model as in the prototype. Therefore, the flow area at such discharge points must be scaled to preserve mass and energy inventory rather than loop kinematics. An overall criterion for similar behavior between the prototype and the model is that the depressurization histories be the same when compared in the respective (scaled) time frames, i.e.,

$$p_m(t_m) = p_p(t_p) \tag{37}$$

This integral condition will be satisfied if the differential pressure change is the same at corresponding times, i.e.,

$$\frac{dp_m}{dt_m} = \frac{dp_p}{dt_p} \tag{38}$$

The scaling criteria for similarity of the friction-dominated natural circulation flows yields the result that the time scale of the model, or laboratory time, is related to the prototype time, by

$$t_m = (1/2)t_p = \tau_R\, t_p \tag{39}$$

and the depressurization rates of the model and the prototype are related by

$$\frac{dp_m}{dt_m} = (1/\tau_R)\frac{dp_p}{dt_p} = (2)\frac{dp_p}{dt_p} \tag{40}$$

This condition will be satisfied if the corresponding component vessel inventories are similar, i.e., ,

$$\left[\frac{M_m}{V_m}\right]_{t_m} = \left[\frac{M_p}{V_p}\right]_{t_p} \tag{41}$$

where M_p and M_m are the prototype and model vessel inventory masses, and Vp and Vm are the respective prototype and model vessel volumes. This relation must hold for each component as well as for the overall system if complete similarity is to be ensured.

Mass Inventory and Mass Flow Scaling

For integral experiments, accurate simulation of the mass and energy inventory is essential. This requires a separate scaling criteria for the system boundary flows such as the break flow and various ECCS injection flows. The scaling criteria, stated in Eq. (5.51), are obtained from the overall control volume balance equations.

By denoting the total volume by V and the mean density by $<\rho>$, for the coolant mass inventory the balance equation can be written in a non-dimensional form that applies to both the model and the prototype system as

$$\frac{d}{dt^*}<\rho^*> = \Sigma m_{in}^* - \Sigma\, m_{out}^* \tag{42}$$

where

$$t^* \equiv t/(l_o/u_o) \tag{43}$$

and

$$m_{in}^* \equiv \frac{m_{in}\,\tau_o}{\rho\, V} \sim \frac{\rho_{in}}{\rho}\left[\frac{a_{in}}{a_o}\right]\left[\frac{u_{in}}{u_o}\right] \tag{44}$$

where $\tau_o = (l_o/u_o)$ for either the prototype or the model. The definition for m_{out}^* can be given similarly. For equal model and prototype pressure simulation, $(\rho_{out}^*)_R = (\rho_{out}/\rho)_R$ is simply unity. Hence, the simulation of the boundary flow requires

$$\left[\frac{a_{out}}{a_o}\,\frac{u_{out}}{u_o}\right]_R = 1 \tag{45}$$

This is a similarity condition for the flow area and velocity combined. Therefore, it is not necessary at discharge points to satisfy the independent conditions for area and flow given by Eqs. (17) and (31), which must be satisfied by the other components of the loop. The form of the discharge scaling criterion given by Eq. (45) is very convenient from the standpoint of practical implementation.

For example, the break flow velocity, u_{out}, can not be independently controlled if choking occurs. In the case of choking, Mach number similarity is maintained. Thus, for a equal-pressure system the break flow is prototypic in the sense that $(u_{out})_R = 1$, whereas the basic scaling $(u_o)_R = (l_o)_R^{1/2}$ and the criterion given in Eq. (40) predict that the break flow area should be scaled according to

$$\left[\frac{a_{in}}{a_o}\right]_R = (l_{oR})^{1/2} \tag{46}$$

which would result in a reduction of the break flow area beyond the geometrical scale used for the loop flows.

Energy Inventory and Energy Flow Scaling

From the control volume balance, the energy inventory is given in non-dimensional form by

$$\frac{dE^*}{dt^*} = q^* - w^* + \Sigma m_{in}^* h_{in}^* - \Sigma m_{out}^* h_{out}^* \tag{47}$$

where

$$m_{in}^* h_{in}^* = m_{in} h_{in} \frac{\tau_o}{\rho V h_o} \sim (\frac{\rho_{in}}{\rho})(\frac{a_{in}}{a_o})(\frac{u_{in}}{u_o})(\frac{h_{in}}{h_o}) \tag{48}$$

In view of Eq. (46), for a full pressure simulation, i.e. $(h_o)_R = 1$, it is necessary to require

$$(h_{in})_R = 1 \quad . \tag{49}$$

This physically implies that the inflow or outflow should have a prototypic enthalpy. The above non-dimensional energy equation also shows that the initial energy inventory should be scaled by the volume ratio.

3.3 Pressure Scaling

The work scope and program objectives of the PUMA are focused on the low-pressure region of operation following the initial depressurization of the vessel. This implies that the prototype pressure maximum is about 150 psi (or 1 MPA). In considering the pressure scaling of the integral test facility, two effects should be evaluated separately. These are:

1. System pressure level, which affects all the thermal-hydraulic properties of the liquid, vapor and phase changes.
2. Individual component or inter-component pressure distributions.

Considering the pressure scaling in these two separate effects is somewhat analogous to the well-known Boussinesq assumption. The prototypic pressure is taken as the system pressure scaling base. Hence, the system pressure and all other fluid properties are considered to be prototypic. This will greatly simplify the scaling procedures. Thus, we have the global pressure scaling given by

$$p_R = 1 \tag{50}$$

Under the above prototypic system pressure scaling, the thermodynamic and transport properties at every component are considered prototypic. However, the pressure distribution in each component may not be prototypic. It should be noted that the pressure distribution within a component or between components can be the controlling factor in determining the flow by forced convection or natural circulation. This aspect of the pressure effect in a reduced-height system should be considered separately. At the initial blowdown phase of a LOCA or other transient, the major intercomponent flow occurs due to the initial pressure difference between the reactor pressure vessel and the containment. For this initial phase, the pressure difference between these two components should be prototypic at the same elevation. Thus,

$$(\Delta P_{ij})_R = 1 \qquad \text{at } Z_R = l_R \tag{51}$$

where the notation i and j stand for the reactor vessel and containment, respectively.

However, in the case of natural circulation-dominated flow, such as the reactor vessel internal circulation, GDCS injection or PCCS venting, the hydrostatic head is the essential driving force. For this case, the differential pressure is scaled by the reduced height scaling. Hence,

$$(\Delta P)_R = l_R \quad (\text{at } \Delta Z_R = l_R) \tag{52}$$

For the PUMA, the initial differential pressure scaling is set by the initialization process with isolated components. At the later stages of accident simulation, most of the significant liquid flows between components are driven by the hydrostatic head. These flows are accurately

simulated by using proper height scaling of all major elements and components based on

$$\Delta Z_R = l_R \tag{53}$$

which implies the complete axial geometrical similarity. This condition, together with the void distribution simulation based on the integral scaling, insures that the differential pressure is scaled by the reduced height scaling.

3.4 Basis for Reduced Height Scaling

Under the prototypic pressure simulation, the system geometry can be determined from the integral system scaling and the boundary flow scaling discussed above. The dynamic scaling requirements for a two-phase flow system are given by Eqs. (19-26). In general it is difficult to match all these similarity criteria for a scaled down system, so a careful evaluation of each of these requirements should be made.

In considering the dynamics of the system, two conditions should be considered separately. The first is on the quasi-steady flow simulation and the second is the dynamic response of the system, including the inertia effect. It is clear that the Froude number and friction number scale the dynamic response. When the inertia forces are not important, only the balance between the frictional resistance and gravitational force should be considered. This can be achieved by taking the product of these two numbers. Thus, natural circulation number is defined as

$$N_{nc} = N_f N_{Fr} = \left[\frac{\text{friction}}{\text{interia}}\right]\left[\frac{\text{inertia}}{\text{gravity head}}\right] \tag{54}$$

This equation can be extended to include the minor loss coefficient as

$$N_{nc} = (N_f + N_o)N_{Fr} \tag{55}$$

Using kinematic and energy similarities a less restrictive requirement is obtained for an approximate dynamic similarity between the inertia term and flow resistance:

$$(N_f + N_o)_R = 1 \tag{56}$$

The advantage of Eq. (56) relative to the two independent requirements of $(N_f)_R = 1$ and $(N_o)_R = 1$ is significant. Under a homogeneous flow assumption, the requirement given by Eq. (56) can be approximated by

$$(N_f + N_o)_R \simeq \left[\frac{fl}{d} + K\right]_R \left[\frac{a_o}{a_i}\right]_R^2 = 1 \tag{57}$$

By using the geometrical similarity criteria,

$$\left[\frac{fl}{d} + K\right]_R = 1 \tag{58}$$

A careful analysis of Eq. (58) clearly indicates the great advantage of using the reduced-height system for a given volume scale in satisfying the dynamic similarity criteria. By reducing the flow area, the hydraulic diameter is reduced by $d_R = \sqrt{a_R}$, except at bundle sections such as the core. For most small integral test facilities, it is necessary to have $l_R > d_R$ in order to maintain a reasonably large axial height so that the naturally existing two-phase level fluctuations do not adversely affect various transient phenomena. In general, the ratio of the first friction term itself is always larger than unity. However, by reducing the height of a facility, this ratio can be made closer to unity by increasing d_R for a fixed value of v_R. The second significant point is that the minor loss coefficient is an easy parameter to adjust through small design modifications in such a way that $K_R < 1$ to compensate for increased friction. Hence by properly modifying the K value, Eq. (58) can be achieved.

In view of the above and the cost consideration, the volume scale of 1/400 and the height scale of 1/4 appear to be most desirable for the Purdue integral test facility. This implies the general area ratio of 1/100.

4. Local Phenomena Scaling (3rd Level)

The global scaling criteria satisfy the system response similarity, the local phenomena may not be satisfied with the global criteria. Hence it is important to study the local phenomena scaling in detail. In the local phenomena (1) Reactor Vessel Flow Dynamics and Instability Scaling, (2) Choked Flow Case, (3) Unchoked Flow Case, (4) Relative Velocity and Flow Regime, (5) Critical Heat Flux Scaling (CHF), (6) Flashing in the Chimney, (7) Condensation in Suppression Pool, (8) Vent Phenomena in Suppression Pool, (9) Mixing in Stratified Fluid Volumes, (10) Natural Circulation, (11) Heat Source and Sink, (12) PCCS Venting into Suppression Pool, (13) Condensation in PCCS Condensers, (14) Stratification in the Drywell, and (15) Stratification in the Suppression Pool are considered. The scaling of these phenomena are considered in detail.

5. Scale of the PUMA Facility

For determining the overall size of the proposed facility, it is necessary to consider four essential factors. They are: (1) the need to scale relations to the existing facility, (2) the need to compensate for the shortcomings of existing facilities or complement the overall data base, (3)

the need for a stand-alone justifiable rationale for the choice of a_R and l_R, and (4) the overall impact on the total cost.

For the PUMA facility, the above factors have been examined in detail. Based on these considerations, a quarter height and 1/400 volume scale have been chosen as the optimum design. The existing or under-construction integral facilities for the SBWR are all full height. The GE's GIST facility [7] is a low pressure, full-height facility, thus $l_R = 1$ and $a_R = 1/508$. The GIRAFFE facility [8] in Japan has $l_R = 1$ and $a_R = 1/400$. The planned PANDA facility [9] has $l_R = 1$ and $a_R = 1/25$. The aspect ratio, l_R/d_R, for these facilities are 22.5, 20 and 5, respectively. In view of the overall cost and the volume scale of these facilities, a new facility at the volume scale of about 1/400 appears to be optimum. This will match the mass and inventory of the GIST and GIRAFFE facilities.

Since the existing facilities are all full height, the impact of the actual total height on various phenomena can be evaluated sufficiently. However, the existing facilities fall into the category of thin and tall systems, which have some major shortcomings. In Table 1, the dimensions of various components of the SBWR are compared between prototype and full-height, 1/4-height and 1/8-height scaled model for a 1/400 volume scaled facility. As shown in Table 1, the 1/8-height scaled model is close to a linearly scaled model. It has very fat vessels, especially the upper drywell and suppression pool. For 1/8 height scale, the required core power is also large. The 1/4 height and $a_R = 1/100$ scaled facility has moderate power requirement and makes the aspect scaling ratio factor to be only 1/2.5 which is very close to the prototype system.

The present quarter-height system with the volume scale of 1/400 has the advantage of well-matched gravity to frictional forces. Furthermore, due to relatively large cross-sectional areas, the important phenomena of two or three dimensional voiding patterns and flow regimes in the core and chimney can be well simulated. This is considered to be particularly important for assessing the effects of various instabilities such as the manometer oscillation, density wave instability, geysering and flashing induced cyclic phenomena on the natural circulation cooling and stability of the GDCS. The scientific design of the PUMA facility is complte and the construction of the facility is underway. The schematic of the PUMA facility is shown in Figure 1. The facility includes models for all the major components of SBWR safety and non-safety sysdtems that are important to the transient response to a postulated LOCA and other transients. Thus it includes the reactor pressure vessel, drywell, suppression pool, GDCS, ICS, PCCS, and auxiliary system like feed water line, CRD line and RWCU/SDC.

References

1. GE Nuclear Energy, "SBWR Standard Safety Analysis Report 25A5113 Rev. A, August (1992).
2. Ishii, M., Kataoka, I., "Similarity Analysis and Scaling Criteria for LWRs under Single Phase and Two-Phase Natural Circulation", NUREG/CR-3267, ANL-83-32 (1983).
3. Kocamustafaogullari, G., Ishii, M., "Scaling Criteria for Two-Phase Flow Natural and Forced Convection Loop and their Application to Conceptual 2x4 Simulation Loop

Design", ANL-83-61, NUREG/CR-3420 (1983).

4. Kocamustafaogullari, G., Ishii, M., "Reduced Pressure and Fluid to Fluid Scaling Laws for Two-Phase Flow Loop", NUREG/CR-4584, ANL-86-19 (1986).
5. Condie, K.G., Larson, T.K., Davis, C.B., McCreery, G.E., "Evaluation of Integral Continuing Experimental Capability (CEC) Concepts for Light Water Reactor Research-PWR Scaling Concepts", NUREG/CR-4824, EG&G 2494 (1987).
6. Boucher, T.J., DiMarzo, M., Shotkin, L.M., "Scaling Issues for a Thermal-Hydraulic Integral Test Facility", NPC Paper.
7. Billig, P.F., "Simplified Boiling Water Reactor (SBWR) Program Gravity-Driven Cooling System (GDCS) Integral Systems Test-Final Report," GEFR-00850, October (1989).
8. Tsunoyama, S., Yokobori, S., Arai, K., "Development of Passive Containment Cooling System," Proc. International Topical Meeting on Advanced Reactor Safety, Hyatt Regency, Pittsburgh, April 17-21 (1994).
9. Yadigaroglu, G., "Scaling of the SBWR Related Test," Report NEDC -32258, November (1993).
10. Han, J.T., Bessett, D.E., Shotkin, L.M., "NRC Confirmatory Testing Program for SBWR," Proceedings of the Twenty-First Water Reactor Safety Information Meeting, Bethesda, Maryland, October 25-27 (1993).

Nomenclature

A	Flow area scale
a	Cross-sectional area [m^2]
B_i	Biot number
c_p	Specific heat [J/kg-C]
D,d	Diameter [m]
E	Energy [J]
F	Total pressure loss coefficient
f	Friction factor, friction
G	Mass velocity [kg-m/s^2]
Gr	Grashof number
g	Gravitational acceleration [m/s^2]
j	Superficial velocity [m/s]
H	Height [m]
h	Enthalpy [J/kg]
K	Minor loss coefficient

L	Axial length scale
l	Length [m]
m,M	Mass [kg]
$\dot{m}$	Mass flow rate [kg/s]
n,N	Number
N_d	Drift flux number
N_{Fr}	Froude number
N_f	Friction number
N_{flash}	Flashing phase change number
N_{nc}	Natural circulation number
N_o	Orifice number
N_{pch}	Phase change number (= Zuber number)
N_{sub}	Subcooling number
N_{th}	Thermal inertia ratio
Nu	Nusselt number
N_{Zu}	Zuber number
p,P	Pressure [Pa]
q	Power [W]
q''	Heat flux [W/m^2]
Qs	Heat source number
R	Richardson number
Ra	Rayleigh number (Gr Pr)
St	Modified Stanton number
t	Time [s]
T	Temperature [°C]
T^*	Time ratio number
u	Velocity [m/s]
u_f	Internal energy of liquid
v,V	Volume [m^3]
V_{gj}	Drift velocity [m/s]
w	Work [J]
x	Quality
z,Z	Distance [m]

Greek Symbols

β	Volumetric thermal expansion coefficient [K^{-1}]
δ	Conduction depth [m]
Δ	Difference
Δh_{fg}	Latent heat of vaporization [J/kg]

α	Void fraction
ρ	Density [kg/m^3]
τ	Time Constant [s]
μ	Dynamic viscosity [kg/m-s]
η	Heated perimeter [m]
ν	Kinematic viscosity [m^2/s]
π	Time constant ratio
σ	Surface tension [N/m]
Σ	Summation
ξ	Wetted perimeter [m]
Ψ	Parameter

Subscripts

a	Ambient
b	Bulk
c	Core
e	Exit
f	Fluid
g	Gas
i	ith component
in	Inlet
m	Model
o	Reference point/component
out	Outlet
p	Prototype
R	Ratio
s	Surface, solid
t	Throat
th	Thermal
v	Vapor

Superscripts

*	Dimensionless quantity

TABLE 1 COMPARISONS FOR MAJOR COMPONENTS AND DIMENSIONS OF DIFFERENT HEIGHT SCALING*

COMPONENT	PROTOTYPE	1/1 HEIGHT	1/4 HEIGHT (PUMA)	1/8 HEIGHT (LINEAR)
REACTOR PRESSURE VESSEL				
Total height (mm)	24600	24600	6150	3075
I.D. (mm)	6000	300	600	848.7
Total volume (m^3)	669	1.67	1.67	1.67
CORE				
Rod material	Zr clad	S.S alloy	S.S alloy	S.S alloy
Active length (mm)	2743	2743	685	342.9
Total power	45 mW	112.5W	225 kW	318.2 kW
Core shroud I.D (mm)	5150	257.5	515	728.4
CHIMNEY SECTION				
Total height (mm)	9000	9000	2250	1125
Partition height	6500	6500	1625	812.5
# of divided areas	25	9	9	9
I.D. of shroud (mm)	4955	247.75	495.5	700.8
CONTAINMENT				
Wall material	Concrete/steel	S.S	S.S	S.S
Upper head volume(m^3)	3770	9.4	9.4	9.4
Upper head height (mm)	6100	6100	1525	762.5
Upper head dia.(mm)	28050	1402.5	2800	3967.5
Lower head volume (m^3)	1696.5	4.24	4.24	4.24
Lower head height (mm)	27200	27200	6800	3400
Lower head dia. (mm)	8911	445.55	891.1	1260.4
SUPPRESSION POOL				
Initial water volume (m^3)	3255	8.13	8.13	8.13
Initial gas space (m^3)	3819	9.55	9.55	9.55
Height (mm)	11950	11950	2987	1493
Diameter (mm)	27450	1372.5	2800	3882.6
GDCS POOL (1 OF 3)				
Diameter (mm)	Not circular	450	900	1273
Height (mm)	6100	6100	1525	762.5
Volume (m^3)	348	0.87	0.87	0.87

*Note: The volume scaling ratio is kept as 1/400 for all different height scaling.

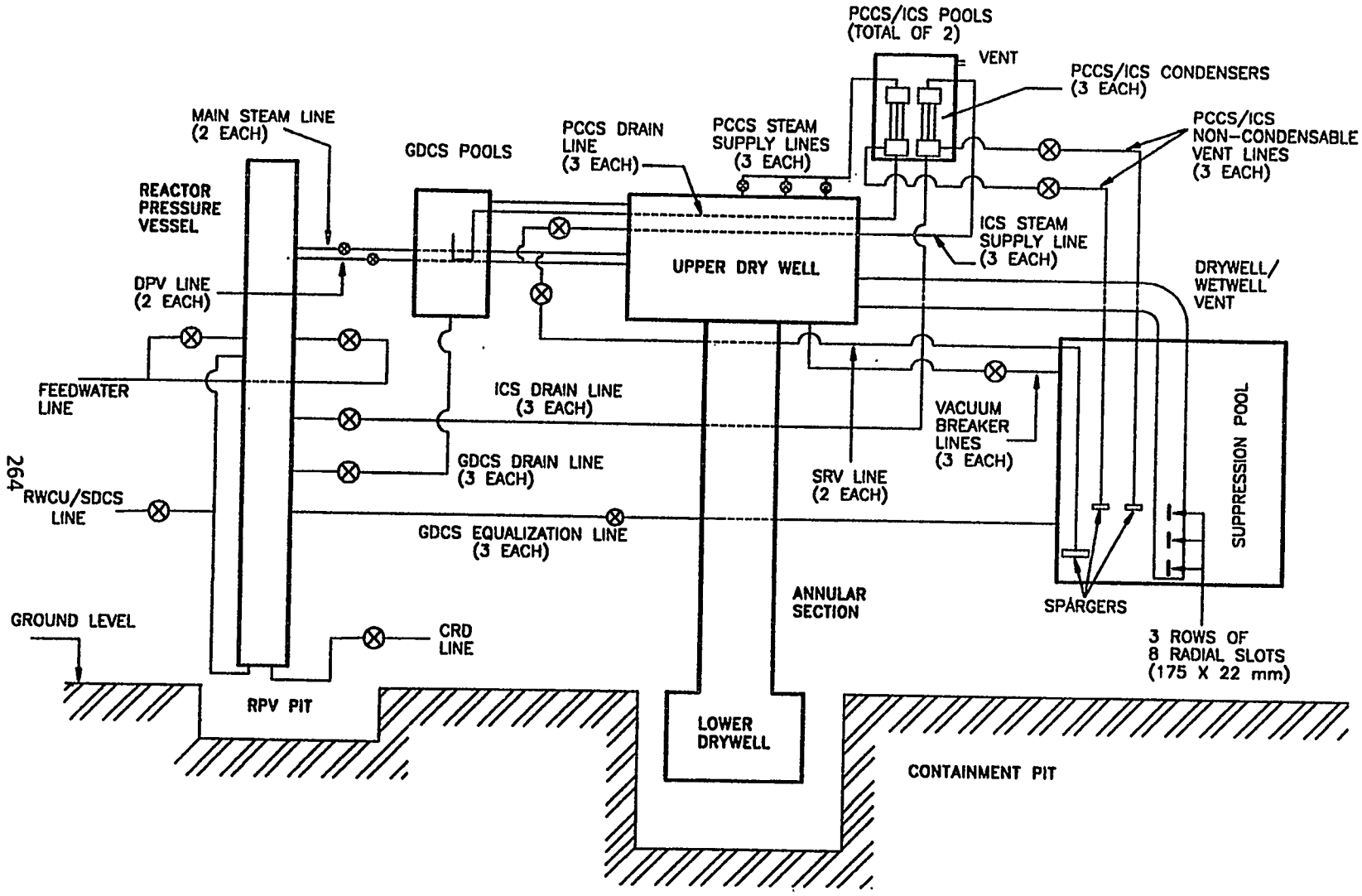

Figure 1 Overall schematic of PUMA facility

Assessment of PUMA Preliminary Design*

Y. Parlatan, J. Jo, U.S. Rohatgi, and G. Slovik
Brookhaven National Laboratory
Department of Advanced Technology
Upton, NY 11973

ABSTRACT

General Electric (GE) has submitted to the United States Nuclear Regulatory Commission (USNRC) an application for a design certification of their Simplified Boiling Water Reactor (SBWR). This reactor system is an advanced light water reactor (ALWR) concept that differs from previous GE BWR designs since the safety systems are based on passive systems. Some of the SBWR unique features include natural circulation during normal plant operation and a passive containment cooling system (PCCS) that condenses steam in the containment and returns the condensate back to the reactor pressure vessel (RPV) by gravity driven flows. During a Loss of Coolant Accident (LOCA), the low water signal in the RPV opens squib valves, actuating the Automatic Depressurization System (ADS) and allows the RPV to depressurize by blowing down into the containment. Depressurization allows the Gravity Driven Cooling System (GDCS) drain into the RPV by static head in a tank to provide the water required to keep the core covered and cooled, and keep the containment and core in safe conditions.

SBWR is an advanced design that introduces several new phenomena. Passive systems are relied upon for plant safety that have never been licensed before by the USNRC. GE has proposed a series of separate and integral test facilities to develop the required data base supporting the performance and interaction of the components to accomplish the safety function in the SBWR. The USNRC is also building a confirmatory integral test facility at Purdue University, which has been given the acronym of PUMA (Purdue University Multi-dimensional Integral Test Assembly). This facility is being designed with the scale of 1/4 in height and 1/400 in volume, with a time scale of 1/2. Transients can be initiated at pressures as high as 1.034 MPa (150 psia). The information obtained from this facility will be used to confirm GE data and to assess the RELAP5 code for application to SBWR. Brookhaven National Laboratory (BNL) is providing technical and analytical support during the development phase of the PUMA facility and will provide pretest and post-test analysis during the operation of the facility.

*This work was performed under the auspicies of the U.S. Nuclear Regulatory Commission

The PUMA facility was designed by matching the important nondimensional groups. The scaling covered the top level approach as well as bottom-up approach. However, this approach may miss the interaction of system components. In order to assess the facility capability to model SBWR transients, the facility design was carefully reviewed. The review was performed at two levels. In the first level, the facility configuration and dimensions were compared with SBWR information. In the second stage, the RELAP5 code was used to simulate a Main Steam Line Break Accident (MSLB) with consistent nodalization to both the SBWR plant and PUMA facility. The predictions for SBWR and PUMA are compared on the same time scale. The preliminary assessment indicated that the RPV pressure and break flow rates were indistinguishable. There were other observations that came from these results that identified the deficiencies in the PUMA facility design, such as oversizing of IC condenser and larger heat transfer area in PCCS.

1. Introduction

GE Nuclear Energy (GENE) has submitted an advanced light water reactor design to United States Nuclear Regulatory commission for design certification. This new design is based on the result of extensive simplifications to the currently operating BWR plants, and therefore, called Simplified Boiling Water Reactor (SBWR) [1]. As the design is based on passive systems that are new, there is a need for experiments to assess the performance of new concepts. Furthermore, the computer codes such as RELAP5 that will be used to provide independent analytic capability, also need to be assessed for new applications. In order to meet these requirements USNRC is sponsoring an integral test facility at Purdue University. The facility is called Purdue University Multi-Dimensional Integral Test Assembly (PUMA) [2].

The objective of this paper is to present an assessment of the PUMA facility. While the PUMA design report was reviewed for any inconsistencies in configuration or dimensions, the interaction of various components could not be addressed. This last item was reviewed by performing systems calculations for design basis accidents using RELAP/MOD3.1.2 for SBWR and PUMA, and comparing the results. These results from the analysis of Main Steam Line Break Accident (MSLB) are presented here.

1.1 SBWR

The primary thermal-hydraulic features that distinguish the SBWR from existing BWRs are natural circulation inside the Reactor Pressure Vessel (RPV) during normal operation, the Gravity Driven Cooling System (GDCS) for emergency core cooling, Isolation Condensers (IC) for removing heat from the RPV and the Passive Containment Cooling System (PCCS) to reject the decay heat from the containment in long term LOCA transients. The driving force for the

recirculation of the coolant in the vessel lacking jet pumps, is provided by the buoyancy head in a tall chimney attached on the top of the core. Figure 1 shows a schematic of SBWR.

Emergency Core Cooling System (ECCS) provides water by gravity head into the RPV during a LOCA. The GDCS tanks provide large amounts of water to RPV near atmospheric pressure. The water initially available in the GDCS tanks is about 1.5 times the total RPV volume. However, for this gravity flow from GDCS to work, the vessel needs to be depressurized. The depressurization of the RPV is initiated by the downcomer low water level (L1) trip and is accomplished by opening in tandem several Safety Relief Valves (SRV) and Depressurization Valves (DPV) located near the RPV steam dome.

The suppression chamber is the main system that limits the initial pressure rise in the containment by condensing large amounts of steam originated in RPV from the primary system and cooling the nitrogen initially present in the inerted atmosphere of the drywell. However, the long term decay heat removal from the containment is provided by the PCCS. These PCCS heat exchangers are located at the top of the drywell inside the tanks filled with water. Hot steam/noncondensable mixture present in the drywell rises into the PCCS where the steam is condensed and the nitrogen is cooled. The condensate is returned to the GDCS tanks and then to RPV while the noncondensable gas is vented to the suppression chamber. The PCCS operation is expected to be of a self-regulating: when the pressure rises in the drywell, the rate of steam condensation increases which in turn decreases the pressure.

Besides the PCCS, SBWR also employs another set of heat exchangers, IC, to limit the overpressurization of the RPV during various transient including LOCA. ICs are directly connected to the RPV steam dome and condense the steam and return the condensate to downcomer. However, ICs become nonoperational in long term during LOCA, since the noncondensable gases that are expected to accumulate in the tubes cannot vent from the system.

1.2 PUMA

The PUMA facility is a full pressure, reduced volume, reduced height, integral effects facility that contains all the major SBWR components to simulate various small and large break LOCA transients. The scaling factors for the length and volume of PUMA are 1/4 and 1/400, respectively. The maximum operating power is 300 kW. Power generation and heat rejection rates, and mass flow rates are scaled by 1/200. The time constants for PUMA are 1/2 of the time constants of SBWR. The maximum pressure allowed in the system is 10.3 bars (150 psia). Therefore, the facility will simulate the LOCA transients beyond the initial blowdown period when the pressure in the RPV has dropped down to 10.3 bars. Figure 2 shows a schematic of PUMA. The results of the scaling study by Ishii and coworkers can be found in [2]. This facility is currently under construction.

2. Analysis

Two sets of calculations are performed using the RELAP5/MOD3 Version 3.1.2 to investigate the phenomena expected to occur in a hypothetical SBWR LOCA transient. One of the calculations was based on the prototypical SBWR and the other on PUMA facility. The parameters predicted in the analysis of the PUMA are modified with the scale factor for that parameter. For example, the time is doubled and the flow rate is multiplied by 200 for PUMA calculations. The modified PUMA results are compared with the SBWR results.

The RELAP5/MOD3 code is based on two-fluid formulation for analyzing the thermal-hydraulic phenomena of two-phase flow [3]. Six equations are used for the conservation of mass, momentum and energy for both the liquid and vapor phases. The constitutive relations are used to model the mass, momentum and energy transfer between the phases, and, wall heat and momentum transfer with the phases. These constitutive relationships are dependent on the flow-regimes, which are determined from flow regime maps.

The input decks used in this study are based on many sources of information including drawings of the SBWR and PUMA. All the major components and safety related devices were modeled. Although the two input decks were developed separately, an effort was made to achieve input deck consistency. One of the criteria used to achieve consistency between the two decks was to match Courant number at steady state. PUMA is scaled such that matching the number of nodes also satisfied the Courant number criterion. A schematic of the nodalization for these input decks is not included in this paper because of space limitations.

The PUMA facility can simulate the phenomena associated with a LOCA transient starting from 10.3 MPa (150 psia). However, the present calculations were started from the normal operating conditions in the RPV, i.e., at a pressure of about 7.2 MPa (1040 psia). In the following sections some of the results are shown.

3. Results and discussion

MSLB type LOCA transient for the SBWR plant and for the PUMA facility were simulated by using RELAP5/MOD3. Two consistent input decks have been used in this study.

The transient following a LOCA can generally be divided into five different phases for SBWR. These are pre-isolation, isolation, depressurization, GDCS refill, and long-term cooling. Pre-isolation is the period starting from the initiation of the transient and lasts only about 5 seconds when the Main Steam Isolation Valves (MSIV) close. Isolation-phase covers the period (on the order 10 minutes) until the downcomer level reaches a low level (L1) and ADS signal actuates the depressurization process. Depressurization covers the period of the opening of all DPVs and SRVs and equalizing of the pressure in the drywell and RPV which lasts about 150 seconds. The GDCS refill period starts with opening of the squib valve in the GDCS injection

line and lasts until the RPV is full and water starts to spill over to lower DW. The long term cooling period is the period where the PCCS becomes the most important system to limit the pressure rise in the containment and remove the decay heat generated in the core.

In a large break transient such as MSLB, the first three phases are not clearly distinguishable. Since the break area is large, the closing of MSIVs cannot isolate the RPV. Similarly, the RPV depressurization starts from the beginning of the transient, and opening of the SRVs and DPVs has only a minor influence on the depressurization process. In the current work, the transient is analyzed for 2000 seconds that covers part of the GDCS refill phase. The heat removal of PCCS and IC has only a minor importance in this period, since the initial stored energy in the RPV fluid and structures as well as decay heat are absorbed in the Suppression Chamber Pool (SP). However, the heat transfer rates can be compared and scaling for PCCS and ICS can be assessed.

In the following figures, the parameters from PUMA simulation have been modified with the scale factors to provide direct comparison with SBWR results. For example, the mass flow rates in PUMA are multiplied by 200, the elevations by 4 and the time by 2.

Following a double ended steam line break, the pressure in the steam dome drops rapidly. As shown in Figure 3, the pressure responses of PUMA and SBWR are indistinguishable. Initially, the PUMA pressure is slightly lower than SBWR pressure. This discrepancy is explained later. The break flow from the broken steam line is choked for approximately the first four hundred seconds. The pressures in the drywell and RPV are equal after about five hundred seconds and are about 3 bars each.

The total break flow, sum of the intact line flow and broken line flow, is shown in Figure 4. The mass flow rate in PUMA is multiplied by 200 in this figure to scale it to SBWR values. Initially, the flow through the break is greater than the rated steam flow rate, since the initial inventory in the steam lines is at high pressure and it discharges into the containment at near atmospheric pressure. Since the MSIVs close at around five seconds and the initial inventory in the steam lines has discharged by then, the limiting area reduces to the area of the flow restrictor located in the steam line, which limits the flow to rated steam flow rate.

The break flow, although still choked, starts to decrease rapidly with the depressurization of the RPV. The break flows from PUMA and SBWR behave similarly, however, PUMA has slightly smaller break flow rate than SBWR for the first 200 seconds, which is again explained later. After 500 seconds, the flow becomes unchoked and the flow rate becomes dependent on the pressure difference between the drywell and the RPV steam dome. At around 700 seconds after the break, the GDCS starts to refill the RPV with cold water. The steam generation in the RPV ceases as the decay heat is used to heat the subcooled water. The predicted break flow rates for SBWR and PUMA are very close.

The SRV and DPV valves can depressurize the RPV quickly having a combined area greater than that of the flow restrictor in the steam lines. However, these valves start to open about 550 seconds into the transient, at which time the RPV is already been depressurized. Therefore, the ADS signal which initiates the opening of the SRV and DPVs as well as the GDCS squib valve do not have a major role in the depressurization process. SRV and DPV flow rates are not shown because of space limitations, but they are small.

Figure 5 shows the so called "Wide Range Reading" (WR), which indicates the water level in the RPV downcomer. The WR shows the collapsed liquid head between two pressure taps (one located near the steam line and the other above the core). The PUMA value is multiplied by four since the length in PUMA is scaled 1/4. This level provides the signal for the initiation of ADS. ADS signal is set when the WR reading falls below a location about 4 m. above the top of active fuel for a period of 10 seconds. The ADS signal is set almost at the same time for PUMA and SBWR. WR, collapsed water level, recovers faster after about 700 seconds in PUMA since the GDCS drains at a faster rate than SBWR (see Figure 6).

Figures 6 and 7 show the GDCS flow rate into the RPV and the level in the GDCS tank as a function of time, respectively. Again, the PUMA flow rate is multiplied by 200 and the tank level by 4. The GDCS starts discharging water into the RPV by gravity head after the squib valves in the injection lines have opened based on the ADS signal. After the valve opening, the flow reaches more than 400 kg/s for both PUMA and SBWR, while the peak flow rate is somewhat higher for PUMA. The GDCS flow rate starts to decline since the RPV water level increases (see Figure 5) and the GDCS tank level decreases (see Figure 7). GDCS flow starts almost at the same time for PUMA and SBWR. Higher GDCS flow rate suggests that the friction in the GDCS line is small.

Figure 8 shows the heat rejection rate in the IC as well as the decay heat generation rate in the core. The heat generation and rejection rates in PUMA are multiplied by 200. Even though the total surface area of IC tubes is roughly half of that of PCCS, the heat rejection rate in IC much larger than that in PCCS. This is expected since the IC draws pure steam from the RPV steam dome at higher saturation temperature, and PCCS draws a mixture of nitrogen and steam from the upper drywell at a lower saturation temperature. The higher condensation rates in the IC for PUMA partly explains the faster pressure drop and slower inventory loss of PUMA, since the condensate returns to RPV downcomer. The higher condensation rates predicted for PUMA is caused by faster draining of water inventory initially present in the IC drain lines in PUMA. Even though IC system in PUMA has a larger inventory in the drain lines, it drains faster than SBWR exposing more heat transfer inside the heat exchanger tubes. As the IC starts to drain, the heat transfer increases until a balance is reached in the increase in the heat transfer area and decrease in the RPV steam temperature. After IC heat exchanger tubes drain completely, the heat transfer essentially follows the RPV pressure curve. Faster draining of inventory suggests that the friction in the IC line is small.

The results shown in the above figures indicate that the primary system in PUMA simulates the global variables, such as break flow, pressure, water inventory and GDCS flow rates for SBWR satisfactorily. However, one can further improve the agreement by eliminating the initial excess water inventory in the IC condensate lines.

Figures 9 and 10 show the pressure response of the drywell and the suppression chamber. The pressure in the containment rises very quickly during the initial period of blowdown. The nitrogen initially present in the drywell (air in case of PUMA) mixes with the steam from the break and discharges into the suppression chamber primarily through the vertical vents. These vents are located inside the suppression chamber and covered by the normal water level. When the pressure in the drywell exceeds the Suppression Chamber (SC) pressure, the vertical vent level is depressed and the vents are cleared. The suppression chamber starts condensing steam and cooling the nitrogen coming from the drywell. This limits the very steep rise of pressure in the containment. The pressure in the suppression chamber keeps increasing at a slower rate due to the flow of nitrogen from the drywell and due to the increase in the temperature of the suppression pool which controls the partial pressure of the steam. The pressure decreases after the GDCS injection to the RPV starts and the steam generation in the core ceases. During this period PCCS continues to operate by condensing steam and hereby, lowering the pressure in the drywell. Vacuum breakers that connect the suppression chamber with drywell open as result of the drywell pressure drop and the nitrogen is redistributed in the containment. The SC pressure in PUMA simulation is higher than in SBWR prediction partly because vertical vent open earlier in PUMA and more air passed to SC leading to higher pressure.

Figure 11 shows the predicted heat rejection rate in PCCS for PUMA and SBWR along with the decay heat generation curve. Condensation process in PCCS slowly stalls after the GDCS flow starts to refill the RPV and prevents steam generation after about 1000 seconds into the transient. PUMA heat rejection rates are higher since the saturation temperature of the pool where the PCCS condenser resides is lower for PUMA. Even though these pools are open to atmospheric conditions, the hydrostatic head of PUMA, and hence the saturation temperature, is lower than those of SBWR. The spikes in PCCS condensation rates are caused by sudden pressure drop in the drywell due to spurious condensation on the surface of GDCS tank water and subsequent opening of vacuum breakers.

RELAP5/MOD3 has some limitations that have caused inaccurate predictions for some of the containment parameters. The partial pressure of the steam in the suppression chamber gas space is probably underestimated in this model because of two reasons:

1) RELAP5 overestimates the interfacial heat transfer between the gas and the liquid in the suppression chamber gas space, making the two at equilibrium at all times.

2) There is considerable recirculation among the three levels of the horizontal vents preventing any stratification effects and therefore, effectively lowering the surface temperature of the pool. These issues need to be resolved.

After the GDCS tank starts to provide water to the RPV, the pressure in the drywell starts to level and then decrease due to the PCCS condensation and the absence of steam generation in the RPV. There are sudden drops in the pressure because of non-physical surface condensation taking place in the GDCS tank. Again the interfacial heat transfer between the cold water in the GDCS tank and the steam above it is overestimated especially when the water level in the tank crosses a cell boundary. These sudden drops in the drywell pressure cause opening of the vacuum breakers, and the nitrogen is redistributed, lowering the pressure in the whole system.

4. Conclusions

The PUMA facility design was assessed by comparing its predicted behavior with that of SBWR for an MSLB transient. We have reached the following conclusions based on this study:

- Global variables related to RPV matched well between the SBWR and PUMA, indicating proper overall scaling.

- The PUMA facility has higher initial water inventory in the IC drain lines compared to SBWR. This discrepancy initially decreases the break flow rate by limiting flashing in the downcomer.

- Both the IC and GDCS drain faster in PUMA suggesting less friction in PUMA facility.

- Drywell pressure responses of PUMA and SBWR are in good agreement.

- IC and PCCS heat rejection rates for PUMA is higher than those for SBWR. IC heat rejection rate is higher since initial water inventory in the IC condenser headers and drain lines drain faster in PUMA exposing more heat transfer area. PCCS heat rejection rate is higher since the saturation temperature of the pool where the condensers reside is lower.

- RELAP5/MOD3 has two major limitation that may affect the containment pressure. First, the code predicts large recirculation among the three rows of horizontal vents in the suppression pool, and therefore, less temperature stratification. The suppression chamber pressure is affected by the surface temperature of the pool. Secondly, the code predicts large condensation at the pool surface of the GDCS tank, when it starts to drain. This shows sudden pressure drops in the containment.

REFERENCES

1. GE Nuclear Energy, "SBWR Standard Safety Analysis Report," 25A5113 Rev. A, August 1992.

2. Ishii, M. et al., "Scientific Design of Purdue University Multi-Dimensional Integral Test Assembly (PUMA) for GE SBWR," (NUREG/CR) PU-NE 94/1, July 1994.

3. Fletcher, C.D., and Schultz, R.R., "RELAP5/MOD3 Code Manual," (NUREG/CR-5535) EGG-2596, January 1992.

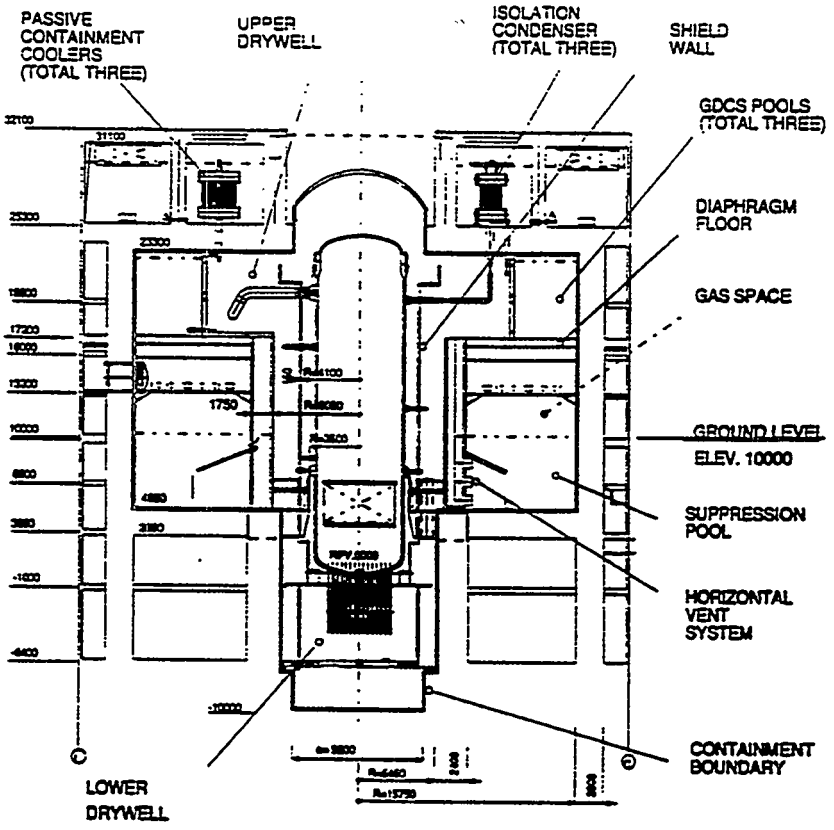

Figure 1. A Schematic of SBWR

Figure 2. A Schematic of PUMA Test Facility

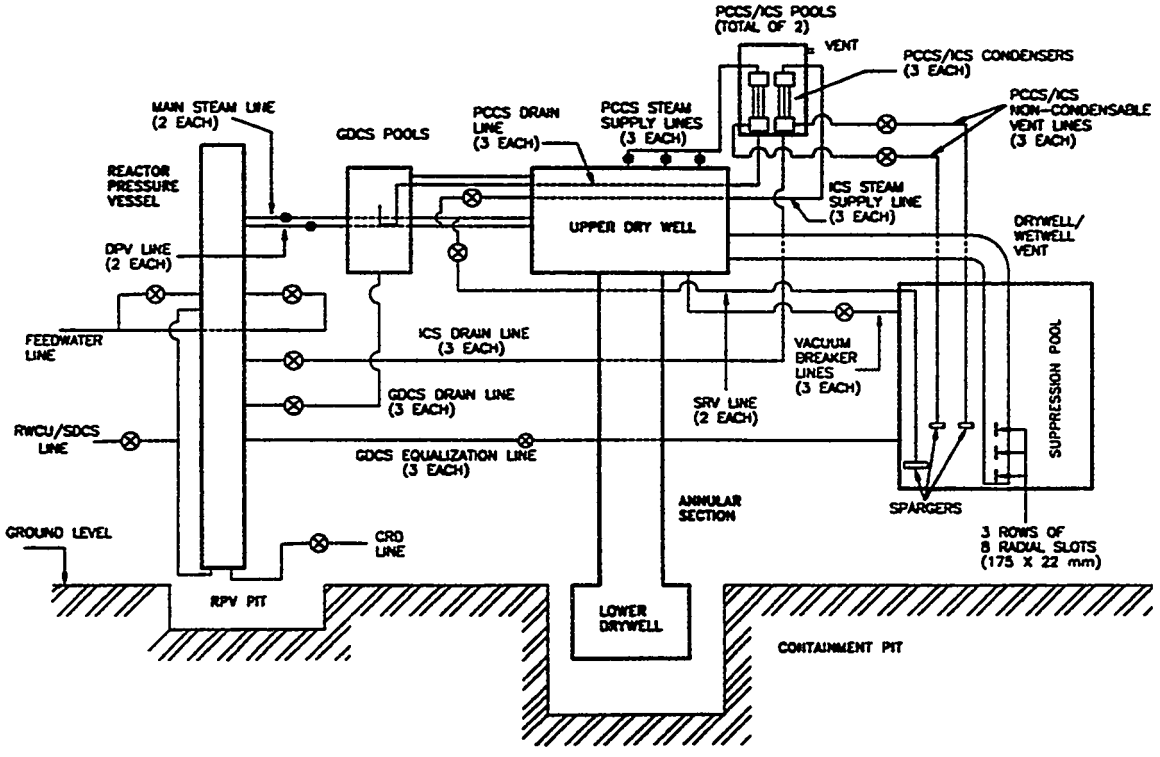

Figure 3. RPV Steam Dome Pressure

Figure 4. Total Break Flow from RPV

Figure 5. Wide Range (collapsed) Level

Figure 6. GDCS Injection Flow Rate

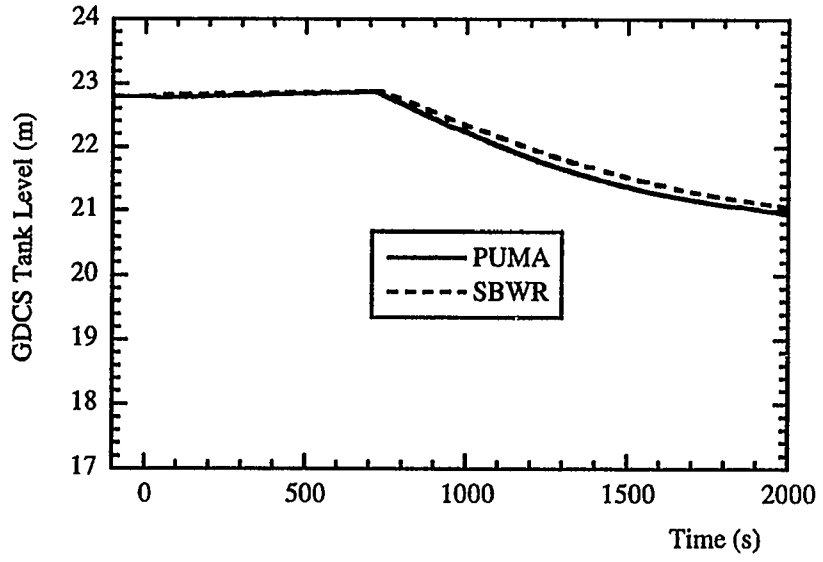

Figure 7. GDCS Tank Level

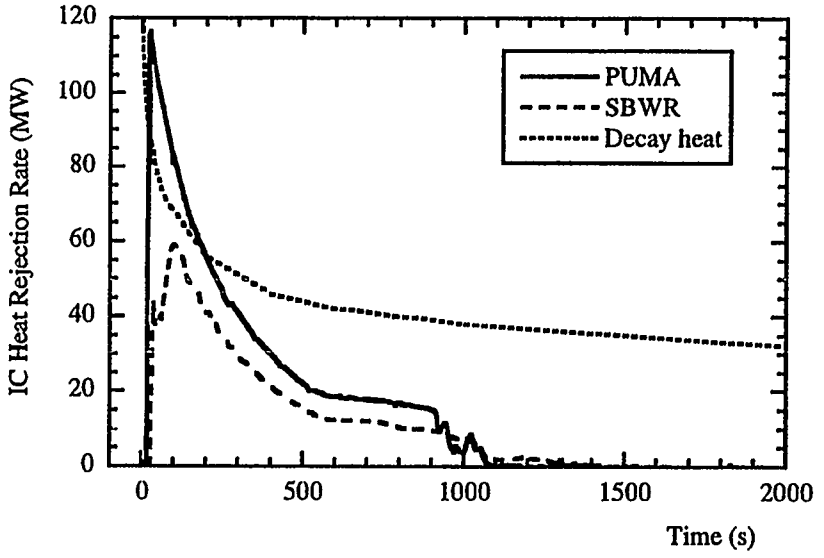

Figure 8. Isolation Condenser Heat Rejection Rate

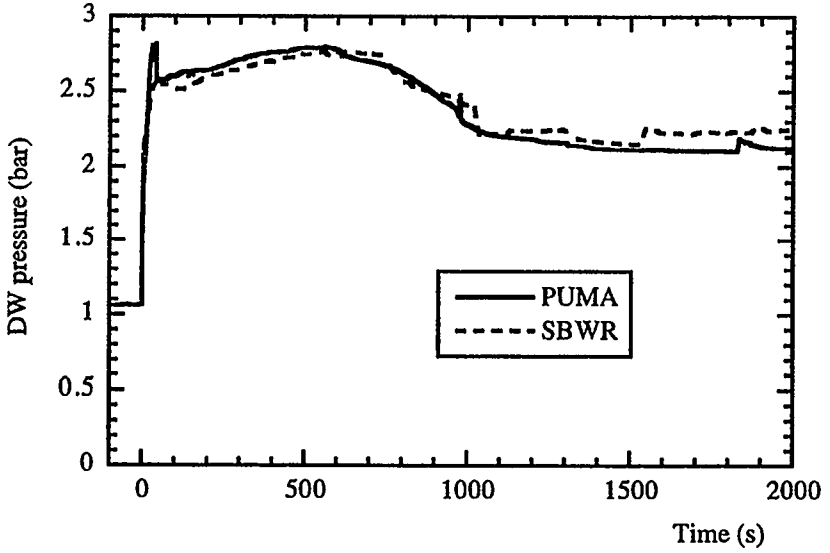

Figure 9. Drywell Pressure

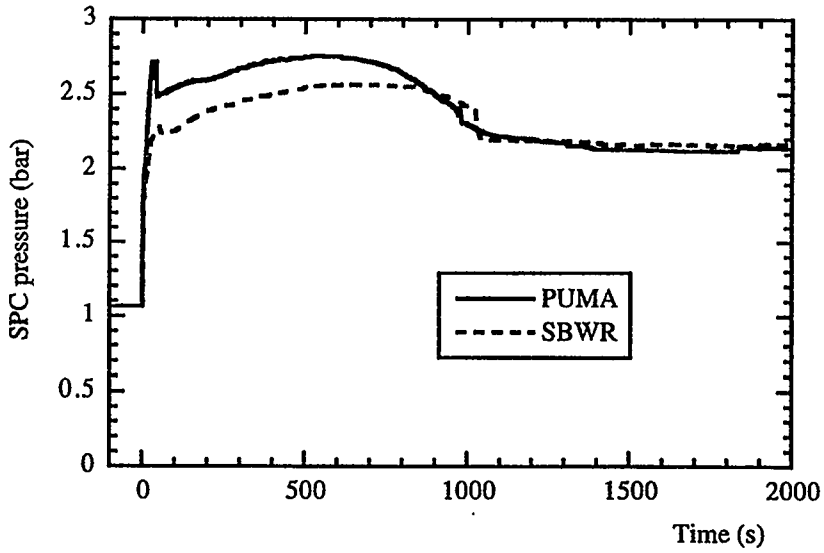

Figure 10. Suppression Pool Chamber Pressure

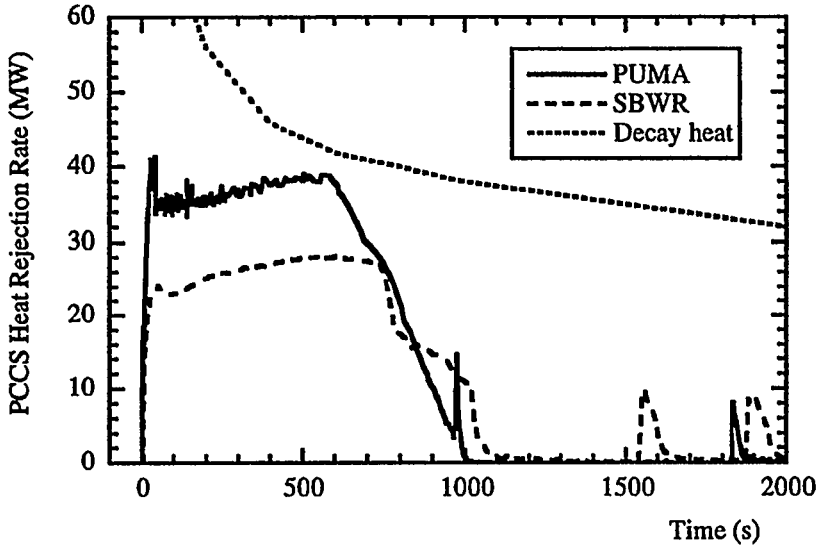

Figure 11. PCCS Condenser Heat Rejection Rate

RELAP5 Model Improvements for AP600 and SBWR

Gary W. Johnsen

Nuclear Research & Engineering
Idaho National Engineering Laboratory
P.O. Box 1625
Idaho Falls, Idaho 83415-3880

ABSTRACT

The United States Nuclear Regulatory Commission is sponsoring improvements to the RELAP5/MOD3 computer code to enable it to credibly model the two advanced light water reactor designs (AP600, SBWR). This paper describes the scope and content of new models and other improvements that are being incorporated to deal with system characteristics and phenomena unique to these new designs.

INTRODUCTION

Since the middle of 1992, the INEL has been engaged in incorporating improvements into the RELAP5/MOD3 computer code for the U.S. Nuclear Regulatory Commission to enable the code to model postulated accident behavior in the AP600 (Westinghouse) and SBWR (General Electric) advanced light water reactor designs.

The AP600 and SBWR designs have some common characteristics. Both rely on natural forces (i.e., gravity, expansion of a compressed gas) to cope with accidents and ensure long-term heat removal. The designs do not depend on "active" engineered safety systems (e.g., emergency coolant pumps) to successfully recover from design-basis accidents. That is why they are sometimes referred to as "passively safe". Both designs call for intentional, controlled, depressurization of the reactor coolant system under prescribed accident conditions, which enables the flow by gravity of makeup coolant from large in-containment water sources into the reactor. Also, both designs rely on the containment as an integral part of long-term decay heat removal strategy.

Analysis of the expected behavior of these systems under the range of postulated accidents that must be studied revealed that the RELAP5 code would need to model a number of characteristics or phenomena that it was either unable or untested to address. Among these are:

- Long transients (up to three days)
- Sharp liquid/gas interfaces
- Small, hydrostatic driving forces
- Strong thermal gradients within liquid pools
- Condensation inside tubes and on walls with noncondensable gas present

These, along with other requirements dictated by specific design attributes, formed the basis for planning improvements to the RELAP5/MOD3 code. Key modeling changes are next described.

DECREASING RUN TIME

Both the AP600 and SBWR are described as not requiring operator intervention for up to three days following certain prescribed accidents. Typical analyses of current generation reactors might

simulate several hours at the most. It was clearly apparent that having to analyze transients that long meant simplifying the input models and incorporating changes that would allow much larger time steps.

Several different approaches were pursued to increase code execution speed, the most significant of them being a new matrix solver and increasing the implicitness of the numerics. The former decreased the "grind time" while the latter enabled larger time steps to be taken. Speed gains of between three and nine times faster have been achieved, as shown in Table 1.

Table 1. Some examples of run time improvements

Problem Description	No. Vols.	Transient Time (sec)	Max Δt	MOD3.1	MOD3.18BA*	Speed up Factor
1. PWR: Feedwater Transient to steady-state	240	100	0.2	586	62.4	9.4
2. Similar to #1, more detailed model	594	20	0.2	452	64.9	7.0
3. Steam generator model, ruptured steam line	130	10	0.004	538	166	3.2
4. Steam generator model, transient to steady-state	52	300	0.02	98.4	34.0	2.9

* Developmental version using Nearly-Implicit Solution Scheme and BPLU matrix solver. All runs CRAY C-90

LEVEL TRACKING AND THERMAL STRATIFICATION MODELS

In both the AP600 and SBWR, well after the reactor coolant system depressurizes, the thermal-hydraulic behavior is characterized by a slow moving transient involving small pressure forces, low flows, and sharp liquid/gas interfaces. Several code improvements were implemented to better represent these conditions.

A level tracking model was added to permit recognition of a liquid level within a RELAP5 control volume. This obviates the need for a fine mesh nodalization, which would ordinarily be needed to capture a sharp void gradient. The model senses the existence of a level based on the void gradient between adjacent cells. When the criterion is satisfied, the model alters the void convected out of the cell. Ordinarily, the code would convect cell-centered, average properties across cell boundaries. However, when a level is detected, the code computes a void fraction above and below the two-phase level. These become the donored quantities, depending on the direction of flow through the volume.

Figure 1. RELAP5 CMT test model

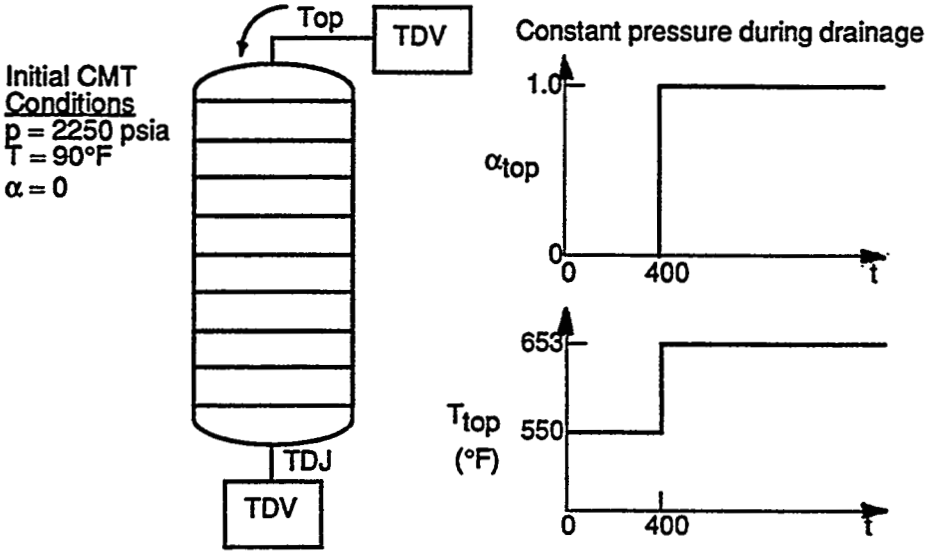

The development of sharp temperature gradients in liquid-filled tanks and pools occurs during accident conditions in both designs. Because of the numerical diffusion inherent in RELAP5 due to upwind differencing, such gradients tend to get numerically "smeared". To overcome this problem a thermal stratification model was added to enable tracking a sharp temperature gradient within a stack of control volumes. The technique used is similar to the level tracking model. A simple tank draining problem illustrates the effect of invoking the new model. Figure 1 shows the nodalization of an AP600 Core Makeup Tank (CMT), along with the prescribed boundary conditions for a draining scenario. The tank is initially filled with 90 degree F water at 2250 psia. Time dependent volumes (TDV) are connected to both ends of the tank. The TDV at the bottom provides a constant pressure boundary condition while the TDV at the top supplies first, 550 degree F water (for 400 seconds), then superheated steam (653 degree F). Figure 2 shows the calculated temperatures at the top, middle, and bottom of the tank as a function of time without the new model. Also included in the plot are the corresponding temperature profiles if perfect separation is assumed. The results show how the donoring scheme used in RELAP5 smears out the temperature gradient, distorting it both time and space. Figure 3 shows the result produced with the thermal stratification model turned on. The smearing is almost completely eliminated.

LOW FLOW PRESSURE DROP MODELS

The low flow wall friction and irreversible form loss models were also improved. A more accurate approximation to the Colebrook equation for wall friction was implemented for turbulent flow (Re>3000). The friction factor is computed using the Zigrang-Sylvester Model[1]:

$$1/\sqrt{f} = -2\log\left[\frac{\varepsilon/D}{3.7} + \frac{2.51}{Re}\left(1.114 - 2\log\left(\frac{\varepsilon}{D} + \frac{21.25}{Re^{0.9}}\right)\right)\right]$$

where f is the friction factor, ε is the pipe roughness, and Re is the Reynolds number. In addition, a "heated wall effect" model was added to recognize the change in viscosity near a heated surface. The modified friction factor is given by:

$$f/f_{ad} = 1 + [p_h/p_w]\left[(\mu_w/\mu_b)^n - 1\right]$$

where f_{ad} is the adiabatic friction factor, p_h is the perimeter of the heated surface, p_w is the wetted perimeter, μ_w is the viscosity of the fluid evaluated at the wall temperature, μ_b is the viscosity of the fluid evaluated at the bulk fluid temperature, and n is a user-supplied constant with a default value of 0.14. A new provision was added to permit users to specify a Reynolds number dependency for form losses. The form expression is given by:

$$K = A + B * Re^C$$

where A, B, and C are user-specified constants.

Figure 2. "Distortion" in axial temperature propagation for drain test problem

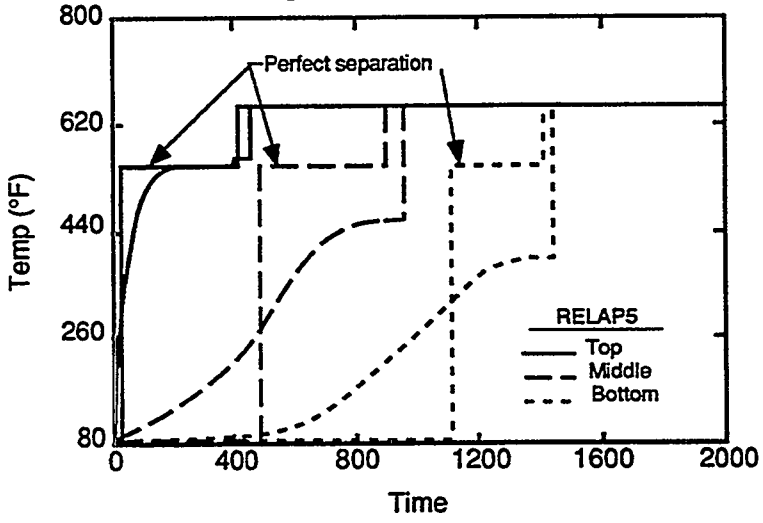

Figure 3. Temperature front propagation using thermal stratification model

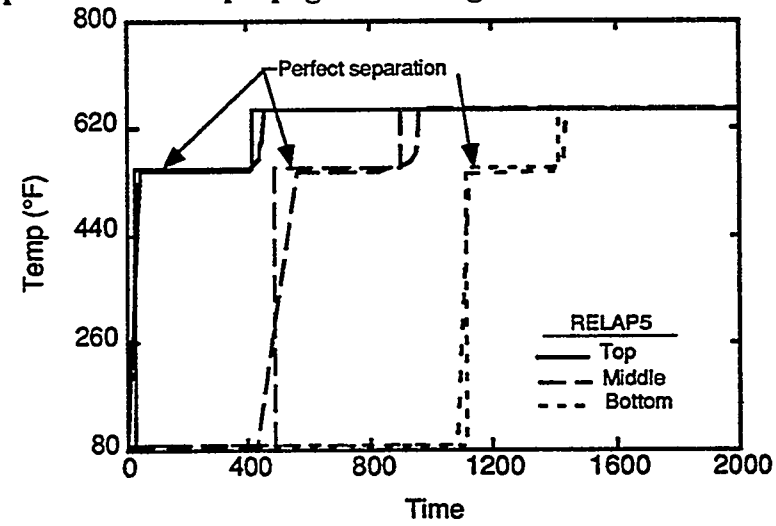

WALL CONDENSATION HEAT TRANSFER

In both reactor designs condensation of steam inside the containment building is the essential mechanism for long-term passive decay heat removal following a design basis accident. In the SBWR condensation occurs inside the tubes of two condensers mounted high in the containment building, whereas the AP600 design relies on condensation on the interior shell wall. In both cases, the condensation process includes the inhibiting effects of the noncondensable containment atmosphere. A new condensation model is being developed that explicitly models the diffusion of water vapor through the noncondensable to the condensing surface. This new model involves altering both the wall heat transfer and interfacial heat transfer models.

DESIGN-SPECIFIC CHANGES

Specific design features necessitated the inclusion of other new models. A mechanistic separator/dryer model was added to enable modeling these components in the SBWR. Also under consideration for the SBWR is a one-dimensional neutron kinetics model that was developed under a DOE-sponsored program.

Figure 4a. AP600 PRHR

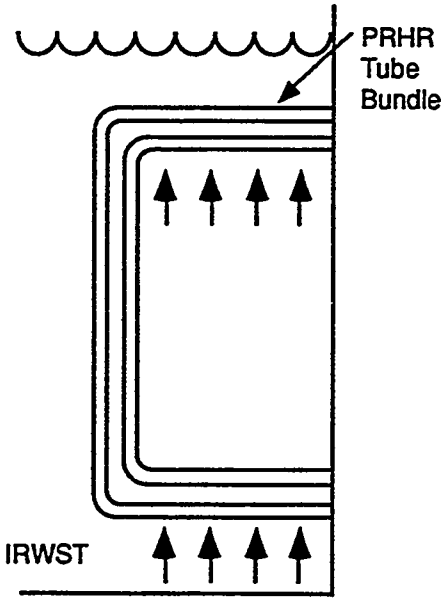

New convective heat transfer models were added to treat the horizontal portions of the tube bundle of the Passive Residual Heat Removal (PRHR) heat exchangers. These heat exchangers allow heat rejection from the reactor coolant system to the In Containment Refueling Water Storage Tank (IRWST). Figure 4a shows a depiction of the PRHR and Figure 4b a comparison of the pool boiling heat transfer characteristics of a single horizontal tube versus a bundle of horizontal tubes. The comparison shows that the bundle average heat transfer coefficient is higher for the bundle but the peak heat flux is lower. Initially, the heat flux is higher for the bundle owing to the turbulence caused by steam rising through the bundle. The peak heat flux seen for the single tube is a result of reaching the boiling crisis (i.e., critical heat flux). In contrast, for the bundle the peak heat flux is associated with the generation of steam on tubes low in the bundle starving the tubes above of liquid. That explains why the roll off in heat flux as wall superheat increases is much more gradual

than it is for the single tube. New boiling and critical heat flux (CHF) models were added to handle horizontal bundles. The boiling heat transfer coefficient suggested by Polley et al[2] was adopted:

$$h = h_{pb} + h_f (1/1-\alpha)^{0.774}$$

where h_{pb} is the pool boiling correlation proposed by Foster and Zuber[3] and h_f is a convective heat transfer coefficient by E.D.S.U[4].The CHF model proposed by Folkin and Goldberg[5] for horizontal tube bundles was incorporated into the code. It is based on Zuber's[6] single tube model and lowers the CHF value as void fraction increases:

$$q_{chf} = q_z (1-1.175\alpha)$$

where q_z is the CHF value given by Zuber's correlation.

Figure 4b. Boiling and CHF for bundle compared to single tube

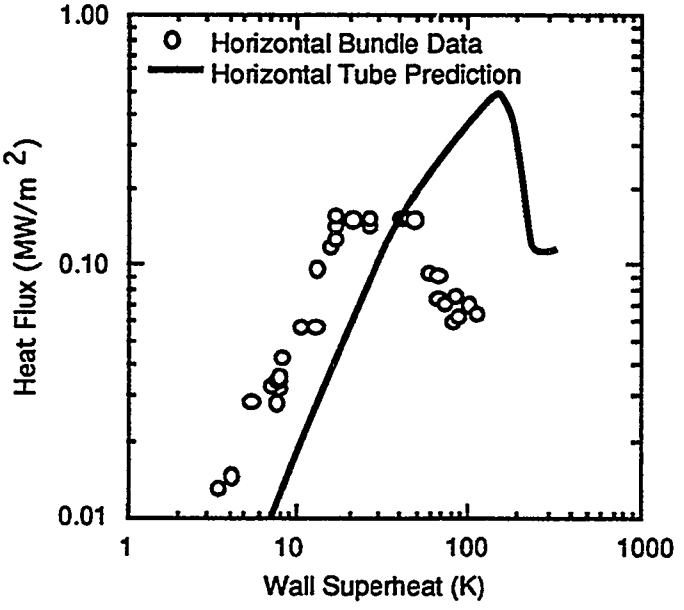

CODE RELEASES

The first version of MOD3 containing some of these improvements was released as version 3.1 in March 1993. Two subsequent internal releases were made in November 1993 and August 1994 (versions 3.1.1 and 3.1.2 respectively). Version 3.1.2 contains nearly all the scheduled improvements and is now undergoing validation and developmental assessment leading to the scheduled release of version 3.2 in February 1995.

REFERENCES

1. D. J. Zigrang and N. D. Sylvester, "A Review of Explicit Friction Factor Equations," Transactions of the ASME 280/Vol. 107, June, 1985.

2. G. T. Polley, T. Ralston, I. D. R. Grant, "Forced Crossflow Boiling in an Ideal In-Line Tube Bundle," ASME 80-HT-46, 1981.

3. H. K. Foster and N. Zuber, "Dynamics of Vapor Bubbles and Boiling Heat Transfer," AICHE, Vol. 1, No. 4, pp. 531-535, December 1955.

E.D.S.U., "Convective Heat Transfer During Crossflow Over Plain Tube Bundles," Item No. 73031, Engineering Science Data Unit, London, 1973.

5. B. S. Folkin and Y. N. Goldberg, "Simulation of Free Convection Boiling Crisis in Vapor Blanketing of a Horizontal Tube Bundle," Heat Transfer Soviet Res., Vol 12, No. 3, 1980, pp. 77-81.

6. N. Zuber, "Hydrodynamic Aspects of Boiling Heat Transfer," AECU-4439, U. S. Atomic Energy Commission, 1959.

SPES-2, THE FULL-HEIGHT, FULL-PRESSURE, INTEGRAL SYSTEM AP600 TEST FACILITY

M. Bacchiani, C. Medich, M. Rigamonti, O. Vescovi
SIET S.p.A.
Via N. Bixio 27
29100 Piacenza, Italy

L. E. Conway
Westinghouse Electric Co.
Pittsburgh, Pa - USA

ABSTRACT

The SPES-2 is a full height, full pressure experimental test facility reproducing the Westinghouse AP600 reactor with a scaling factor of 1/395. The experimental plant, designed and operated by SIET in Piacenza, consists of a full simulation of the AP600 primary core cooling system including all the passive and active safety systems. In 1992, Westinghouse, in cooperation with ENEL (Ente Nazionale per l' Energia Elettrica), ENEA (Ente per le Nuove Tecnologie,l' Energia e l' Ambiente), SIET and ANSALDO developed an experimental program to test the integrated behaviour of the AP600 passive safety systems. The SPES-2 test matrix, concluded in October '94, has examined the AP600 passive safety system response for a range of small break LOCAs at different locations on the primary system and on the passive system lines; single steam generator tube ruptures with both passive and active non-safety systems, and a main steam line break transient to demonstrate the boration capability of passive safety systems for rapid cooldown. Each of the tests has provided detailed experimental results for verification of the capability of the analysis methods to predict the integrated passive safety system behaviour. Colds and hot shakedown tests have been performed on the facility to check the characteristics of the plant before to start the experimantal campaign.
The paper first presents a description of the SPES-2 test facility then same results of the main tests compared with predictions performed using Relap5/mod3/80 obtained by ANSALDO through agreeement with U.S.N.R.C. The SPES-2 nodalization and RELAP Code results will be presented by ANSALDO in a second paper.

INTRODUCTION

Westinghouse Electric Corporation, in conjunction with the U.S.Department of Energy and the Electric Power Research Institute, has developed an advanced light water reactor design, known as AP600. AP600 is a 1940 MWt, 600MWe two-loop pressurized water reactor (PWR) that utilizes passive safety systems and modular design and construction techniques to reduce the capital costs, construction time and operational and maintenance cost.
The AP600 primary system utilizes a four-cold-leg, two-hot-leg configuration with canned-motor primary reactor coolant pumps. The pressurizer used in the AP600 design has a volume which is 30% larger than operating two-loop PWR's.. The larger pressurizer allows the unit to tolerate operational transients with increased margin. The average power has been reduced by 20%, the lower power density provides additional critical heat flux (DNB) margins for postulated design basis accident such as the large-break loss-of-coolant accident (LOCA). The primary loop design also results in a smaller cold legs for AP600 compared to a current PWR as a result, the break flow is reduced for the postulated large LOCAs resulting in an increased margin for AP600. Also, injection flow is injected directly into the reactor vessel downcomer so that less cooling water is lost through large breaks, making the passive safety systems more effective. The most significant unique features of the AP600 are the use of a safety grade passive core cooling system (PXS) and a passive containment cooling system (PCS) to mitigate the consequences of postulated accidents.
The passive safety systems are comprised of:

- two full pressure Core Make-up Tanks (CMT) providing borated makeup water to the primary system in the event of a loss of reactor coolant or reactor cooldown;
- two accumulators discharging high flow water into the core in the event of a large loss of reactor coolant;
- a set of valves connected to the pressurizer steam space and on the two hot legs, constituting the (ADS) which provides a controlled depressurization;
- an In-Containment Refuelling Water Storage Tank (IRWST) that is the long term gravity fed core cooling water reservoir and in which the ADS from the pressurizer are discharged;

- a Passive Residual Heat Removal System (PRHR) supplied with a C shaped heat exchanger submerged inside the IRWST that removes decay heat during loss of steam generator inventory.

A comprehensive test and analysis program has been developed to confirm the passive safety features of the AP600 design. The program includes large-scale separate effects tests on the major components and two integral system experimental campaigns: the experimental results obtained at SPES-2 facility are to be used in conjunction with one-quarter scale, low pressure Oregon State University facility to obtain the final design approval of the AP600 and to verify the capability of the analysis methods to predict the integrated passive safety systems behaviour.-

For SPES-2,Westinghouse, ENEA, ENEL and Ansaldo have a co-operative agreement for SIET to perform a set of integral system tests to simulate the operation of the AP600 passive safety systems. The SPES facility located in Piacenza,Italy (Fig.1) and operated by SIET was modified to simulate the AP600 reactor vessel, reactor coolant system, and passive safety injection system.

Originally the SPES facility was commissioned by ENEA to simulate a Westinghouse 312 pressurised water reactor with Italian specific design features.

The modified SPES facility,SPES-2 (Fig.2), is a full height, full pressure, 1/395th volume scale simulation of the AP600.

SYSTEM DESCRIPTION

Scaling criteria

The facility simulates the AP600:

. primary circuit;
. secondary circuit up to the steam isolation valve;
. all the passive safety systems: CMT's, IRWST, PRHR, ADS;and accumulators.
. the non safety systems: CVCS, NRHRS and Start-up Feed water (SFW).

The following general scaling criteria have been applied to the design of the SPES-2 test facility:

1. conservation of thermodynamic conditions (pressure and temperature);
2. power over volume ratio conservation in each component;
3. power over mass flowrate conservation;
4. fluid transit time preservation (as a consequence of 1, 2, 3);
5. heat flux conservation in heat transfer components (core and steam generator);
6. elevations maintained in lines and components;
7. preservation of Froude number in the primary circuit loop piping (hot leg and cold legs) inorder to preserve the flow regime transition to a stratified flow that would be expected for small break LOCA situations in horizontal piping.

Further specific scaling criteria have been applied to some components or lines to better duplicate the AP600 behaviour.

The overall scaling factor of the facility is 1/395, the main operating parameters are:

. process fluid	water
. number of loops	2
. number of reactor coolant pumps	2
. primary operating pressure, MPa	15.5
. secondary operating pressure, MPa	4.9
. primary operating temp.(HL/CL) , °C	. 315/276
. secondary operating temperature, °C	262
. full power, Mw	4.991
. elevation scaling	1/1
. primary core flowrate (kg/s)	23.

Primary piping

The primary piping consists of two loops each one including one hot leg and two cold legs. The hot leg, connecting the reactor vessel to a steam generator, duplicates the AP600 up to the pressurizer surge line nozzle by maintaining the AP600 L/D in the horizontal section and the same 55° angle in the inclined section.

The AP600 two cold legs per loop design, is duplicated however they detach from a single coolant pump vertical discharge (Fig.5). The split from the single pump discharge into the two cold legs is positioned at the elevation of the AP600 SG channel head in order to preserve the same geodesic flow path that the fluid must take from the unbroken cold leg to the broken one during a cold leg break transient (Fig.6) .

Due to the great importance of surge line during ADS depressurization the line has been designed preserving the friction pressure drops.

Rod bundle

The rod bundle is electrically heated and consists of 97 skin heated inconel rods reproducing, in the active zone, the same geometry (rod pitch, rod diameter and length) as the AP600 bundle. The axial power profile is uniform for all the rods, radially the profile is also uniform with the exception of two rods with a peaking factor of 1.19. The heater rods are single ended and are connected to a ground bus at the top of the bundle at the upper core plate elevation. The maximum bundle power is 9 Mw and the

maximum current is 70 kA. The scaled full power used for the AP600 transients is 4.89 MW (x 1.02)

Power channel downcomer

The downcomer is composed of an annular section in which the four cold legs and two direct vessel injection (DVI) nozzles are attached (Fig. 3,4). Below these nozzles a pipe connects this annular downcomer section to the lower plenum. In this fashion, the four cold leg/two hot leg characteristics of the AP600 can be preserved along with the downcomer injection features.
The annular and the tubular downcomer sections have the same friction pressure drops. The circumferential pressure drop of the annulus has been equalized to the AP600 . There are turning devices to direct the ECC injection flow downward in the annular downcomer as in the AP600. The total volume is scaled by the scaling factor.

Pressurizer

The pressurizer controls primary system pressure during normal and transient plant operation and consists of a cylindrical flanged vessel equipped with 2 immersion type heaters each having a maximum controlled power of 16 kw and 6 external heaters each generating 3 kW. The pressurizer volume is scaled and the bottom elevation is preserved. The level swelling is preserved by ensuring that the average void fraction in the test is equal to AP600 for similar thermo-hydraulics conditions using the Wilson bubble rise models. The experiments performed in the original SPES test series indicated that this was a proper scaling approach.

Pumps

Two primary pumps (one per loop) drive primary coolant into the PC downcomer to remove the generated heat. The pumps are centrifugal-single stage-horizontal shaft type, the suction line is horizontal while the delivery is directed downwards discharging in a 3" pipe common to the two cold legs. A flywheel is provided to have an inertia closer to the AP600. The rotational speed can be controlled in the range +/- 190% of the nominal value and the speed variations can be programmed by a means of a motor driven regulator.

Steam Generators

The facility has two identical generators to transfer thermal power from the primary to the secondary circuit. The steam generator primary side consists of a tube bundle and inlet/outlet plena. The SG bundle includes 13 inconel 600 U-tubes assembled in a square array.
The secondary side volumes are scaled by 1/395, and all the vertical elevations are preserved up to the top of the steam separator (the steam dome has no influence on the natural circulation phenomena).

Passive safety systems

- The Core Make up Tanks (CMTs) design is unique and has been developed by SIET engineers so that the CMT metal mass is scaled to the AP600 CMT. The CMT design uses a thin-walled vessel inside a thicker pressure vessel with the space between the two vessel pressurised with air at 70 bar. In this manner the rate of steam condensation on the walls is preserved. Since the CMTs are full height and operate at full pressure, the surface area to volume and total metal mass of a single pressure vessel would have been excessive resulting in very large wall steam condensation effects.

- - two Accumulators with volume scaled;

- one Passive Residual Heat Removal (PRHR) with a full height C shaped heat exchanger with friction pressure drops maintained and the heat transfer area is scaled such that the natural circulation behaviour of the AP600 PRHR is simulated.

- In-containment Refuelling Water Storage Tank (IRWST) at atmospheric pressure with water volume scaled and elevation maintained;

- four stages of Automatic Depressurization System (ADS) simulated by means of ball valves (one per stage) with an orifice in series to achieve the proper scaled flow area. The two ADS valve pacheges connected to the steam space of the pressurizer in the AP600 are combined into a single set with the first, second and third stage valves in SPES-2. The three ADS valves share a common discharge line to a condenser and a collection tank that has load cells to measure the mass accumulation. A similar measuring arrangement is also used for the two ADS fourth stages, one of which is located on each hot legs of the primary piping.

The injection capability of the AP600 non passive systems such as CVCS, NRHR and SFW can be provided in order to illustrate any safety/non safety system interaction. The friction pressure drops of all the connecting lines are maintained. Small break are simulated using a spool piece which contains a break orifice and quick opening valve. The break, ADS and secondary relief valve discharges are collected into different catch tanks with load cells to measure the mass accumulation.

TEST OBJECTIVES

The overall and specific objectives of the AP600, SPES-2 Integral Systems Test are:

1. - Simulate the AP600 thermal-hydraulic phenomena and behaviour of the AP600 following specified small-break loss of coolant accidents (LOCA's), steam generator tube ruptures (SGTR's), and steam line breaks (SLB's).

2. - Obtain detailed experimental results for verification of accident analysis computer codes.

3. - Provide detailed measurements of the operation of the AP600 Core Makeup Tanks (CMT's) Following initiation of the specified transients.

4. - Observe the effects of the injection of nitrogen gas from the safety-injection accumulators following their water delivery.

5. - Provide in-sight on the ability of the automatic Depressurization System (ADS) to depressurize the reactor coolant system sufficiently to permit gravity injection following any postulated event.

6. - Provide information on interactions between the AP600 Passive Safety Injection System (PXS) and non safety active systems.

TEST MATRIX AND RESULTS

The transient tests which were performed are listed and described in Table 1. These tests include:

1.- Test Nos. 1,3 and 4 which are 1-inch and 2-inch pipe size, primary system cold leg breaks. These breaks were located in the bottom of the cold leg that contains the balance line to the normally instrumented CMT (test No.2 will not be performed).

2.- Test Nos. 5 and 6 are breaks in the direct vessel injection line of 2-inch pipe size and a double ended guillotine break of the DVI nozzle. The 2-inch break was located in the DVI line and both breaks were located in the DVI line connected to CMT-B.

3.- Test Nos. 7 and 8 are a 2-inch pipe size break and a double-ended break of the CL to CMT balance line. These breaks were located in the balance line to the CMT-B.

4.- Test Nos. 9, 10, and 11 are simulated steam generator tube ruptures (SGTR's). Test 9 and 10 are to simulate a single ruptured tube; one with operator action and active systems, and one with just the passive systems and automatic actuations for accident mitigation with no operator actions. Test No.11 simulates single ruptured tube with only passive system and with ADS initiated shortly after (2.5 minutes) reactor trip.

5.- Test No. 12 is a large, single-ended steamline Break (SLB) at the steam discharge nozzle of steam generator A:

6.- Test No. 13 is similar to No.1, a 1-inch cold leg break, but with all three PRHR-HX tubes in operation.

Tests 1 through 11 and 13 were initiated from conditions simulating AP600 full power operation. Initial conditions for Test 12, the large steamline break, simulate plant start-up condition, 0% power, no decay heat, with RCP's initially operating.
The response of the facility is shown below and is compared with pre-test analysis which were performed by ANSALDO using RELAP5/mod3/80 in Figures 7 to 18. The above initial conditions and automatic actuations in the sequence of events simulate the AP600 full power conditions and safety actuation signal set points.

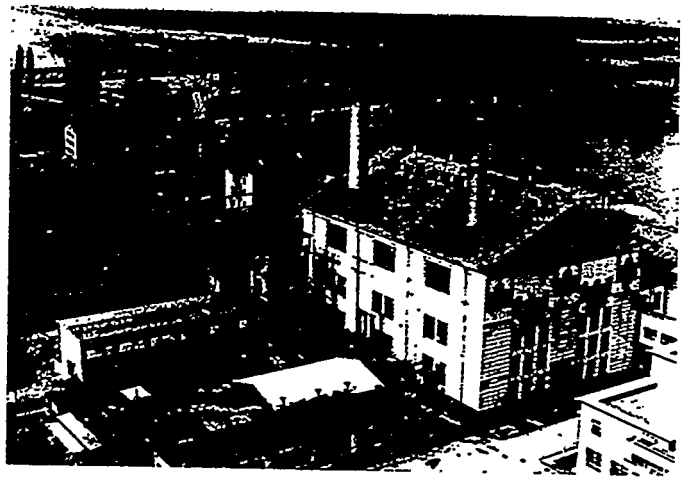

Fig. 1 SIET Laboratory in Piacenza

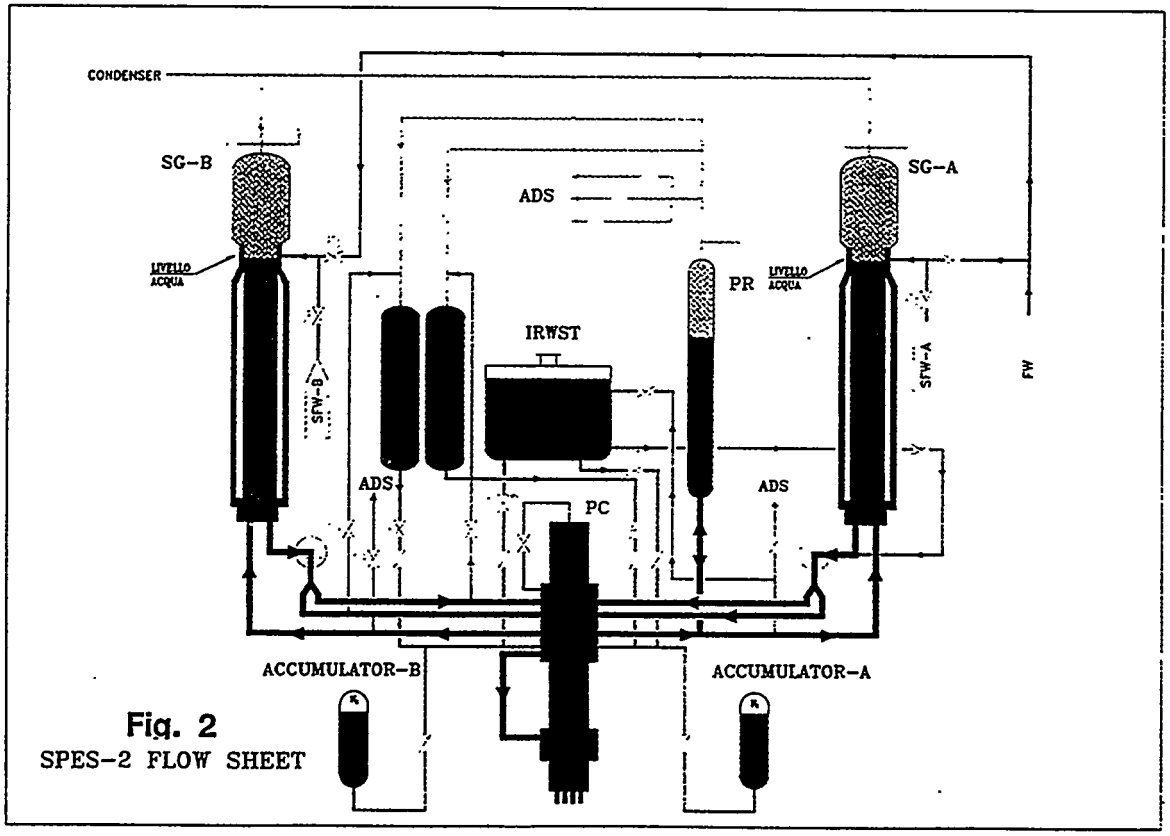

Fig. 2
SPES-2 FLOW SHEET

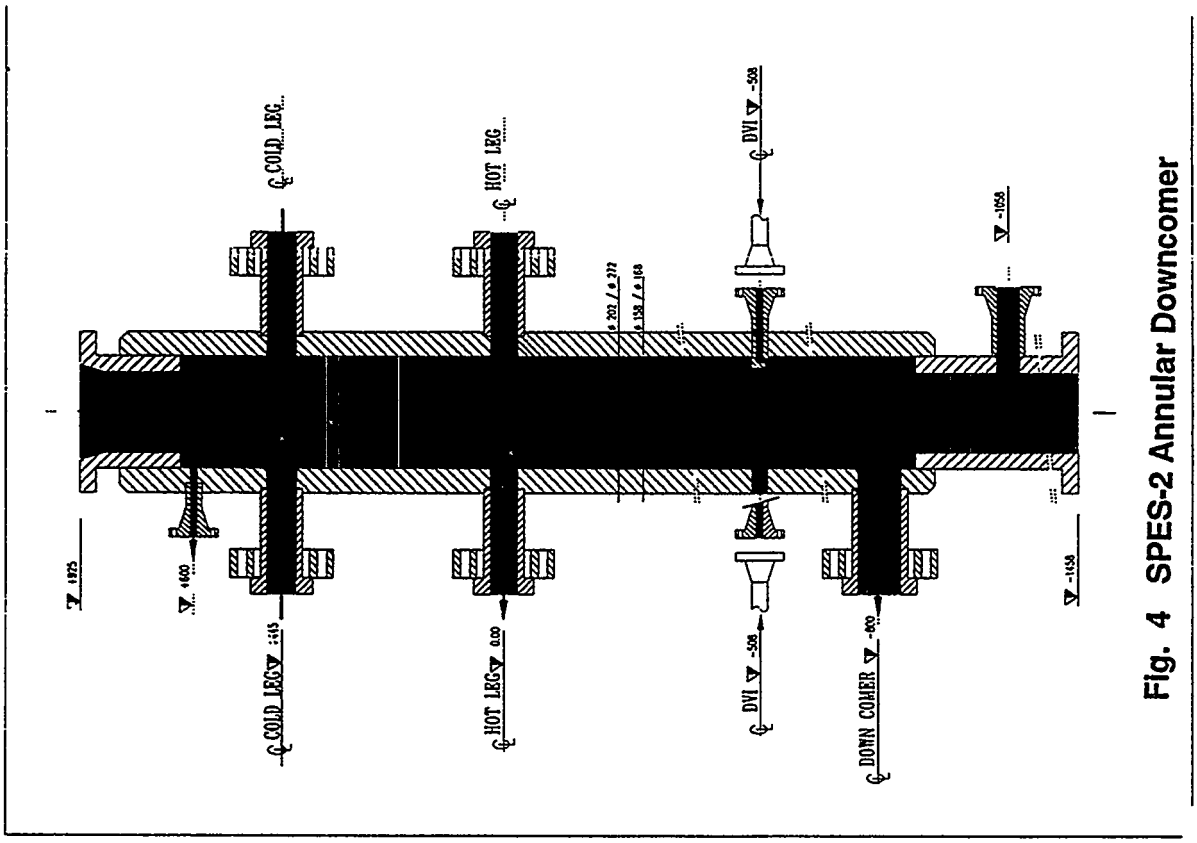

Fig. 4 SPES-2 Annular Downcomer

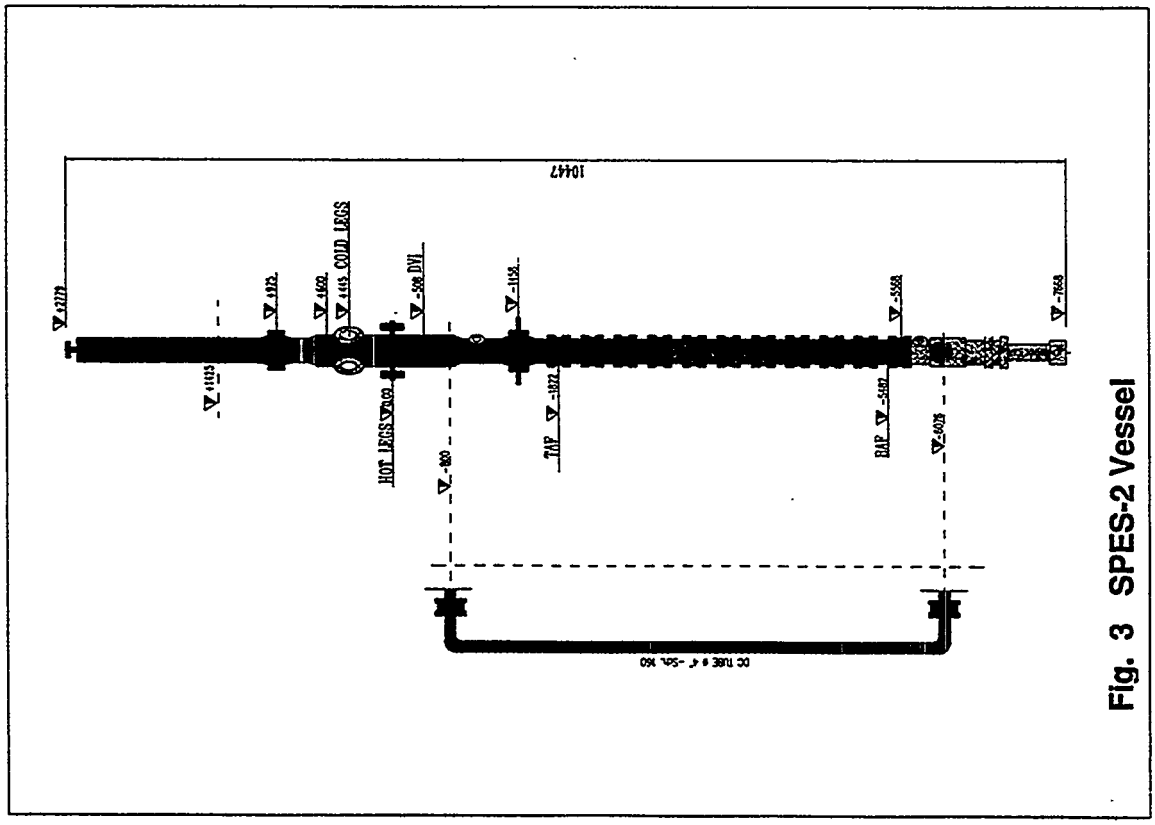

Fig. 3 SPES-2 Vessel

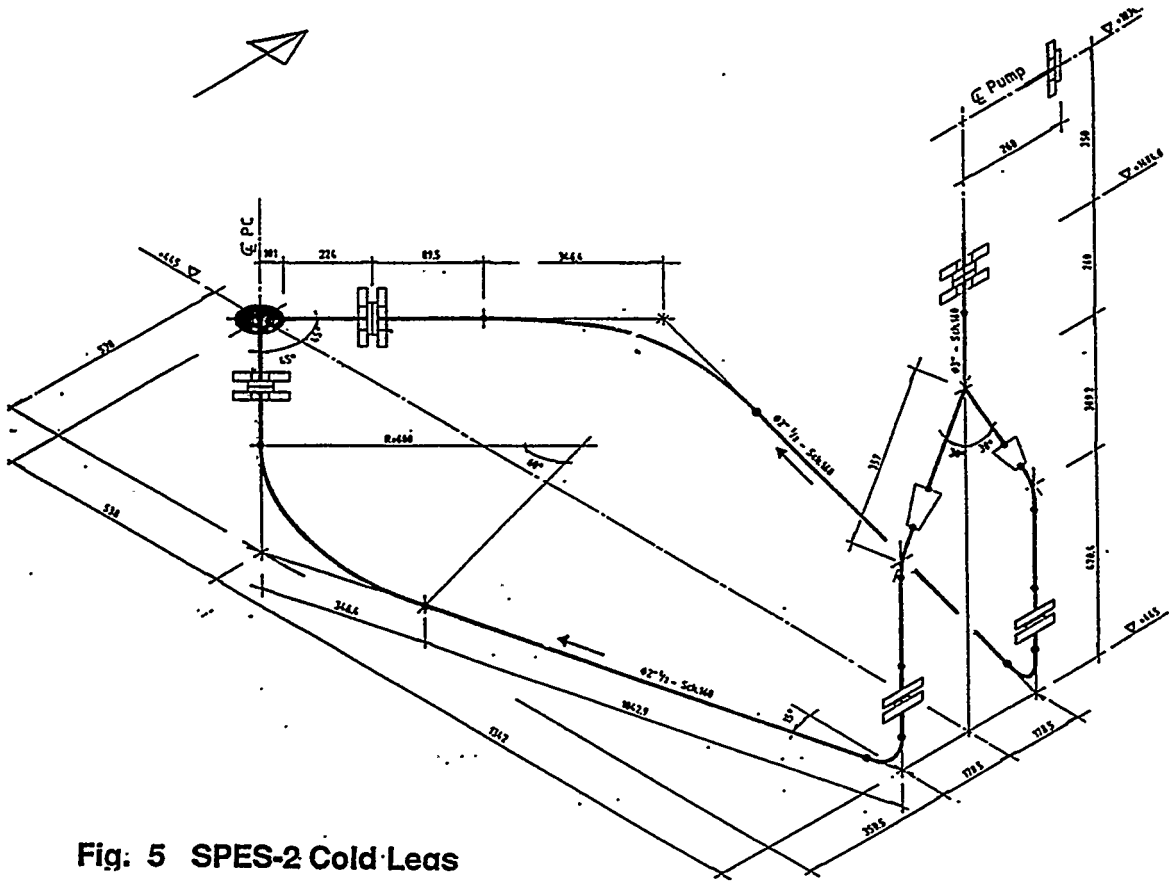

Fig. 5 SPES-2 Cold Leas

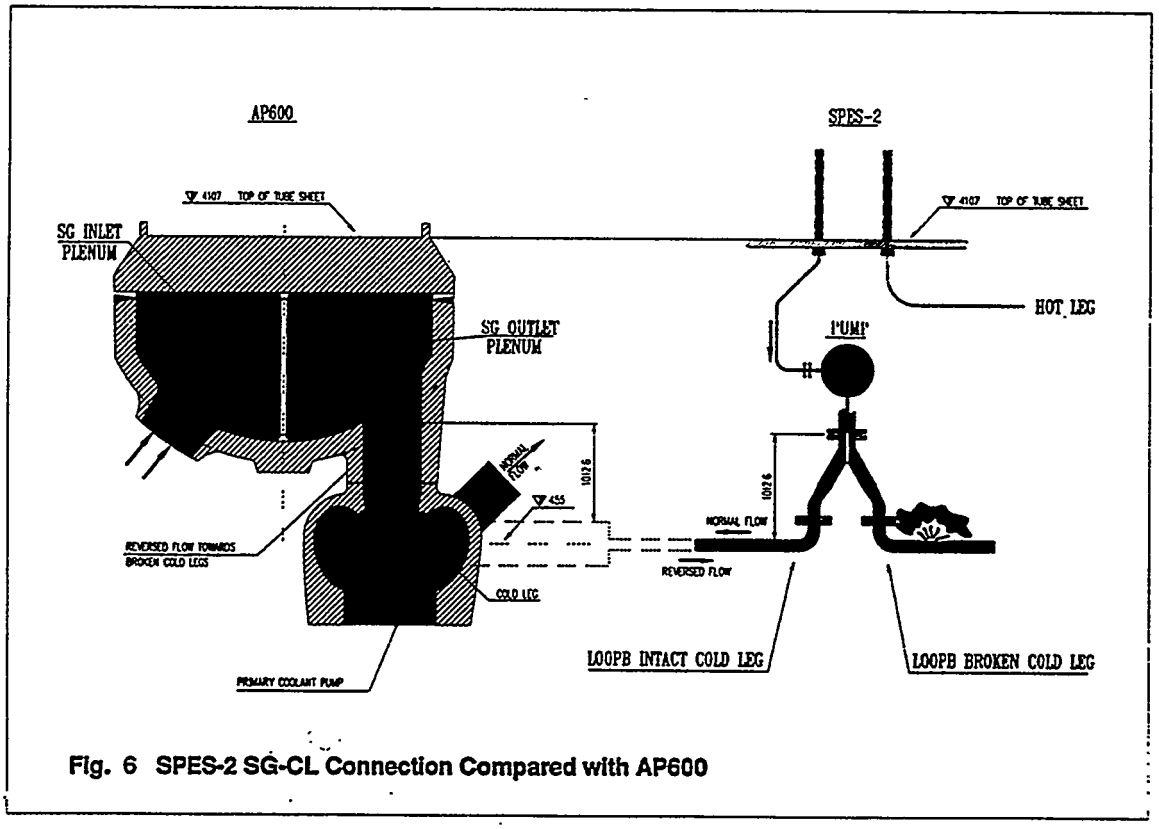

Fig. 6 SPES-2 SG-CL Connection Compared with AP600

Comparison between experimental data and ANSALDO pretest calculation.

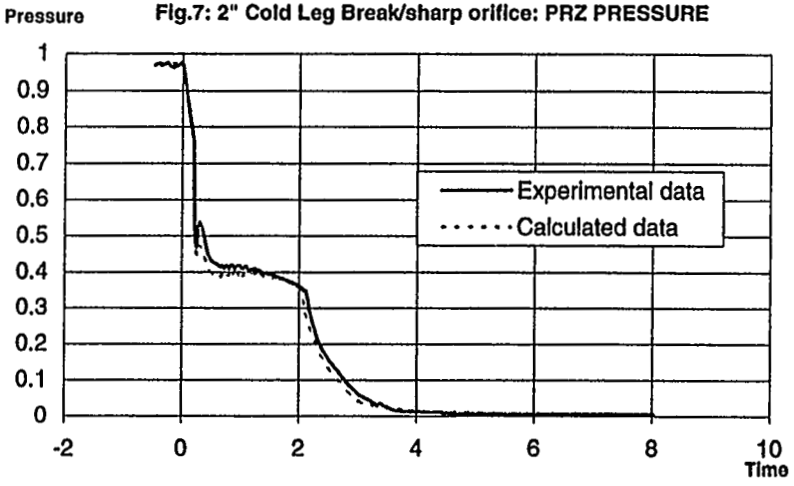

Fig.7: 2" Cold Leg Break/sharp orifice: PRZ PRESSURE

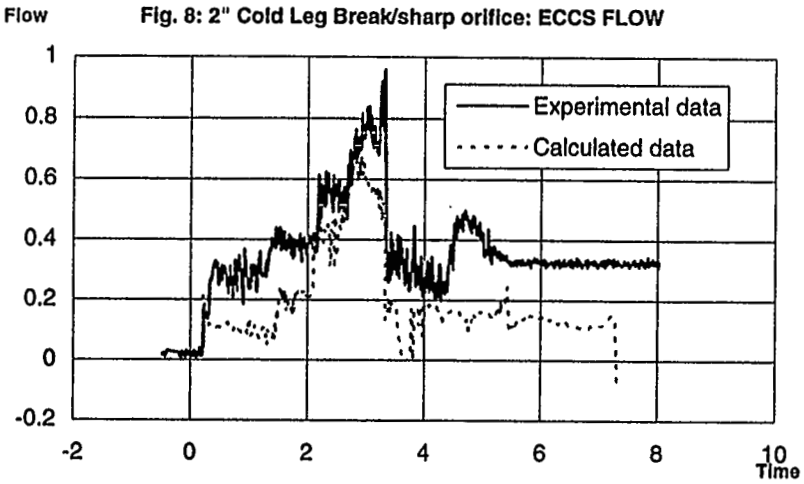

Fig. 8: 2" Cold Leg Break/sharp orifice: ECCS FLOW

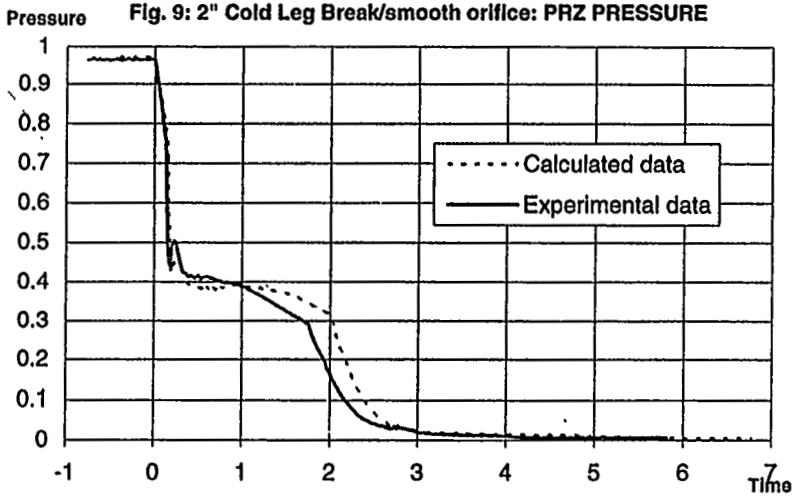

Fig. 9: 2" Cold Leg Break/smooth orifice: PRZ PRESSURE

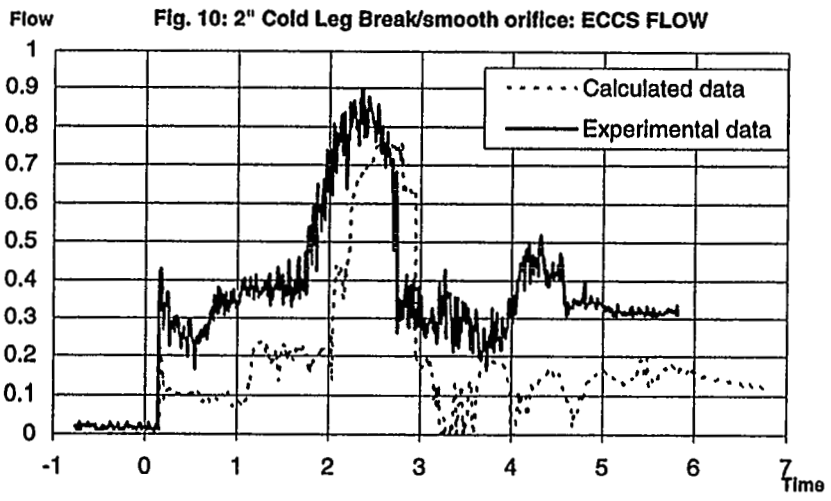

Fig. 10: 2" Cold Leg Break/smooth orifice: ECCS FLOW

All the scales are normalized

Comparison between experimental data and ANSALDO pretest calculation.

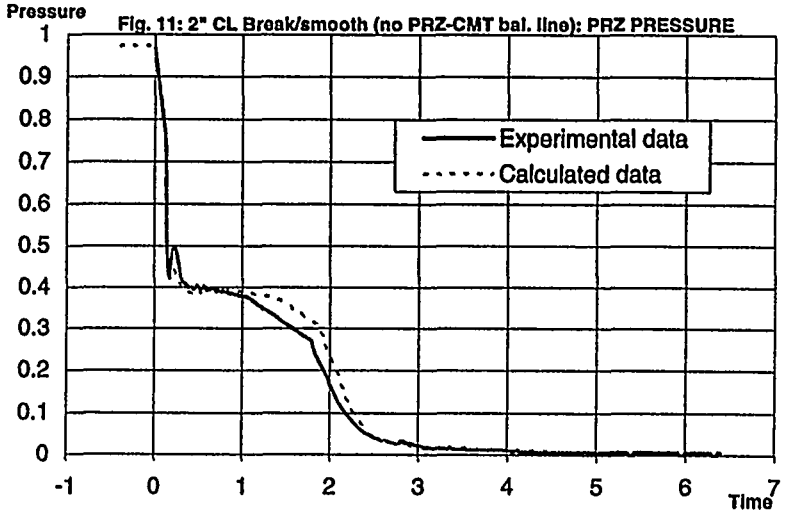

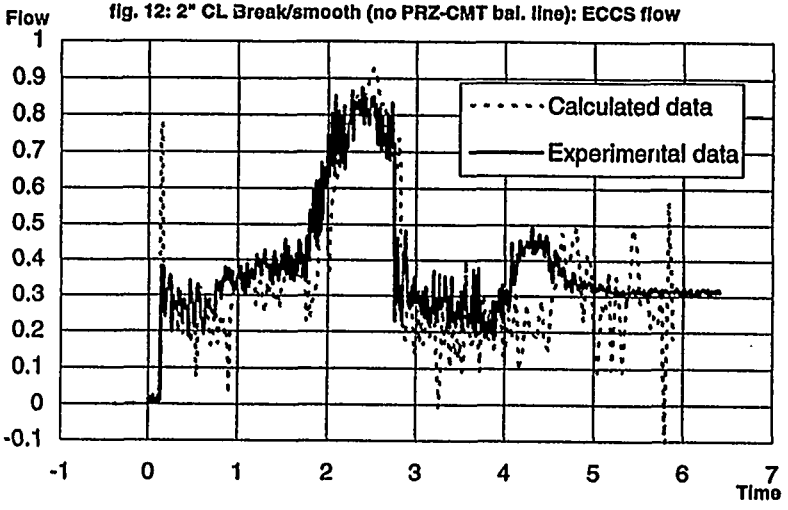

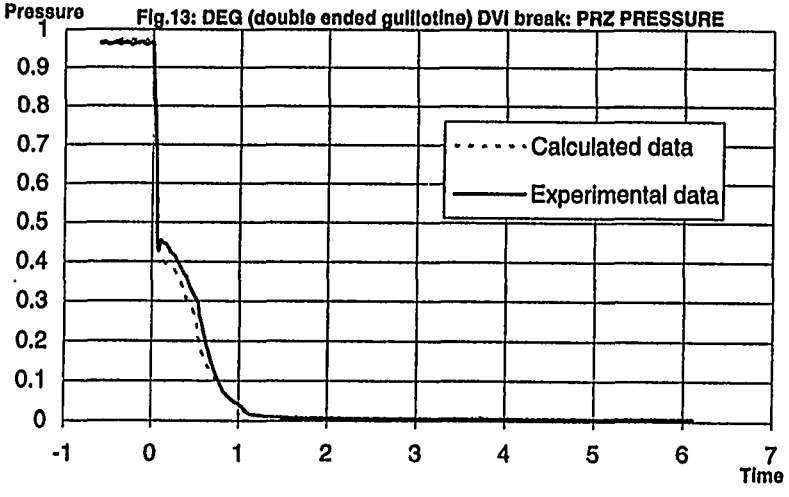

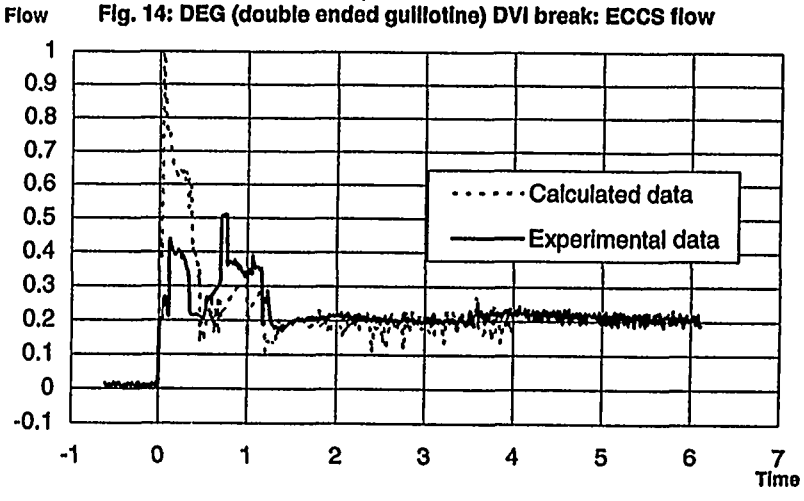

All the scales are normalized

Comparison between experimental data and ANSALDO pretest calculation.

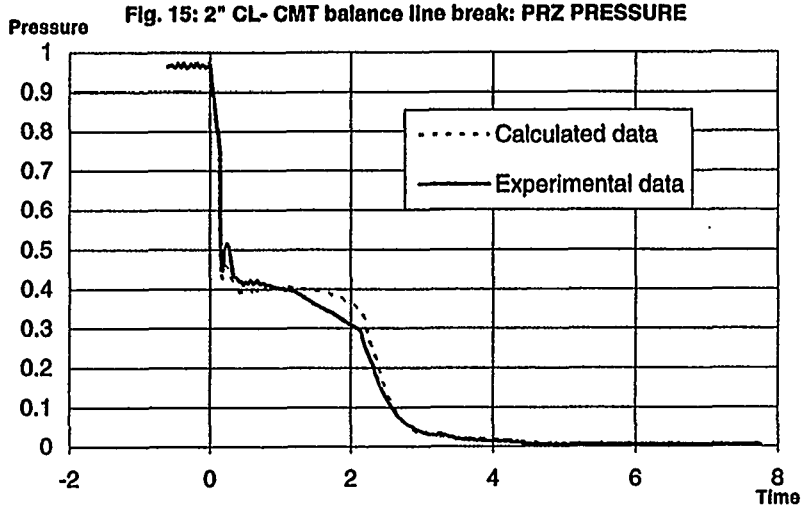

Fig. 15: 2" CL- CMT balance line break: PRZ PRESSURE

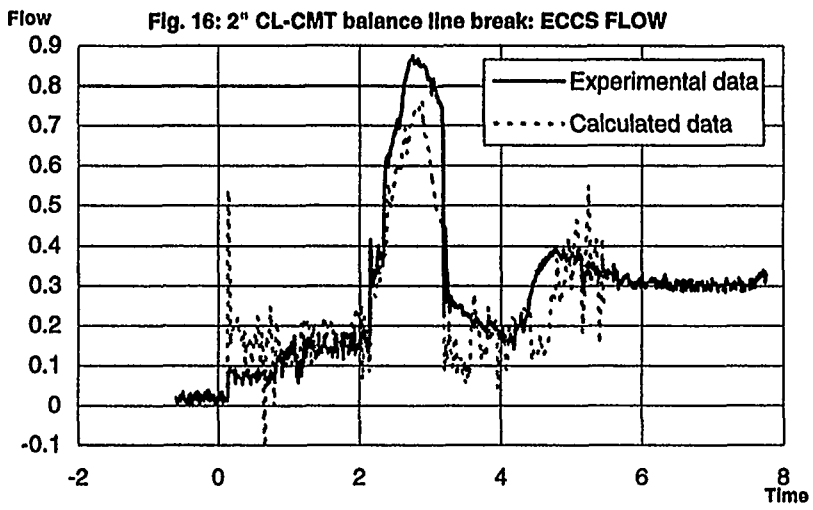

Fig. 16: 2" CL-CMT balance line break: ECCS FLOW

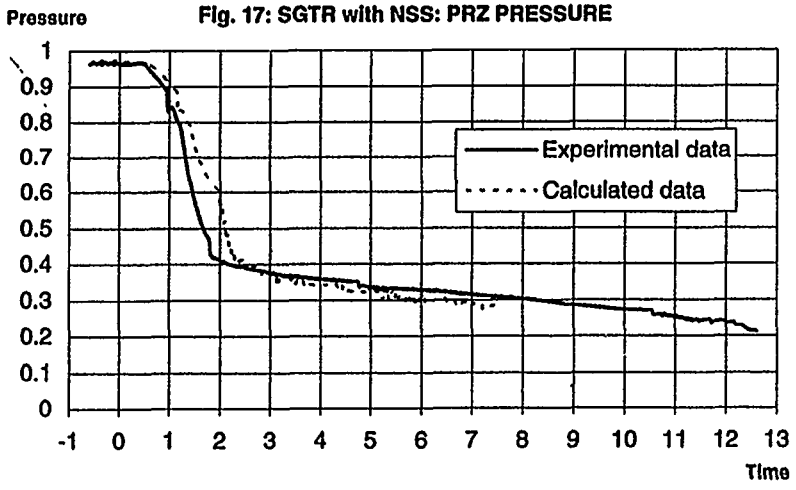

Fig. 17: SGTR with NSS: PRZ PRESSURE

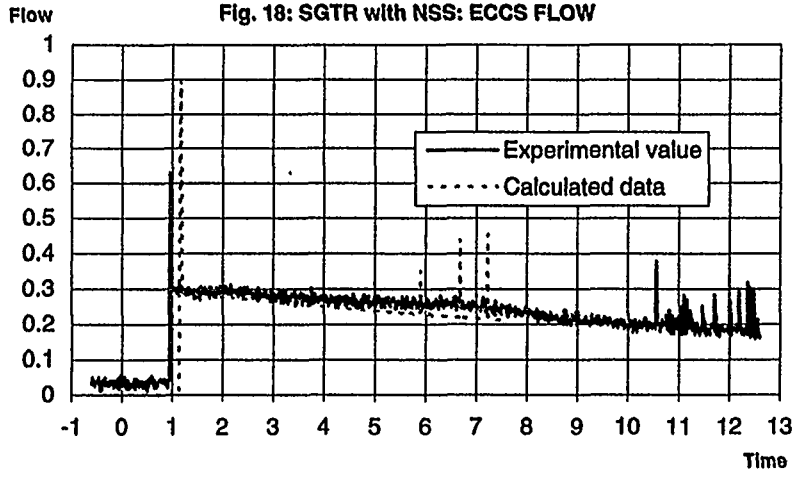

Fig. 18: SGTR with NSS: ECCS FLOW

All the scales are normalized

TABLE -1 SPES-2, TEST MATRIX					
Test No.	Test Type	Test Description (AP600 Transient Simulated)	Status Non-safety Systems	Single Failure	Comment
1	SBLOCA	1-inch CL break (Note 2) of Loop B (Note 1)	CVCS, NRHR, and SFW Off	1 of 2 4th stage valves on Loop B	Maximize CMT heatup prior to ADS actuation
2	SBLOCA	1-inch CL break of Loop B	CVCS, NRHR Off; SFW On (Note 3)	1 of 2 4th stage valves on Loop B	This test delete due to AP600 design changes
3	SBLOCA	2-inch CL break, bottom of Loop B	CVCS, NRHR, and SFW Off	1 of 2 4th stage valves on Loop B	Reference CL break
4	SBLOCA	2-inch CL break, bottom of Loop B	CVCS, NRHR, and SFW On (Note 3)	No effect - no 4th stage actuation expected	Non-safety/passive system interactions
5	SBLOCA	2-inch DVI break	CVCS, NRHR and SFW Off	1 of 2 4th stage valves on Loop B	Asymmetric CMT performance
6	SBLOCA	DEG break of DVI	CVCS, NRHR, and SFW Off	1 of 2 Stage 1 and Stage 3 valves	Complete loss of one-of-two PXS subsystems
7	SBLOCA	2-inch break of a CL/CMT balance line	CVCS, NRHR, and SFW Off	1 of 2 4th stage valves on Loop B	Examine effect on CMT drain down
8	SBLOCA	DEG break of a CL/CMT balance line between valve and CMT	CVCS, NRHR, and SFW Off	1 of 2 Stage 1 and 1 of 2 Stage 2 ADS valves	No delivery from faulted CMT
9	SGTR	Design basis SGTR (1 tube)	CVCS, SFWS On; Operator action to isolate SG, subcool, depressurize	No effect	Recovery with proper operator action; show recovery, margin

TABLE -1 (Continued)
SPES-2, TEST MATRIX

Test No.	Test Type	Test Description (AP600 Transient Simulated)	Status Non-safety Systems	Single Failure	Comment
10	SGTR	Design basis SGTR (1 tube)	No CVCS. SFWS is on until isol. by HI SG level or LO T-cold, no operator action	No effect	Recovery with no operator action
11	SGTR	Design basis SGTR (1 tube) with manual ADS actuation	No CVCS, or SFW, no additional operator actions.	1 of 2 4th stage valves on Loop B	Cause SG to primary flow observe dilution rate, ADS performance.
12	SLB	SL break at zero power. A 1.388 ft^2 single ended SLB on SGA discharge.	No CVCS, NRHR	SFW not isolated on Tcold signal	Show CMT's do not drain and no ADS actuation occurs.
13	SBLOCA (with 3 PRHR HX tubes in service)	1-inch CL break (Note 2) of Loop B (Note 1)	CVCS, NRHR, and SFW off	1 of 2 4th stage valves on Loop B	Show effect of 2 PRHR HX's on cold leg temperature.

Notes:

1) Loop B is the CMT side of plant, Loop A is PZR and PRHR side of plant.
2) Break sizes are "a broken pipe of the indicated diameter", e.g., 2-inch break is 3.146 $in.^2$
3) SG main feedwater isolated on S-signal and SFW initiated, SFW on until isolated on HI SG level or LO-Tcold.
4) Selected repeat test may be performed.

SPES-2 RELAP5/MOD3 NODING AND 1" COLD LEG BREAK TEST S00401

Alemberti A., Frepoli C., Graziosi G.
ANSALDO Nuclear Division
Genova , Italy

22nd Water Reactor Safety information Meeting
WASHINGTON D.C. October 24-26 1994

ABSTRACT

SPES-2 is a full height, full pressure experimental facility scaled 1/395 respect to the Westinghouse AP600 plant. The SPES-2 facility designed and operated by SIET in Piacenza is the evolution of the previous existing SPES-1 facility. The SPES-2 test matrix provide a complete set of experiments from Cold Leg break accidents to Steam Generator Tubes Ruptures and Main Steam Line break. The SPES-2 test program is performed under the technical cooperation agreement among ENEL, ENEA, ANSALDO and WESTINGHOUSE.
In the frame of the SPES-2 activities ANSALDO carried out pre-test calculations for the facility as well as comparisons with full plant behaviour to support the facility scaling criteria.
SPES-2 calculations were carried out using a nodalization developed by ANSALDO for the Relap5/mod3/V80 code.
The facility noding was developed mainly with the usual hand calculations while for some aspects of the facility 3-D calculations were carried out to provide guidelines for the noding development.
The paper presents some of the particular aspects of the facility analyzed using the CFDS-FLOW3D code (developed by Harwell Laboratory) as well as the final Relap5/mod3 noding for SPES-2.
The main purpose of this presentation will be to show how a 3-D code can be used to develop user guidelines for the Relap5 noding to deal with particular aspects of the facility (or plant) not automatically handled by the code itself.
After the presentation of such noding details, and considerations on Relap5 modelling limitations as well as possible solutions, a comparison of the calculations performed for the 1" Cold Leg break with experimental data is also presented.

INTRODUCTION

In the following the SPES-2 Relap5/mod3 noding developed by ANSALDO is presented. The noding is briefly described to give an idea of the extension of the noding itself while particular aspects of the facility solved with the help of 3-D calculations will be presented in detail. Others components of the SPES-2 noding where developed by comparison of experimental results with pre-test calculations gaining in this way a better knowledge on how to simulate the system taken into consideration. This work is mainly devoted to the presentation of user guidelines, developed during the SPES-2 activity, able to improve the response of the Relap5/mod3 code.

The following parts of the facility have been analyzed with 3-D calculations resulting in modifications to the original SPES-2 noding:

- Annular-Tubular downcomer behaviour
- Annular downcomer (hot leg) form losses

Noding was also reviewed by comparison of the facility behaviour with pre-test predictions for:

- CMTs noding
- IRWST noding

The paper presents the final noding and conclusion for each of the above cited aspects of the simulation.

Relap5 modelling limitation are analyzed, were they exists, and possible solutions briefly outlined to improve the code response in future releases.

Finally the results of the 1" C.L. break simulations are compared with experimental data to show the degree of reproduction of the experimental data obtained.

SPES-2 NODING

The general arrangement of the SPES-2 noding is presented in Fig.1. Total number of volumes is 457 while junction connections are 542. Each volume is provided by its own heat structure exchanging heat with the environment since heat losses simulation is very important for facility scaled like SPES-2 (1/395). A complete noding description is not here reported. We are going to concentrate our attention on parts of the noding were unusual approaches have been used for the noding development.

ANNULAR-TUBULAR DOWNCOMER BEHAVIOUR

During small break accidents the facility behaviour is characterized by a constant pressure phase in which the downcomer situation is rather stable with cold water injected by the CMTs through the DVIs lines and core flow driven by natural circulation.
In AP600 were the annular downcomer extends to the inlet plenum is clear that the cold water injected by DVIs is able to reach the lower plenum while hot water is recirculated to the upper part of the downcomer. For this reason the AP600 noding was provided by a quasi 2-D simulation which allows Relap5 to represent such situation at least qualitatively .
The SPES-2 facility is provided by an annular downcomer in the upper part and tubular downcomer connecting the annular downcomer to the lower plenum.
A 1-D simulation of the tubular downcomer will not permit cold water to reach the inlet plenum of the facility until hot water already present in the tubular downcomer is pushed through the core. In the facility it was not really clear if the cold water injected is able to flow into the tubular downcomer or not. To solve this problem a 3-D simulation of the annular-tubular downcomer was performed using the CFDS-FLOW3D code (developed by Harwell Laboratory) to better understand the behaviour of the annular-tubular downcomer flows.

The SPES-2 CFDS-FLOW3D noding is shown in Fig.2. Only the upper part of the noding is presented to give details about the grid used. The full grid extends to the inlet plenum connections and core inlet section. The annulus is partitioned in the radial direction with 6 cells, in the azimuthal direction with 50 cells and in the vertical direction with 77 cells. The tubular downcomer is provided by a 6x6 mesh in the cross section and subdivided in the axial with about 150 cells. Lower plenum is simulated by 11x11 mesh in the horizontal section and 72 cells in the vertical direction.
Boundary conditions have been applied to the annular downcomer top (upflow to the break location) and injected DVIs flow resulting in a core flow rate equal to the difference of the two above cited values. The difference scheme used by the code is the hybrid scheme.
The coriolis force has been also included in the simulation to improve the response of the code respect to the interaction of the injected flow and hot water recirculating in the tubular downcomer.

Figures 3,4 and 5 shows the annular-tubular downcomer connection at different times 31, 35 and 120 seconds respectively. The cold water stream located just above the annular-tubular downcomer connections is characterized by an unstable behaviour switching from left to right due to the interaction with the hot water coming in the opposite direction from the tubular downcomer. The simulation of this interesting behaviour of the cold water stream was possible only with the introduction of the coriolis force which added a force term able to produce this unstable interaction.
Velocity vectors and temperature field in the upper part of the tubular downcomer are shown in Figure 6. Here it is possible to observe the recirculation path in the tubular downcomer with hot water coming up from the lower plenum and cold water directed to the lower plenum. However as shown in the previous plots the cold water level in the upper part of the tubular downcomer is not already stable and some degree of mixing is predicted by the code. Plot of the temperature distribution on the lower part of the tubular downcomer is shown in figure 7 were a much more stable situation is predicted. Although the situation here described is ideal (the calculation was performed without the PRHR flow contribution) it is clear that the facility can exhibit such a behaviour so that adequate noding should be provided to Relap5 input deck.

Figure 9 shows the Relap5 tubular downcomer noding. Two pipes were used (130 and 131) and each volume of the first pipe is connected by means of cross flow junction to the correspondent volume in the second pipe.
This noding enable the code to qualitatively simulate the tubular downcomer behaviour allowing a recirculation flow path for hot and cold water in the tubular downcomer.

A plot of the SPES2 measurements in the lower part of the tubular downcomer is presented and comparison with temperatures of pipe 130 and 131 is performed in Figure 8. Temperatures measurements were made in the lower and upper part of the tube and as can be clearly seen the Relap5 prediction well agree with experimental data.

ANNULAR DOWNCOMER (HOT LEG) FORM LOSS

Hot leg penetration into the annular downcomer is provided in the SPES2 facility configuration. Relap5 noding uses a quasi 2-D simulation of the annular downcomer as shown in Fig. 1.
However it is not easy to develop form losses to be used in the Relap5 noding due to the flow obstruction caused by hot leg. For this reason another 3-D simulation was performed using the CFDS-FLOW3D code.
Steady state conditions at full power were simulated obtaining the results shown in fig. 10 .
CFDS-FLOW3D provided the flow field behaviour and pressure distribution inside the annular downcomer.
From the results obtained equivalent form losses were computed and applied to the Relap5 quasi 2-D noding.

CMTs NODING

As shown in Figure 1 CMTs have been noded using a large amount of volumes. Each CMTs is nodalized using 62 volumes, the height of each volume is 10 cm.
Such an expensive noding in terms of cpu time has been used due to the first results obtained in SPES-2 pre-test analysis. Using a larger size volumes resulted in several

stops of the injected flows due to steam condensation and consequent local pressure decrease.
The unexpected behaviour is due to the following two reasons:

- when the CMT level crosses the interface between two volumes the steam is able to exchange energy with the cold water of the hydrodynamic volume just reached. However the liquid temperature where the level is now located can be still subcooled so that a large steam condensation is predicted by the code.

- Another reason for steam condensation is due to the heat exchange with the heat structure attached to the hydrodynamic volume. In fact the whole heat structure area is used to compute the heat exchange with the steam without taking into account the level position inside the volume.

The second effect is however of the second order. Sensitivity analysis performed using completely insulated CMTs shown that CMTs injected flows reductions were still present.

Both the lack of a thermal stratification model for the liquid inside a vertically stratified volume and the absence of the heat structure area partitioning for heat exchange calculations below and above liquid level affected the Relap5 code response producing overestimation of the steam condensation and consequent unrealistic CMTs injection stops.
The only way to solve the problem was (from the users point of view) to implement a so detailed noding to help the code in the prediction of the thermal stratification preventing the unrealistic steam condensation.
In this way the CMTs injected flows were stabilised and no stops were predicted by the code.

Possible solutions for this problem require code development for vertical stratified volumes from the point of view of both liquid thermal stratification and heat structures area partitioning below and above liquid level.

IRWST NODING

From the first comparisons performed between experimental results and pre test predictions it was clear that PRHR outlet temperature was higher than experimental data of about 40-50 C being the total mass flow well predicted.
It was finally realized that IRWST noding was not adequate to represent what really takes place in the facility.
The PRHR tube (C-shaped) is immersed in the IRWST and when heat exchange takes place a natural convection cell develops in the tank. We have no information's on the extension of the IRWST upflow close to the PRHR tube in the facility. However we finally realized that to obtain a good reproduction of the experimental data we have first to make a 2-D noding of the IRWST to create a recirculation flow path as well as to decrease the size of the IRWST volumes connected to the PRHR heat structure to better represents the convection cell.
The final IRWST noding was tested on SPES2 test N.9 an SGTR test were flow conditions at PRHR inlet were in sigle phase conditions for most of the transient.

A good agreement was found with the last developed IRWST noding between experimental PRHR outlet temperature and Relap5 calculated value.

1" COLD LEG BREAK COMPARISON

Comparison of the test results with Relap5/mod3/V80 is made in the following figure from 11 to 18.
The following table presents the experimental sequence of events fro the SPES-2 1" cold leg break Test S00401.

SPES-2 test s00401 - Sequence of events	Time (sec.)
Break opens	0.0
Reactor Trip Signal "R"	244.5
Main Steam line isolation	247
"S" Signal	255.5
Main Feed Water isolation	257
CMTs and PRHR I.V. begin to open	258
Reactor Coolant Pumps trip	273
Accumulators injection starts	2498
ADS stage 1	4598
ADS stage 2	4693
ADS stage 3	4813
ADS stage 4	5655
IRWST injection starts	5775/5806

Figure 11 presents the comparison between experimental and calculated primary and secondary pressure.
The calculated behaviour of the primary pressure is very similar to the experiment, only a small pressure overprediction is present before first stage ADS.
The secondary pressure is on the contrary underpredicted by the code in the second part of the transient.
This fact however does not influence the primary pressure since primary and secondary side in this phase of the transient are nearly completely decoupled. The underprediction is due to an incorrect evaluation of the secondary side heat losses caused by the external heat transfer coefficient applied as a boundary condition to the secondary side heat structures.

Figure 12 compares pressurizer level behaviour. The initial pressurizer draining is very well computed by the code and also the pressurizer level increase at ADS opening is well reproduced. Some difference is still present in the slow and small increase of the level in the central part of the transient as well as in the final draining of the pressurizer due to fourth stage opening, anticipated in the code prediction.

Cmt injection flows, Figure 13, are very well reproduced.
The single phase recirculation value in the first part of the transient is captured by the code as well as the following injection flow decrease due to the change of the gravity head available caused by CMT heat-up. The onset of the two phase recirculation is very close to experiment.
For this transient the CMTs two phase recirculation is not very stable and some liquid entrainement is still present in the cold leg balance line. The predictions of the code follows very close the experimental results. An injection flow increase at ADS opening is present in both the experiment

and the prediction. The final CMT draining is slightly anticipated.

CMT level comparison is made in the following figure 14 and shows a good reproduction of the experimental data.

Figure 15 presents both the accumulator and IRWST injection flows. The code predictions clearly shows the effect of the ADS stages on accumulator injection as in the experimental data. The accumulator injection stop is slightly different and delayed respect to the experiment.
IRWST injection is anticipated but the injection value is correctly calculated by the code.

Figure 16 presents the total discharged mass from the primary system taking into account the contribution of the break flow and ADS stages. The reproduction of the experimental data is very good before and after the ADS opening.

Finally figure 17 and 18 presents respectively the PRHR mass flow and inlet-outlet temperature. As it can be observed the PRHR mass flow is underpredicted and this fact has some influence on the overall energy balance (primary pressure overprediction) since the inlet and outlet temperature are well predicted. Before the run here presented and IRWST renoding the outlet temperature was overpredicted with a correspondent increase of the primary pressure overprediction.
The IRWST renoding permitted to match the PRHR outlet temperature although more work is needed to improve the PRHR mass flow calculation (note that in single phase condition during the first part of the transient the PRHR mass flow is well computed by the code).

The overall behaviour of the code compared with experimental results was very good.
Events timing as well as quantitative predictions of the main transient variables are correctly calculated showing that the code is able to reproduce all phenomenologies taking place during the transient.
The development and improvement of the SPES-2 input deck played an important role on the degree of reproduction of the experimental data. Development of special noding arrangement enabled the simulation of the facility aspects not automatically handled by Relap5 modelling.

Some work can still be done to improve the Relap5 code predictions for what the overall energy balance is concerned, however such improvement should be done in the frame of an extended post test calculation activity.

CONCLUSIONS

The SPES-2 noding developed by ANSALDO has been briefly presented and particular aspects of the facility simulation discussed.
The use of three dimensional calculation to help the development of the SPES-2 noding has been presented for what annular and tubular downcomer in the facility are concerned.
The work shown that three dimensional calculations can be very helpful to develop Relap5 input deck giving to the user new insights into the phenomena to be simulated in order to help the code handling aspects of the system taken into consideration not automatically described by the code modelling capability.
Moreover the comparison of the code predictions with experimental data were very useful to identify input deck limitations and to improve the SPES-2 noding.

Finally prediction for the 1" Cold Leg Break transient test S00401 were compared with experimental data.
The results indicate that Relap5 was able to deal with the facility phenomenology both from a qualitative and quantitative point of view.
Sequence of events was very close to experiment while calculated values of the main variables of the transient were in good agreement with experimental data.

ACKNOWLEDGEMENTS

The authors wish to thanks Dr. L.E. Hochreiter, L.E. Conway from Westinghouse and the SIET SPES-2 group for the information's and useful discussions on the AP600 plant and the SPES-2 facility.
The ANSALDO SPES-2 noding development and pre-test analysis activity was possible thanks to ENEL funding.

NOMENCLATURE

ADS	Automatic Depressurization system
CMTIV	Core Make-up Tank Isolation valve
DVI	Direct Vessel Injection line
IRWST	In containment Refuelling Water Storage Tank
MSIV	Main Steam Line Isolation Valve
PRHR	Passive Residual Heat Removal
CFDS	Computational Fluid Dynamics Services

REFERENCES

Alemberti A., Frepoli C., Graziosi G. 1994
SPES-2 cold break experiments: Scaling approach for decay power, heat losses compensation and metal heat release.
International Conference - New Trends in Nuclear System Thermohydraulics - Pisa, May 30th-June 2nd

Alemberti A., Frepoli C., Graziosi G. 1994
Comparison of the SPES-2 pre-test predictions and AP600 plant calculations using Relap5/mod3
International Conference - New Trends in Nuclear System Thermohydraulics - Pisa, May 30th-June 2nd

M.Bacchiani,C.Medich,M.Rigamonti (SIET) - L.E.Conway (Westinghouse) *SPES-2, AP600 Integral System Test - Inadvertent ADS opening and Cold Leg Break Transients* Internat. Conference - Pittsburgh Pa April 17-21 ARS-94

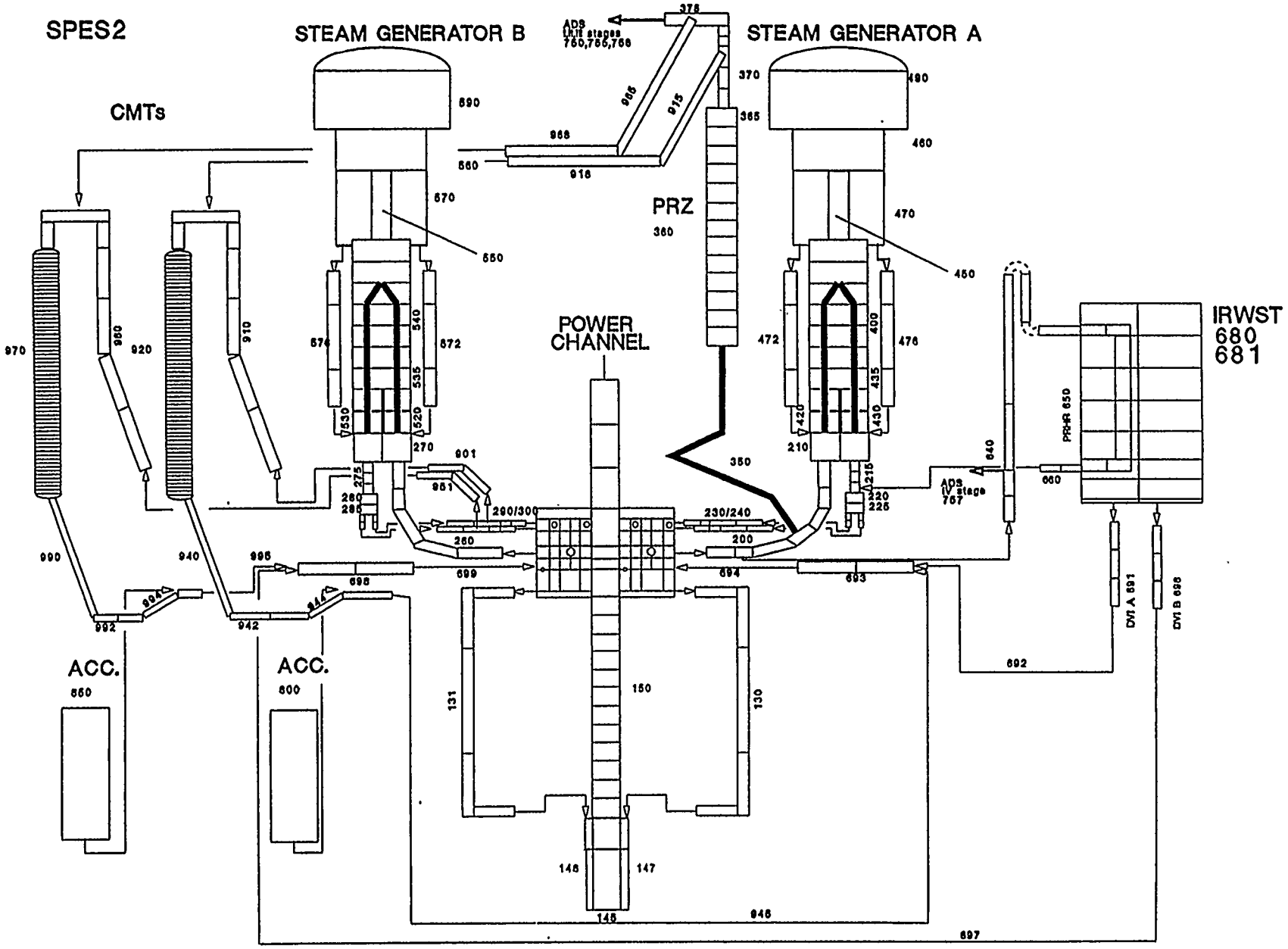

Figure 1 - SPES-2 Relap5/mod3 noding

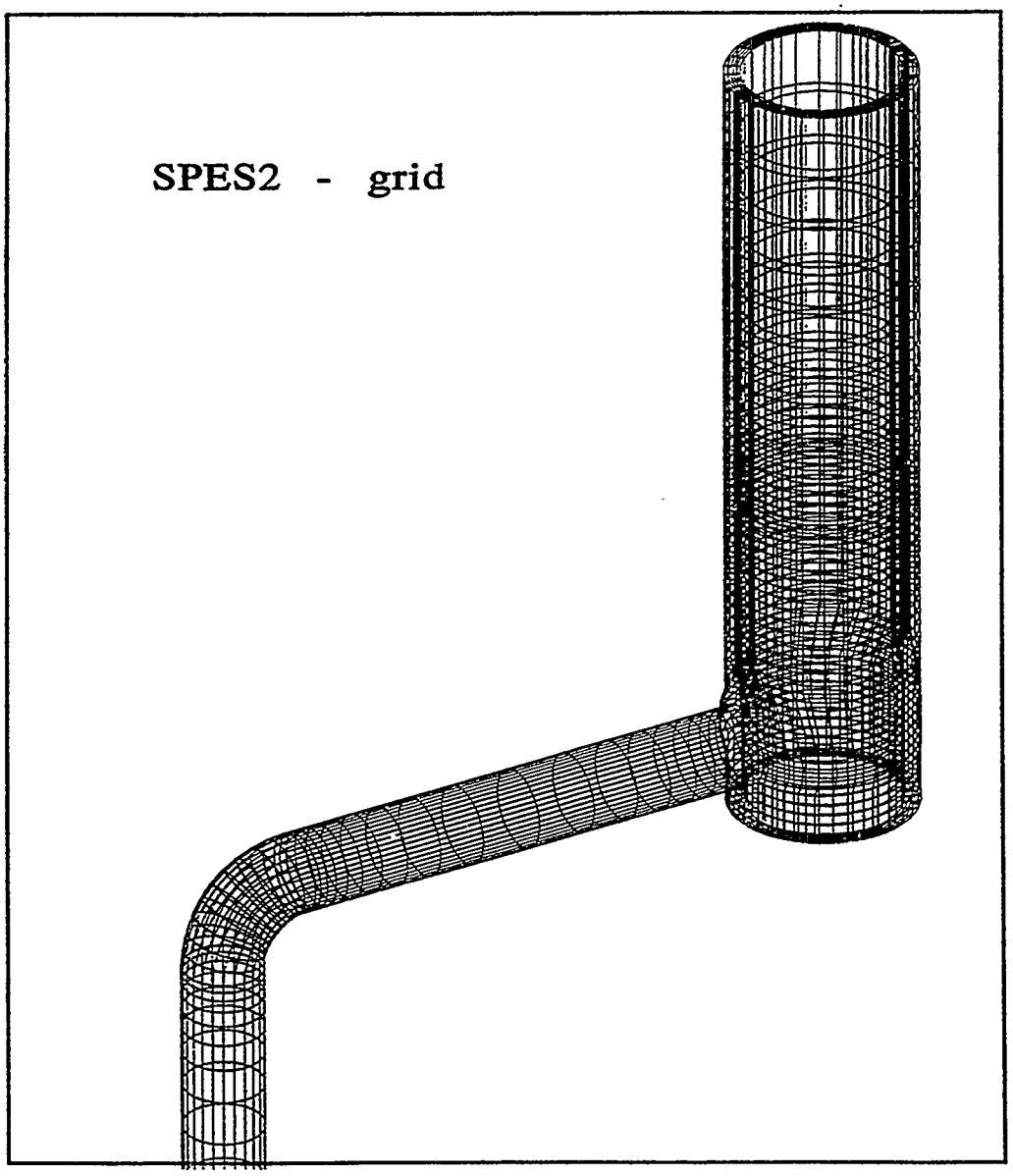

Figure 2 - SPES-2 CFDS-FLOW3D annular - tubular downcomer grid

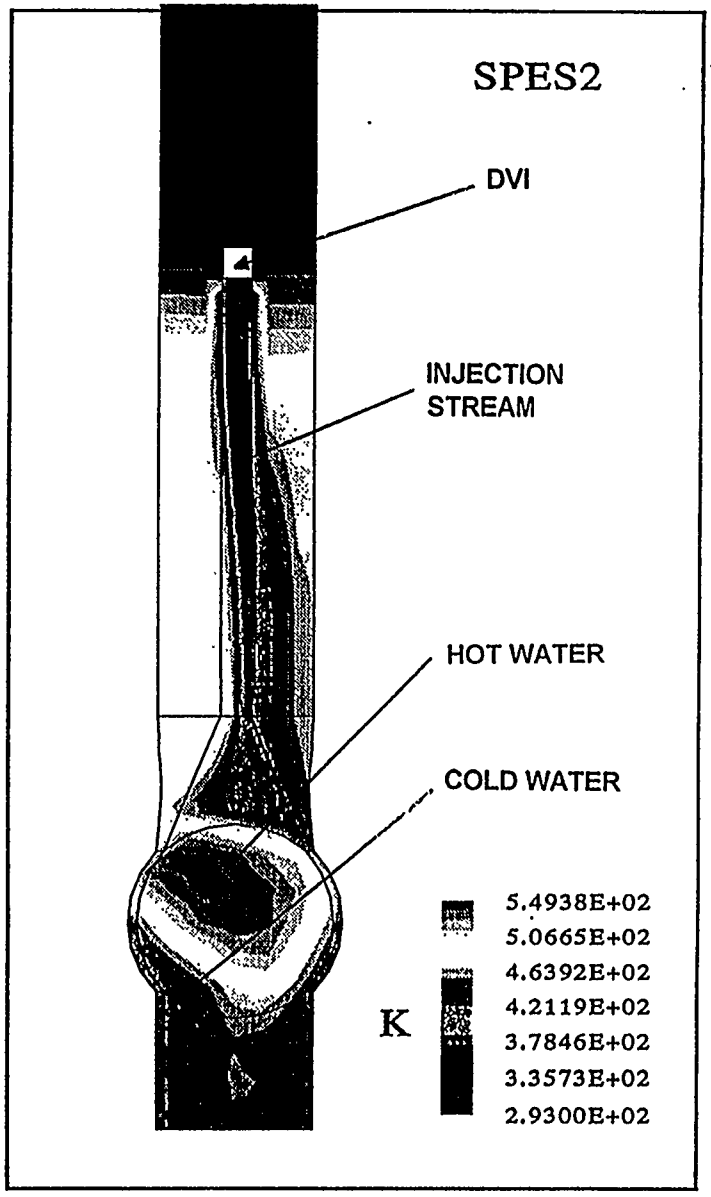

Figure 3 - Annular-tubular downcomer connection
Temperature distribution at 31 seconds

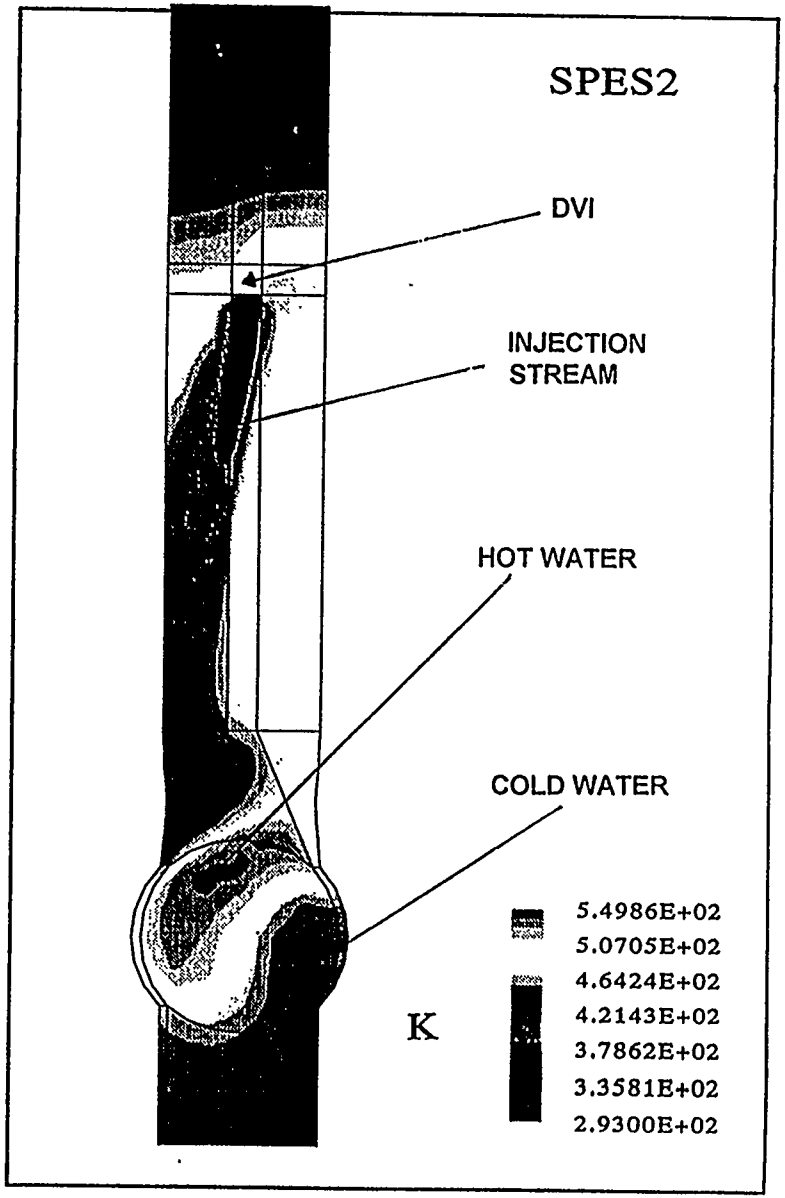

Figure 4 - Annular-tubular downcomer connection
Temperature distribution at 35 seconds

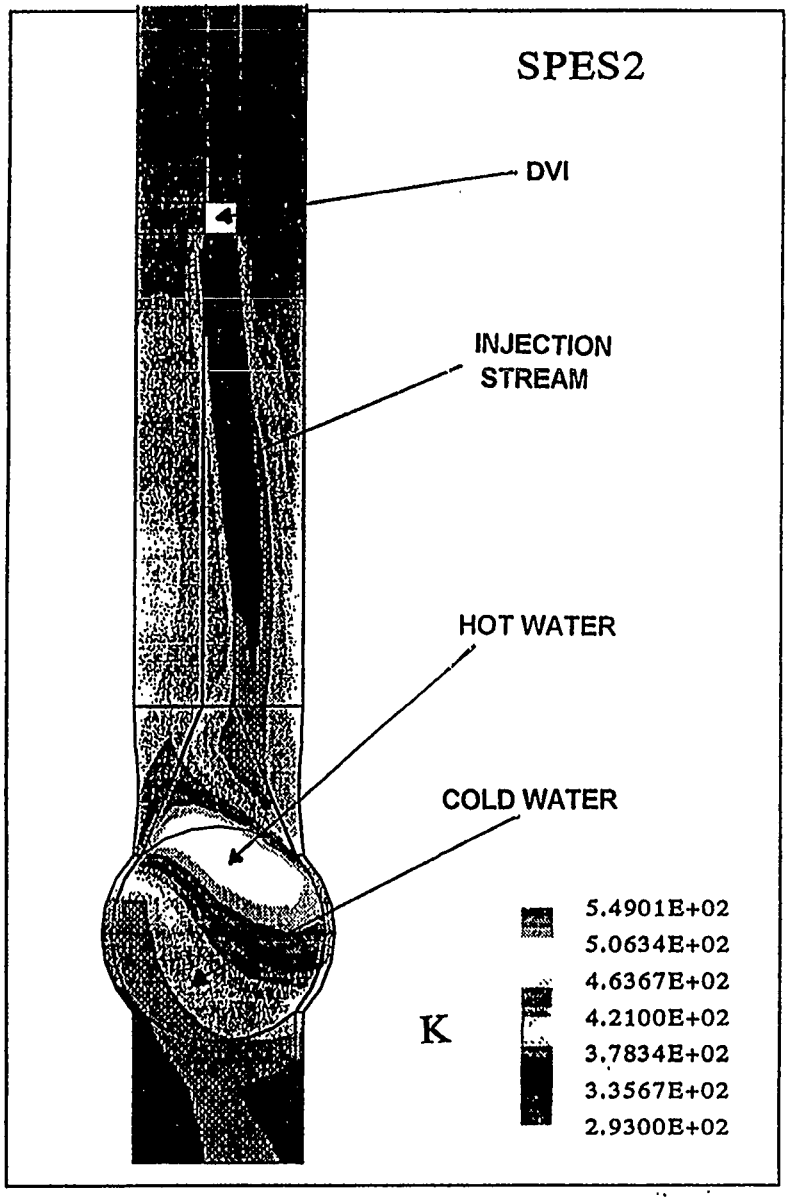

Figure 5 - Annular-tubular downcomer connection
Temperature distribution at 120 seconds

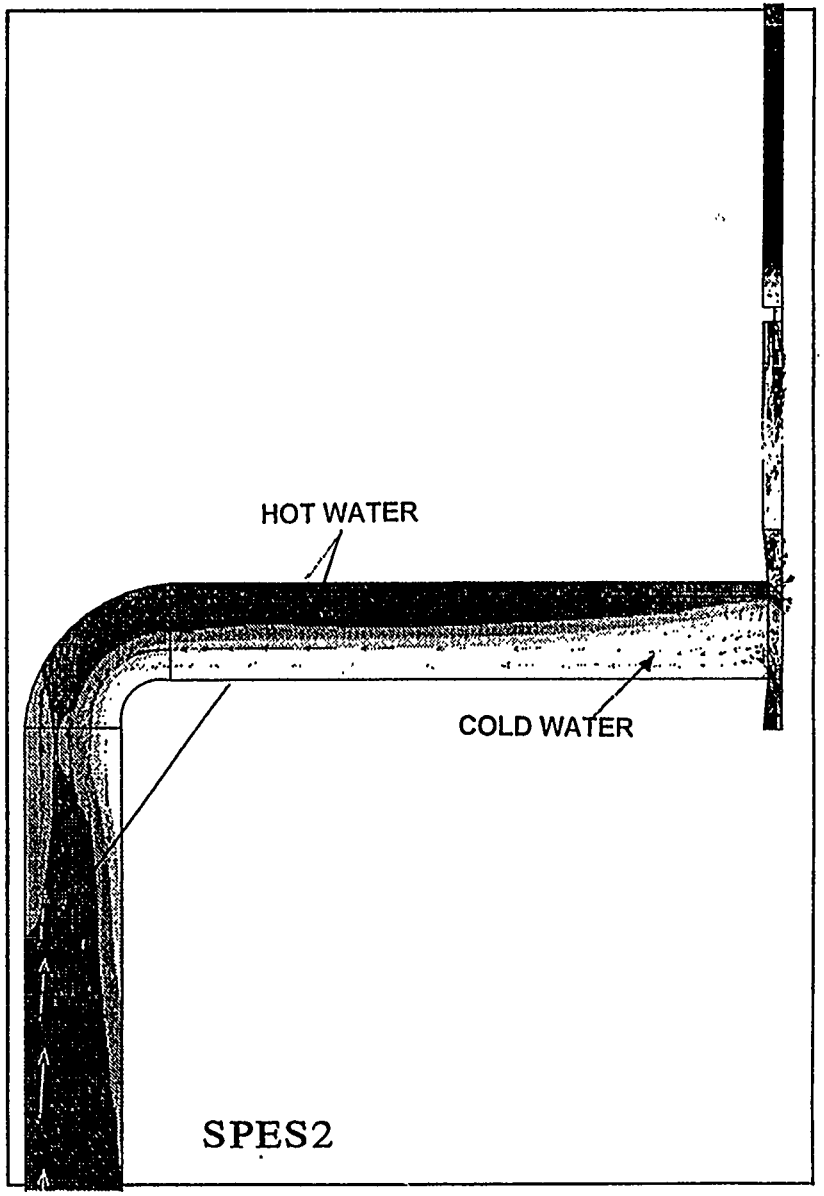

Figure 6 - Tubular downcomer (upper part) flow field and
Temperature distribution at 35 seconds

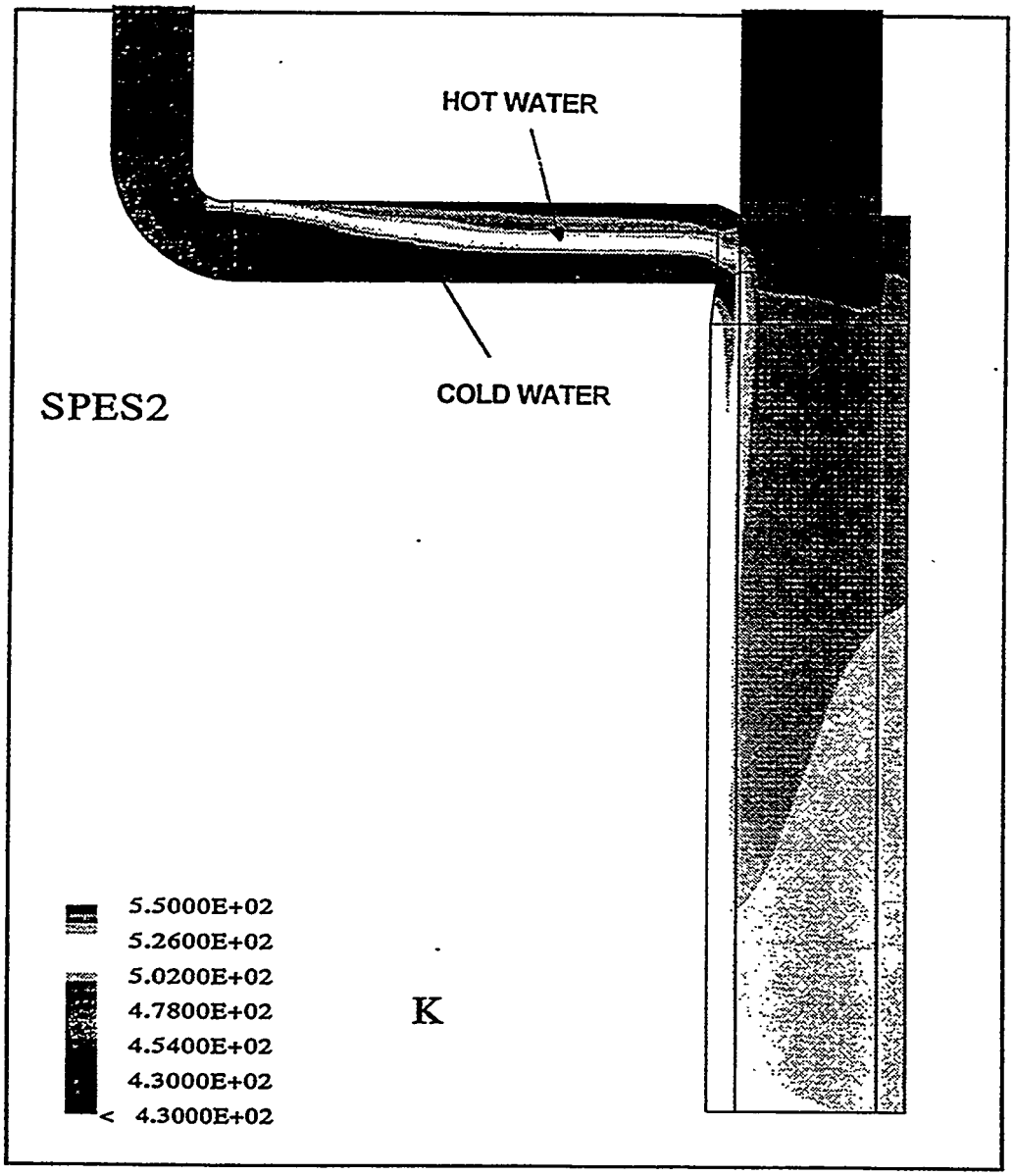

Figure 7 - Tubular downcomer (lower part)
Temperature distribution at 120 seconds

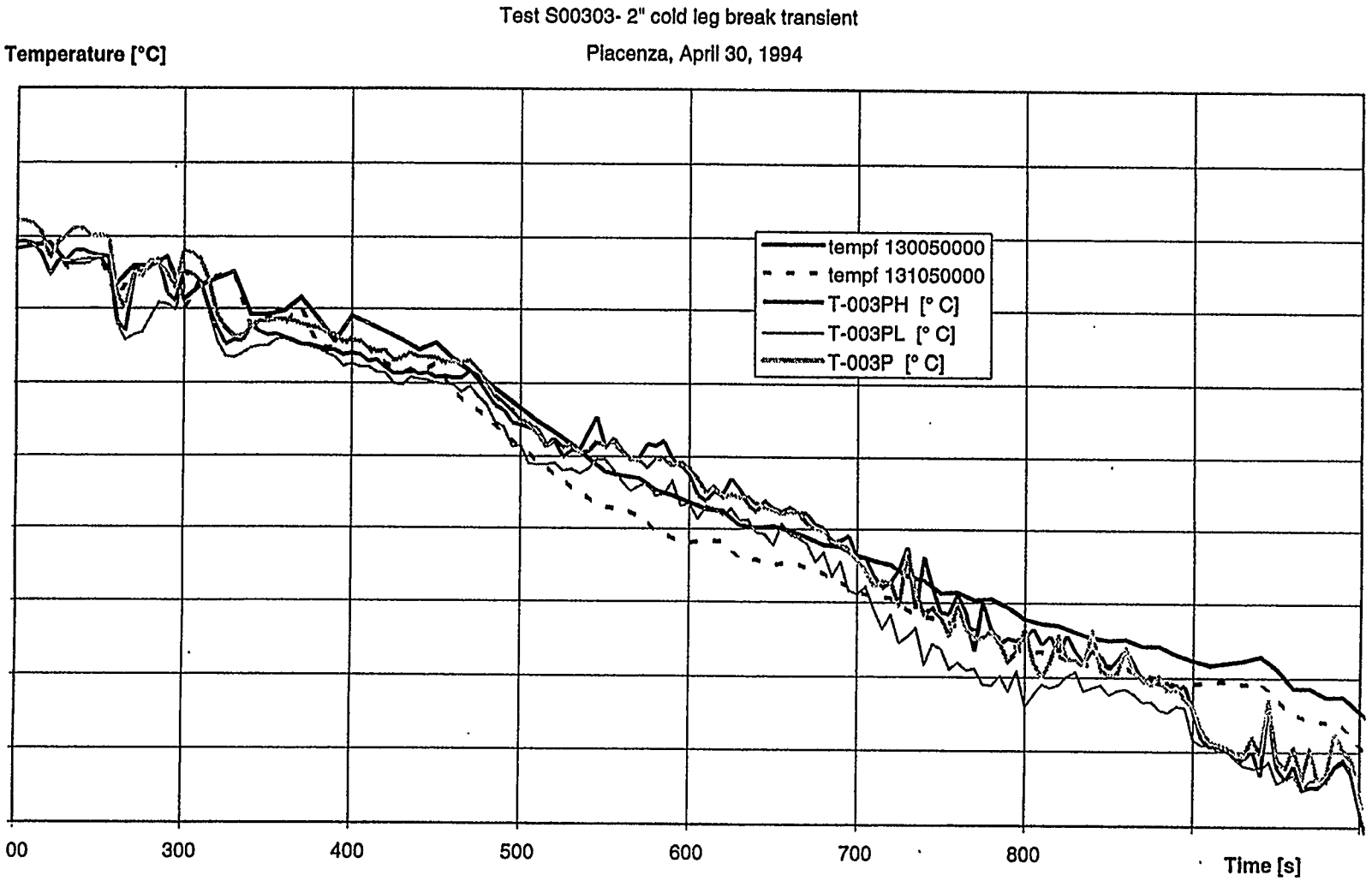

Figure 8 - Comparison of the lower and upper SPES-2 fluid temperatures in the lower part of the tubular downcomer and Relap5/mod3 predictions

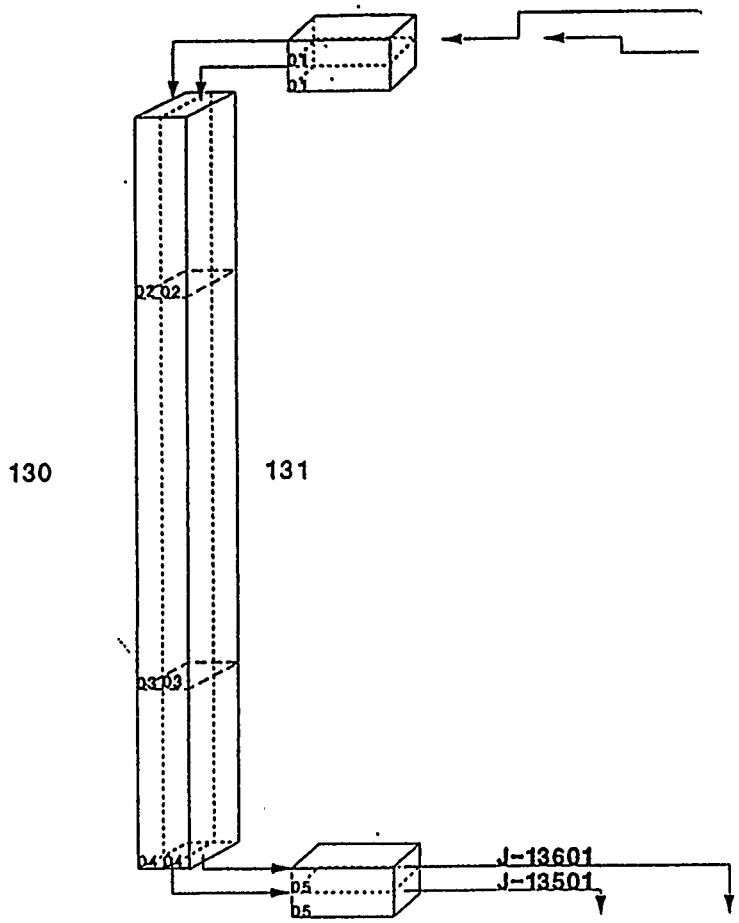

Figure 9 - SPES-2 Relap5/mod3 tubular downcomer noding

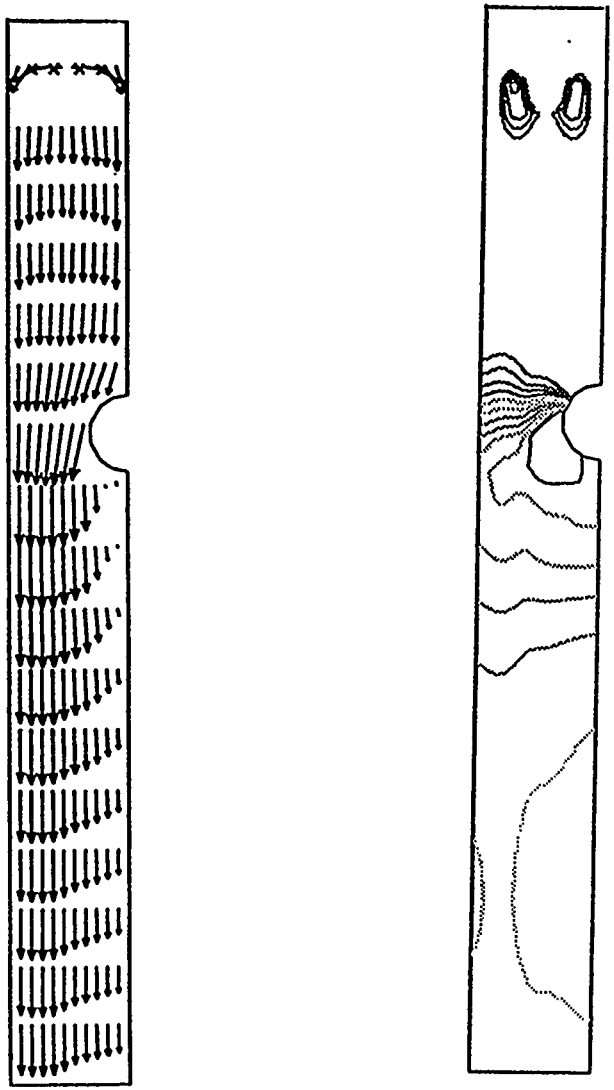

Figure 10 - SPES-2 Annular downcomer - Hot leg intersection
CFDS-FLOW3D simulation of the flow field and pressure distribution

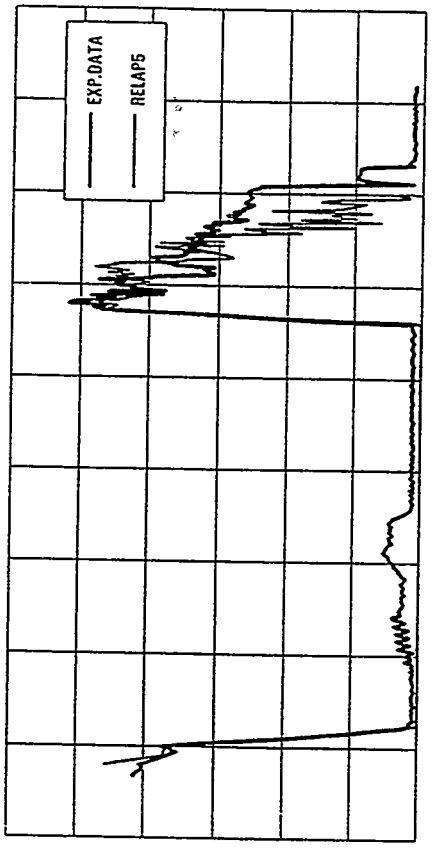

Fig. 12 Pressurizer level

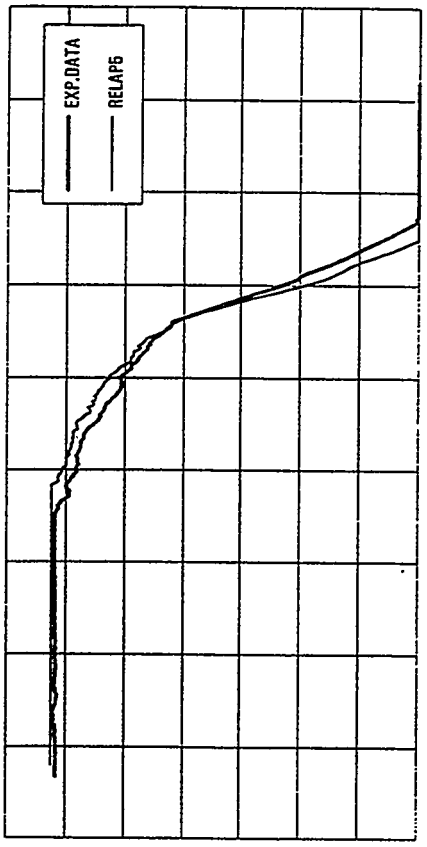

Fig. 14 CMT level

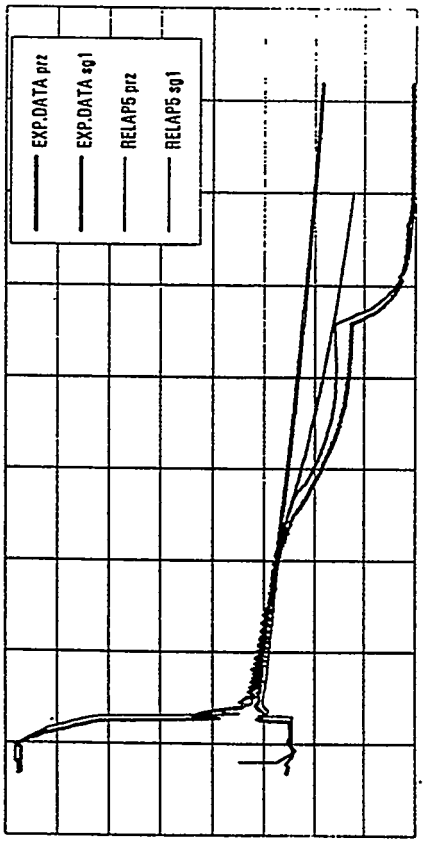

Fig. 11 Primary and Secondary Pressure

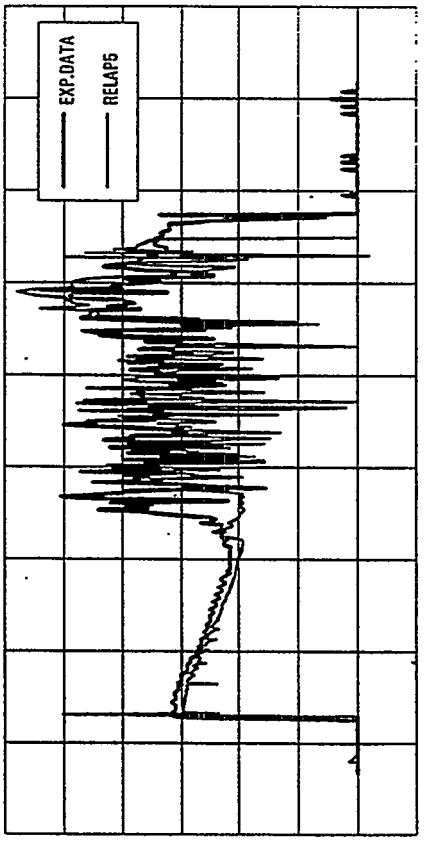

Fig 13 CMTs injection flows

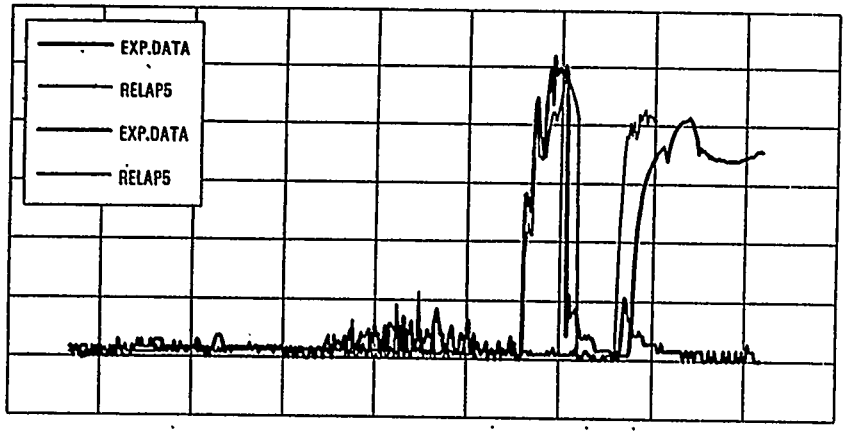

Fig. 15 Accumulator and IRWST injection flows

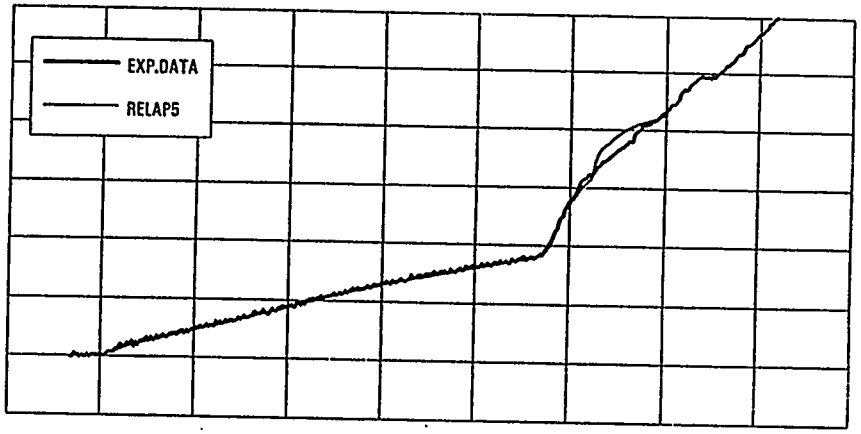

Fig. 16 Total discharged mass (Break and ADS)

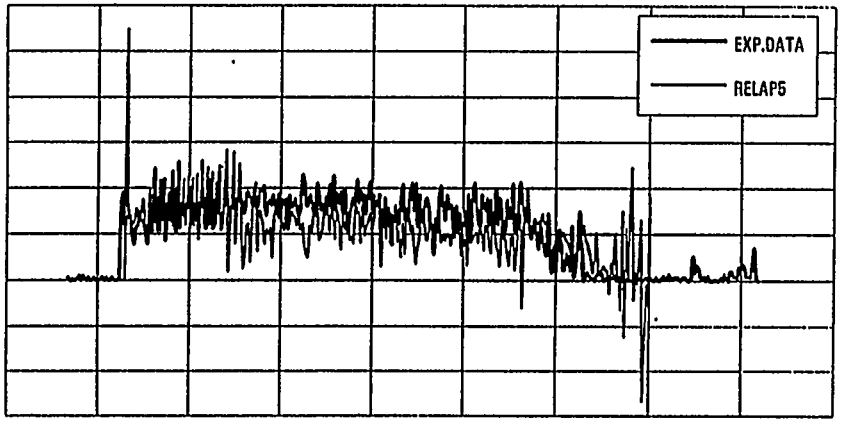

Fig. 17 PRHR mass flow

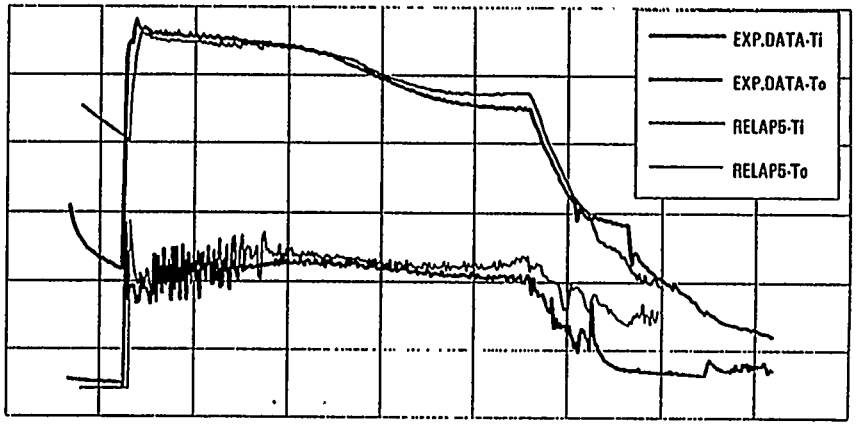

Fig. 18 PRHR inlet-outlet temperatures

22nd WATER REACTOR SAFETY INFORMATION MEETING
SESSION 11
HIGH-BURNUP FUEL BEHAVIOR
R. Meyer, Chair

INTRODUCTION

Welcome to Session 11 on High-Burnup Fuel Behavior, with special emphasis on reactivity-initiated accidents. These are design-basis accidents that are analyzed in safety analysis reports for all licensed power reactors. It has been a long time since there was so much interest in fuel behavior under conditions of design-basis accidents, so I thought I would take a few minutes to provide a little background.

In the 1970s, the NRC had a strong program of licensing and research in the area of fuel behavior. That program was driven to a large degree by commitments from the earlier ECCS hearings and by fuel anomalies that were occurring in operating power reactors. By the late 1970s, results from that program had been used to define regulatory practices that were described in the NRC's Standard Review Plan (Ref. 1).

Within a few years after the accident at TMI in 1979, that NRC fuels program was idled. Resources were reassigned to address severe accident issues as risk-based considerations were taken into account. The kind of fuel-related phenomena addressed in the Standard Review Plan were not seen as precursors to severe accidents, and fuel performance in operating reactors had improved.

The data base on which the regulatory practices had been founded covered fuel burnups up to the range of 20,000 to 40,000 MWd/t. For example, the ANS Standard Fission Product Release Model (1982) had to use LMFBR data above 19,000 MWd/t because well characterized LWR data were not available. And the highest burnup fuel rod that had been tested under reactivity transient conditions (in the CDC core of SPERT) had a burnup of 32,000 MWd/t. Nevertheless, burnups in that range were thought to be adequate for the exposures that would be achieved in commercial power reactors.

During the 1980s, fuel performance in operating reactors remained good, and fuel burnup increased to levels not expected a decade earlier. Experimental data at higher burnups also became available from programs such as the Halden Project. During that time period, the NRC maintained its participation in the Halden Project and in Studsvik's fuel research projects, but results were merely archived and no research activities were pursued by NRC. NRC's research attention remained focused on severe accidents.

By the early 1990s, it had become clear that burnups in commercial power reactors were exceeding the burnup range for the validation of NRC's fuel behavior computer codes and related fuel damage criteria. Fuel suppliers were providing high-burnup performance data to support the licensing of higher burnup fuel designs, but the NRC's independent capability had not been updated. Therefore, on October 4, 1993, a formal memorandum was sent from NRC's licensing office to the research office requesting assistance on high-burnup fuels. The memorandum asked for work in three areas: (1) fuel performance model changes (e.g., UO_2 thermal conductivity, fission gas release, etc.), (2) fuel performance code updates (i.e., FRAPCON and resultant effects on LOCA stored energy), and (3) fuel failure threshold assessment (for reactivity transients).

The first of three contracts, which were initiated to respond to the need, was placed at Battelle's Pacific Northwest Laboratories, and that contract was for fuel performance model changes. A number of specific modeling areas are being addressed, and this work will be described in greater detail in a subsequent paper at this meeting.

The second contract was placed at the Idaho National Engineering Laboratory. This contract has two different activities. One will take the revised models from the Battelle contract and incorporate them into the FRAPCON code for steady-state fuel behavior analysis, thus updating FRAPCON for high-burnup applications. Updates will also be made to the transient fuel-behavior code FRAP-T and to the MATPRO program for materials properties. Validation, peer review, and documentation are all planned for the updated codes. This work will also be mentioned in more detail in the subsequent paper to be presented by INEL.

The other activity in the Idaho contract is an assessment of fuel damage criteria for reactivity transients in high-burnup fuel. This assessment will reevaluate NRC's cladding failure criteria for reactivity accidents in light of the experimental data coming out of completed and ongoing in-reactor test programs.

The third contract was placed at Brookhaven National Laboratory to perform best-estimate calculations of plant transients for reactivity-initiated events of the type addressed in licensing safety analysis reports. Such results are needed to determine the energy input into the fuel during reactivity accidents; this energy input is needed to assess the impact of any reduced damage thresholds that might be indicated by emerging high-burnup fuels data. This work was initiated only recently, and no further discussion of it will be given here.

During the past year, as the above work was getting underway, important fuel behavior data were obtained in the Cabri test

reactor in France (Ref. 2) and in the NSRR test reactor in Japan (Refs. 3-4). Additional testing of this type has also been done in the IGR test reactor in Kazakhstan by the staff at the Russian Research Center (Kurchatov Institute). All of this work will be reported in the following papers.

The importance of this experimental work on reactivity-initiated accidents will be determined by its impact on current licensing criteria and the way we do the related safety analyses. Let me summarize the licensing criteria currently used in the U.S.

The present licensing criteria for fuel behavior during reactivity transients involve two enthalpy values: one at 280 cal/g and the other at 170 cal/g. The 280 cal/g value is used as a limit "to ensure that core damage will be minimal and that both short-term and long-term core cooling capability will not be impaired" (Ref. 5). The 170 cal/g value is used as an indicator of cladding failure for BWR reactivity transients initiated at zero or low power; thermal margin criteria are used for all other BWR and PWR reactivity transients (see Ref. 1).

In the papers that follow, it will be seen that cladding failure is observed at enthalpy values significantly below 170 cal/g at very high burnups. Fuel loss from the test section was found in some cases. These kinds of observations could have an impact on the enthalpy values that are used as licensing criteria.

To obtain a preliminary assessment of the impact, the NRC staff performed a brief review of plant analyses described in licensing safety analysis reports that had been previously approved for a typical BWR and a typical PWR. The review was to identify the transients that are likely to result in reactivity insertion levels on the order of 15 cal/g (the approximate added enthalpy at the time of failure in the Cabri test at 65,000 MWd/t). It was found that, for high-burnup fuel in typical loading patterns, only a few of the analyzed transients would result in some fuel approaching or exceeding a 15 cal/g increase. These transients are:

- BWR Rod Drop
- PWR Rod Ejection
- BWR Flow Controller Failure with Recirculation Flow Increase
- BWR Power Oscillations

The NRC staff concluded that the immediate public health and safety significance of the new high-burnup transient tests is small, but the potential impact on plant operation and planning -- for future cores with higher burnup and longer operating

cycles -- may be large. Results from the Brookhaven study mentioned above, and results that might be obtained from reactor manufacturers, will clarify the importance of these new data.

On August 31, 1994, an NRC Information Notice was sent to all licensees and fuel suppliers in the U.S. to alert them to recent information on high-burnup fuel performance that could affect previously approved fuel burnup limits and enthalpy limits for high burnup fuel. By the fall of 1995, all of the activities described above will be at a stage where a more informed conclusion can be reached and the need for any revision of fuel behavior criteria can be defined.

REFERENCES

1. U.S. Nuclear Regulatory Commission, "Standard Review Plan," Section 4.2 (Fuel System Design), NUREG-0800, Rev. 2, July 1981.

2. F. Schmitz, et al., "Investigation of the behavior of high burn-up PWR fuel under RIA conditions in the CABRI test reactor," *Trans. 22nd WRSM*, NUREG/CP-0139, October 1994, p. 107.

3. K. Yanagisawa, et al., "Transient FGR and PCMI of PWR Fuels Preirradiated to 42 MWd/kgU," *Proc. 1994 International Topical Meeting on Light Water Reactor Fuel Performance*, American Nuclear Society, April 1994, p. 248.

4. T. Fujishiro and K. Ishijima, "NSRR Experiments to Study the Effects of Burnup on the Fuel Behavior under Reactivity-Initiated Accident Conditions," *Trans. 22nd WRSM*, NUREG/CP-0139, October 1994, p. 109.

5. U.S. Nuclear Regulatory Commission, "Assumptions used for Evaluating a Control Rod Ejection Accident for Pressurized Water Reactors," Regulatory Guide 1.77, May 1974.

THE RIM EFFECT AND OTHER HIGH BURNUP MODELING FOR NRC FUEL PERFORMANCE CODES

C. E. Beyer, D. D. Lanning, and M. E. Cunningham
Pacific Northwest Laboratory[a]

Abstract

Pacific Northwest Laboratory (PNL) has recently initiated a program sponsored by U.S. Nuclear Regulatory Commission (NRC) to review data on the material properties of fuel and cladding at high burnup levels and to update models within NRC fuel performance codes. As part of this program PNL is updating those models that may have a significant impact on predicting fuel performance during reactivity initiated accidents (RIAs) occurring at high burnup levels. Recent RIA experimental tests indicate that fuel failures occur at decreasing energy deposition levels with increasing fuel burnup. Factors contributing to failures at reduced energy levels are believed to be increased power deposition in the rim of the fuel, high pressure gas bubbles in the fuel that release mechanical energy, and cladding with reduced ductility and impact strength.

Introduction

The U. S. Nuclear Regulatory Commission (NRC) has recently initiated a new program to review data on the material properties of fuel and cladding at high burnup levels. The objective of this program is to update fuel performance models within NRC fuel performance codes to improve their predictive capability to rod-average burnup levels of 60 GWd/MTU and higher. Models being reviewed for improvement at the higher burnup levels are fission gas release, fuel swelling, gap conductance, fuel thermal conductivity, fuel specific heat, fuel rim structure, burnable poison properties, radial power distribution, cladding corrosion/hydriding, and cladding mechanical properties. In addition, the NRC is examining the results from the latest experimental tests that simulate reactivity initiated accidents (RIA).[1,2,3,4] Preliminary examination of these data show fuel failures occurring at decreasing energy deposition levels with increasing fuel burnup levels.

As part of this NRC program, Pacific Northwest Laboratory (PNL) is evaluating those fuel performance models that may have a significant impact on predicting fuel performance during reactivity initiated accidents occurring at high burnup levels. Those models that may have an impact are the fuel pellet

---

(a) Pacific Northwest Laboratory is operated for the U.S. Department of Energy by Battelle Memorial Institute under Contract DE-AC06-76RLO 1830.

rim structure, the radial power distribution within the fuel pellet, cladding corrosion, and cladding mechanical properties. The first two are interdependent because three interrelated phenomena in the fuel surface, or rim, change with increasing burnup: 1) there is a significant buildup of plutonium in a thin region at the fuel surface due to ^{238}U resonance absorption of neutrons, which results in higher fission rates and burnup; 2) a highly porous structure develops within the rim with up to 30% porosity (bubbles) filled with fission gases; and 3) a fine subgrain structure of ≤ 1 μm grains develops, as compared to the as-fabricated grain structure of 10-20 μm. In addition, the width of this rim increases with increasing burnup, with a width of 150-200 μm at a pellet average burnup of 60 GWd/MTU.

Fuel Rim Effects

The increased plutonium in the rim with increasing burnup significantly changes the radial power distribution. For example, the volumetric heat generation rate in the pellet rim at 50 to 60 GWd/MTU (pellet average) has been estimated to be a factor of two to three greater than the pellet average as illustrated in Figure 1 (taken from Reference 5). The increase in both plutonium and power within the rim with increasing burnup will be modeled in the NRC fuel performance codes using the RADAR radial power profile algorithm[6] with modifications as proposed by Lassmann[5] to explicitly describe the increasing plutonium isotopes.

In addition, increased fission products and bubbles in the rim will decrease the thermal conductivity in that region. Therefore, the higher volumetric heat generation rate and the lower thermal conductivity in the rim combine to produce slightly higher fuel rim temperatures (in the same neutron flux) at higher burnups than lower burnups.

The fine subgrain structure (≤ 1 μm) that forms in the rim results in a large quantity of gas bubbles on the subgrain boundaries that were not evident prior to rim formation (Figures 2 to 4). The rim formation appears to be dependent on the local burnup level within the fuel. Both Cunningham[7] and Kameyama[8] estimate that the local burnup level for rim formation is between 70 to 80 GWd/MTU. Kameyama also shows that this burnup level remains applicable over a wide range of rim widths. Therefore, the NRC fuel performance codes will assume that rim formation begins at a local fuel burnup of 75 GWd/MTU and will calculate the rim width based on the radial burnup distribution in the fuel pellet.

The noble gases (xenon and krypton) produced in the fuel and stored in the matrix and bubbles are the most likely source of cladding loading during transient power increases. For slower power transients on the order of several minutes to hours, the fuel will swell due to bubble growth from gas atom and bubble diffusion that will load the cladding in the radial and axial directions. However, for the faster RIAs, where the transient power increase

is over in milliseconds, the diffusion kinetics for the fission gas is not significant in this time period except for those extreme high energy RIAs where fuel temperatures are near melting. The source of cladding loading for these lower energy RIAs is most likely due to the high pressure bubbles that have been recently observed in pressurized water reactor (PWR) fuel irradiated at low temperatures typical of commercial operation.[9,10] These bubbles have been observed to have high strain fields around them and pressures on the order of 10^4 bar at room temperature and therefore, mechanical energy that can load the cladding when released. As their numbers increase with burnup, there is a large degree of microcracking and bubble interlinkage observed that weakens the grain boundaries, particularly near the pellet surface. It is further hypothesized that the very fast transients induce high thermal stresses in the pellets that along with the high pressure bubbles on the grain and rim subgrain boundaries create severe microcracking at the grain boundaries releasing significant quantities of fission gas resulting in cladding loading. A significant question that still needs to be addressed through fuel examination is whether this microcracking during RIAs is limited to the fuel rim (where power density is greatest in high burnup fuel) or is it experienced within the whole pellet. Modeling of this phenomena will depend on these examinations.

Cladding Effects

Zircaloy-4 cladding from PWRs has exhibited a significant decrease in ductility when local fuel burnups exceed 55 GWd/MTU and fast fluences exceed $8x10^{21}$ n/cm^2 (> 1.0 MeV) as illustrated in Table 1. At fast fluences of 5 to $7x10^{21}$ n/cm^2 measured elongation is typically 2 to 3% near normal in-reactor cladding temperatures, however, when fast fluences reach $8x10^{21}$ n/cm^2 and greater uniform ductility drops to 1% or less. Even though yield strength remains high in the Zircaloy-4 cladding it is likely that the impact strength is decreasing with the ductility and the cladding loadings due to RIAs are probably closer to an impact load. Therefore, the cladding cannot withstand the same impact loads at these high fluences/burnups as experienced at lower burnup levels. The cause for the decrease in Zircaloy-4 cladding ductility is believed to be due to high levels of corrosion, i.e., hydriding, and fast neutron damage at extended burnup levels.

There is a large amount of in-reactor Zircaloy-4 corrosion data indicating that corrosion is accelerating at burnup levels greater than 50 GWd/MTU.[14,15] This accelerated corrosion leads to oxide thickness levels greater than 100 μm particularly in high coolant temperature plants as illustrated in Figure 5 taken from Reference 15. The hydride levels in the cladding proportionally increase with oxide thickness with peak hydride levels reaching 400 to 700 ppm when oxide thickness exceeds 100 μm.[13] Therefore, the ductility decrease is believed due to a combination of irradiation damage at fast fluences greater than $8x10^{21}$n/cm^2 and hydride levels greater than

400 ppm. This is confirmed by the fact that unirradiated Zircaloy-4 with hydrogen levels of 700 ppm have shown a smaller decrease in ductility than the extended burnup cladding. Conversely, Zircaloy-4 with fluences greater than $9x10^{21}n/cm^2$ but with hydrogen levels less than 100 ppm also shows greater ductility than the extended burnup cladding with hydrogen levels greater than 400 ppm.[13]

Cladding corrosion (hydride levels) and fast fluence levels will both be considered in the modeling of cladding properties.

Summary

Fuel failures have been observed at decreasing energy deposition levels with increasing burnup in reactivity initiated tests of high burnup fuel rods.[1,2,3,4] Factors contributing to failure at reduced energy levels are believed to be increased power deposition in the rim, high pressure gas bubbles in the fuel that release mechanical energy, and cladding with reduced ductility and impact strength.

Fuel and cladding data and information are currently being collected by PNL so that the rim structure and cladding properties can be modeled at high burnup levels. These models will be updated within the NRC fuel performance codes by September 1995.

References

1. Schmitz et al. 1994. "Investigation of the Behavior of High Burnup PWR Fuel Under RIA Conditions in the CABRI Test Reactor," 22nd Water Reactor Safety Information Meeting, October 24-26, 1994, NUREG-CP-0140.

2. Fujishiro, T. and K. Ishijima. 1994. "NSRR Experiments to Study the Effects of Burnup on the Fuel Behavior Under Reactivity-Initiated Accident Conditions," 22nd Water Reactor Safety Information Meeting, October 24-26, 1994. Safety Information Meeting, October 24-26, 1994, NUREG-CP-0140.

3. Asmolov, V. and L. Yegorova. 1994. "Russian Experience with Experimental Studies of Burnup Effects under RIA Conditions," 22nd Water Reactor Safety Information Meeting, October 24-26, 1994, NUREG-CP-0140.

4. McCardell, R. 1994. "Reassessment of the Basis for NRC Fuel Damage Criteria for Reactivity Transients," 22nd Water Reactor Safety Information Meeting, October 24-26, 1994, NUREG-CP-0140.

5. Lassmann, K. 1994. "The Radial Distribution of Plutonium in High Burnup UO_2 Fuels." Journal of Nuclear Materials, Vol. 208, pp. 223-231.

6. Palmer, I. D. 1982. "A Model for Predicting the Radial Power in a Fuel Pin." Proceedings of the IAEA Specialists' Meeting on Water Reactor Element Performance Computer Modeling, Preston, UK, March 15-19, 1982.

7. Cunningham, M. E. et al. 1992. "Development and Characteristics of the Rim Region in High Burnup UO_2 Fuel Pellets." Journal of Nuclear Materials, Vol. 188, pp. 19-27.

8. Kameyama, T., T. Matsumura, and M. Kinoshita. 1991. "Analysis of Rim Structure Formation in Battelle High Burnup Program." ANS/ENS International Topical Meeting on LWR Fuel Performance, Avignon, France, pp. 620-626.

9. Thomas, L. E., C. E. Beyer, and L. A. Charlot. 1992. "Microstructural Analysis of LWR Spent Fuel at High Burnup." Journal of Nuclear Materials, Vol. 188, pp. 80-89.

10. Matzke, H. 1992. "On the Rim Effect in High Burnup UO_2 LWR Fuels." Journal of Nuclear Materials, Vol. 188, pp. 141-148.

11. Balfour, M. G., et al. 1982. Zorita Research and Development Program: Volume 1, Final Report. WCAP-10180, Vol. 1.

References (con't)

12. Newman, L. W. 1990. Development of an Extended Burnup Mark B Design-Thirteenth Progress Report, July 1987 to December 1989 and Project Summary. DOE/ET/34213-16, BAW-1532-13.

13. Garde, A. M. 1986. Hot Cell Examination of Extended Burnup Fuel from Fort Calhoun. DOE/ET/34030-11, CEND-427.

14. Kilp, G. R. et al. 1991. "Corrosion Experience with Zircaloy and ZIRLO™ in Operating PWRs." ANS/ENS International Topical Meeting on LWR Fuel Performance, Avignon, France, pp. 730-741.

15. Limback, M., et al. 1994. "Corrosion and Hydriding Performance of Zircaloy-2 and Zircaloy-4 Cladding Materials in PWRs." ANS/IAEA International Topical Meeting on LWR Fuel Performance, West Palm Beach, Florida, pp. 286-295.

TABLE 1. Irradiation Effects on Tensile Test Results for Zircaloy Cladding Tubing Mechanical Properties

Cladding Condition	Reactor (Reference)	Test Temperature, °C	Local Fast Fluence, 10^{21} n/cm^2	Yield Strength, MPa	Uniform Elongation, %	Total Elongation, %
Unirradiated	Zorita(11)	385	--	340	?	14 to 15
Irradiated	Zorita(11)	316	5 to 7	620	2 to 3	3 to 6
Unirradiated	ANO-1(12)	343	--	390	3.9	14.6
Irradiated	ANO-1(12)	343	9	563	2 to 3	4 to 11 (6.9 avg)
Unirradiated	Oconee-1(12)	343	--	404	3.1	20
Irradiated, 4-cycle	Oconee-1(12)	343	7	546	2.1 avg.	15.5 avg.
Irradiated, 5-Cycle	Oconee-1(12)	343	9	606	1.3 avg.	12.7 avg.
Unirradiated	Calhoun(13)	400	--	240-310	---	27-27
Irradiated 6 cycles	Calhoun(13)	400	11	519	0.75	6.19

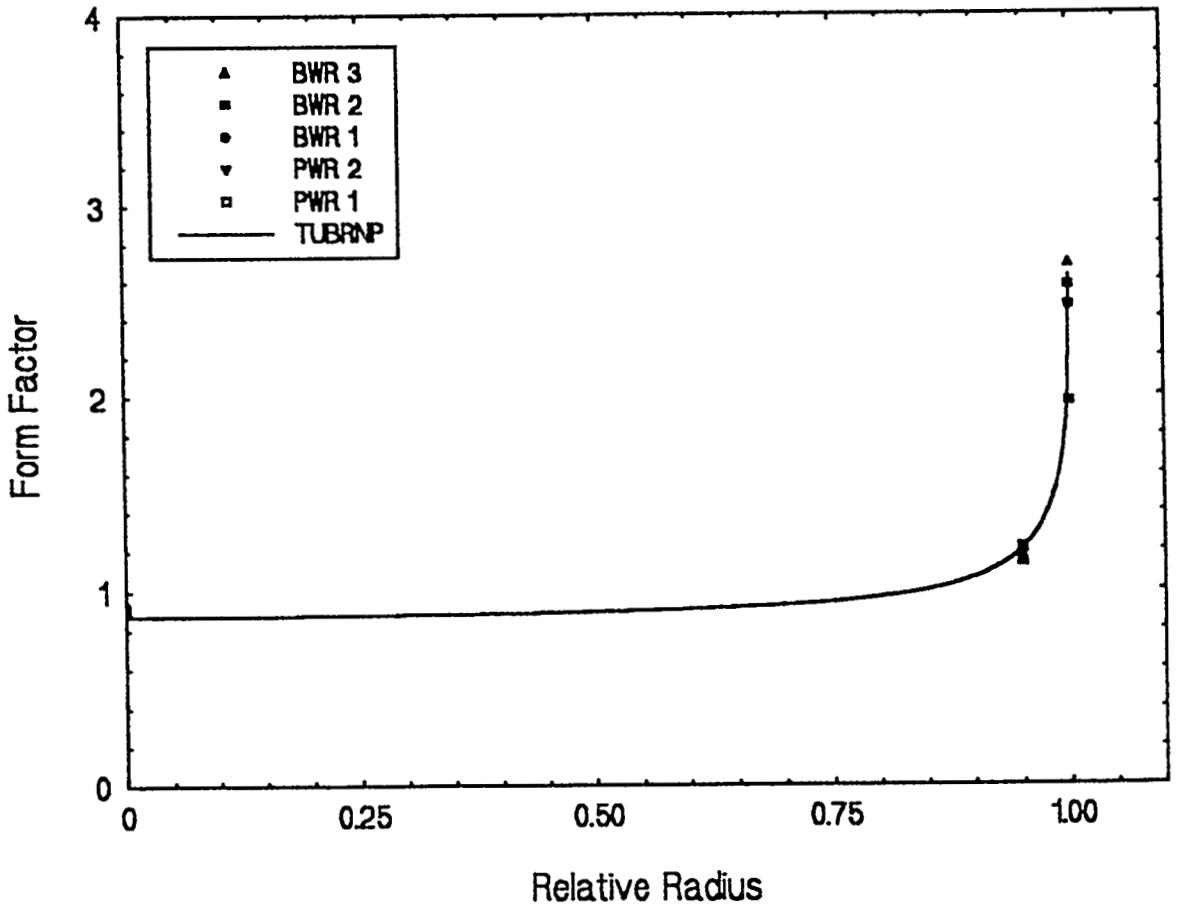

Figure 1. Calculated Radial Power Density Function at 50 GWd/MTU Burnup for several Fuel Types (from Lassmann, Reference 5). Initial Fuel Enrichment was 5%.

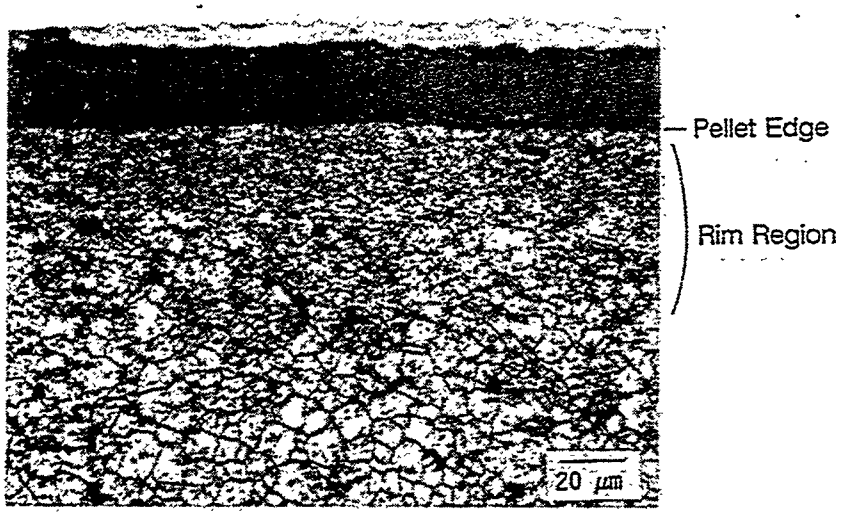

Figure 2. Example of Rim Region Microstructure at 54.2 GWd/MTU from Reference 9.

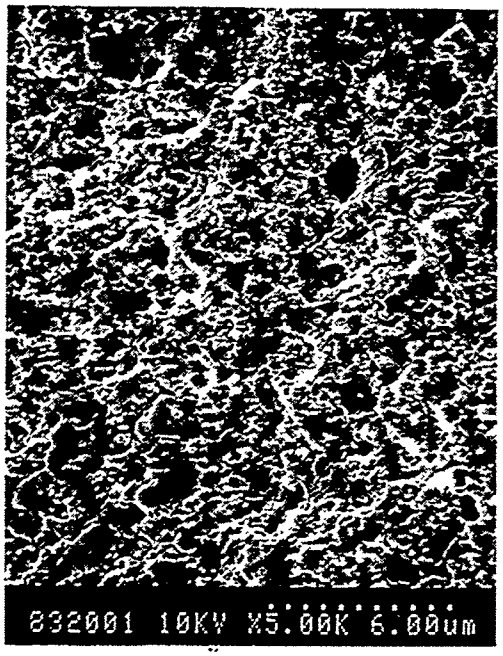

Figure 3. SEM Photo of Fracture Surface in Rim Region at 83 GWd/MTU (Pellet Average) from Reference 9.

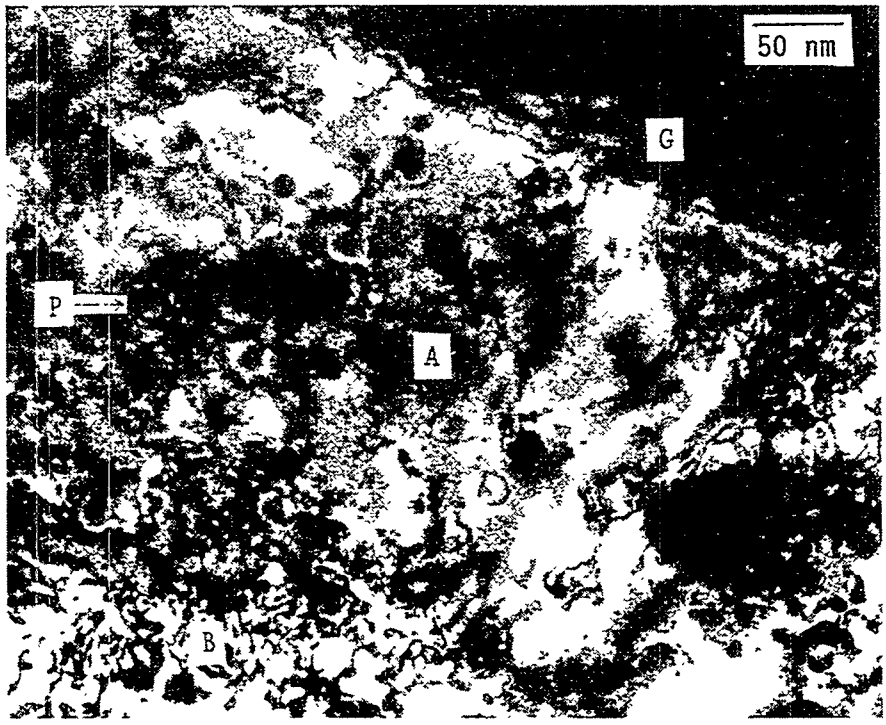

Figure 4. TEM photo illustrating as-fabricated grain boundary (G), matrix structure (A), tangled dislocation (B), and fission product precipitates or bubbles (P).

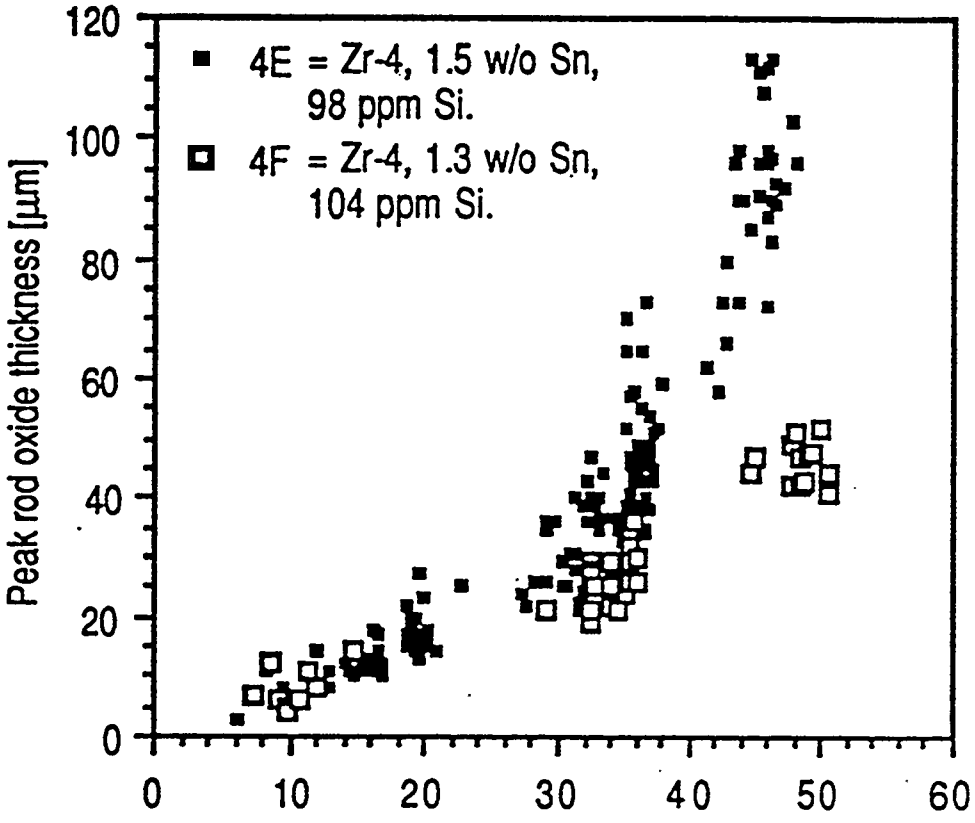

Figure 5. Typical Range of PWR Waterside Corrosion Layer Thickness as a Function of Burnup (from Reference 15).

Investigation of the behaviour of high burn-up PWR fuel under RIA conditions in the CABRI test reactor

-:-:-:-:-:-

F. SCHMITZ, J. PAPIN, M. HAESSLER, J.C. NERVI
Commissariat à l'Energie Atomique
Institut de Protection et de Sûreté Nucléaire, CADARACHE

P. PERMEZEL.
Electricité de France, SEPTEN Lyon

Abstract

In the frame of burn-up increase of the Pressurized Water Reactors (PWR), the French Nuclear Safety and Protection Institute (IPSN) is performing theoretical and experimental studies in the field of Reactivity Initiated Accidents (RIA). This work is performed in close cooperation with Electricité de France (EdF).

The basic goal of this work is to develop and to validate the computer code SCANAIR as a reference tool for transient fuel behaviour under reactivity accident conditions, in particular for fuel at high burn-up.

The presently available experimental data base is insufficient. High burn-up effects resulting from clad corrosion, fission product accumulation and from the so-called RIM effect must be evaluated by exposing high burn-up fuel to rapid power transients under representative conditions. This experimental effort is performed in the French test reactor CABRI.

In a first programme stage (1993 - 1996), which covers 6 to 8 experiments, high burn-up fuel, both UO_2 and MOX is tested in the sodium loop of CABRI. The scope of this programme stage only concern the fuel behaviour phenomena up to fuel rod failure.
In 1997 a pressurized water loop will be implemented into the CABRI test channel. The future CABRI REP programme will then allow to study the full sequence of transient behaviour including post failure events resulting from fuel dispersion.
In the present paper we present the major results of the first CABRI REP-Na experiments.

1. Introduction

Fuel cycle and fuel management economics are the motivation for the world-wide trend to increase the burn-up at discharge of the LWRs and in particular of the PWRs.

A broad international data base is available for the demonstration that burn-up of more than 60 GWd/t(U) can be reached reliably with improved fuel assemblies. Steady state operation and operational transients are covered by this demonstration of satisfactory fuel behaviour.

However, a similar degree of experimental knowledge has not been achieved in the field of high burn-up fuel behaviour under design basis accident conditions, in particular RIA

Reactivity Initiated Accident). More precisely, at high burn-up (> 30 GWd/t), the fuel service limits and safety margins are unknown for the reference RIA, resulting from a postulated ejection of a control rod bundle. For this scenario the presently valid safety criteria are supposed to prevent from any severe damage to the reactor core and its structures.

In France, the RIA safety criteria have been formulated essentially on basis of the SPERT, PBF experiments :

- Maximum mean fuel enthalpy : $\overline{H}_{max} \leq 200$ cal / g (UO_2)
- Maximum clad temperature : $\overline{T}_c$ (max) $\leq 1482°C$
- Maximum fuel melt fraction : $F_{melt} \leq 10\ \%$

These criteria, as formulated presently, are independent on burn-up.

Since the early SPERT experiments (1967-1970) however there is clear evidence "that the mode of fuel rod failure is strongly affected by the previous irradiation" [1]. Similar conclusions were drawn from more recent Japanese NSRR experiments [2] when, nearly 20 years after the SPERT-CDC tests, fuel at a significant burn-up level was once again exposed to the conditions of rapid power transients.

No experimental data beyond ~ 30 GWj/t(U) with sufficient energy deposition for fuel behaviour under RIA conditions were available at the end of the 1980's. Russian experiments at 47 MWd/t performed in the IGR- test reactor [3] in Kasakhstan were known ; however the hollow pellet geometry of the WWER fuel and the specific cladding were considered to be to far from representativity for western fuel design.

In fact,there is clear evidence however for fuel transformations at high burn-up which might worsen the consequences of the hypothetical reactivity accident :

1/ formation of significant oxide layers on the ZIRCALOY cladding and related hydrogen pick-up which leads to embrittlement and reduced mechanical strength of the clad material.

2/ steadily increasing retention of gaseous and volatile fission products in the fuel which lead to transient fuel swelling under rapid heating conditions causing severe PCMI (pellet clad mechanical interaction).

3/ formation at the fuel surface of a porous, high burn-up zone with very small grains and high fissile material content.

4/ strong pellet to clad contact.

As a consequence of these transformations it is expected that the critical fuel enthalpy which leads to unacceptable consequences decreases with increasing burn-up. The early rod failure resulting from PCMI loading of brittle cladding might produce undelayed expulsion of finely fragmented solid fuel together with the gases retained in the RIM region and originate a new type of fuel coolant interaction, FSFCI (Fragmented Solid Fuel Coolant Interaction).

2. The transient response of the fuel to RIA accident conditions

The american (SPERT, PBF) and japanese (NSSR) in-pile experiments have established a broad data base for fresh fuel rod behaviour for experimental fuel exposed to fast, close to adiabatic, power transients.

The conclusions drawn from the results of these test programmes have largely determined the formulation of the RIA safety criteria :

a) no failure without departure from nucleated boiling (DNB).
b) no fuel dispersion without melting.

The failure mode of the cladding was strain rupture due to ballooning at high clad temperature.

Molten fuel ejection and subsequent molten fuel coolant interaction (MFCI) only occurred at high fuel enthalpy levels when substantial melting was reached.

Some of the last SPERT CDC tests (756 and 859 at ~ 32 GWd/t) and more recent NSRR experiments (JM4 and JM5 at ~ 26 GWd/t), gave unrefutable evidence for a totally different transient fuel behaviour with regard to fresh fuel. Failure occurred at significantly lower enthalpy levels than for fresh fuel, as low as 85 cal/g in SPERT 859, however either no or very little fuel was dispersed.

In addition, both test series are suffering from major unrepresentativities with regard to PWR fuel :

- high preirradiation power level for the GEX pellet fuel used in SPERT CDC (~ 550 W/cm (max)),
- highly enriched (10 %) experimental fuel irradiated under helium and tested in NSRR at 20°C initial capsule water temperature conditions under 1 bar pressure.

The three already mentioned high burn-up effects which are supposed to change significantly the fuel behaviour at high burn-up must be analysed in detail.

If the accumulation of fission products with irradiation and also the clad embrittlement could be prognosticated, this was not the case for the RIM effect in 1971 when the guide-lines for safety criteria were formulated.

2.1. Clad corrosion

The in-pile clad corrosion process is the major life limiting factor for nominal fuel operation.

In the upper part of the fuel rod, at high burn-up and for first generation clad material, oxide layers of more than 100 μ thickness may be observed and the hydrogen content of the underlying metal could be larger than 600 ppm. This corrosion is accompanied by the radiation

damage due to fast neutrons and to the potential action of aggressive fission products on the inner surface of the fuel clad.

Hydrogen has some solubility in ZIRCALOY at the operating temperature of ~ 300°C. When cooling down, hydride phases could precipitate perpendicularly to the stress field in case of very high tensile stress in the cladding. A circumferential orientation of the hydride platelets is observed in metallographic examinations of irradiated cladding giving evidence of the loading from external pressure [4]. Stress inversion would lead to radial orientation of the hydrides which might initiate cracking [5].

2.2. Fission product retention

At 52 GWd/t (U) the fuel contains 1.4 cm^3/g of fission gas, Xenon and Krypton essentially, which is contained in microscopic, fine bubbles and confined by the lattice and grain boundary forces of the fuel (surface tensions). Under rapid transient heating this gas inventory is activated (released), progressively at solid state of the fuel and completely and instantaneously upon melting. This process produces the internal pressurisation of the fuel and the transient fuel swelling before the escape of the gas into the free volumes of the fuel rod. The inert fission gas effect might be raised up by a factor of up to two if volatile fission products (Cs, Rb...) or part of them would behave in a similar way like noble gases.

2.3. The RIM effect

At high burn-up, beyond 40 to 45 GWd/t(U) a typical zone appears at the radial periphery of the fuel. This zone, approximately 200 μ thick, is characterized by both its structure and composition [6 - 8]:

- very high local burn-up (~ 2 x $\bar{\tau}$),
- high local Pu content (~ 2 x cPu),
- submicron size fuel grains due to subdivision resulting from high fission product content at low temperature,
- high local porosity.

This peripheral zone is the product of the flux gradient in the pellet and of resonance neutron captures close to the fuel surface.

During the rapid power excursion the RIM zone plays a key role because the already peaking fission density in homogeneous fuel is amplified by the high Pu content and the increased gas content is boosted up by the locally high fuel temperatures. In case of fuel rod failure, this peripheral zone may be finely fragmented and dispersed into the coolant channel together with the fission gas retained in the RIM region.

3. The French theoretical and experimental programme of RIA studies

The basic objective of the IPSN/EDF programme on RIA's is the development, qualification and validation of computer tools.

TOSURA-REP (IPSN) [9] and METEOR (CEA-DRN) [10] are the codes which describe the state of the fuel at the beginning of the power transient (t_o-state).

SCANAIR (IPSN) [11] is specially developed for the high burn up fuel response to rapid power excursions. These codes are presently available for the preparation and interpretation of the RIA experiments and for sensitivity studies in reactor application. In a first step in the attempt to improve the experimental knowledge at high burn-up, IPSN has established the association to the japanese programme NSRR. Rapidly a good insight was gathered, especially on basis of the JM4 and JM5 experiments [12]. In 1991 however, on basis of 8 experiments with irradiated fuel in NSRR, the IPSN specialists came to the conclusion that the NSRR programme alone could not satisfy the French safety needs due to the NSRR limitations :

- unsufficient capacity of the amount of energy deposition into industrial fuel at high burn-up,
- no precise detection of failure and post-failure events,
- unsatisfactory initial thermohydraulic conditions (stagnant water, 1 bar, 20°C),
- non representative test rods only allowed to reach significantly high fuel enthalpies at high burn-up (JMTR fuel with 10 % enrichment and no corrosion).

As a consequence it was decided to initiate in the CABRI test reactor in CADARACHE an experimental programme in two stages with distinct objectives :

- Phase 1 of the CABRI RIA programme : REP-Na, RIA experiments in the sodium loop of CABRI.
- Phase 2 : CABRI-REP, after implementation of a pressurised water-loop into CABRI, experiments in representative PWR conditions.

3.1. RIA experiments in the sodium loop of CABRI [14]

The early, precocious failures which have been observed in SPERT 859 as well as in NSRR JM4, JM5 had demonstrated that PCMI failure at high burn-up occurs on cold cladding, early in the transient. No significant thermal-hydraulic effect is to be expected before failure. For this phenomenology experiments in the sodium loop of CABRI could be envisaged. The nature of the coolant, if compatible with ZIRCALOY, should not play a role before failure and fuel ejection.

A limited number of tests has thus been defined aiming at the determination of the fuel failure enthalpy at high burn-up and at the evaluation of the safety margin to fuel ejection.

For this programme phase a number of 6 to 8 experiments are envisaged with fuel burn-up as the major test parameter.

3.1.1. The CABRI REP-Na test matrix and the test parameters

In fact four parameters are studied already in the first phase of the CABRI tests :

- burn-up,
- clad corrosion,
- ramp rate,
- fuel type.

1. Burn-up

The global aspect of irradiation effects is studied at 3 burn-up levels :

~ 30, ~ 50, ~ 60 GWd/t

A fresh fuel test in CABRI cannot be envisaged because the sodium coolant environment does not allow to simulate the sequence of clad overheating and ballooning after DNB.

2. Clad corrosion

The effect of various degrees of corrosion is studied by the use of either standard or improved clad material or by selecting lower or upper sections of a commercial fuel rod at the same burn-up level.

3. Power ramp rate

In a first stage a fast power pulse of ~ 10 ms width at half maximum similar to the NSRR and SPERT ramps, is applied.

In a second stage a pulse of ~ 80 ms width at half maximum as calculated from reactor neutronics, will be applied. It is expected that the power ramp rate could have some influence on the behaviour of the fission product populations resulting from the significantly different temperature history and radial distribution.

4. Fuel type

The introduction of mixed U-Pu fuel - MOX - into the french PWRs has already started and will be amplified in a near future. The fabrication mode of MOX fuel may lead to local inhomogeneities especially for the fuel fabrication mode which is based on the mixing of UO_2 with a U/Pu masterblend (MIMAS procedure). Fuel from this fabrication route may contain Pu rich agglomerates which would reach local burn-up levels very much higher than average. Rapid transient heating would overheat and overpressurize these agglomerates. Fresh fuel tests have been performed by FRESHLEY and al. in the early 70's [14]. No data base is available for highly irradiated MOX fuel. A few experiments at various burn-up are foreseen already in the sodium loop of CABRI.

The CABRI test matrix beyond REP-Na3 is still provisional and is shown in table 1.

3.1.2. The CABRI-REP water programme

In 1997 the CABRI facility will be equipped with a pressurized water loop. At this time some major questions will have been resolved thanks to the sodium experiments.

The essential part of the questioning and finally the validation basis for computer codes must be delivered however by the fully representative experiments in the pressurised water environment.

IPSN

TABLE 1 MATRIX OF RIA TESTS IN THE CABRI SODIUM LOOP

Name	Fuel (U5 enrichi)	Max. Mean Fuel Enthalpy (estimated)	Objective	Date
REP Na-1	EDF 65 GWd/t (4.5 %) SGL 5/6	120	Failure ?	Nov. 1993 (made)
REP Na-2	BR3 35 GWd/t (6.85 %)	200	Failure	June 1994 (made)
REP Na-3	EDF 50 GWd/t (4.5 %) SGL 5/6	140	Failure	Sept. 94 (made)
REP Na-4	EDF 50 GWd/t (4.5 %) SGL 2/3 or EDF 30 GWd/t (4.5 %) SGL5/6	140 160	Failure ? Failure ?	Fin 94/ Début 95
REP Na-5	EDF 50 GWd/t (4.5 %) SGL 5/6 Reactor Ramp or EDF 30 GWd/t (4.5 %) SGL 5/6 Reactor Ramp	140 160	Failure ? Failure ?	95
REP Na-6	MOX Fuel not yet chosen	180	Failure	95

SGL = spacer grid level.

INSTITUT DE PROTECTION ET DE SURETE NUCLEAIRE
DEPARTEMENT DE RECHERCHES EN SECURITE
Centre d'Etudes de Cadarache - Bâtiment n°702 - 13108 SAINT PAUL LEZ DURANCE CEDEX - Téléphone : 33 42 25 77 36 - Fax : 33 42 25 29 29 - Télex : CEACA 440678 F

As already mentioned, the experiments under sodium are only valid in their early phase. Early failure if occuring is significant. Once the rod has survived the early loading, the overcooling under sodium causes thermal and thermal-hydraulic non-representativity.

Furthermore, the transient fission gas behaviour has to be validated under realistic pressure conditions. The most important aspect of the PWR loop however is given by the possibility to study post failure events, in particular the fragmented-solid-fuel-coolant-interaction (FSFCI) which represents at present time a major threat. Without any precise knowledge, a conservative approach must be adopted presently such that finely fragmented fuel once ejected, which continues to be heated by the on-going power pulse and exchanges heat directly with the pressurised water.

On the contrary, experimental evidence is expected to show that the real process is considerably mitigated by the presence of the fission gas which was blown out simultaneously with the fuel.

Together with the number of advantages of the CABRI facility [15] :

- hodoscope,
- precise energy deposition,
- precise failure time and location,
- temperature, pressure, flow measurements,
- on site examination.,

the pressurised water loop will open a new field for important safety studies.

4. First results from REP-Na tests

Three experiments of the CABRI REP-Na test matrix have been performed.

The test fuel was selected in accordance with the global matrix objectives. The experimental fuel rods were carefully elaborated and submitted to detailed non destructive testing and inspection before introduction into the CABRI test section.

After introduction and transportation to the CABRI site, the test rods are again radiographied and γ-scanned before loading into the CABRI test loop.

This is the usual CABRI procedure which is followed then by the flowmeter calibration and the measurement of the neutronic coupling between the test pin and the CABRI driver core.

Immediately before and just after the power transient a HODOSCOPE recording is made at low power which establishes the state of the fuel just before and immediately after the test.

All the three experimental rods have been exposed to the same driver core power pulse, close to the maximum capabilities of CABRI, both in kinetics and in amplitude. The energy deposition into the test rod is finally determined by the reactivity of the test fuel resulting from fissile material content and from burn-up.

All tests are carefully precalculated :

- t_o-state : TOSURA (REP).
- transient : SCANAIR

4.1. The test REP-Na 1

For this first test the most penalising conditions have been chosen :

- highest burn-up,
- important corrosion.

4.1.1. The fuel rod

The tested fuel is a 570 mm long section cut-off from a commercial fuel rod at the level of the spacer grids 5/6. The 4.5 % U-5 enriched fuel was irradiated in the EDF power-plant GRAVELINES during 5 cycles, 3 of them under load follow operation mode.

The local burn-up is 63 GWd/t. The test rod was elaborated according to the FABRICE procedure and filled with a He/Xe gas mixture simulating the calculated plenum gas composition at 1 bar (ntp).

4.1.2. The CABRI test

The test rod was subjected to a 9.5 ms large power pulse which deposited a local maximum average energy of 116 cal/g (UO_2). The coolant channel conditions were :

- sodium inlet temperature : 280°C,
- sodium flow rate : 4 m/s,
- coolant pressure (outlet) : 2 bars.

4.1.3. Test results

The fuel rod failed early into the transient at a local average energy deposition of only ~ 15 cal/g corresponding to an average maximum enthalpy of ~ 30 cal/g (UO_2). Failure was detected by microphones and pressure and flow events were recorded.(see fig 1) Channel thermocouples measured temperature up to 1350°C.

Post test non-destructive examinations showed multiple brittle failures (see fig 2), fuel loss from the rod and fuel accumulation on channel filters.

4.2. The test REP-Na 2

The objective of this test was to explore the safety margin at ~ 30 GWj/t (U) and to qualify the sodium channel testing at the level of the previous SPERT-CDC tests 756 and 859.

FIG. 1 :

REP-Na1

In-pile
Diagnostics

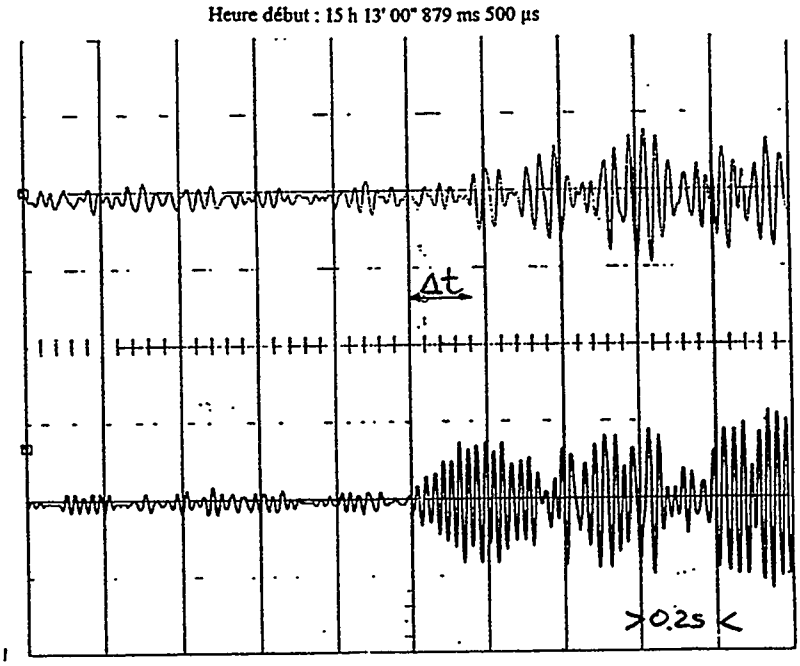

Fig. 1a : Microphone Signals

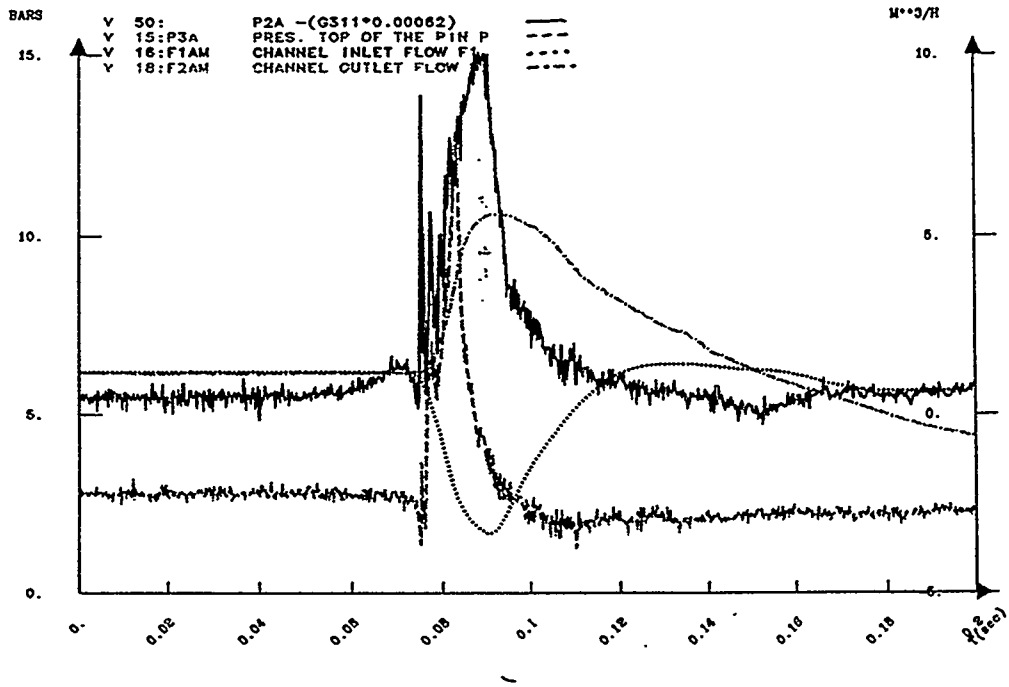

Fig. 1b : Pressure and Flow Signals

INSTITUT DE PROTECTION ET DE SURETE NUCLEAIRE
DEPARTEMENT DE RECHERCHES EN SECURITE
Centre d'Etudes de Cadarache - Bâtiment n°702 - 13108 SAINT PAUL LEZ DURANCE CEDEX - Téléphone : 33 42 25 77 36 - Fax : 33 42 25 29 29 - Télex : CEACA 440678 F

REP-Na1

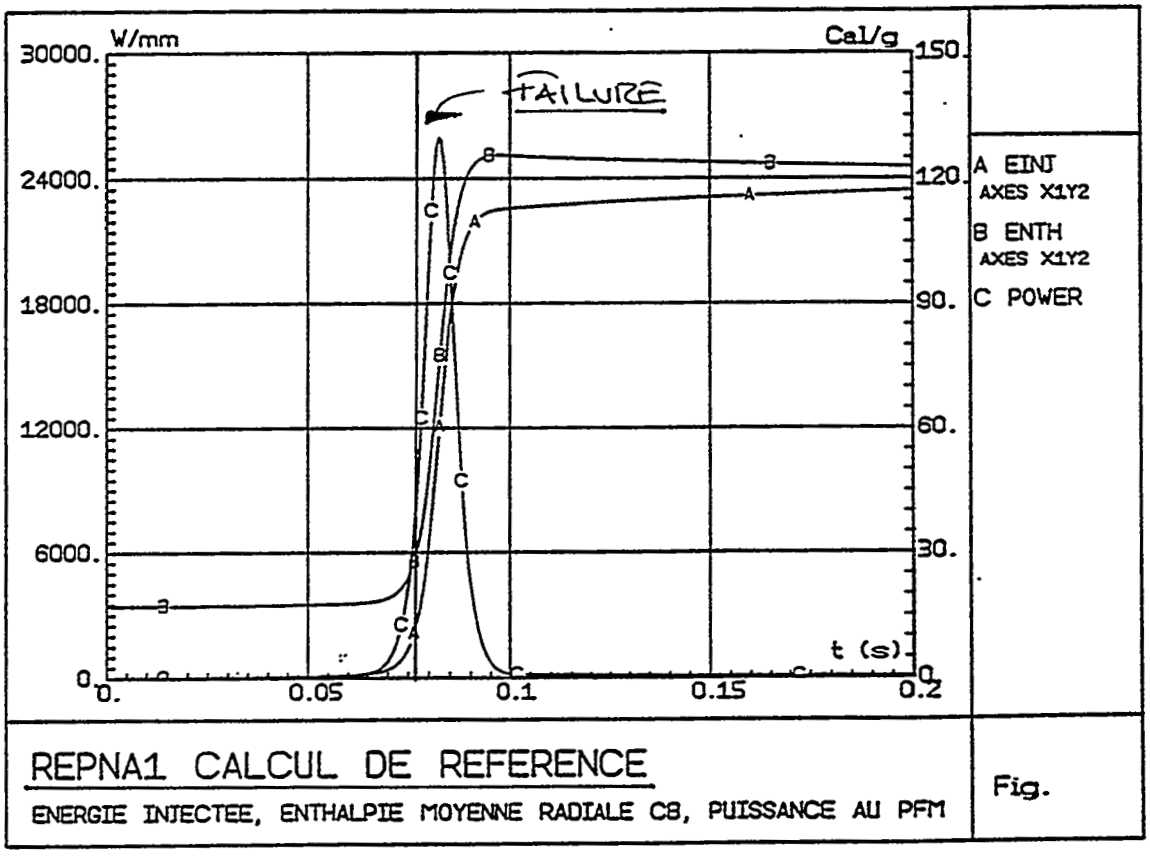

Fig. 1c : Power Pulse, Energy Injection and Failure Time Indication

INSTITUT DE PROTECTION ET DE SURETE NUCLEAIRE
DEPARTEMENT DE RECHERCHES EN SECURITE
Centre d'Etudes de Cadarache - Bâtiment n°702 - 13108 SAINT PAUL LEZ DURANCE CEDEX - Téléphone : 33 42 25 77 36 - Fax : 33 42 25 29 29 - Télex : CEACA 440678 F

Cabri test REP Na-1

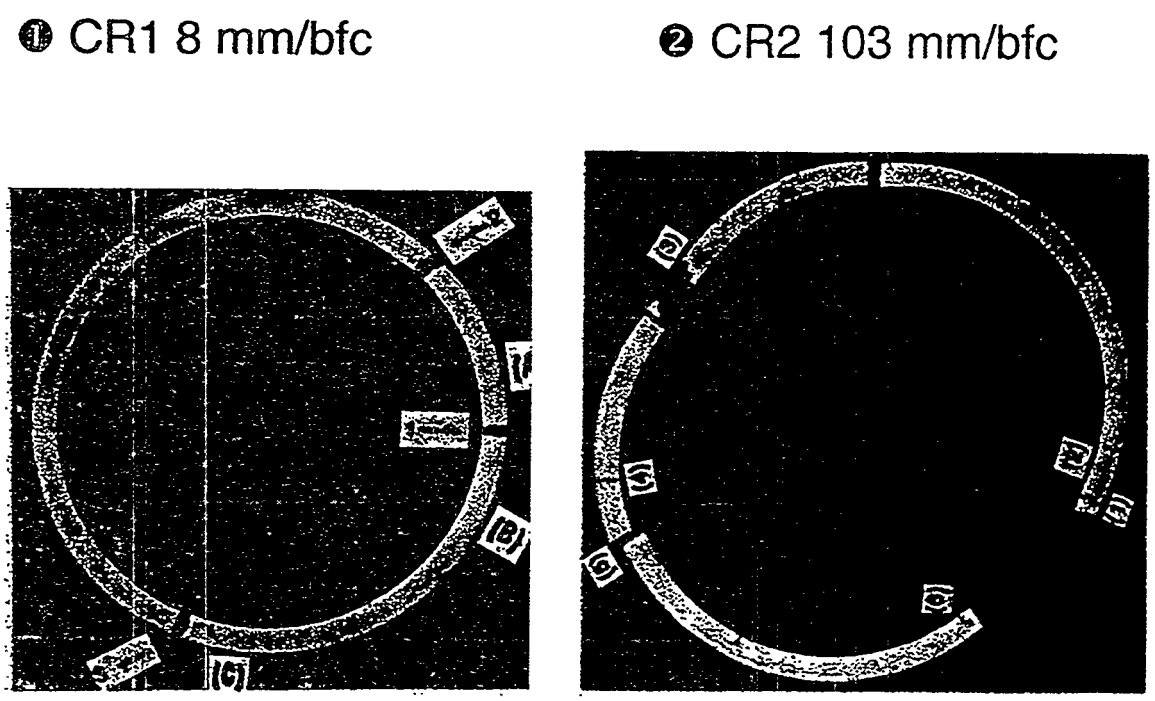

FIG. 2 : Radial cuts of REP-Na1 showing multiple brittle failure sites

4.2.1. The fuel rod

The test rod of this test is a full length BR3 fuel rod of 1000 mm fissile length. The 6.85 % enriched fuel was irradiated in the belgian reactor BR3 during 2 cycles to a maximum burn-up of 33 GWd/t. The only transformation of the fuel rod consisted in replacing the original fill gas by pure helium at atmospheric pressure in order to avoid an abnormal pressure gradient in the CABRI test channel.

4.2.2. The CABRI test

The test rod was subjected to a 9 ms large power pulse which deposited a local maximum average energy of 202 cal/g (UO_2) (see fig 3). The coolant channel conditions were identical to REP-Na 1.

4.2.3. Test results

The fuel rod did not fail. During the test the flow meters measured a so-called TOP effect which is attributed to the expulsion of a small coolant volume which corresponds to the transient volume change of the test pin (see fig 3). A slight permanent flow reduction was detected indicating a significant plastic fuel rod deformation. A permanent cladding growth of 10 mm and a fuel growth of 8 mm was registered.

4.3. The test REP-Na 3

The objective of this experiment was to test the response to the RIA transient of a commercial fuel rod with improved clad material at goal burn-up.

4.3.1. The fuel rod

The tested fuel is a segmented fuel rodlet of 436 mm fissile length irradiated in commercial conditions in the EDF power plant GRAVELINES during 4 cycles under load follow. The 4.5 % U-5 enriched fuel reached a local burn-up of 53 GWd/t. The segmented rodlet was located at the spacer-grid-level 5/6 during irradiation.

The preparation for CABRI testing consisted in removal of structure elements and replacing the original fill gas by pure helium at 3 bar (ntp) pressure. In fact after REP-Na 2 it was considered preferable to improve the failure detection by a slight overpressure in the pin compared to the channel pressure.

IPSN

FIG. 3 : REP-Na2 In Pile Diagnostics
Fig. 3a : Reactor Power and Core Energy Deposition
Fig. 3b : Inlet Flow (F1) and Outlet Flow (F2)

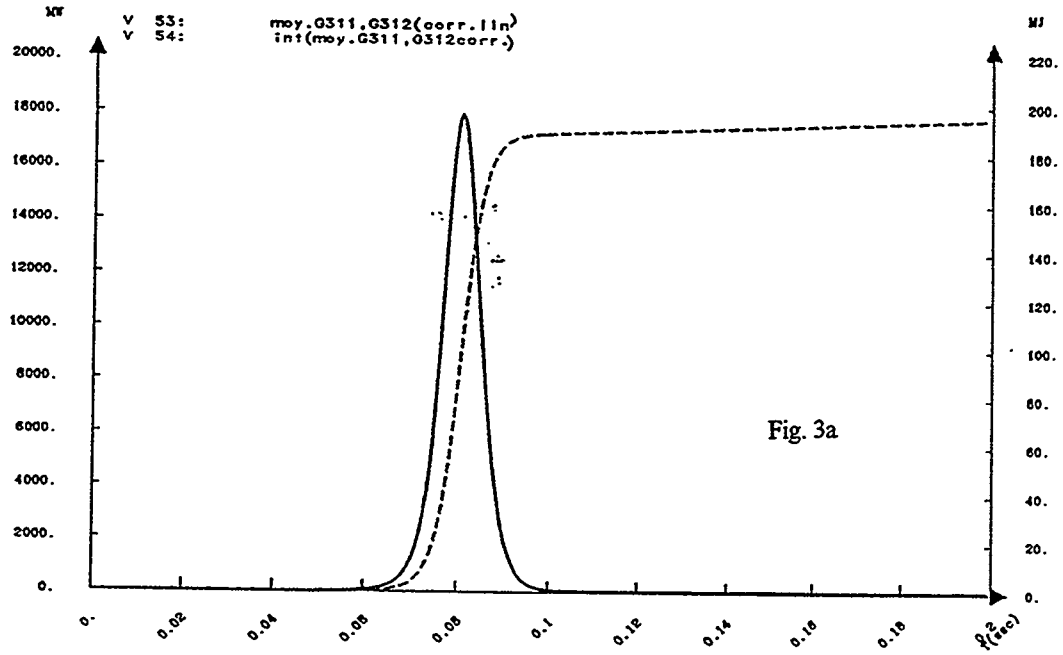

Fig. 3a

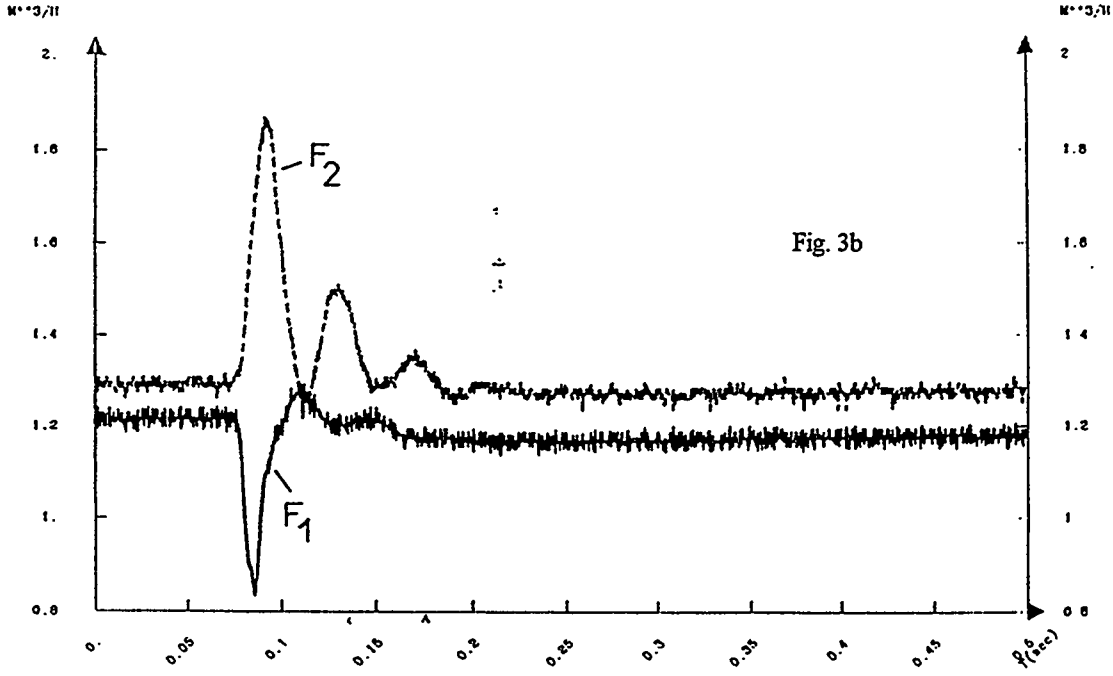

Fig. 3b

INSTITUT DE PROTECTION ET DE SURETE NUCLEAIRE
DEPARTEMENT DE RECHERCHES EN SECURITE
Centre d'Etudes de Cadarache - Bâtiment n°702 - 13108 SAINT PAUL LEZ DURANCE CEDEX - Téléphone : 33 42 25 77 36 - Fax : 33 42 25 29 29 - Télex : CEACA 440678 F

FIG. 4 : REP-Na3 In Pile Diagnostics
Fig. 4a : Reactor Power and Core Energy Deposition
Fig. 4b : Inlet Flow (F1) and Outlet Flow (F2)

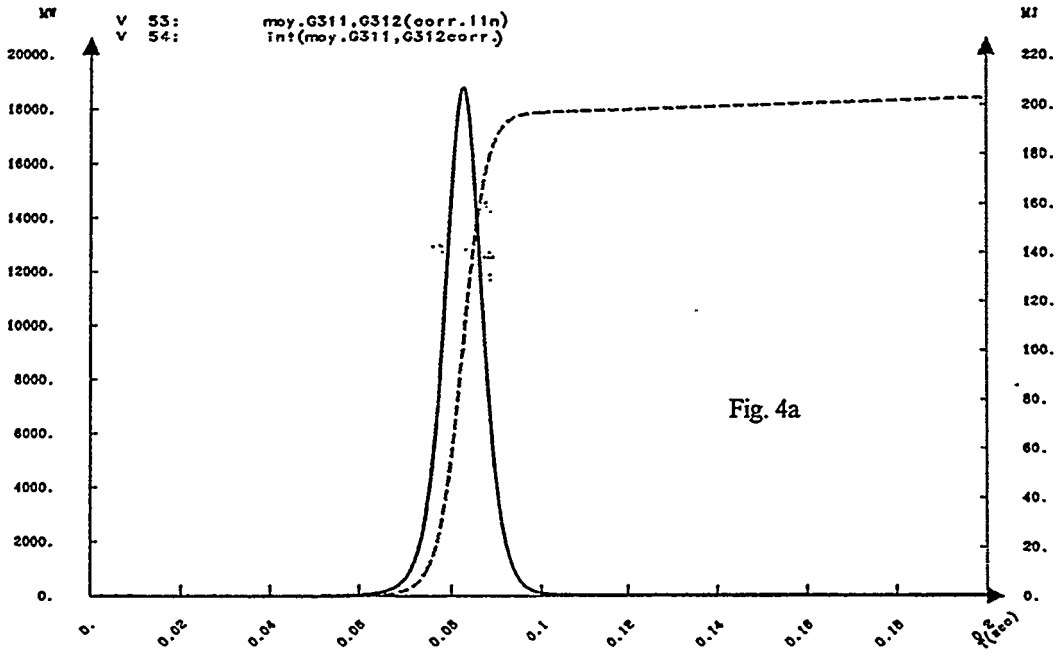

Fig. 4a

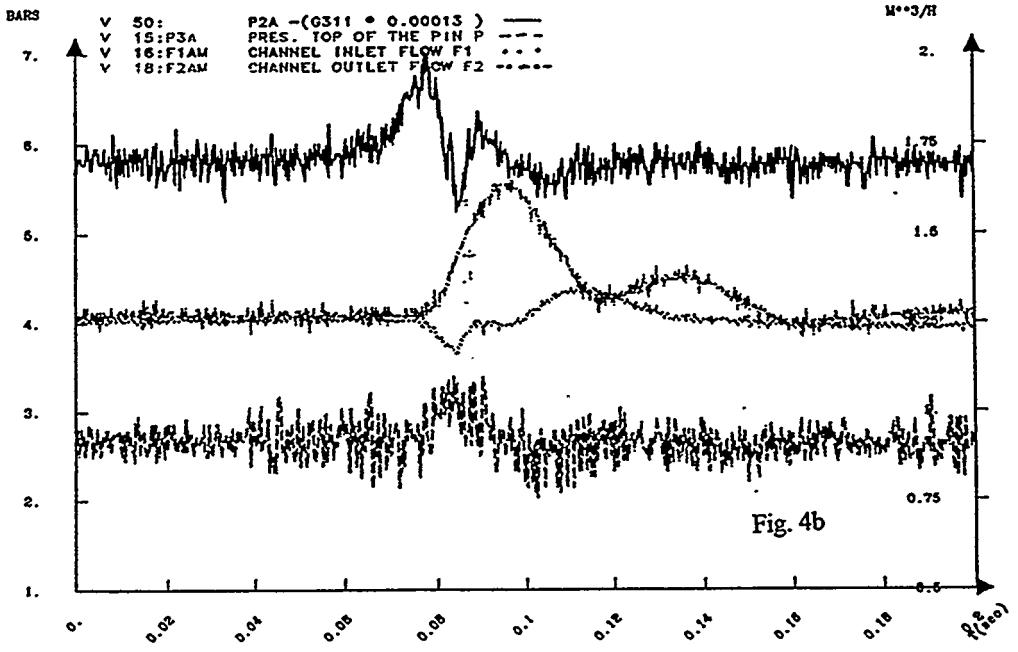

Fig. 4b

INSTITUT DE PROTECTION ET DE SURETE NUCLEAIRE
DEPARTEMENT DE RECHERCHES EN SECURITE
Centre d'Etudes de Cadarache - Bâtiment n°702 - 13108 SAINT PAUL LEZ DURANCE CEDEX - Téléphone : 33 42 25 77 36 - Fax : 33 42 25 29 29 - Télex : CEACA 440678 F

4.3.2. The CABRI test

The test rod was subjected to a 9.5 ms large power pulse which deposited a local maximum energy of ~ 120 cal/g (UO_2) (see fig 4). The coolant channel conditions were nominal, identical to the previous tests.

4.3.3. Test results

The fuel rod did not fail. A similar TOP effect like in REP Na2 has been detected by the flow-meters (see fig 4). If confirmed, a significaant plastic straining of the cladding is to be expected.

5. Discussion

The first three CABRI REP-Na experiments gave important, and to a large extend, unexpected results.

After REP-Na 1, critics and doubts were formulated as to the representativity and the compatibility of the ZIRCALOY with the sodium test channel.

These experimental conditions may be considered as qualified by the tests REP-Na 2 and REP-Na 3. Nevertheless, an important destructive examination programme has been performed and to an important part devoted to the identification of eventual "system effects". This extensive examination programme which is performed in the CEA/DRN hot-cells at CADARACHE and SACLAY is nearly terminated.

There is no evidence for untypical material behaviour and in particular for incompatibility between ZIRCALOY and sodium.

The extremely early and moreover violent failure of CABRI REP Na1 can only be explained by a specific action of the RIM region which is the only part of the fuel which had reached thermal conditions largely beyond the nominal operation conditions due to the power peaking in the periphery (see fig 5). This action of the RIM is most probably coinciding with a considerably reduced clad resistance due to corrosion and especially to hydrogen embrittlement and a strong radial PCMI.

REP-Na2 has demonstrated a good thermomechanical behaviour. The final interpretation however must take into consideration the very low cladding oxidation and the relatively low fast neutron dose. An important clad plastic straining has been measured. The essential part of it seemsto be attribuable to transient swelling.

REP-Na3 is of highest interest. At 50 GWd/t the RIM is expressed and activated during the transient. The test rod has survived the RIA transient. This is most probably attribuable to the good mechanical behaviour of the improved cladding and to the reduced extension of the RIM region..

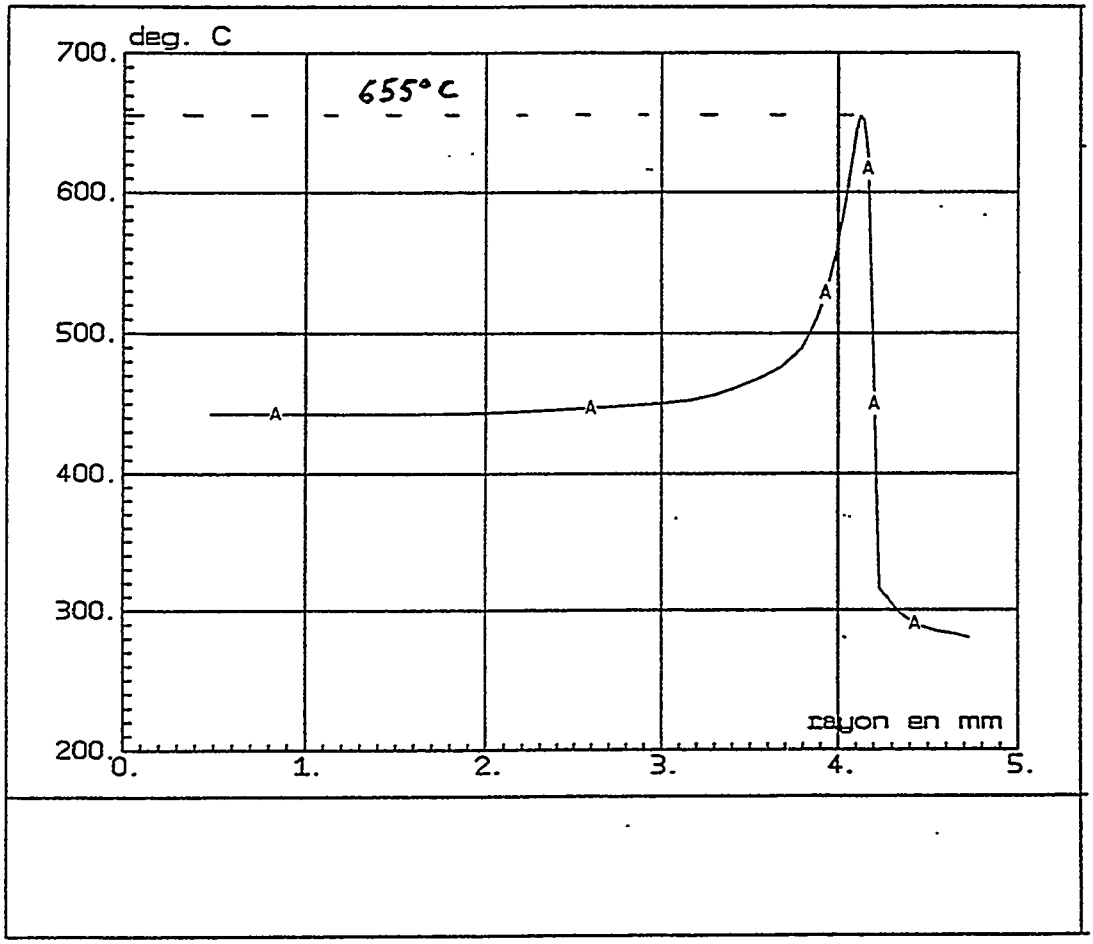

FIG. 5 : REP-Na1 reference calculation of radial temperature distribution at the time of rod failure

INSTITUT DE PROTECTION ET DE SURETE NUCLEAIRE
DEPARTEMENT DE RECHERCHES EN SECURITE
Centre d'Etudes de Cadarache - Bâtiment n°702 - 13108 SAINT PAUL LEZ DURANCE CEDEX - Téléphone : 33 42 25 77 36 - Fax : 33 42 25 29 29 - Télex : CEACA 440678 F

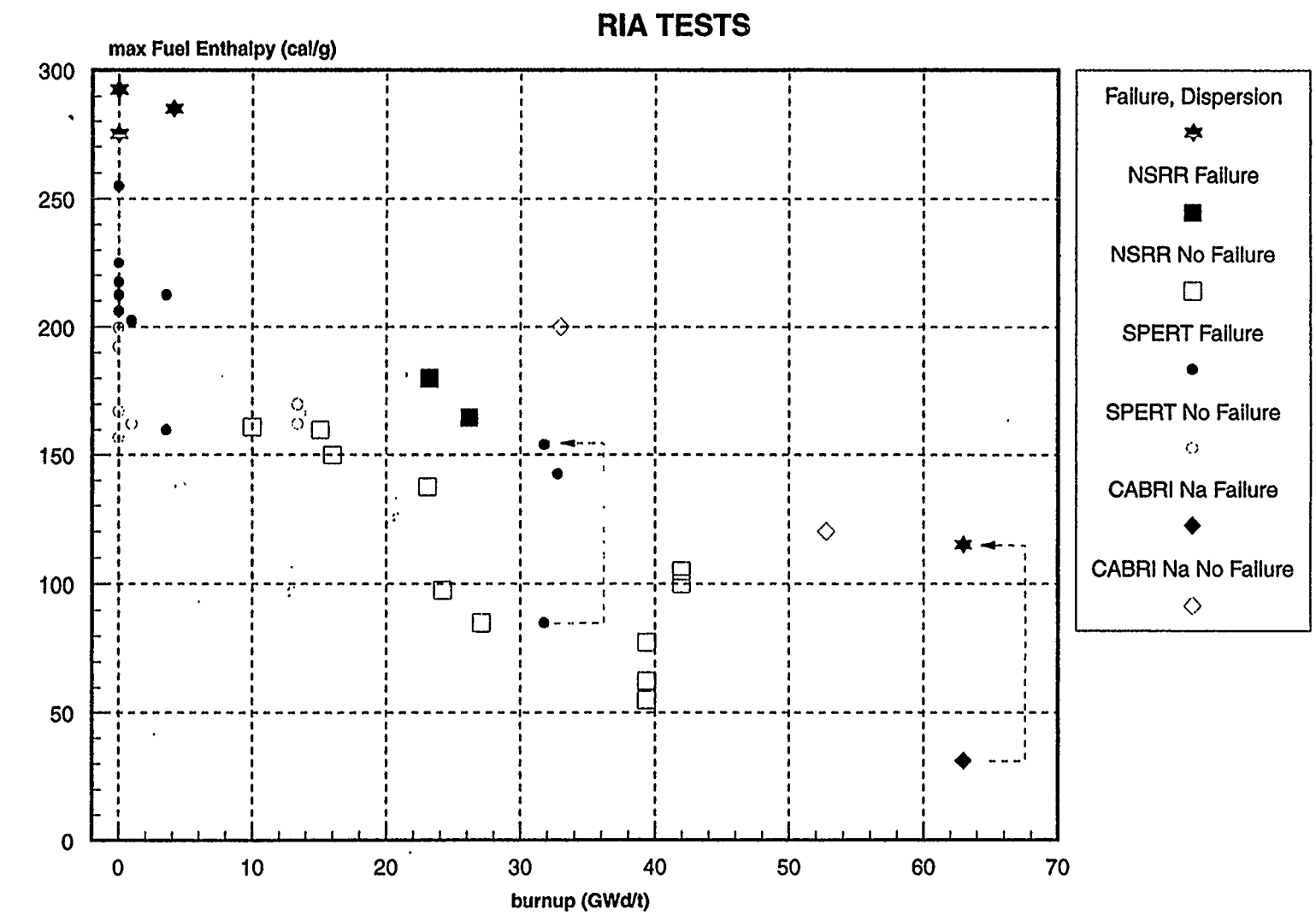

FIG. 6 : Data base of RIA tests

INSTITUT DE PROTECTION ET DE SURETE NUCLEAIRE
DEPARTEMENT DE RECHERCHES EN SECURITE
Centre d'Etudes de Cadarache - Bâtiment n°702 - 13108 SAINT PAUL LEZ DURANCE CEDEX - Téléphone : 33 42 25 77 36 - Fax : 33 42 25 29 29 - Télex : CEACA 440678 F

6. CONCLUSION

The REP-Na test matrix has been formulated as a bundle of tests which are complementary for understanding. A synthesis will be established once the UO_2 tests are terminated. Presently it appears that understanding is complicated by missing data in the field of the dynamic mechanical properties of irradiated ZIRCALOY.

Furthermore a better understanding of transient fission gas behaviour is urgently needed.

From table.2 and fig. 6, it is obvious that low corrosion seems to improve the transient response of the PWR fuel to the RIA transient.

The future tests should reveal the impact of the energy injection rate and possibly the cliff-edge behaviour when corrosion degraded clad can not resist to the transient fuel swelling (PCMI) and the finely fragmented fuel of the RIM region is dispersed into the coolant channel when high burn-up fuel fails at an early stage, due to PCMI.

Last but not least, the need to perform tests in a pressurised water-loop is the indispensable condition for final code validation and so for the reassessment of safety criteria which most probably must include a corrosion limitation in addition to burn-up.

Acknowledgement :

The authors of this paper acknowledge gratefully the qualified work of the specialist teams involved in the broad effort on RIA experiments : test fuel characterization at EDF (CHINON), test rod fabrication and control at LECI (SACLAY) and TUI (KARLSRUHE), test preparation and performance by DRS/SREAS and SEA at CADARACHE, theoretical preparation by computer code applications by DRS/SEMAR and EDF/SEPTEN and fruitful, safety analysis related contributions from IPSN/DES.

Table 2 : REP-Na Test data summary

(tbd = to be determined)	REP-Na1	REP-Na2	REP-Na3
Test fuel rod	FABRICE	BR 3 rod	Segmented
Cladding	Standard	Standard	Improved
Pressure (P_{pin}-$P_{channel}$)	0	0	2
Enrichment	4.5 %	6.85 %	4.5 %
Burn-up	63 GWd/t	33 GWd/t (max)	53 GWd/t
Corrosion (μ)	80	10	40
Hydrogen (ppm)	760	tbd	tbd
Test Energy Deposition	116 cal/g	202 cal/g	117 cal/g
Power Pulse Width	9.5	9	9.5
Maximum Fuel Temperature	2230°C	2750°C	2300°C
Main Result	Failure	No Failure	No Failure
Load follow	3 of 5 cycles	No	all 4 cycles

REFERENCES

[1] P.E. MAC DONALD et al.
Assessment of Light-Water-Reactor Fuel Damage During a Reactivity-Initiated-Accident.
Nuclear Safety vol. 21 - N°5 (1980).

[2] K. ISHIJIMA et al.
Behaviour of preirradiated LWR. Fuel Rods under Reactivity Initiated Accident conditions.
IAEA TECDOC-706 - Aix-en-Provence 1992.

[3] L.A. EGOROVA.
Results of Cose Experiments in Investigation of Fuel Failure Mechanisms For The UUER - 1000 in RIA Conditions.
IAEA TECDOC 706 Aix-en-Provence 1992.

[4] P. GUEDENEY et al.
Standard PWR Fuel Rod Characterization at High Burn-up.
International Topical Meeting on LWR Fuel Performance, Avignon 1991.

[5] C. LEMAIGNAN, A.T. MOTTA
Zirconium Alloys in Nuclear Applications Material Science and Technology.
Volume 10B - Nuclear Materials VCH - 1994.

[6] M.E. CUNNINGHAM et al.
Development and Characteristics of the RIM Region in High Burn-up UO_2 Fuel Pellets.
Journal of Nuclear Materials 188 (1992) 19-27.

[7] J.P. PIRON et al.
Fuel Microstructure and RIM Effect at High Burn-up.
International Topical Meeting on Light Water Reactor Fuel Performance.
West Palm Beach, Fl (1994).

[8] R. MANZEL, M. COQUERELLE, M.R. BILLAUX.
Fuel Rod Behaviour at Extended Burn-up.
International Topical Meeting on Light Water Reactor Fuel Performance.
West Palm Beach, Fl 1994.

[9] F. D. LEMOINE.
Adaptation du Code TOSURA aux REP.
To be published.

[10] C. STRUZIK et al.
Fuel Modelling at Extended Burn-up Comparison Between METEOR 1/ TRANSURANUS Calculations and Examinations on Fuel Rods Irradiated Up to 60 GWj/t.

International Topical Meeting on Light Water Reactor Fuel Performance, West Palm Beach, Fl (1994).

[11] J.C. LATCHE.
High Burn-up Fuel and Reactivity Accident.
Meeting Franco/Finlandais (June 1994).

[12] J. PAPIN et al.
Irradiated Fuel Behaviour During Reactivity Insertion Accidents of L
WRs.
IAEA - TECDOC 706 Aix-en-Provence 1992.

[13] J. PAPIN, J.P. MERLE.
Irradiated Fuel Behaviour During Reactivity Initiated Accidents in LWRS. Status of Research and Development studies in France.
21st WRSM, Bethesda (1993).

[14] M.D. FRESHLEY et al.
Behaviour of Discrete Plutonium. Dioxide Particles in Mixed Oxide Fuel During Rapid Power Transients.
Nuclear Technology - Vol. 15 (1972).

[15] J.DADILLON, J.M. AUJOLLET and G. KUSSMAUL
The CABRI Facility - Generation and Control of the Transient Conditions, Instrumentation of the Test Section.
International Colloquium on Irradition Tests for Reactor Safety Programmes.
Petten, Netherlands (1979).

NSRR EXPERIMENTS TO STUDY THE EFFECTS OF BURNUP ON THE FUEL BEHAVIOR UNDER REACTIVITY INITIATED ACCIDENT CONDITIONS

T. FUJISHIRO, K. ISHIJIMA
Department of Reactor Safety Research,
Tokai Research Establishment,
Japan Atomic Energy Research Institute,
Tokai, Ibaraki, Japan

Abstract

Since 1975, extensive studies on fuel behavior under reactivity initiated accident conditions have been continued in the Nuclear Safety Research Reactor of Japan Atomic Energy Research Institute. New experimental program with preirradiated LWR fuel rod as a test sample has recently been started. In this program, the effects of fuel burnup on the transient behavior, the failure threshold, the failure mechanisms and the consequences of the failure will be studied. Thirty two tests have been performed so far with commercial PWR and BWR rods, and PWR type rods preirradiated in the Japan Materials Testing Reactor (JMTR rods). The experiments indicated significant effects of burnup on fuel behavior such as large fuel pellet swelling causing hard pellet–cladding mechanical interaction and significant release of gaseous fission products.

1. INTRODUCTION

In the Nuclear Safety Research Reactor (NSRR) operated by Japan Atomic Energy Research Institute (JAERI), extensive experimental studies on the fuel behavior under reactivity initiated accident (RIA) conditions have been continued since the start of the test program in 1975[1]. Accumulated experimental data were used as the fundamental data base of the safety evaluation guideline for reactivity initiated events in light water cooled nuclear

power plants established by the nuclear safety commission on January 19th, 1984.

All of the data used to establish the guideline were, however, limited to those derived from the tests with fresh fuel rods as test samples because of the lack of experimental facility to handle highly radioactive materials. In time past, the tests with preirradiated fuel rods were conducted in the SPERT-CDC and the PBF projects at Idaho National Engineering Laboratory in the United States[2]. The number of the tests performed in these projects was, however, limited to thirteen runs in all, and seems to be insufficient for clearly understanding the influences of fuel burnup on fuel behavior under RIA conditions. The present Japanese safety evaluation guideline, therefore, introduces the peak fuel enthalpy of 85 cal/g·fuel which was adopted from the SPERT-CDC data as a provisional failure threshold of preirradiated fuel rod and says that this value should be revised based on the NSRR experiments in future.

This provisional failure threshold of 85 cal/g·fuel was introduced the embrittlement of the cladding tube and the possibility of PCMI (Pellet-cladding Mechanical Interaction) failure and is used to count the number of failure rods during the course of an RIA and to evaluate the source term for radiation hazard calculation. The present guideline has two other criteria 230 cal/g for accidents to eliminate the possibility of mechanical energy generation and the acceptable fuel design limit for abnormal transients as a function of pressure difference between inside and outside of the cladding tube. The latter partially considers the effect of fuel burnup, that is, accumulation of gaseous fission products. All of these criteria should be reevaluated for high fuel burnup conditions.

According to the above requirement, new NSRR experimental program with preirradiated fuel rod as a test sample was started in 1989. Test fuel rods are prepared by refabrication of fuel rods preirradiated in commercial PWRs and BWRs into short segments and by preirradiation of short-sized test fuel rods in the Japan Materials Testing Reactor (JMTR). Fuel rods already procured from commercial power reactors include PWR fuel rods from Mihama-2, Genkai-1 and Ohi-1,2 reactors, and BWR fuel rods from Tsuruga-1 reactor.

Preirradiation of 29 capsules (containing 87 test fuel rods) in the JMTR had completed or been progressing. These test fuel rods will accumulate fuel burnups ranging from 10 to 40 GWd/t. Among them, some rods have higher initial enrichment (20%) or different rod design

(e.g. gap width).

The major interests in the current research activities are PCMI which might cause cladding failure at a low fuel enthalpy, fission gas release behavior under rapid heating conditions and the possibility of fuel dispersion at a relatively low fuel enthalpy.

2. EXPERIMENTAL METHOD

2.1. Outline of the NSRR facilities

Since the NSRR, program is directed towards the study RIA fuel behavior, test fuel rods should be irradiated by a rapid power burst which should be similar to an RIA power burst in an LWR. TRIGA–ACPR, which generates pulsing power slightly more rapidly than an LWR, was selected as the NSRR reactor. As shown in Fig. 1, the reactor core is mounted on the bottom of 3.6 m wide, 4.5 m long and 9 m deep open pool. At the center of the NSRR core, there is a large experimental cavity, where test fuel rods contained in a capsule or a loop are subjected to power bursts.

The pulse operation which generates a power burst from zero power can simulate an RIA from cold startup or hot stand–by. The reactivity insertion of up to \$4.7 is licensed to produce the maximum reactor power of 23,000 MW with the minimum reactor period of approximately 1.2 ms and to bring the maximum burst energy of 130 MJ.

2.2. Test fuel rod

The test fuel rods used in the current test program are 14x14 and 17x17 type PWR rods and 7x7 type BWR rods. The as–fabricated characteristics of the test rods are listed in Table 1. Burnup of the commercial PWR rods ranged from 39 GWd/t to 50 GWd/t and that of the BWR rods was 26 GWd/t.

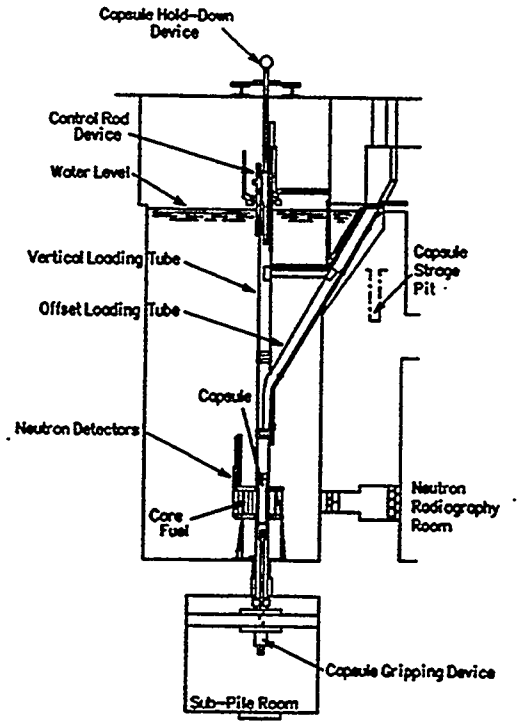

Fig. 1 NSRR facility

Table 1 Summary of as-fabricated characteristics of the test fuel rods

Item	PWR rod (14x14)	PWR rod (17x17)	BWR rod	JMTR rod
Fuel	Sintered UO_2	Sintered UO_2	Sintered UO_2	Sintered UO_2
Density (g/cc)	10.41 (95%TD)	10.41 (95%TD)	10.41 (95%TD)	10.41 (95%TD)
Pellet O.D.(mm)	9.29	8.1	12.37	9.29
Pellet length (mm)	15.2	9.0	21.0	10.0
Enrichment (w/o)	2.6(1) or 3.4(2)	3.4	2.79	10.0(3), 5.0, Nat.
End shape	Dished end	Dished end	Dished end	Chamfered end
Cladding	Stress relieved zircaloy-4	Stress relieved zircaloy-4	Stress relieved zircaloy-4	Stress relieved zircaloy-4
Cladding O.D.(mm)	10.72	9.5	14.3	10.72
Wall thickness (mm)	0.62	0.62	0.81	0.62

(Note) : MH rod (2) GK rod (3) Main part of fuel stack

The fuel rods are refabricated from the preirradiated commercial reactor fuel rods. As an example, Fig. 2 shows the design of BWR type test fuel rod. A short segment is cut off from the axial position with relatively flat burnup distribution. A new top end fitting containing a magnetic iron core to measure the elongation of fuel stack and a new bottom end fitting with a pressure sensor for the measurement of rod internal pressure are welded to it. The active lengths and the fill gases of the test fuel rods are given in Table 2. The pressure and the compositions of the fill gases for the PWR and the BWR rods are determined based on the results of rod puncture tests. Table lists the measured fission gas release during preirradiation for each type of the test fuel rod.

JMTR rods which are shortened PWR type rods containing highly enriched fuel pellets (10%) were preirradiated in the JMTR to accumulate fuel burnup. The fuel stack contains a 5%-enriched and a natural UO_2 pellets in each end. The rod was filled with pure helium gas of 0.1 MPa. These rods were installed in a capsule filled with pure helium gas of atmospheric pressure and subjected to the preirradiation. The linear heat rate during the preirradiation ranged from 20 to 40 kW/m. The fission gas release of 0.2% was measured for the reference rod after the completion of the preirradiation.

2.3. Experimental capsule and instrumentation

Figure 3 shows the schematic of the experimental capsule and the instrumentation. Each test fuel rod was instrumented with thermocouples (Pt/Pt-13%Rh : 0.2 mmϕ) to measure cladding surface temperature. The shortened commercial reactor fuel rod was equipped with a pressure sensor in the bottom end fitting to measure rod internal pressure. In some tests, linear variable differential transformers (LVDTs) were used to measure transient elongation of the cladding tube and the fuel pellet stack. The instrumented test fuel rod was contained in a doubly sealed (double container type) capsule which is newly developed for the test with preirradiated fuel rod. The capsule was filled with water of ambient temperature and atmospheric pressure, and subjected to a pulse irradiation in the NSRR.

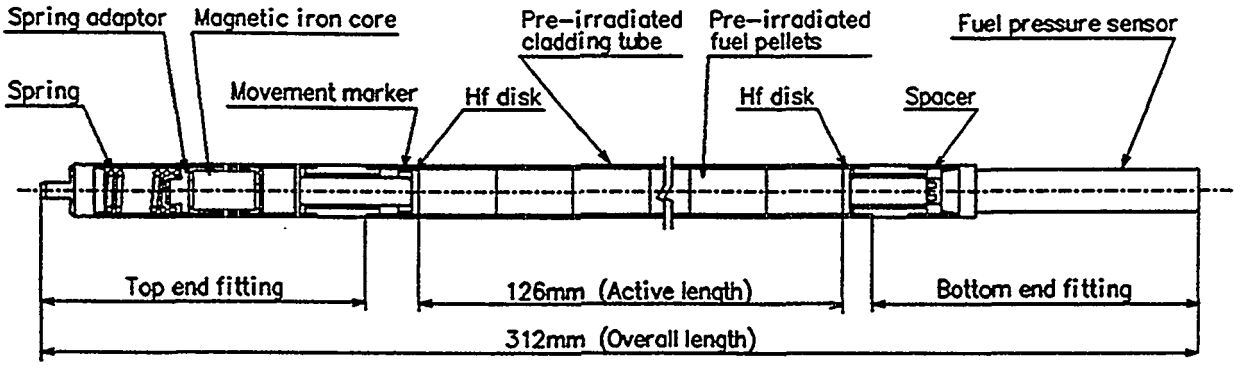

Fig. 2 Schematic of the test fuel rod
(BWR type rod)

Table 2 Test fuel rod design

Item	PWR rod (14x14)	PWR rod (17x17)	BWR rod	JMTR rod
Acitive length (mm)	122	133	126	100(1)
Overall length (mm)	308	314	312	220
Fill gas (MPa)	He(4.2~4.6)	He (0.1)	Mix. (1.1) or He (1.1)(2)	He (0.1)

(Note) : (1) 10%-enriched fuel region
(2) TS-3 rod

Table 3 FGR during preirradiation

PWR rod	BWR rod	JMTR rod
0.18(%) (1) 0.47(%) (2) 0.24(%) (3)	17%	0.20

(Note) : (1) MH rod
(2) GK rod
(3) OI rod

3. EXPERIMENTAL RESULTS

3.1. Test condition

In each experiment, a single fuel rod supported at the bottom in the stagnant water in the test capsule was subjected to a pulse irradiation. The long-term burnup (base burnup) due to the preirradiation and the short-term burnup (energy deposition) due to the pulse irradiation in the NSRR were evaluated by the chemical FP analyses of the samples taken from the test fuel rods after the completion of the pulse irradiation.

Base burnup measurement was performed by determining the fractional amounts of isotopes of neodymium, uranium and plutonium using the isotopic dilution method. Evaluated base burnups for PWR and BWR rods are described in section 2.2. Estimated values for JMTR rods ranged from 16 to 27 GWd/t.

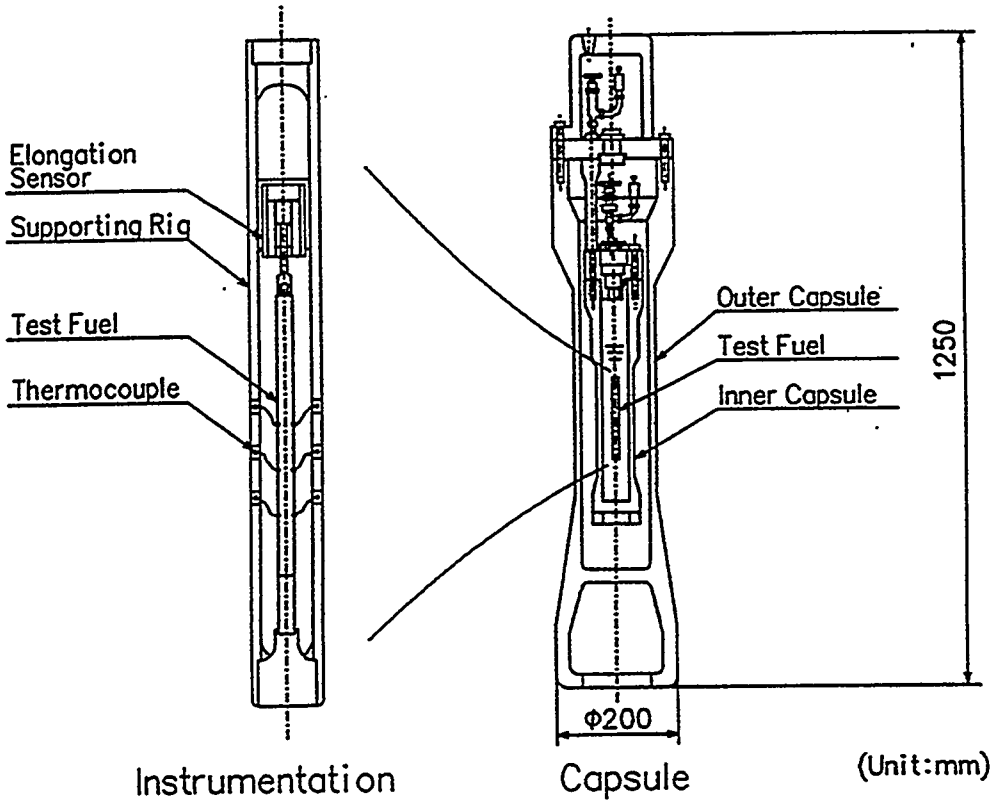

Fig. 3 Experimental capsule and instrumentation

Evaluation of the energy deposition due to the pulse irradiation includes severe difficulty because of the presence of large amount of γ-ray emitting FPs due to the preirradiation. Therefore, barium was chemically separated from the sample with the cation exchange method in nitric acid system. Post test examination including the evaluation of energy deposition was completed for the first thirteen experiments. The results are summarized in Table 4.

3.2. Cladding surface temperature

The measured maximum cladding surface temperatures are plotted in Fig. 8. The DNB (Departure from Nucleate Boiling) phenomenon on the cladding surface was observed in some cases. Durations of the film boiling were, however, very short and less than 1 s. Figure 4 gives the histories of the cladding surface temperatures measured in Test JM-4 as an typical example which shows the occurrence of DNB on the cladding surface.

Table 4 Summary of the test results

Test No.		Fuel burnup (GWd/t)	Peak fuel enthalpy (cal/g)	Fuel failure
PWR	MH-1	39	44	No
	MH-2	39	52	No
	MH-3	39	65	No
	GK-1	42	89	No
	GK-2	42	85	No
	OI-1	39	101	No
	OI-2	39	103	No
	HBO-1	50	(76)	Yes
	HBO-2	50	(39)	No
BWR	TS-1	26	55	No
	TS-2	26	61~71	No
	TS-3	26	88	No
	TS-4	26	89	No
	TS-5	26	98	No
JMTR	JM-1	22	87	No
	JM-2	27	80	No
	JM-3	17	124	No
	JM-4	21	168	Yes
	JM-5	26	158	Yes
	JM-6	15	148	No
	JM-7	13	139	No
	JM-8	20	152	No
	JM-9	(23)	155	No
	JM-10	(20)	159	No
	JM-11	(30)	157	No
	JM-12	(36)	168	Yes

(Note): (1) Values in ( ) are not fixed yet.

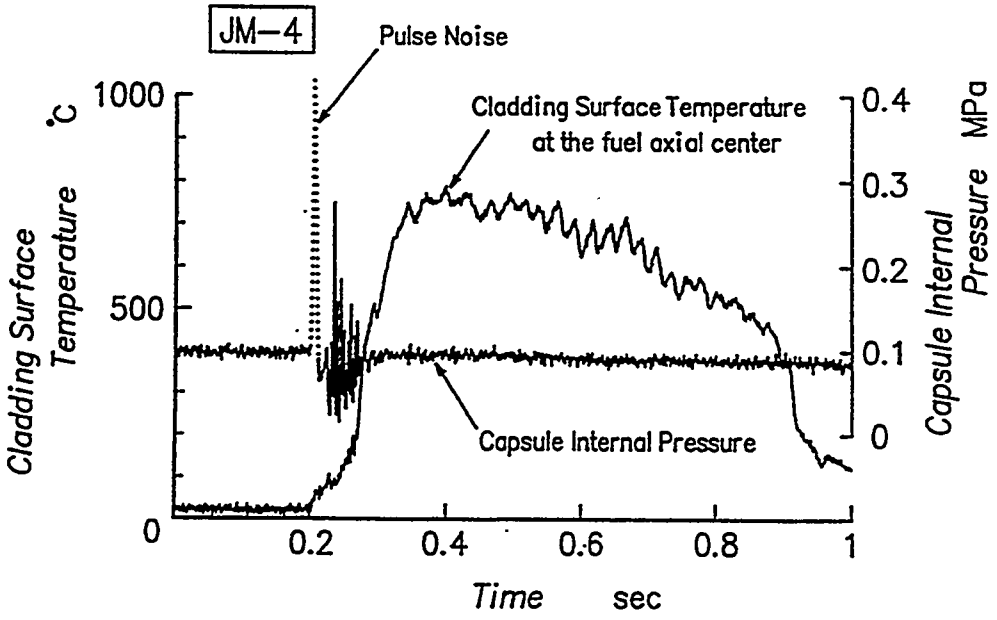

Fig. 4 Cladding surface temperature and capsule internal pressure measured in Test JM–4

3.3. Fuel rod deformation

Residual deformation of the cladding tube was observed in many tests. Figure 5 gives the measured axial profiles of some JMTR rods. The maximum hoop strain of the cladding tube reached approximately 7.5% in JM–4 rod. As shown in the figure, the profiles of JM–4 and –5 rods have 10 peaks and the position of each peak nearly corresponds to the axial center of each 10%–enriched fuel pellet. This kind of deformation behavior was not so clear in the PWR rods.

Transient elongations of the fuel pellet stack and the cladding tube were successfully measured in many tests. The cladding elongations of the PWR rods are most significant among them. Figure 6 shows the histories of the elongations of the fuel pellet stack and the cladding tube measured in Test JM–3.

3.4. Fission gas release during pulse irradiation

Fission gas releases (FGRs) during the pulse irradiation were measured by puncturing test. FGRs of the PWR rods and the JMTR rod were 2~4% except GK-1 rod (~12%). FGRs of the BWR rods were 10~13% and fairly higher than those of PWR rods except GK-1 rod. In the tests with the PWR and the BWR rods, very sharp increases of the rod internal pressure were observed indicating the additional FGR occurred at the very early stage of the transient.

3.5. Fuel failure

Fuel failure occurred at the fuel enthalpy of approximately over 150 cal/g·fuel for JMTR rods. By the visual inspection, generation of small defects of the cladding tube including penetrated ones were observed. Figure 7 shows typical defects of the cladding tube observed in JM-4 rod. Type of the defect is a small axial crack of a few millimeters. Regarding commercial LWR rods, fuel rods irradiated to the burnup of 40 GWd/t or less did not fail for the maximum fuel enthalpy of about 110 cal/g·fuel. Recently a commercial PWR rod preirradiated to 50 GWd/t failed in a case in which fuel enthalpy of about 80 cal/g·fuel was planned. Though the exact value of the fuel enthalpy has not yet been obtained through the procedure described in 3.1, the results suggest the effects of high burnups to the failure thresholds. The failure mode is the generation of axial cracks on the cladding probably by PCMI in all cases.

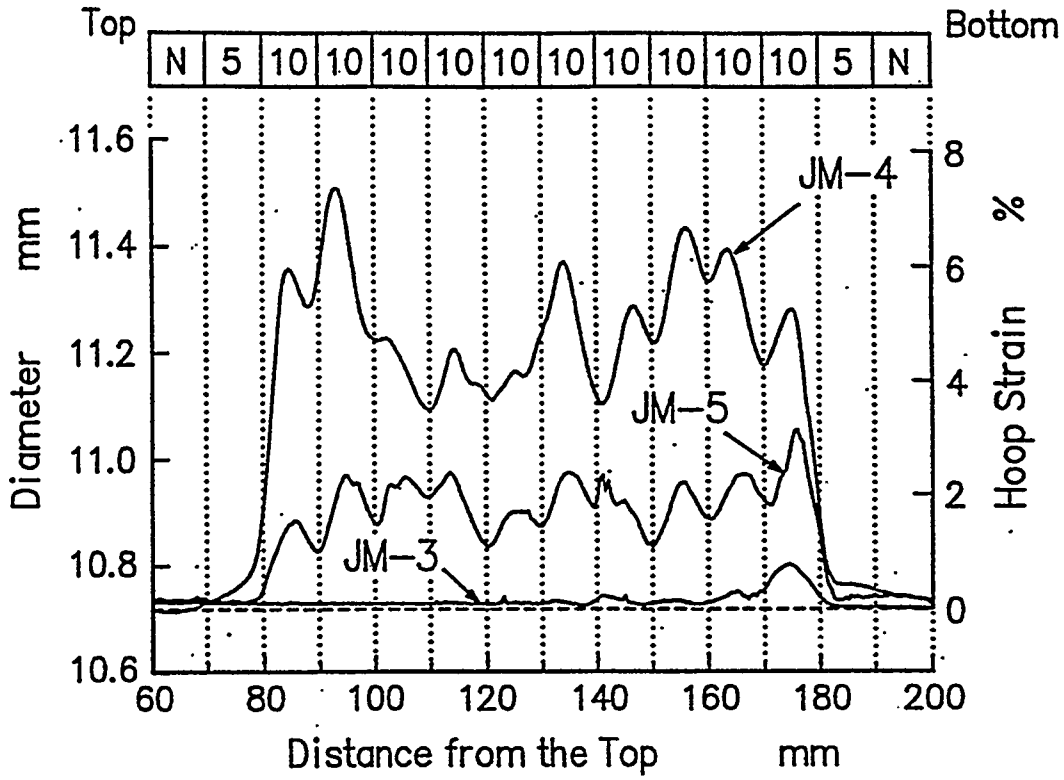

Fig. 5 Axial profiles of the JMTR rods

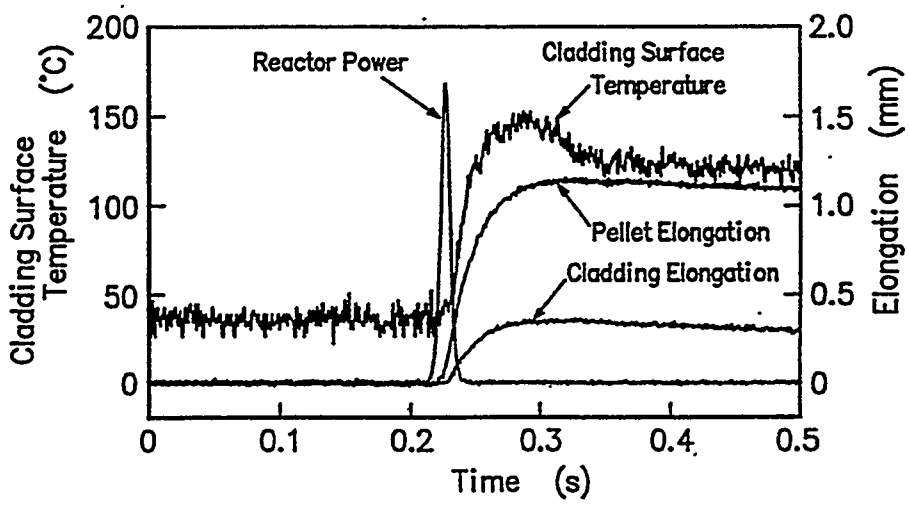

Fig. 6 Transient deformation of the fuel rod in Test JM–3

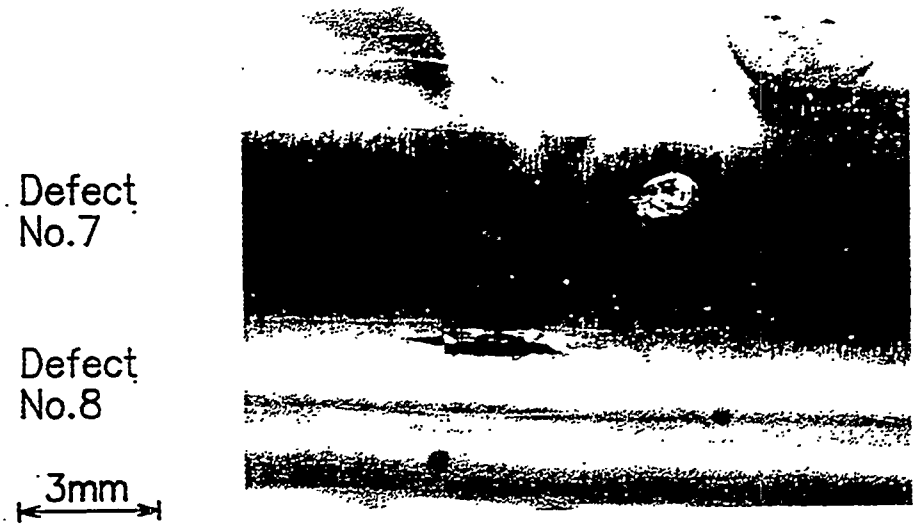

Fig. 7 Defects of the cladding tube observed in JM-4 rod

4. DISCUSSIONS

4.1. Cladding surface temperature

Figure 8 shows the maximum cladding surface temperature as a function of peak fuel enthalpy. The difference in the thresholds of DNB between the PWR and the JMTR rods can be explained by the significant creep down of the cladding tube in the PWR rods. The JMTR rod preirradiated in the helium environment of atmospheric pressure showed no creep down. Creep down in the PWR rod means the decrease of gap width and , therefore, the initiation of PCMI at lower enthalpy. The cladding tube of the BWR rod shows milder creep down than that of the PWR rods and it can easily be supposed that the threshold of DNB generation for the BWR rod may be somewhere between those for the PWR and the JMTR rods.

The maximum cladding surface temperature of the JMTR rod was 500~800℃ and duration of the film boiling was less than 1 s when the peak fuel enthalpy was 160~180 cal/g·fuel. In this enthalpy range, the maximum cladding surface temperature of a fresh rod is much higher than 1000℃ and the film boiling continues for

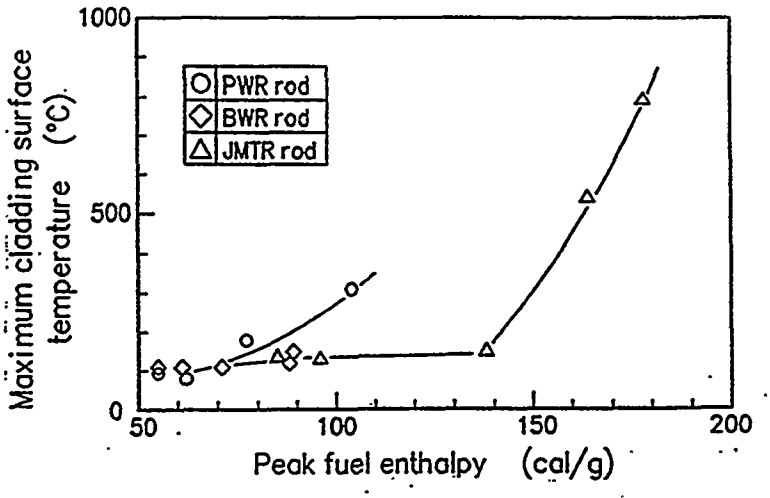

Fig. 8 The maximum cladding surface temperature as a function of peak fuel enthalpy

more than 10 s. Once we have performed repeated irradiations for a fresh rod and observed similar difference between the 1st and the 2nd irradiations. That is, in the 2nd irradiation, the maximum temperature was much lower and the duration of the film boiling was much shorter than those in the 1st irradiation. This may be due to the oxidation of the cladding surface by the 1st irradiation. For the preirradiated rod, however, the additional effects of burnup such as change of thermal conductivity of fuel pellet should be considered.

4.2. Fuel rod deformation

Figure 9 gives the longitudinal section of JM-4 rod showing the significant deformation of the cladding tube. As shown in the figure, the deformation was brought by the swelling of 10% enriched UO_2 pellet. The axial profiles of the JMTR rods given in Fig. 5 indicate that main part of the deformation was formed during the very early stage of the transient and PCMI played an important role on it. Figure 10 gives the measured maximum residual hoop strains of the cladding tube as a function of peak fuel enthalpy. The figure shows that the PWR rods had the most severe PCMI due to the significant creep down of the cladding tube. This well corresponds to the behavior of the cladding surface temperature shown in Fig. 8.

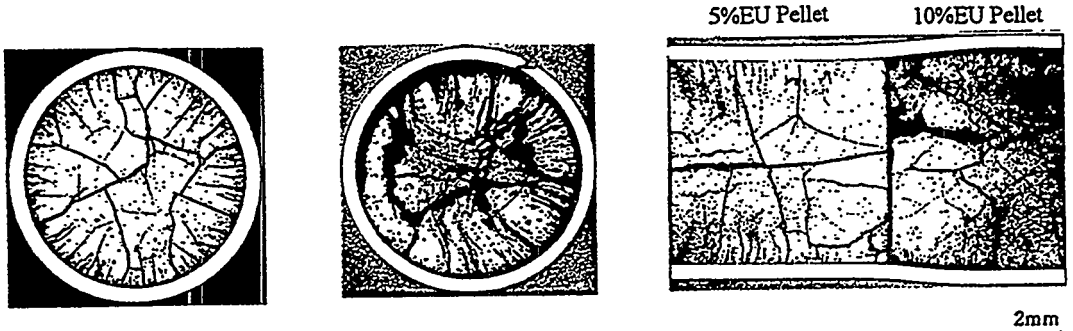

Fig. 9 Macroscopic photographs of the JMTR rods after pulse irradiation

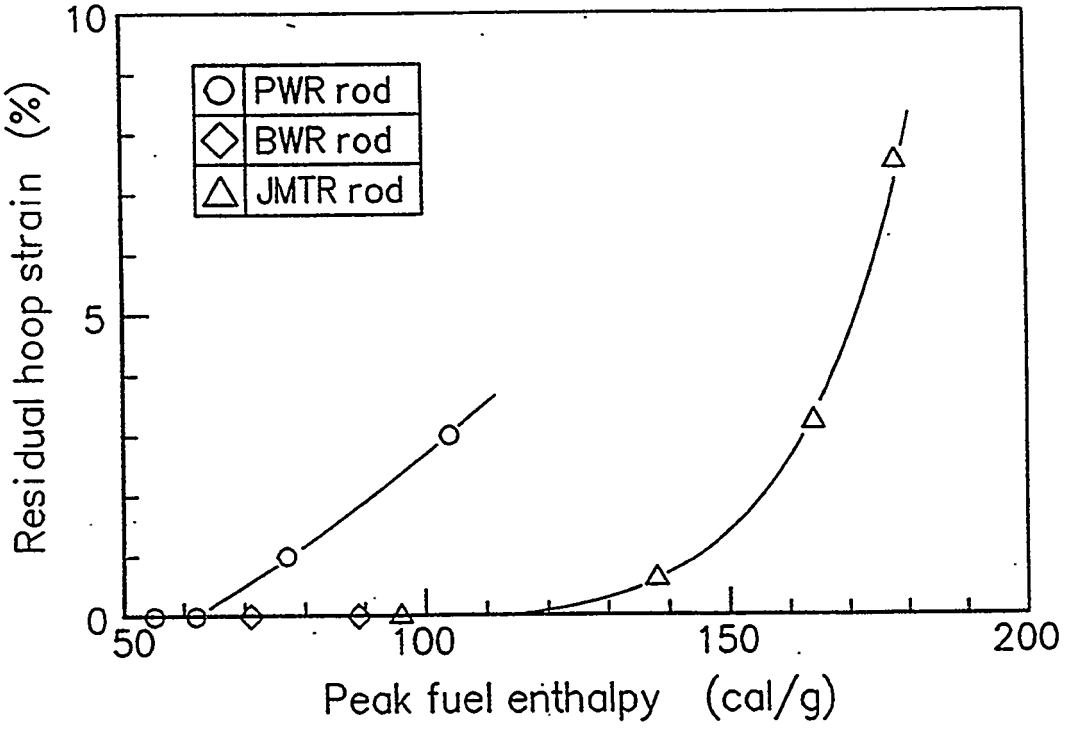

Fig.10 Residual cladding hoop strain as a function of peak fuel enthalpy

Figure 11 gives the results of the fuel pellet density measurements. The samples were taken from the various axial positions of JM-4 and -5 rods which showed significant deformation of the cladding tube. Horizontal axis is the increase of the fuel rod diameter at the position where the sample was taken. The figure shows that the density of the fuel pellet decreases almost linearly with the increase of the fuel rod deformation. This change in the density, however, is not sufficient to explain the amount of the deformation.

Figure 12 shows the microstructures of the fuels in JM-3 and -4 rods. The microstructure of the fuel in JM-3 rod which showed slight deformation has no significant change comparing with that observed in the reference rod. On the other hand, the microstructure of fuel in JM-4 rod which showed significant deformation has significant separation of the grain boundaries. The increase of pores in fuel pellet was not evident. The decrease of the pellet density, therefore, is due to the separation of the grain boundaries. This separation may be caused by the transient FGR and the increase of the pressure at the separated boundaries might contribute to the deformation of the fuel pellet and, therefore, of the cladding tube.

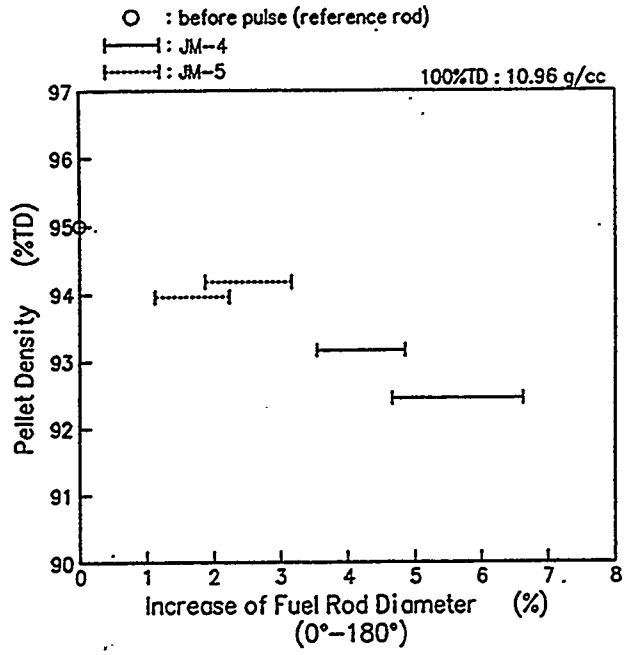

Fig. 11 Density measurements for the JMTR rods

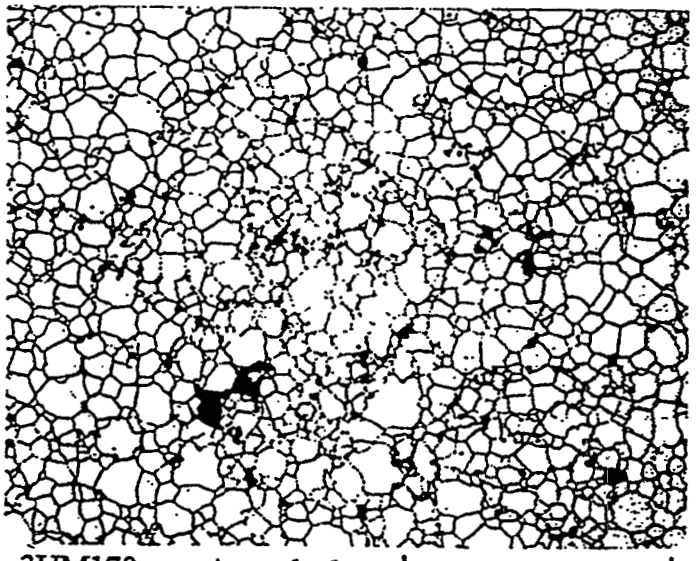

Fig. 12 Microstructures of the fuels in JM–3 and –4 rods

4.3. Fission gas release during irradiation

Figure 13 shows the FGR during pulse irradiation as a function of peak fuel enthalpy. Among PWR rods, GK–1 rod showed the highest value. This is because the rod had the highest fuel burnup, the highest linear heat rate during preirradiation and the highest peak fuel enthalpy. FGR in JM–3 rod is much lower than that GK–1 rod in spite of higher peak fuel enthalpy and higher linear heat rate during the preirradiation. This indicates that the fuel burnup is the most effective parameter on FGR during pulse irradiation within the present peak fuel enthalpy range.

Figure 9 gives the cross–sectional view of JM–3 rod. Many radial cracks can be observed at the peripheral region of the fuel pellet. This kind of crack generation is also observed in the PWR and the BWR rods. The cause of the generation of these cracks may be due to the large temperature gradient at the periphery of the pellet immediately after the initiation of the pulse irradiation. It is easily expected that generation of these cracks has large contribution to the transient FGR because the large fraction of the fissions occurs in the periphery region of the fuel pellet. In the higher peak fuel enthalpy case, however, separation of the grain boundaries will have additional contribution to it as discussed in Sec. 4.2.

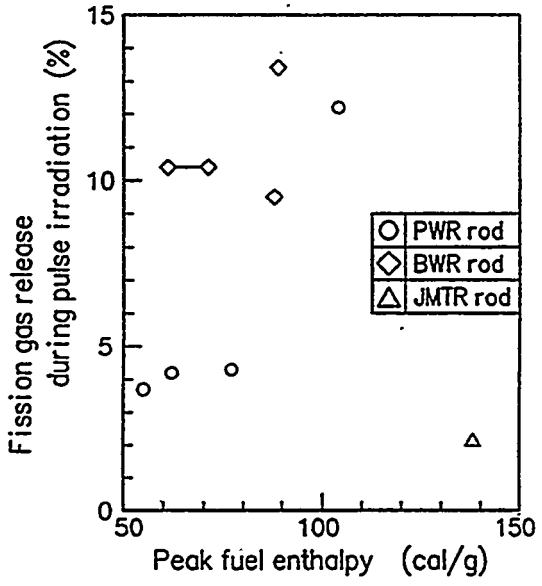

Fig. 13 FGR as a function of peak fuel enthalpy

4.4. Fuel failure

Figure 9 includes the cross-sectional view of JM-4 rod which shows the failure of the cladding tube. Figure 4 gives the behavior of the capsule internal pressure measured in test JM-4. It can be seen that the pressure pulses were generated at the time when the cladding surface temperature was still low. Therefore, we can conclude that the cause of the cladding defect is overstress due to PCMI taking the shape of the defect into account.

Commercial PWR rods of about 40 GWd/t did not fail up to the condition of cladding residual strain of about 3%. This indicates that the cladding had the ductility to endure the severe PCMI. However, in the rod of 50 GWd/t, decrease of cladding ductility due partly to irradiation and partly to oxidation and hydride formation might result in the failure at a lower enthalpy. The threshold enthalpy for fuel failure will thus be the strong function of cladding mechanical properties. Detailed studies on cladding embrittlement as well as the dynamic PCMI behavior will be needed for quantifying the failure threshold.

Figure 14 summarizes the results of preirradiated rod tests performed in the NSRR. The figure also includes the results from the SPERT-CDC and PBF programs in the United States. It can be seen that no failure occurred except SPERT Run 859 at the peak fuel enthalpies below 140 cal/g·fuel for the fuel burnup of 42 GWd/t or less.

In the case of SPERT Run 859, fuel failure was detected during transient at the energy deposition of 85 cal/g·fuel in the experiment of peak fuel enthalpy of 190 cal/g·fuel. This energy deposition was applied as a provisional fuel failure criteria in the Japanese safety guideline. However, it is not known whether the test rod would fail at the peak fuel enthalpy of 85 cal/g·fuel. No failure were observed for the peak fuel enthalpy of 140 cal/g·fuel in all the tests with Japanese fuel rods. So it can be concluded that the provisional fuel failure criteria of 85 cal/g·fuel has a large safety margin as far as the fuel burnup is lower than 42 GWd/t.

For higher burnup cases of over 50 GWd/t, however, the NSRR experiments suggests the lower fuel failure thresholds. Further studies will be needed to quantify the fuel failure threshold.

5. FUTURE PLAN

Figure 15 gives the tentative long-term plan of the major NSRR experiments. Study of the effects of fuel burnup on the mechanical energy generation and the tests for the rods with extended burnup are the major tasks in future in the frame of preirradiated UO_2 fuel rod test program. Mixed oxide fuel rod test is another important research item to contribute to the project on the plutonium utilization in LWRs which is supported by the government.

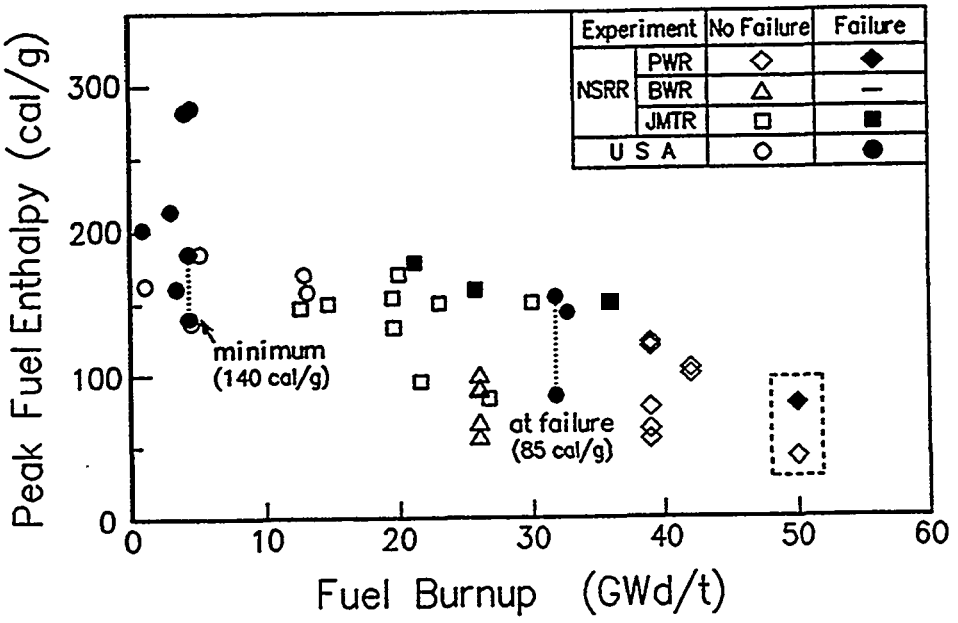

Note : Values in dotted box are not fixed yet.

Fig. 14 Summary of the preirradiated fuel rod tests

6. SUMMARY

New experimental program with preirradiated fuel rod as a test sample was started in the NSRR. The major results obtained so far can be summarized as follows;

(1) The cladding surface temperature was strongly influenced by the degree of creep down of the cladding tube during the preirradiation. JMTR rod showed significantly lower cladding surface temperature than that of fresh rod under the same peak fuel enthalpy condition probably due to preoxidation of the cladding surface during the preirradiation.

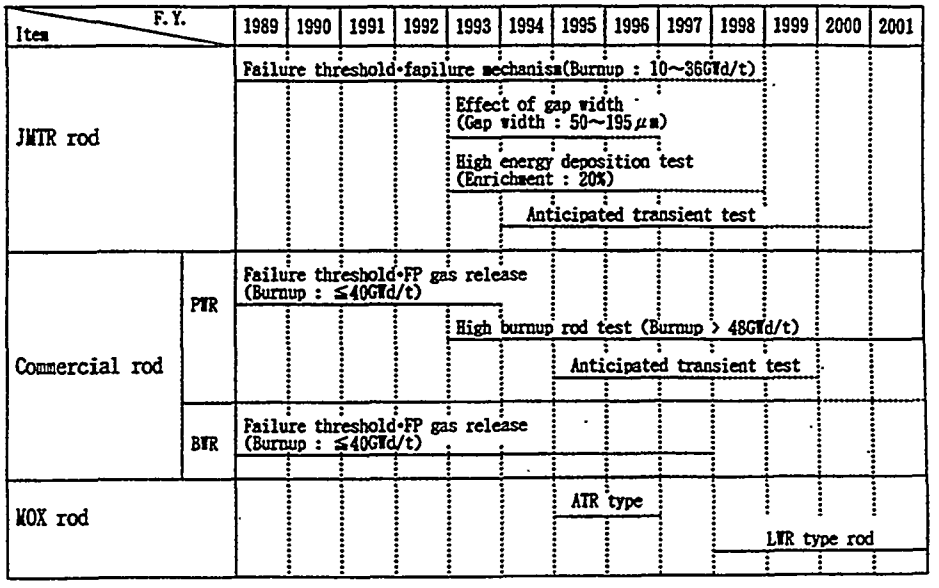

Fig. 15 Tentative long-term plan of the NSRR experiments

(2) Measured residual cladding strains clearly reflected the effect of the creep down of the cladding tube on the PCMI. Very large deformation of the fuel rods observed in the tests with JMTR rods suggested that the transient FGR during pulse irradiation might have significant effect on the deformation.

(3) The transient FGRs of 2~13% were observed. The causes of the significant releases might be the formation of micro-cracks at the periphery region of the fuel pellet and the separation of the grain boundaries especially in the higher peak fuel enthalpy cases.

(4) Fuel failures were observed in the tests with JMTR rods. The PCMI played an important role on the generation of the through-wall cracks. The fuel rod integrity was confirmed at the peak fuel enthalpy below 100 cal/g for the burnup of up to 42 GWd/t. However, lower fuel failure threshold was suggested in recent experiments with a high burnup rod irradiated up to 50 GWd/t. Further study is needed to identify the threshold as a function of fuel burnup.

ACKNOWLEDGEMENTS

The authors wish to thank all of the JAERI staffs who are engaged in the project on the preirradiated fuel rod tests in the NSRR for their collaboration and many useful discussions. The authors also thank Kansai Electric Power Company and Mitsubishi Heavy Industries for their strong supports to this work.

REFERENCES

[1] ISHIKAWA, K. and SHIOZAWA, S., A Study of Fuel Behavior under Reactivity Initiated Accident Conditions – Review, J. Nucl. Mat. 95 1&2 (1980) 1

[2] MACDONALD, P.E. et al., Assessment of Light–Water–Reactor Fuel Damage During a Reactivity–Initiated Accident, Nuclear Safety, 21 5 (1980) 582

[3] ISHIJIMA, K., TANZAWA, S., FUKETA, T., FUJISHIRO, T., Behavior of Preirradiated Fuels under Simulated RIA Condiitons, Proc. Int. Top. Mtg. on Safety of Thermal Reactors, Portiand, Oregon, (1991)

[4] FUJISHIRO, T., YANAGISAWA, K., ISHIJIMA, K. and SHIBA, K., Transient Fuel Behaviorfof Preirradiated PWR Fuels Under Reactivity Initiated Accident Conditions, J. Nucl. Mat., 188(1992) 1622

[5] FUKETA, T. et al., Behavior of Pre–Irradiated Fuel under a Simulation RIA Condition, [Results of NSRR Test JM–3], JAERI–Research 94–006 (1994)

[6] NAKAMURA, T. et al., Boiling Water Reactor Fuel Behavior at Burnup of 26 GWd/tonne U under Reactivity–Initiated Accident Conditions, Nucl. Technol., 108 (1994) 45

Russian Approach to Experimental Studies of Burnup Effects under RIA Conditions

V. Asmolov, L. Yegorova

Nuclear Safety Institute of the "Kurchatov Institute" Russian Research Center

During the period of 1989 - 1992 the Nuclear Safety Institute of the "Kurchatov Institute" Russian Research Center (NSI KI RRC, Moscow) in cooperation with the Research Institute of Atomic Reactors (RIAR, Dimitrovgrad) and the Joint Expedition of the "Luch" Scientific and Industrial Association (JE "Luch" SIA, Semipalatinsk) prepared and performed a complex of experimental studies that included reactor tests of high burnup fuel rods of VVER type under RIA conditions.

This cycle of research was the final stage of the experimental program carried out by NSI KI RRC in 1983 - 1992 and aimed at studying the behavior features of VVER-1000 - type fuel elements under reactivity initiated accidents.

The main purpose of preirradiated fuel rod tests was the determination of the energy deposition that corresponds to the failure threshold and the identification of specific features of failure mechanisms of high burnup fuel elements.

The capsule tests of 23 single fuel rods (13 - preirradiated fuel and cladding, 10 - fresh fuel and preirradiated cladding) were performed at the IGR pulse reactor (JE "Luch" SIA, Semipalatinsk).

As the test object we used refabricated fuel rods of VVER-1000 type, that were specially designed and manufactured in RIAR, Dimitrovgrad, made of VVER-1000 standard fuel elements .which operated for three years at the power unit No. 5 of Novovoronezh nuclear power plant (burnup was about 49000 MW days/t).

The program overline was based on the following main principles:

- test parameters and geometric dimensions of preirradiated fuel rods were maximally close to corresponding parameters of fresh fuel tests;
- set of variable parameters of the tests (including the fuel element design) must provide credible information on fuel element failure mechanisms and their interrelation with test parameters.

The practical implementation of these provisions in the form of the experimental program allowed us to obtain a set of experimental data characterizing the behavior of preirradiated fuel rods in a wide range of the total energy deposition (60 - 280 Cal/g UO_2).

At present the obtained data are the basis for the analysis of the processes of deformation and failure of preirradiated fuel rods of pressurized water reactors under RIA conditions.

1982 year - the preparation of the experimental Programm to study the behavior of the WWER-1000 type fuel elements in RIA conditions - was started at the Kurchatov Institute of Atomic Energy.

WWER-1000/RIA Programm.

WWER-1000/RIA
Stage 3

Institutes-Participants WWER-1000/RIA Programm

--- Nuclear Safety Institute,
RRC "Kurchatov Institute" (Moscow, Russia)

--- Institute for Nuclear Reactors,
RRC "Kurchatov Institute" (Moscow, Russia)

--- Research Institute of Atomic Reactors
(Dinitrovgrad, Russia)

--- Institute of Atomic Energy,
Kazakhstan Republic National Nuclear Centre
(Semipalatinsk, Kazakhstan)

Possible alternatives to develop the WWER-1000/RIA program:

1. **Realization of the specifically national program without reference to the experience and data base for PWR/RIA programs.**

2. **The data base, obtained within the frames of WWER-1000/RIA program is to be sufficient for WWER-PWR/RIA comparison analysis.**

Decision - selection of the second alternative.

Structure of Technical Requirements for WWER-1000/RIA program:

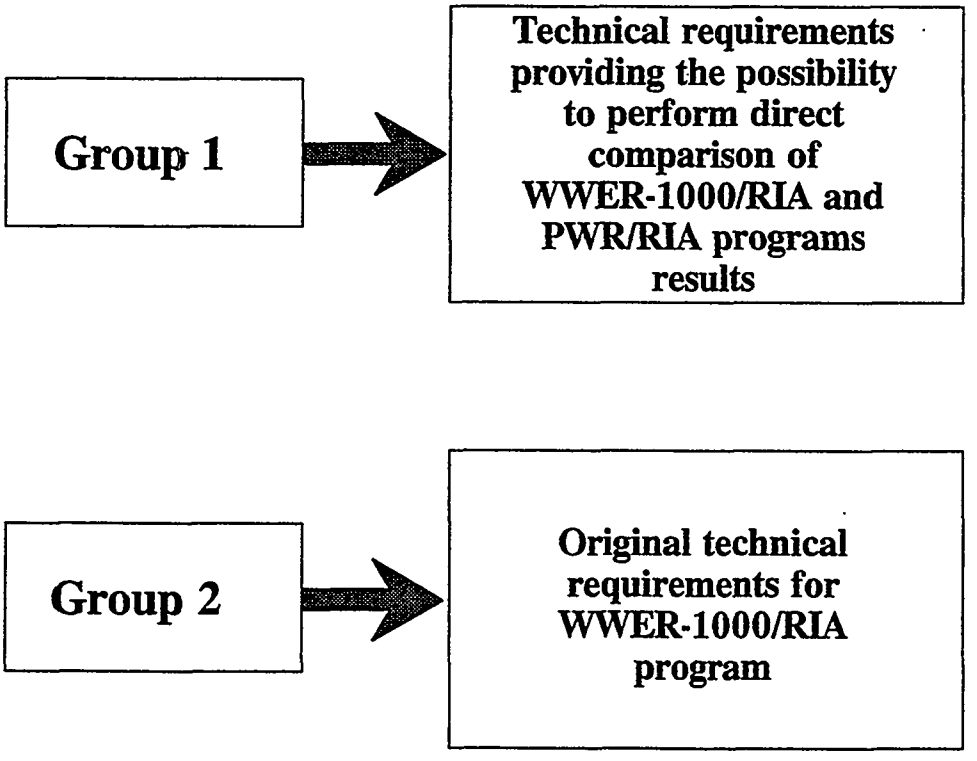

Structure of Technical Requirements for Group 1:

Test type	reactor, capsule, non-flow
Coolant initial parameters: temperature pressure	 environment temperature atmospheric
Fuel element power initial level	corresponds to reactor power physical level
Typical half-width of reactor power pulse	several milliseconds
Range of fuel element energy deposition change	up to 220 cal/g UO2
Type of fuel element	shortened fuel element of WWER-1000 geometry fuel length = 150 mm
Initial value of gas pressure in fuel element	0.1-2.5 MPa
Burn-up	0 MW day/t
Number of fuel elements per capsule	1

Structure of Technical Requirements for Group 2:

Test type	reactor, capsule, non-flow
Coolant initial parameters: temperature pressure	 environment temperature up to 16.0 MPa
Fuel element power initial level	corresponds to reactor power physical level
Typical half-width of reactor power pulse	up to 1.5 s
Range of fuel element energy deposition change	up to 1000 cal/g UO_2
Type of fuel element	shortened fuel element of WWER-1000 regular radial geometry
Initial value of gas pressure in fuel element	0.1-2.5 MPa
Burn-up	up to 50000 MW day/t

Main Logical Principles of Comparison Analysis Performing of WWER-1000/RIA Programm Results

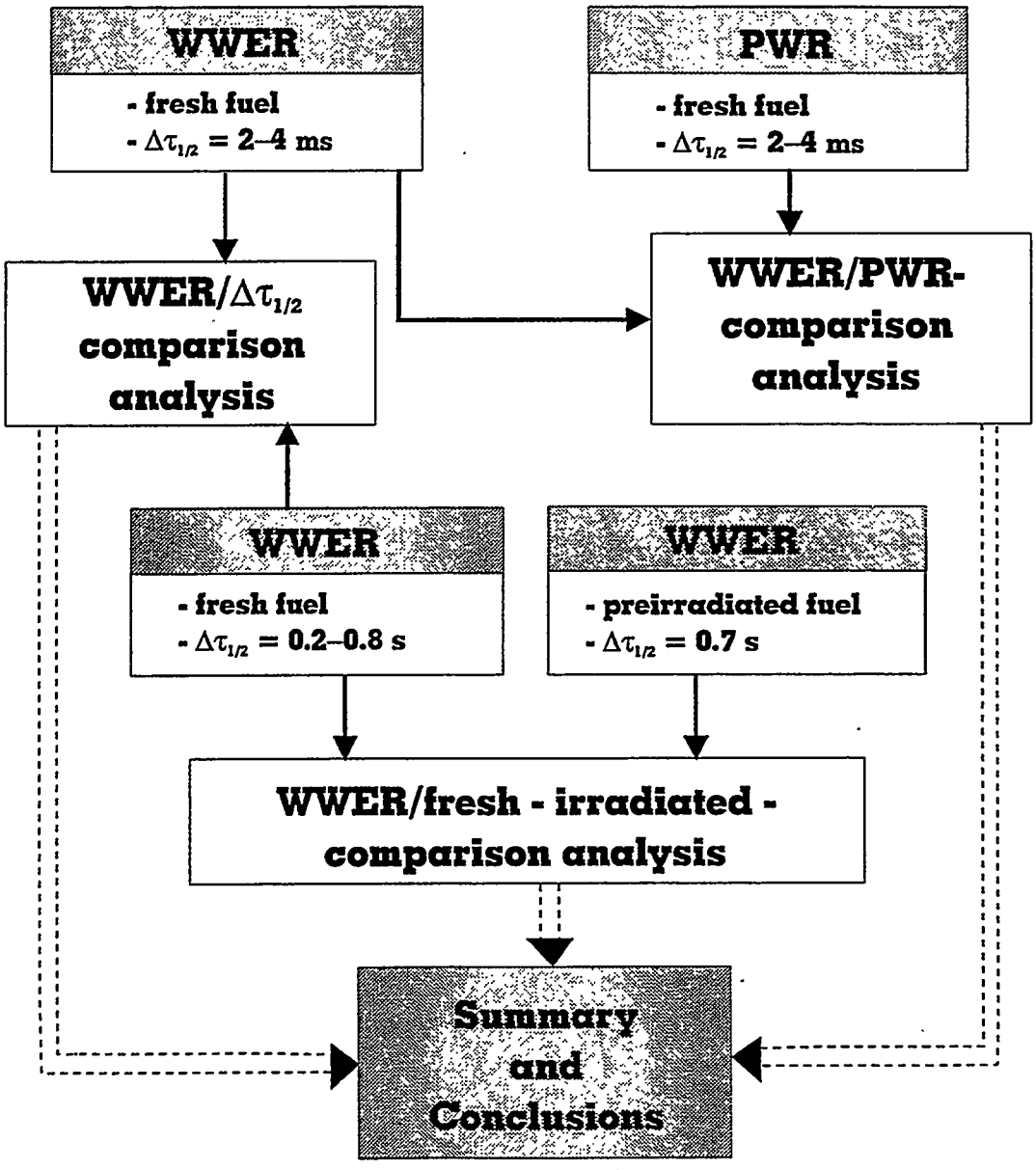

NSI RRC "Kurchatov Institute"

Schedule of WWER-1000 Programm Implementation

1983-1989 (stage 1)	Tests of non-irradiated fuel element in "HYDRA" reactor
1983-1992 (stage 2)	Tests of non-irradiated fuel element in "IGR" reactor
1990-1992 (stage 3)	Tests of pre-irradiated fuel elements in "IGR" reactor

The Main Aim of the 1st Stage of Pre-Irradiated Fuel Rods Testing

- to obtain experimental results characterising a range of values variety of energy deposition rupture thresholds for WWER-1000 fuel rods design elements both at the beginning and at the end of lifetime

Methodological Basis for WWER-1000 Pre-irradiated Experimental Fuel Elements Testing

- the maximum similarity of technical parameters of WWER-1000 commercial reactors fuel elements and experimental fuel elements (for the given burn-up level)

- the maximum similarity of geometric parameters of experimental pre-irradiated and non-irradiated fuel elements

- the maximum similarity of test conditions of pre-irradiated and non-irradiated fuel elements

WWER-1000/RIA
Stage 3

List of the main problems	Methods of problems solution
1. IGR Safety ensuring under testing of pre-irradiated fuel rods	1. Ensuring of capsule unit tightness taking into account all possible outcomes
2. Lack of reliable prior information on rupture threshold of pre-irradiated fuel rods	2. Energy deposition step-by-step increase in the chosen experimental area
3. Impossibility of operative post-test examination of fuel rods	3. Tests performing in 2 stages. Examination of fuel rods after 1-st stage and correction of testing modes for the 2-nd stage
4. Limited number of fuel rods	4. Reduction of number of varying parameters

WWER-1000/RIA
Stage 3

Technological Cycle
of pre-irradiated fuel elements tests preparing and performing

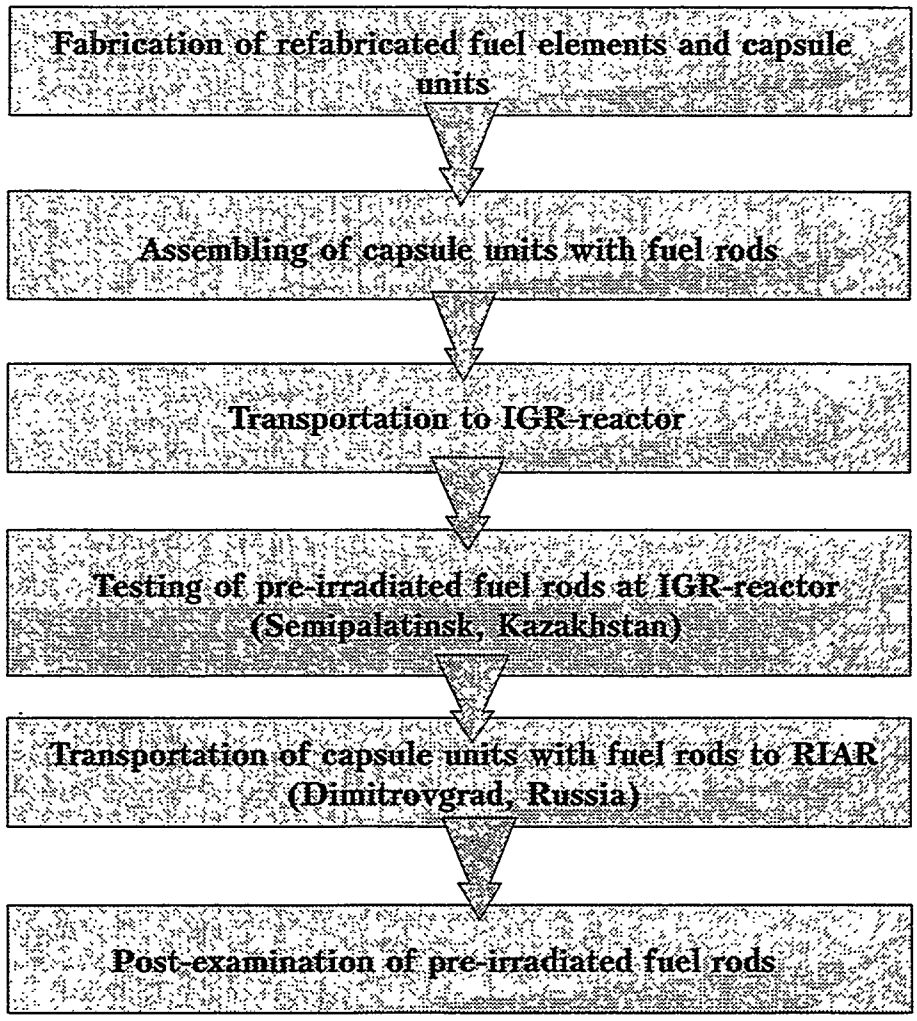

NSI RRC "Kurchatov Institute"

WWER-1000/RIA
Stage 3

Technological Production Scheme of Pre-irradiated Fuel Elements.*

1. Fabrication of specimen(s) for experimental fuel elements by means of cutting of regular fuel element

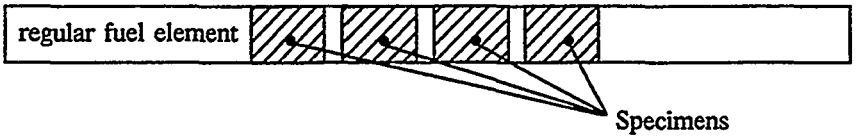

2. Withdrawing of part of fuel column out of each specimen by means of drilling

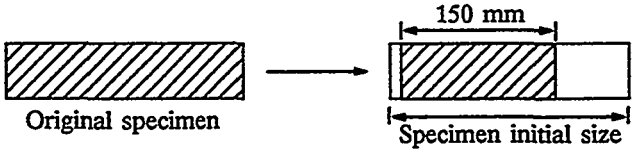

3. Joining of end seals by means of welding

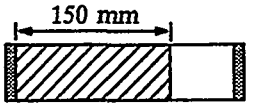

4. Fuel element filling with gas (He) and its sealing

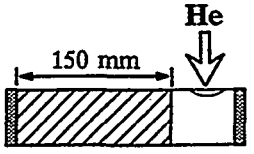

*Scheme was develop and implemented in RIAR (Dimitrovgrad, Russia)

NSI RRC "Kurchatov Institute"

WWER-1000/RIA
Stage 3

General view of WWER-1000 type refabricated fuel rods before IGR pulse testing

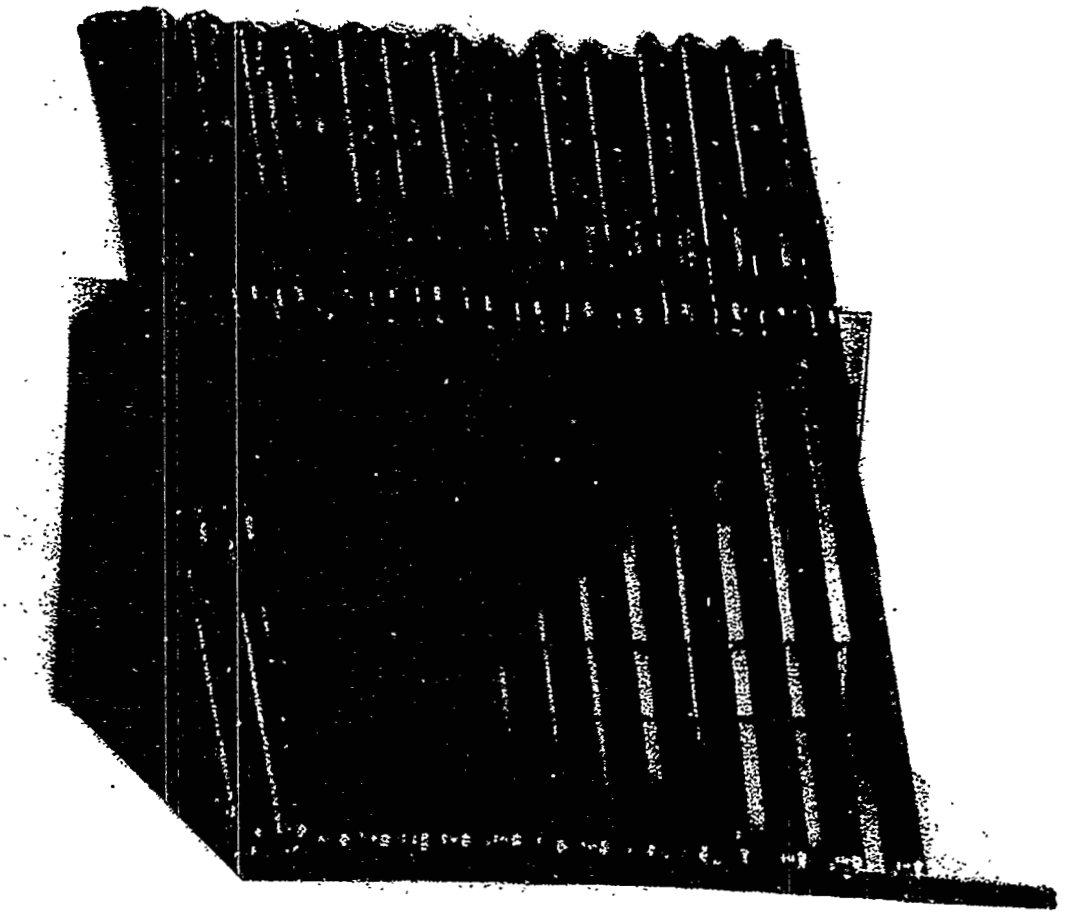

NSI RRC "Kurchatov Institute"

RIA Study

IGR reactor

Cross-section and time behaviour of reactor power (4.5 β eff)

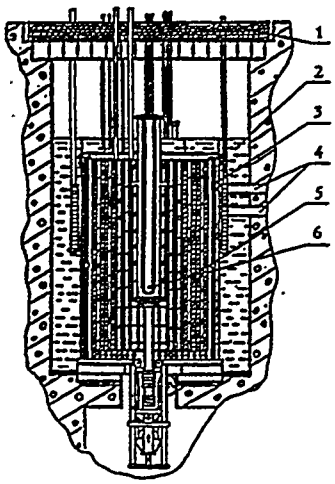

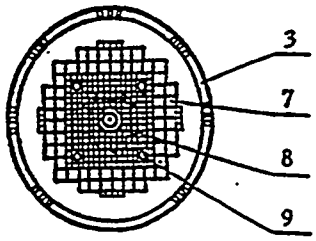

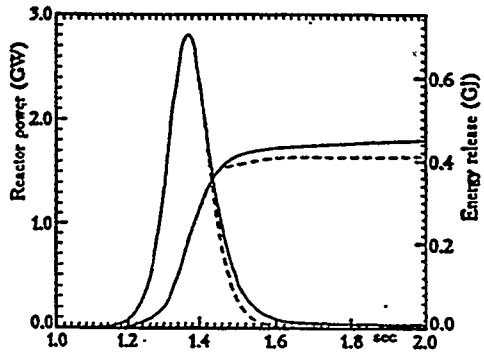

1. Biological shield plate
2. Water vessel
3. Reactor vessel
4. Helium pipes
6. Experimental channel
7. Reflector
8. Reactor core
9. Lateral experimental channel

Material Scheme of Capsule Unit With Fuel Rods

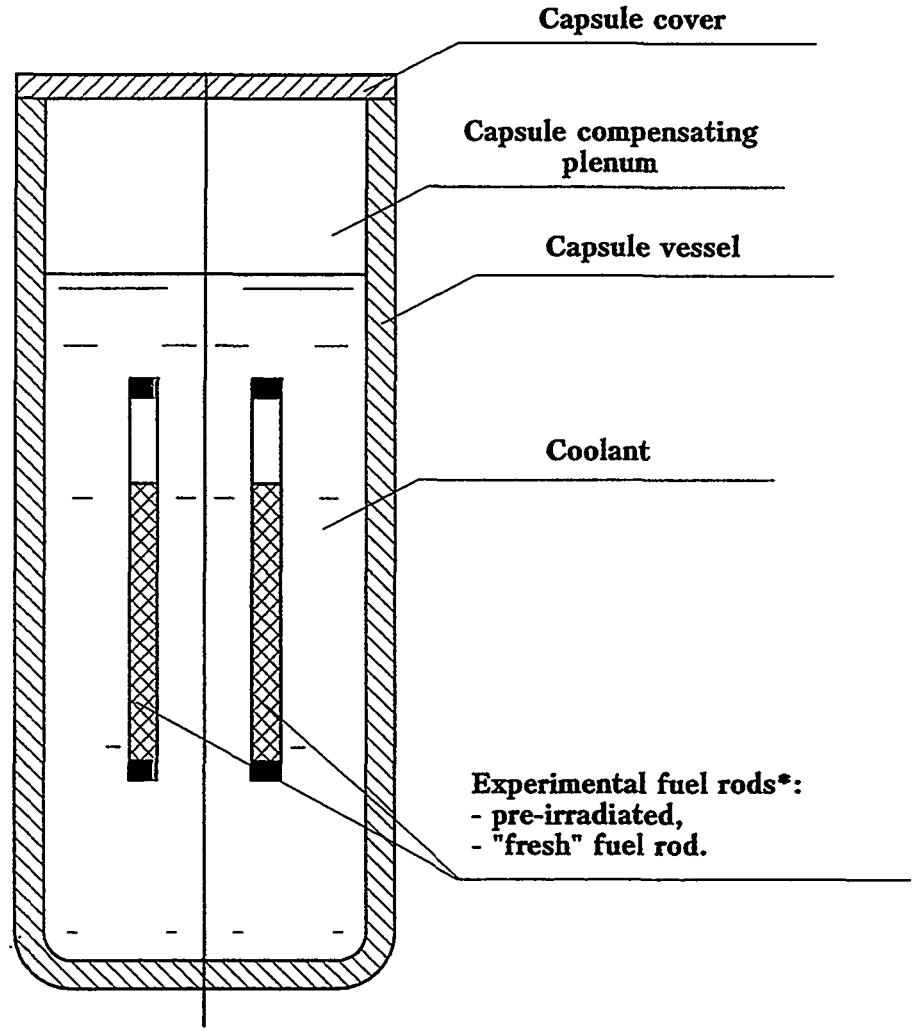

• - Tests were carried out both with use of the arrangement given in this figure and with a single pre-irradiated fuel rod in capsule unit

NSI RRC "Kurchatov Institute"

Parameters of fuel rods

Type of experimental fuel elements	WWER-1000
Fabrication of experimental fuel elements	refabrication out of commercial reactor fuel elements (Zr, 1% Nb)
Original material for refabrication	regular fuel element from NV NPP reactor diameters (mm): center hole = 2.2 pellet = 7.5 rod = 9.15
Burn-up reference value	50,000 MW day/t
Length of fuel column in experimental fuel elements	150 mm
Type of fuel elements	"A" and "B" "A" having pre-irradiated fuel and cladding "B" having fresh fuel and pre-irradiated cladding

Test parameters of Pre-Irradiated Fuel Rods

Half-width of reactor power pulse	0.7 s
Coolant	water, air
Coolant initial parameters	environment temperature, atmospheric pressure, non-flow mode
Gas initial pressure in fuel rod	2.5 MPa
Given range of energy deposition changing	80-250 cal/g UO_2
Number of fuel rods supplied for testing	13

Scheme of Energy Deposition Changing in Experimental Pre-Unirradiated Fuel Rods for Two Types of Coolant in Capsule

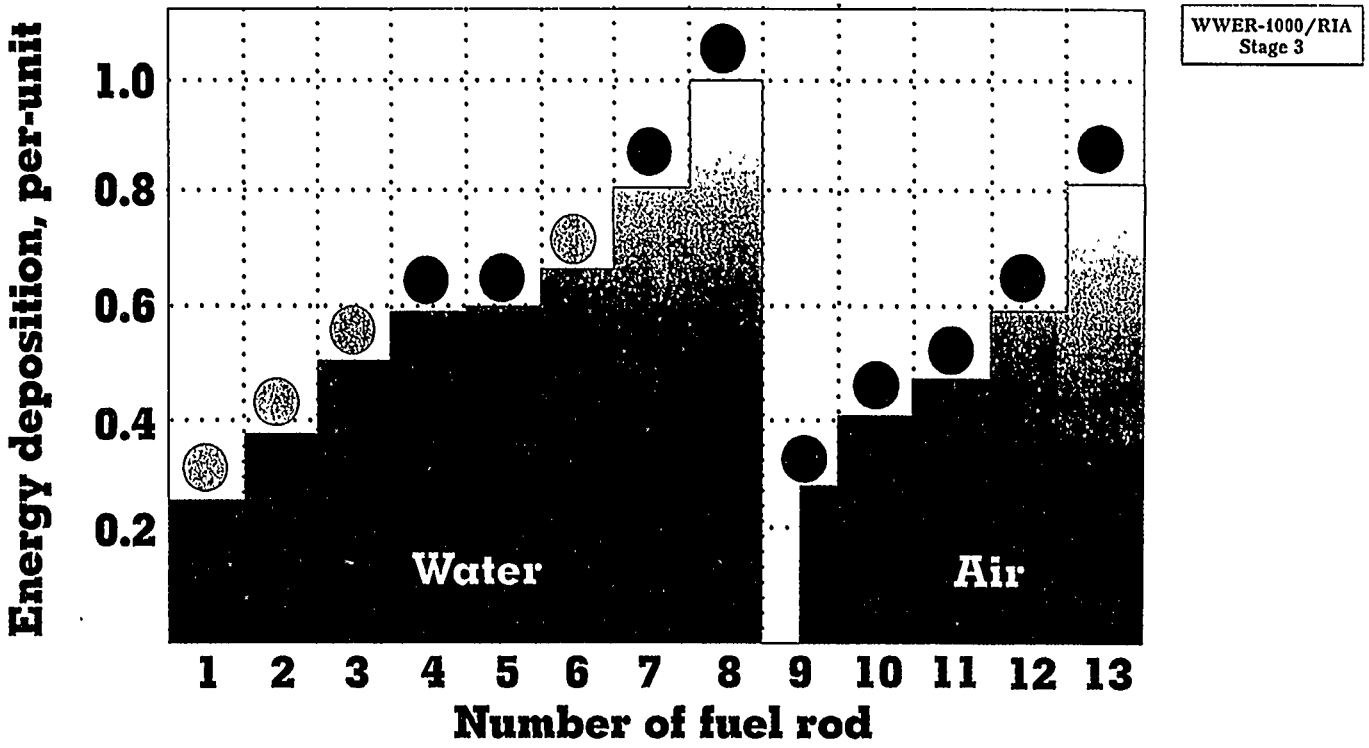

Fuel rods post-test state:

fuel rod without cladding rupture; **fuel rod with cladding rupture;**

NSI RRC "Kurchatov Institute"

WWER-1000/RIA
Этап 3

Cross-sections general veiw of pre-irradiated fuel rods after the pulse irradiation in IGR reactor (from initial state to maximum mode)

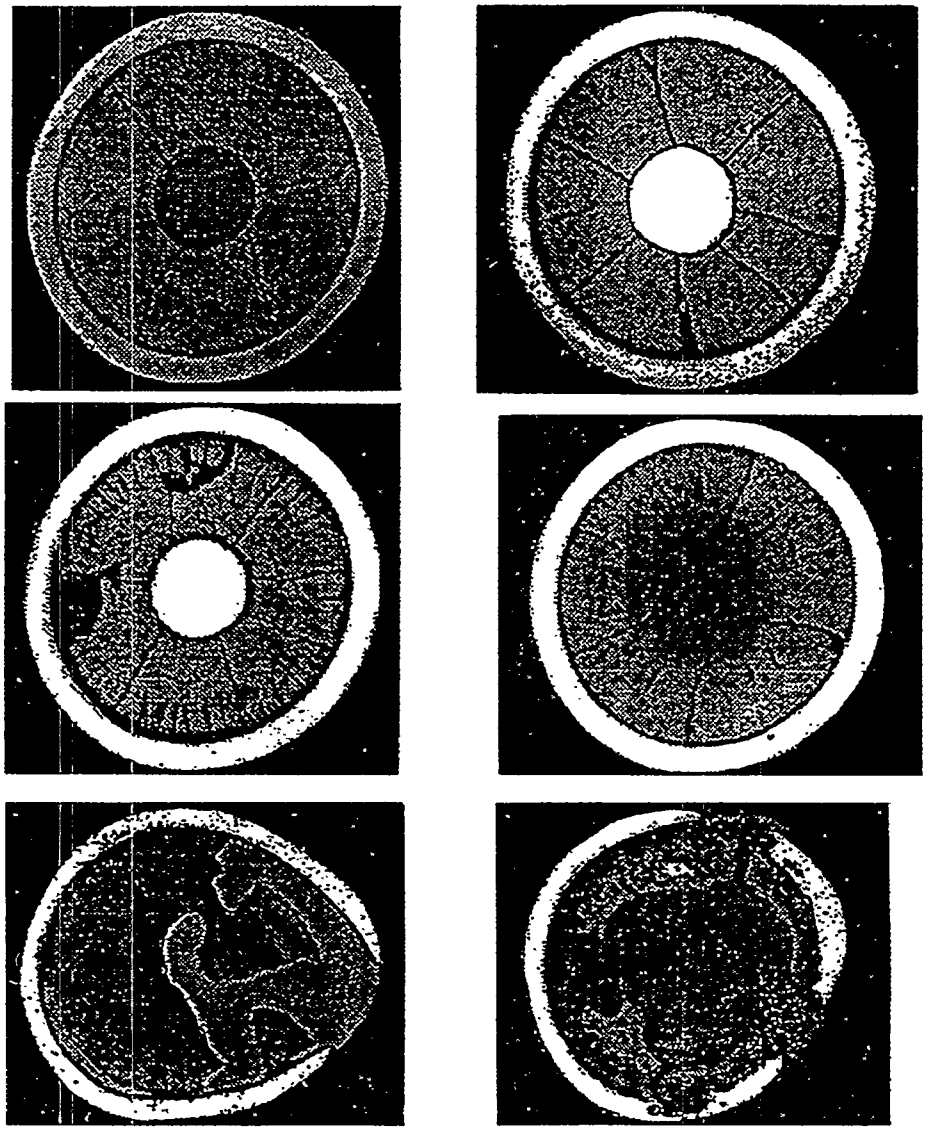

NSI RRC "Kurchatov Institute"

Reassessment of the Technical Basis for NRC Fuel Damage Criteria for Reactivity Transients

R. K. McCardell
Idaho National Engineering Laboratory

ABSTRACT

Recent experimental results on the radial average peak fuel enthalpy required to cause the failure of irradiated fuel rods have indicated that the failure enthalpy may decrease with increasing burnup. This possibility is not accounted for in the present NRC fuel damage criteria for reactivity transients, and therefore a reassessment of the technical basis for the NRC criteria is being made. This paper briefly describes the original data on which the present NRC criteria were based, reviews the results of the testing of 10 irradiated fuel rods in the INEL Capsule Driver Core (CDC) in the early 1970s, describes the results of the testing of both unirradiated and irradiated fuel rods in the INEL Power Burst Facility (PBF) in the early 1980s, and compares the results of the CDC, PBF, and very recent Nuclear Safety Research Reactor of Japan and the CABRI reactor of France. Conclusions are followed by a brief description of future work for the NRC at the INEL reassessing the technical basis for NRC fuel damage criteria for reactivity transients.

INTRODUCTION

The present basis for the United States Nuclear Regulatory Commission (USNRC) Fuel Damage Criteria for Reactivity Initiated Accidents (RIAs) was obtained from experiments performed in the Special Power Excursion Reactor Test (SPERT) IV Reactor Capsule Driver Core (CDC) at the Idaho National Engineering Laboratory (INEL) between 1967 and 1970[1,2,3]. Most of the CDC test fuel rods were previously unirradiated and the failure threshold for these unirradiated fuel rods was measured to be about 200 calories per gram of UO_2 radially averaged fuel enthalpy at the axial peak-power location. The CDC data also indicated that the failure consequences were insignificant for *total energy depositions* below 300 cal/g UO_2 for both unirradiated and irradiated UO_2 fuel rods subjected to rapid power excursions. Therefore, an *axial peak, radial average* fuel enthalpy of 280 cal/g UO_2 was considered a conservative maximum limit to insure minimal core damage and maintenance of both short term and long term core cooling capability. The NRC requires that light water reactors (LWRs) operated within the United States must be designed such that a worst case RIA will not result in a radial average fuel enthalpy greater than 280 cal/g UO_2 at any axial location in any fuel rod[4]. Offsite dose consequences must be within the guidelines of 10 CFR 100 and are calculated assuming that any fuel rod that departs from nucleate boiling fails and any BWR fuel rod subjected to a radial average peak fuel enthalpy of 170 cal/g UO_2 or above fails [5].

Note that the USNRC expressed the RIA criteria in terms of radial average peak fuel enthalpy, whereas the SPERT tests, which were used to develop the present design requirements, were

originally reported in terms of radial average total energy deposition. Radial average peak fuel enthalpy is less than the associated radial average total energy deposition because of heat transfer from the fuel to the cladding and coolant during the power transient, and the relatively large fraction of the total energy which is due to delayed fissions (10 to 25% depending on the reactor design). The SPERT test rods that were subjected to a total energy deposition of 280 cal/g UO_2 reached a radial average peak fuel enthalpy of about 230 cal/g UO_2.

The SPERT CDC RIA tests were initiated from ambient conditions (room temperature water at no flow and at atmospheric conditions) and the irradiated fuel rods were preirradiated in the Engineering Test Reactor (ETR) at the INEL at atypically high power levels. Because of these atypical conditions, further RIA tests were conducted in the Power Burst Facility (PBF)[6] at the INEL at typical BWR hot startup conditions using typical preirradiated rods from the Saxton Reactor. Experimental results for irradiated test fuel rods from both the SPERT CDC and PBF tests indicated that the failure threshold for RIAs decreased with increasing burnup. The desire to expose nuclear fuel in commercial power plants to higher and higher burnups has made more important the question of whether the peak fuel enthalpy required to cause fuel failure during an RIA decreases with increasing burnup. New data obtained from irradiated fuel rod tests performed in the NSRR[7], and CABRI[8] reactors also indicate a downward trend in peak fuel enthalpy with burnup. Therefore, a reassessment of the technical basis for NRC fuel damage criteria was undertaken. The following sections of this paper briefly describe the results of the CDC RIA tests on irradiated fuel, the results of the PBF tests on irradiated fuel, and the future efforts planned on the reassessment of the technical basis for the NRC fuel damage criteria.

CDC RESULTS

Ten preirradiated test fuel rods were exposed to RIA transients in the CDC. Six of these test fuel rods had burnups below about 4 GWd/MTU. Two of the fuel rods had burnups of about 12 GWd/MTU, and two of the fuel rods had burnups of about 32 GWd/MTU. Test conditions and results for these 10 CDC tests are summarized in Table 1. The eight fuel rods designated GEX had an outside diameter (OD) of 0.79 cm (5/16-in.) and the two GEP test fuel rods had an OD of 1.43 cm (9/16-in.). The overall length of the GEX and GEP type test fuel rods were 22.58 cm (8.89-in.) and 22.1 cm (8.70-in.), respectively. Pellet type fuel with an active length of about 13.21 cm (5.2-in.) was used in both types of fuel rods with hafnium disks and natural UO_2 pellets located on each end of the active pellet stacks to reduce flux peaking (hafnium) and for thermal insulation (UO_2). The 7% enriched pellets had a density of 10.30 g/cm^3. The GEX type fuel rods had a zircaloy-2 cladding thickness of 0.05 cm (20 mils) and a pellet to cladding gap width of 0.005 cm (2 mils). The GEP type fuel rods had a zircaloy-2 cladding thickness of 0.089 cm (35 mils) and a pellet-to-cladding gap of 0.01 cm (4 mils). Both the GEX and GEP fuel rods had upper plenums with springs and iron cores which, when calibrated with the associated magnetic fields, yielded measurements of pellet stack growth during the transient.

Table 1. Summary of conditions for irradiated fuel rods tested in CDC.

CDC test number	Rod type	CDC reactor period (ms)	Power burst half width (ms)[a]	Average burnup (MWd/MTU)	Total energy deposition (cal/g UO_2)	Radially averaged peak fuel enthalpy (cal/g UO_2)	Condition of rod F=failed NF=not failed
571	GEX	7.80	31	4,550	161	137	NF
568	GEX	6.06	24	3,480	199	161	F
567	GEX	4.53	18	3,100	264	214	F
569	GEX	3.55	14	4,140	348	282	F
703	GEP	3.68	15	1,140	192	163	NF
709	GEP	3.10	13	990	238	202	F
685	GEX	5.75	27	13,100	186	158	NF
684	GEX	5.12	20	12,900	200	170	NF
756	GEX	4.42	17	32,700	176	143	F
859	GEX	3.94	16	31,800	190	85	F

[a]Width of power burst at half maximum power.

The GEX and GEP test fuel rods were preirradiated in the ETR at the INEL. The preirradiation conditions were a pressure of 6.9 MPa (1000 psi), an inlet temperature of 511 K (460 F), and linear powers of 460 W/cm to 755 W/cm (14 to 23 kW/ft). For the high preirradiation powers, centerline melting occurred in the test fuel rods.

For all of the ten transient CDC experiments performed, the following measurements were made: (1) reactor power (from which peak fuel enthalpy is calculated), (2) velocity of the capsule water column above the test fuel rod, (3) axial growth of the fuel rod, (4) axial growth of the fuel column, (5) dynamic pressure inside of the fuel rod, and (6) dynamic pressure inside the test capsule.

Figure 1 shows posttest photographs of the four GEX fuel rods tested at peak fuel enthalpies of 137, 161, 214, and 282 cal/g of UO_2. These fuel rods had burnups ranging from 3100 to 4550 MWd/MTU. The rod tested to 137 cal/g of UO_2 peak fuel enthalpy did not fail. The rod tested at 161 cal/g of UO_2 failed by a longitudinal split just above the 3-in. mark indicated on Figure 1 (the complete severence of the fuel rod near the bottom occurred during handling). The rod tested at 214 cal/g of UO_2 peak fuel enthalpy failed by a longitudinal split between 2 and 3 inches on Figure 1. The rod tested at 282 cal/g UO_2 melted completely through at the 3.5-inch location on Figure 1. Thus, these four tests illustrated in Figure 1 indicate that the failure threshold is near 161 cal/g of UO_2 for these low burnups.

Figure 2 shows the posttest condition of the GEP fuel rod tested at 202 cal/g of UO_2 peak fuel enthalpy. The rod failed by a longitudinal tear in the cladding (between 4 and 5 inches on Figure 2). The GEP fuel rod tested at 163 cal/g of UO_2 peak fuel enthalpy did not fail.

Two intermediate burnup fuel rods (13.1 and 12.9 GWd/MTU) were exposed to peak fuel enthalpies of 158 and 170 cal/g, respectively in the CDC and the fuel rods did not fail. Figure 3 shows the posttest condition of the fuel rod tested at 170 cal/g of UO_2 peak fuel enthalpy.

Two higher burnup CDC test fuel rods failed with peak fuel enthalpies of 143 and 154 cal/g, respectively. One of the fuel rods (32.7 GWd/MTU) failed near the end of the transient at 143 cal/g peak fuel rod enthalpy. The failure was by one very small longitudinal split as shown in Figure 4. The other fuel rod (31.8 GWd/MTU) failed early in the transient after only 85 cal/g of UO_2 peak fuel enthalpy. This rod failed by three very large longitudinal cracks. Two of these longitudinal cracks (one on the side and one on the top) are shown in Figure 5 together with a closeup edge view of the crack on the side. The other large longitudinal crack on this rod is shown in Figure 6. These cracks appear to be caused by pellet-cladding mechanical interaction (PCMI). Not much fuel appears to have been washed out from the large cracks and the test rod remained in a coolable geometry. This 85 cal/g failure did not result from waterlogging. Waterlogged fuel rods fail by violent rupture leaving large ballooned cladding regions with torn cladding as shown in Figure 7[9]. Results of the CDC tests are summarized in Table 2.

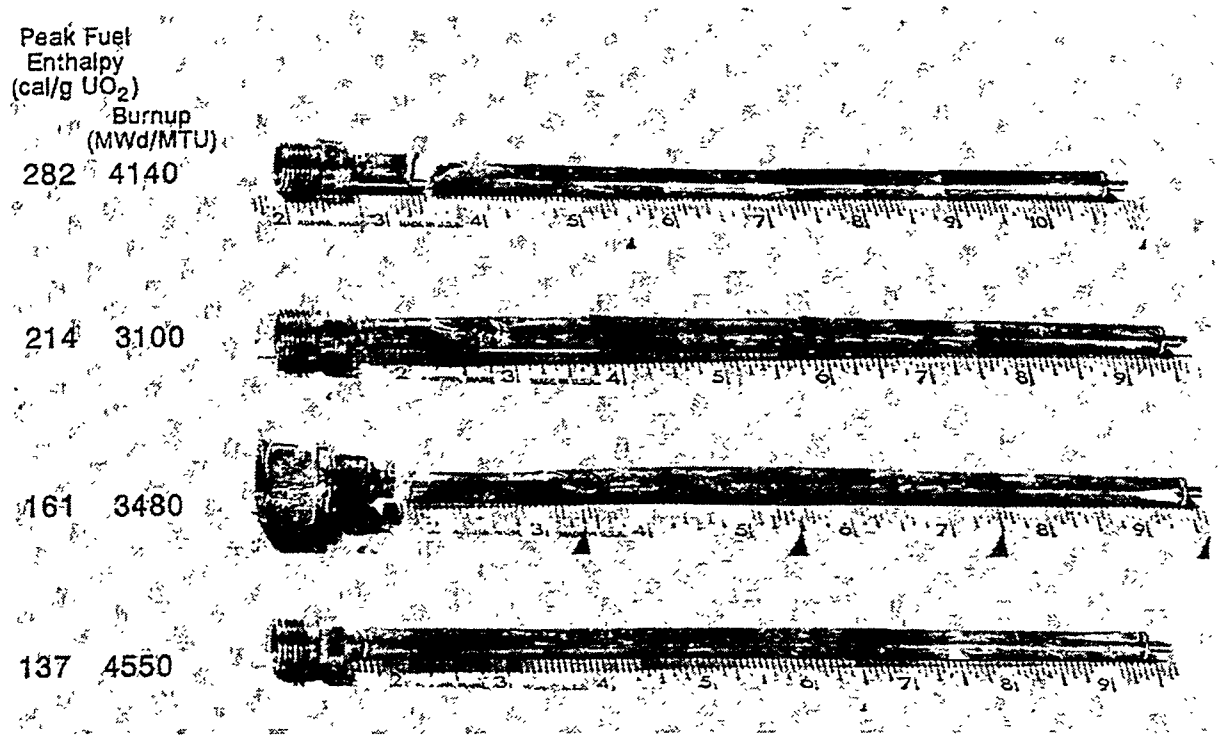

Figure 1. Posttest photograph of four GEX fuel rods tested in the Capsule Driver Core (CDC).

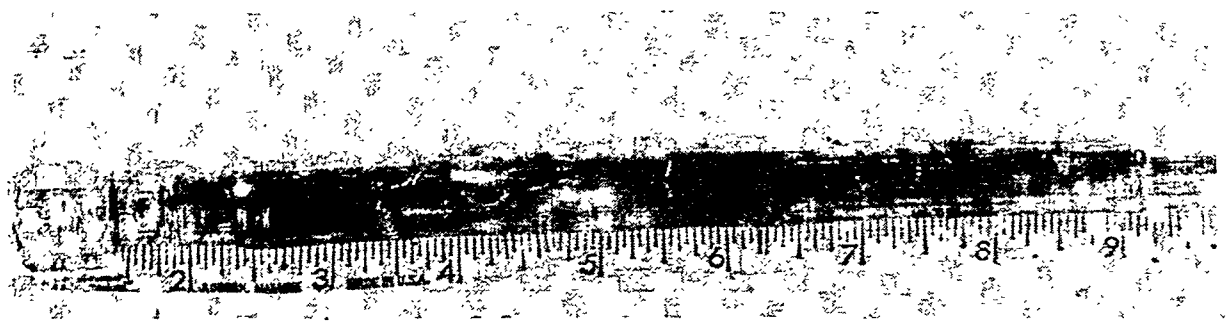

Figure 2. Posttest photograph of GEP fuel rod tested in CDC. Peak fuel enthalpy 202 (cal/g UO_2); burnup 990 (MWd/MTU).

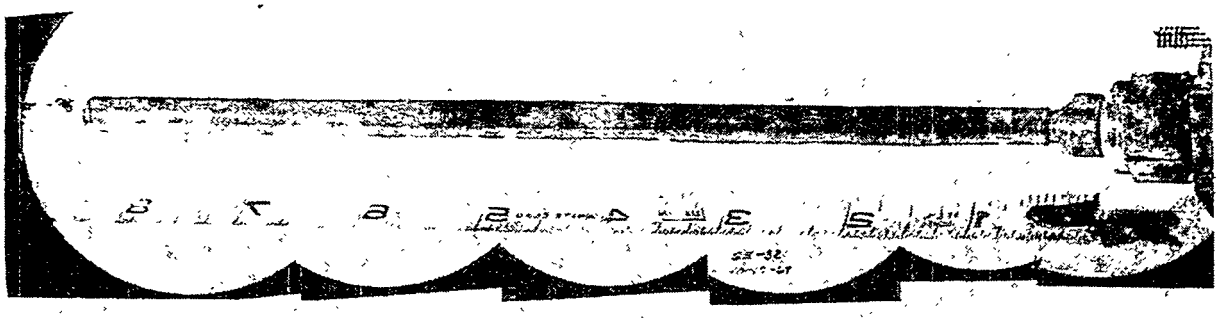

Figure 3. Posttest photograph of GEX fuel rod tested in CDC. Peak fuel enthalpy 170 (cal/g UO_2); burnup 12,900 (MWd/MTU).

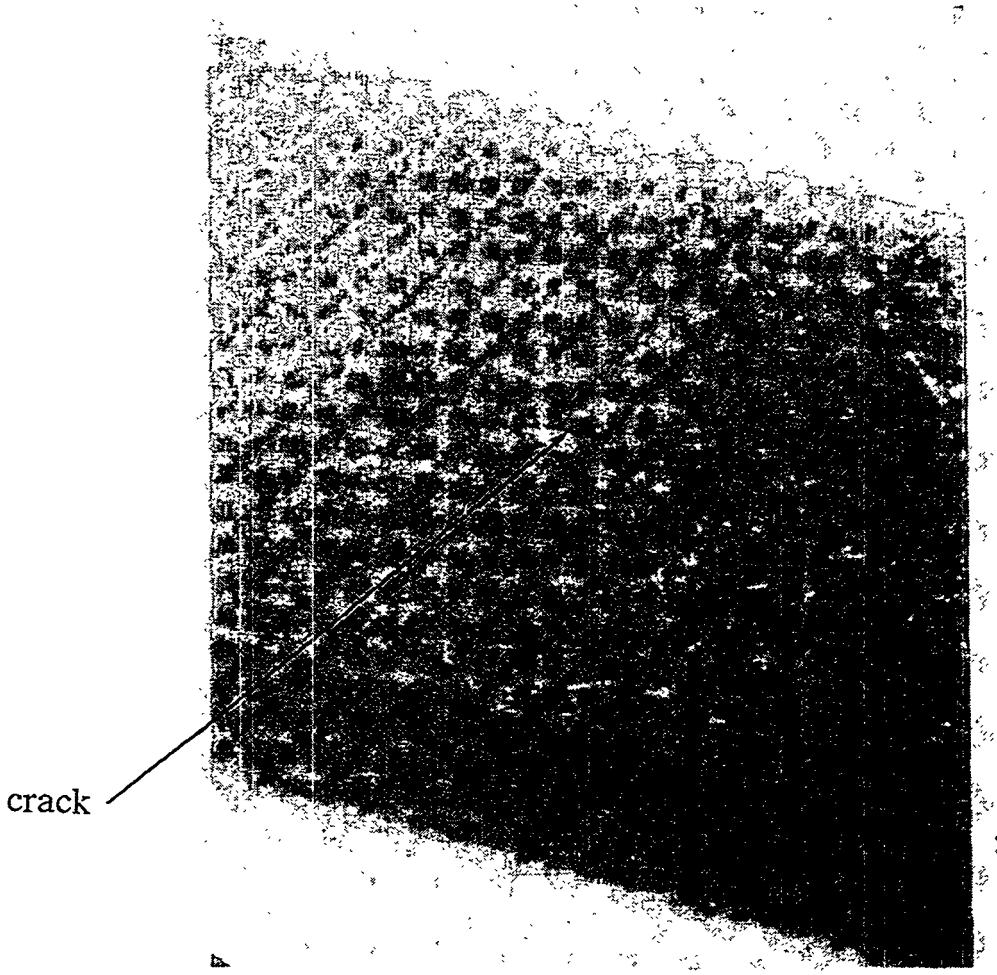

Figure 4. Posttest photograph of GEX fuel rod tested in CDC. Peak fuel enthalpy 143 (cal/g UO_2); burnup 32,700 (MWd/MTU).

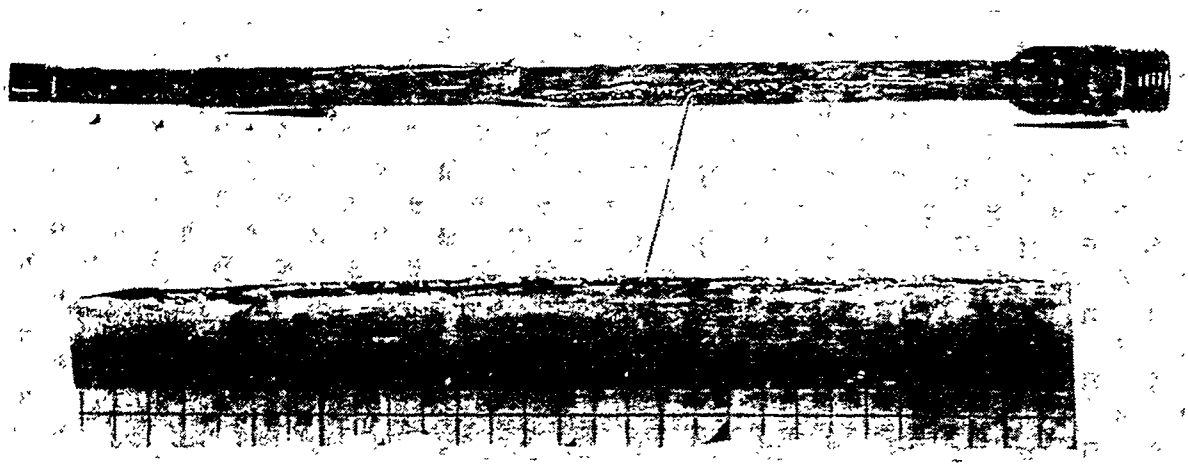

Figure 5. Posttest photograph of GEX fuel rod tested in CDC. Peak fuel enthalpy 154 (85)(cal/g UO_2); burnup 31,000 (MWd/MTU).

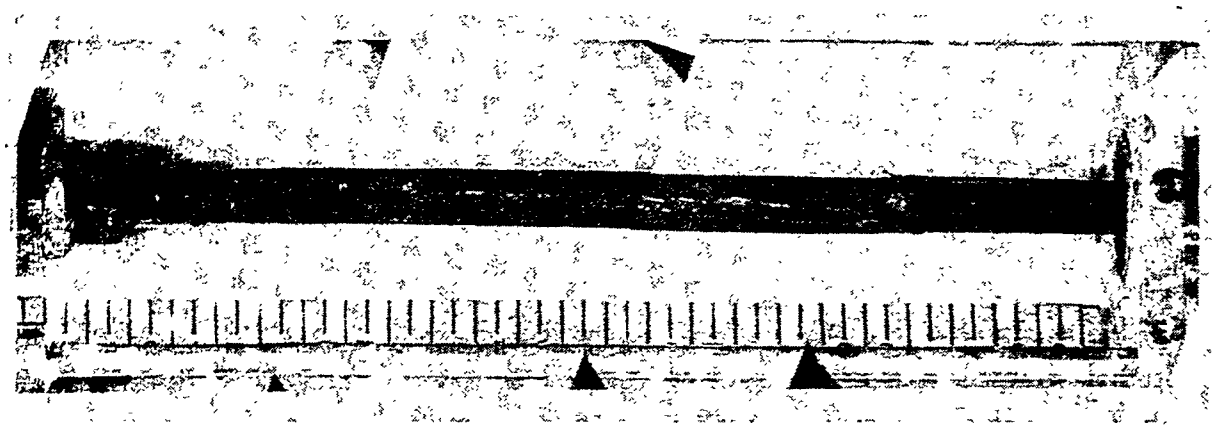

Figure 6. Close-up of longitudinal split of GEX fuel rod tested in CDC. Peak fuel enthalpy 154 (85) (cal/g UO_2); burnup 31,000 (MWd/MTU).

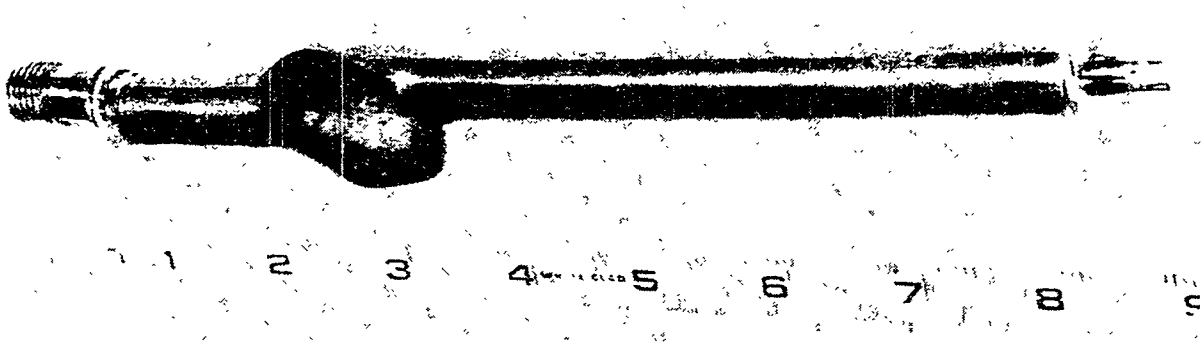

Figure 7. Typical waterlogged fuel rod failure.

Table 2. CDC test data.

Test rod condition	Radial average peak fuel enthalpy (cal/g)
Unirradiated:	
Failure threshold	SPXM Rods 205-225 GEP Pellet Rods 171-206 GEX Pellet Rods 189-217
Loss-of-coolable geometry	≈ 245
Prompt fuel dispersal	≈ 300
Irradiated:	
Failure threshold	85 to 200

PBF RESULTS

The PBF RIA Test Series was designed to address the following key safety issues: (1) Will there be a loss of coolable fuel rod geometry when LWR fuel is subjected to a radial average peak fuel enthalpy of 280 cal/g of UO_2? (2) Will energetic molten fuel-coolant interactions occur during a severe RIA and result in the production of a significant pressure pulse? (3) What is the mechanism and threshold enthalpy for failure of LWR fuel during an RIA? As part of the PBF RIA Program, four-single rod tests and two four-rod tests were performed. Each fuel rod was tested in an individual flow shroud. The initial conditions for the tests were a shroud inlet temperature of 538 K (509 F), a coolant pressure of 6.45 MPa (935 psi), a shroud coolant flow of 85 cm^3/s (5.19 $in.^3/s$), and zero rod power. Seven PBF RIA experiments are discussed in this paper. Test conditions and results for these seven PBF RIA tests are summarized in Table 3.

The four single rod tests were designated Scoping Tests, and the characteristics of the unirradiated test fuel rods used in the scoping tests are given in Table 4. The first four-rod test was designated the RIA 1-1 test, which used two irradiated Saxton Reactor type fuel rods and two unirradiated fuel rods. The characteristics of the RIA 1-1 test are listed in Table 5. The second four-rod test was designated the RIA 1-2 test which used four irradiated Saxton Reactor type fuel rods. Characteristics of the irradiated Saxton Reactor type fuel rods are listed in Table 6.

The PBF RIA Scoping Tests were performed to define the radially averaged peak fuel enthalpy failure threshold for unirradiated fuel rods at hot startup conditions (RIA-ST-1, RIA-ST-2, and RIA-ST-3) and to determine if destructive pressure pulses could result from large radially averaged peak fuel enthalpy (RIA-ST-4). The RIA-ST-1 test fuel rod was exposed to two power bursts, one that yielded a radial averaged peak fuel enthalpy of 185 cal/g of UO_2, during which the test rod did not fail; and the second power burst which yielded a radially averaged peak fuel enthalpy of 250 cal/g of UO_2, during which the test fuel rod did fail. The RIA-ST-2 fuel rod was exposed to 260 cal/g of UO_2 and it failed. The RIA-ST-3 fuel rod was exposed to 225 cal/g of UO_2 and it did not fail. Figure 8 shows the posttest condition of the RIA-ST-1,-2,and -3 fuel rods. As shown in Figure 8, the RIA-ST-1 fuel rod failed by large gaping longitudinal cracks and had extensive cladding oxidation, but retained its rod-like geometry. The RIA-ST-2 fuel rod, with only 10 cal/g of UO_2 larger than the RIA-ST-1 fuel rod, crumbled and lost its rod-like geometry in the central region. The remainder of the RIA-ST-2 test rod that maintained rod-like geometry appears much like the RIA-ST-1 fuel rod with extensive oxidation and large gaping longitudinal gaps. From this data the failure threshold for unirradiated LWR fuel at hot startup conditions is between 225 and 250 cal/g of UO_2 radially averaged peak fuel enthalpy. This may be compared with a failure threshold of between 205 and 225 cal/g of UO_2 for unirradiated CDC SPXM test fuel rods; a failure threshold of between 171 and 206 cal/g of UO_2 for unirradiated CDC GEP-Pellet type fuel rods; and a failure threshold of between 189 and 217 cal/g of UO_2 for unirradiated CDC GEX pellet type fuel rods.

Large cladding wall thickness variations (defined as thickening and thinning) were observed for both RIA-ST-1 and RIA-ST-2. The thickness variations probably occurred as a result of extensive plastic flow of the hot cladding driven by variations in the local coolant pressure associated with rapid heating of the coolant early in the transient, shortly after peak power. An example of cladding thickening and thinning is shown in Figure 9 for the RIA-ST-1 test fuel rod. Oxygen embrittlement occurs after the thickening and thinning has occurred as evidenced in Figure 10, which shows ZrO_2 on the outside layer of the cladding, and, in the thinned region, the internal and external oxygen-stabilized alpha zirconium meet with almost no beta zirconium apparent. However, in the thickened region a large fraction of the cladding thickness (about half) is beta zircaloy with massive alpha zircaloy incursions. The cladding always failed in the totally oxidized thin cladding regions, probably during fuel rod quench.

Table 3. Summary of conditions for unirradiated and irradiated fuel rods tested in PBF.

PBF test Number	Rod type	PBF reactor period (ms)	Power burst half width (ms)[a]	Avcrage burnup (MWd/MTU)	Total energy deposition (cal/g UO_2)	Radially averaged peak fuel enthalpy (cal/g UO_2)	Condition of rod F=failed NF=not failed
RIA-ST-1 Burst 1	PWR[b] #800-1	5.7	22	0	250	185	NF
RIA-ST-1 Burst 2	PWR[b] #800-1	4.4	17	0	330	250	F
RIA-ST-2	PWR[b] #800-2	4.6	17	0	345	260	F
RIA-ST-3	PWR[b] #800-3	5.2	20	0	300	225	NF
RIA-ST-4	PWR[c] #800-4	3.85	16	0	695	350	F
RIA 1-1	Saxton[d]	3.1	13		365	285	
four rod	#801-1			4,600			F
test	#801-2			4,650			F
	#801-3			0			F
	#801-5			0			F
RIA 1-2	Saxton[d]	4.3	16		240	185	
four rod	#802-1			5,220			NF
test	#802-2			5,110			NF
	#802-3			4,430			F
	#802-4			4,530			NF

[a]Width of power burst at half maximum power
[b]17x17 PWR
[c]15x15 PWR
[d]The Saxton reactor was a small, prototype, closed cycle, pressurized LWR designed by Westinghouse Electric Corporation for the USAEC.

Table 4. Nominal fuel rod design characteristics for test RIA-St.

Characteristic	Rods 800-1,2,3	Rod 800-4
Fuel		
Material	UO_2	UO_2
Pellet outside diameter (mm)	8.23	9.3
Pellet length (mm)	15.2	15.49
Pellet enrichment (wt%)	5.8	20
Density (% theoretical density)	94	93
Fuel stack length (m)	0.914	0.914
End configuration	Dished	Dished
Burnup	0	0
Cladding		
Material	Zircaloy-4	Zircaloy-4
Tube outside diameter (mm)	9.70	10.73
Inside diameter (mm)	8.42	9.50
Tube wall thickness (mm)	0.64	0.61
Fuel Rod		
Overall length (m)	1.0	1.0
Fill gas	Helium	Helium
Initial gas pressure (MPa)	0.19	3.79

Table 5. Test RIA 1-1 fuel rod design characteristics.

Characteristic	Irradiated Rods 800-1,-2[a]	Unirradiated Rods 801-3, -4, -5
Fuel		
Material	UO_2	UO_2
Pellet outside diameter (mm)	8.59	8.53
Pellet length (mm)	15.2	15.2
Pellet enrichment (wt%)	5.7	5.8
Density (% theoretical density)	94	94.5
Fuel stack length (m)	0.914	0.914
End configuration	Dished	Dished
Cladding		
Material	Zircaloy-4	Zircaloy-4
Tube outside diameter (mm)	9.99	9.93
Tube wall thickness (mm)	0.572	0.533
Yield strength (MPa)	570	570
Ultimate strength (MPa)	700	700
Fuel Rod		
Overall length (mm)	(801-1/-2/-3) 1.072	(801-4/801-5) 1.068
Fill Gas	77.7% Helium[b] 22.3% Argon	Helium
Initial gas pressure (MPa)	0.103	0.103
Gas plenum length (mm)	45.7	45.7
Insulator pellets	None	None

[a]Data are pre-irradiation values.
[b]Rod 801-1 was filled with a mixture of 77.7% helium and 22.3% argon and Rod 801-2 was unopened.

Table 6. Test RIA 1-2 fuel rod design characteristics.

Characteristic	Rods 802-1/-2/-3/-4[a]
Fuel	
Material	UO_2
Pellet outside diameter (mm)	8.59
Pellet length (mm)	15.2
Pellet enrichment (wt%)	5.7
Density (% theoretical density)	94
Fuel stack length (m)	0.914
End configuration	Dished
Cladding	
Material	Zircaloy-4
Tube outside diameter (mm)	9.99
Tube wall thickness (mm)	0.572
Yield strength (MPa)	570
Ultimate strength (MPa)	700
Fuel Rod	
Overall length (mm)	1.033
Gas plenum length (mm)	45.7
Initial gas pressure (MPa)	(802-1, 0.103) (802-2/-4, 2.41)[b]
Fill gas	77.7% Helium 22.3% Argon
Insulator pellets	None

[a]Data are pre-irradiation values of the fuel rods.
[b]Rod 802-3 was unopened.

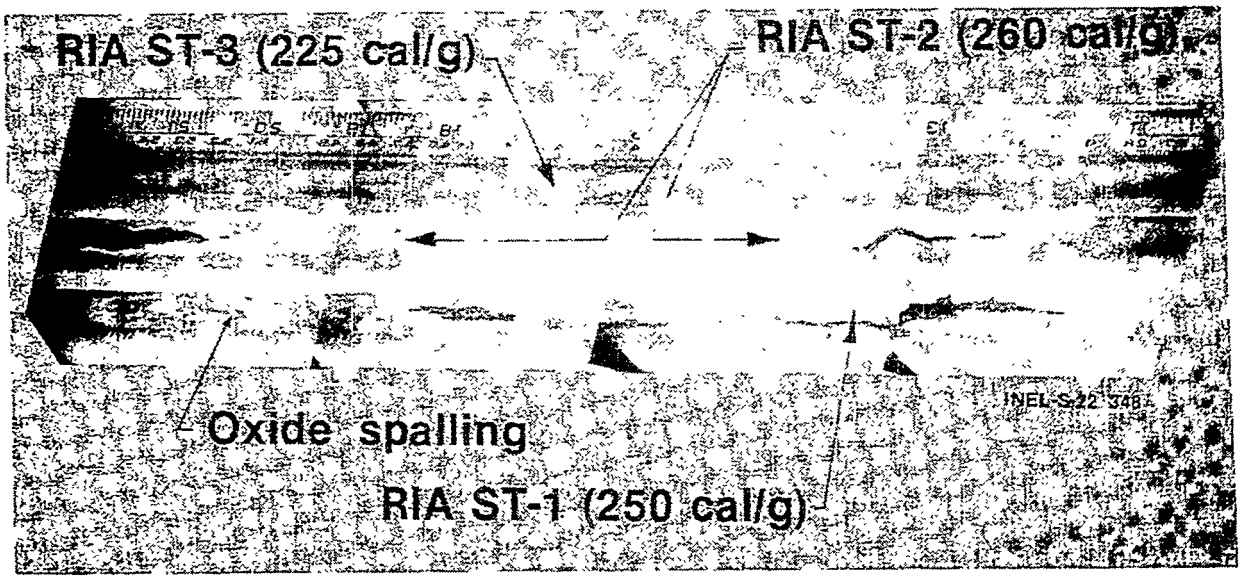

Figure 8. Posttest photograph of RIA Scoping Test 1, 2, and 3 fuel rods.

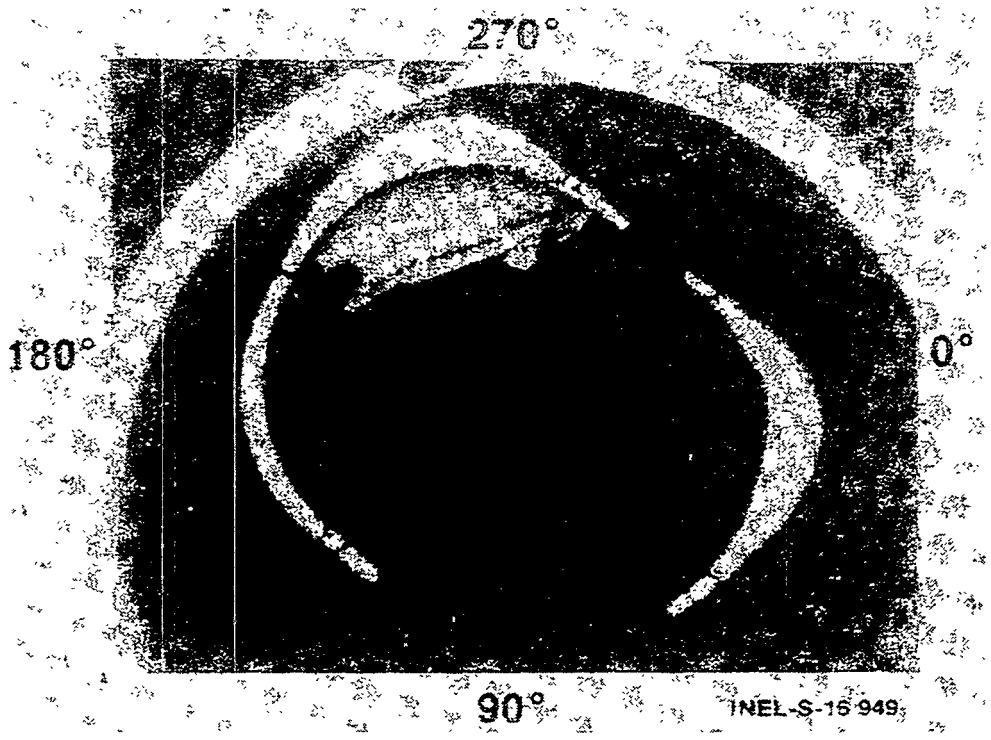

Figure 9. Posttest photograph of RIA ST-1 cladding at 0.35-m elevation.

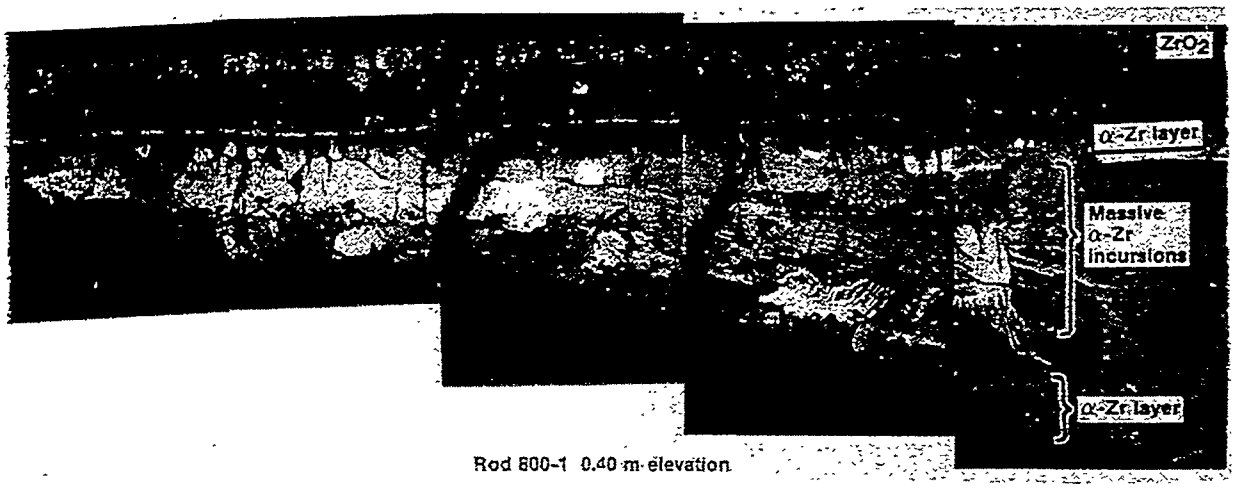

Figure 10. Posttest photograph of RIA scoping test cladding microstructures, Rod 800-1, 0.40 m elevation.

The RIA-ST-4 test did result in a molten fuel coolant interaction about 3 milliseconds after peak power when the peak fuel enthalpy was 350 cal/g of UO_2. At 3 milliseconds a large pressure pulse (34.6 MPa) was measured near the bottom of the experiment. The test rod was completely destroyed. Seventy-five percent of the test fuel rod was adhered to the inside of the flow shroud in a previously molten state. The remaining 25% was nearly spherical previously molten debris.

The objectives of the PBF RIA 1-1 and RIA 1-2 experiments were to (1) characterize the response of previously irradiated fuel rods during an RIA event at BWR hot-startup conditions, (2) evaluate the effect of internal rod pressure on preirradiated fuel rod response; and (3) provide data on the failure threshold peak fuel enthalpy for previously irradiated rods. The radially averaged peak fuel enthalpy for Test RIA 1-1 was 285 cal/g of UO_2 (near the 280 cal/g NRC limit), and the radially averaged peak fuel enthalpy for RIA 1-2 was 185 cal/g of UO_2 (near the suspected failure threshold).

For Test RIA 1-1, all four test rods failed early in the power burst. Complete flow channel blockage occurred for the two irradiated Saxton fuel rods, 801-1 and 801-2. Based on flow shroud inlet flow meters, the flow shroud for rod 801-1 blocked 4 to 5 seconds after power burst initiation. The flow shroud inlet flowmeter for rod 801-2 indicated shroud blockage 3 seconds after power burst initiation. Although flow reduction occurred for the two RIA 1-1 unirradiated test rods (801-3 and 801-5), complete flow blockage did not occur until after the test was completed. The flow channel blockage for RIA 1-1 is illustrated in Figure 11 which indicates "foaming" of the preirradiated fuel.

All four test rods used in the RIA 1-2 test were irradiated Saxton rods. Two of the test fuel rods (802-2 and 802-4) were instrumented, opened, and prepressurized to about 2.4 MPa to simulate end-of-life rod internal pressure. Rod 802-1 was opened, instrumented, and backfilled to an internal pressure of 0.105 MPa. Rod 802-3 was neither instrumented nor opened. Only one of

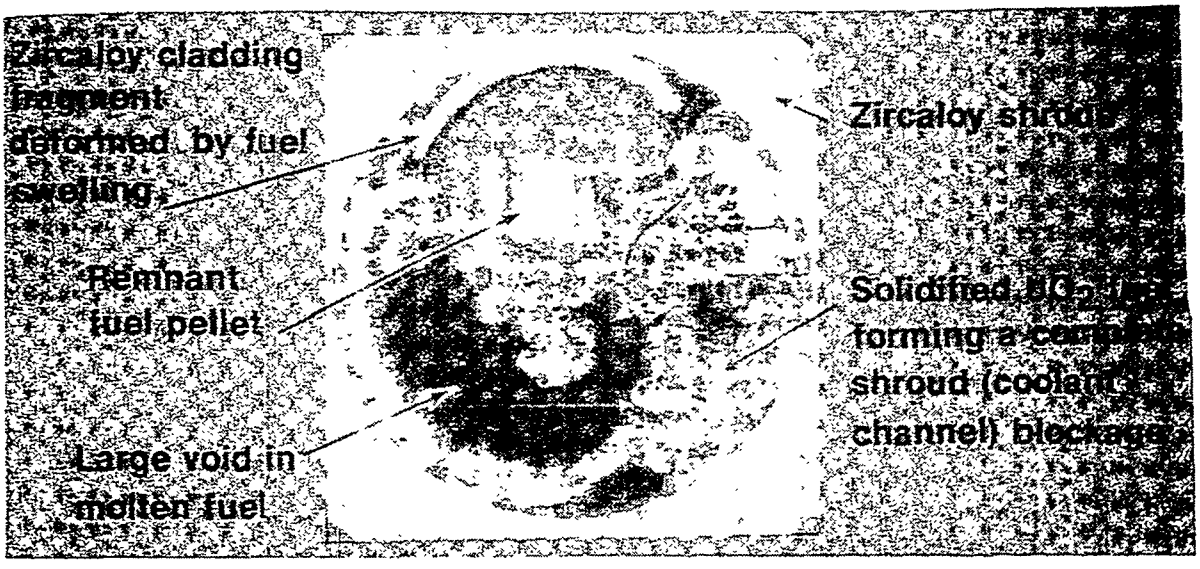

Figure 11. Posttest photomicrograph showing complete shroud blockage for Test RIA 1-1, Rod 801-1, irradiated fuel and cladding.

the four test fuel rods (802-3) failed as a result of the 185 cal/g of UO_2 radially averaged peak fuel enthalpy. The rod failed by 22 longitudinal cracks that appear to be caused by pellet-cladding mechanical interaction PCMI. The longitudinal cracks started at about 14.5 cm from the bottom of the rod and extended to 68.1 cm from the bottom of 91.4-cm-long rod. The radially averaged peak fuel enthalpy at the 14.5- and 68.1-cm locations was 140 cal/g of UO_2. Figure 12 shows three of the small longitudinal PCMI cracks. A close-up photomicrograph of the upper end of one of the through-wall cracks (taken in a region where the crack does not extend completely through the cladding) is shown in Figure 13. This photomicrograph confirms that the PCMI failures occurred early in the transient before significant oxidation occurred, because the oxidation layer inside the crack is the same depth as the oxidation on the outside surface of the cladding.

The failure thresholds for unirradiated and irradiated fuel rods determined from CDC and PBF tests are listed in Table 7. A plot of radially averaged peak fuel enthalpy versus burnup for CDC, PBF, NSRR, and CABRI test results is shown in Figure 14. The decrease of radially averaged peak fuel enthalpy required to cause fuel rod failure with increasing burnup is apparent in Figure 14.

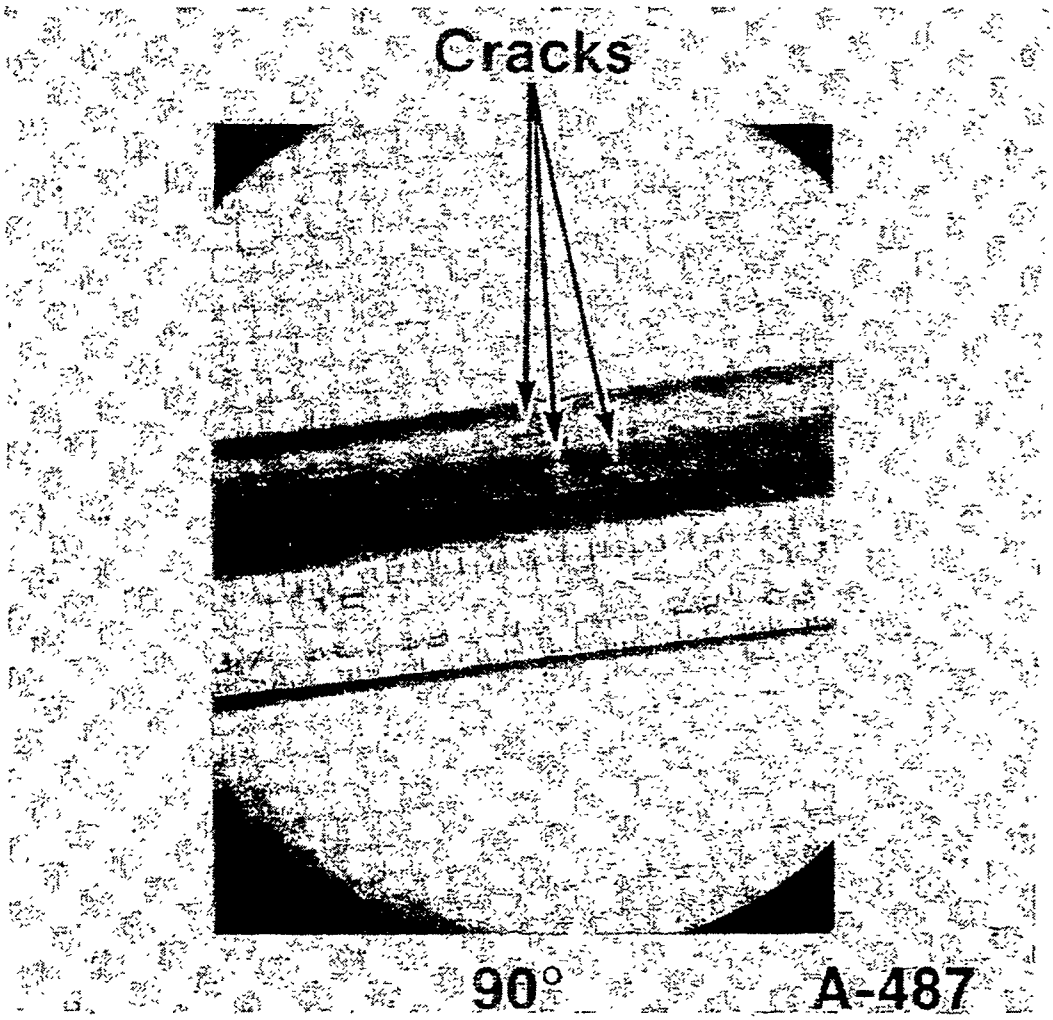

Figure 12. Pellet-clad mechanical interaction induced longitudinal cladding cracks. Test RIA 1-2, Rod 802-3.

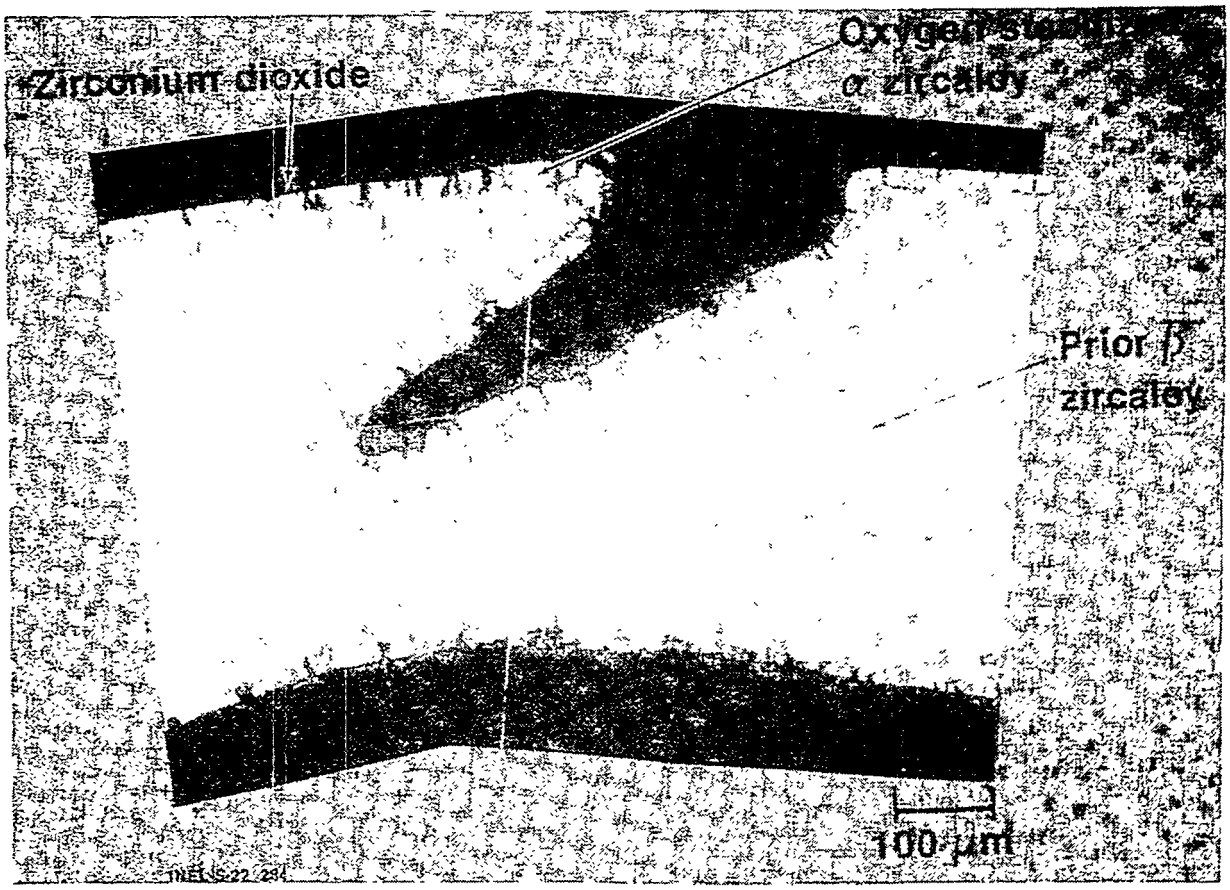

Figure 13. Close-up of upper end of through-wall crack (which is not completely through cladding) indicating that cracking occurred early in transient before significant oxidation. RIA 1-2 Rod 802-3, 0.3800-m elevation.

Table 7. Comparison of CDC and PBF test data.

	Radial/average-peak fuel enthalpy (cal/g)	
Test rod condition	CDC	PBF
Unirradiated:		
Failure threshold	SPXM Rods 205-225	225-250
	GEP Pellet Rods 171-206	
	GEX Pellet Rods 189-217	
Loss-of-Coolable Geometry	≈ 245	≈ 250
Prompt fuel dispersal	≈ 300	Less than 350
Irradiated:		
Failure threshold	85 to 200	140

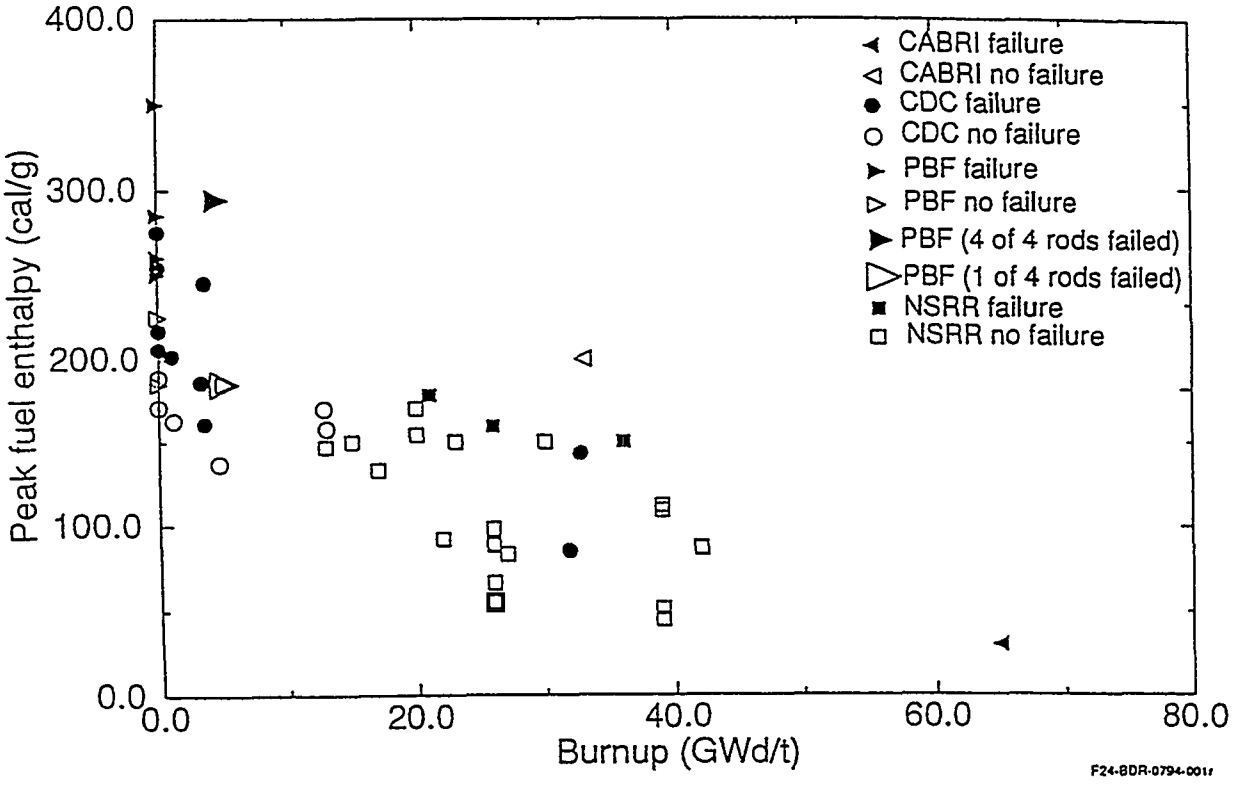

Figure 14. Radially averaged peak fuel enthalpy versus burnup for CDC, PBF, NSRR, and CABRI data.

CONCLUSIONS

The failure mechanism for unirradiated and irradiated fuel rods is different. Irradiated fuel rods fail during heatup, before the fuel rod departs from nucleate boiling, possibly because of mechanical interaction between the pellet and the cladding. The failure threshold for irradiated rods occurred at a radially averaged peak fuel enthalpy as low as 140 cal/g of UO_2 in PBF tests and 85 cal/g of UO_2 in CDC tests.

In PBF tests the failure mechanism for unirradiated rods occurred after the cladding plastically deformed (thinned and thickened), oxidized completely through the thinned regions, and quenched. This failure type occurred at 225 to 250 cal/g of UO_2.

The probability of fuel rod failure at lower radially averaged peak fuel enthalpy appears to increase with increasing burnup, but there is considerable scatter in the data. Further evaluation of test data will be performed before a new technical basis for the NRC fuel damage criteria for reactivity transients can be established.

FUTURE EFFORTS

Future efforts on the reassessment of the basis for NRC fuel damage criteria for reactivity transients will include (a) analyzing data from France, Japan, and Russia (IGR Test Reactor in Kazakhstan)[10]; (b) estimating the reasonableness of the data scatter for brittle fracture of the cladding; (c) inserting the new burnup dependent models developed by PNL[11] into the FRAPCON 2 and MATPRO computer codes; (d) performing parametric studies with the FRAP-T6 code; (e) analyzing the data with the updated FRAP-T6 (high-burnup models added) code to understand the PCMI failure mechanism during reactivity transients with high burnup rods; (f) determining the compatibility of the data and analysis from the different reactors; and (g) preparing a report summarizing the results of the work and providing the technical basis for possible revision of the NRC failure criteria.

REFERENCES

1. R. W. Miller, *The Effects of Burnup on fuel Failure: I. Power Burst Tests on Low Burnup UO_2 Fuel Rods*, IN-ITR-113, July 1970.

2. R. W. Miller, *The Effects of Burnup on Fuel Failure: II. Power Burst Tests on Fuel Rods with 13,000 and 32,000 MWd/MTU Burnup*, IN-ITR-118, April 1971.

3. P. E. MacDonald et al., "Assessment of Light-Water-Reactor Fuel Damage During a Reactivity-Initiated Accident", *Nuclear Safety* , Volume 21, No. 5, September-October 1980.

4. "Assumptions Used for Evaluating a Control Rod Ejection Accident for Pressurized Water Reactors", NRC Regulatory Guide 1.77, May 1974.

5. "Fuel System Design, Section 4.2," in *Standard Review Plan for the Review of Safety Analysis Reports for Nuclear Power Plants*, NUREG-0800, July 1981.

6. R. S. Semken et al., *Reactivity Initiated Accident Test Series, RIA Scoping Tests, Fuel Behavior Report*, NUREG/CR-1360, EGG 2024, April 1980.

7. T. Fujishiro and K Ishijima, "NSRR Experiments to Study the Effects of Burnup on the Fuel Behavior Under Reactivity Initiated Accident Conditions," *Proceedings of the Twenty-Second Water Reactor Safety Information Meeting, Bethesda, Maryland, October 24-26, 1994*, NUREG/CP-0140.

8. F. Schmitz et al., "Investigation of the Behavior of High-Burnup PWR Fuel under RIA Conditions in the CABRI Test Reactor," *Proceedings of the Twenty-Second Water Reactor Safety Information Meeting, Bethesda, Maryland, October 24-26, 1994*, NUREG/CP-0140.

9. L. A. Stephan, *The Effects of Cladding Material and Heat Treatment on the Response of Waterlogged UO_2 Fuel Rods to Power Bursts*, IN-ITR-111, January 1970.

10. V. Asmolov and L. Yegorova, "Russian Approach to Experimental Studies of Burnup Effect under RIA Conditions,"*Proceedings of the Twenty-Second Water Reactor Safety Information Meeting, Bethesda, Maryland, October 24-26, 1994*, NUREG/CP-0140.

11. C. E. Beyer, D. D. Lanning, and M. E. Cunningham, "The Rim Effect and Other High Burnup Modeling for NRC Fuel Performance Codes," *Proceedings of the Twenty-Second Water Reactor Safety Information Meeting, Bethesda, Maryland, October 24-26, 1994*, NUREG/CP-0140.

NRC FORM 335 (2-89) NRCM 1102, 3201, 3202

U.S. NUCLEAR REGULATORY COMMISSION

BIBLIOGRAPHIC DATA SHEET

(See instructions on the reverse)

1. REPORT NUMBER (Assigned by NRC. Add Vol., Supp., Rev., and Addendum Numbers, if any.)
NUREG/CP-0140
Vol. 2

2. TITLE AND SUBTITLE
Proceedings of the Twenty-Second Water Reactor Safety Information Meeting
Severe Accident Research, Thermal Hydraulic Research for Advanced Passive LWRs, High-Burnup Fuel Behavior

3. DATE REPORT PUBLISHED
MONTH: April
YEAR: 1995

4. FIN OR GRANT NUMBER
A3988

5. AUTHOR(S)
Compiled by Susan Monteleone, BNL

6. TYPE OF REPORT
Conference Proceedings

7. PERIOD COVERED *(Inclusive Dates)*
October 24-26, 1994

8. PERFORMING ORGANIZATION – NAME AND ADDRESS *(If NRC, provide Division, Office or Region, U.S. Nuclear Regulatory Commission, and mailing address; if contractor, provide name and mailing address.)*
Office of Nuclear Regulatory Research
U. S. Nuclear Regulatory Commission
Washington, DC 20555-0001

9. SPONSORING ORGANIZATION – NAME AND ADDRESS *(If NRC, type "Same as above"; if contractor, provide NRC Division, Office or Region, U.S. Nuclear Regulatory Commission, and mailing address.)*
Same as Item 8 above

10. SUPPLEMENTARY NOTES
Proceedings prepared by Brookhaven National Laboratory

11. ABSTRACT *(200 words or less)*

This three-volume report contains papers presented at the Twenty-Second Water Reactor Safety Information Meeting held at the Bethesda Marriott Hotel, Bethesda, Maryland, during the week of October 24-26, 1994. The papers are printed in the order of their presentation in each session and describe progress and results of programs in nuclear safety research conducted in this country and abroad. Foreign participation in the meeting included papers presented by researchers from Finland, France, Italy, Japan, Russia and United Kingdom. The titles of the papers and the names of the authors have been updated and may differ from those that appeared in the final program of the meeting.

12. KEY WORDS/DESCRIPTORS *(List words or phrases that will assist researchers in locating the report.)*
BWR type reactors-reactor safety, international organizations-meetings, PWR type reactors-reactor safety, water cooled reactors-proceedings, Human Factors, Leading Abstract, Reactor Control Systems, Reactor Instrumentation, Probabilistic Estimation, Risk Assessment

13. AVAILABILITY STATEMENT
Unlimited

14. SECURITY CLASSIFICATION
(This Page)
Unclassified
(This Report)
Unclassified

15. NUMBER OF PAGES

16. PRICE